



저작자표시-비영리-변경금지 2.0 대한민국

이용자는 아래의 조건을 따르는 경우에 한하여 자유롭게

- 이 저작물을 복제, 배포, 전송, 전시, 공연 및 방송할 수 있습니다.

다음과 같은 조건을 따라야 합니다:



저작자표시. 귀하는 원저작자를 표시하여야 합니다.



비영리. 귀하는 이 저작물을 영리 목적으로 이용할 수 없습니다.



변경금지. 귀하는 이 저작물을 개작, 변형 또는 가공할 수 없습니다.

- 귀하는, 이 저작물의 재이용이나 배포의 경우, 이 저작물에 적용된 이용허락조건을 명확하게 나타내어야 합니다.
- 저작권자로부터 별도의 허가를 받으면 이러한 조건들은 적용되지 않습니다.

저작권법에 따른 이용자의 권리는 위의 내용에 의하여 영향을 받지 않습니다.

이것은 [이용허락규약\(Legal Code\)](#)을 이해하기 쉽게 요약한 것입니다.

[Disclaimer](#)

Doctor of Philosophy

**Mechanical Exfoliation of 2D-Materials and
Formation of Nanocomposites with Transition
Metal Compounds by Vacuum Kinetic Spray
Process for Energy Conversion and Sensing
Applications**

The Graduate School of
the University of Ulsan

School of Mechanical Engineering

Ahmed Galal Abdelrehim Rashwan

**Mechanical Exfoliation of 2D-Materials and
Formation of Nanocomposites with Transition
Metal Compounds by Vacuum Kinetic Spray
Process for Energy Conversion and Sensing
Applications**

Supervisor: Professor Doo-Man Chun

A Dissertation

Submitted to the Graduate School of the University of Ulsan in Partial
Fulfillment of the Requirements for the Degree of
Doctor of Philosophy

by

Ahmed Galal Abdelrehim Rashwan

School of Mechanical Engineering

University of Ulsan, South Korea

August 2021

**Mechanical Exfoliation of 2D-Materials and
Formation of Nanocomposites with transition
Metal Compounds by Vacuum Kinetic Spray
Process for Energy Conversion and Sensing
Applications**

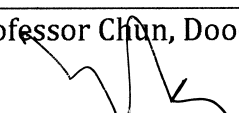
This certifies that the thesis of **Ahmed Galal Abdelrehim Rashwan** is
approved



Committee Chair: Professor Chung, Koo-Hyun



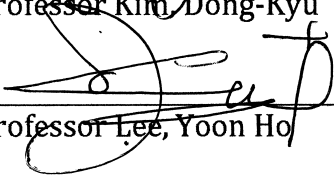
Committee Member: Professor Chun, Doo-Man



Committee Member: Professor Kim, Chung-Soo



Committee Member: Professor Kim, Dong-Kyu



Committee Member: Professor Lee, Yoon Ho

School of Mechanical Engineering

University of Ulsan, South Korea

August 2021

Ahmed Galal Abdelrehim Rashwan 의 공학박사 학위

논문을 인준함

심사위원장

정구현



심사위원

천두만



심사위원

김충수



심사위원

김동규



심사위원

이윤호



울산대학교 대학원

2021년 08월

Acknowledgments

I would like to express my deep and sincere gratitude to many people who made this Ph.D. thesis possible. Special thanks are due to my supervisor **Professor Doo-Man Chun** for his insight in resolving many problems encountered throughout research and thesis writing, for his inspiring and encouraging way to guide me to a deeper understanding of research, and for his invaluable comments during my graduate study.

I would thank all my friends in the Hybrid Manufacturing Technology (HMT) laboratory for their valuable assistance all over my study period.

I would like to thank my thesis defense committee members Professors Koo-Hyun Chung, Chung-Soo Kim, Dong-Kyu Kim, and Yoon Ho Lee for their valuable comments that helped me to further improve my dissertation.

Dedication

I dedicate this work to:

- ✓ *My beloved mother and father for their endless love, encouragement, support, and sacrifices.*
- ✓ *My dear wife (Manar Abd-Elrahman) for her continuous helping and support.*
- ✓ *My two lovely daughters (Mennatallah and Mariam).*
- ✓ *My **brother and sister** for their love and encouragement.*

Ahmed Galal Abdelrahim

Abstract

The wide spreading of using two dimensional (2D) materials (i.e., graphene, MoS₂, and Boron nitride) and their hybrid nanocomposites (NCs) with functional semiconductor compounds in electrochemical applications related to energy conversion, energy storage, and non-enzymatic sensing applications require a cost-effective technique that is amenable to large size production. This goal cannot be simply achieved because there is no single system for the fabrication of 2D materials and their hybrid NCs in one process. The top-down approaches based on the mechanical exfoliation of layered materials are commonly used for the mass production of pure 2D materials. The conventional methods for layered materials exfoliations through the mechanical approach are ball milling (wet or dry) and sonochemical techniques. In these techniques, the pure 2D materials were prepared in successive steps for a very long time. Also, these techniques require solvents with suitable surface energy that match with the type of the layered material to facilitate the stacked layers' exfoliation. The use of chemicals and solvents require further cleaning from waste product and the product only in the powder form. This requires hard labor work and increases the fabrication cost. Furthermore, the fabrication of 2D-materials hybrid NCs with a functional nanosized semiconductor cannot be achieved in one process, in which the pure 2D materials and the nanosized semiconductor materials are prepared individually. Then, both materials were mixed by chemical approach to form interfacial bonding between them. This would further increase the fabrication time consumption and reduce the overall cost efficiency.

The dry spray coating based on the vacuum kinetic spray process was utilized for the direct deposition of nanosized thin films in one step from the corresponding micron powder at room temperature without any chemical treatment. There is various low-temperature dry manufacturing process such as cold spray, aerosol deposition (AD), as well as the nanoparticle deposition system (NPDS). The main difference between these techniques is the optimized pressure range for micron powder feeding as well as deposition pressure. The cold spray and AD techniques have similar system configurations of particle deposition but have some limitations on particle size range and type, which strongly affect the ability of deposition. As an example, the cold spray technique is mostly used for the deposition of metallic powder whereas the AD technique is frequently used for ceramic films. This indicated the limitation of deposition of metal/ceramics composites by these techniques. In contrast, the NPDS system has the optimum pressure range for deposition of either nano-sized ceramics or metallic as well as their hybrid NCs thin films at room temperature in one step. Furthermore, the graphene thin films were successfully deposited by the

NPDS in one step on various substrate types. The kinetic induced transformation of graphite-staked layers to graphene nanosheets in one step by the NPDS at room temperature was explained in terms of the mechanical exfoliation of graphite stacked layers at impact velocity higher than a critical value. This would provide a new route for layered materials mechanical exfoliation based on the vacuum kinetic spray process that differs from the conventional technique that follows either sonochemical or ball milling approaches

The ability of graphite stacked layers separation by the NPDS in one step motivated us to examine the ability of mechanical exfoliation of other graphene-like materials (i.e., layered materials) with a similar hexagonal structure such as molybdenum disulfide (MoS_2) and boron nitride (BN) by the NPDS without the need of any chemical assistance. Hence, we could use the NPDS as a single system for the mechanical exfoliation for various layered materials. Moreover, the NPDS was used to fabricate graphene-based hybrid NCs with various functional nanosized semiconductors. So, we investigated the ability of hybrid NCs formation with another graphene-like material especially MoS_2 to demonstrate the benefit of using the NPDS system as a single system for layered materials exfoliation and formation of hybrid NCs with other functional materials, which reduce the fabrication time and consequently enhance the fabrication cost efficiency.

To improve the charge transfer kinetics at the electrode/electrolyte interface in the electrochemical energy applications the 2D-nanomaterials (NMs) like graphene and MoS_2 nanosheets are commonly used. The hybridization between the 2D-NMs and the other functional nano-sized semiconductor would result in the improvement of overall activity toward various electrochemical applications. Optimization of modified electrode performance is strongly dependent on the composition constituent at the heterostructure interfaces. This indicates the need to study the effect of the composition ratio between the 2D NMs and the other functional materials on the electrochemical performance of the fabricated electrodes.

The main objectives of this study are classified into three main parts:

First, we want to provide a new mechanical approach for pure layered materials exfoliation using the NPDS according to the vacuum kinetic spray process. This was achieved by studying the mechanical exfoliation of various layered materials with a similar hexagonal phase such as graphite, MoS_2 , and BN

using the same deposition condition by the NPDS. This indicated the applicability of NPDS as a single and solvent-free system for layered materials exfoliation.

Second, we fabricated various graphene-based hybrid NCs with various transition metals (TMs) compounds (i.e., $\text{Ni}(\text{OH})_2$, Co_3O_4 , Mn_3O_4 , and ZnO) by the NPDS at room temperature in a one-step process on various substrate type (i.e., porous nickel foam and flat titanium sheet). All fabricated electrodes revealed the successful exfoliation of graphite stacked layers to graphene nanosheets in one step as well as the strong synergy improvement between the formed graphene nanosheets and the TMs species. The observed synergy improvement resulted in the activity enhancement toward water splitting-based energy conversion and non-enzymatic H_2O_2 detection applications. The catalytic activity of TMs-graphene hybrid NCs towards the water splitting through various routes including electrocatalytic, photocatalytic, and photo-electrocatalytic as well as non-enzymatic H_2O_2 sensing was found to be strongly dependent on the initial ratio of TMs: graphite mixture, in which the optimum combination was estimated for each application.

Third, we fabricated various MoS_2 -based hybrid NCs with spinel transition metals (TMs) compounds (i.e., Co_3O_4 and Mn_3O_4) by the NPDS at room temperature in a one-step process on various substrate type (i.e., porous nickel foam and flat titanium sheet). All fabricated electrodes revealed the successful exfoliation of MoS_2 stacked layers to small MoS_2 nanosheets and strong synergy improvement between the formed MoS_2 nanosheets and the spinel TMs species. The observed synergy improvement resulted in the activity enhancement toward water splitting-based energy conversion and non-enzymatic H_2O_2 sensing applications. The catalytic activity of TMs- MoS_2 hybrid NCs towards the electrocatalytic water splitting and non-enzymatic H_2O_2 sensing was found to be strongly dependent on the initial ratio of TMs: MoS_2 mixture, in which the optimum combination was estimated for each application.

The obtained results indicated that the NPDS technique is an efficient and eco-friendly technique for layered materials exfoliation and fabrication of hybrid NCs with high efficiency in various energy and sensing applications in one deposition step at room temperature in a short fabrication time. This indicated the improvement of fabrication cost efficiency compared with other conventional processes.

Contents

Abstract.....	I
Contents.....	IV
List of Figures:	IX
List of Tables:	XXII
List of Abbreviations.....	XXV
<i>Chapter 1: Introduction.....</i>	<i>27</i>
1. 1. 2D NMs properties	28
1. 2. 2D NMs synthetic approaches	29
1. 2. 1. The bottom-up synthetic approach of 2D NMs	29
1. 2. 2. The top-down synthetic approach of 2D NMs	29
1. 3. Formation of TMs-based hybrid NCs with 2D NMs	37
1. 4. Vacuum kinetic spray process for NMs deposition	38
1. 5. Research goals and objectives	40
1. 6. Thesis Organization.....	41
<i>Chapter 2: Experimental Conditions</i>	<i>45</i>
2. 1. Materials	46
2. 1. 1. Layered materials	46
2. 1. 2. Transition metals compounds	46
2. 1. 3. Substrate	46
2. 1. 4. Electrolytes and solvents	46
2. 2. Fabrication of nano-sized thin films by the NPDS	47
2. 3. Surface Characterization techniques	50
2. 4. Electrochemical measurements.....	51

2. 4. 1.	Electrocatalytic water splitting	51
2. 4. 2.	PEC water splitting	52
2. 4. 3.	H ₂ O ₂ sensing	53
<i>Chapter 3:</i>		54
<i>One-Step Mechanical Exfoliation and Deposition of Nanosheets of Layered Materials by a Room Temperature Vacuum Kinetic Spray Process</i>		54
3. 1.	Overview	55
3. 2.	Mechanism of 2D materials exfoliation and deposition	56
3. 3.	Results and discussion	58
3. 3. 1.	X-ray diffraction	58
3. 3. 2.	Morphological analysis of the layered materials powder and deposited thin films	63
3. 3. 3.	Raman studies	64
3. 4.	Summary	69
<i>Chapter 4:</i>		71
<i>Composition Dependent Electrocatalytic Activity of Ni(OH)₂-Graphene Hybrid Catalyst Deposited by One-Step Vacuum Kinetic Spray Technique</i>		71
4. 1.	Overview	72
4. 2.	Results and discussion	74
4. 2. 1.	Structural analysis of the Ni(OH) ₂ -graphene composites	74
4. 2. 2.	Raman spectra of the Ni(OH) ₂ -graphene composites	76
4. 2. 3.	Surface analysis of the Ni(OH) ₂ -graphene composite/Ni foam thin films	79
4. 2. 4.	Morphological and elemental analysis of the Ni(OH) ₂ -graphene composites	83
4. 2. 5.	Electrochemical characterization	88
4. 3.	Summary	98
<i>Chapter 5:</i>		99

<i>Fabrication of Efficient Nanostructured Co₃O₄-Graphene Bifunctional Catalysts: Oxygen Evolution, Hydrogen Evolution, and H₂O₂ Sensing</i>	99
5.1. Overview	100
5.2. Results and discussion	103
5.2.1. XRD analysis of Co ₃ O ₄ -graphene composites	103
5.2.2. Raman studies on Co ₃ O ₄ -graphene composites.....	106
5.2.3. Surface Morphology and composition analysis of Co ₃ O ₄ -graphene composites	111
5.2.4. XPS analysis of the Co ₃ O ₄ -graphene composites thin films	120
5.2.5. Electrochemical active surface area.....	127
5.2.6. Oxygen evolution reaction activity of Co ₃ O ₄ -graphene hybrid catalysts.....	128
5.2.7. Hydrogen evolution activity of Co ₃ O ₄ -graphene hybrid catalysts.....	131
5.2.8. H ₂ O ₂ electrochemical sensing by Co ₃ O ₄ -graphene hybrid catalysts	132
5.3. Summary	136
<i>Chapter 6:</i>	138
<i>Facile One-Step Deposition of ZnO-Graphene Nanosheets Hybrid Photoanodes for Enhanced Photoelectrochemical Water Splitting</i>	138
6.1. Overview	139
6.2. Results and discussion.....	142
6.2.1. X-ray diffraction analysis of ZnO-graphene composites	142
6.2.2. Surface morphology of ZnO-graphene composites	143
6.2.3. FTIR and Raman studies on ZnO-graphene composites.....	150
6.2.4. Surface bonding characterization of ZnO-graphene NCs	155
6.2.5. The optical band gap of ZnO-graphene nanosheets photoanodes	162
6.2.6. Photoluminescence studies on ZnO-graphene nanosheets hybrid photoanodes.....	164
6.2.7. Photoelectrochemical water splitting measurements	165

6.3.	Summary.....	170
<i>Chapter 7:</i>		<i>172</i>
<i>Room-Temperature Deposition of ZnO-Graphene Nanocomposite Hybrid Photocatalysts for Improved Visible-Light-Driven Degradation of Methylene Blue.....</i>		<i>172</i>
7.1.	Overview	173
7.2.	Results and Discussion	176
7.2.1.	XRD patterns of ZnO-graphene NCs hybrid photocatalysts	176
7.2.2.	Raman studies on ZnO-graphene NCs	177
7.2.3.	Surface morphology of ZnO-graphene nanocomposites photocatalysts.....	180
7.2.4.	Investigation of the surface bonding states on ZnO-graphene NCs/NF hybrid photocatalysts.....	187
7.2.5.	The optical band gap of ZnO-graphene NCs/NF hybrid photocatalysts.....	191
7.2.6.	Photocatalytic activity of ZnO-graphene nanocomposite photocatalysts	193
7.3.	Summary	197
<i>Chapter 8:</i>		<i>199</i>
<i>Nanosized Co₃O₄-MoS₂ Heterostructure Electrodes for Improving the Oxygen Evolution Reaction in an Alkaline Medium.....</i>		<i>199</i>
8.1.	Overview	200
8.2.	Results and discussion	202
8.2.1.	XRD patterns of Co ₃ O ₄ -MoS ₂ composites	202
8.2.2.	Raman spectra of Co ₃ O ₄ -MoS ₂ composites.....	204
8.2.3.	Morphology investigation of Co ₃ O ₄ -MoS ₂ composites	208
8.2.4.	Surface bonding states of Co ₃ O ₄ -MoS ₂ hybrid electrocatalysts	219
8.2.5.	Electrochemical active surface area	224
8.2.6.	Electrocatalytic activity of Co ₃ O ₄ -MoS ₂ heterogeneous electrodes	225

8.3. Summary	228
<i>Chapter 9:</i>	<i>229</i>
<i>Facile One-step Deposition of Co₃O₄-MoS₂ Nanocomposites using a Vacuum Kinetic Spray Process for Non-Enzymatic H₂O₂ Sensing</i>	<i>229</i>
9.1. Overview	230
9.2. Results and Discussion	231
9.2.1. XRD analysis of Co ₃ O ₄ -MoS ₂ composites.....	231
9.2.2. Surface morphology of Co ₃ O ₄ -MoS ₂ composites.....	233
9.2.3. Raman studies on Co ₃ O ₄ -MoS ₂ heterostructure composites	243
9.2.4. XPS studies on Co ₃ O ₄ -MoS ₂ nanostructure composites	248
9.2.5. Electrocatalytic active surface area evaluation.....	254
9.2.6. Electrocatalytic activity of Co ₃ O ₄ -MoS ₂ NCs toward H ₂ O ₂ oxidation.....	255
9.3. Summary	262
<i>Chapter 10:.....</i>	<i>264</i>
<i>Heterostructured Mn₃O₄-2D Materials Nanosheets: One-Step Vacuum Kinetic Spray Deposition and Non-Enzymatic H₂O₂ Sensing</i>	<i>264</i>
10.1. Overview	265
10.2. Results and Discussion	267
10.2.1. XRD analysis of Mn ₃ O ₄ -2D-layered materials composites	267
10.2.2. Investigation of the surface structural phase of Mn ₃ O ₄ -2D materials hybrid composites 270	
10.2.3. Surface morphology of Mn ₃ O ₄ -2D materials composites.....	274
10.2.4. XPS studies on Mn ₃ O ₄ -2D materials composites	279
10.2.5. Electrocatalytic activity of Mn ₃ O ₄ -2D materials toward H ₂ O ₂ reduction	286
10.3. Summary.....	290

<i>Chapter 11: Conclusions</i>	292
<i>References</i>	297

List of Figures:

Figure 1. 1: Schematic diagram for two mechanical based approach of layered materials exfoliation [21, 22].....	30
Figure 1. 2: An illustrative procedure of the Scotch-tape based micro-mechanical cleavage graphite-to-graphene transformation [23].....	31
Figure 1. 3: (a) highly crystalline graphite mounted and trimmed to a pyramid shape. (b) Setup showing the wedge alignment with graphite layers [24].....	31
Figure 1. 4: Schematic diagram for the mechanical mechanism for exfoliation via sonication process [40, 41]	34
Figure 1. 5: Schematic diagram for the mechanical mechanism for exfoliation via ball milling [42].	35
Figure 1. 6: Ball milling exfoliation of carbon nanofibers into graphene by using melamine as an exfoliating agent [48, 53].	36
Figure 1. 7: Schematic of the soluble salt-assisted ball-milled route to graphene nanosheet powder [54].	37
Figure 1. 8: Comparison of the pressures in the deposition chamber and the powder feeder of the cold spray, nano-particle deposition, and aerosol deposition systems	39
Figure 2. 1: Thin film fabrication steps by the nanoparticle deposition system	48
Figure 3. 1: Schematic of the mechanical exfoliation and deposition of the 2D materials using the nanoparticle deposition system (NPDS) on a sapphire substrate.	57

Figure 3. 2: XRD patterns of micro-sized graphite powder and the deposited nano-sized graphite thin film on a sapphire substrate.....	60
Figure 3. 3: XRD patterns of micro-sized MoS ₂ powder and the corresponding deposited nano-sized thin film on a sapphire substrate.....	62
Figure 3. 4: XRD patterns of micro-sized boron nitride powder and the resulting deposited nano-sized thin film on a sapphire substrate.....	62
Figure 3. 5: SEM Images of the (a) micro-sized powder and (b) the deposited nano-sized thin film of graphite on a sapphire substrate, the (c) micro-sized powder and (d) the deposited nano-sized thin film of MoS ₂ on a sapphire substrate. the (e) micro-sized powder and (f) the deposited nano-sized thin film of BN on a sapphire substrate.....	63
Figure 3. 6: Raman spectra of the micro-sized graphite powder and the deposited nano-sized thin films of graphite on a sapphire substrate.....	65
Figure 3. 7: Raman spectra of the (a) micro-sized MoS ₂ powder and deposited nano-sized thin films of MoS ₂ on a sapphire substrate. Raman peak fitting for the (b) powder and (c) deposited nanosized thin film spectra.....	67
Figure 3. 8: Raman spectra of (a) the micro-sized BN powder and the deposited nano-sized thin films of BN on a sapphire substrate. Raman peak fitting for the (b) powder and (c) deposited nanosized thin film spectra.....	68
Figure 4. 1: XRD patterns of the Ni(OH) ₂ -graphene composite powder at different Ni(OH) ₂ contents	75
Figure 4. 2: XRD patterns of Ni(OH) ₂ -graphene composite/NF at different Ni(OH) ₂ contents	76
Figure 4. 3: Raman spectra of (a) graphite, (b) 20 wt.% Ni(OH) ₂ , (c) 80 wt.% Ni(OH) ₂ , and (d) Ni(OH) ₂ powder.....	77
Figure 4. 4: Raman spectra of the (a) graphene/NF, (b) 20 wt.% Ni(OH) ₂ -80 wt.% graphene/NF, (c) 80 wt.% Ni(OH) ₂ -20 wt.% graphene/NF, and (d) Ni(OH) ₂ /NF	78

Figure 4. 5: XPS survey spectrum, (b) Ni 2p spectrum, (c) deconvolution of O 1s spectrum, and (d) deconvolution of C 1s spectrum of 20 wt.% Ni(OH) ₂ -80 wt.% graphene/NF	80
Figure 4. 6: XPS survey spectrum (a) , Ni 2p spectrum (b) , O 1s spectrum (c) , and C 1s spectrum (d) of 20 wt.% Ni(OH) ₂ -80 wt.% graphene/NF before and after OER test.....	81
Figure 4. 7: XPS survey spectrum, Ni 2p spectrum (b) , deconvolution of O 1s spectrum (c) , and deconvolution of C 1s spectrum (d) for 80 wt.% Ni(OH) ₂ -20 wt.% graphene/NF	82
Figure 4. 8: SEM images of the micro-sized graphite particles (a, b) , SEM images, and the EDS analysis of the composite (c, d, e) with 20 wt.% Ni(OH) ₂ . SEM images and the EDX analysis of the composite (f, g, h) with 80 wt.% Ni(OH) ₂ , and SEM images of Ni(OH) ₂ powder (i, j)	84
Figure 4. 9: SEM images of bare Ni foam (a, b) , SEM images and EDS spectrum of graphene/NF (c-e) , and 20 wt.% Ni(OH) ₂ -80 wt.% graphene/NF (f-h)	85
Figure 4. 10: SEM images and EDs spectrum of 80 wt.% Ni(OH) ₂ - 20 wt.% graphene/NF (a-c) , and Ni(OH) ₂ /NF (d-f)	86
Figure 4. 11: SEM images and the elemental analysis mapping of the 20 wt.% Ni(OH) ₂ -80 wt.% graphene/NF	87
Figure 4. 12: SEM images and the elemental analysis mapping of the 80 wt.% Ni(OH) ₂ -20 wt.% graphene /NF.....	87
Figure 4. 13: SEM images and the corresponding EDs spectrum of 20 wt.% Ni(OH) ₂ -80 wt.% graphene/NF directly after OER test (a-d) , and after 25 hours OER stability test in 1.0 M KOH (d-f)	88
Figure 4. 14: Plots of current density difference at 0.15 V vs. RHE as a function of scan rate.....	89
Figure 4. 15: CV plots of the graphene/Ni foam NF (a) , Ni(OH) ₂ -graphene/Ni foam NF (b-e) , and Ni(OH) ₂ /Ni foam NF (f) at different scan rates	91
Figure 4. 16: OER LSV curves (a) and Tafel plots (b) for Ni(OH) ₂ -graphene hybrid catalysts/NF; The variation of the overpotential (η) and Tafel slope values with changing Ni(OH) ₂ content (c) . Chronoamperometric curves of 20 wt.% Ni(OH) ₂ -80 wt.% graphene composites/NF at an overpotential of 330 mV for 25 h (d)	92

Figure 4. 17: HER LSV curves and **(b)** Tafel plots for Ni(OH)₂-graphene hybrid catalysts /NF. **(c)** The variation of the overpotential η and Tafel slope values with changing Ni(OH)₂ content. **(d)** Chronoamperometric curves of 80 wt.% Ni(OH)₂- 20 wt.% graphene hybrid catalysts /NF with 80 wt.% at an overpotential η of 154 mV for 25 h..... 94

Figure 4. 18: The wettability behavior of **(a)** the bare Ni foam, **(b)** the pure graphene/NF, **(c)** the composite with 20 wt.% Ni(OH)₂, **(d)** the composite with 80 wt.% Ni(OH)₂, and **(e)** pure Ni(OH)₂/NF..... 95

Figure 4. 19: **(a)** Nyquist plots of Ni(OH)₂-graphene composite/NF, and **(b)** the change in the charge transfer resistance R_{ct} at different Ni(OH)₂ contents, **(c)** water electrolysis LSV curves in two-electrode configuration with a composite of 20 wt.% Ni(OH)₂ as the anode and 80 wt.% Ni(OH)₂ as the cathode, compared with the symmetric Ni foam couple at a scan rate of 5 mV/s. **(d)** The chronoamperometric curve of water electrolysis for the asymmetric configuration at a static potential of 1.75 V. 96

Figure 5. 1: XRD patterns of the used graphite powder **(a)**, Co₃O₄-graphite composite **(b-d)**, and pure Co₃O₄ **(e)** 105

Figure 5. 2: XRD patterns of Co₃O₄-graphene composite/NF at different Co₃O₄ contents..... 105

Figure 5. 3: Raman spectra of the used powder before deposition of the pure phases of graphite **(a)**, and Co₃O₄ **(e)**..... 107

Figure 5. 4: Raman spectra of the Co₃O₄-Graphite mixed powder before deposition at different Co₃O₄ content (25, 50, and 75 wt.%). 108

Figure 5. 5: Raman spectra of graphene/NF **(a)**, Co₃O₄-graphene composites **(b-d)**, and Co₃O₄/NF **(e)** 110

Figure 5. 6: SEM images of the micro-sized particles of **(a, b)** graphite powder, and **(c, d)** mixed Co₃O₄-Graphite powder before the deposition with 25 wt.% Co₃O₄ content. 112

Figure 5. 7: SEM images of the micro-sized particles of Co₃O₄-Graphite composites with Co₃O₄ content of 50 wt.% **(a, b)**, 75 wt.% **(c, d)**, and the pure phase of **(e, f)** Co₃O₄ powder. 113

Figure 5. 8: Elemental analysis of the used micro-sized powder before deposition.....	114
Figure 5. 9: SEM images of graphene/NF (a, b) , and composites with 25 wt.% Co ₃ O ₄ /NF (c, d)	115
Figure 5. 10: SEM images of composites with 50 wt.% (a, b), 75 wt.% (c, d) Co ₃ O ₄ /NF, and pure Co ₃ O ₄ /NF (e, f).....	117
Figure 5. 11: Elemental analysis and the corresponding mapping of graphene/NF and composite with 25 wt.% Co ₃ O ₄ /NF.....	118
Figure 5. 12: Elemental analysis and the corresponding elemental mapping of Co ₃ O ₄ -Graphene/NF composite with 50, and 75 wt.% Co ₃ O ₄ content.	119
Figure 5. 13: Elemental analysis and the corresponding elemental mapping of Co ₃ O ₄ /NF thin film.	120
Figure 5. 14: Wide-scan XPS survey spectra of the Nanostructured pure phases of graphene and Co ₃ O ₄ electrocatalysts, and their hybrid catalysts with different Co ₃ O ₄ content.	121
Figure 5. 15: Co 2p XPS spectra of Co ₃ O ₄ -graphene composites.	122
Figure 5. 16: O 1s XPS spectra of Co ₃ O ₄ -graphene composites	124
Figure 5. 17: C 1s XPS spectra of Co ₃ O ₄ -graphene composites (a-d).....	126
Figure 5. 18: CV plots of Co ₃ O ₄ -composites at different scan ranges in the non-Faradic region from 0 to 0.2 vs. Hg/HgO.....	129
Figure 5. 19: Plots of the current density vs. scan rate of Co ₃ O ₄ -graphene composite.....	130
Figure 5. 20: LSV, the derived Tafel plot, and the stability test @50 mA.cm ⁻² of OER (a, b, c) and of HER (d, e, f) of Co ₃ O ₄ -graphene hybrid catalysts.....	130
Figure 5. 21: Nyquist plot in 1.0 M KOH of the Co ₃ O ₄ -graphene catalysts at an overpotential 300 mV correspond for the (a) OER, and (b) at an overpotential of 100 mV correspond HER.....	131
Figure 5. 22: Cyclic voltammogram from 0 to -0.7 vs. Hg/HgO at a scan rate of 50 mV.s ⁻¹ without and with 5 mM of H ₂ O ₂ in 0.1 M NaOH (a) and the corresponding amperometric response at -0.45 V of Co ₃ O ₄ -graphene hybrid catalyst at various Co ₃ O ₄ content.....	133

Figure 5. 23: Calibration curves of current-induced response to H ₂ O ₂ concentration by Co ₃ O ₄ -graphene catalyst at different Co ₃ O ₄ contents.....	134
Figure 5. 24: Schematic diagram for illustration the H ₂ O ₂ detection mechanism by the Co ₃ O ₄ -Graphene hybrid catalysts	135
Figure 6. 1: XRD patterns of mixed micro-sized ZnO-graphite powder (a) and nano-sized ZnO-graphene thin film deposited on a titanium sheet (b)	143
Figure 6. 2: SEM image and the corresponding EDS elemental analysis of pure ZnO powder (a) , mixed ZnO-graphite micro-sized powder with 25 wt.% (b) , 50 wt.% (c) , and 75 wt.% graphite contents (d)	144
Figure 6. 3: SEM image and the corresponding EDS elemental analysis mapping of ZnO nanosheet thin films on a titanium sheet.	145
Figure 6. 4: SEM image and the corresponding EDS elemental analysis mapping of the ZnO-graphene NCs thin films with 25 wt.% graphite contents on a titanium sheet.	146
Figure 6. 5: SEM image and the corresponding EDS elemental analysis mapping of ZnO-graphene NCs thin films with 50 wt.% graphite contents on a titanium sheet.....	147
Figure 6. 6: SEM image and the corresponding EDS elemental analysis mapping of the ZnO-graphene NCs thin films with 75 wt.% graphite contents on a titanium sheet.....	148
Figure 6. 7: Cross-sectional view (a) , and the corresponding EDS elemental analysis mapping (b-d) of ZnO-graphene with 50 wt.% graphite content on titanium sheets.....	149
Figure 6. 8: HRTEM image and the corresponding interplanar distance histogram analysis of ZnO-graphene nanosheet thin films on titanium sheets.	150
Figure 6. 9: FTIR spectra of ZnO and ZnO-graphite mixed powder (a, b) , nanostructured ZnO and ZnO-graphene thin films on a titanium sheet (c, d)	151
Figure 6. 10: Raman spectra of the ZnO micropowder (a), ZnO-Graphite micro powder mixture (b), nanostructured ZnO thin film (c), and nanostructured ZnO-Graphene thin films on a titanium sheet.	154

Figure 6. 11: XPS survey spectrum (a) and, high-resolution XPS scans of Zn 2p (b) , and O 1s (c) , and C 1s (d) of ZnO-graphene NCs on titanium sheet	156
Figure 6. 12: Deconvoluted Zn 2p XPS scan of pure ZnO (a) and ZnO-graphene NCs/Ti-sheet thin films on titanium sheet with 25 wt.% (b) , 50 wt.% (c) , and 75 wt.% (d) graphite content.	158
Figure 6. 13: Deconvoluted O 1s XPS scan of pure ZnO (a) and ZnO-graphene NCs/Ti-sheet thin films with 25 wt.% (b) , 50 wt.% (c) , and 75 wt.% (d) graphite content.....	159
Figure 6. 14: Deconvoluted C 1s XPS scans of nano-sized ZnO/Ti-sheet (a) , and ZnO-graphene NCs/Ti-sheet thin films with 25 wt.% (b) , 50 wt.% (c) , and 75 wt.% (d) graphite content.....	160
Figure 6. 15: XPS survey spectrum (a) and, high-resolution XPS scans of Zn 2p (b) , and O 1s (c) , and C 1s (d) of ZnO-graphene NCs on titanium sheet after the photoelectrochemical water splitting measurements.....	161
Figure 6. 16: Diffuse reflectance spectra and the corresponding Kubelka-Munk plot (a, b) , Valence band estimation from the XPS survey spectrum (c) , and demonstrative band structure diagram of ZnO-graphene hybrid photoanodes with different graphite contents (d)	163
Figure 6. 17: Photoluminescence emission spectra of ZnO-graphene hybrid photoanodes at different excitation wavelengths (λ_{ex}) and the corresponding radiative center illustrative band diagram.....	165
Figure 6. 18: Photocurrent density vs. applied potential (a), Nyquist plot under illumination at 1.23 V vs. RHE (b), Mott-Schottky (M-S) plot in the dark state (c), the change in the open circuit potential (ΔOCP) with light illumination (d), incident photon-to-electron conversion efficiency (IPCE) vs. potential (e), and response current stability for 10 cycles (f) of ZnO-graphene hybrid photoanodes at different graphene contents.....	166
Figure 6. 19: Schematic band diagram to illustrate the effect of graphene on the band structure of ZnO-based photoanodes	169
Figure 7. 1: XRD patterns of ZnO-graphite micro-sized powders at different graphite contents (a) , and the corresponding deposited nanostructured thin films on the NF porous substrate (b)	176

Figure 7. 2: Raman spectra of the ZnO micro-sized powder and the corresponding nanostructured thin film (a, b), ZnO-graphite mixed micro-sized powders, and the corresponding nanostructured thin films (c, d).....	179
Figure 7. 3: SEM image and the corresponding EDS elemental analysis of pure ZnO powder (a), mixed ZnO-Graphite micro-sized powder with 25 wt.% (b), 50 wt.% (c), and 75 wt.% graphite contents (d).	181
Figure 7. 4: SEM images of nanostructured ZnO/NF thin film (a), and ZnO-graphene NCs/NF thin films at graphite content of 25 wt.% (b), 50 wt.% (c), and 75 wt.% (d).....	182
Figure 7. 5: The elemental composition analysis and the corresponding lateral mapping of nanostructured ZnO/NF photocatalyst.....	183
Figure 7. 6: Elemental composition analysis and the corresponding lateral mapping of ZnO-graphene /NF nanocomposites photocatalyst with 25 wt.% graphite contents.	184
Figure 7. 7: Elemental composition analysis and the corresponding lateral mapping of ZnO-graphene/NF nanocomposites photocatalyst with 50 wt.% graphite contents.....	185
Figure 7. 8: Elemental composition analysis and the corresponding lateral mapping of ZnO-graphene /NF nanocomposites photocatalyst with 75 wt.% graphite contents.	186
Figure 7. 9: XPS survey spectra (a) and high-resolution XPS scans of Zn 2p(b), O 1s (c), and C 1s (d) of ZnO-graphene NCs/NF hybrid photocatalysts at different graphite contents.	187
Figure 7. 10: Deconvoluted Zn 2p XPS scans of nanostructured ZnO/NF (a) and ZnO-graphene NCs/NF hybrid photocatalysts with 25 wt.% (b), 50 wt.% (c), and 75 wt.% graphite contents (d).	188
Figure 7. 11: Deconvoluted O 1s XPS scans of nanostructured ZnO/NF (a) and ZnO-graphene NCs/NF hybrid photocatalysts with 25 wt.% (b), 50 wt.% (c), and 75 wt.% (d) graphite content.	189
Figure 7. 12: Deconvoluted C 1s XPS scans of ZnO-graphene NCs/NF hybrid photocatalysts with 25 wt.% (a), 50 wt.% (b), and 75 wt.% (c) graphite content.	190

Figure 7. 13: Optical absorbance spectra and the corresponding Tauc plots (a, b), valence band estimation from the XPS survey spectrum (c), and a demonstrative band structure diagram of ZnO-graphene NCs/NF hybrid photocatalysts with different graphite contents. 192

Figure 7. 14: Schematic diagram for ZnO-graphene NCs hybrid photocatalysts formation and MB degradation mechanism under visible light illumination 194

Figure 7. 15: The variation of MB optical absorbance with illumination time in the presence of nanostructured ZnO/NF photocatalyst (a), and ZnO-graphene NCs photocatalysts with 25 (b), 50 (c), and 75 wt.% (d) graphite content under a visible light intensity of $50 \text{ mW}\cdot\text{cm}^{-2}$ 195

Figure 7. 16: Optical absorbance spectra at 2 h illumination time (a), the photocatalytic degradation efficiency at different illumination times τ (b), and the linear relation of $\ln(C_0/C)$ vs. the illumination time τ (c) of the ZnO-graphene NCs/NF hybrid photocatalysts. 196

Figure 8. 1: XRD patterns of Co_3O_4 - MoS_2 composites in powder form (a) and thin film deposited on Ni foam substrate. 203

Figure 8. 2: Raman spectra of mixed Co_3O_4 - MoS_2 microparticles at different MoS_2 contents 206

Figure 8. 3: Raman spectra of the MoS_2 /NF (a), Co_3O_4 - MoS_2 heterostructure composites (b-d), and Co_3O_4 /NF (e). 207

Figure 8. 4: SEM images of the micro-sized particles of (a, b) MoS_2 , and (c, d) composites with 75 wt.% MoS_2 content 210

Figure 8. 5: SEM images of the micro-sized particles of composites with (a, b) 50 wt.%, (c, d) 25 wt.% MoS_2 content, and (e, f) pure Co_3O_4 powder 211

Figure 8. 6: Elemental analyses from the EDS spectra of the used micro-sized powder before deposition of Co_3O_4 - MoS_2 composites at different MoS_2 contents. 212

Figure 8. 7: SEM images of pure MoS_2 /NF (a, b), and 75 wt.% MoS_2 /NF (c, d). 213

Figure 8. 8: SEM images of composites with 50 wt.% MoS_2 /NF (a, b), 25 wt.% MoS_2 /NF (c, d), and pure Co_3O_4 /NF (e, f). 214

Figure 8. 9: Elemental analysis from EDS spectrum and the corresponding maps of the MoS ₂ thin film on the 3D Ni foam substrate.	215
Figure 8. 10: Elemental analysis from EDS spectrum and the corresponding maps of the pure phase Co ₃ O ₄ thin film on the 3D Ni foam substrate.	215
Figure 8. 11: Elemental analysis from EDS spectrum and the corresponding maps of the heterostructure composite with 75 wt.% MoS ₂ thin film on the 3D Ni foam substrate.....	216
Figure 8. 12: Elemental analysis from the EDS spectrum and the corresponding maps of the heterostructure composite with 50 wt.% MoS ₂ thin film on the 3D Ni foam substrate.....	217
Figure 8. 13: Elemental analysis from EDS spectrum and the corresponding maps of heterostructure composite with 25 wt.% MoS ₂ thin film on the 3D Ni foam substrate.....	218
Figure 8. 14: XPS survey spectrum (a) and, high-resolution XPS scans of S 2p (b), and Mo 3d (c), O 1s (d), and Co 2p (e) of Co ₃ O ₄ -MoS ₂ heterostructure thin films.....	220
Figure 8. 15: Deconvoluted S 2p XPS scan of pure MoS ₂ (a), 75 wt.% MoS ₂ (b), 50 wt.% MoS ₂ (c), and 25 wt.% MoS ₂ (d) heterostructure thin films.	221
Figure 8. 16: Deconvoluted Mo 3d XPS scan of pure MoS ₂ (a), 75 wt.% MoS ₂ (b), 50 wt.% MoS ₂ (c), and 25 wt.% MoS ₂ (d) heterostructure thin films.	222
Figure 8. 17: Deconvoluted O 1s XPS scan of 75 wt.% MoS ₂ (a), 50 wt.% MoS ₂ (b), 25 wt.% MoS ₂ (c) heterostructure thin films, and pure Co ₃ O ₄ thin films (d).....	223
Figure 8. 18: Deconvoluted Co 2p XPS scan of 75 wt.% MoS ₂ (a), 50 wt.% MoS ₂ (b), 25 wt.% MoS ₂ (c) heterostructure thin films, and pure Co ₃ O ₄ thin films (d).....	224
Figure 8. 19: CV plots of Co ₃ O ₄ -MoS ₂ hybrid catalysts at different scan ranges in the non-faradic region from 0.924 to 1.024 vs. RHE (0 to 0.2 vs. Hg/HgO)	226
Figure 8. 20: OER LSV curves (a), Tafel plots (b), Nyquist plots (c), and stability test at 50 mA.cm ⁻² for 50 hours using Co ₃ O ₄ -MoS ₂ heterostructure electrodes (d), and the current density vs. scan rates plot in the non-faradic region at different MoS ₂ contents (e).	227

Figure 9. 1: XRD patterns of $\text{Co}_3\text{O}_4\text{-MoS}_2$ composites in powder form (a) and nanostructured thin film deposited on titanium sheet.	233
Figure 9. 2: SEM images of micro-sized particles of (a, b) MoS_2 , and (c, d) composites with 25 wt.% Co_3O_4	234
Figure 9. 3: SEM images of micro-sized particles of composites with (a, b) 50 wt.%, (c, d) 75 wt. % Co_3O_4 , and (e, f) pure Co_3O_4 powder.....	235
Figure 9. 4: Elemental analysis of EDS spectra of micro-sized powder before deposition of $\text{Co}_3\text{O}_4\text{-MoS}_2$ composites at different Co_3O_4 contents.....	236
Figure 9. 5: SEM images of MoS_2/Ti (a, b), and 25 wt.% $\text{Co}_3\text{O}_4/\text{Ti}$ (c, d).....	237
Figure 9. 6: SEM images of composites with 50 wt.% $\text{Co}_3\text{O}_4/\text{Ti}$ (a, b), 75 wt.% $\text{Co}_3\text{O}_4/\text{Ti}$ (c, d), and $\text{Co}_3\text{O}_4/\text{Ti}$ (e, f).....	238
Figure 9. 7: Elemental analysis using EDS spectrum and corresponding mapping of nanostructured Co_3O_4 thin films on a titanium substrate.	239
Figure 9. 8: Elemental analysis using EDS spectrum and the corresponding mapping of MoS_2 thin films on titanium sheet substrate.	240
Figure 9. 9: Elemental analysis using EDS spectrum and corresponding mapping of nanocomposites with 25 wt.% Co_3O_4 thin films on a titanium sheet substrate.....	241
Figure 9. 10: Elemental analysis using EDS spectrum and corresponding mapping of nanocomposite with 50 wt.% Co_3O_4 thin films on a titanium substrate.....	242
Figure 9. 11: Elemental analysis using EDS spectrum and corresponding mapping of nanocomposite with a 75 wt.% Co_3O_4 thin film on a titanium substrate.....	243
Figure 9. 12: Raman Spectra of mixed $\text{Co}_3\text{O}_4\text{-MoS}_2$ micro powders at different Co_3O_4 contents.	245
Figure 9. 13: Raman spectra of MoS_2 (a), nanocomposites of $\text{Co}_3\text{O}_4\text{-MoS}_2$ (b-d), and Co_3O_4 (e) nanostructured thin film on titanium sheets.....	247
Figure 9. 14: XPS survey spectra (a), high-resolution XPS scans of S 2p (b), and Mo 3d (c), O 1s (d), and Co 2p (e) of $\text{Co}_3\text{O}_4\text{-MoS}_2$ nanocomposite thin films.....	249

Figure 9. 15: Deconvoluted S 2p XPS scan of pure MoS ₂ (a) , nanocomposites with 25 wt.% (b) , 50 wt.% (c) , and 75 wt.% Co ₃ O ₄ (d) thin films.	250
Figure 9. 16: Deconvoluted Mo 3d XPS scan of pure MoS ₂ (a) , nanocomposites with 25 wt.% (b) , 50 wt.% (c) , and 75 wt.% Co ₃ O ₄ (d) thin films.	251
Figure 9. 17: Deconvoluted O 1s XPS scan of nanocomposites with 25 wt.% (a) , 50 wt.% (b) , 75 wt.% Co ₃ O ₄ (c) , and pure Co ₃ O ₄ (d) thin films.....	252
Figure 9. 18: Deconvoluted Co 2p XPS scan of nanocomposites with 25 wt.% (a) , 50 wt.% (b) , 75 wt.% Co ₃ O ₄ (c) , and pure nanostructured Co ₃ O ₄ (d) thin films.....	253
Figure 9. 19: CV plots of Co ₃ O ₄ -MoS ₂ nanocomposites electrodes at different scan range in the non-faradic region from 0.924 to 1.024 vs. RHE (0 to 0.1 vs. Hg/HgO).	256
Figure 9. 20: Plot of double-layer capacitive current at different scan rates (a) and the corresponding ECSA of Co ₃ O ₄ -MoS ₂ NCs in the non-faradic region at different Co ₃ O ₄ contents (b).	257
Figure 9. 21: CVs of MoS ₂ /Ti (a) , nanocomposite Co ₃ O ₄ -MoS ₂ (b-d) , and pure nanostructured Co ₃ O ₄ /T (e) at different scan rates in 0.1 M NaOH. The linear regression of anodic and cathodic peaks vs. scan rate of Co ₃ O ₄ nanocomposite electrodes (f)	258
Figure 9. 22: CV curves recorded from 0 to 0.8 vs. Hg/HgO at a scan rate of 50 mV.s ⁻¹ without and with 5 mM of H ₂ O ₂ in 0.1 M NaOH (a) , the amperometric response at 0.6 V (b) , a Nyquist plot in 0.1 M NaOH at a DC potential of 0.5 V and 5 mM H ₂ O ₂ , and the corresponding behavior of charge-transfer resistance (c, d) , oxidation selectivity test using amperometric response at 0.6 V with the addition of 1 mM from H ₂ O ₂ , NaCl, saccharose, and glucose in 0.1 M NaOH (e) of Co ₃ O ₄ -MoS ₂ Nanocomposite electrodes at various Co ₃ O ₄ contents	259
Figure 9. 23: Calibration curves of current-induced response to H ₂ O ₂ concentration by Co ₃ O ₄ -MoS ₂ nanocomposites electrodes at different Co ₃ O ₄ contents.	261
Figure 10. 1: XRD patterns of Mn ₃ O ₄ -2D material composites in powder form (a) and corresponding nano-sized film on the NF porous substrate (b) . Magnified XRD peak related to the	

c-axis of the (002) plane in the powder and deposited thin films with graphite (c) and MoS ₂ (d)	268
Figure 10. 2: Raman spectra of the micro-sized powder and the corresponding thin films of MoS ₂ (a) , graphite (b) , Mn ₃ O ₄ (c) , Mn ₃ O ₄ -MoS ₂ (d) , and Mn ₃ O ₄ -graphite (e) composites.	273
Figure 10. 3: SEM images of the micro-sized powders and the deposited nano-sized thin films on the NF porous substrate: MoS ₂ (a-c) , graphite (d-f) , and Mn ₃ O ₄ (g-i)	276
Figure 10. 4: SEM images of the micro-sized powders and the deposited nano-sized thin films on the NF porous substrate: Mn ₃ O ₄ -MoS ₂ (a-d) , and Mn ₃ O ₄ -graphite (d-f) composites.....	276
Figure 10. 5: Micron powder EDS elemental composition analysis of MoS ₂ (a) , graphite (b) , Mn ₃ O ₄ (c) , Mn ₃ O ₄ -MoS ₂ composite (d) , and Mn ₃ O ₄ -graphite composite (e)	277
Figure 10. 6: EDS elemental mapping analysis of MoS ₂ (a) , graphene (b) , and Mn ₃ O ₄ (c) thin films on the NF porous substrate.....	278
Figure 10. 7: EDS elemental mapping analysis of Mn ₃ O ₄ -MoS ₂ NCs on the NF porous substrate.	278
Figure 10. 8: EDS elemental mapping analysis of Mn ₃ O ₄ -graphene NCs on the NF porous substrate.	279
Figure 10. 9: XPS survey spectra (a) and high resolution XPS scans of S 2p (b) , Mo 3d (c) , C 1s (d) , O 1s (e) , and Mn 2p (e) of Mn ₃ O ₄ -2D material NCs/NF thin films.....	280
Figure 10. 10: High-resolution S 2p scan of MoS ₂ (a) and Mn ₃ O ₄ -MoS ₂ NC (b) thin films	281
Figure 10. 11: High-resolution Mo 3d scan of MoS ₂ (a) and Mn ₃ O ₄ -MoS ₂ NC (b) thin films	282
Figure 10. 12: High-resolution C 1s scan of graphene (a) and Mn ₃ O ₄ -graphene NC (b) thin films	282
Figure 10. 13: High-resolution O 1s scan of Mn ₃ O ₄ (a) Mn ₃ O ₄ -MoS ₂ NC (b) , and Mn ₃ O ₄ -graphene NC (c) thin films	283
Figure 10. 14: High-resolution Mn 2p scan of Mn ₃ O ₄ (a) Mn ₃ O ₄ -MoS ₂ NC (b) , and Mn ₃ O ₄ -graphene NC (c) thin films	284
Figure 10. 15: CV plots measured from 0 to -0.7 V vs. Hg/HgO at a scan rate of 50 mV.s ⁻¹ without and with 5 mM H ₂ O ₂ in 0.1 M NaOH (a) . Electrocatalytic reduction selectivity test using the	

amperometric response at -0.4 V with the addition of 1 mM H₂O₂, NaCl, saccharose, and glucose **(b)** for the pure Mn₃O₄ phase and Mn₃O₄ NCs with MoS₂ and graphene nanosheets. 287

Figure 10. 16: Chronoamperometric response at -0.4 V **(a)**. The calibration curves of the current induced response with increasing H₂O₂ concentration by the pure Mn₃O₄ phase **(b)** and Mn₃O₄ NCs with MoS₂ **(c)** and graphene nanosheets **(d)**..... 289

List of Tables:

Table 2. 1: Deposition conditions of Layered materials on the sapphire wafer substrate..... 48

Table 2. 2: Deposition conditions of Ni(OH)₂-graphite NCs on nickel foam..... 48

Table 2. 3: Deposition conditions of Co₃O₄-graphite NCs on nickel foam..... 49

Table 2. 4: Deposition conditions of Co₃O₄-MoS₂ NCs on nickel foam 49

Table 2. 5: Deposition conditions of Co₃O₄-MoS₂ NCs on titanium-sheet..... 49

Table 2. 6: Deposition conditions of ZnO-graphite NCs on nickel foam..... 49

Table 2. 7: Deposition conditions of ZnO-graphite NCs on titanium-sheet 49

Table 2. 8: Deposition conditions of Mn₃O₄-2D materials (graphite, MoS₂) NCs on nickel foam... 50

Table 3. 1: internal structural parameters of the hexagonal crystalline phase along the (002) planes in the micro-sized powder (P) and the corresponding thin films (TF) on a sapphire wafer substrate. 61

Table 4. 1: Electrocatalytic activity and kinetic parameters of Ni(OH)₂-graphene hybrid catalysts/NF for OER and HER..... 97

Table 5. 1: Electrocatalytic activity of Co₃O₄-graphene composite/Ni foam for OER and HER.... 132

Table 5. 2: Comparison of the electrochemical performance between the present work and recently published work of Co-based nonenzymatic amperometric H ₂ O ₂ sensors.....	136
Table 6. 1: XPS band centers according to the deconvolution of the high-resolution XPS scans of Zn 2p, O 1s, and C1s of ZnO-graphene nanosheet hybrid photoanodes at different graphite contents (wt.%).....	157
Table 6. 2: Analysis of the high-resolution XPS scans of Zn 2p, O 1s, and C1s of ZnO-graphene NCs hybrid photoanodes at different graphite contents (wt.%) after the photoelectrochemical water splitting measurements	162
Table 6. 3: The estimated donor concentration (N _D), flat band potential (V _{fb}), and width of the space charge layer (W _{SCL}) of ZnO-graphene NCs/Ti-sheet hybrid photoanodes at different graphite content.....	170
Table 7. 1: Deconvoluted high-resolution XPS bands of Zn 2p, O 1s, and C1s scans of ZnO-graphene NCs/NF hybrid photocatalysts at different graphite contents (wt.%)	191
Table 8. 1: Identification of Raman modes in the mixed Co ₃ O ₄ -MoS ₂ powder at different MoS ₂ contents (wt.%).....	205
Table 8. 2: Identification of active Raman modes in the nanostructured Co ₃ O ₄ -MoS ₂ heterostructure electrodes at different MoS ₂ contents (wt.%)	208
Table 8. 3: EDS elemental analyses of Co ₃ O ₄ -MoS ₂ mixed powder	209
Table 8. 4: EDS elemental analyses of heterostructure composites of Co ₃ O ₄ -MoS ₂ /NF thin films.....	213
Table 8. 5: XPS peaks positions estimated from the deconvolution of XPS scans of S 2p, Mo 3d, O 1s, Co 2p of Co ₃ O ₄ -MoS ₂ heterostructure composites at different MoS ₂ contents (wt.%)	221
Table 8. 6: Values of η, Tafel slope, R _{ct} , and ECSA of the modified electrode with Co ₃ O ₄ -MoS ₂ composites at various MoS ₂ contents.....	228

Table 9. 1: EDS elemental analysis of mixed $\text{Co}_3\text{O}_4\text{-MoS}_2$ microparticles.....	234
Table 9. 2: EDS elemental analysis of nanocomposite $\text{Co}_3\text{O}_4\text{-MoS}_2$ thin films a titanium sheet. ..	235
Table 9. 3: Raman active modes in the $\text{Co}_3\text{O}_4\text{-MoS}_2$ microparticles at different Co_3O_4 content (wt.%).	244
Table 9. 4: Raman peaks of titanium modified electrodes with $\text{Co}_3\text{O}_4\text{-MoS}_2$ NCs at different Co_3O_4 contents.	246
Table 9. 5: Characteristic peaks of S 2p, Mo 3d, O 1s, and Co 2p deconvoluted XPS scans in nanocomposite $\text{Co}_3\text{O}_4\text{-MoS}_2$ thin films.....	253
Table 9. 6: Comparison of electrochemical performance of the present work and recently published work of Co-based nonenzymatic amperometric H_2O_2 sensors.	262
Table 10. 1: Raman active vibrations peaks of $\text{Mn}_3\text{O}_4\text{-2D}$ materials composites in the form of powder (P) and the corresponding thin film (TF) on NF porous substrate.	274
Table 10. 2: Characteristic peaks of S 2p, Mo 3d, C 1s, O 1s, and Mn 2p deconvoluted XPS scans in $\text{Mn}_3\text{O}_4\text{-2D}$ material NC thin films.	285
Table 10. 3: Comparison of the electrochemical performance between the present work and the recently published work of $\text{Mn}_3\text{O}_4\text{-based}$ nonenzymatic amperometric H_2O_2 sensors.	288

List of Abbreviations

NF	Nickel Foam
CF	Carbon Foam
3D	Three dimensions
2D	Two dimensions
NPDS	Nanoparticles deposition system
TMs	Transition metals
TMOs	Transition metals oxides
TMDs	Transition metals dichalcogenides
SoD	Standoff distance
NCs	Nanocomposites
NPs	Nanoparticles
XRD	X-ray diffraction
XPS	X-ray photon electron spectroscopy
EDXS	Energy dispersive X-ray spectroscopy
FTIR	Fourier transform infrared
FE-SEM	Field emission Scanning electron microscope
HR-TEM	High resolution transmission electron microscope
ECSA	Electro-chemical active surface area
CV	Cyclic voltammogram
LSV	Linear sweep voltammetry
CA	Chronoamperometry
R_{ct}	Charge Transfer resistance
PEC	Photo-electrocatalytic

MB	Methylene blue
OER	Oxygen evolution reaction
HER	Hydrogen evolution reaction
LDH	Layered double hydroxide
TMs	Transition metals
CC	Carbon cloth
EG	activated graphite-graphene matrix
GC	Glassy carbon
GO	Graphene oxide
rGO	Reduced graphene oxide
NPG	Nanoparticles gold
PB	phosphate buffer
CNTs	Carbon nanotubes
QDs	Quantum dots
DGF	Three-dimensional graphene foam
AD	aerosol deposition
CVD	Chemical vapor deposition
PVD	Physical vapor deposition

Chapter 1: Introduction

1. 1. 2D NMs properties

The fascinating properties of 2D NMs compared with their corresponding bulk layered materials have gotten much interest from both academic and industrial points of view for the last two decades [1-6]. The graphene nanosheets are the most known 2D NMs, which exhibited superior intraplanar characteristics compared with the graphite bulk phase. The graphene nanosheets exhibited the highest theoretical specific surface area of $2630 \text{ m}^2 \cdot \text{g}^{-1}$, very high transparency (i.e., 97%) all over the visible spectral region, as well as very high mechanical strength with Young's modulus of 1.0 TPa. Another interesting feature is the 2D confinement of excited charge carriers that enables extraordinary charge carrier transportation over several micrometers without scattering. These characteristics make the graphene nanosheets possess superior carrier mobility and excellent electrical conductivity [7]. The dramatic enhancement of structural and sensitive physical properties that are associated with the exfoliation of bulk graphite phase to small size graphene nanosheets arises the research curiosity to study the change in the properties of other layered materials when their size is reduced to the nanosize range. This is because all layered materials exhibited stronger intraplane chemical bonding compared with the weak interplane van der Waals interactions. The exfoliated layered materials in the form of two-dimensional (2D) nanosheets with enhanced surface-to-volume ratio help improving the performance in energy and sensing applications [8, 9]. There are several categories belongs to layered materials such as TMDs (e.g., MoS_2 , WS_2 , ReS_2), nitrides (e.g., BN), phosphorene (black phosphorus (BP)), and MXenes (e.g., Ti_3C_2 , Ta_4C_3). TMDs are 2D semiconductors with the general formula MX_2 , in which "M" refers to the transition metal (i.e., Mo or W), and "X" is the chalcogen element (i.e., S, Se, or Te). The atomic spatial configuration TMDs inside the layered structure is created by inserting a layer of transition metals atoms "M" between two chalcogens "X" atomic layers. The intraplanar bonding is commonly covalent, meanwhile, the stacked layers are weakly bonded by van der Waals interactions. There are several configurations that the TMDs layers can be stacked with such as one tetragonal (1T), two hexagonal (2H), and three rhombohedral (3R) symmetries. Another interesting example is hexagonal BN (h-BN) that is an isomorph for the layered graphite phase and consists of intraplane covalently bonded B and N atoms [10]. Both h-BN and 2H- MoS_2 nanosheets are widely used in energy conversion and storage applications [11-15]. Due to the growing demand for 2D NMs, it becomes increasingly important to develop cost-effective and scalable methods for producing 2D NMs. There are various synthesis techniques for 2D NMs that follow either bottom-up or top-down approaches as described below.

1. 2. 2D NMs synthetic approaches

1. 2. 1. The bottom-up synthetic approach of 2D NMs

The Bottom-up approaches depend on the direct buildup of 2D nanomaterials with the constituent building block atoms. There are various bottom-up synthetic techniques involves CVD, PVD, molecular beam epitaxy, atomic layer epitaxy, and wet chemical syntheses. These methods generally require harsh reaction conditions (e.g., high temperature, high vacuum) and complicated post-treatment steps (e.g., substrate transfer and purification). Considering graphene as an atypical example, much effort has been made to develop bottom-up routes for its preparation. Representatively, CVD on catalytic metal substrates, such as copper or nickel, has shown rich potential for producing large-area, high-quality graphene. However, CVD growth requires a high reaction temperature, sacrificial metal catalyst, and multistep substrate transfer process. Many variables must be precisely controlled to produce high-quality graphene, including such parameters as the mixing ratio, feeding rate, and amount of source gases, reaction temperature, and cooling rate. Chemical synthesis can be performed at a lower temperature (<200 °C) and may allow for better control at an atomic level. However, syntheses of large-area 2D nanomaterials by such bottom-up methods still need further development [16-20].

1. 2. 2. The top-down synthetic approach of 2D NMs

For the scalable production of 2D NMs, the top-down approach is widely used because it can be performed near ambient conditions and capable of producing dispersions of few-layer nanosheets using either a chemical or physical approach. These techniques are based on the mechanical exfoliation of weakly interacted stacked layers into few-layer nanosheets, in which various driving forces can be employed to break the weak van der Waals interactions. Various mechanical-based exfoliation techniques such as sonication and ball-milling are widely used for large-size production of 2D NMs that can be further illustrated below:

1. 2. 2. 1. *Mechanical exfoliation mechanism*

In the ideal process of layered materials exfoliation, the stacked layers can be peeled from the bulk phase layer by layer. There are two approaches of mechanical exfoliation either by using normal force or lateral force as shown in **Figure 1. 1**. One can exert normal force to overcome the van der Waals attraction when peeling two stacked layers apart. This can be practically done by techniques such as micromechanical cleavage by Scotch tape techniques [21, 22]. Because the layered materials have a self-lubricating ability

in the lateral direction, one can also exert lateral force to promote the relative motion between the stacked layers. These two mechanical approaches can occur individually or as a combination based on the optimized techniques for the efficient transformation from the bulk phase to small-size nanosheets. The fragmentation process is expected to occur during exfoliation, as shown in **Figure 1. 1**. The force generated by the exfoliation technique can also fragment the large-size micron powder into smaller ones. This fragmentation can reduce the lateral size of layered materials and make reduce the collective van der Waals interaction forces between the stacked layers in the small grains.

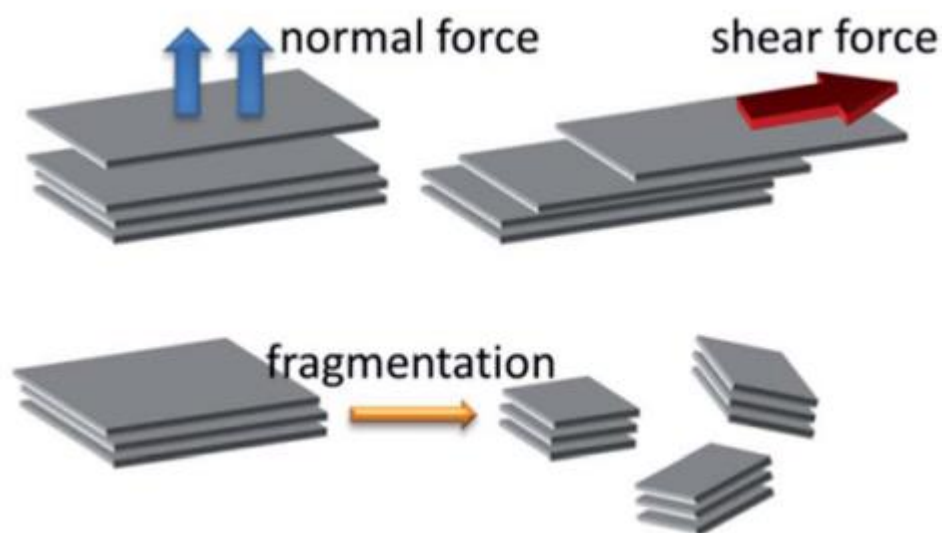


Figure 1. 1: Schematic diagram for two mechanical based approach of layered materials exfoliation [21, 22].

1. 2. 2. 2. Mechanical exfoliation techniques

a) Micromechanical cleavage

The micromechanical cleavage was the first technique to obtains small graphene nanosheets from stacked layers of crystalline graphite phase [23]. The main idea of this technique is the cleavage of graphene layers from the surface of the bulk graphite phase according to procedures illustrated in **Figure 1. 2**. The exfoliation mechanics of this method are that the Scotch tape is applied to the bulk graphite surface and thus exerts a normal force. If one takes great pains to repeat this normal force numerous times, the graphitic layer becomes thinner until becomes single-layer graphene. The exfoliation mechanics are dominated by a normal force. This method can be used to prepare high-quality and large-area graphene flakes. However, this method is extremely labor-intensive and time-consuming. It is limited to laboratory research and seems impossible to scale up for industrial production.

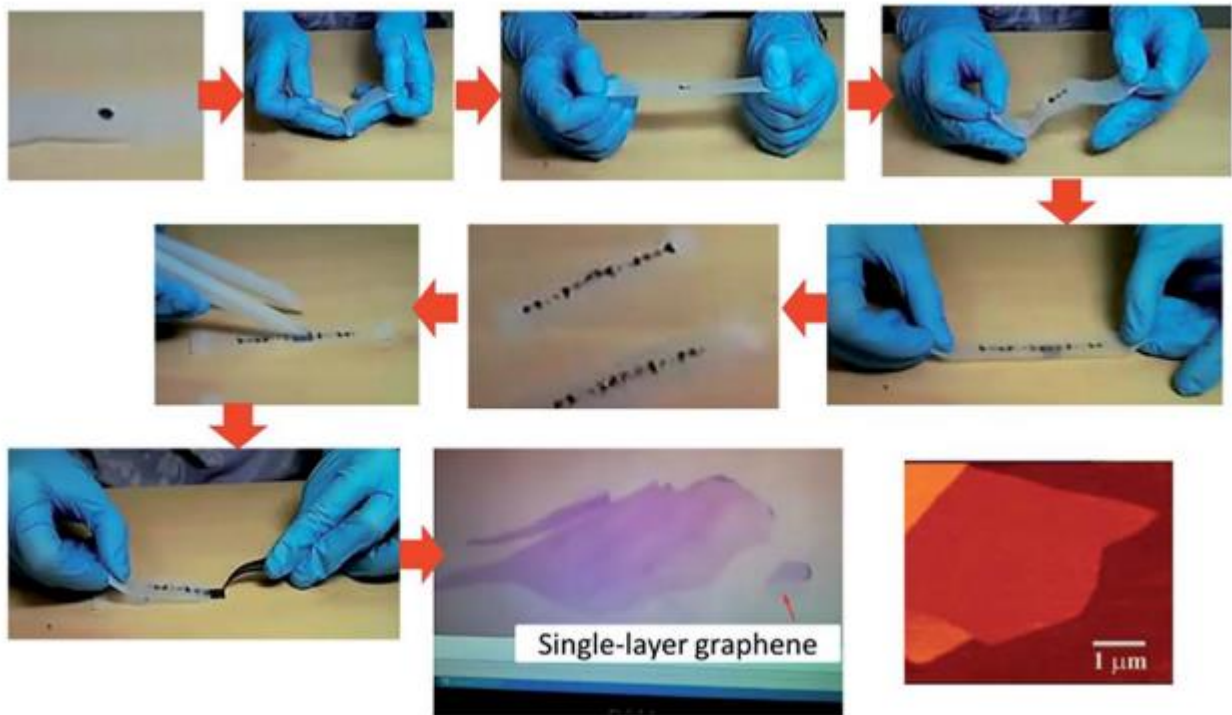


Figure 1. 2: An illustrative procedure of the Scotch-tape based micro-mechanical cleavage graphite-to-graphene transformation [23].

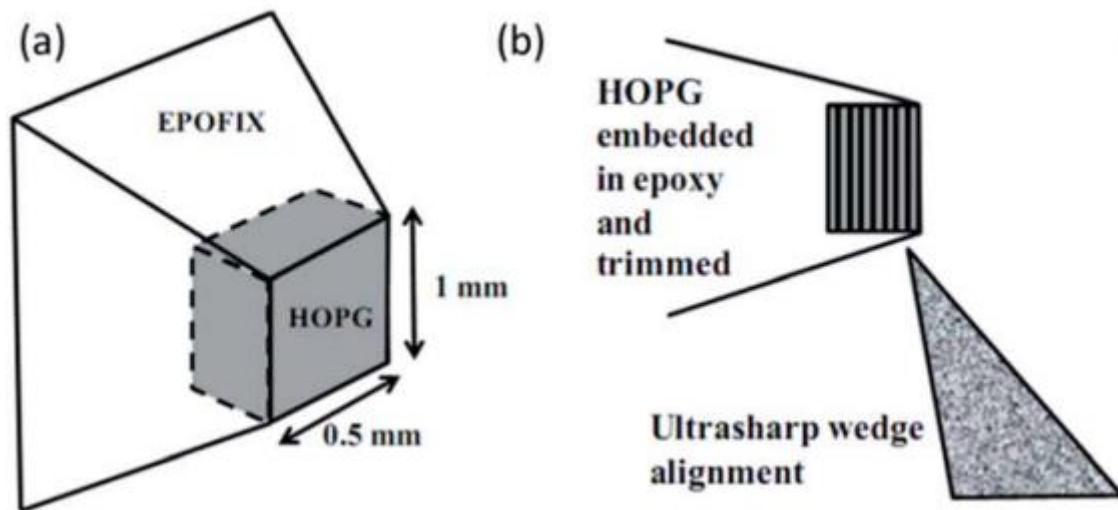


Figure 1. 3: (a) highly crystalline graphite mounted and trimmed to a pyramid shape. (b) Setup showing the wedge alignment with graphite layers [24].

To save time and enhance the exfoliation performance, Jayasena et al [24] have developed a lathe-like experimental setup to cleave graphite samples for generating graphene flakes As shown in **Figure 1. 3**, in which the crystalline graphite is trimmed into a pyramid shape. The tool for cleaving graphite is an ultrasharp single-crystal diamond wedge. The diamond wedge is mounted onto an ultrasonic oscillation system and is aligned carefully concerning the graphite mount. When the ultrasharp wedge is held fixed and the work material is fed slowly downwards towards the wedge, lathe-like behavior happens and the lathed products sliding off the diamond wedge surface are cleaved graphite flakes. This method is lathe-like and can be scaled up to available lathe techniques, but the obtained thin flakes have a thickness of tens of nanometers. Further precise control of the diamond wedge is required for achieving high-quality graphene. The micromechanical cleavage technique was also optimized to exfoliate other 2D NMs [25-27].

b) Sonication

The sonication-assisted liquid-phase exfoliation of layered materials is commonly used for the large-scale production of 2D NMs [28-31]. In the typical procedures, the layered materials are dissolved in specific organic solvents, such as N, N-dimethylformamide (DMF), and N-methyl- pyrrolidone (NMP), followed by sonication and centrifugation. This method is suitable for the large-scale and low-cost production of 2D NMs. However, the low transformation rate (e.g., graphite-to-graphene transformation) that requires long fabrication times. This restricts the spreading of this technique in real-life applications. Researchers attempted to overcome this restriction by increasing the sonication time, increasing the initial graphite concentration, adding surfactants and polymers, solvent exchange methods, and mixing solvents [32-35]. Hernandez et al., [28] demonstrated that the liquid-phase exfoliation of graphite is attributed to the small net energetic cost during the ultrasound-induced exfoliation process, in which the energy balance for the 2D materials nanosheets and used solvent system is expressed as the enthalpy of mixing per unit volume as described below:

$$\frac{\Delta H_{mix}}{V_{mix}} \approx \frac{2}{T_{flake}} (\delta_G - \delta_{sol})^2 \Phi \quad Eq. 1$$

in which T_{flake} is the thickness of a graphene flake, Φ is the graphene volume fraction, and δ is the square root of the surface energy of either layered materials or the used solvent. δ is defined as the energy per unit area required to overcome the van der Waals forces when peeling two sheets apart. This demonstrates that when the surface energy of the layered materials and the used solvent is close to each other the mixing enthalpy will be smaller and the exfoliation has more probability to occur. Therefore, choosing the

appropriate solvent with suitable surface energy that matches the desired layered materials is of great importance for sonochemical-assisted exfoliation. However, If the solvent temperature is elevated or the sonication time is increased the surface energy and the surface tension will be changed. Hence, the used solvents would suffer from degradation and their properties will also be changed These may make the large-scale production of 2D NMs is difficult. Lin et al., [36] have noticed the tuning of solvent surface energy with the variation of temperature reaction temperature during the reduction of graphene oxide using the solvothermal technique. The obtained results helped them to establish a temperature-dependent model of surface energy engineering for the large-scale production of graphene. The mechanical exfoliation according to the sonication mechanism is originating from the liquid cavitation as shown in **Figure 1. 4**. The produced bubbles by the localized cavitation will distribute around the layered materials flakes. Besides, due to the bubbles' collapse, instant micro-jets and shock waves will act on the surface of the layered material. This will produce compressive stress waves which propagate throughout the stacked layers of the bulk phase. When the propagated compressive waves reach the second interface between the layered materials surface and the surrounding solvent, a tensile stress wave will be reflected in the layered materials body according to the theory of stress waves [37]. The numerous collapses of micro-bubbles could produce intensive tensile stress that responsible for the layered materials exfoliation. Furthermore, a secondary process is possible that the unbalanced lateral compressive stress can also separate two adjacent flakes by a shear effect. Also, the micro-jets may split the micro-flakes just as a wedge is driven into the interlayer. Although, the sonochemical-assisted liquid-phase exfoliation of 2D NMs has some limitations that can be further illustrated as follows: I) the 2D NMs prepared by the sonication method has a high concentration of defects. This behavior is caused by the sonication-induced cavitation that is accompanied by a dramatic increase in the localized thermodynamics parameters (i.e., pressure and temperature) [38, 39]; II) the distribution and intensity of the cavitation strongly dependent on the vessel size and shape; and III) The low efficiency of exfoliation due to the fixed position of the used ultrasonic source (i.e., bath or ultrasonic probe), which mostly accompanied by a static distribution of cavitation. This is not favorable for efficient exfoliation, because the layered materials flakes be exfoliated in the region of high cavitation intensity better than the region of low cavitation intensity [40, 41].

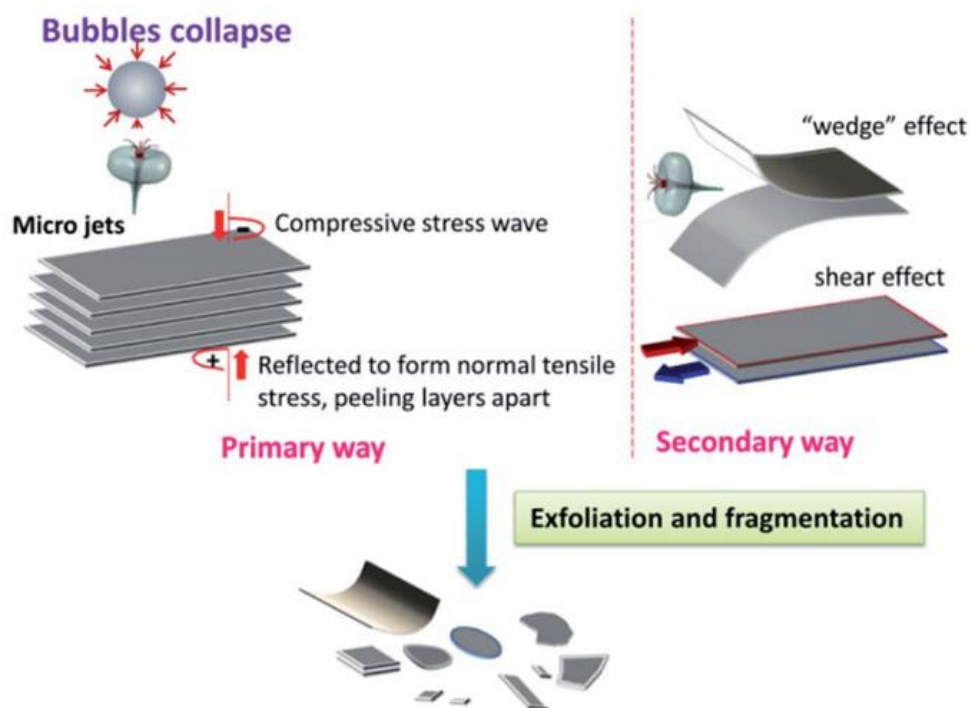


Figure 1. 4: Schematic diagram for the mechanical mechanism for exfoliation via sonication process [40, 41]

c) Ball milling

As previously discussed, sonication-based exfoliation is depending on normal force. The shear force can also be utilized for lateral exfoliation of layered materials as illustrated in **Figure 1. 1**. The ball milling technique is a good candidate for generating shear force, which is widely used in the powder fabrication industry. The mechanical exfoliation mechanism according to ball milling is schematically demonstrated in **Figure 1. 5** [42]. There are two possible ways responsible for the exfoliation and fragmentation effects. The primary one is the shear force, which is thought to be an excellent mechanical route for exfoliation. This way is highly desired for achieving large-sized 2D NMs. The secondary one is the collisions or vertical impacts applied by the balls during rolling actions. This is expected to fragment the large grains into small ones. There are two approaches used in ball milling exfoliation either dry or wet- ball milling that is further illustrated as follows: In the beginning, the ball milling was used to reduce the size of graphite. The flake thickness was reduced to around 10 nm but still possesses the graphite nature [43, 44]. To produce graphene, a suitable liquid was used like the sonication-based liquid-phase exfoliation of graphene. There are two types of ball milling techniques planetary ball mills [45, 46], and stirred media mills [47, 48]. The choice of dispersing solvent for graphite that matched the surface energy of the graphite

is important to overcome the van der Waals forces of stacked layers. Various solvent types can be used for graphite dispersion such as dimethylformamide (DMF) and N-methyl-2-pyrrolidone (NMP). Zhao et al.[49] used a planetary mill for wet ball milling to get graphene. This scheme depends on long-time milling (30 h) and the rotating tray should be controlled at a low speed (300 rpm) to ensure that the shear stress is dominant. Yao et al., [50] used sodium dodecyl sulfate aqueous solutions as the wet medium for ball milling graphite. However, the exfoliation degree is relatively low and subsequent sonication is required. Strong aqueous exfoliants (i.e., 1-pyrene carboxylic acid and methanol) combined with energy ball milling were used to increase the exfoliation degree of layered materials and efficiency. This approach provided a faster exfoliation rate compared with the usage of DMF as dispersing solvent [51].

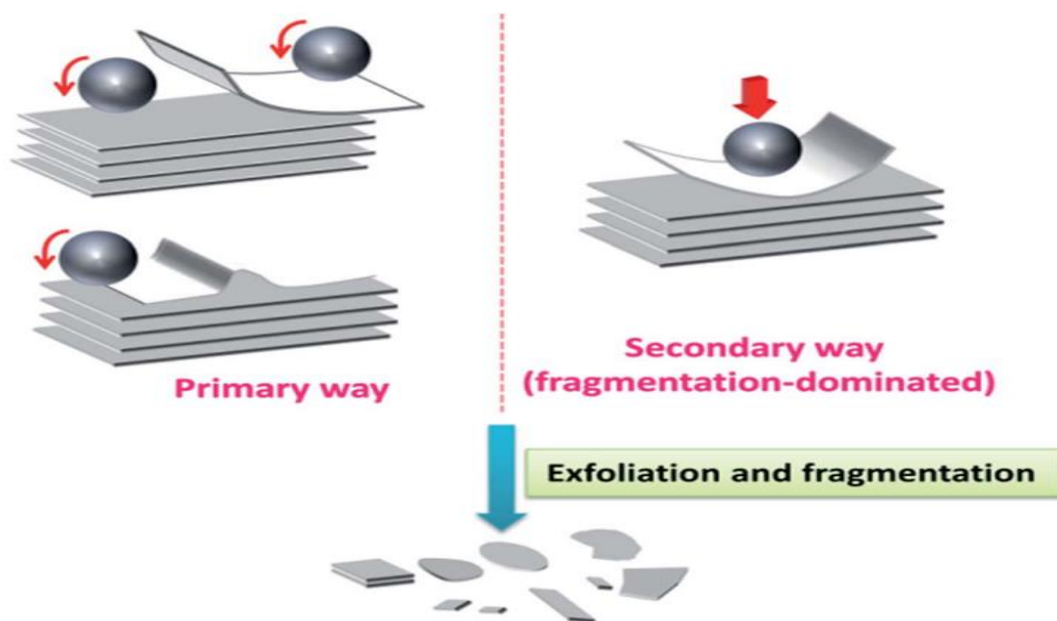


Figure 1. 5: Schematic diagram for the mechanical mechanism for exfoliation via ball milling [42].

Similarly, Rio-Castillo et al. [52] recently used melamine an exfoliating agent for the intercalation of graphite layers and found that adding a small amount of solvent during the ball milling process can enhance the intercalation and promote exceptional exfoliation of carbon nano-fibers into graphene nanosheets as schematized in **Figure 1. 6**. The previous reports used high-energy planetary ball milling, which is favorable for combined functionalization and exfoliation. Meanwhile, a drawback is the long processing time (several ten hours) and/or requirement of sonication-assisted post-dispersing steps. On the other hand, the planetary ball mills used wet stirred media mills which operate with much smaller grinding media and allow better temperature control during the processing [48, 53]. Another strategy was followed in the ball

milling-based mechanical exfoliations, in which the dry ball milling through mixing graphite micron powder with chemically inert water-soluble inorganic salts such as Na_2SO_4 . This would result in interlayer separation that is followed by subsequent water washing and/or sonication of the milling products to obtain final graphene powders as shown in **Figure 1. 7** [54].

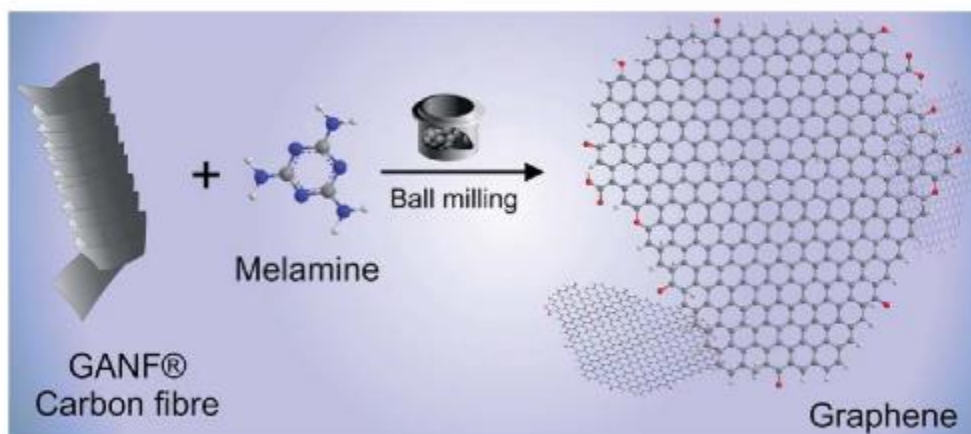


Figure 1. 6: Ball milling exfoliation of carbon nanofibers into graphene by using melamine as an exfoliating agent [48, 53].

In the dry ball milling technique, the exfoliated 2D NMs can be functionalized with other elements such as sulfur, which the large electronegativity difference between the graphene and the incorporated sulfur atoms would result in composites with better performance compared with the bare graphene nanosheets [55]. In contrast to these methods which suffer from the basal plane functionalization of graphene, Jeon et al. put forward an edge functionalization route for the scalable production of graphene by dry ball milling. They dry milled graphite in the presence of hydrogen, carbon dioxide, sulfur trioxide, or a carbon dioxide/sulfur trioxide mixture. Upon exposure to air moisture, the resultant hydrogen-, carboxylic acid-, sulfonic acid-, and carboxylic acid/sulfonic acid-functionalized graphene flakes were obtained [56, 57]. The edge-carboxylated graphite is highly dispersible in various solvents and can self-exfoliate into mono- and few-layer graphene nanosheets. These examples of edge-selectively functionalized graphene proved to be of high quality. Though the ball milling technique is thought of as an intriguing method for the large-scale production of graphene, the defects induced by the high-energy collision of grinding media are less clear. Since collisions among the grinding media cannot be prevented during the milling process, fragmentation and defects are unavoidable.

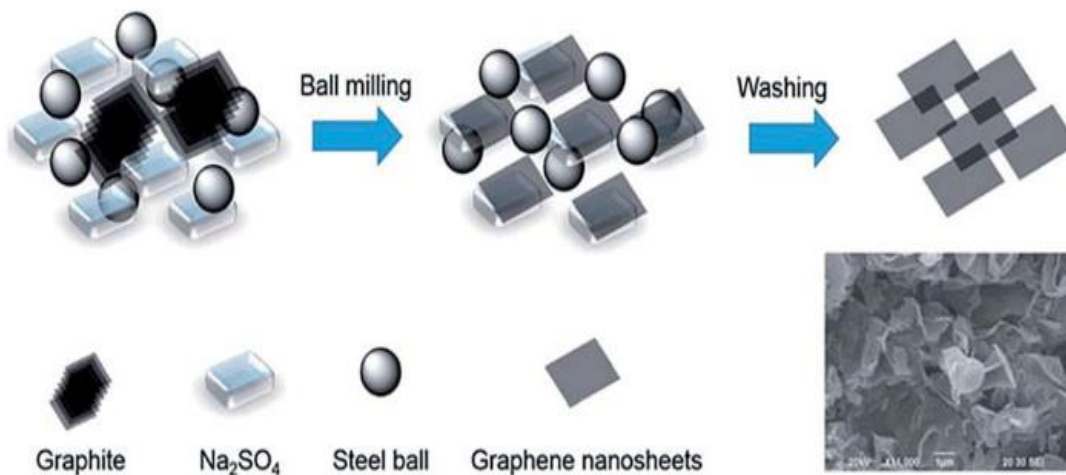


Figure 1. 7: Schematic of the soluble salt-assisted ball-milled route to graphene nanosheet powder [54].

1. 3. Formation of TMs-based hybrid NCs with 2D NMs

In general, there is no single process to fabricate TMs-based hybrid NCs with 2D NMs, which one of each material (i.e., TMs or 2D NMs) are separately prepared and then the mixing or chemical bonding with other materials through a chemical process that can be further illustrated as follows: Masjedi-Arani et al., [58] have prepared CdSnO_3 -graphene hybrid NCs via microwave-assisted sonochemical technique. Firstly, the CdSnO_3 NPs were separately synthesized using the sonochemical technique. Then the obtained CdSnO_3 powder was mixed with the pre-synthesized graphene and stirred at $90\text{ }^\circ\text{C}$ for 30 min. Finally, the mixed CdSnO_3 -graphene NCs powder was exposed to microwave irradiation for 15 min and dried in an oven. Li et al., [59] have synthesized TiO_2 @rGO heterostructure NCs using the alkaline hydrothermal technique. The pre-synthesized powder of TiO_2 NPs and rGO was mixed in NaOH aqueous solution. Then, the mixture was transferred to a Teflon-lined stainless steel autoclave and heated to $180\text{ }^\circ\text{C}$ at different times. The obtained sediment was washed in water and HCl solution. The samples were freeze-dried and then calcined at $400\text{ }^\circ\text{C}$ for 2 h under an N_2 atmosphere. Barakat et al., [60] have prepared $\text{Ni}(\text{OH})_2$ - TiO_2 @graphene NCs using chemical precipitation technique. The pre-synthesized TiO_2 and graphene powder were mixed in an aqueous alkaline solution, which the Ni^{2+} source was added dropwise until under a fixed stirring process. The reaction time was around 2 h and the reaction pH was controlling by NaOH solution. To make sure of composite formation, the formed precipitate was stirred for 48 hands the obtained powder after several cleaning processes were dried in an oven at $100\text{ }^\circ\text{C}$ for 18 h. Duan et al., [61] fabricated

Co₃O₄-MoS₂ hybrid NCs using microwave plasma chemical vapor deposition (MOCVD). The individual micron powder of MoS₂ and Co₃O₄ micron powder were individually prepared using the solution drying method. The mixture was deposited using the MPCVD technique. The resulted Co₃O₄-MoS₂ composites exhibited a large size of about 6 μm. Wang et al., [62] have prepared the core-shell structure of CoFe₂O₄@MoS₂ hybrid NCs using the solvothermal technique. First, the CoFe₂O₄ NPs were prepared using 1 h ultrasound followed by the solvothermal process at 200 °C for 4 h. The obtained powder was dried in the oven at 60 °C for 12 h. The final powder was used to form a composite with MoS₂ nanosheets using ultrasound and solvothermal process at 200 °C for 24 h. The fine precipitate of CoFe₂O₄-MoS₂ hybrid NCs was filtered and dried in the oven. Kumar et al., [63] have used the microwave-assisted technique to synthesis Mn₃O₄-Fe₂O₃/Fe₃O₄@rGO ternary hybrid NCs.

1. 4. Vacuum kinetic spray process for NMs deposition

The deposition process for nano-sized ceramic and metallic films on different substrate types can be performed using the high-velocity impact of micron powder in one step at room temperature according to the vacuum kinetic spray process using various strategies such as cold spray, the aerosol deposition (AD) technique and nano-particle deposition system (NPDS) [64-67]. The dry-spray deposition has general advantages like a) room temperature deposition; b) no thermal damage for the substrate; c) no use for hazardous chemicals; and d) one-step deposition in a short time. In general, the dry-spray deposition mechanism of the nano-sized thin film involves the transportation of micron powder (i.e., either metallic or ceramics) at a high-pressure carrier gas through a nozzle. Followed by the high-velocity impact of micron powder with the substrate and the formation of the bonded layer at the substrate surface. The main difference between the dry-spray deposition techniques (i.e., cold spray, AD, and NPDS) is the range of powder feeding pressure and deposition pressure, see **Figure 1. 8**, according to Chun et al [68]. The deposition mechanism of micron powder in the AD technique involves the micron ceramics powder fragmentation and bonding with substrate interface [69]. However, the derived localized thermodynamic parameters (i.e., the pressure of 2.5 GPa and temperature of 500 K) from the numerical simulation of single-particle impact according to Akedo et al., [64] is not enough for interfacial bonding between the fragmented particles and the used substrate. Also, the simulation results did not show any clear particle fragmentation after the impact. So, the deposition mechanism of ceramics powder is not understood in the case of AD deposition. The deposition mechanism of metallic powder using the cold spray technique is recognized as adiabatic shear instability, in which the high plastic strain at the particle/substrate interface

results in micron powder fragmentation and softening due to adiabatic heating. Hence, the bonding between the NPs and the substrate is possible. The NPDS was used for NPs deposition from either metals or ceramics on various types of substrates for metals and ceramics nano-sized thin films.

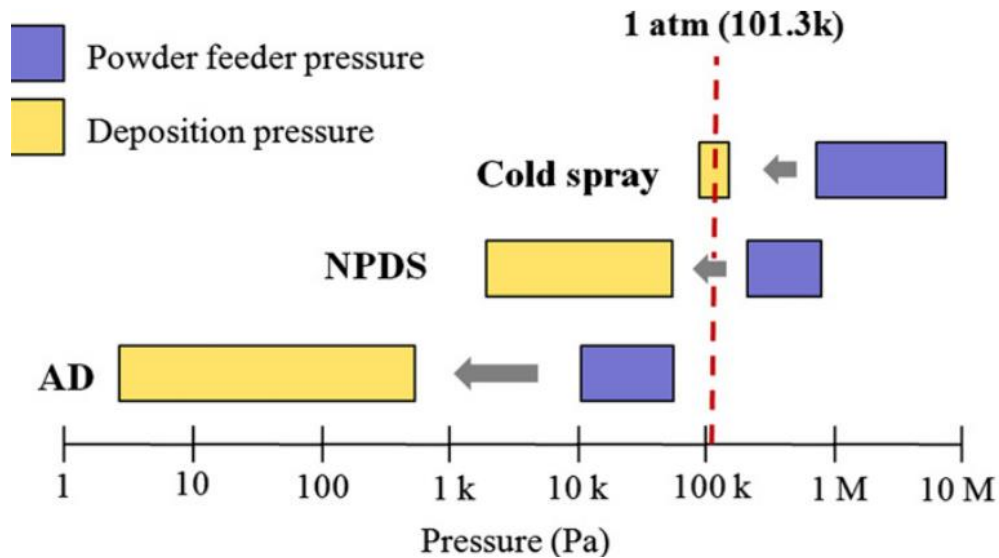


Figure 1. 8: Comparison of the pressures in the deposition chamber and the powder feeder of the cold spray, nano-particle deposition, and aerosol deposition systems

The typical deposition conditions according to the NPDS involve the fragmentation of submicron ceramic particles into nanoparticles due to shock compaction waves produced by the successive impact of submicron particles. The accompanied adiabatic energy transfer results in a sharp increase in the localized pressure and temperature, which are saturated within several nanoseconds from the impact. This would provide sufficient interfacial bonding energy of the small NPs and the used substrate surface [70]. The dry-spray deposition using the AD process is mainly used for ceramics materials [64, 69]. Besides, the nozzle configuration in the AD technique cannot control the supersonic flow that is considered as a limitation in the deposition metal micron powder that requires a high critical velocity exceeds the sound speed in the air [71]. The cold spray deposition was used depositing metals and ceramics but each material type needs a different system configuration [72]. In the cold spray process, the micron powder that is carried out by supersonic flow is deposited on the substrate at atmospheric pressure. The high-pressure flow creates a strong shock wave around the substrate. The small particles cannot penetrate the substrate and fragmentation is expected due to the high impact velocity [73]. There is a limitation for the used micron powder size in the cold spray technique, in which the minimum micron particle size is around 10 μm . The second limitation appears when using ceramic micron powder with a large particle size that could erode the substrate similar to

powder blasting mechanical etching [74]. In contrast, the used nozzle in the NPDS has a converging inlet-diverging outlet configuration in a vacuum, which helps to reduce the shock wave strength and control the supersonic flow. The converging-diverging geometrical configuration of the nozzle in the NPDS will increase the dispersed particle speed and make the NPDS system able to deposit more materials compared with the AD system. Moreover, the aerosol generators used for AD have low controllability, especially for heavy powders, so a fluidized bed powder feeder is used in NPDS.

1. 5. Research goals and objectives

2D NMs materials and their heterostructure NCs are widely used in a variety of applications related to energy and sensors. To expand the commercial use of such materials, the fabrication cost efficiency and the ability for large-size production must be considered. As previously illustrated. This goal cannot be achieved by the conventional mechanical exfoliation technique of layered materials such as ball milling (wet or dry) and sonochemical techniques. Since these techniques used to prepare 2D NMs in several separate steps that consume long labor work time and need further post-treatment for waste products. Furthermore, the formation of hybrid NCs with other materials can not be prepared in the same process, in which each material is separately prepared and mixing of two materials is performed in extra steps. As we illustrated in the previous section, the vacuum kinetic spray process according to the NPDS technique was successfully used for the fabrication of several nanosized materials (i.e., metals and semiconductors) in one step at room temperature. Also, the graphene nanosheets and their hybrid were directly deposited on several substrates from the corresponding graphite micron powder in a single step.

The ability of graphene nanosheets deposition and formation of hybrid NCs formation with several functional nano-sized TMs compounds by the NPDS in one step motivated us to examine the ability of mechanical exfoliation of other graphene-like materials (i.e., layered materials) with a similar hexagonal structure such as molybdenum disulfide (MoS_2) and boron nitride (BN) by the NPDS without the need of any chemical assistance. Hence, we could use the NPDS as a single system for the mechanical exfoliation of pure layered materials and formation of the formation of hybrid NCs with other functional materials in a single process, which reduces the fabrication time and consequently enhance the fabrication cost efficiency for commercial life applications.

The fabricated hybrid electrodes by the NPDS technique were utilized in energy conversion applications related to water splitting and non-enzymatic sensing of H_2O_2 in alkaline medium to

demonstrate the performance improvement compared with 2D NMs-based electrodes that were fabricated by other conventional techniques as

1. 6. Thesis Organization

The detailed plan for the present thesis is divided into several chapters that are concerned with specific goals.

Chapter 1 focuses on several issues that are mainly concerned with the ability of production of 2D NMs from the mechanical exfoliation of layered micron powder by a cost-effective and scalable technique. Firstly, we presented the room temperature deposition of ceramics and metals-based nanoparticles from the corresponding micron powder using several vacuum kinetic spray techniques including aerosol deposition, cold spray, and the NPDS. The advantages and drawbacks of each technique were illustrated in detail. The second issue to recognize the characteristics of various layered materials types (e.g., graphene, TMDs, etc.). Due to the wide spreading of 2D NMs in technological applications, we demonstrated the recently available technique to recognize which is better for large-size production. Finally, we demonstrated the role of 2D NMs in improving the performance of water splitting-energy conversion applications through various routes (i.e., electrocatalysis, photocatalysis, and photo-electrocatalysis) as well as the non-enzymatic electrochemical sensor in alkaline medium

Chapter 2 demonstrates information about the used materials in the deposition process of pure phases or heterostructure electrodes by the NPDS from the initial micron powders on either metal or ceramic substrates. The deposition conditions of 2D NMs pure phases and their nanocomposites (NCs) with transition metal compounds are explained in detail. Also, the experimental measurements for evaluating the electrochemical performance of the fabricated hybrid electrodes toward the water splitting and non-enzymatic H₂O₂ sensing applications are illustrated in various configurations.

In **chapter 3**, we investigate the feasibility of the direct mechanical exfoliation and deposition of various layered material types such as graphite, MoS₂, and boron nitride (BN) in one step at room temperature under low vacuum conditions using NDPS. The deposited nano-sized thin films are studied by various surface characterization x-ray diffraction (XRD), scanning electron microscope (SEM), and Raman spectroscopy. Based on the obtained results we verified the occurrence of mechanical exfoliation of layered materials to small-size nanosheets due to the micron powder fragmentation and interlayer separation of their stacked structure layers.

After checking the feasibility of mechanical exfoliation of the layered materials pure phases (graphite, MoS₂), we will check the ability of NCs formation between either graphene or MoS₂ nanosheets with functional transition metal compounds for water splitting based energy conversion applications and non-enzymatic electrocatalytic detection of H₂O₂. These applications depend strongly on the induced water splitting species (i.e., oxygen or hydrogen) that can be used in different forms such as electrochemical energy storage or directly for the degradation of industrial waste products. For the occurrence of the water-splitting, an external energy source should be applied, which can be either photon, electricity, or hybrid in the form of photo-electrocatalytic water splitting. The formation of functional hybrid NCs with 2D materials nanosheets is widely used for these applications to improve the efficiency of power transferring or accelerating the charge transfer process at the interface between the fabricated electrodes and the used electrolyte. Each graphene or MoS₂ can verify this goal but with different synergy mechanisms between the hybrid NCs species. To illustrate this, we investigated the effect of hybridization between one of the 2D materials nanosheets and various types of transition metal compounds. Besides, the formed NCs hybrid electrodes were utilized for improving overall performance by variation of materials composition ratio.

- **Graphene nanosheets-based hybrid NCs**

Hybrid NCs between graphene nanosheets and either nano-sized Ni(OH)₂ or Co₃O₄ were directly deposited in one step at room temperature on nickel foam (NF) porous substrate to study the electrocatalytic water splitting in the alkaline medium (i.e., 1.0 M KOH) as demonstrated in **chapter 4& 5**. In both studies, the graphite content in the initial micron powder was changed relative to the used TMs material for thin deposition by the NPDS. To demonstrate the hybridization between the graphene and TMs species in the deposited nano-sized thin films various surface sensitive techniques such as XRD, FE-SEM, Raman spectra, and x-ray photoelectron spectroscopy (XPS) were used. Besides, to study the electrochemical performance of the fabricated heterostructure nano-sized electrodes toward the overall water splitting, the kinetic of each oxygen evolution reaction (OER) and the hydrogen evolution reaction (HER) were separately evaluated in the three-electrode configurations. The utilized working electrode (WE) was based on the hybrid NCs at different graphite content. The optimum composition ratio between the graphite species and the TMs materials for each the OER and the HER was recognized, in which the higher graphite content in the fabricated hybrid NCs exhibited better electrochemical performance toward the OER due to the overall improvement in the charge transfer kinetics. Whereas the fabricated electrodes with hybrid NCs that contain a high percentage of TMs showed better electrochemical performance toward the HER. Furthermore, Co₃O₄-graphene hybrid NCs/NF at different graphite content in **chapter 5** was

also, utilized for the investigation of electrochemical reduction of H_2O_2 in alkaline medium (0.1 M NaOH). The results revealed the overall improvement of H_2O_2 reduction with the increase of graphene content in the fabricated hybrid NCs due to the improvement of both the charge transfer kinetics and the density of electrocatalytic active centers. This makes the deposited Co_3O_4 -graphene hybrid NCs/NF with an optimum composition ratio a good candidate as an electrochemical non-enzymatic sensor for H_2O_2 in an alkaline medium.

Graphene hybrid NCs uses for water splitting applications that depend only on photon excitation or hybrid with electricity in the form of photoelectrochemical was also investigated in **chapter 6 & 7**, in which ZnO-graphene NCs hybrid photoanodes at different graphite content were deposited in NF porous substrate and titanium sheet substrate in one-step by the NPDS at room temperature. The formation of NCs and the hybridization between the ZnO and graphene nanosheets in the hybrid NCs were characterized by several techniques such as XRD, FE-SEM, as well as various spectroscopic techniques (i.e., Raman, UV-visible absorption, photoluminescence, and x-ray photoelectron spectroscopy). The modified electrodes with ZnO-graphene NCs hybrid photoanodes were utilized for studying the photoelectrochemical water splitting in an alkaline medium (i.e., 0.5 M Na_2SO_3) as well as photocatalytic degradation of methylene blue under visible-light irradiation. We find that the synergy improvement between the graphene nanosheets and nano-sized ZnO species in the NCs hybrid photoanodes resulted in overall transfer in the photogenerated carrier separation and transfer, which in turn enhanced the solar energy harvesting. This was accompanied by an enhancement in photocatalytic water oxidation as well as the improvement of MB degradation kinetics. Furthermore, the stoichiometric ratio (i.e., 50: 50 wt.%) exhibited the optimum composition with the highest solar energy conversion efficiency.

- **MoS₂ nanosheets-based hybrid NCs**

Hybrid NCs between MoS₂ nanosheets and Co₃O₄ was deposited in one step at room temperature on NF porous and titanium sheet substrate to study the electrocatalytic water splitting in the alkaline medium (i.e., 1.0 M KOH) as well as the electrochemical oxidation of H_2O_2 in an alkaline medium (0.1 M NaOH) as illustrated in **chapter 8 & 9**. In both cases, the ratio of Co₃O₄ to MoS₂ content in the micro-sized powder was mixed using the ball milling technique, which is used in the thin film deposition process by the NPDS. The hybridization between the MoS₂ nanosheets and nanostructure Co₃O₄ in the fabricated thin films was examined by several techniques like XRD, FE-SEM, Raman spectra, and XPS. The fabricated Co₃O₄-MoS₂ NCs/NF was used as an anode for testing the OER in 1.0 M KOH as demonstrated in **chapter 8**. We

found that the synergy improvement between the Co_3O_4 and MoS_2 species resulted in an improvement of the OER reaction kinetics as well as the decrease of water oxidation overpotential. Furthermore, the hybrid NCs with high MoS_2 nanosheets contents exhibited better electrocatalytic activity toward the OER compared with other composites. Whereas Co_3O_4 - MoS_2 hybrid NCs with high Co_3O_4 content exhibited better electrocatalytic activity and selectivity toward H_2O_2 oxidation compared with other composites, as demonstrated in **chapter 9**.

In **chapter 10**, we tried to compare the effect of different synergy behavior between the nano-sized Mn_3O_4 and various types of 2D materials such as MoS_2 and graphene nanosheets, which directly exfoliated and deposited in one step using the NPDS. The fabricated Mn_3O_4 - hybrid NCs were utilized for studying the H_2O_2 reduction in the alkaline medium (0.1 M NaOH). In both cases, the initial ratio of Mn_3O_4 to the layered material (i.e., MoS_2 or graphite) content was kept 1: 1 in the micro-sized powder, which the mixed process was performed by the ball milling technique. The mixed micron powder was used in the deposition process on the NF porous substrate by the NPDS. The hybridization between the 2D materials nanosheets and the nanosized Mn_3O_4 in hybrid NCs was examined by several techniques like XRD, FE-SEM, Raman spectra, and XPS. The electrocatalytic reduction of H_2O_2 was investigated in the 3 electrode cell configuration, in which the synergy improvement between the Mn_3O_4 and either graphene or MoS_2 nanosheets resulted in an improvement of the H_2O_2 reduction kinetics compared with the pure Mn_3O_4 phase. The real-time detection of H_2O_2 was performed using the chronoamperometric (CA) techniques, which revealed a wide linear detection range and high sensitivity toward the H_2O_2 reduction.

Chapter 2: Experimental Conditions

2. 1. Materials

2. 1. 1. Layered materials

The used layered materials powder with micro-size range and hexagonal structural phase are:

- graphite (size $\leq 10 \mu\text{m}$, MGF 10 995A, Samjung C&G, Gyeongsan, Korea).
- MoS_2 (size $\approx \mu\text{m}$, assay 98%, CAS#1317-33-5, Sigma-Aldrich, USA).
- Boron Nitride powders (size $\approx 5 \mu\text{m}$, assay 99.8%, CAS#10043-11-5, US Research Nanomaterials, Inc, USA).

2. 1. 2. Transition metals compounds

Various type of transition metal compounds with micro-size range are used based on the application category as illustrated below:

- $\text{Ni}(\text{OH})_2$ powder (size $< 5\mu\text{m}$, CAS#: 12054-48-07, Aldrich, MW: 92.71 g/mol, mp: 230 °C, d: 4.1 g/mL, Germany).
- Co_3O_4 powder (size $\approx 2.5 \mu\text{m}$, CAS#: 1308-06-1, US Research Nanomaterials, Inc, USA).
- Mn_3O_4 powder (size $\approx 2.5 \mu\text{m}$, CAS#: 1317-35-7, US Research Nanomaterials, Inc, USA).
- ZnO microparticles (size $< 5\mu\text{m}$, assay 99.9%, CAS#1314-13-2, Sigma-Aldrich, USA).

2. 1. 3. Substrate

The used substrates are:

- Ni foam (NF) substrate (99.5%, 110 PPI, $d=350 \text{ g}\cdot\text{m}^{-2}$, and thickness of 1.6 mm, Invisible, Inc., Korea)
- Single side polished sapphire wafer (orientation: C(001) $0.2^\circ \pm 0.05$; diameter: 2 inch; thickness: $430 \pm 25 \mu\text{m}$, i-Nexus Inc. Korea).
- titanium sheet (99.5%, and 0.5 mm thick, Nilaco Corporation, Japan).

2. 1. 4. Electrolytes and solvents

- A 1.0 M KOH electrolyte was used (CAS#: 1310-58-3, Daejung, Korea) was used to study the electrocatalytic water measurements (i.e., OER and HER) in the alkaline medium.
- A 0.1 M NaOH electrolyte (CAS#: 1310-73-2, Samchun, Korea) was used as an electrolyte for the non-enzymatic detection of H_2O_2 in an alkaline medium.

- A 0.5 M Na₂SO₃ electrolyte with a pH of 9.8 (CAS#: 7757–83–7, Duksan, Korea) was used for studying the PEC water splitting in an alkaline medium.
- Methylene blue (MB; Catalog No. 5578-4125, Daejung Co. Ltd., Busan, Korea) with a concentration of 5 mg·l⁻¹ was used to evaluate the kinetics of photodegradation under visible light irradiation.

2.2. Fabrication of nano-sized thin films by the NPDS

Various types of functional semiconductors in the form of pure materials or mixed phases were deposited in one step using the NPDS under low vacuum conditions at room temperatures. In the typical condition of thin film deposition, the initial micro-sized powder was directly used in the deposition process. In the case of hybrid NCs, the desired weight percent mixtures of the micro-sized powders were first prepared by mixing in a ball mill for 6 hours (5-mm diameter zirconium, 1:10 ball to mass ratio, and 600 rpm). The mixed powders were then utilized in the NPDS system for direct deposition on the desired substrate with a total area of 4 cm². As previously mentioned, the main concept in our deposition system is accelerating particles to acquire high kinetic energy, which results in the fragmentation of the micro-sized particles due to the inelastic collision with the substrate. The mechanism of accelerating powders is illustrated in the provided schematic diagram, **Figure 2. 1**. First, the deposition chamber was evacuated using a rough vacuum for ≤ 3 torrs. Then, initial dispersion for the powder was performed by a powder feeder (cylindrical piston) and a rotating brush system. The vertical movement of the piston was precisely controlled with various speeds ranging from 0 to 4250 rpm, which was used with the rotating brush with rotation speed ranging from 7000 to 8000 rpm speed to adjust the loading mass of the deposited films. Then, an influx of compressed air at 3 ~ 3.5 bars carried the dispersed powder to reach the nozzle slit with dimensions (0.2 mm width, and height of 50 mm). The nozzle was a converging-diverging type, in which the input air powder mixture would experience pressure difference in the slit opening causing further acceleration to the particles included in the air. After that, the existing powder impacted the desired substrate fixed on the 3D stage at a normal incidence to the slit opening with a standoff distance (SoD) of 3 ~ 5 mm. The inelastic collision between moving particles with high kinetic energy and the fixed substrate is the main reason for the fragmentation

of the micro-powders to nanostructured thin films. The detailed parametric conditions of the deposited nano-sized thin films for each compound are illustrated in the next **Tables**.

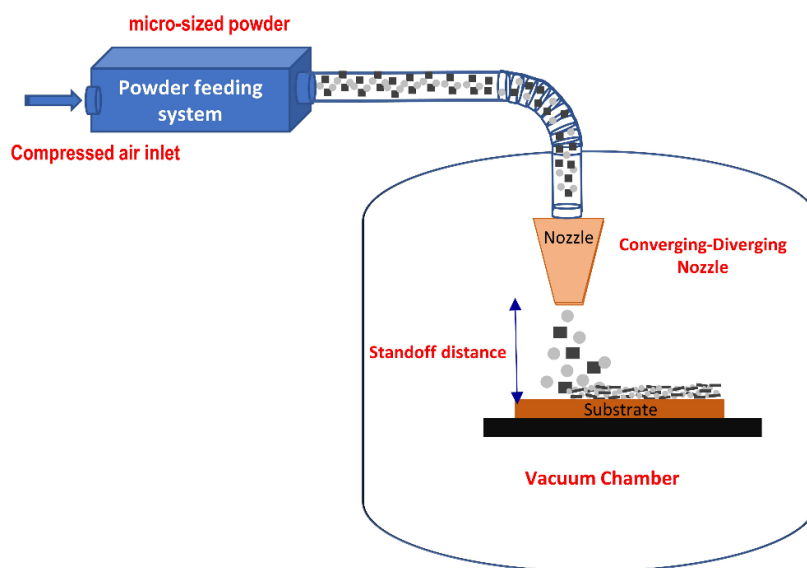


Figure 2. 1: Thin film fabrication steps by the nanoparticle deposition system

Table 2. 1: Deposition conditions of Layered materials on the sapphire wafer substrate

Material	Area h*w cm ²	Powder pressure (bar)	SOD (mm)	Piston speed (rpm)	Brush speed (rpm)	Scan speed (rpm)	Chamber pressure (torr)	Flow rate (l/min)
Graphite								
Molybdenum disulphide	4	3.5	3	3500	8000	250	320	45
Boron nitride								

Table 2. 2: Deposition conditions of Ni(OH)₂-graphite NCs on nickel foam

Composition (%)		Area h*w cm ²	Powder pressure (bar)	SOD (mm)	Piston speed (rpm)	Brush speed (rpm)	Scan speed (rpm)	Chamber pressure (torr)	Flow rate (l/min)	Loading mass mg/cm ²
Co ₃ O ₄	Graphite									
0	100									0.5
20	80			4250						
40	60	4	2	5	7000	375	100 ~150	25	2 ~2.5	
60	40									3000
80	20									
100	0									2000

Table 2. 3: Deposition conditions of Co_3O_4 -graphite NCs on nickel foam

Composition (%)		Area h*w cm ²	Powder pressure (bar)	SOD (mm)	Piston speed (rpm)	Brush speed (rpm)	Scan speed (rpm)	Chamber pressure (torr)	Flow rate (l/min)	Loading mass mg/cm ²
Co_3O_4	Graphite									
0%	100%	4*1	3	5	4250	7000	250	300~320	38	0.5
25%	75%				3500					
50%	50%				2500					
75%	25%				2000					
100%	0%									

Table 2. 4: Deposition conditions of Co_3O_4 - MoS_2 NCs on nickel foam

Composition (%)		Area h*w cm ²	Powder pressure (bar)	SOD (mm)	Piston speed (rpm)	Brush speed (rpm)	Scan speed (rpm)	Chamber pressure (torr)	Flow rate (l/min)	loading mass mg/cm ²
Co_3O_4	MoS_2									
0%	100%	4*1	3	5	2000	7000	250	300~320	38	1~1.25
25%	75%									
50%	50%									
75%	25%									
100%	0%									

Table 2. 5: Deposition conditions of Co_3O_4 - MoS_2 NCs on titanium-sheet

Composition (%)		Area h*w cm ²	Powder pressure (bar)	SOD (mm)	Piston speed (rpm)	Brush speed (rpm)	Scan speed (rpm)	Chamber pressure (torr)	Flow rate (l/min)	loading mass mg/cm ²
Co_3O_4	MoS_2									
0%	100%	4*1	3	5	2000	7000	250	300~320	38	~0.1
25%	75%									
50%	50%									
75%	25%									
100%	0%									

Table 2. 6: Deposition conditions of ZnO -graphite NCs on nickel foam

Composition (%)		Area h*w cm ²	Powder pressure (bar)	SOD (mm)	Piston speed (rpm)	Brush speed (rpm)	Scan speed (rpm)	Chamber pressure (torr)	Flow rate (l/min)	loading mass mg/cm ²
ZnO	graphite									
25%	75%	4*1	3~3.2	3	2000	8000	250	320-350	40	~3
50%	50%									
75%	25%									
100%	0%									

Table 2. 7: Deposition conditions of ZnO -graphite NCs on titanium-sheet

Composition (%)		Area h*w cm ²	Powder pressure (bar)	SOD (mm)	Piston speed (rpm)	Brush speed (rpm)	Scan speed (rpm)	Chamber pressure (torr)	Flow rate (l/min)	loading mass mg/cm ²
ZnO	graphite									
25%	75%	4*1	3~3.2	3	2000	8000	250	320-350	40	~0.1
50%	50%									
75%	25%									
100%	0%									

Table 2. 8: Deposition conditions of Mn_3O_4 -2D materials (graphite, MoS_2) NCs on nickel foam

Composition (%)			Area h*w cm ²	Powder pressure (bar)	SOD (mm)	Piston speed (rpm)	Brush speed (rpm)	Scan speed (rpm)	Chamber pressure (torr)	Flow rate (l/min)	loading mass mg/cm ²
Mn_3O_4	graphite	MoS_2									
0	100	0									~ 0.5
0	0	100									
100	0	0	4*1	3.5	3	2000	8000	250	320	45	2 ~ 2.5
50	50	0									
50	0	50									

2. 3. Surface Characterization techniques

- The crystal structures the micro-sized powder, and the corresponding thin films were investigated by the Ultima IV X-ray diffractometer in the diffraction angle range from 10 to 100° with a diffraction angle step size of 0.02°.
- The surface morphology and the corresponding elemental analysis of the used powders and the deposited thin films were analyzed using the energy-dispersive X-ray spectra (EDS) by the JEOL JSM-6500F field emission scanning electron microscope (FE-SEM). For depicting the interfacial bonding between various species in the deposited thin films, the surface morphology was further examined by a high-resolution transmission electron microscope (HR-TEM model: JEM-2100F, JEOL), in which the sample was prepared and loaded on the grid using a focused ion beam (model: Helios 450HP FIB).
- The active molecular vibrations related to various species in the micro-sized powder and the corresponding thin films were identified using the Fourier transform infrared (FTIR) spectrometer (model: Varian 670/620, wavenumber range from 650 up to 4000 cm^{-1}) as well as the micro-Raman spectroscopy (a 532 nm Raman spectrometer with a 1 mW laser source, Alpha 300R, WITec. GmbH).
- The interfacial states on the surface of the deposited thin films were scanned using the k_{α} X-ray photoelectron spectrometer (XPS: Thermo Fisher Scientific, US) in the binding energy range 0 to 1400 eV.
- The optical band gap was estimated from the optical diffuse reflectance spectra in the range from 200 to 800 nm using the UV-VIS-NIR spectrophotometer (Cary 5000, Agilent, US).

- The Photoluminescence (PL) emission spectra were recorded for the deposited thin films in the range from 300 nm to 600 nm using a fluorescence spectrophotometer (Cary Eclipse, Agilent, US).

2.4. Electrochemical measurements

2.4.1. Electrocatalytic water splitting

The electrochemical performance of the fabricated hybrid NCs electrocatalysts by the NPDS toward the OER and the HER in 1.0 M KOH was investigated using the electrochemical workstation (C350, Wuhan Corr-test Instruments Corp. Ltd., China) in the 3-electrode cell configuration, which the modified electrodes with 1 cm² area were used as working electrode, either 1 cm² Pt mesh or Pt wire were used as a counter electrode, and either Ag/AgCl in 1.0 M KCl or Hg/HgO in 1.0 M KOH were used as a reference electrode. Both the OER and HER potentials were IR-corrected and calibrated to RHE according to the following equation [75]:

$$E_{RHE} = E_{Ref.} + E_{Ref.}^{\circ} + 0.059 * pH \quad Eq. 2.1$$

Here, $E_{Ref.}^{\circ}$ is the standard potential vs. NHE ($E_{Ref.}^{\circ} = 0.098$ V for Hg/HgO, and 0.235 V for Ag/AgCl) and $E_{Ref.}$ is the applied potential difference vs. the used reference electrode in 1.0 M KOH. Linear sweep voltammetry (LSV) curves were measured in the potential range from 1.2 to 1.8 V vs. RHE at 5 mV/s scan rate for the OER and from -0 to -6 V vs. RHE for the HER in 1.0 KOH with the pH =14. The overpotential (η) values corresponding to the OER and HER were estimated from the following relations [76]:

$$\eta_{OER} = E_{OER} - E_{OER}^{\circ} - IR \quad Eq. 2.2$$

$$\eta_{HER} = E_{HER} - E_{HER}^{\circ} - IR \quad Eq. 2.3$$

where E_{OER} and E_{HER} are the applied potentials on the working electrode vs. RHE for the OER and the HER, respectively. E_{OER}° is the standard potential of water oxidation of 1.23 V vs. RHE, meanwhile, E_{HER}° is the standard water reduction potential of 0 V vs. RHE, and IR is the potential correction due to the electrolyte nuisance resistance.

The electrocatalytic reaction kinetics can be investigated using Tafel analysis, in which the estimated overpotential for either the OER or the HER is drawn on the y-axis vs. the log scale of the produced current according to the Tafel equation illustrated below [77]. The estimated slope exhibits the electrocatalytic reaction kinetics of the modified working electrode:

$$\eta = b \log \left(\frac{j}{j_0} \right) \quad \text{Eq. 2. 4}$$

where j is the current density, j_0 is the exchange current density, and b is the Tafel slope.

The electrochemical active surface area (ECSA) of the modified electrodes with hybrid NCs was determined using capacitance components corresponding to double-layer [78] in which the potential was linearly scanned in the non-faradaic range from 0 to 0.1 vs. Hg/HgO in 1.0 M KOH electrolyte. The C_{DL} represents the slope of the linear relationship between the current density (ΔJ) at various scan rate (v) as described below:

$$\Delta J = J_{anode} - J_{cathode} = C_{DL} v \quad \text{Eq. 2. 5}$$

The cyclic voltammogram (CV) plots of the modified electrodes were recorded at various scan rates from 10 to 100 $\text{mV} \cdot \text{s}^{-1}$. A linear relationship based on the above-mentioned equation between ΔJ at 0.05 vs. Hg/HgO and v were plotted for all modified electrodes. The obtained C_{DL} from the slope refers to the ECSA in the unit of $\text{mF} \cdot \text{cm}^{-2}$.

2. 4. 2. PEC water splitting

The PEC water splitting was measured in a 0.5 M Na_2SO_3 (pH = 9.8) electrolyte using the electrochemical workstation in the three-electrode configuration. The fabricated hybrid NCs photoanodes by the NPDS were utilized as working electrodes. The counter electrode was a 1 cm^2 Pt mesh and the reference electrode was Hg/HgO in 1.0 M KOH. A halogen lamp with an incident light intensity of $85 \text{ mW} \cdot \text{cm}^{-2}$ (Photo-Optic LAMP 12V 100W) was used as the illumination source and the incident light flux was measured using a digital luxmeter (model: LX1330B). The Mott-Schottky plots were produced using the electrochemical impedance spectroscopy (EIS) in the dark state in the potential range from -1 to 0 V vs. Hg/HgO using an AC signal (5 mV amplitude, 1 kHz frequency). The photo-response current under the incident visible light was estimated from the current difference between the illumination and dark conditions using the linear sweep voltammetry from 0.5 to 1.8 V vs. RHE at the same scan rate. The charge transfer resistance (R_{ct}) under illumination was measured using a Nyquist plot with AC signal amplitude of 5 mV in the frequency range of 100 kHz to 1 Hz at DC bias potential of 1.23 V vs. RHE. Additionally, the photocurrent stability was examined using the chronoamperometric (CA) technique at the DC bias potential of 1.23 V vs. RHE for successive 10 cycles. The measured potential vs. Hg/HgO was calibrated to the RHE scale according to **Eq. 2. 1**:

2. 4. 3. H₂O₂ sensing

The electrochemical non-enzymatic response for the H₂O₂ by the fabricated hybrid NCs electrodes was investigated by the CV plots at 50 mV·s⁻¹ in the absence and the presence of H₂O₂ in the potential range from 0 to -0.7 V vs. Hg/HgO for H₂O₂ reduction and from 0 to 0.8 V vs. Hg/HgO for H₂O₂ oxidation. Then, the performance of the hybrid NCs electrodes as a non-enzymatic sensor for H₂O₂ was quantitatively evaluated using the chronoamperometric (CA) plots, in which a gradual amount of H₂O₂ was added at a specific potential.

Chapter 3:

*One-Step Mechanical Exfoliation and Deposition of
Nanosheets of Layered Materials by a Room Temperature
Vacuum Kinetic Spray Process*

3.1. Overview

The transformation of three-dimensional (3D) materials with multiple stacked layers to two-dimensional (2D) nanosheets is accompanied by a dramatic enhancement in various physical and chemical characteristics. The improved properties of 2D materials have led to their widespread adoption in various electrochemical applications. There are various types of 2D materials, such as graphene, molybdenum disulfide (MoS_2), and hexagonal boron nitride (h-BN), that can be functionalized to form nanocomposites (NCs) that improve the overall performance of energy-related applications. For instance, graphene and MoS_2 can improve the charge transfer kinetics in hybrid NCs and subsequently enhance the power rate in energy conversion applications [79-81]. In contrast, h-BN nanosheets are characterized by ultrahigh insulation, which is necessary for enhancing the energy density of dielectric capacitors that operate at high temperatures and voltage [82-84].

Challenges to large-scale production currently limit the further implementation of 2D-material NCs. In addition, the stacked layers in the bulk structure of MoS_2 and h-BN exhibit stronger interlayer interactions [85, 86] than do the layered structure of graphite [87], indicating the higher energy required for the exfoliation of these materials. There are several existing techniques used for 2D material exfoliation, of which the top-down approach is the most widely used for large size and mass production. The exfoliation of 2D materials through the top-down approaches can be achieved by either a chemical or a physical route. The chemical-based techniques for 2D material exfoliation can involve oxidization, dissociation, or intercalation with highly reactive chemical species, such as KMnO_4 , H_2SO_4 , and H_2O_2 [88-90]. Several techniques use external energy sources to accelerate the chemical exfoliation rates of 2D materials such as sonochemical-assisted exfoliation [91, 92]. These techniques are usually not preferable for mass production because they exhibit a low exfoliation efficiency and require extensive precautions and waste treatment to avoid chemical hazards. The exfoliation process for 2D materials using physical routes can be achieved using either peeling or shearing forces in the process such as micromechanical cleavage [93], shear exfoliation [94], exfoliation using dry and wet ball milling [54, 95]. Zhu et al. [96] reported the physical exfoliation of h-BN through a thermally assisted gas exfoliation process. The exfoliation process is divided into two successive steps. First, the bulk h-BN is expanded at a high temperature of ~ 800 °C. Then, the thermally heated powder is immediately immersed into liquid N_2 until complete gasification. The sudden dramatic decrease in temperature and the sudden increase in the volume of N_2 gas result in the exfoliation of the bulk h-BN and the formation of few-layered BN nanosheets.

Recently, many hybrid techniques that involve both physical and chemical routes for 2D materials exfoliation, such as mechanochemical assisted exfoliation, have been reported. In this hybrid approach, the micro-sized powder of layered materials is exposed to ball milling that is assisted by chemical solvents. Then, the yield product is dispersed using ultrasonication and collected via centrifugation at very high speed, $\sim 10,000$ rpm, which removes large particles, including partially exfoliated and unexfoliated micro-sized grains [49, 97, 98].

The aforementioned techniques for layered materials exfoliation exhibit good performance. However, these methods are more suitable for the small size production used for research and development purposes than they are for industrial applications. Further, these techniques only yield exfoliated products in powder form, which requires a binder to attach to electrode surfaces for use in energy conversion and storage applications. The existing exfoliation techniques have many limitations, such as high production costs, long preparation times due to successive steps, use of harmful chemicals as a reactant, production of undesirable waste products, and the inability to produce large electrodes that are suitable for energy-related applications. Unlike these existing techniques, the top-down process for mechanical exfoliation of 2D materials nanosheets and the formation of hybrid NCs with other functional compounds using NPDS has several favorable characteristics: a) vacuum kinetic spray deposition in one stage at room temperature; b) no substrate damage by thermal heating; c) binder-free; d) no secondary products or waste; and e) applicable for the large-size area [99].

In this work, we present a simple technique for the direct mechanical exfoliation and deposition of various layered material types, including graphite, MoS_2 , and BN, on a sapphire wafer substrate. The exfoliation process was performed using a one-step vacuum kinetic process at room temperature via the NPDS. The exfoliation of the 2D materials was verified with several characterization techniques, including SEM, XRD, and Raman spectroscopy.

3. 2. Mechanism of 2D materials exfoliation and deposition

The deposition of layered structure materials using a vacuum kinetic spray process via the NPDS involves the fragmentation of the micro-sized powder, layer separation at high impact velocity, and interfacial bonding between the exfoliated layers and the substrate, as schematically illustrated in **Figure 3. 1**. In the initial step, the micro-sized powder of the layered structure materials (i.e., graphite, MoS_2 , or BN) is provided to the powder feeding system at a constant rate. Then, the supported powder is carried

out by pressurized air flow to the converging-diverging nozzle. This nozzle's geometrical design in the NPDS helps increase the kinetic energy of the accelerated particles due to the difference in the pressure between the powder pressure at the nozzle inlet and the deposition pressure in the vacuum chamber. This system allows for good control of the accelerated particle velocity in the supersonic flow. The accelerated particles impact the hard substrate, resulting in fragmentation of the micro-sized powder for particles in the nano-size range. One-step exfoliation and deposition of the 2D materials nanosheets on the substrate can be realized at room temperature. According to Chun et al. [100], the fragmentation of the micro-sized powder to produce nano-size particles using the NPDS is caused by the shock compaction wave produced from the supersonic flow collapse within the substrate followed by the successive impact with other micro-sized particles, which causes a sharp and spontaneous temperature increase due to adiabatic thermal heating. These extraordinary conditions are spatially localized and stabilized within a few nanoseconds after the impact, providing enough energy to bind the nanosheets to the substrate surface without any damage. Concerning layer separation, Nasim et al. [101] used molecular dynamic simulations to show that layer separation in 2D materials can occur in the vacuum kinetic spray of the NPDS if the impact velocity of the accelerated particles exceeds a critical limit.

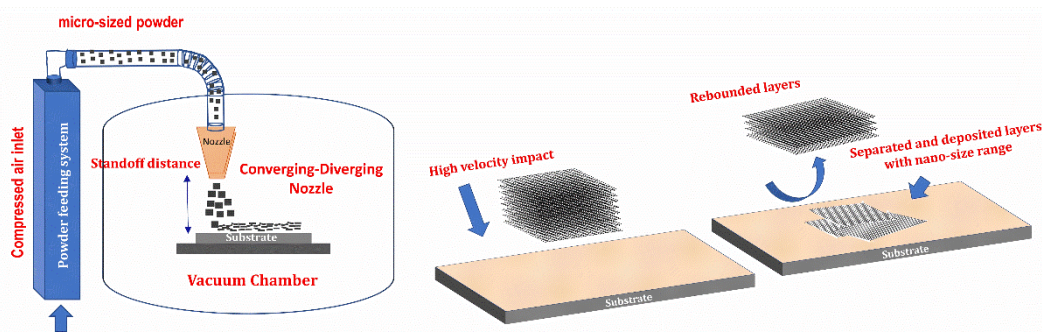


Figure 3. 1: Schematic of the mechanical exfoliation and deposition of the 2D materials using the nanoparticle deposition system (NPDS) on a sapphire substrate.

In our experiment, the high impact velocity provides enough energy for layer separation to form small nanosheets that bond with the substrate as well as the rebounding of unbonded layers. The typical deposition conditions of the 2D materials nanosheets thin films on sapphire wafer substrate using the NPDS (**Figure 3. 1**) proceeds as follows. The sapphire wafer substrate is placed on a three-dimensional stage below the nozzle opening slit with a standoff distance of 3 mm. The deposition chamber is sealed, and the pressure is reduced to < 3 torrs using a rotary vacuum pump. Then, a micro-sized powder of layered materials (i.e., graphite, MoS₂, and BN) is provided to the powder-feeding system using a rotating

brush. Subsequently, the dispersed micro-sized powder was carried by compressed air, with a pressure of 3.5 bar and flow rate of 45 liters · min⁻¹, to the converging-diverging nozzle (slit width = 50 mm and slit height = 0.2 mm). The pressure difference between the nozzle inlet and outlet increases the kinetic energy of the moving particles. Thus, the impact of the micro-sized powder with high kinetic energy on the sapphire wafer substrate induces a large number of fractures and interlayer separations in the incident micro-sized particles and reduces the domain size to the nano-size range. The adiabatic energy transfer during the impact of the accelerated particles with high kinetic energy on the stationary substrate leads to a sharp increase in the localized thermal energy of the interfacial atoms, providing bonding energy for the deposited layer.

3.3. Results and discussion

3.3.1. X-ray diffraction

The internal crystalline structures of the 2D layered materials and the corresponding nano-sized thin films on a sapphire wafer substrate were identified using XRD. The variation in the internal lattice spacing (d_{hkl}) is estimated from the XRD peak position (θ) and X-ray wavelength (λ) of 1.540593 Å using Bragg's law for the first-order diffraction ($n=1$), as follows [102]:

$$2d_{hkl}\sin\theta = n\lambda \quad \text{Eq. 3.1}$$

The crystalline domain size (D_{hkl}) and the associated internal local strain (ε_{hkl}) are estimated from the XRD peak position and the corresponding peak broadening (β_{hkl}) based on the Scherrer formula, as follows [103, 104]:

$$D_{hkl} = \frac{K\lambda}{\beta_{hkl}\cos\theta} \quad \text{Eq. 3.2}$$

$$\varepsilon_{hkl} = \frac{\beta_{hkl}\cos\theta}{4} \quad \text{Eq. 3.3}$$

Where K is the shape factor. The 2θ , d_{hkl} , D_{hkl} , and ε_{hkl} corresponding to the c -plane along the (002) direction of the hexagonal structure of the experimental micro-sized powders and the thin films were estimated using **Eq. 3. (1-3)** and recorded in **Table 3. 1**. The induced variations in the structural phase of the layered materials due to the high-velocity impact with the hard substrate are discussed below for each material.

3. 3. 1. 1. Graphite to graphene reduction

Figure 3. 2(a) exhibits the XRD patterns of the micro-sized graphite powder and the corresponding nano-sized thin film on sapphire wafer substrate in the 2θ range 10° to 100° . The XRD pattern of the micro-sized graphite powder exhibits two diffraction peaks related to the hexagonal layered structure of graphite at 26.52° and 54.62° . The most intense peak at 26.52° corresponds to the c-plane that is oriented along the (002) direction. The second, lower intensity peak at 54.62° corresponds to the c-plane along the (004) direction. The bulk hexagonal phase of graphite powder has lattice parameters $a = 2.643 \text{ \AA}$ and $c = 6.714 \text{ \AA}$ and crystal symmetry operations described by the P63/MMC space group (ICDD: 00-056-016, PDF 2010). In addition, the intercalation of some oxygen-related functional groups between the stacked layers of hexagonal graphite powder results in the observation of other XRD peaks at 23.92° with a higher interplanar distance of 3.72 \AA [105]. After depositing the graphite powder on a sapphire wafer substrate, the XRD peak corresponding to the c-plane along the (002) direction of the hexagonal graphite phase is strongly diminished in intensity, as shown in **Figure 3. 2(b)**. The peak position is also slightly shifted to lower 2θ value, see **Table 3. 1**. In addition, the interplanar distance increases from 3.357 \AA to 3.367 \AA . This behavior demonstrates the strong separation of the stacked graphite layers due to the high-velocity impact between the accelerated graphite powder and the sapphire wafer substrate. Furthermore, the crystalline peak corresponding to oxygen-containing functional groups disappears and is replaced by a broad band located at 16.5° as shown in **Figure 3. 2(c)**. These diffraction patterns were taken on single crystalline sapphire wafer substrates, which do not have any broadened bands in the same range that would overlap the amorphous-like graphene band. This XRD data illustrates the successful kinetic-induced exfoliation of layered hexagonal-structure graphite to form nano-sized graphene layers in one step using the NPDS [106, 107].

3. 3. 1. 2. MoS₂

Figure 3. 3(a) shows the XRD patterns of the micro-sized MoS₂ powder and the deposited MoS₂ thin film on the sapphire wafer substrate. The XRD pattern of the stacked layers of MoS₂ powder exhibits numerous diffraction peaks at $14.38, 28.96, 32.62, 33.44, 35.82, 39.4, 44.1, 49.74, 55.94, 58.28,$ and 60.1 ; these peaks are matched with the (002), (004), (100), (101), (102), (103), (006), (105), (110), and (008) crystalline planes, respectively, of the bulk phase of hexagonal MoS₂

(space group: $P6_3/mmc$, ICDD: 00-037-1492, PDF 2010). After the deposition of the MoS_2 on the sapphire wafer substrate, the XRD pattern reveals decreased intensity for all XRD peaks due to the micro-sized powder fragmentation by the high impact velocity with the hard sapphire wafer substrate.

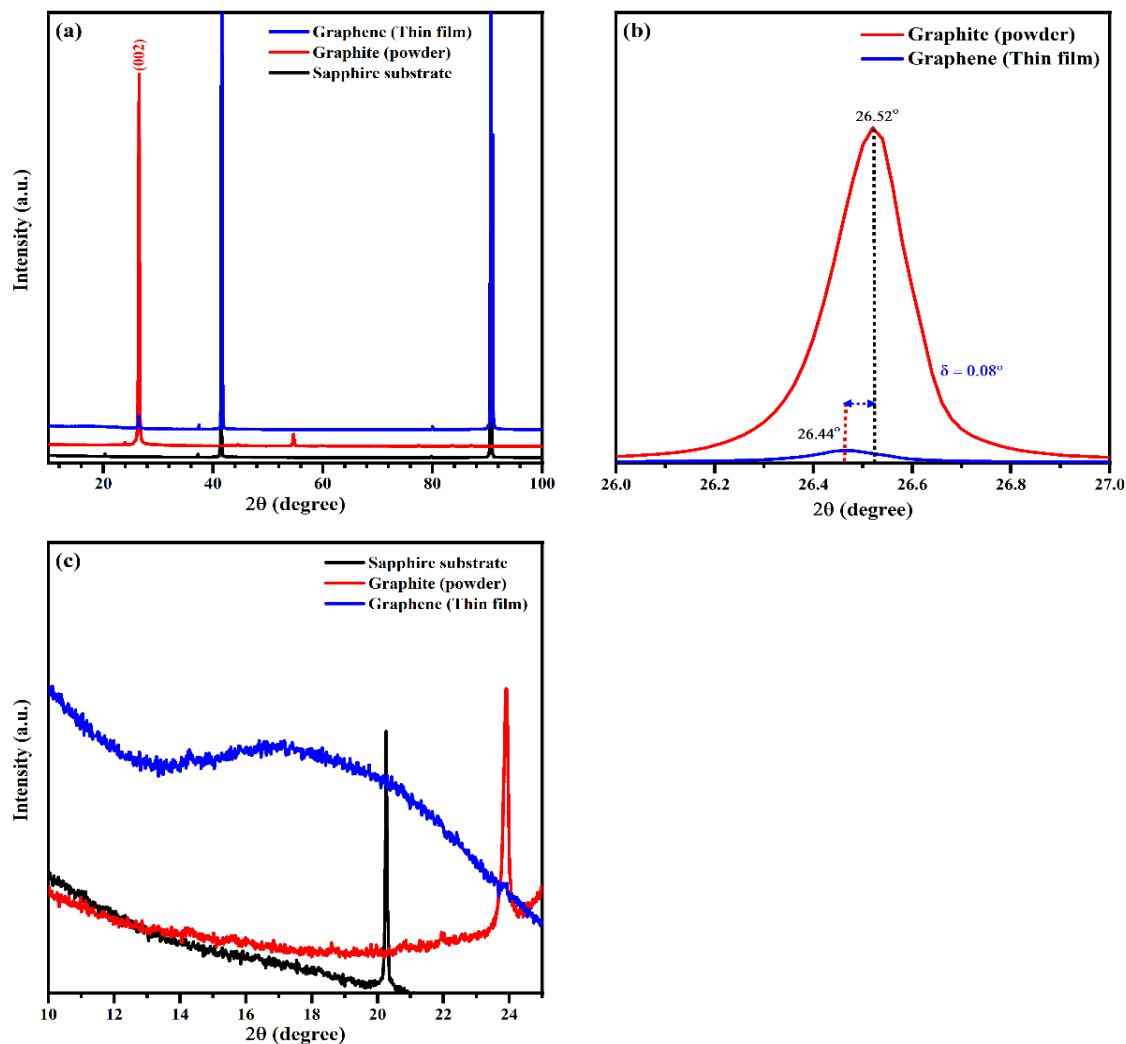


Figure 3. 2: XRD patterns of micro-sized graphite powder and the deposited nano-sized graphite thin film on a sapphire substrate.

The XRD peak of the micro-sized MoS_2 powder and the deposited thin-film corresponding to the (002) crystalline plane is magnified in **Figure 3. 3(b)** to identify the size variation in the crystalline domain. It can be observed that the XRD peak position is shifted to lower 2θ values upon deposition, as recorded in **Table 3. 1**. This shift indicates that the interplanar distance increased from 6.15 to 6.22 Å. Furthermore, the crystalline domain size, as determined by the Scherrer

equation, decreases from about 45 to 18 nm, which is accompanied by a greater than 2-fold increase in the local internal lattice strain, see **Table 3. 1**. This data confirms that the impact velocity in the vacuum kinetic spray process of the NPDS leading effectively causes micro-sized particle fragmentation as well as stacked-layer separation of layered MoS₂ material.

3. 3. 1. 3. BN

Figure 3. 4(a) exhibits the XRS patterns of the micro-sized powder of BN and the deposited nano-sized BN thin film on the sapphire wafer substrate. The XRD pattern of the micro-sized BN powder shows two main diffraction peaks at 26.72° and 55.12° that are related to the c-axis of the layered hexagonal structure of the BN phase. The most intense peak at 26.72° corresponds to the c-plane that is oriented along the (002) direction. The second peak, with lower intensity at 55.12°, corresponds to the c-plane along the (004) direction. The lattice parameters of the bulk hexagonal phase of the BN powder are $a = 2.5 \text{ \AA}$ and $c = 6.661 \text{ \AA}$, and the crystal symmetry operations are described by the P6₃/mmc space group (ICDD: 01-073-2095, PDF 2010) [96]. To demonstrate the induced structural changes in the layered structure of BN due to the high impact velocity of micro-sized powder with a hard substrate, the XRD patterns corresponding to the c-axis along the (002) crystalline plane orientation is magnified in **Figure 3. 4(b)**. It is obvious that the XRD peak position of the deposited BN shifts to lower 2θ values upon deposition, see **Table 3. 1**.

Table 3. 1: internal structural parameters of the hexagonal crystalline phase along the (002) planes in the micro-sized powder (P) and the corresponding thin films (TF) on a sapphire wafer substrate.

Materials	$2\theta_{(002)}^{\circ}$	$d_{(002)}(\text{\AA})$	$\beta_{(002)}^{\circ}$	$D_{(002)}(\text{nm})$	$\varepsilon_{(002)} \times 10^{-3}$
Graphite (P)	26.52 ^o	3.357	0.169	47.73	0.71844
Graphite (TF)	26.44 ^o	3.367	0.175	46.1	0.744
MoS ₂ (P)	14.38 ^o	6.152	0.175	45.20	0.758
MoS ₂ (TF)	14.22 ^o	6.220	0.436	18.15	1.889
BN (P)	26.72 ^o	3.332	0.203	39.70	0.863
BN (TF)	26.48 ^o	3.362	0.245	32.90	1.042

The observed shift is associated with an interplanar distance increase from 3.332 to 3.362 Å. Furthermore, according to the Scherrer equation, the crystalline domain size is decreased from about 39.7 to 32.9 nm increasing the internal lattice strain, see **Table 3. 1**. This indicates that the high-velocity impact in the vacuum kinetic spray process of the NPDS leads to fragmentation of the micro-sized BN particles and the deposition of very thin h-BN layers with lower stacking order

in the c direction compared to the initial micro-sized powder [108, 109]. These structural changes demonstrate the applicability of the vacuum kinetic spray of the NPDs for the effective mechanical exfoliation of micro-sized flake h-BN into nano-sized thin layers.

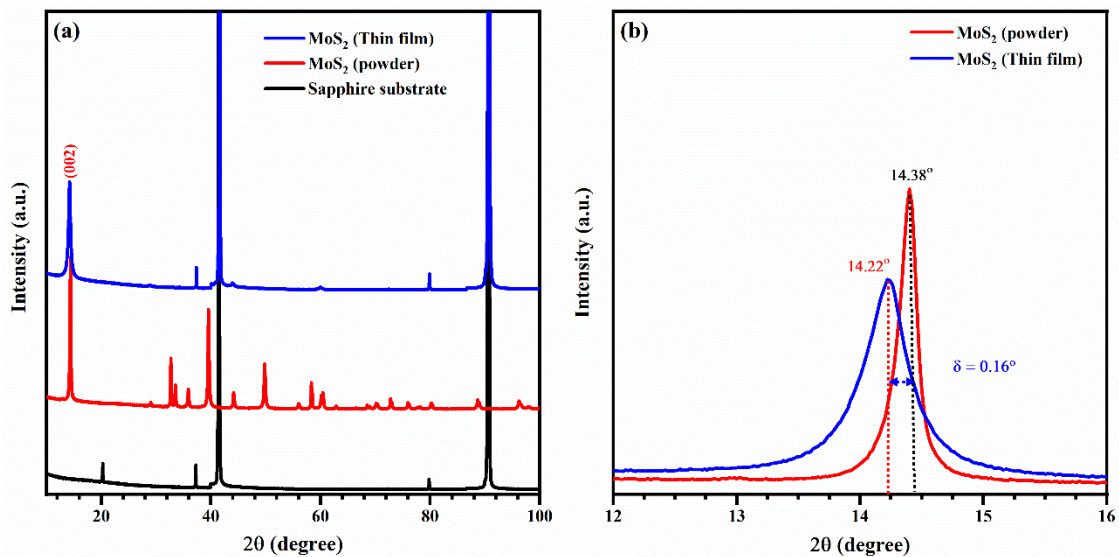


Figure 3. 3: XRD patterns of micro-sized MoS_2 powder and the corresponding deposited nano-sized thin film on a sapphire substrate

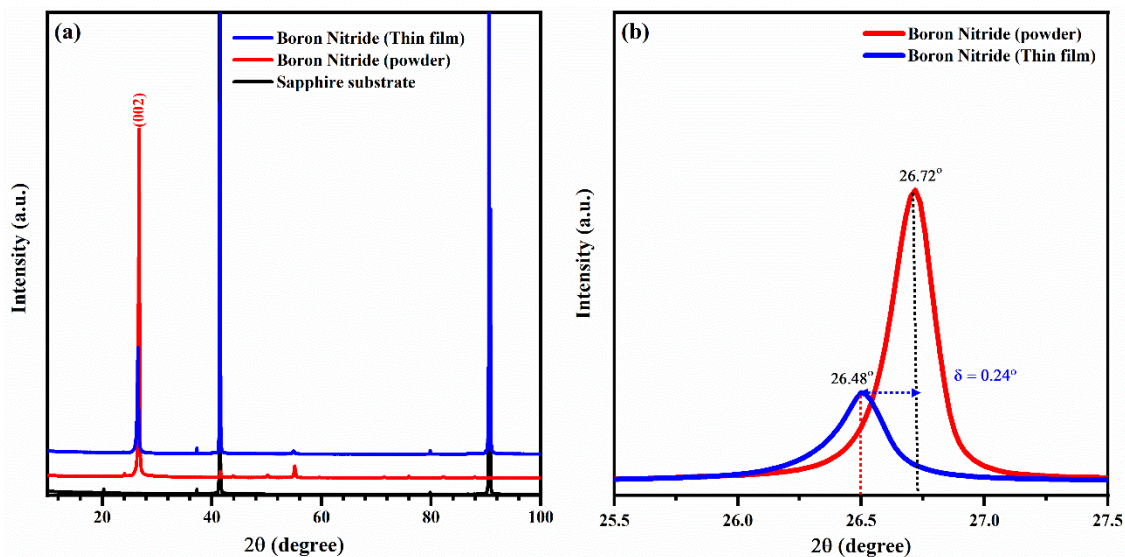


Figure 3. 4: XRD patterns of micro-sized boron nitride powder and the resulting deposited nano-sized thin film on a sapphire substrate

3. 3. 2. Morphological analysis of the layered materials powder and deposited thin films

Analysis of the surface morphology of the layered structure materials can visually demonstrate the reduction of particle size due to both the fragmentation and interlayer separation. **Figure 3. 5** exhibits the SEM images of graphite, MoS₂, and BN micro-sized powder and the corresponding thin films on the sapphire wafer substrate. The SEM images of all selected micro-sized powders reveal flake-like morphology with multiple stacked layers that are randomly oriented.

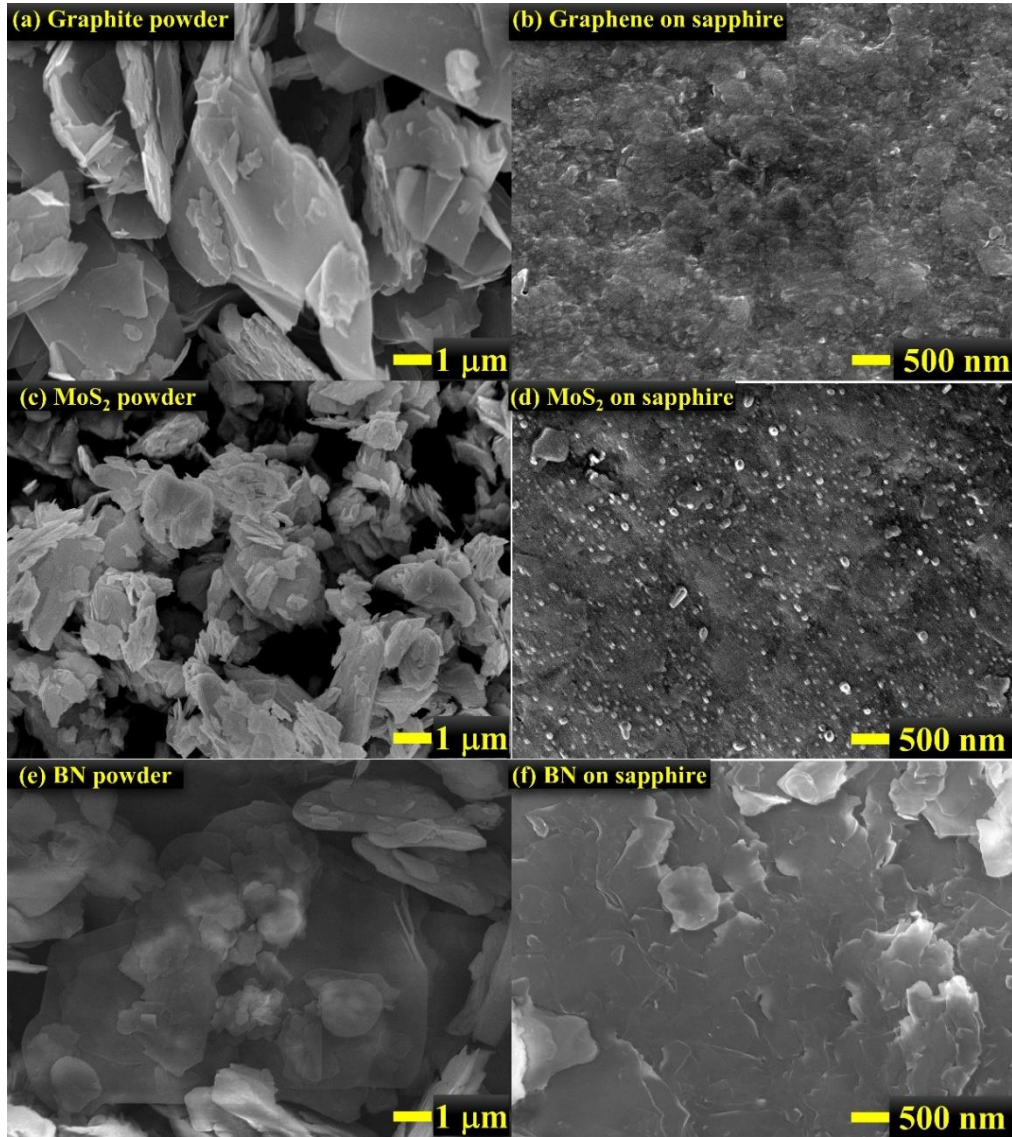


Figure 3. 5: SEM Images of the (a) micro-sized powder and (b) the deposited nano-sized thin film of graphite on a sapphire substrate, the (c) micro-sized powder and (d) the deposited nano-sized thin film of MoS₂ on a sapphire substrate. the (e) micro-sized powder and (f) the deposited nano-sized thin film of BN on a sapphire substrate.

The selected powders were chosen based on their commercial availability in the micro-size range, extending from 1 to 10 μm . After the deposition of the layered structure materials using the vacuum kinetic spray process of the NPDS on the sapphire wafer substrate. The SEM images of the deposited thin films exhibit a sharp reduction in the flake size to the nano-size range. The observed reduction in the particle size results from the fragmentation and interlayer separation process caused by the high-velocity impact of the micro-sized powder with the hard sapphire wafer substrate [101]. The sizes of the deposited graphene and MoS_2 nanosheets are less than 100 nm, whereas the deposited h-BN nanosheets show a lower degree of fragmentation, with sizes in the range of several hundreds of nanometers. Furthermore, the deposited nanosheets exhibit a low degree of stacking compared to the corresponding micro-sized flakes. This data demonstrates the interlayer separation of the powders and the applicability of kinetic-induced mechanical exfoliation of layered materials in a one-step NPDS process. The interlayer separation and particle fragmentation are further verified using Raman spectroscopy, as illustrated in the next section.

3. 3. 3. Raman studies

Micro-Raman spectroscopy is a powerful tool for detecting small variations in the structural phases of crystalline materials. The active Raman symmetry modes of the crystalline materials are strongly affected by grain size modifications. Hence, we used this technique to illustrate the effect of the kinetic induced micro-sized particle fragmentation and the accompanied exfoliation of stacked layers of the NPDS 2D on the size of the materials. The variation in the micro-Raman spectra of the various 2D materials studied, i.e., graphite, BN, and MoS_2 , are discussed in more detail as follows.

3. 3. 3. 1. Reduction of hexagonal graphite layered structure to graphene nanosheets

Figure 3. 6 shows the Raman spectra of the micro-sized graphite powder and the corresponding nano-sized thin films on the sapphire wafer substrate. The micro-Raman spectrum of the graphite powder exhibits several active vibrations at 1346, 1575, 2703, and 3231 cm^{-1} . The first-order vibration at 1346 cm^{-1} is attributed to those of the interfacial defects at the crystalline domain boundaries that are related to the D-symmetry mode of the micro-sized graphite powder. The first-order G-band of the graphite powder caused by the E_{2g} -symmetry mode is observed at 1575 cm^{-1} . This symmetry mode is related to the large degree of crystallinity in the micro-sized graphite powder [110]. Furthermore, the second-order vibrations at the Raman shifts of 2703 and

3231 cm^{-1} are attributed to active vibrations caused by the 2D-intervalley and 2D'-symmetry modes, respectively [111, 112]. In the case of the deposited graphite thin films on sapphire substrates, the Raman spectrum reveals several active vibrations at the Raman shift centers of 1350, 1587, 1619, 2693, and 2936 cm^{-1} . The first-order vibrations at 1350 and 1587 cm^{-1} in the nano-sized thin film corresponding to the characteristic D and G-bands, respectively, of the hexagonal graphite phase. These peak positions exhibit higher Raman shift values compared to those of the micro-sized powder. In contrast, the second-order vibration at 2693 cm^{-1} that is related to the 2D-symmetry mode has a lower Raman shift value in the thin film. The observed shifts of the first- and second-order vibrations can be attributed to the evolution of surface defects that are caused by the fragmentation and interlayer separation of the micro-sized powder to the very small sizes of the resulting nanosheets [113]. In addition, other structural defect-induced vibrations are observed at 1619 and 2936 cm^{-1} , which are ascribed to the translational displacement of carbon atoms from the internal lattice sites into the grain boundary interfaces, and the enhancement of the disorder-induced G'' band, respectively [114].

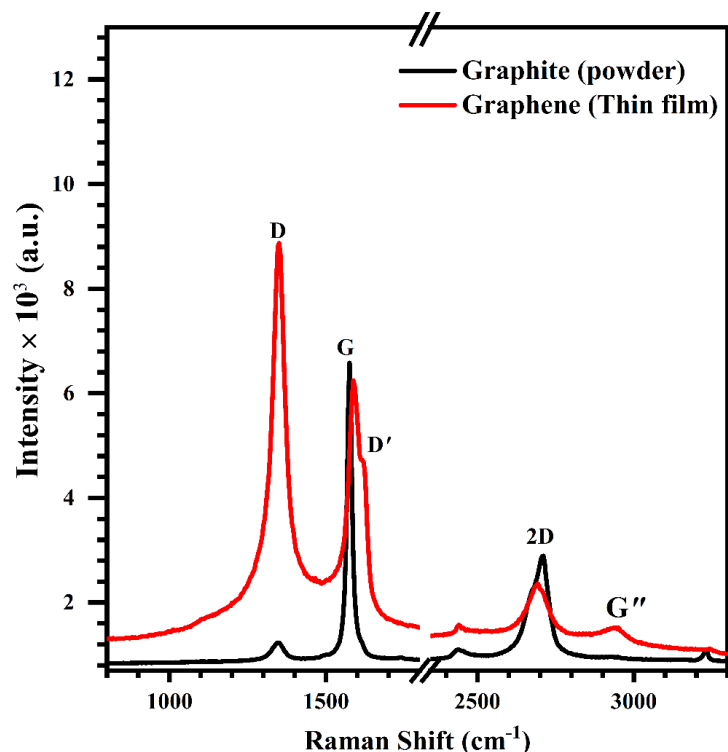


Figure 3. 6: Raman spectra of the micro-sized graphite powder and the deposited nano-sized thin films of graphite on a sapphire substrate.

The graphite to graphene nanosheets transformation through the microparticle size fragmentation and interlayer exfoliation is recognized from the improvement of disorder-related Raman modes (i.e., D and G^{''}) and the reduction of crystallinity-related Raman modes (i.e., G and 2D). This process can be verified from the Raman intensity ratio between the D and G-bands (I_D/I_G). In the case of the micro-sized graphite powder, the I_D/I_G ratio is 0.187, and this ratio dramatically increases to 1.42 for the deposited nano-sized thin film. This sharp increase in I_D/I_G indicates the fragmentation and layer separation of the micro-crystalline graphite to form small graphene nanosheets that are accompanied by the evolution of a high density of edge defects [115]. The reported I_D/I_G ratio of 1.42 is higher than those of other reports that achieved graphite exfoliation using other techniques [116-118]. This Raman data demonstrates the complete exfoliation of the graphite layered structure to result in graphene nanosheets in the one-step NPDS process.

3. 3. 3. 2. Reduction of hexagonal MoS₂ layered structure to small nanosheets

Figure 3. 7(a) exhibits the micro-Raman spectra of the micro-sized MoS₂ powder and the corresponding NPDS-fabricated nano-sized thin films on a sapphire wafer substrate. The spectra were fitted to evaluate the changes in Raman peak broadening induced by the interlayer separation and particle fragmentation of the deposition process (**Figure 3. 7(b, c)**). The Raman spectrum of the micro-sized MoS₂ powder exhibits two active Raman vibrations at 374 and 400 cm⁻¹. The first-order active vibration at 374 cm⁻¹ is ascribed to the in-plane vibration of the Mo-S bond corresponding to the E_{2g}¹-symmetry mode, whereas the first-order vibration at the higher Raman shift value of 400 cm⁻¹ is attributed to the out-of-plane vibration corresponding to the A_{1g}-symmetry mode. The peak position difference between the observed first-order vibration modes is 26 cm⁻¹. These peaks are characterized by the hexagonal MoS₂ structural phase [119-123]. After the deposition process, there is a spectral shift of around 3 cm⁻¹ to higher Raman shift values in both active Raman vibrations as well as a decrease in the peak intensity. The decrease in the Raman peak intensity is accompanied by a slight increase in the peak broadening. This behavior results from improvement of the lattice disorder caused by the fragmentation and interlayer separation of the micro-sized grains due to the high impact velocity during deposition [124].

3. 3. 3. 3. Reduction of hexagonal BN layered structure to small nanosheets

As previously mentioned, thickness variation has a profound effect on the active Raman vibrations of the symmetry modes of few-layer graphene, which can be observed from the change in the intensity ratio between the characteristic D and G bands of the layered graphite hexagonal

structure. Additionally, the hexagonal layered structure of MoS₂ exhibits thickness and size dependence of the characteristic Raman frequency of E_{12g} and A_{1g} bands. In the case of h-BN, there are no disorder-sensitive bands like the D-band of the layered graphite structure. Further, the variation in the characteristic G-band frequency of h-BN is not strongly affected by the number of stacked layers.

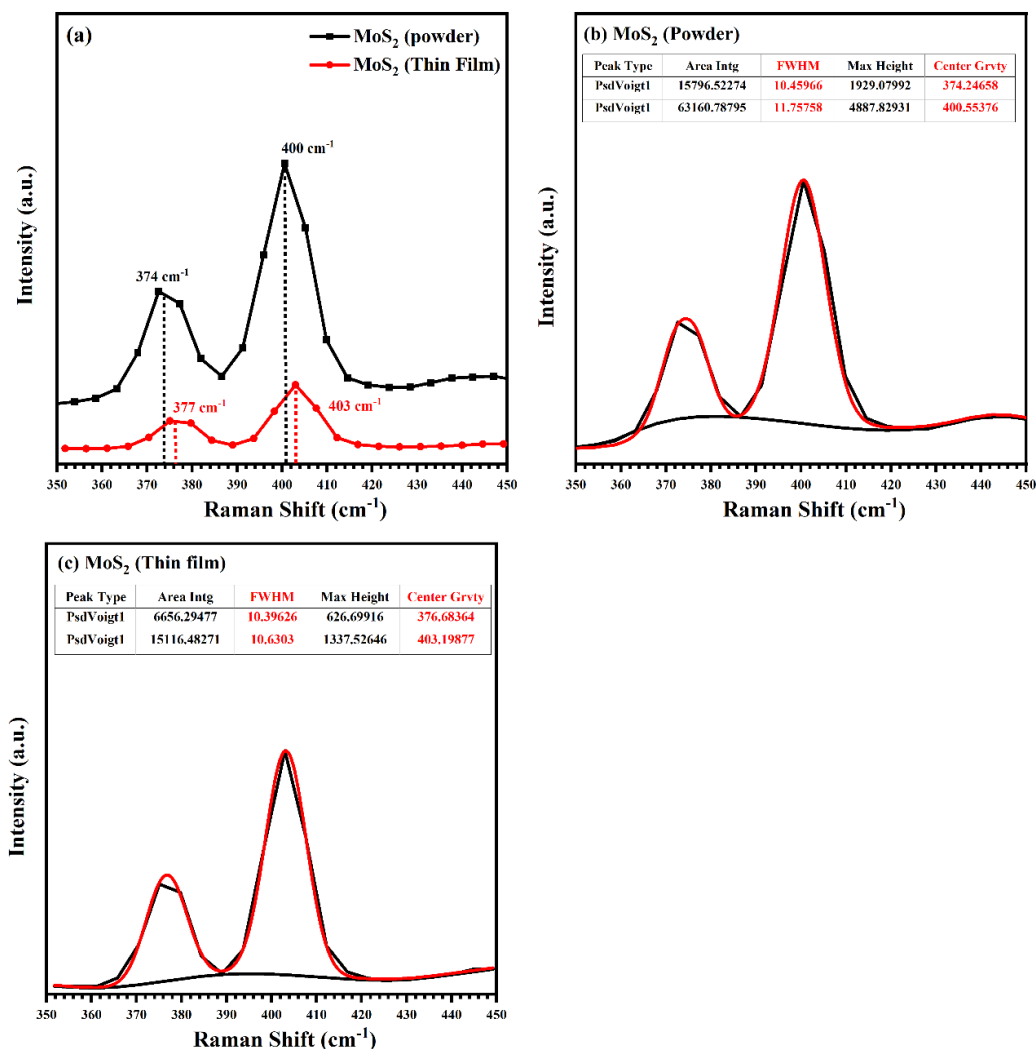


Figure 3. 7: Raman spectra of the (a) micro-sized MoS₂ powder and deposited nano-sized thin films of MoS₂ on a sapphire substrate. Raman peak fitting for the (b) powder and (c) deposited nanosized thin film spectra.

These characteristics pose challenges to recognizing the layer separation and size reduction induced by the mechanical exfoliation process using Raman spectroscopy. However, the induced internal lattice strain caused by the mechanical exfoliation process is expected to have a slight effect on the G-band frequency and a strong effect on the peak width and intensity [125]. **Figure 3. 8(a)** reveals the micro-Raman spectra of the micro-sized BN powder and the corresponding

nano-sized thin film of the sapphire wafer substrate. For quantitative analysis of the induced changes in the characteristic G-band of h-BN layered structure, a curve fitting process was performed on the peak, as shown in **Figure 3. 8(b, c)**.

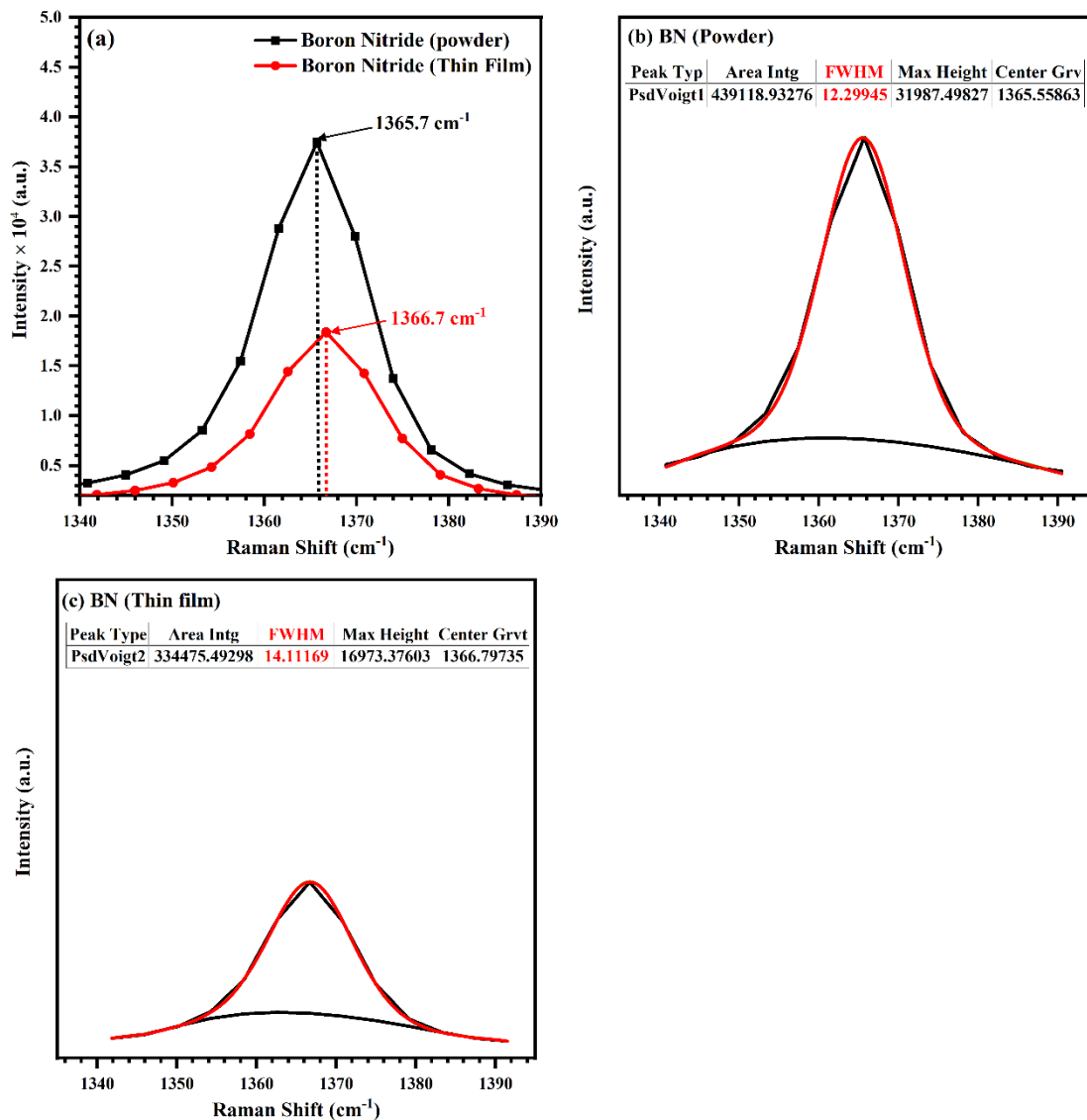


Figure 3. 8: Raman spectra of (a) the micro-sized BN powder and the deposited nano-sized thin films of BN on a sapphire substrate. Raman peak fitting for the (b) powder and (c) deposited nanosized thin film spectra.

The micro-Raman spectrum of the micro-sized h-BN powder exhibits an intense peak at a Raman shift of 1365.56 cm^{-1} that corresponds to the G-band of the layered h-BN structure [96]. After depositing the h-BN on the sapphire wafer substrate, the Raman spectrum profile of the G-band has various changes, such as a peak position upshift to 1366.8 cm^{-1} and a reduction of the peak intensity. The slight shift in the G-band frequency is believed to arise from the decrease of the

number of stacked layers in h-BN that is associated with the increase of in-plane strain and the weakness of the “lip-lip” interlayer interaction of nearby layers [126]. Furthermore, the full width at half the maximum of the G-band profile broadens from 12.3 to 14.11 upon deposition. This behavior indicates the interlayer separation and thinning of the layered h-BN to form smaller particles in the nano-size range and the enhancement of surface scattering at the grain boundary interfaces after the mechanical exfoliation process [127].

3.4. Summary

The mechanical exfoliation of the layered materials of graphite, MoS₂, and BN was successfully demonstrated using the room temperature vacuum kinetic spray process of the NPDS. The deposited nanostructured thin films on the sapphire substrate were analyzed using several techniques, including XRD, SEM, and Raman spectroscopy. The XRD pattern of deposited graphite thin films revealed a strong decrease in intensity of the XRD peak corresponding to the c-plane along with the (002) orientation as well as a shift of this peak’s position to a lower diffraction angle value. This result indicates the possibility of layer separation in the layered materials that was accompanied by interplanar distance increase. Furthermore, the disappearance of the oxygen-related XRD peak and the evolution of the broad band at 16.5° in the deposited thin film exhibited the total transformation of bulk graphite phase to small graphene nanosheets. The XRD patterns of the deposited MoS₂ and BN thin films also showed intensity reduction of all peaks, demonstrating the crystalline domain of micro-sized powder fragmentation to smaller sizes. Furthermore, the XRD peak of the c-plane along the (002) orientation revealed a decrease in the intensity and shift to lower 2θ. This behavior results from the interlayer separation of the material’s stacked layers, which is associated with interplanar distance increase due to the weakness of interlayer interaction. Comparison of SEM images of the powder of the layered materials (i.e., graphite, MoS₂, and BN) before and after the deposition exhibited the fragmentation and layer thinning of the micro-sized flakes morphology to small size nanosheets morphology upon deposition. The observed degree of kinetic-induced fragmentation and layer thinning in the micro-sized graphite and MoS₂ powder was greater than that of the BN powder. The Raman spectrum of the deposited graphite thin film revealed the total transformation of the crystalline graphite bulk phase to few-layers graphene nanosheets, in which the intensity of the disorder-related D-band is strongly improved and the intensity of the characteristic G-band was strongly diminished compared to the bulk crystalline graphite phase. The interlayer separation in the deposited MoS₂ and BN thin films was recognized from the observed variation in the Raman active E¹_{2g}

and A_{1g} -symmetry modes of the hexagonal MoS_2 phase and the G-band for the hexagonal BN phase. The Raman peak profiles of these symmetry modes exhibited an intensity decrease, FWHM increase, and spectral shift to higher wavenumber values in the deposited thin films. These features demonstrated the applicability of using the one-step vacuum kinetic spray process in the low vacuum condition for the mechanical exfoliation of layered materials using the NPDS. This simple and effective technique provides good insight for how to achieve mechanical exfoliation and large-size deposition of layered materials in a short time with a reasonable cost, which is desirable for the implementation in real-life applications.

Chapter 4:

Composition Dependent Electrocatalytic Activity of Ni(OH)₂-Graphene Hybrid Catalyst Deposited by One-Step Vacuum Kinetic Spray Technique

4. 1. Overview

The need to replace nonrenewable energy sources has become the main interest of many researchers all over the world. This arises from the dramatic increase in environmental problems (e.g., global warming and air pollution) because of the huge consumption of fossil fuel energy sources. Electrochemical water splitting is a promising technology for storing electrical energy without pollution since the electrocatalytic reaction secondary products are hydrogen and oxygen [128]. However, the two reaction parts involved in the overall water electrolysis (i.e., the oxygen evolution reaction [OER] and hydrogen evolution reaction [HER]) still face some limitations that either decrease the electrochemical efficiency or increase the manufacturing costs of the noble metal-based catalysts used for the overall water electrolysis [129].

Ni metal is a relatively earth-abundant element with a low price compared with other metals. In addition, a 3D porous structure of Ni foam (NF) with superior conductivity was used as a conductive substrate for many efficient electrocatalysts [75, 130, 131]. Ni-based catalysts revealed electrocatalytic activities with high efficiency and long-term stability in an alkaline medium. Hence, Ni-based catalysts are considered to be promising candidates for many electrochemical applications such as Li-ion batteries [132], supercapacitors [133, 134], and water oxidation in an alkaline medium, as demonstrated by Louie et al., [135] who investigated the OER activity of electrodeposited Ni-Fe catalysts. They found that the incorporation of Fe enhances the OER compared to the bare Ni catalyst. Du et al., [136] have investigated theoretically and experimentally the effect of transition metal doping (Co, Cu, and V) on the electrocatalytic activity of NiSe/Ni foam catalyst toward the overall water splitting. They found that V-NiSe/Ni foam exhibited high activity toward the OER, meanwhile, Cu-NiSe/Ni foam revealed high activity toward the HER. Ni(OH)₂/Ni foam catalysts revealed high efficiency toward overall water splitting and stability in an alkaline medium. This is due to the efficiency of Ni(OH)₂ in H-OH bond cleaving, which is useful in the first step of water dissociation. In addition, Ni foam is distinguished by the high adsorption and recombination characteristics toward adsorbed hydrogen [137]. Subbaraman et al. [138] reported that the decoration of a Pt electrode by nanostructured Ni(OH)₂ improved the electrocatalytic activity toward the HER significantly compared with the bare Pt electrode. They attributed this improvement to the enhanced water dissociation rate and the production of hydrogen intermediate. Gao et al. [139] compared the electrocatalytic activity of α and β -Ni(OH)₂ structural phases toward the OER in 0.1 M KOH. Their results showed that α -Ni(OH)₂ has a higher OER activity and longer temporal stability compared with β -Ni(OH)₂. Rao et al. [129] prepared Ni(OH)₂ nanosheets on Ni foam by the hydrothermal technique that

revealed good electrocatalytic activity toward OER and HER with long term stability up to 24 hours in 1.0 M KOH. Lee et al. [140] decorated Ni(OH)₂ nanosheets with a small layer of RuO₂ using Ni foam corrosion in a RuCl₃ aqueous solution. They found that their composite has a better overall water splitting efficacy than the commercial Pt wire electrode. Kong et al. [141] designed Zn-embedded Ni(OH)₂ nanosheets using a sol-gel method. The obtained catalysts exhibited higher OER activity than the pristine Ni(OH)₂. Du et al. [142] synthesized hierarchical Ni(OH)₂-Ni₃S₂/Ni foam nanosheets using a two-step method involving co-precipitation and sulfurization. They showed that the synergetic effect between Ni(OH)₂ and Ni₃S₂ improved the overall water splitting and produced 10 mA·cm⁻² with a low cell potential of 1.57 mV in 1.0 M KOH. Xu et al. [143] synthesized self-assembled ultrathin Ni(OH)₂/Ni₃S₂ heterogeneous nanosheets with strong quantum confinement (dimensions~1.8nm) that revealed superior electrocatalytic activity toward both OER and HER with high stability. Trotochaud et al.[144] investigated the OER electrocatalytic activity of several Ni-based composites in 1.0 M KOH. They found that the Ni_{0.9}Fe_{0.10x} composite had the highest OER activity. In addition, this composite catalyst delivered 10 mA·cm⁻² at an overpotential of 336 mV with a Tafel slope of 30 mV·dec⁻¹. Klaus et al. [145] revealed an improvement in the OER activity of a Ni(OH)₂/Au-Ti quartz cell in 1.0 M KOH due to the addition of Fe as an impurity in the electrolyte. The hybridization between Ni(OH)₂ and graphene in composites was intensively investigated for use in many electrochemical applications [146-152]. Chen et al. [134] reported that the incorporation of ternary hydroxides (i.e., Ni-Co double hydroxide) into N-doped graphene catalysts could improve the OER activity. Subramanya et al. [153] illustrated that Co-Ni-graphene composites have a higher HER activity compared with the bare Co-Ni composite in an alkaline medium. Huang et al. [154] demonstrated that adding Ni to graphene catalysts improved the electrocatalytic activity toward the HER in the alkaline medium. Xue et al., [155] reported the role of anchoring graphdiyne by single atoms with a very narrow size distribution of Ni (1.02 Å) on the improvement of electrocatalytic activity and stability toward the HER. Moreover, Xing et al., [156] illustrated that using the three-dimensional porous fluorographdiyne exhibited improvement in the catalytic activity toward both the OER and HER in KOH. Long et al. [157] illustrated that NiFe double-layered hydroxide-graphene composites reveal a high OER activity in 1.0 M KOH since it could provide 10 mA·cm⁻² at an overpotential value of 195 mV. Tang et al. [158] revealed that a NiFe double-layered hydroxide-hybrid with carbon quantum dots possessed a high OER activity with a current density of 10 mA·cm⁻² at an overpotential of 235 mV. However, the preparation of graphene-based composites was extensively studied by various fabrication techniques there is still a great need for other techniques that capable to be scaled up for large

size production with reasonable production cost and relatively short fabrication time. Hence, we report a one-step preparation of graphene-based composites using a modified kinetic spray technique called nanoparticle deposition system (NPDS). This technique is a simple and economical coating technique for the direct deposition of nano-sized thin films using a starting micro-sized powder at room temperature without binders or any other chemical treatment, short fabrication time relative to other techniques. In addition, it is easy to scale up for commercial production [70, 100]. Several previous papers have illustrated the applicability of the NPDS in the deposition of various types of metal, ceramic [159-162], and carbon-based composites thin film [163-168]. Moreover, the deposition mechanism of graphene nanosheets on metal substrates was theoretically investigated through our research group by Nasim et al. [101], which illustrated that at a specific critical impact velocity the graphene nanosheets is deposited on the metal substrate surface after the interlayer separation of the initial bulk graphite powder. The effect of the NPDS deposition parameters on the electrochemical performance as supercapacitor for the graphene nanoflakes and Ni(OH)₂ nanosheets were separately investigated through our research group by Mohamed et al. [167, 169].

In the present research, we illustrate the deposition of Ni(OH)₂-graphene nanosheet hybrid catalysts on Ni foam by NPDS with relatively cheap and abundant micro-sized particles of Ni(OH)₂ and graphite powder without any chemical treatment. In addition, we investigated the effect of composition variation on the electrocatalytic activity of the Ni(OH)₂-graphene composites toward the oxygen evolution reaction (OER), and the hydrogen evolution reaction in 1.0 M KOH.

4. 2. Results and discussion

4. 2. 1. Structural analysis of the Ni(OH)₂-graphene composites

4. 2. 1. 1 Ni(OH)₂ -graphite composite powder before deposition

Figure 4. 1(a) shows the XRD pattern of the initial graphite powder. The most intense peak at 26.5° corresponds to the preferred orientation of the crystalline plane (002) along the c-axis of the hexagonal bulk structure of the graphite (ICDD: 00-056-016, PDF 2010). In addition, the observed sharpness, and the high intensity of the XRD peaks indicate the large size of the crystalline domain. **Figure 4. 1(d)** illustrates the XRD pattern of the Ni(OH)₂ powder that consists of several diffraction peaks matching the trigonal structure of the bulk β-Ni(OH)₂ (ICDD: 00-057-0907, PDF 2010). Moreover, the XRD peaks showed variations in their broadening due to the polycrystalline nature of the Ni(OH)₂ powder [170]. In the cases of the mixed Ni(OH)₂-graphite composites at either 20 or 80 wt.% of Ni(OH)₂, the XRD patterns

in **Figure 4. 1(b, c)** exhibit peaks for the individual structural phases of Ni(OH)₂ and graphite without any noticeable change in the peak position or any new XRD peaks corresponding to a new hybrid structural phase. Moreover, the XRD patterns of the mixed Ni(OH)₂-graphite composites had broader peaks with smaller diffraction peak intensity due to the relative fragmentation of the powder particles during the ball milling process and the decrease in crystalline domain size.

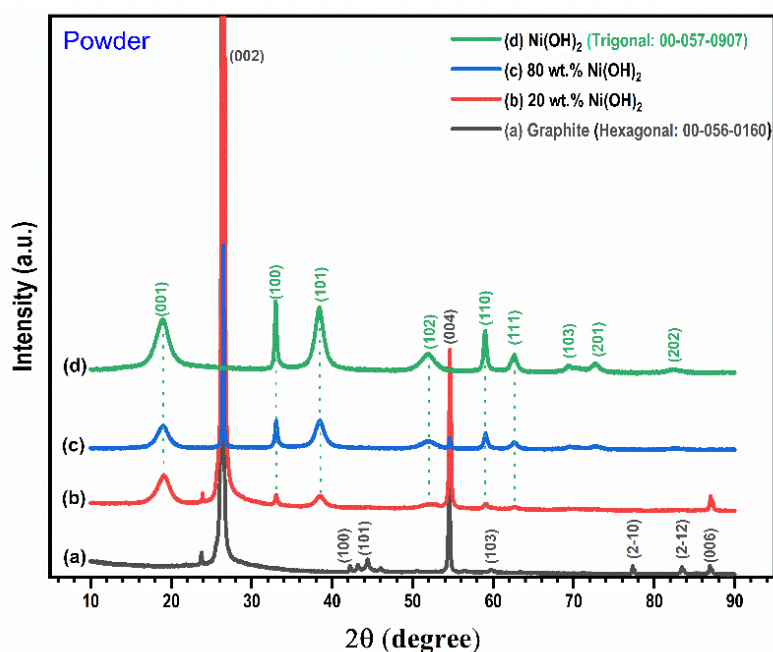


Figure 4. 1: XRD patterns of the Ni(OH)₂-graphene composite powder at different Ni(OH)₂ contents

4. 2. 1. 2 Ni(OH)₂ -graphene composite/Ni foam thin films

Figure 4. 2 reveals the XRD patterns of the pure phases of Ni(OH)₂ and graphite, as well as their composites deposited on the porous Ni foam substrate. All XRD peaks of the deposited films for the pure phases and their composites with Ni(OH)₂ content either at 20 or 80 wt.% correspond to the cubic structure of the Ni foam (ICDD: 00-004-0850, PDF 2010), with no detectable diffraction peaks related to the micro-sized particles of either graphite or Ni(OH)₂ powder. This behavior could be ascribed to the short-range order of the deposited crystalline domains (i.e., low crystallinity) and the low loading mass of the deposited films (~ 2.5 mg·cm²) compared with the Ni foam substrate that has high crystallinity. Moreover, the observed broadened XRD peak in the 2θ range of 16–18° for the pure phases (i.e., graphite or Ni(OH)₂) could arise from the fragmentation of micro-sized particles and the formation of polycrystalline domains with very short-range order, as they tend to be amorphous [147]. So, other techniques such as Raman spectroscopy and SEM images at various magnifications were used to identify the presented

phases in the deposited thin film and to determine the size range of the deposited layers after the fragmentation process.

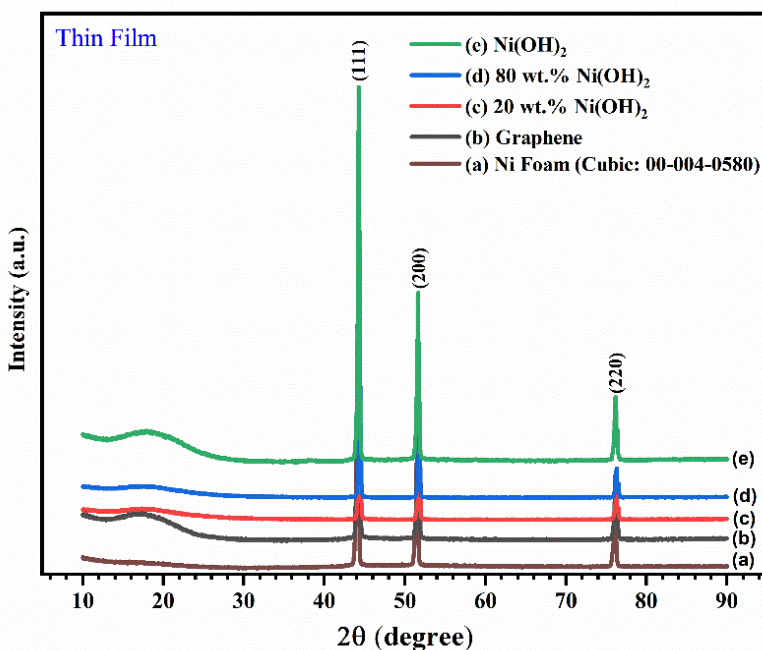


Figure 4. 2: XRD patterns of $\text{Ni}(\text{OH})_2$ -graphene composite/NF at different $\text{Ni}(\text{OH})_2$ contents

4. 2. 2. Raman spectra of the $\text{Ni}(\text{OH})_2$ -graphene composites

4. 2. 2. 1. $\text{Ni}(\text{OH})_2$ -graphite composite powder before deposition

Figure 4. 3(a) illustrates the Raman spectrum of the graphite powder that consists of 3 main vibration peaks located at 1352, 1582, and 2720 cm^{-1} corresponding to the D, G, and 2D vibration bands, respectively. The observed intense peak (i.e., G-band) at 1582 cm^{-1} arises from the double degeneracy of the zone center in E_{2g} mode [171]. The Raman spectrum of $\text{Ni}(\text{OH})_2$ powder in **Figure 4. 3(d)** reveals three characteristic vibration bands at 310, 445, and 3570 cm^{-1} . The observed vibration band at 3570 cm^{-1} is attributed to the symmetric stretching of the O-H bond from either the lattice hydroxyl group (OH) or intersheet H_2O [172]. The observed Raman peaks at 445 and 310 cm^{-1} were assigned to the stretching vibration Ni-O and the E-type vibration of the Ni-OH lattice, respectively [173]. In the case of the $\text{Ni}(\text{OH})_2$ -graphite powder composites with $\text{Ni}(\text{OH})_2$ contents of 20 and 80 wt.%, Raman spectra in **Figure 4. 3(b, c)** revealed the existence of the three main vibration bands of the graphite powder with slight variations in the peak positions (5-7 cm^{-1}). There were no other peaks related to the pure $\text{Ni}(\text{OH})_2$ powder. Moreover, the evolution of a small vibration band in the range from 3236-3240 cm^{-1} for both composites (20 and 80 wt.% $\text{Ni}(\text{OH})_2$ content) was caused by the formation of free hydroxyl anions [174].

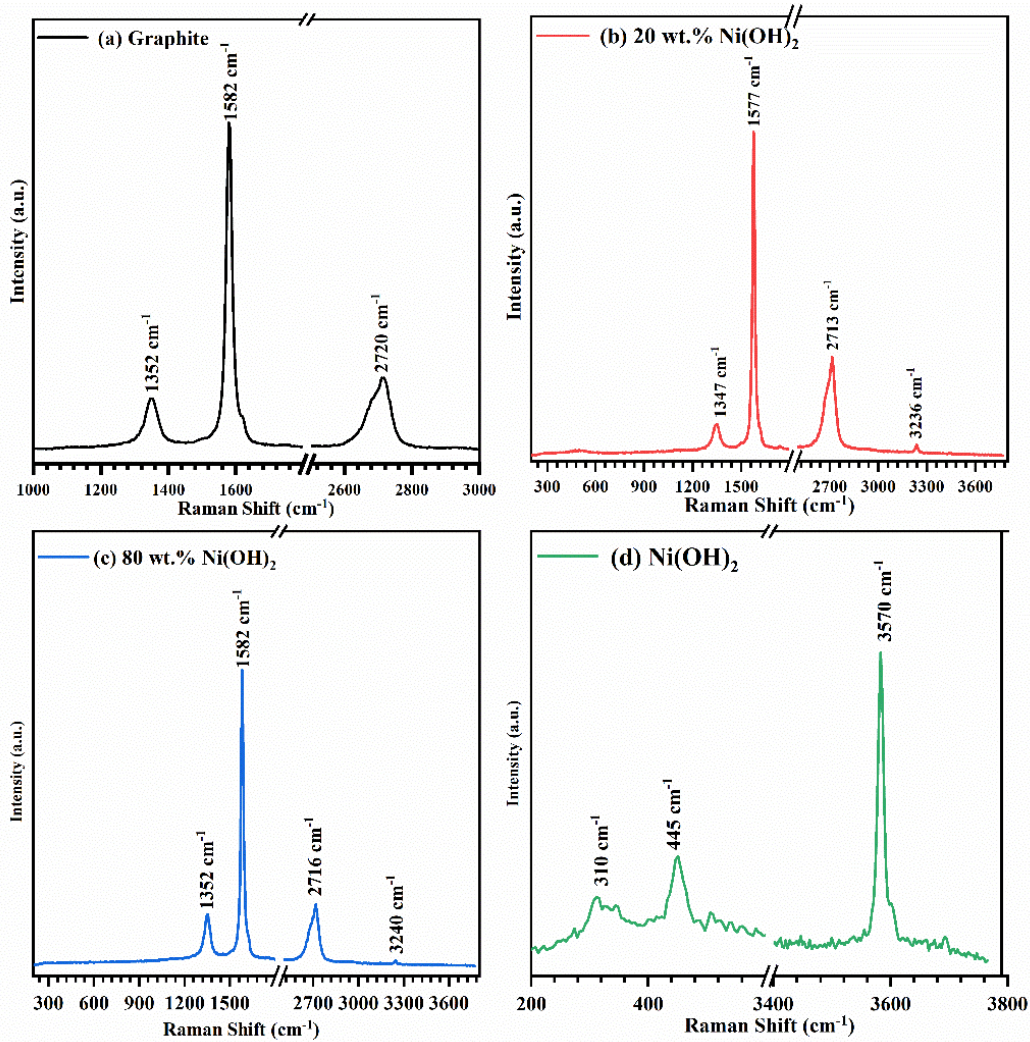


Figure 4. 3: Raman spectra of (a) graphite, (b) 20 wt.% Ni(OH)₂, (c) 80 wt.% Ni(OH)₂, and (d) Ni(OH)₂ powder.

4. 2. 2. 2. Ni(OH)₂ -graphene composite/Ni foam thin films

Figure 4. 4(a) demonstrates the Raman spectrum of the deposited graphite thin films on Ni foam that possess vibration bands at 1352, 1592, and 2695 cm⁻¹ with slight variations in peak position relative to the initial graphite powder. The observed vibration peak at 1352 cm⁻¹ is due to the first-order vibration band D. The second peak at 1592 cm⁻¹ is due to the first-order vibration band G. Meanwhile, the characteristic second-order vibration band 2D was observed at 2695 cm⁻¹. The intensity ratio between D/G vibration bands in the case of the deposited thin film (ID/IG=1.32) was higher than the corresponding value in the graphite powder (ID/IG=0.34), **Figure 4. 3(a)**.

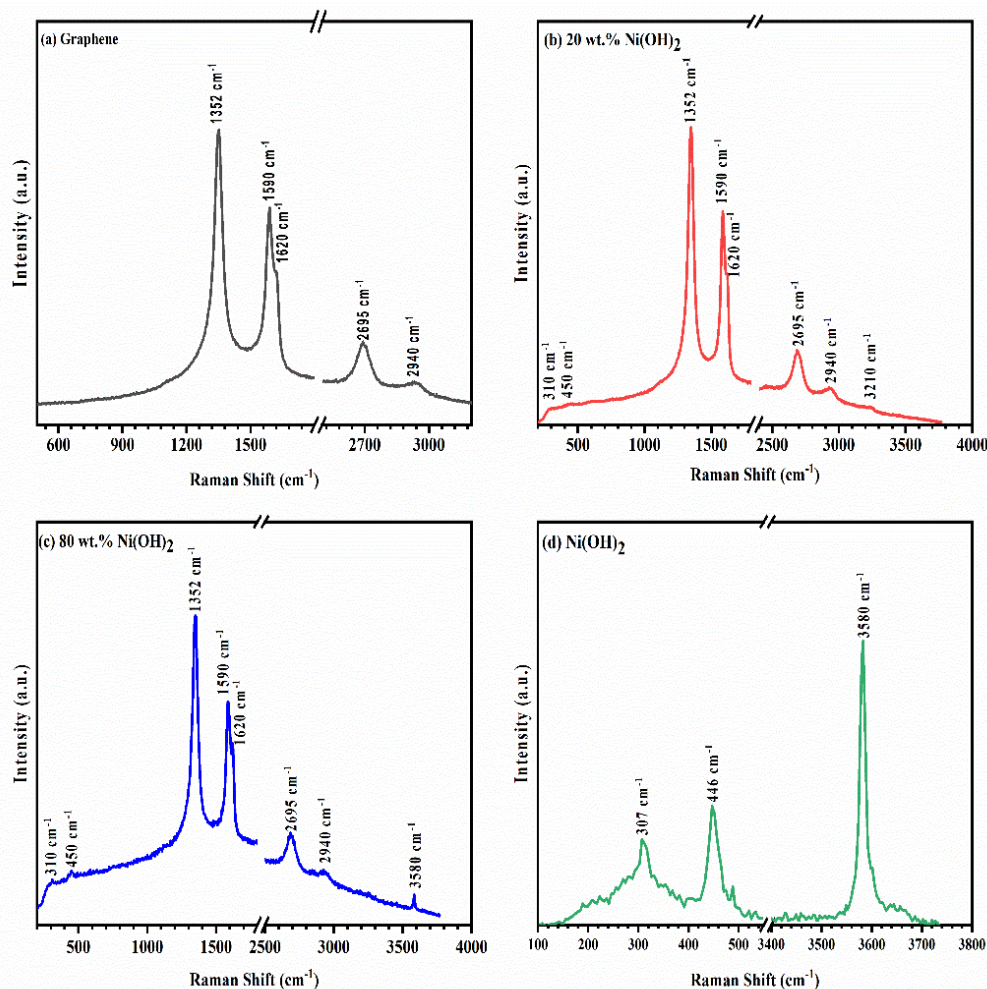


Figure 4. 4: Raman spectra of the (a) graphene/NF, (b) 20 wt.% Ni(OH)₂-80 wt.% graphene/NF, (c) 80 wt.% Ni(OH)₂-20 wt.% graphene/NF, and (d) Ni(OH)₂/NF

This behavior is commonly observed due to the fragmentation of the micro-sized graphite flakes to thinner graphene layers in the nano-size range (i.e., the decrease of domain size in the sp² plane), accompanied by the formation of a large number of edge defects [115]. The Raman spectrum, **Figure 4. 4(d)**, of the deposited Ni(OH)₂/NF, revealed the same vibration bands related to the powder at 307, 445, and 3580 cm⁻¹ with slight variations in the positions of the peaks. The Raman spectra of the deposited Ni(OH)₂-graphene composites with Ni(OH)₂ contents of 20 and 80 wt.%, **Figure 4. 4(b, c)**, revealed first-order vibration bands of D at 1352 cm⁻¹ and G at 1590 cm⁻¹. The second-order vibration band of 2D was observed at 2695 cm⁻¹ and was accompanied by a very weak band corresponding to the second-order 2G at 3210 cm⁻¹. The vibration bands corresponding to Ni(OH)₂ at 310, and 445 cm⁻¹ had very low intensity compared to the other active vibration modes in the composite. The intensity ratios (ID/IG) in the case of composites with Ni(OH)₂

contents of 20 and 80 wt.% were 1.33 and 1.17, respectively. This indicates the existence of a small graphene layer in each composite.

4. 2. 3. Surface analysis of the Ni(OH)₂-graphene composite/Ni foam thin films

Further investigations on the composition and the nature of the chemical bonding of the deposited Ni(OH)₂-graphene hybrid catalysts on the surface of the NF substrate were carried out using x-ray photoelectron spectroscopy (XPS). **Figure 4. 5(a)** reveals the survey spectrum of the Ni(OH)₂-graphene composite with 20 wt.% Ni(OH)₂ content. The XPS survey spectrum verified the presence of Ni, O, and C elements in the deposited composite. **Figure 4. 5(b)** shows the XPS spectrum of the Ni 2p orbital with two main spin-orbital states corresponding to 2p_{3/2} and 2p_{1/2} at 856.6, and 874.2 eV, respectively. The spin energy separation between the main Ni 2p orbitals is 17.6 eV [48]. We also observed satellite peaks at 862.4 eV and 880.5 eV corresponding to 2p_{3/2}(s), and 2p_{1/2}(s), respectively. These satellite peaks are caused by the degeneracy of the main spin-orbital states in the Ni(OH)₂ phases [115, 151, 152]. The deconvoluted spectrum of the O 1s orbital, **Figure 4. 5(c)**, indicates various oxygen-related bonded states such as C-O-Ni, C=O/O-Ni, and C-OH/C-O-C at 531.36, 532.14, and 533.1 eV, respectively. On the other hand, the deconvoluted XPS spectrum of the C 1s band in **Figure 4. 5 (d)** revealed the existence of multiple functional groups that include oxygen, such as C-O at 285.62 eV, and O=C-OH at 289.3 eV as well as the characteristic single-bonded carbon atoms C-C at 284.63 eV [115, 150, 175, 176]. Most of the above-mentioned functional groups detected in either O 1s or C 1s are hydrophilic groups that enhance the wettability of the electrode surface. They also induce more active sites at the electrode surface and improve the electrochemical properties at the electrode/electrolyte interface [177]. For demonstrating the mechanism of water oxidation in the alkaline medium in terms of surface chemistry modifications of the real catalyst during OER due to changes in the transition metal-based catalysts oxidation state, XPS analysis was performed for the Ni(OH)₂-graphene hybrid catalysts with 20 wt.% Ni(OH)₂ content after OER test and after OER stability test for 25 hours in 1.0 M KOH as shown in **Figure 4. 6**. XPS survey spectrum of the Ni(OH)₂-graphene hybrid catalyst, **Figure 4. 6(a)**, revealed the presence of Ni, O, and C elements after the OER test, which have the same origin for the as-deposited hybrid catalyst with 20 wt.% Ni(OH)₂. **Figure 4. 6(b)** revealed the high-resolution XPS spectrum for the Ni 2p orbitals, which consists of two main spin-orbital 2p_{3/2} at 855.6 eV, and 2p_{1/2} at 873.2 eV, which possessed the same spin energy separation between the main Ni 2p orbitals is 17.6 eV. As well as the

accompanied satellite peaks at 861.4 eV and 879.5 eV corresponding to $2p_{3/2}(s)$, and $2p_{1/2}(s)$, respectively.

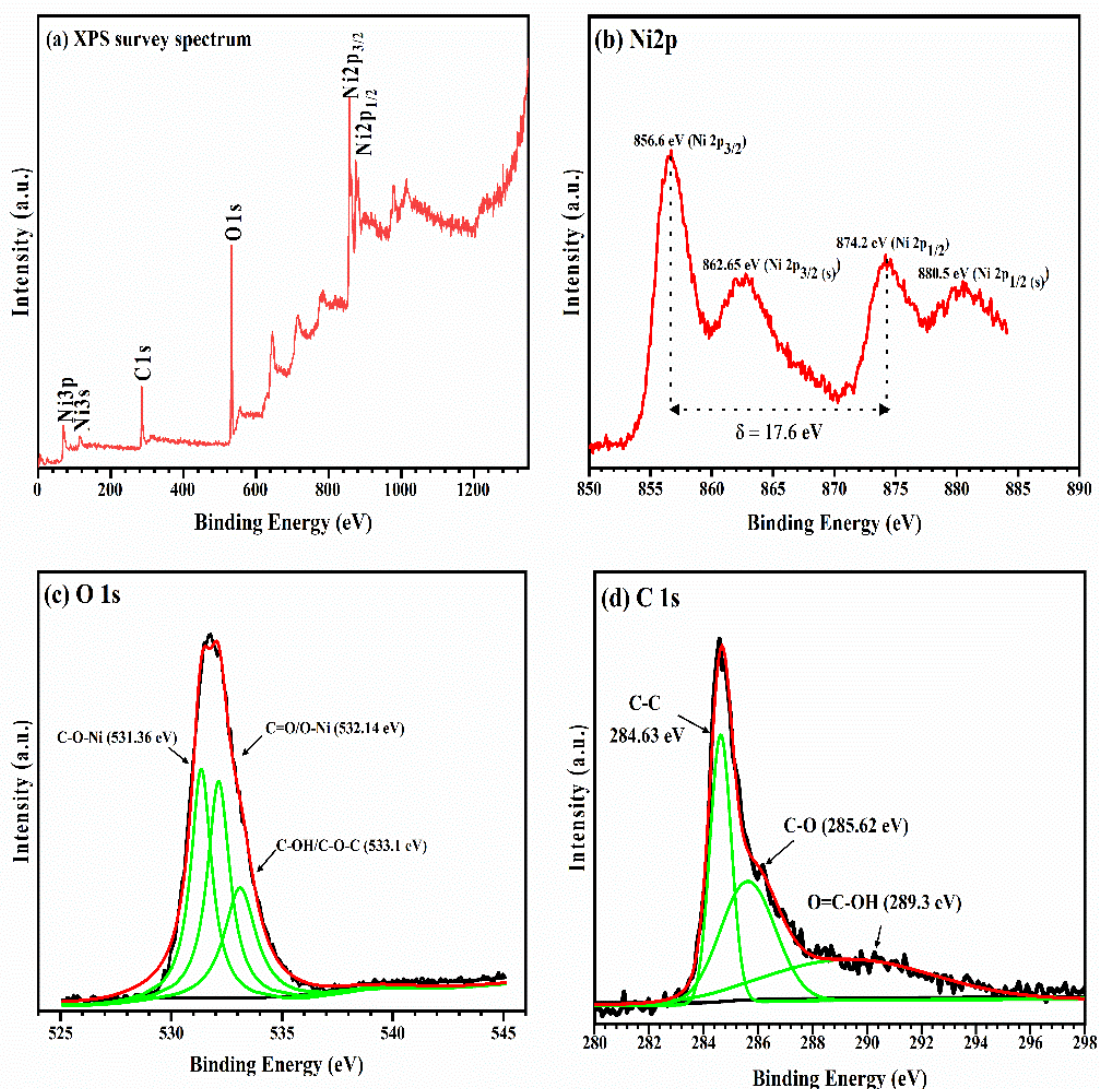


Figure 4. 5: XPS survey spectrum, **(b)** Ni 2p spectrum, **(c)** deconvolution of O 1s spectrum, and **(d)** deconvolution of C 1s spectrum of 20 wt.% Ni(OH)₂-80 wt.% graphene/NF

It can be observed that all Ni 2p XPS peaks are shifted to a lower binding energy side by about 1 eV after the OER. This chemical shift in the binding energy is ascribed to the electrochemical induced phase transformations of Ni(OH)₂ to layered structured of Ni(OH)₂/NiOOH on the surface of the hybrid catalysts, which is more active toward the OER. This phase transformation is accompanied by an increase of Ni oxidation state from Ni²⁺ to Ni³⁺ during the oxygen evolution reactions [178]. Similar behavior was observed in the case of O 1s orbital, in which the

corresponding high-resolution XPS spectrum in **Figure 4. 6(c)** revealed the chemical shift by about 1 eV in the binding energy to the lower energy side. This feature is also related to the formation of NiOOH on the surface of the catalyst [142, 179]. The high-resolution XPS spectrum of C 1s after OER revealed no significant shift in the main band in addition to the evolution of new surface states at nearly 292.5 eV, and 295.3 eV. It can be observed that the first band at 292.5 eV is increased after the OER stability test, which can be ascribed to the evolution of the carboxyl function group as a result of hybrid catalysts interaction with oxygen during the OER [180]. Meanwhile, the weak band at nearly 295.3 eV did not change after the OER stability test, which can be attributed to the K 2p_{3/2} of the adsorbed of the used KOH electrolyte in the OER test [181]. The XPS survey spectrum of the 80wt.% Ni(OH)₂-20 wt.% graphene composite/Ni foam in **Figure 4. 7(a)** reveals the existence of Ni, O, and C elements in the deposited composite.

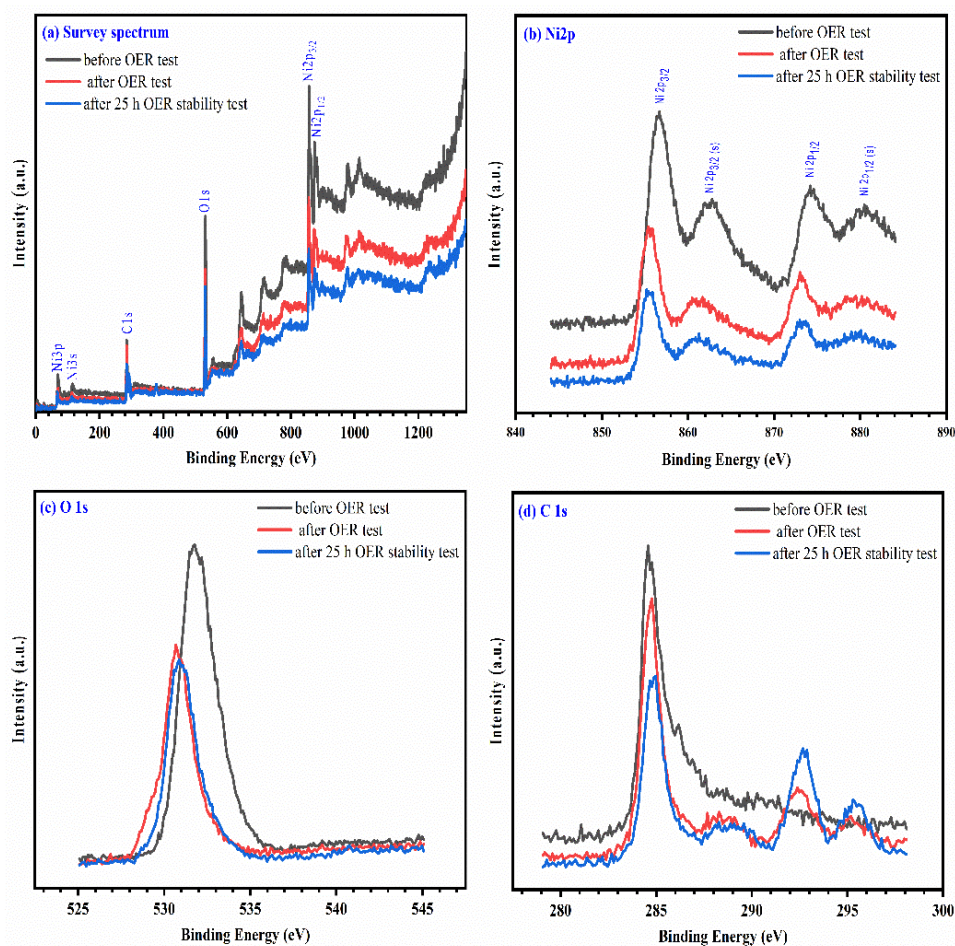


Figure 4. 6: XPS survey spectrum **(a)**, Ni 2p spectrum **(b)**, O 1s spectrum **(c)**, and C 1s spectrum **(d)** of 20 wt.% Ni(OH)₂-80 wt.% graphene/NF before and after OER test

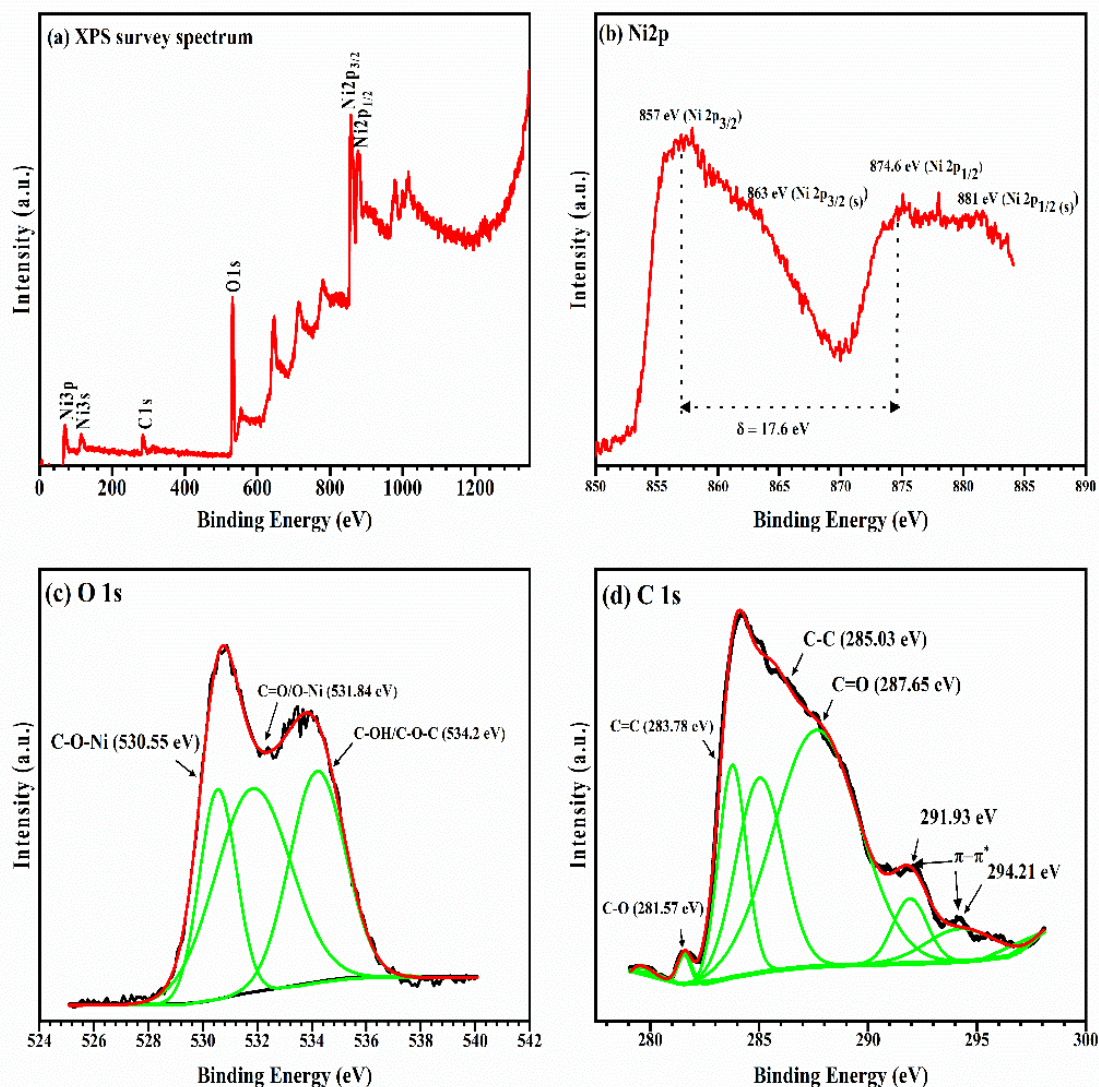


Figure 4. 7: XPS survey spectrum, Ni 2p spectrum **(b)**, deconvolution of O 1s spectrum **(c)**, and deconvolution of C 1s spectrum **(d)** for 80 wt.% Ni(OH)₂-20 wt.% graphene/NF

The XPS spectrum of Ni in **Figure 4. 7(b)** is like the composite with 20 wt.% Ni(OH)₂ with a small shift to the higher energy side (~0.5 eV). The same degenerate states of the 2p_{3/2} orbital at 857 and 863 eV were observed as well as the 2-degenerate states of 2p_{1/2} orbital at 874.6 and 881 eV. The main differences between the two deposited composites (20 and 80 wt.% Ni(OH)₂) are illustrated in the deconvoluted XPS spectra of the O 1s and C 1s. The deconvoluted spectrum of O 1s of the composite with 80 wt.% Ni(OH)₂ in **Figure 4. 7(c)** reveals XPS peaks at 530.55, 531.84, and 534.2 eV. These correspond to the multiple oxygen-related bond states as C-O-Ni, C=O/O-Ni, and C-OH/C-O-C, respectively. In addition, the relative intensity of the C=O/O-Ni, and C-OH/C-O-C bonds is higher in the composite of 80 wt.% Ni(OH)₂ than the other composite with

lower Ni(OH)₂ content. On the other hand, the deconvoluted XPS spectrum of C 1s in **Figure 4. 7(d)** reveals several bonded states in which the intensities were higher in the 20 wt.% Ni(OH)₂ such as C-O at 281.57 eV, C=C at 283.78 eV, C-C at 285.03 eV, and C=O at 287.65. In addition, we observed the evolution of a weak shake-up satellite peak corresponding to π - π^* transfer at 291.93 and 294.21 eV due to the delocalization of π conjugates [182].

4. 2. 4. Morphological and elemental analysis of the Ni(OH)₂-graphene composites

4. 2. 4. 1. Ni(OH)₂-graphite composite powder

SEM images of the graphite powder in **Figure 4. 8(a, b)** exhibit micro-sized flake morphologies with various flake dimensions ($\geq 10\mu\text{m}$) and orientations. Meanwhile, the initial micro-sized Ni(OH)₂ powder had a semispherical shape with a polydisperse particle size distribution, as shown in **Figure 4. 8(i, j)**. The elemental analysis of the mixed Ni(OH)₂-graphite powder before the deposition process is shown in **Figure 4. 8(c, f)**, where the composite with low Ni(OH)₂ content showed a composition weight ratio (wt.%) of 84.83 for C_k, 13.11 for O_k, and 2.06 Ni_k in the mixed composite. Meanwhile, the composite with higher Ni(OH)₂ content showed a composition weight ratio of 24.64 for C_k, 43.89 for O_k, and 31.47 for Ni_k. SEM images of the mixed Ni(OH)₂-graphite composites powder with low Ni(OH)₂ content (20 wt.%) reveal mixed micro-sized flakes and a semispherical morphology as shown in **Figure 4. 8(d, e)**. The flake morphology showed a relatively high content related to the graphite powder. Whereas, the higher content of Ni(OH)₂ (80 wt.%) had a relatively higher concentration of the semispherical shaped particles compared to the flake morphology, as demonstrated in **Figure 4. 8(g, h)**.

4. 2. 4. 2. Ni(OH)₂ -graphene composites/Ni foam thin films

Figure 4. 9(a, b) reveals the SEM images of the bare Ni foam surface at two different magnification powers before the deposition process to illustrate differences between the bare supporting substrate and the deposited films at the same length scale. The elemental analysis of the deposited graphene/Ni foam, **Figure 4. 9(c)**, reveals the existence of a relatively low concentration of carbon from the deposition compared with the higher concentration of the Ni that resulted from the substrate. **Figure 4. 9(d, e)** shows the SEM images of the deposited graphene on the Ni foam substrate. The low magnification image at a scale length of 2 μm revealed a flake morphology with various dimensions and orientations.

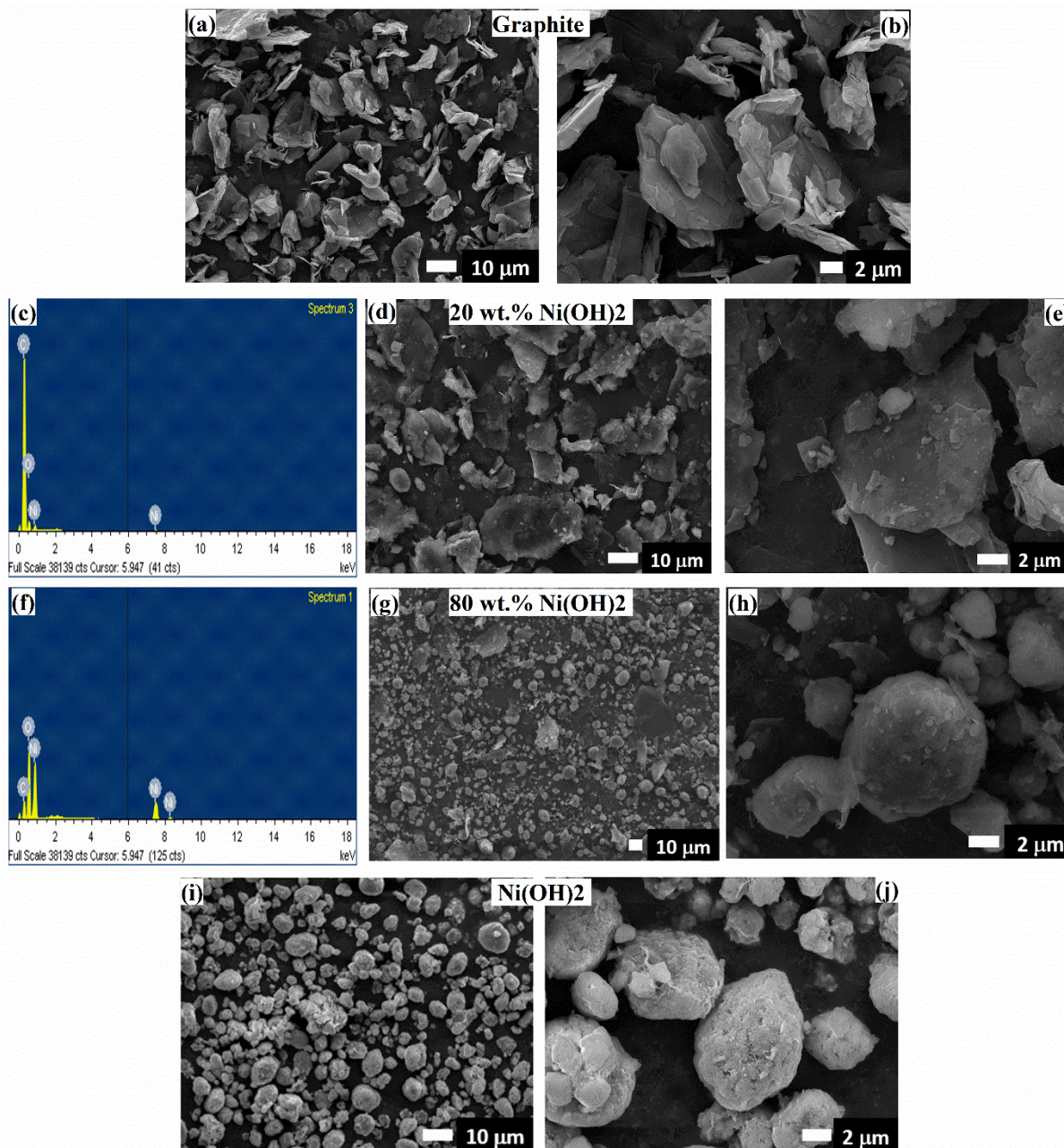


Figure 4. 8: SEM images of the micro-sized graphite particles (**a, b**), SEM images, and the EDS analysis of the composite (**c, d, e**) with 20 wt.% Ni(OH)₂. SEM images and the EDX analysis of the composite (**f, g, h**) with 80 wt.% Ni(OH)₂, and SEM images of Ni(OH)₂ powder (**i, j**).

The higher magnification image at a length scale of 200 nm exhibited that these flakes consisted of smaller merged sheets with smaller dimensions in the nano-size range (200 to 400 nm) that resulted from the fragmentation of the initial graphite powder with initial flake dimensions in the range of $\geq 10 \mu\text{m}$, **Figure 4. 8(a, b)**. The elemental analysis in the case of the pure phase of Ni(OH)₂ thin film, **Figure 4. 10(d)** revealed the existence of O due to the deposition, as well as Ni from

either the deposition or the used substrate. The low magnification SEM image of the deposited Ni(OH)₂/Ni foam thin films in **Figure 4. 10(e)** shows the deposited film with stacked particles with merged boundaries. Moreover, the higher magnification SEM image in **Figure 4. 10(f)** shows a sheet morphology with overlapped boundaries with lateral dimensions in the nano-size range (≤ 100 nm). This illustrates the fragmentation of the initial powder with the micro-sized semispherical Ni(OH)₂ with an average particle size of 5 μ m, **Figure 4. 8(i, j)**.

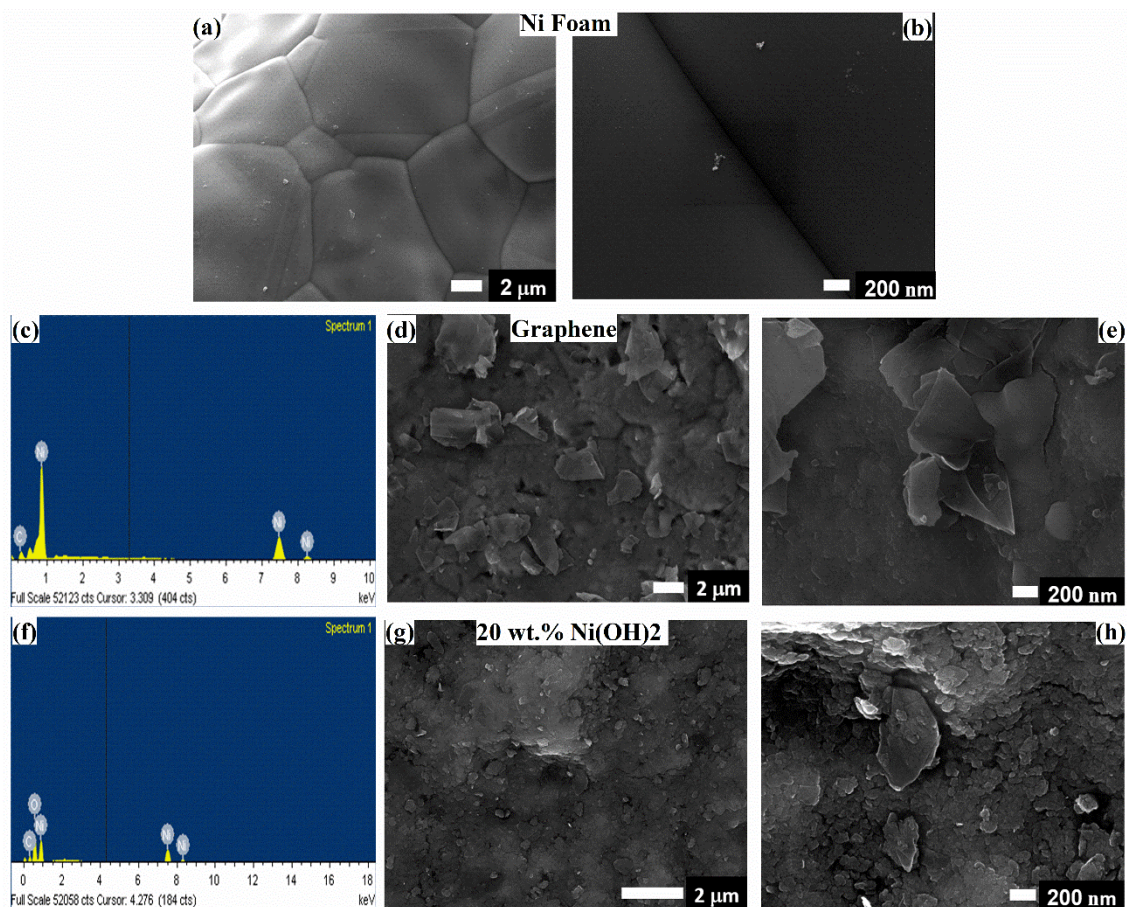


Figure 4. 9: SEM images of bare Ni foam **(a, b)**, SEM images and EDS spectrum of graphene/NF **(c-e)**, and 20 wt.% Ni(OH)₂-80 wt.% graphene/NF **(f-h)**

The elemental analysis using the EDS spectra of Ni(OH)₂-graphene/NF hybrid catalysts is shown in **Figure 4. 9(f)** and **Figure 4. 10(a)** for composites with Ni(OH)₂ contents of 20 and 80 wt.%, respectively. The observed EDS peaks in the deposited thin films were assigned to C_k, Ni_k, and O_k. Moreover, the uniform spatial distribution of these elements in both composites (20 and 80 wt.% Ni(OH)₂) were verified from the corresponding elemental maps in **Figure 4. 11** and **Figure 4. 12**, which revealed the

homogenous deposition of the Ni(OH)₂-graphene composites on the supporting substrate (Ni foam) using the NPDS. In the case of the low Ni(OH)₂ content (20 wt.%), the low magnification SEM image in **Figure 4. 9(g)** revealed aggregated particles with merged grain boundaries in the deposited film. In addition, a higher magnification SEM image in **Figure 4. 9(h)** reveals a mixed morphology from nanoflakes with sizes ranging from 200 to 400 nm and nanosheets with lateral dimensions ≤ of 100 nm. Meanwhile, the SEM image corresponding to the higher Ni(OH)₂ content (80 wt.%) revealed dominant nanosheet morphologies in the size range from 100 to 200 nm, **Figure 4. 10(b, c)**. The morphology and the elemental composition of Ni(OH)₂-graphene hybrid catalyst with 20 wt.% Ni(OH)₂ were examined directly after the oxygen evolution reaction (OER) test and after 25 hours OER stability test for verifying the long stability of our hybrid catalyst, as shown in **Figure 4. 13**. It can be observed that no observable change in the morphology (either size range or shape) and the corresponding elemental analysis during the OER test, which supports the long-term stability of the Ni(OH)₂-graphene hybrid catalyst in the used alkaline medium (1.0 M KOH).

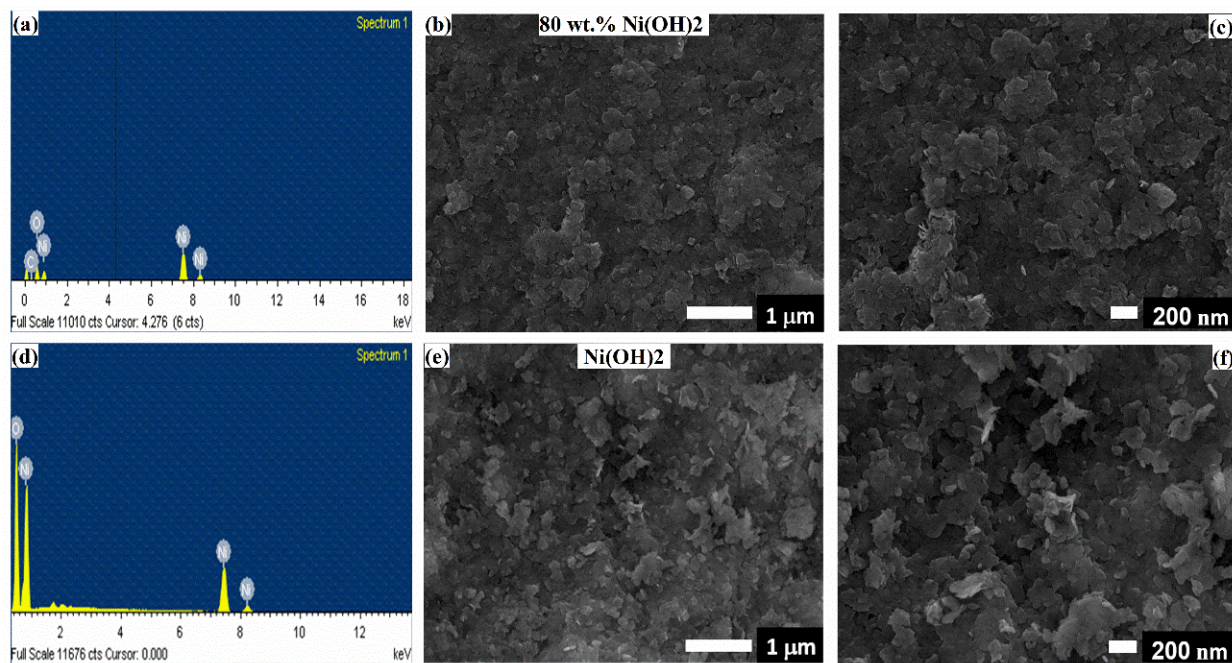


Figure 4. 10: SEM images and EDs spectrum of 80 wt.% Ni(OH)₂-20 wt.% graphene/NF (**a-c**), and Ni(OH)₂/NF (**d-f**).

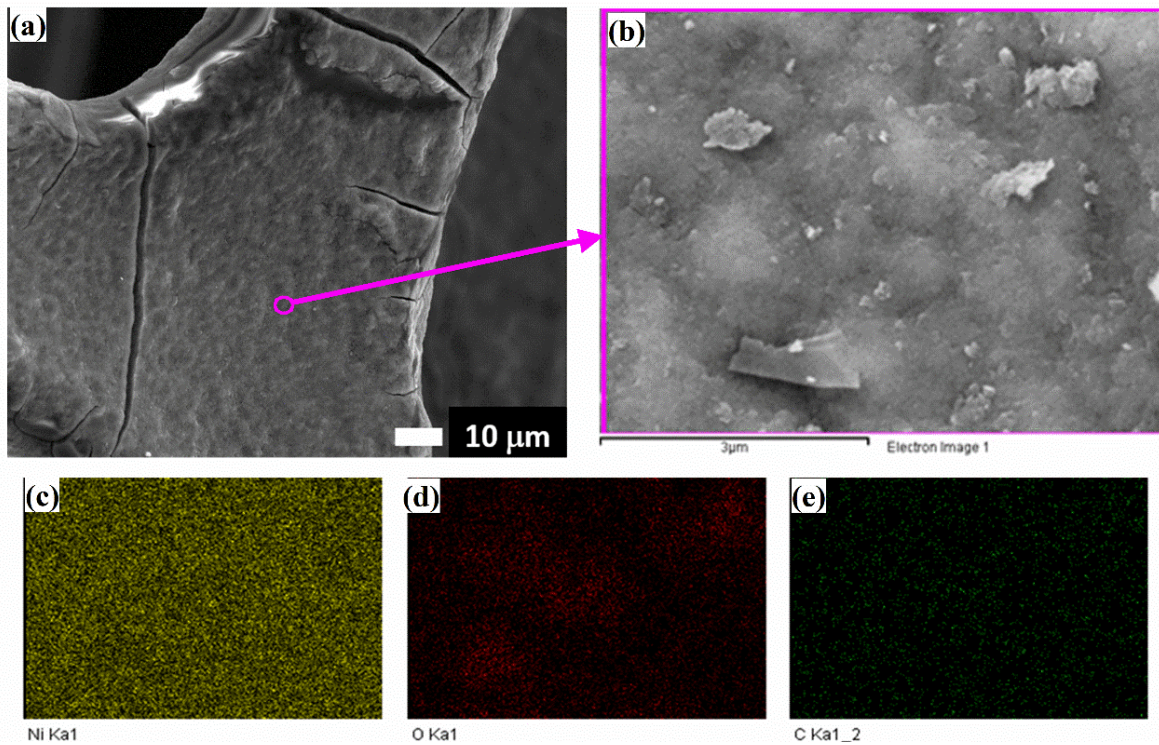


Figure 4. 11: SEM images and the elemental analysis mapping of the 20 wt.% Ni(OH)₂-80 wt.% graphene/NF

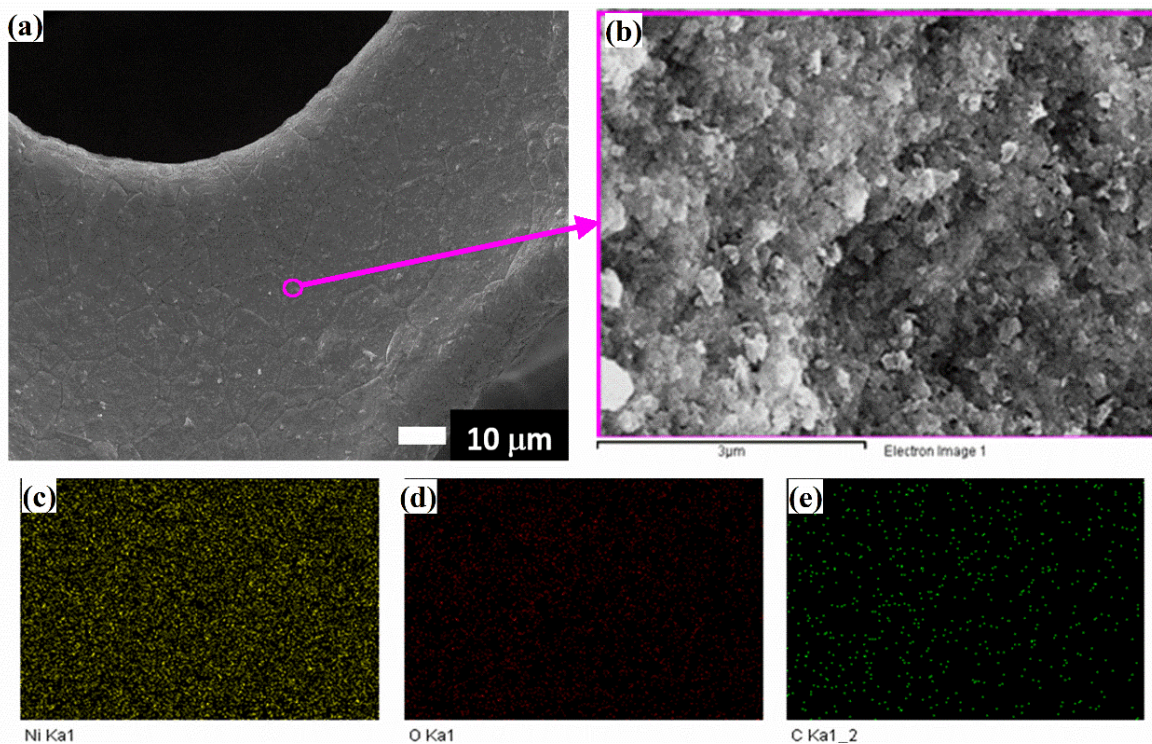


Figure 4. 12: SEM images and the elemental analysis mapping of the 80 wt.% Ni(OH)₂-20 wt.% graphene /NF.

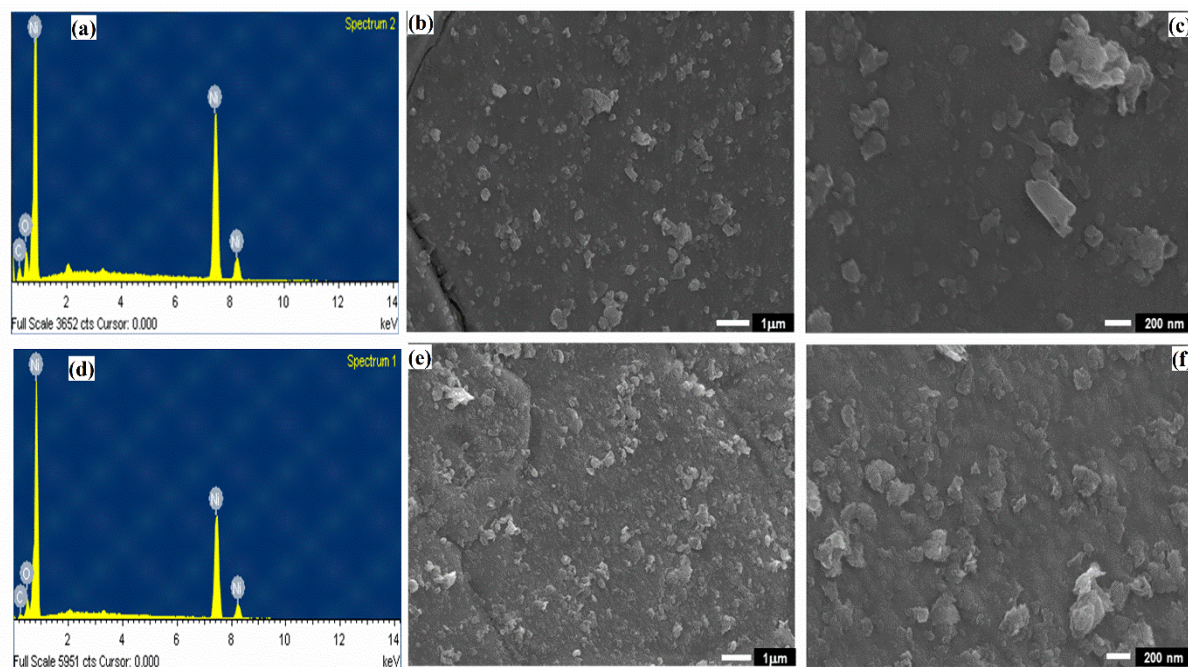


Figure 4. 13: SEM images and the corresponding EDs spectrum of 20 wt.% Ni(OH)₂-80 wt.% graphene/NF directly after OER test (a-d), and after 25 hours OER stability test in 1.0 M KOH (d-f)

4. 2. 5. Electrochemical characterization

The overall electrocatalytic water splitting mechanism mainly consists of two half-cell reactions, i.e., the OER at the anode and the HER at the cathode. The key performance parameters of the overall water splitting reaction depend on the activity of the chosen catalyst toward the HER and the OER as illustrated below.

4. 2. 5. 1. Electrochemical active surface area

The electrochemically active surface areas (ECSA) of the Ni(OH)₂-graphene hybrid catalysts were measured by the double-layer capacitance (C_{DL}) method [183] in the potential range from 1 to 1.1 V vs. RHE in 1 M KOH electrolyte, where no Faradaic current is observed. The C_{DL} values were calculated by the scan-rate-dependent of cyclic voltammetry (CV) plots according to **Eq. 2. 5**. CV plots of the pure phases of Ni(OH)₂/NF and graphene/NF, as well as, Ni(OH)₂-graphene/NF hybrid catalyst at different Ni(OH)₂ content (20, 40, 60, and 80 wt.%) were recorded at different scan rates (10, 20, 30, 40, 50, 60, 70, 80, 90 and 100 mV·s⁻¹), as shown in Error! Reference source not found.(a-c). Then, a linear relationship between ΔJ at 1.05 V vs. RHE and scan rate was plotted for all working electrodes, **Figure 4. 14**. The obtained ECSA represented by C_{DL} values are 2, 4, 2.53, 2.89, 3.56, 4.58, and 3 mF·cm⁻²

corresponds to bare Ni foam (NF), graphene/NF, hybrid catalysts with Ni(OH)₂ content from 20 to 80 wt.%, and pure Ni(OH)₂/NF, respectively. It can be observed that the pure graphene/NF catalyst has a relatively higher ECSA compared with the pure Ni(OH)₂/NF catalysts. In addition, the hybrid catalysts with lower Ni(OH)₂ (20 and 40 wt.%) possess lower ECSA compared with pure phases. Meanwhile further increase in the Ni(OH)₂ contents resulted in more improvement in the ECSA, which hybrid catalysts with 80 wt.% Ni(OH)₂ revealed the highest ECSA of 4.58 mF.cm⁻² compared with the pure catalysts of graphene and Ni(OH)₂, as well as, the other hybrid catalysts. Consequently, it has a larger concentration of active sites on the surface of the hybrid catalyst.

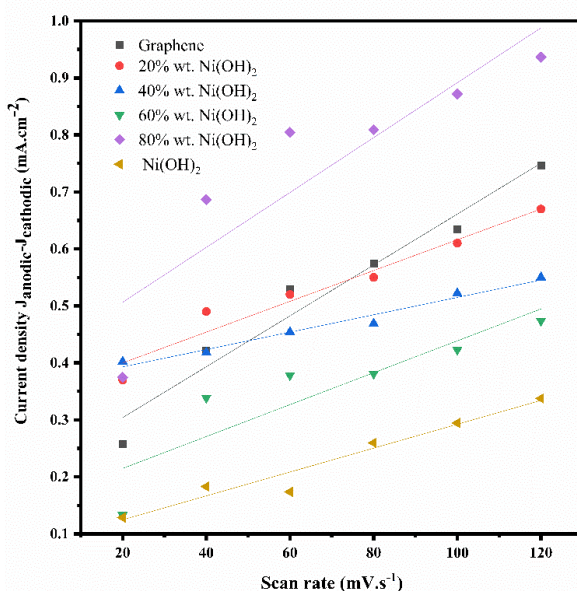
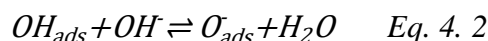


Figure 4. 14: Plots of current density difference at 0.15 V vs. RHE as a function of scan rate

4. 2. 5. 2. Mechanism of oxygen evolution reaction in the alkaline medium

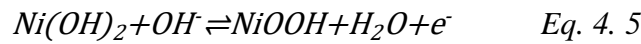
The water oxidation mechanism at the interface of Ni-based catalysts for the oxygen evolution was described by Bronoel et al. [184]. They illustrated that water oxidation mainly consists of two successive discharge (i.e., charge transfer) processes. The first step starts with OH⁻ discharge, followed by the recombination of the adsorbed hydroxyl group (OH_{ads}) with the hydroxyl ions of the electrolyte (OH⁻) to form O_{ads}⁻, and then, discharging of the adsorbed oxygen anions to form oxygen molecules according to the following chemical reactions:





4. 2. 5. 3. Oxygen evolution reaction activity of Ni(OH)₂-graphene hybrid catalysts

The electrocatalytic activities of the pure phases and the Ni(OH)₂-graphene hybrid catalysts /NF thin film as a working electrode for the oxygen evolution reaction (OER) were examined in 1.0 M KOH. **Figure 4. 16(a, b)** reveal the LSV curves and the corresponding Tafel plots of Ni(OH)₂/NF, graphene/NF, and Ni(OH)₂-graphene hybrid catalysts /NF with various Ni(OH)₂ contents (20, 40, 60, and 80 wt.%). The estimated overpotentials (η) values at current densities of 20, 50, 100, 150, and 200 mA·cm⁻², as well as the kinetic parameter (b, Jo) for each catalyst, are recorded in **Table 4. 1**. Ni(OH)₂/NF catalysts exhibited an OER electrocatalytic activity with a relatively high η of 340 mV @ 20 mA·cm⁻² and slow reaction kinetics with a high Tafel slope of 185.5 dec·mV⁻¹. Meanwhile, the graphene/NF-modified catalysts showed very fast reaction kinetics toward OER with a small Tafel slope value of 57.79 dec·mV⁻¹, but with a relatively high η of 340 mV @ 20 mA·cm⁻². The observed oxidation peak at nearly 1.42 V vs. RHE in the LSV plot, **Figure 4. 16(a)**, of the Ni(OH)₂/NF catalyst, can be ascribed to the surface Faradaic reaction of the pure Ni(OH)₂ due to the structural phase transformation from Ni^(II) to Ni^(III) [129, 146]. Meanwhile, the mass transport surface faradic reaction is the main reason for the observed oxidation peak in the case of the pure graphene catalyst [148] as illustrated below:



It was observed that in the case of Ni(OH)₂-graphene hybrid catalysts/NF, the incorporation of Ni(OH)₂ in the graphene/NF catalyst results in a shift of the oxidation peaks to lower potential values, accompanied by an overall improvement in the OER electrocatalytic activity, which Ni(OH)₂-graphene hybrid catalysts/NF with 20 wt.% Ni(OH)₂ content exhibited the lowest oxidation potential of 1.37V, as well as, a current density higher than 200 mA·cm⁻², a low overpotential (η) value of 330 mV @ 50 mA·cm⁻², fast interfacial reaction kinetics with a low Tafel slope value of 78 mV·dec⁻¹, as well as, low charge transfer resistance as shown in **Figure 4. 19(a)**. To quantitatively demonstrate the composition effect on the OER electrocatalytic activity, the variation in η @50 mA·cm⁻² and the corresponding Tafel slopes are illustrated in **Figure 4. 16(c)**. In addition, further increase in Ni(OH)₂ content from 20 wt.% to 80 wt.% resulted in a shift of the oxidation peak potential to higher values, an increase in the charge transfer resistance (R_{ct}), an

increase in the corresponding Tafel slope, and an overall decrease in the OER electrocatalytic activity.

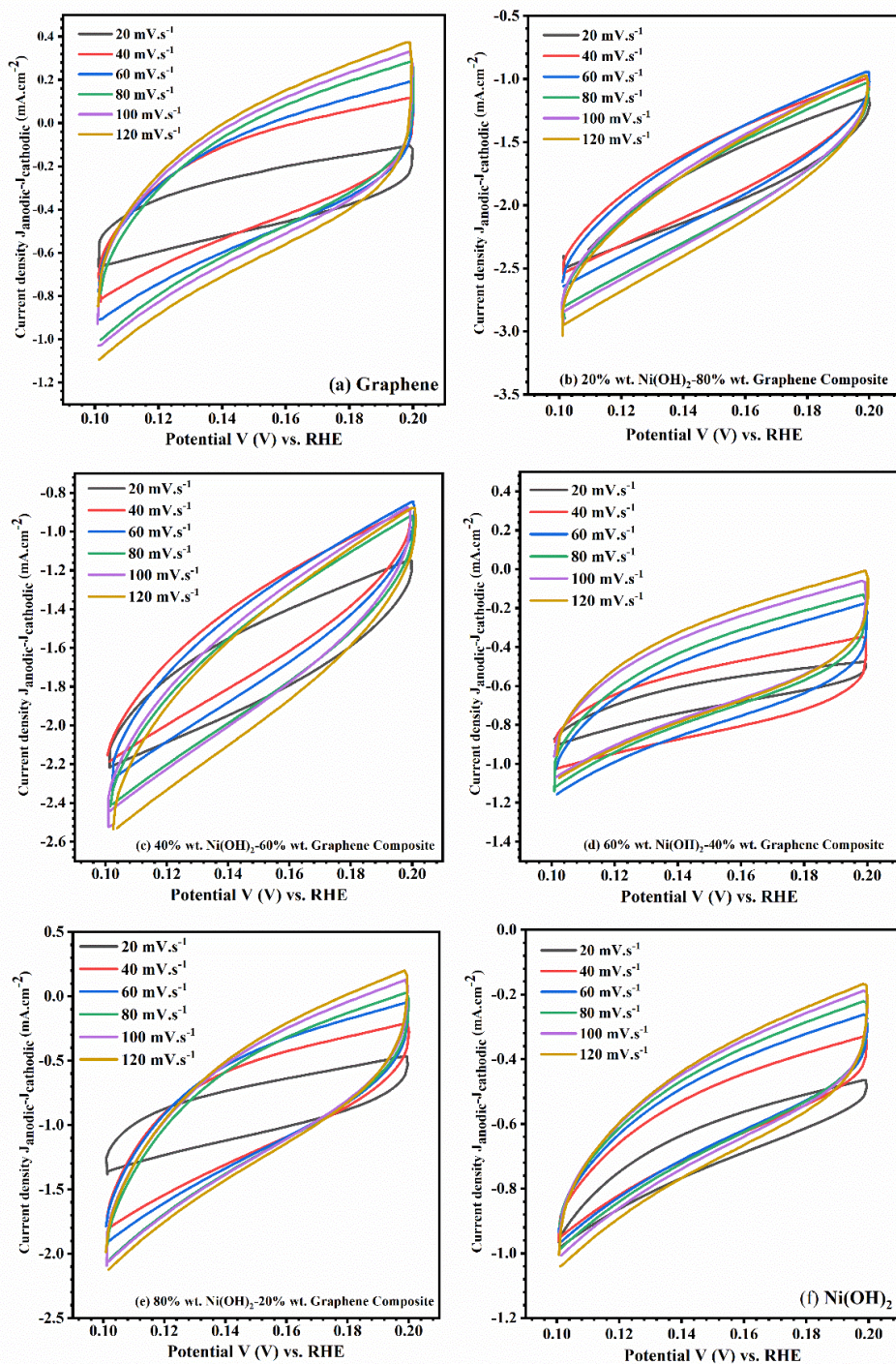


Figure 4. 15: CV plots of the graphene/Ni foam NF **(a)**, Ni(OH)₂-graphene/Ni foam NF **(b-e)**, and Ni(OH)₂/Ni foam NF **(f)** at different scan rates

This makes 20 wt.% Ni(OH)₂-80 wt.% graphene composite/NF the optimum working electrode for OER. This behavior can be explained according to the suggested OER mechanism that consists mainly of two consecutive steps (i.e., discharge of both OH⁻, and O⁻), which depends on the charge transfer kinetics; hence, the high graphene content in this composite improved the rate of charge transfer and the overall OER electrocatalytic activity.

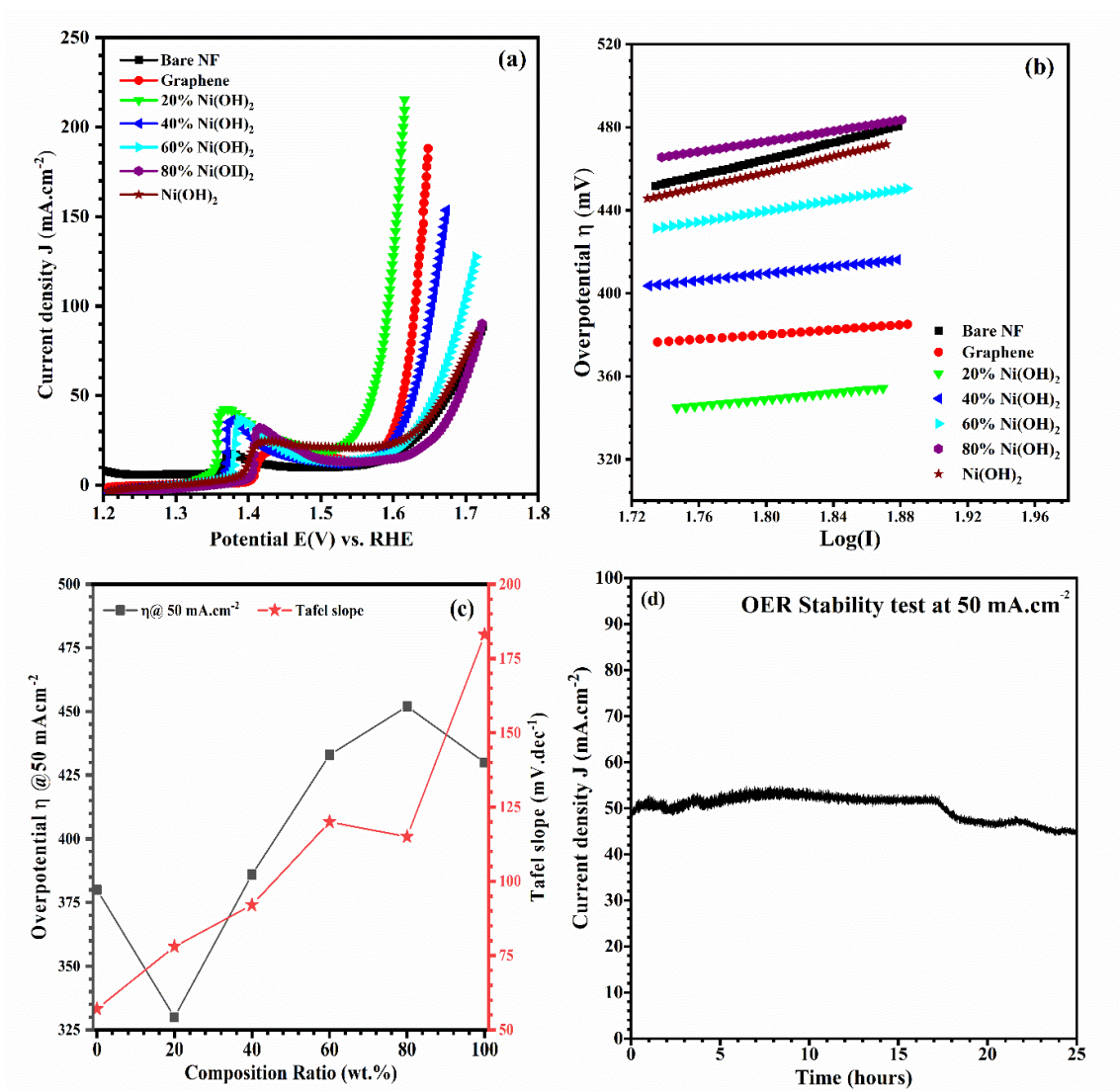


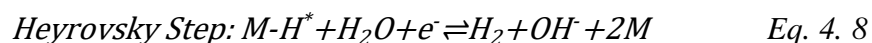
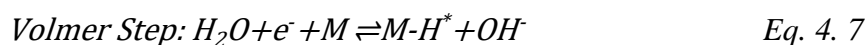
Figure 4. 16: OER LSV curves (a) and Tafel plots (b) for Ni(OH)₂-graphene hybrid catalysts/NF; The variation of the overpotential (η) and Tafel slope values with changing Ni(OH)₂ content (c). Chronoamperometric curves of 20 wt.% Ni(OH)₂-80 wt.% graphene composites/NF at an overpotential of 330 mV for 25 h (d).

The long-term stability of the Ni(OH)₂-graphene hybrid catalysts/NF with 20 wt.% Ni(OH)₂ in 1.0 KOH toward OER was verified using chronoamperometry at a static potential of 1.56 V (an

overpotential η of 330 mV), which delivered around $50 \text{ mA}\cdot\text{cm}^{-2}$ for more than 17 hours, followed by a slight reduction ($< 5\%$), which continued up 25 hours as shown in **Figure 4. 16(d)**.

4. 2. 5. 4. Mechanism of hydrogen evolution in the alkaline medium

The water reduction mechanism in the alkaline medium for the hydrogen evolution reaction consists of three main steps, namely, Volmer, Heyrovsky, and Tafel steps according to **Eq. 4. (7-9)** [185, 186]. The water molecules adsorbed on the working electrode surface are reduced to H and adsorbed hydroxyl groups (OH^-), followed by the formation of hydrogen intermediate (H^*) and the generation of H_2 . The formation of H^* and the desorption mechanism of OH^- are the controlling steps for hydrogen evolution in an alkaline medium [187, 188].



Here, M represents the active sites on the working electrode surface. The Volmer step is a charge transfer step. Meanwhile, the Heyrovsky step arises from coverage of the electrode surface with reduced water anions. The adsorption improvement for electrolyte species (H^* , H_2O) at the electrode/electrolyte interface could speed up the forward reaction in the Heyrovsky step, eq#12, and produce more active sites on the electrode surface [185]. In addition, the charge transfer from the Volmer step is balanced with the charge transfer from the back reaction of the Heyrovsky step.

4. 2. 5. 5. Hydrogen evolution activity of $\text{Ni}(\text{OH})_2$ -graphene hybrid catalysts

The HER electrocatalytic activity of the pure phase $\text{Ni}(\text{OH})_2/\text{NF}$, graphene/NF, and the $\text{Ni}(\text{OH})_2$ -graphene hybrid catalysts/NF were examined in 1.0 M KOH. **Figure 4. 17(a, b)** reveals the LSV and the corresponding Tafel plots of the pure $\text{Ni}(\text{OH})_2/\text{NF}$, graphene/NF, and the $\text{Ni}(\text{OH})_2$ -graphene hybrid catalysts/NF thin films with $\text{Ni}(\text{OH})_2$ contents of 20, 40, 60, 80 wt.%. The estimated overpotential (η) values at the corresponding current densities of 10, 20, 50, 100, 150, and $200 \text{ mA}\cdot\text{cm}^{-2}$, as well as kinetics parameters (b , J_0), are recorded in **Table 4. 1**. A pure $\text{Ni}(\text{OH})_2/\text{NF}$ thin-film working electrode revealed an HER electrocatalytic activity with a relatively high η of 206 mV at $20 \text{ mA}\cdot\text{cm}^{-2}$ and relatively slow reaction kinetics with a Tafel slope of $159 \text{ dec}\cdot\text{mV}^{-1}$. Meanwhile, the pure graphene/NF thin film exhibited a relatively higher HER

electrocatalytic activity that possesses a lower η of 178 mV @ 20 mA·cm⁻² and faster reaction kinetics with a Tafel slope of 107.6 mV·dec⁻¹ compared with the pure Ni(OH)₂/NF.

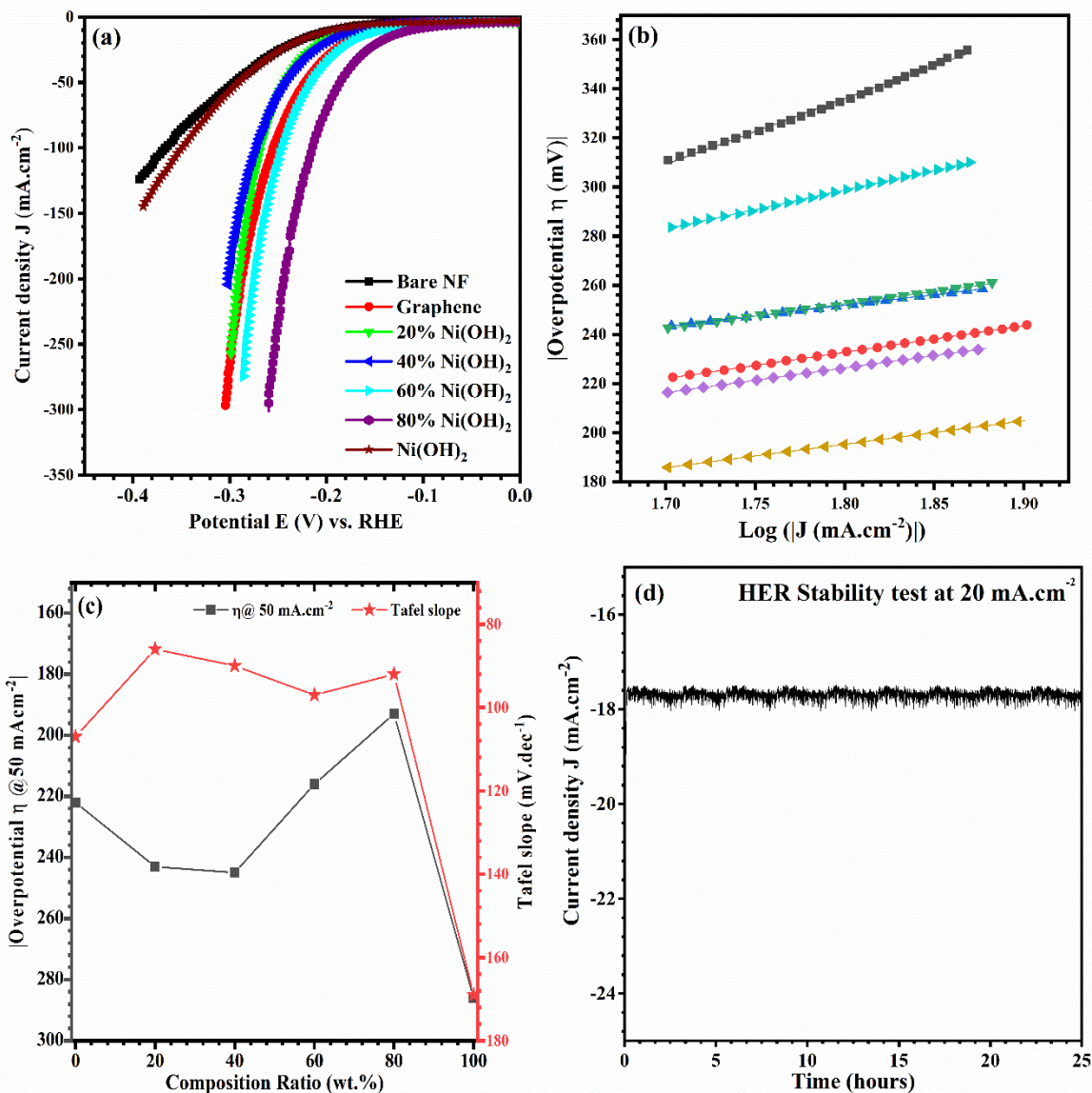


Figure 4. 17: HER LSV curves and **(b)** Tafel plots for Ni(OH)₂-graphene hybrid catalysts /NF. **(c)** The variation of the overpotential η and Tafel slope values with changing Ni(OH)₂ content. **(d)** Chronoamperometric curves of 80 wt.% Ni(OH)₂- 20 wt.% graphene hybrid catalysts /NF with 80 wt.% at an overpotential η of 154 mV for 25 h.

Figure 4. 17(c) reveals the variation in the overpotential η @50 mA·cm⁻² and the estimated Tafel slope values with various Ni(OH)₂ contents. It was noticed that increasing Ni(OH)₂ content resulted in an improvement in the HER electrocatalytic catalytic activity. In addition, the hybrid catalyst with 80 wt.% Ni(OH)₂ was the optimum for the HER electrocatalytic activity because they possess the lowest overpotential (η) value of 154 mV@20 mA·cm⁻², a high exchange current density (J_0) of 0.562 mA·cm⁻²

as well as a low Tafel slope of $92 \text{ mV}\cdot\text{dec}^{-1}$. To illustrate the effect of electrode surface wettability on the HER activity of the $\text{Ni}(\text{OH})_2$ -graphene hybrid catalysts/NF, the contact angle for a $\sim 1 \text{ }\mu\text{m}$ water droplet was examined for the bare Ni foam, graphene/NF, $\text{Ni}(\text{OH})_2$ /NF, and $\text{Ni}(\text{OH})_2$ -graphene composites /NF with different $\text{Ni}(\text{OH})_2$ contents (20 wt.% and 80 wt.%) as shown in **Figure 4. 18**. It can be observed from **Figure 4. 18(a, b)** that the bare Ni foam and the deposited graphene/NF exhibited a hydrophobic nature with average contact angles of 118° and 124° , respectively. Meanwhile, in the case of composites with 20 wt.% $\text{Ni}(\text{OH})_2$ content, the contact angle was reduced to 76° , because of the improvement in the surface wettability (i.e., improvement in the hydrophilic tendency), **Figure 4. 18(c)**. Moreover, a further increase in the $\text{Ni}(\text{OH})_2$ content up to 80 wt.% results in further enhancement in the surface wettability due to the strong hydrophilic tendency with no detectable contact angle as shown in **Figure 4. 18(d)**. The observed improvement in the surface wettability with increasing $\text{Ni}(\text{OH})_2$ content in the deposited $\text{Ni}(\text{OH})_2$ -graphene composites has a pronounced effect on enhancing the electrolyte diffusion within the electrolyte/electrode interface as well as increasing the electrode affinity towards electrolyte ions [189].

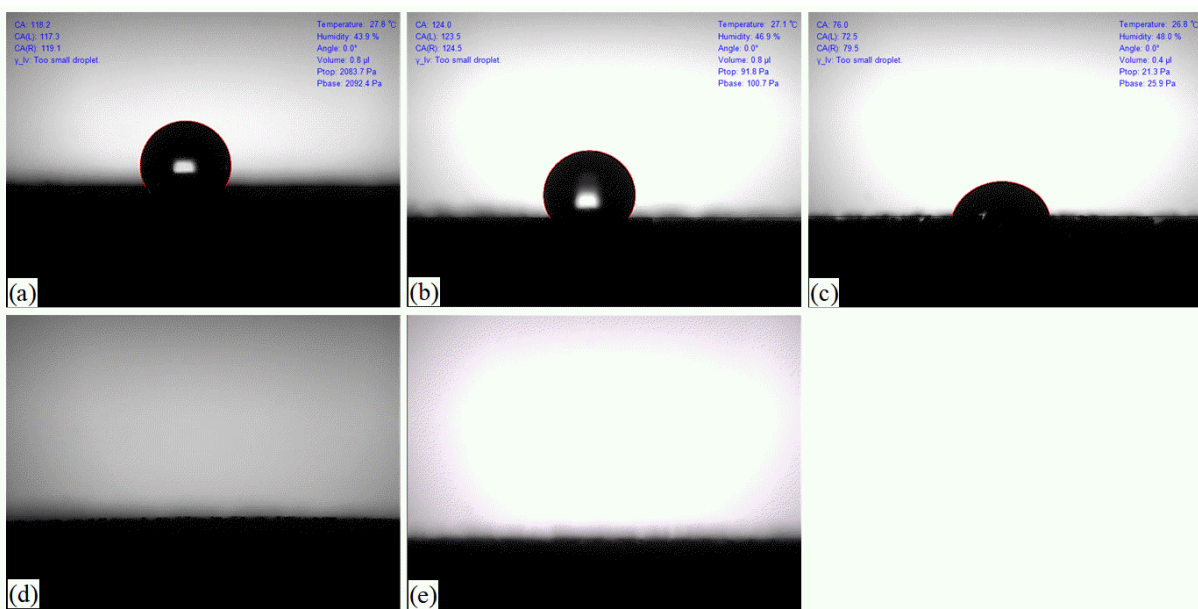


Figure 4. 18: The wettability behavior of (a) the bare Ni foam, (b) the pure graphene/NF, (c) the composite with 20 wt.% $\text{Ni}(\text{OH})_2$, (d) the composite with 80 wt.% $\text{Ni}(\text{OH})_2$, and (e) pure $\text{Ni}(\text{OH})_2$ /NF.

The observed high HER activity of $\text{Ni}(\text{OH})_2$ -graphene composites with high $\text{Ni}(\text{OH})_2$ content can be ascribed to several reasons as follows. I) Synergetic effects were obtained between the $\text{Ni}(\text{OH})_2$

and the graphene in this composite through the formation of various hydrophilic groups as bonding states (e.g., C=O, C-O, and C-OH/C-O-C, and C-O-Ni bonds). These active hydrophilic groups could improve the electrode surface wettability by interacting with water molecules through hydrogen bonding and introduce new active sites at the electrode/electrolyte interface [134, 177, 190], as demonstrated from the XPS spectra in **Figure 4. 7(c, d)**.

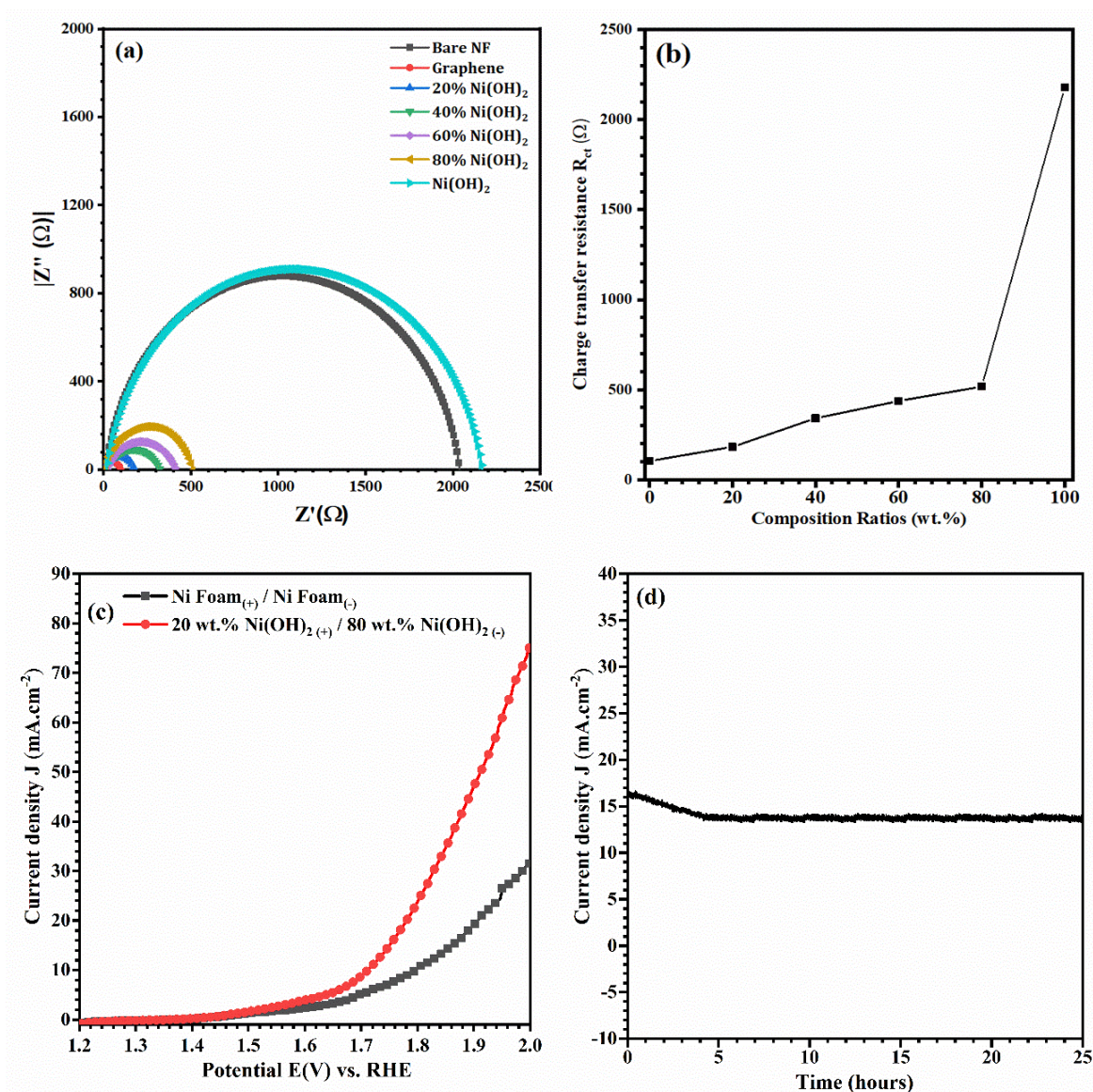


Figure 4. 19: (a) Nyquist plots of Ni(OH)₂-graphene composite/NF, and (b) the change in the charge transfer resistance R_{ct} at different Ni(OH)₂ contents, (c) water electrolysis LSV curves in two-electrode configuration with a composite of 20 wt.% Ni(OH)₂ as the anode and 80 wt.% Ni(OH)₂ as the cathode, compared with the symmetric Ni foam couple at a scan rate of 5 mV/s. (d) The chronoamperometric curve of water electrolysis for the asymmetric configuration at a static potential of 1.75 V.

II) The surface coverage by the adsorbed water molecules increased due to the improvement of the surface wettability, which in this case is the rate-determining step that depends mainly on the Heyrovsky step [59]. III) Ni(OH)₂-graphene composites with 80 wt.% Ni(OH)₂ content had the highest relative ECSA of 4.58 mF·cm⁻², due to the improvement of surface coverage by reduced water molecules and the increase in the number of active sites on the electrode surface. The long-term stability of the Ni(OH)₂-graphene composite/NF with 80 wt.% Ni(OH)₂ in 1.0 KOH toward HER was tested using chronoamperometry at an overpotential of 154 mV, which delivered around 20 mA·cm⁻² for 25 hours as shown in **Figure 4. 17(d)**. Based on the obtained results, we constructed an electrolyzer with a two-electrode system consisting of 20 wt.% Ni(OH)-80 wt.% graphene hybrid catalysts/NF as an anode and 80 wt.% Ni(OH)₂-20 wt.% graphene hybrid catalysts /NF as a cathode. We also made an asymmetric electrolyzer from the bare Ni foam for testing the overall water splitting. The LSV and the long-term stability at 1.75 V static potential corresponding to the overall water splitting are illustrated in **Figure 4. 19(c, d)**, which shows that the electrolyzer revealed good stability without noticeable decay for 25 hours.

Table 4. 1: Electrocatalytic activity and kinetic parameters of Ni(OH)₂-graphene hybrid catalysts/NF for OER and HER

Composition (wt.%)		Overpotential η (mV)						Tafel Analysis			
Ni(OH) ₂	Gr	10	20	50	100	150	200	B	A	J ₀ *10 ⁻³	
		mA·cm ⁻²						mV·dec ⁻¹	mV	mA·cm ⁻²	
OER	Bare Ni Foam	290	379	438	-	-	-	199.4	105.7	295	
	0	100	-	357	384	400	411	-	57.79	276	0.0168
	20	80	-	-	330	355	368	384	78.7	207.2	2.34
	40	60	-	345	386	411	-	-	84	258	0.848
	60	40	-	-	433	471	-	-	129.5	206.3	25.52
	80	20	-	405	461	-	-	-	125.5	247.3	10.7
	100	0	-	340	430	-	-	-	185.5	124.4	213.49
HER	Bare Ni Foam	-	240	310	404	-	-	267	145	286.4	
	0	100	-	178	220	255	273	287	107.6	39	434
	20	80	-	206	243	269	281	292	86.32	96.44	76.63
	40	60	-	204	243	273	291	302	93	71	172
	60	40	-	172	212	242	260	270	97	45	343
	80	20	-	154	192	220	236	247	92	23	562
	100	0	-	206	286	370	456	-	159	12	840

4.3. Summary

Nanostructured Ni(OH)₂-graphene hybrid bifunctional catalysts with different Ni(OH)₂ contents were directly deposited on Ni foam supporting substrate using micro-sized particles of Ni(OH)₂ and graphite without any chemical treatment. The deposited composites exhibited nanosheet morphology. The synergetic effect between the Ni(OH)₂ and the graphene improved the electrocatalytic activity of the Ni(OH)₂-graphene hybrid catalysts toward the OER and the HER. The Ni(OH)₂-graphene hybrid catalysts with low Ni(OH)₂ content (20 wt.%) revealed higher OER activity compared with other composites due to the improvements in the reaction kinetics and the decrease in the corresponding charge transfer resistance, which resulted in the acceleration of the discharge process of the free hydroxyl anions OH⁻ and the adsorbed oxygen anions (O_{ads}⁻) at the electrode surface according to the suggested mechanism for the OER. On the other hand, the catalyst with a higher Ni(OH)₂ content of 80 wt.% exhibited excellent electrocatalytic activity toward the HER due to an increase in bonding states related to hydrophilic groups that caused an improvement in the surface wettability and consequently an increase in the number of active sites. Both optimum working electrodes for OER and HER showed long-term stability for 25 hours without noticeable decay. In addition, the electrolyzer in the two-electrode configuration using the efficient composite for OER as an anode and the efficient composite for HER as a cathode revealed long-term stability that delivered nearly 15 mA·cm⁻² at a static potential of 1.75 V for 25 hours.

Chapter 5:

*Fabrication of Efficient Nanostructured Co₃O₄-Graphene
Bifunctional Catalysts: Oxygen Evolution, Hydrogen
Evolution, and H₂O₂ Sensing*

5.1. Overview

Cobalt-based (metallic and non-metallic Co compounds) electrocatalysts are strong candidates for many electrochemical energy conversion and storage applications as well as, various biosensor applications [191] due to abundance, low cost, high chemical durability, and high corrosion resistance [192, 193]. In addition, the performance of these applications not only depends on the elemental, but it is also affected by the internal microstructures, the distribution, and the concentration of the interfacial active sites on the working electrode surface. Chen et al., [194] reported the reduction of Co_3O_4 nanoparticles (NPs) in a metal-organic framework resulted in an improvement in the electrocatalytic activity toward the oxygen evolution reaction (OER), which provided $10 \text{ mA}\cdot\text{cm}^{-2}$ with relatively small overpotential (η) of 320 mV and small Tafel slope of $71 \text{ mV}\cdot\text{dec}^{-1}$, as well as improving the cyclic stability related to supercapacitor application. Yu et al., [195] reported the effect of modifying the CoS/CoP interface on the OER and hydrogen evolution reaction (HER) in the alkaline medium. They illustrated that the disordered structure at the interface could improve the overall electrocatalytic activity toward the OER and HER, in which the optimized catalyst afforded the OER current density of $10 \text{ mA}\cdot\text{cm}^{-2}$ at an overpotential at of 313 mV and a Tafel slope of $93 \text{ mV}\cdot\text{dec}^{-1}$. Malik et al., [196] demonstrated that the decoration of CoPt NPs by $\text{Co}(\text{OH})_2$ NPs improved the electrocatalytic activity toward the OER, which provided $10 \text{ mA}\cdot\text{cm}^{-2}$ at an overpotential of 334 mV and 226 mV at $50 \text{ mA}\cdot\text{cm}^{-2}$ for the HER.

Recently, many electrocatalysts based on polycrystalline or amorphous nanostructured materials such as Co-Fe-O alloys showed electrocatalytic activity toward the overall water splitting better than the counterparts crystalline materials [197]. Anantharaj and Noda [198] illustrated that amorphous-based nanostructured electrocatalysts exhibited several advantages such as self-adapting with the electrocatalyst that improved both volume and surface confinement of electrocatalytic species, in contrast to crystalline materials that only provide surface confinement for the electrolyte species. Moreover, the high concentration of surface and interfacial defects results in the improvement in the concentrations of the electrocatalytic active sites that in turn enhance the electrocatalytic activity toward the OER [199, 200]. Bergmann et al., [201] illustrated that the reversible amorphization of the nanocrystalline Co_3O_4 by generating reactive amorphous surface layers of the catalyst further enhanced the OER efficiency. In addition, several reports concerned by amorphous nanostructured cobalt oxide electrocatalysts revealed good electrochemical performance toward the water oxidation and reduction in the basic medium [202-205]. Nanostructured carbon-based materials such as graphene nanosheets and carbon nanotubes (CNT)

are widely used as heterostructure electrodes with high catalytic activity for water splitting [206, 207] and biosensing applications [206, 208] due to their superior conductivity and their large surface area.

Co_3O_4 -hybrid catalysts for overall water splitting applications were prepared by several techniques to optimize the electrochemical performance toward the half-cell reaction included in the overall water splitting (i.e., OER and HER). Liang et al. [209] reported that synthesizing Co_3O_4 /reduced graphene oxide (rGO) catalysts by a modified Hummers method. The prepared catalyst was used for the OER in 1.0 M KOH, which affords a current density of $10 \text{ mA}\cdot\text{cm}^{-2}$ at an overpotential (η) value of 310 mV and a small Tafel slope of $67 \text{ mV}\cdot\text{dec}^{-1}$. However, the prepared catalysts exhibited good electrocatalytic activity toward water oxidation (i.e., OER). The preparation method requires an extended time of more than 15 hours, also consuming a large amount of energy thereby increasing the production cost. Besides, it cannot be scaled up for large-scale production required in real-life applications. Liu et al., [189] have fabricated the graphite-graphene structure decorated by Co_3O_4 nanoparticles (NPs) hybrid catalyst by a hydrothermal technique at 150°C . The total time for catalyst fabrication is approximately 4 hours. The formed catalyst exhibited wrinkled and cross-linked graphene sheets on the conductive graphite foil. Also, it exhibited good electrocatalytic activity toward the OER in 1.0 M KOH, which provides $10 \text{ mA}\cdot\text{cm}^{-2}$ at 301 mV and a small Tafel slope of $47 \text{ mV}\cdot\text{dec}^{-1}$. Li et al., [78] prepared ultrathin Co_3O_4 nanosheets using a surfactant-free cyanogel- NaBH_4 method. The obtained Co_3O_4 nanosheets catalyst revealed good electrocatalytic activity toward the OER in 1.0 M KOH, which afforded $10 \text{ mA}\cdot\text{cm}^{-2}$ at η of 307 mV and a small Tafel slope of $76 \text{ mV}\cdot\text{dec}^{-1}$. This strategy for preparation is suitable for small-scale production and consumes a large amount of energy due to the long period of preparation and drying at 80°C (> 24 hours). Muthurasu et al., [210] prepared a $\text{Co}_3\text{O}_4/\text{MoS}_2$ heterostructure in a metal-organic framework using several consecutive steps: a) pyrolysis at high temperature (300°C) for 1 hour; b) immersion in dimethylformamide (DMF) solution containing MoS_2 for several hours; and, c) hydrothermal processing at 200°C for 10 hours. This catalyst revealed good activity toward the HER, in 1.0 M KOH that provides $10 \text{ mA}\cdot\text{cm}^{-2}$ at 205 mV with a Tafel slope of $128 \text{ mV}\cdot\text{dec}^{-1}$. Fiaz et al., [211] demonstrated that the introduction of Co_3O_4 NPs into a metal-organic framework (UiO-66) by a hydrothermal technique at 140°C for more than 24 hours. They illustrated that the $\text{Co}_3\text{O}_4/\text{UiO-66}$ catalyst revealed good electrocatalytic activity toward the HER in 2.0 M KOH, which supports $10 \text{ mA}\cdot\text{cm}^{-2}$ at 220 mV.

Co_3O_4 -based materials are promising electrocatalysts for the H_2O_2 reduction and electrochemical sensing in the alkaline medium because Co_3O_4 -based catalysts have various polar termination sites on

their grain boundaries, which help to detect any small variation at the interface of the working electrode [212, 213]. Wang et al., [214] reported the preparation of hollow structure Co_3O_4 /glassy carbon using pyrolysis of Co-based zeolitic imidazolate frameworks (ZIF-67) in air. This combination product was used for H_2O_2 sensing in 0.1 M NaOH, in which the detection of H_2O_2 revealed low sensitivity of $120.55 \mu\text{A} \cdot \text{mM}^{-1} \cdot \text{cm}^{-2}$ and linear detection range from 0.4 μM to 2.2 mM. Pei et al., [215] synthesized the preparation of a Co_3O_4 -gold composite by a modified electrodeposition technique. The modified catalyst revealed good electrocatalytic activity toward glucose oxidation in 0.1 M NaOH with a linear range from 2 μM to 2.11 mM and high sensitivity of $4470.4 \mu\text{A} \cdot \text{mM}^{-1} \cdot \text{cm}^{-2}$. On the other hand, it exhibited good activity toward the H_2O_2 reduction with a linear range from 20 μM to 19.1 mM and high sensitivity of $1338.7 \mu\text{A} \cdot \text{mM}^{-1} \cdot \text{cm}^{-2}$. Although, the technique used was only suitable for small-scale production and cannot be used for large-scale production. Dai et al., [216] prepared $\text{Au}@C\text{-Co}_3\text{O}_4$ NPs composites using the pyrolysis technique at 450 °C for 4 hours, followed by mild oxidative calcination at 250 °C for 2 hours. The fabricated catalyst provides high sensitivity toward the H_2O_2 reduction of $7553 \mu\text{A} \cdot \text{mM}^{-1} \cdot \text{cm}^{-2}$ within a narrow detection linear range from 0.05 to 100 μM .

The above-mentioned techniques were focusing on improving the electrocatalytic activity of Co_3O_4 based electrocatalysts toward the H_2O_2 sensing via the modification of interfacial active sites by altering either the morphology or particle size, as well as, decorating of the working electrode with expensive materials. On the other hand, nowadays the combination of Co-based materials characterized by the existence of a high concentration of electrocatalytic active sites with nanostructured carbon-based materials (i.e., carbon nanotubes, reduced graphene oxide, and graphene) is promising because the obtained hybrid catalyst revealed better electrochemical performance toward the H_2O_2 sensing. This behavior results from the combination between the large concentration of active sites, as well as the improvement in the charge transfer kinetics at the interface of the used hybrid electrodes. Kong et al [217] have synthesized Co_3O_4 nanowires on reduced graphene oxide via two subsequent steps hydrothermal followed by thermal treatment. The obtained composites revealed good electrocatalytic activity toward the H_2O_2 reduction with a high sensitivity of $1140 \mu\text{A} \cdot \text{mM}^{-1} \cdot \text{cm}^{-2}$. Kogularasu et al [218] reported the preparation of 3D graphene oxide-cobalt oxide polyhedrons via hydrothermal techniques. They illustrated that the improvement in the synergetic effect between the graphene oxide and the cobalt oxide polyhedrons results in H_2O_2 detection with high sensitivity of $3450 \mu\text{A} \cdot \text{mM}^{-1} \cdot \text{cm}^{-2}$ in the linear detection range from 0.05-400 μM of H_2O_2 . Heli and Pishahang [219] reported the preparation of Co_3O_4 NPs on carbon

nanotubes using the microwave decomposition method, which revealed electrocatalytic activity toward the H₂O₂ reduction in 0.1 M NaOH with 1002.8 $\mu\text{A}\cdot\text{mM}^{-1}\cdot\text{cm}^{-2}$ sensitivity in the linear range from 20 to 430 μM .

Based on the above-mentioned preparation methods of the Co₃O₄-based catalyst, we found that the reported techniques revealed good electrochemical performance toward the overall water splitting and H₂O₂ sensing application. However, these techniques may ignore the cost-efficiency that is necessary for commercializing water splitting electrochemical energy conversion, the use of dangerous chemicals, a very long preparation time in several separate steps that increase the production cost, and a difficult scaled-up for large size production in commercial applications. The nanoparticle deposition system (NPDS) is one of the top-down techniques used for direct deposition of binder-free nanostructured ceramic materials films and their composites by spraying the initial microparticles at room temperature, which prevents the thermal damage of the used substrate [220, 221]. Besides, deposition with NPDS is easy to be scaled up for films with large deposition area and suitable for mass production that reduces the cost of fabrication for real-life commercial applications [68]. Sung-Ik Park [99] has fabricated an electrochromic device using the deposited WO₃ thin films with a 1 m² geometrical area by the NPDS system. In the present study, we fabricate efficient Co₃O₄-graphene hybrid catalysts with different Co₃O₄ contents (25, 50, and 75 wt.%) using a one-pot deposition technique by a modified vacuum spray technique. Compared with the other reported techniques, our fabrication technique is a simple, one-step deposition for composite catalysts in a short time, with no chemical hazards, suitable for scaled-up to large size production. Also, the effect of changing Co₃O₄ content on the oxygen evolution reaction, hydrogen evolution reaction, as well as H₂O₂ sensing in the alkaline medium was investigated.

5.2. Results and discussion

5.2.1. XRD analysis of Co₃O₄-graphene composites

5.2.1.1. Initial micro-sized powder

The internal microcrystal structure of the pure graphite, Co₃O₄, and the ball-milled powder mixtures with 25, 50, and 75 wt.% Co₃O₄ were identified from XRD patterns as shown in Figure 1S. The XRD pattern of graphite powder, **Figure 5. 1(a)**, revealed two characteristic diffraction peaks at 26.5° and 56.42°, which matched well with the crystalline planes (002), and (004), respectively, of the bulk graphite hexagonal structure with lattice parameters $a = 2.643 \text{ \AA}$, and c

= 6.714 Å of the space group P63/mmc (ICDD: 00-056-016, PDF 2010). In addition, no secondary peak was detected related to any other impurity. On the other hand, the XRD pattern of the micro-sized Co_3O_4 powder, **Figure 5. 1(e)**, revealed several diffraction peaks that are in good agreement with the bulk structure of Co_3O_4 face-centered cubic phase with space group Fd-3m, (ICDD: 43-1003) [222]. Moreover, XRD patterns of the Co_3O_4 -graphite mixture with 25, 50, and 75 wt.% Co_3O_4 content, **Figure 5. 1(b-d)**, exhibited the existence of both phases, cubic Co_3O_4 , and hexagonal graphite phase, without the evolution of new phases due to the ball milling before the deposition process.

5. 2. 1. 2. Nanostructured Co_3O_4 -graphene composites thin films

Figure 5. 2 shows XRD patterns of the bare Ni foam (NF) substrate without deposition, the deposited films of the graphene/NF, Co_3O_4 /NF, as well as the deposited Co_3O_4 -graphene composites with different Co_3O_4 content (25, 50, and 75 wt.%) on Ni foam. In the case of the bare Ni foam, three main diffraction peaks were observed at 2θ values of 44.19, 51.54, and 76.09° corresponding to the (111), (200), and (220) crystalline planes of the face-centered structure with Fm-3m space groups (ICDD: 00-004-0850) of cubic Ni with preferable orientation along (111). It can be observed that in the case of the bare graphene/NF no diffraction peaks were detected except characteristic peaks of the cubic structure of the Ni foam substrate. Meanwhile, Co_3O_4 and Co_3O_4 -graphene composites thin-films revealed some peaks with a very small intensity corresponding to the crystalline peaks (311), (511), and (400) of the face-centered cubic structure of Co_3O_4 . The observed small intensity of these peaks may arise from the fragmentation of the initial microparticles to a large number of randomly oriented domains with a very small domain size that tends to be amorphous structures. The observed low crystallinity for the Co_3O_4 -based catalysts was also observed by Du et al [223] when they prepared Co_3O_4 nanosheets by phase transfer process with no detectable XRD peaks correspond to the Co_3O_4 phase. They attributed that to the low degree of crystallinity and the evolution of a higher concentration of metal oxide interfacial defects that act as an electrocatalytic active center for the oxygen evolution reaction.

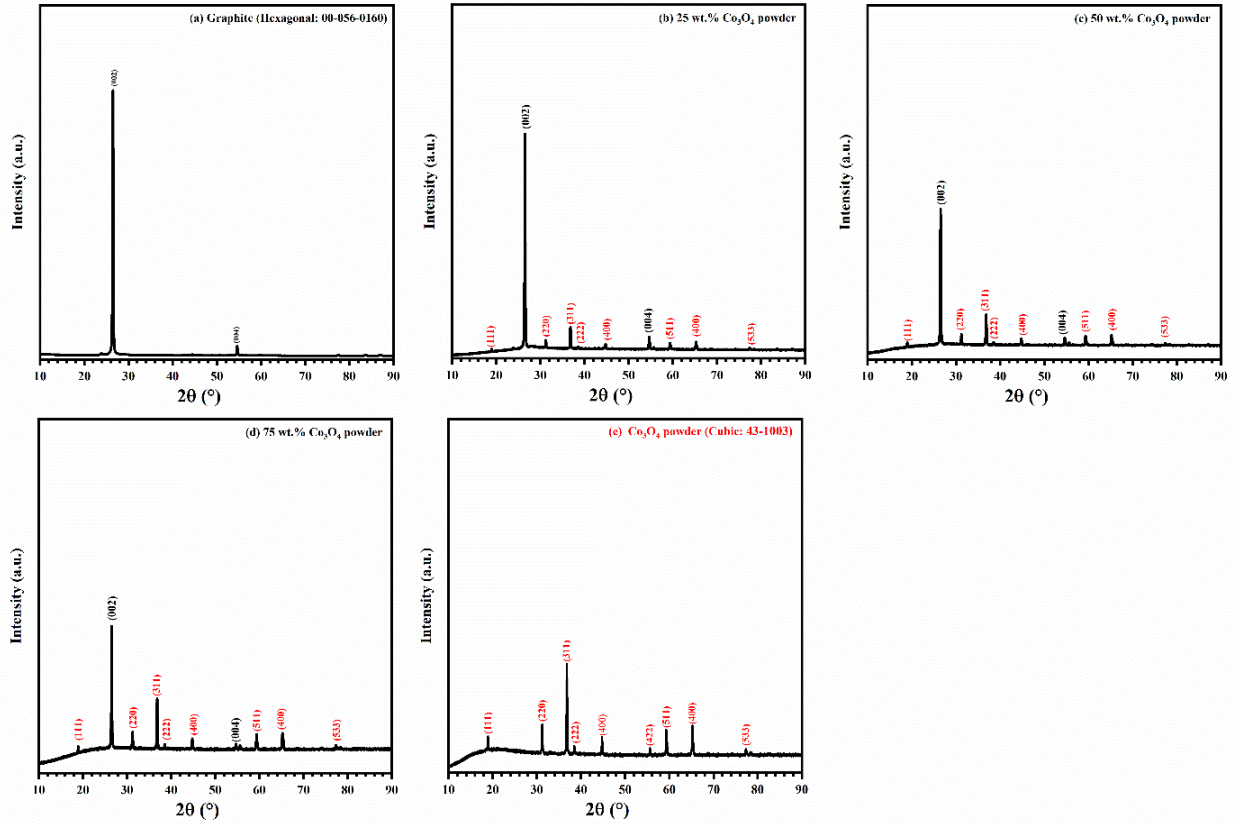


Figure 5. 1: XRD patterns of the used graphite powder **(a)**, Co_3O_4 -graphite composite **(b-d)**, and pure Co_3O_4 **(e)**

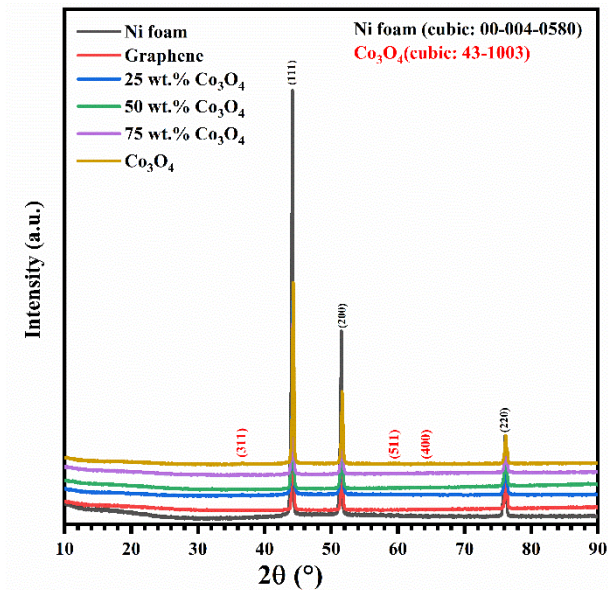


Figure 5. 2: XRD patterns of Co_3O_4 -graphene composite/NF at different Co_3O_4 contents

5. 2. 2. Raman studies on Co₃O₄-graphene composites

5. 2. 2. 1. *Micro-sized powder before deposition*

Raman spectrum of the micro-sized graphite powder in **Figure 5. 3(a)** shows various active Raman modes centered at 1354, 1584, 2722, and 3253 cm⁻¹. The main G band at 1584 cm⁻¹ corresponds to the E_{2g}-symmetry mode, which is characteristic for the lattice vibration of the large crystalline graphite powder; meanwhile, the interfacial defect-related lattice vibration D mode is noticed at 1354 cm⁻¹[110]. In addition, the second-order 2D symmetry mode is observed at around 2722 cm⁻¹[111]. Moreover, the Raman band at 3253 cm⁻¹ is actually at a frequency higher than the double of the G band frequency, which is attributed to another second-order vibration mode called intravalley 2D'-mode [112]. **Figure 5. 3(b)** shows the Raman spectrum of Co₃O₄ powder, which consists of several characteristic bands centered at a Raman shift of 188, 474, 515, 611, and 679 cm⁻¹. These active Raman modes correspond to the A_{1g}+E_g+3F_{2g} combination of the Co₃O₄ spinel structure. The most intense band centered at 679 cm⁻¹ is ascribed to the characteristic octahedral site (CoO₆) related to the A_{1g} mode of the O7h spectroscopic symmetry; Raman bands with mid-range intensity at 474 and 515 cm⁻¹ are ascribed to the E_g and F⁽²⁾_{2g} mode, respectively; in addition, bands at 192 and 611 cm⁻¹ are caused by the F⁽³⁾_{2g} and F⁽¹⁾_{2g} symmetry modes, respectively, of the tetrahedral sites of CoO₄ [224-226]. During the Raman spectra scan of the ball-milled mixtures of the Co₃O₄-graphite powders with 25, 50, and 75 wt.% Co₃O₄, we observed that both Co₃O₄ and graphite micro-structure grains still separately existed. The characteristic Raman active modes for each powder were identified from separate positions, in which Raman active modes belonging to pure graphite powder were matched with the bright grains at a 30 μm length scale, whereas the dark grains were matched with the Co₃O₄ spinel pure phase. For each of the mixed powders of Co₃O₄-graphite, Raman spectra were recognized for the two main features dark (i.e., pure phase of Co₃O₄) and bright grains (i.e., pure phase graphite). It can be observed that all Raman spectra of all mixed powders exhibit the same characteristic Raman bands at the same positions related to the pure phases of Co₃O₄ and graphite powder. This indicates the existence of both phases in the prepared powders before the deposition process, **Figure 5. 4(a-f)**.

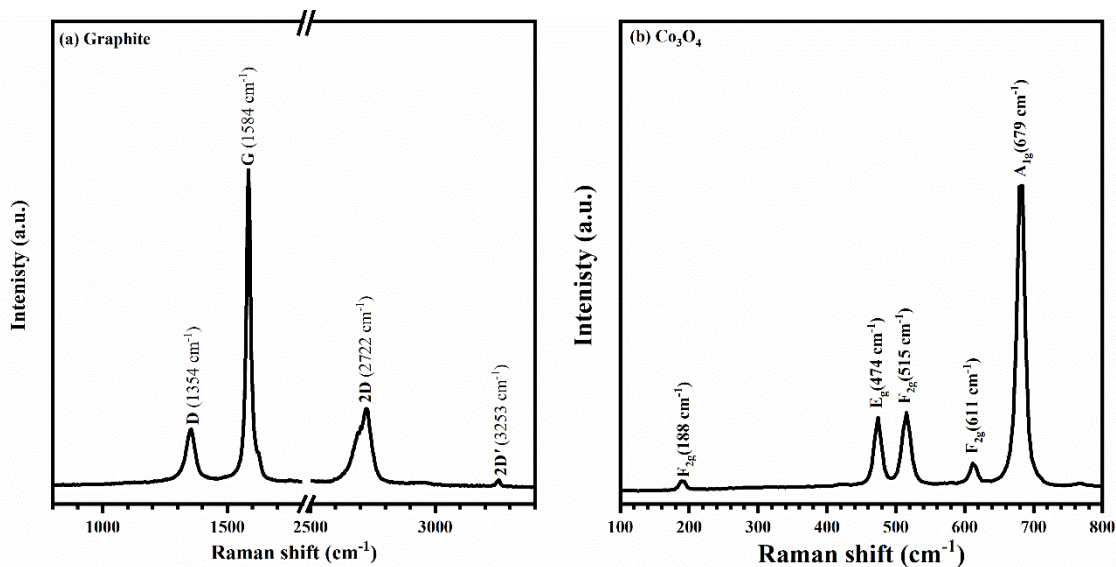


Figure 5. 3: Raman spectra of the used powder before deposition of the pure phases of graphite **(a)**, and Co_3O_4 **(e)**

5. 2. 2. 2. Nanostructured deposited thin films

It worth mentions that XRD patterns of the deposited thin films cannot detect any phase in the deposited Co_3O_4 -graphene thin films, hence micro-Raman spectroscopy was used because it is a more sensitive technique to provide information regarding the phase that exists on the deposited thin film surfaces. The Raman spectrum in **Figure 5. 5(a)** of the deposited graphene/NF nanosheets exhibits three main active Raman modes at 1352, 1590, and 2694 cm^{-1} , the evolution of the shoulder peak at 1620 cm^{-1} , as well as, the improvement of the disorder-induced G'' vibration mode at 2940 cm^{-1} [112]. The peak position of the three main active modes has the same origin as the micro-sized graphite powder with little shift in the position and variation in the width of the Raman peaks due to the induced defect at the grain boundary of the lattice [113]. The first band centered at 1352 cm^{-1} can be ascribed to the first-order vibration mode D; the second band at 1590 cm^{-1} is due to the first-order vibration mode G; Besides the observation of characteristic second-order vibration mode 2D at 2694 cm^{-1} . The observed peak shoulder at 1620 cm^{-1} corresponds to the D' -symmetry mode is ascribed to the displacement of carbon atoms inside the crystal lattice to the surface layer [110, 114]. The main characteristic that enables us to distinguish between the large crystalline structure of graphite powder and the few graphene layers caused by the fragmentation process is the change in the intensity ratio (I_D/I_G) between the vibration modes D and G in the Raman spectra.

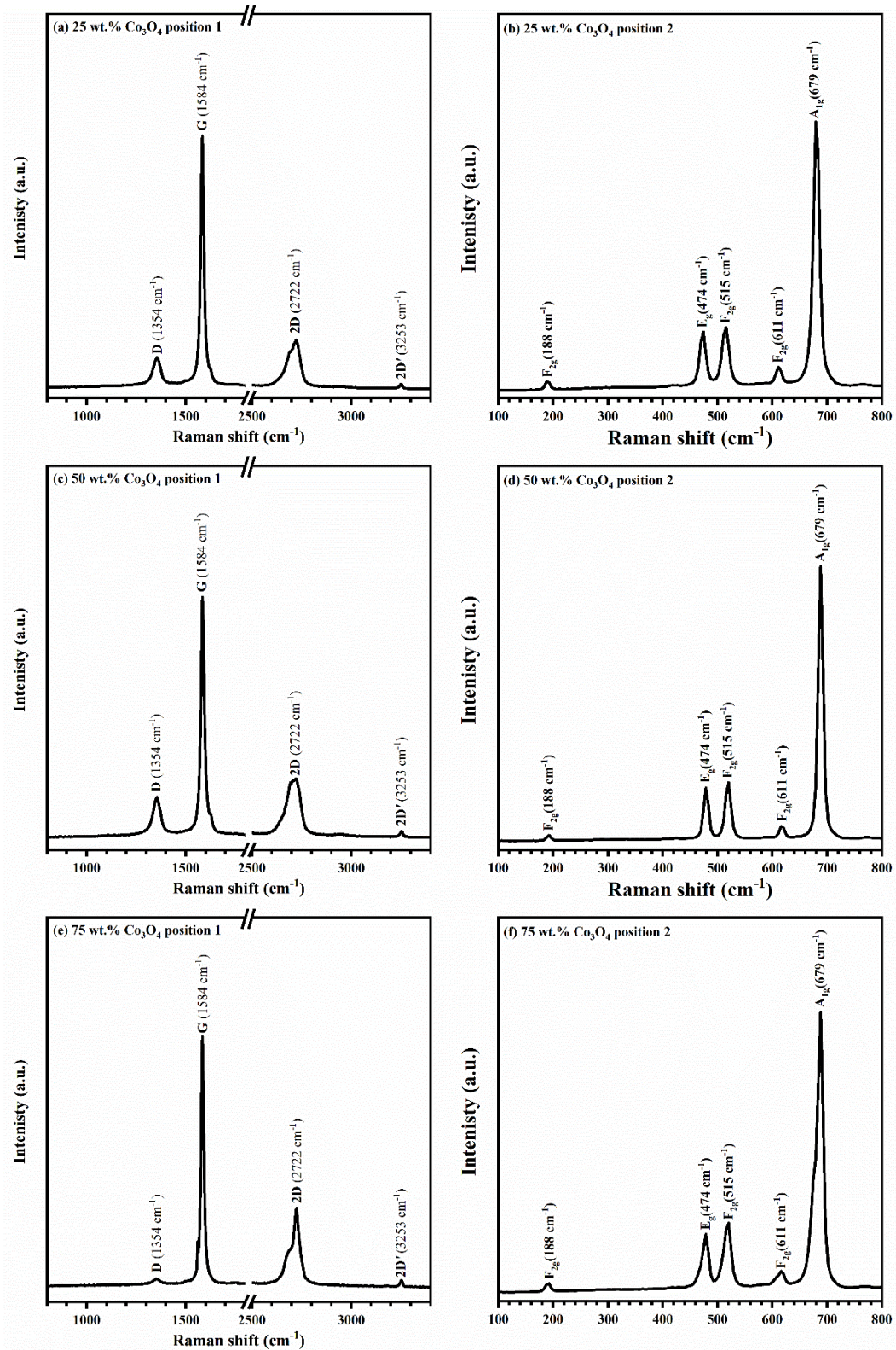


Figure 5. 4: Raman spectra of the Co₃O₄-Graphite mixed powder before deposition at different Co₃O₄ content (25, 50, and 75 wt.%).

The fragmentation of the initial micro-sized graphite powder during the deposition process is associated with the improvement of either defect or disorder-related Raman modes (D, G''), whereas the G and 2D band that distinguishes crystallinity or order degree is relatively reduced. The intensity ratio in the deposited graphene/NF of 1.34 is higher than the corresponding I_D/I_G ratio in the used micro-sized graphite powder with an intensity ratio of 0.43, **Figure 5. 4(a)**. This change in the intensity ratio is mostly caused by the layer separation due to the micro-sized particle fragmentation to a few graphene layers in the nanosized regime, as well as the evolution of a high concentration of edge-related defects [115].

The Raman spectrum in **Figure 5. 5(e)** of the deposited nanostructured $\text{Co}_3\text{O}_4/\text{NF}$ reveals several distinctive bands with peaks positioned at 192, 483, 525, 620, and 690 cm^{-1} . The observed bands correspond to multiple active Raman modes ($A_{1g}+E_g+3F_{2g}$) of the Co_3O_4 spinel structure, confirms the existence of Co_3O_4 phase species on the surface of the deposited thin films. The most intense band centered at 690 cm^{-1} is ascribed to the characteristic octahedral site (CoO_6) related to the A_{1g} mode of the O_{7h} spectroscopic symmetry. Raman bands with mid-range intensity at 483 and 525 cm^{-1} are ascribed to the E_g and $F^{(2)}_{2g}$ mode, respectively; meanwhile, the lower intensity Raman band at 620 cm^{-1} is caused by $F^{(1)}_{2g}$ mode. In addition, the Raman band with very low intensity at 192 cm^{-1} is ascribed to $F^{(3)}_{2g}$ mode that is related to the tetrahedral sites of CoO_4 [224-226]. Furthermore, by comparing peak positions with the corresponding Raman peaks in the spectrum of the Co_3O_4 powder, **Figure 5. 4(b)**, we noticed that, in general, there is a positive shift toward the higher Raman shift value for all characteristic peaks. This shift in peak positions of active Raman modes of nanostructure Co_3O_4 would arise from various size-dependent effects in the nanometric size range such as variation in the tensile stress caused by lattice disorder and low range crystalline domains. Besides, the spontaneous local thermal heating that occurred during the deposition process may cause the observed peak position shift in the Raman active modes of the Co_3O_4 nanoparticles [124, 227]. Raman spectra of the deposited Co_3O_4 -graphene composites on Ni foam with 25, 50, and 75 wt.% Co_3O_4 contents are illustrated in **Figure 5. 5(b-d)**, which reveals the existence of various Raman active modes that belong to both the Co_3O_4 spinel structure and the few graphene layers. Moreover, the change in the intensity ratio (I_D/I_G) that related to layer separation of graphite powder during the deposition process ranged from 1.25 to 1.28, demonstrates the formation of a few layers of graphene nanosheets in all composites.

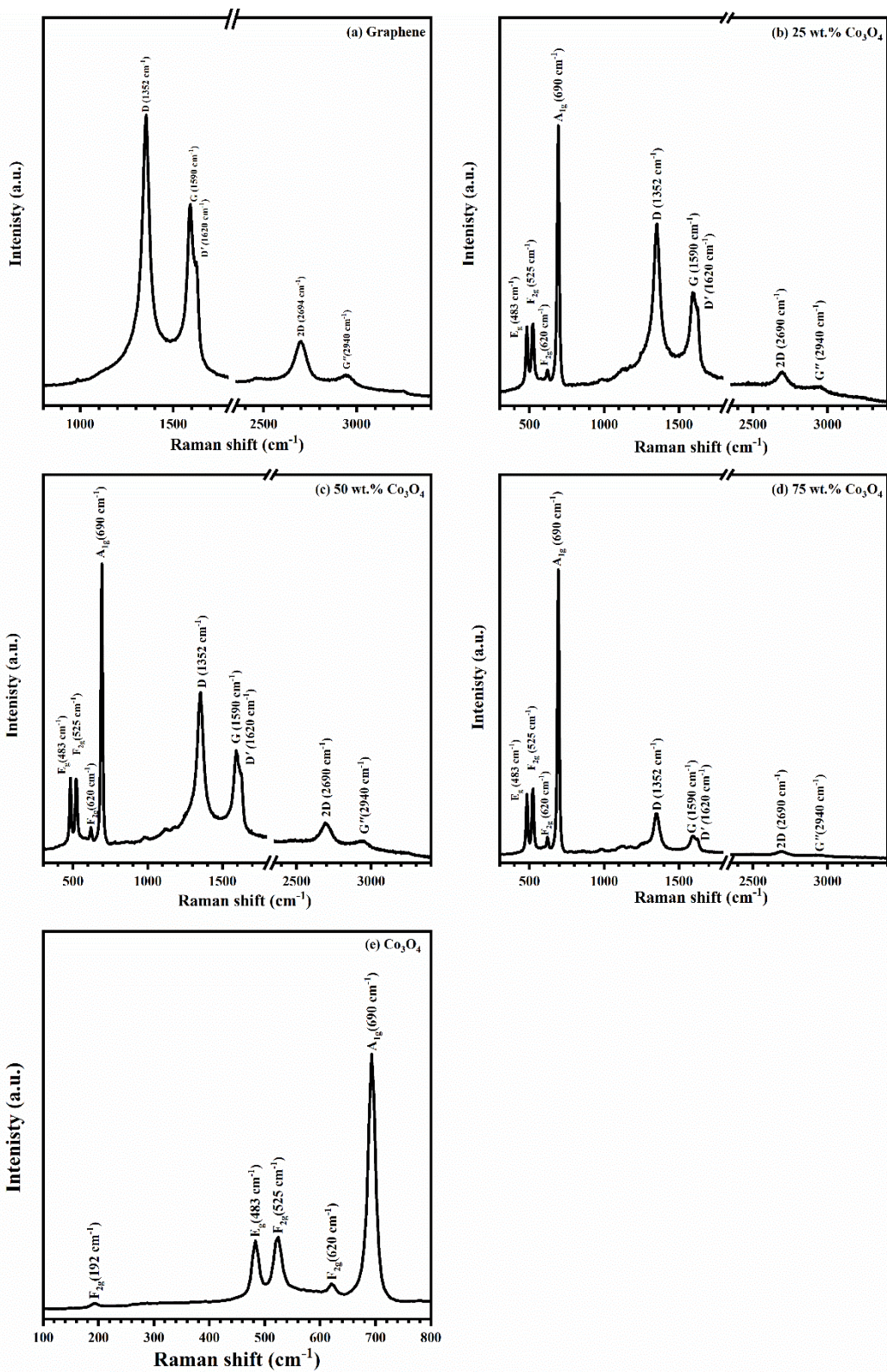


Figure 5.5: Raman spectra of graphene/NF **(a)**, Co₃O₄-graphene composites **(b-d)**, and Co₃O₄/NF **(e)**

5. 2. 3. Surface Morphology and composition analysis of Co₃O₄-graphene composites

5. 2. 3. 1. *Micro-sized powder before deposition*

Morphological and elemental analysis for the initially micro-sized particles were performed for the powder of graphite, Co₃O₄, and the mixtures with 25, 50, and 75 wt.% Co₃O₄ content. As mentioned in our previous works, the graphite powder possessed flake morphology with various dimensions and orientation with mean lateral dimension $\leq 10 \mu\text{m}$ [228], **Figure 5. 6(a, b)**. In addition, the EDS elemental analysis of the graphite powder exhibited C and O elements with 93.47 at. %, and 6.53 at. %, respectively, **Figure 5. 8(a)**. The SEM image of Co₃O₄ powder in **Figure 5. 7(e, f)** revealed a semi-spherical shape with a relatively broad size distribution in the micro-size range from less than 1 μm to $\leq 5 \mu\text{m}$, in which the observed size distribution broadening in the particle size may arise from the aggregation tendency caused by the magnetic properties of the Co₃O₄. The EDS spectrum of the micro-sized powder of Co₃O₄, **Figure 5. 8(e)** exhibited that the elemental atomic ratio (Co_k/O_k) of 0.347 with 22.47 at. %, Co_k content, and 64.77 at. % of O_k. Also, C_k with 12.76 at. % was observed to originate from the contribution of carbon film on the Cu-grid for holding the sample. The estimated elemental ratio of Co_k to O_k in the powder is less than the theoretical value of 0.75 [229]. This difference represents a large deficiency of Co content in the sample accompanied by a high concentration of Co vacancies at the octahedral (Co³⁺), tetrahedral (Co²⁺), or both sites in the spinel structure of Co₃O₄ nanoparticles [227].

SEM images of the Co₃O₄-graphite mixtures with different Co₃O₄ contents (25, 50, and 75 wt.%) in **Figure 5. 6(c, d)** and **Figure 5. 7(a-d)** revealed mixed morphology from the micro-sized flake and a semi-spherical shape within the same size range that was mentioned in the pure phases of graphite and Co₃O₄ powder. The EDS elemental analysis of the mixed powders of 25 wt. % Co₃O₄ content, **Figure 5. 8(b)**, exhibits C, O, and Co elements of 41.11, 46.3, 12.6 at. %, respectively, which possessed a Co_k/O_k ratio of 0.272. For the mixed powder with 50 wt.%, Co₃O₄, the elemental contributions are 57.12, 34.16, and 8.72 at.% corresponding to C_k, O_k, and Co_k, respectively, with a Co_k/O_k ratio of 0.255. The mixed powder with 75 wt.% Co₃O₄ contained an atomic percentage of C_k of 37.98, O_k of 47.38, as well as Co_k of 14.64 with a Co_k/O_k ratio of 0.31. Based on the calculated Co_k/O_k from the EDS spectra of all mixed powders, we observed that all mixed powders possessed lower Co_k/O_k ratios compared with the pure phase of Co₃O₄ powder, which illustrated that normal mixing using ball milling results in more deficiency in the Co content in the Co₃O₄ spinel structure.

5. 2. 3. 2. Nanostructured thin films

The suggested deposition mechanism of Co_3O_4 -graphene composites on the Ni foam substrate using the NPDS can be explained according to Chun et al. [100]. They reported that the deposition and bonding mechanism of ceramic particles on a substrate by the NPDS, where the bonding nature occurred in successive steps within a very short time (few nanoseconds). Firstly, the impact between the accelerated micro-sized ceramic particle with the substrate results in the fracture to a smaller size in the nano-size range due to the shock compaction wave; followed by successive impact with the micro-sized particles that cause dramatic local thermal heating and pores-filling (packing) of the deposited thin films. The lateral local thermal heating would cause solid-state diffusion and strong bonding at the interface between the deposited film and the substrate [230]. For the deposited Co_3O_4 -graphene composites thin films, graphene plays an important role in reducing the grain boundaries aggregation of the deposited Co_3O_4 nanoparticles due to the improvement in the heat dissipation during the deposition process that illustrated from the following SEM analysis of the deposited pure phase Co_3O_4 /NF thin, as well as composites with different graphene content.

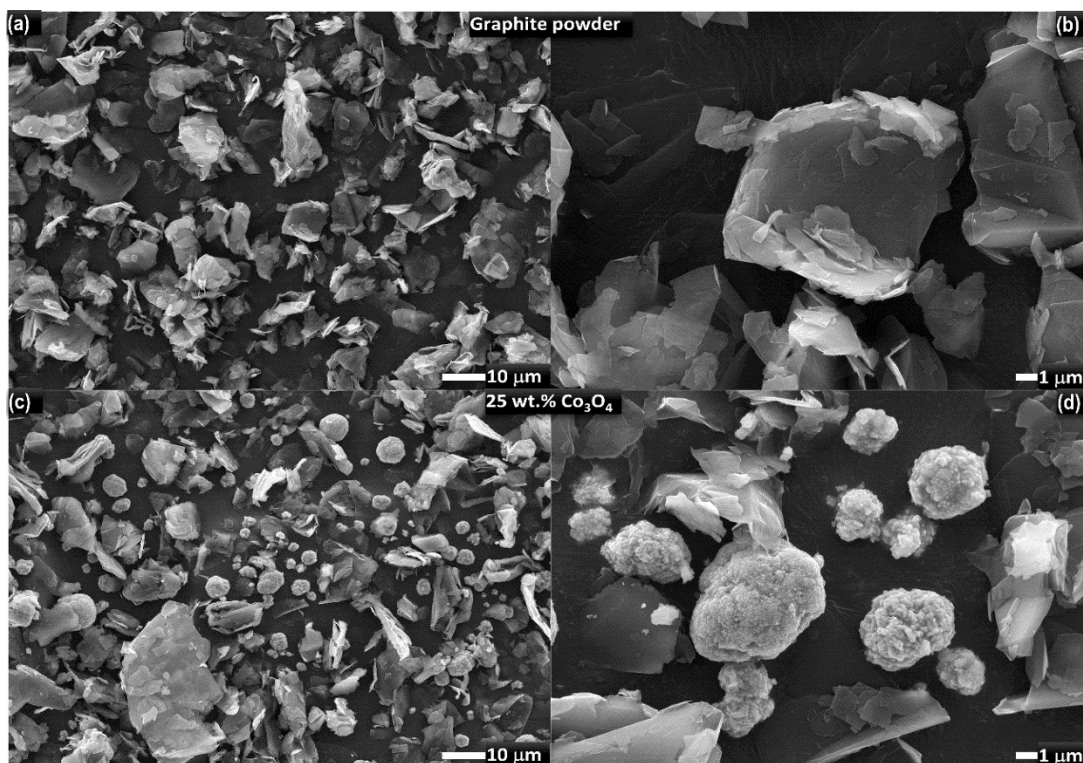


Figure 5. 6: SEM images of the micro-sized particles of (a, b) graphite powder, and (c, d) mixed Co_3O_4 -Graphite powder before the deposition with 25 wt.% Co_3O_4 content.

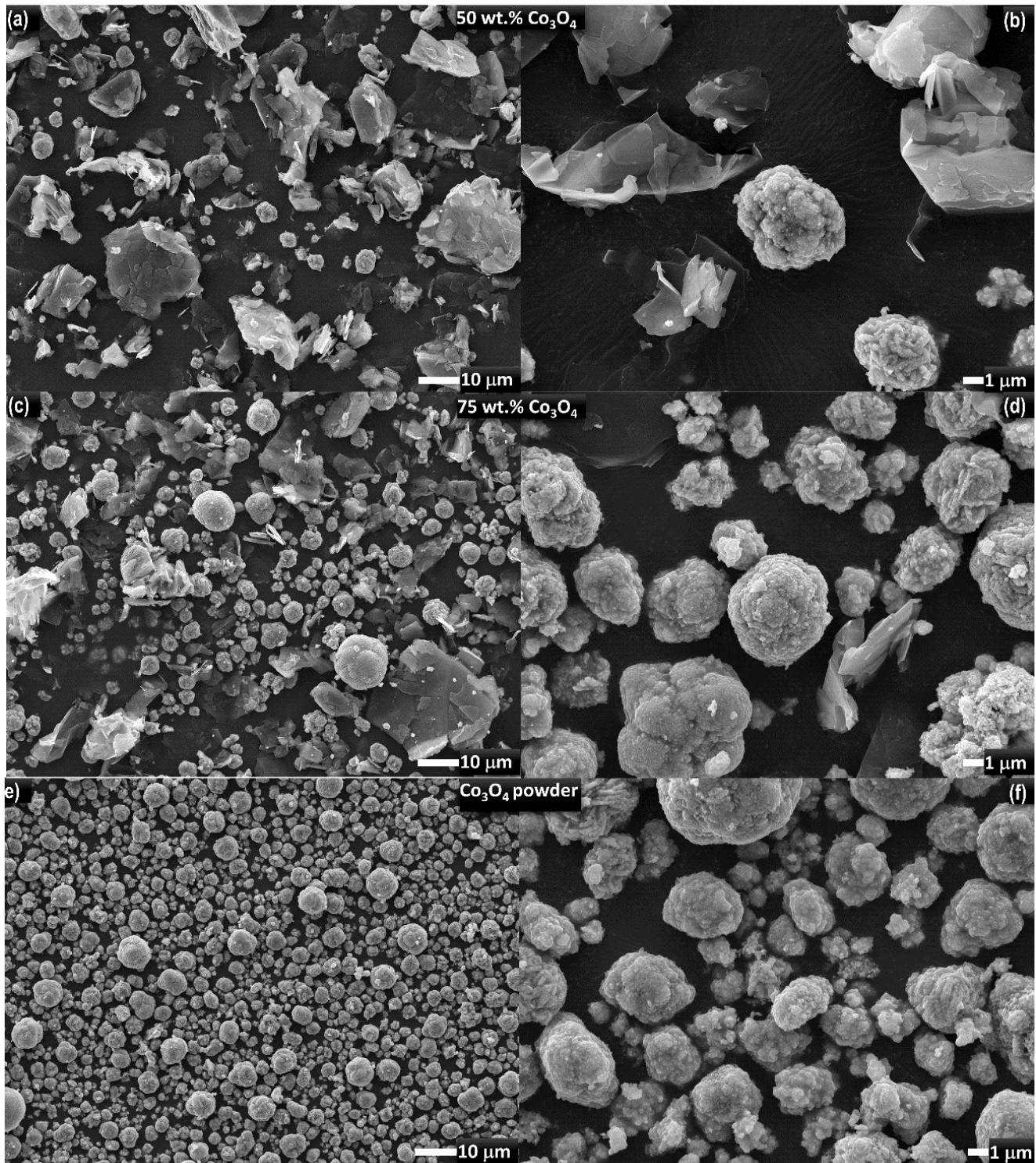


Figure 5. 7: SEM images of the micro-sized particles of Co_3O_4 -Graphite composites with Co_3O_4 content of 50 wt.% (a, b), 75 wt.% (c, d), and the pure phase of (e, f) Co_3O_4 powder.

SEM images of the deposited graphene on the 3D Ni foam substrate, **Figure 5. 9(a, b)** show the deposited film morphology with a two-length scale 1 μm and 100 nm, in which the SEM image with a lower length scale exhibited several nanosized sheets with merged grain boundaries. The observed grain size range of the deposited films varies from less than 100 nm to 200 nm that confirms the fragmentation process of the micro-sized graphite powder, **Figure 5. 9(a, b)**, due to the collision between the accelerated particles with high kinetic energy and the metallic substrate in use.

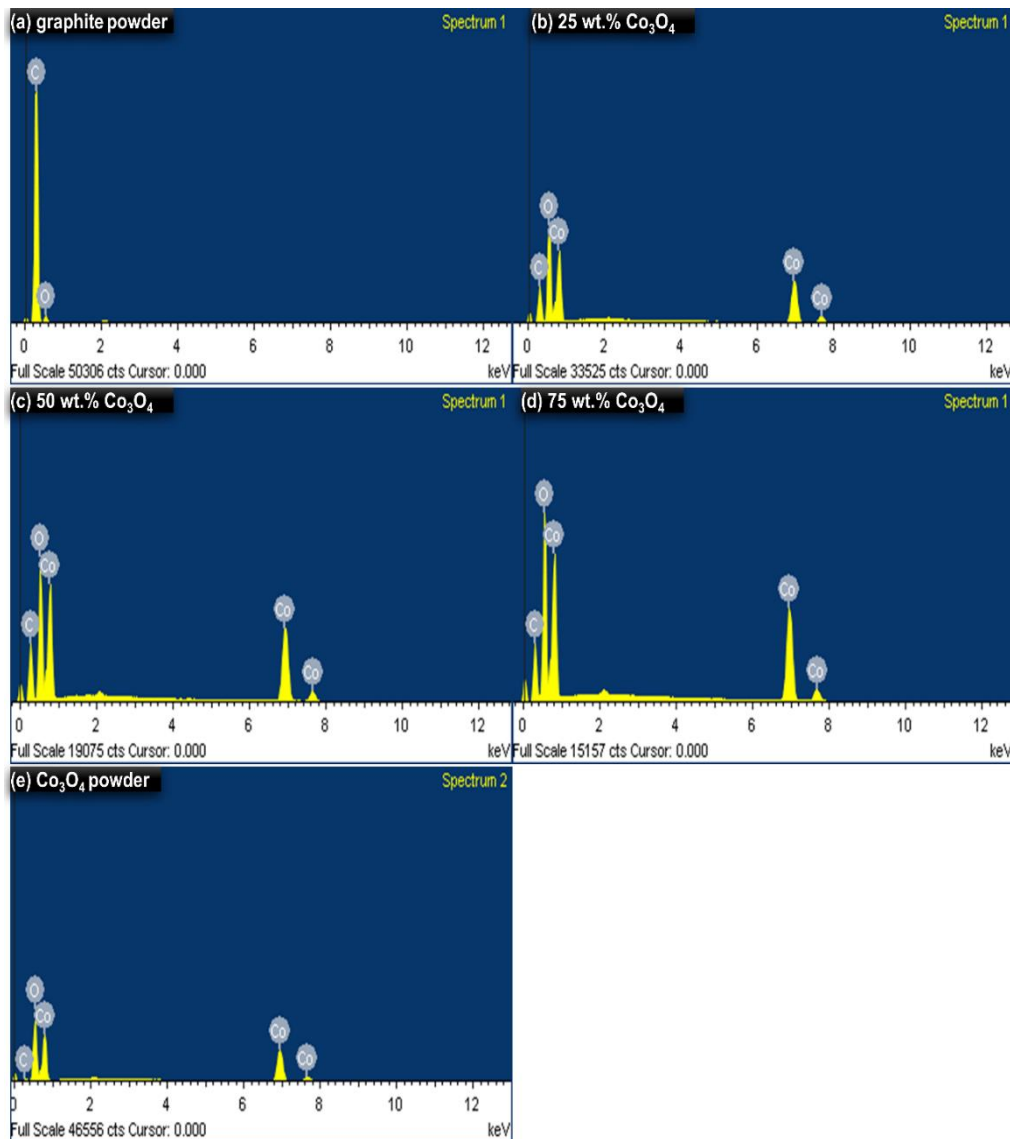


Figure 5. 8: Elemental analysis of the used micro-sized powder before deposition

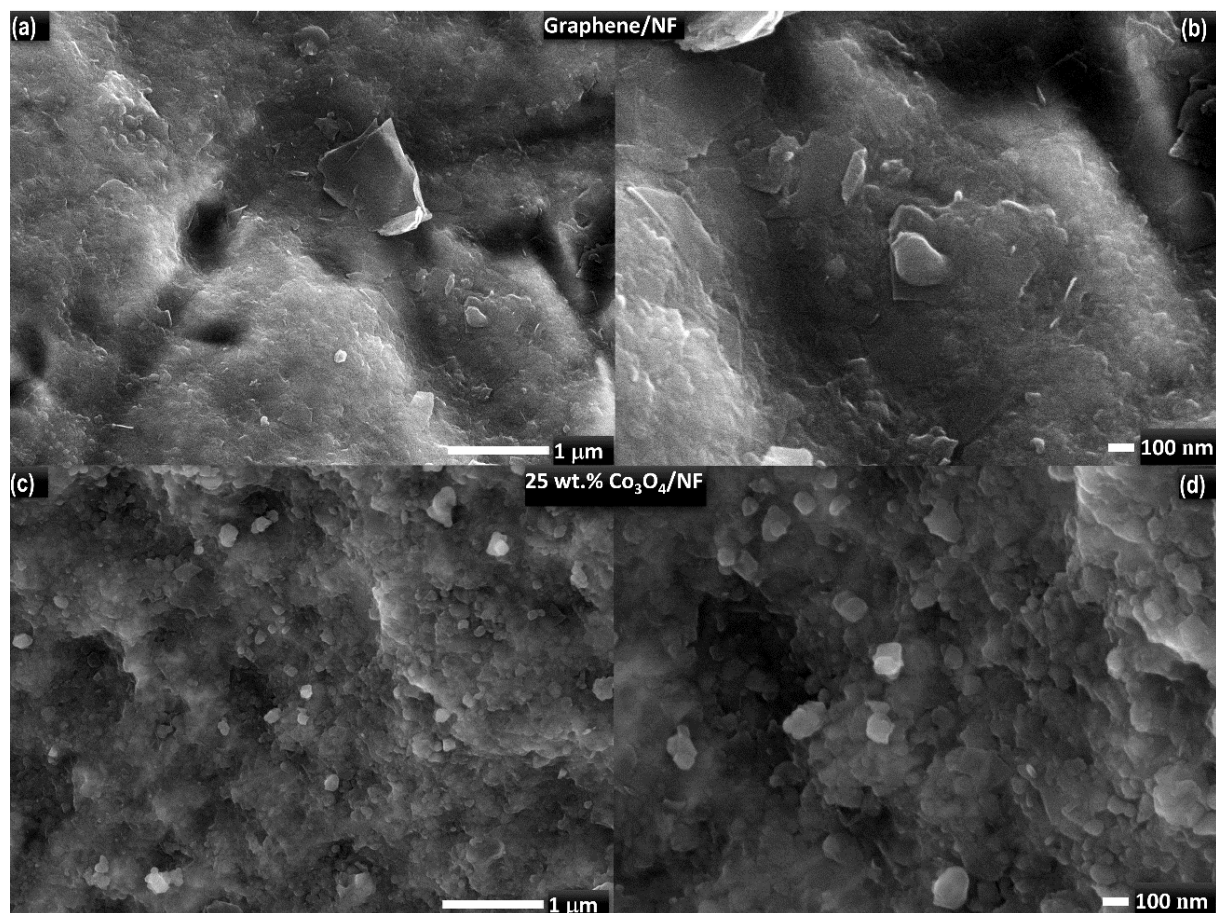


Figure 5. 9: SEM images of graphene/NF (a, b), and composites with 25 wt.% Co₃O₄/NF (c, d)

The EDS spectrum and the corresponding microstructure elemental mapping of the deposited graphene thin film in **Figure 5. 11** exhibit 62.51 at.% as carbon content and 37.49 at.% Ni that comes from the supporting Ni foam holding substrate. The surface morphology of the deposited nanostructured Co₃O₄ thin film on the Ni foam is illustrated in **Figure 5. 10(e, f)**. It can be observed that the large-scale length SEM image in **Figure 5. 10(e)** exhibited a large agglomeration tendency in some parts that resulted in ambiguous grain boundaries and difficulty in the observation of well-defined particle edges, as well as forming irregular plate structure. Other parts of the image reveal particles with small particle sizes due to the fragmentation process. The observed aggregation of the small particles in some spots in the SEM images of the deposited Co₃O₄/NF thin films is expected due to the sharp local thermal heating and slow dissipation compared with the very abrupt temperature increase (nanoseconds) that results in surface melting of some particles and welding of small particles together to form particles with larger sizes according to the explosive liquid phase sintering process [231]. The EDS spectrum and the corresponding elemental mapping of the

deposited nanostructured Co_3O_4 thin film, **Figure 5. 13**, demonstrated 30.69 at. % O, 14.68 at.%, as well as 34.43 at.% Ni from the holding substrate. The Co_k/O_k ratio in the deposited nanostructured Co_3O_4 film is 0.478, which is higher than the corresponding Co/O ratio in the micro-sized powder of 0.347. However, there is still a large deficiency in the Co species content compared with the theoretical stoichiometric value of the bulk spinel structure Co_3O_4 , the obtained stoichiometric Co_k/O_k ratio by our deposition technique that is relatively higher compared with earlier research that obtained Co_k/O_k ratio of 0.45 at an annealing temperature of 450 °C by Gawali et al.,[227], and at an annealing temperature of 800 °C by George et al.[232]. Moreover, the lateral elemental mapping reveals the homogeneous elemental distribution of Co and O all over the localized deposition area. For estimating the approximated size range of the deposited $\text{Co}_3\text{O}_4/\text{NF}$ thin film, SEM image at higher magnification was provided, **Figure 5. 10(f)**, which demonstrated particles with semi-spherical morphology and wide size distribution. The lateral size range of the deposited particles was less than 50 nm; however, the aggregation tendency was still noticed. The observed aggregation tendency in the case of $\text{Co}_3\text{O}_4/\text{NF}$ thin film may arise from the sharp increase in the temperature within a short time during the collision with the metallic substrate. In the case of nanostructured Co_3O_4 -graphene composites thin films with 25, 50, and 75 wt.% Co_3O_4 content, small particles were observed with a size range extending from less than 50 nm to 100 nm that mixed with nanostructured sheets representing graphene layers. Besides, less aggregation tendency was observed in SEM images of the composite thin films compared with the pure Co_3O_4 thin film, see **Figure 5. 9(c, d)** and **Figure 5. 10(a-d)**. The observed inhibition of the aggregation tendency of the Co_3O_4 -graphene composites/NF thin films compared with the $\text{Co}_3\text{O}_4/\text{NF}$ thin film can be understood through the proposed mechanism. The existence of graphene nanosheets in the deposited Co_3O_4 could improve the overall thermal conductivity of the deposited films, and hence the time rate of thermal energy dissipation during the successive impact of the incident micro-sized particles with the fragmented layers. This enhancement in the thermal energy dissipation prevents unnecessary further local heating and reduces the possibility of an explosive liquid phase sintering process. The EDS spectrum of the deposited Co_3O_4 -graphene composite with 25 wt.% Co_3O_4 content in **Figure 5. 11** showed the existence of C, O, and Co elements with 27.04, 34.18, and 10.31 at. %, as well as 28.47 at.% from the Ni holding substrate. This composite has a Co_k/O_k ratio of 0.3. The EDS spectrum of the Co_3O_4 -graphene composite thin film with 50 wt.% Co_3O_4

content, **Figure 5. 12**, demonstrated 18.74, 48.72, 10.65, and 21.89 at.% of elements C, O, Co, and Ni, respectively, with a Co_k/O_k ratio of 0.2186.

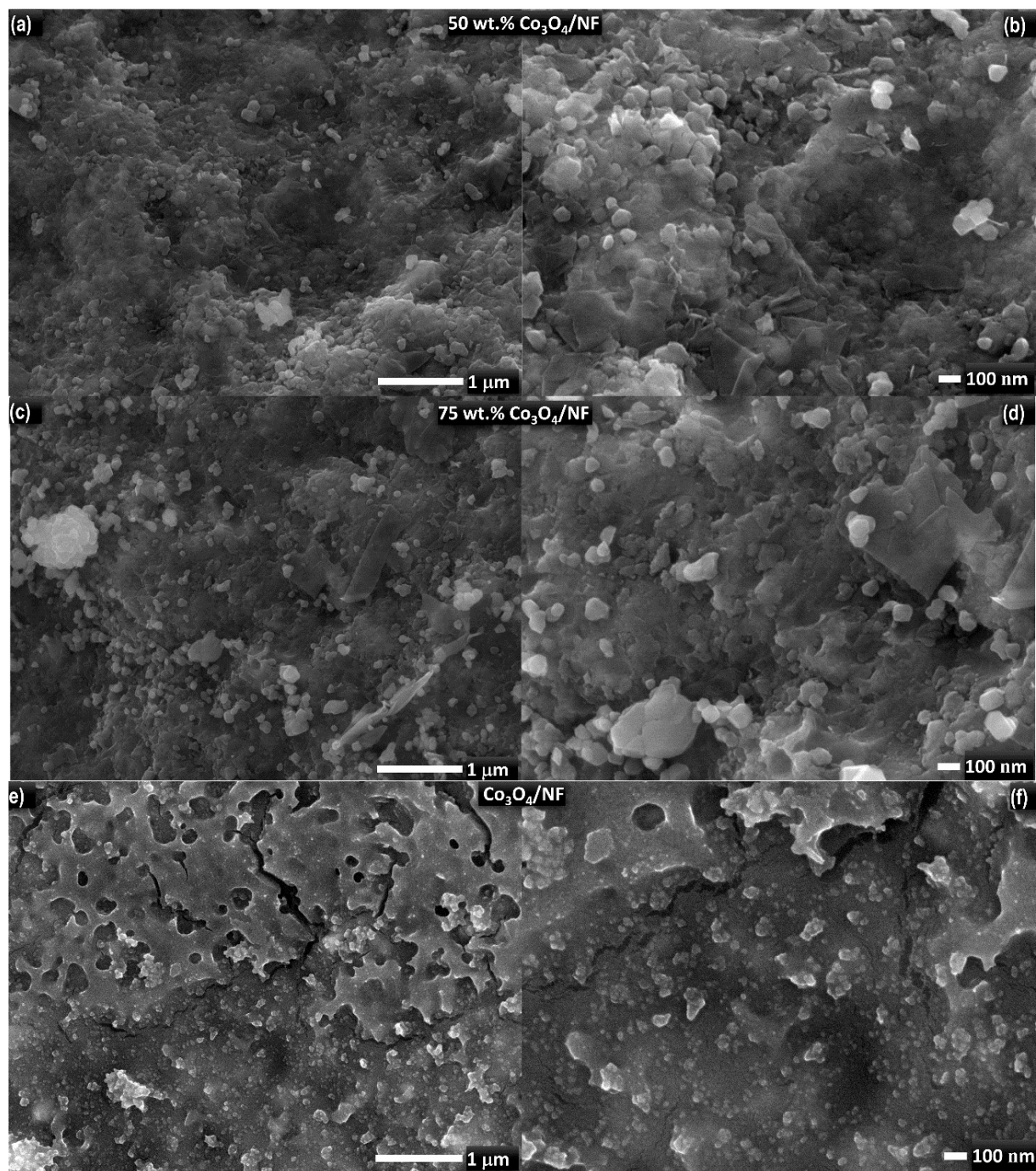


Figure 5. 10: SEM images of composites with 50 wt.% (a, b), 75 wt.% (c, d) $\text{Co}_3\text{O}_4/\text{NF}$, and pure $\text{Co}_3\text{O}_4/\text{NF}$ (e, f)

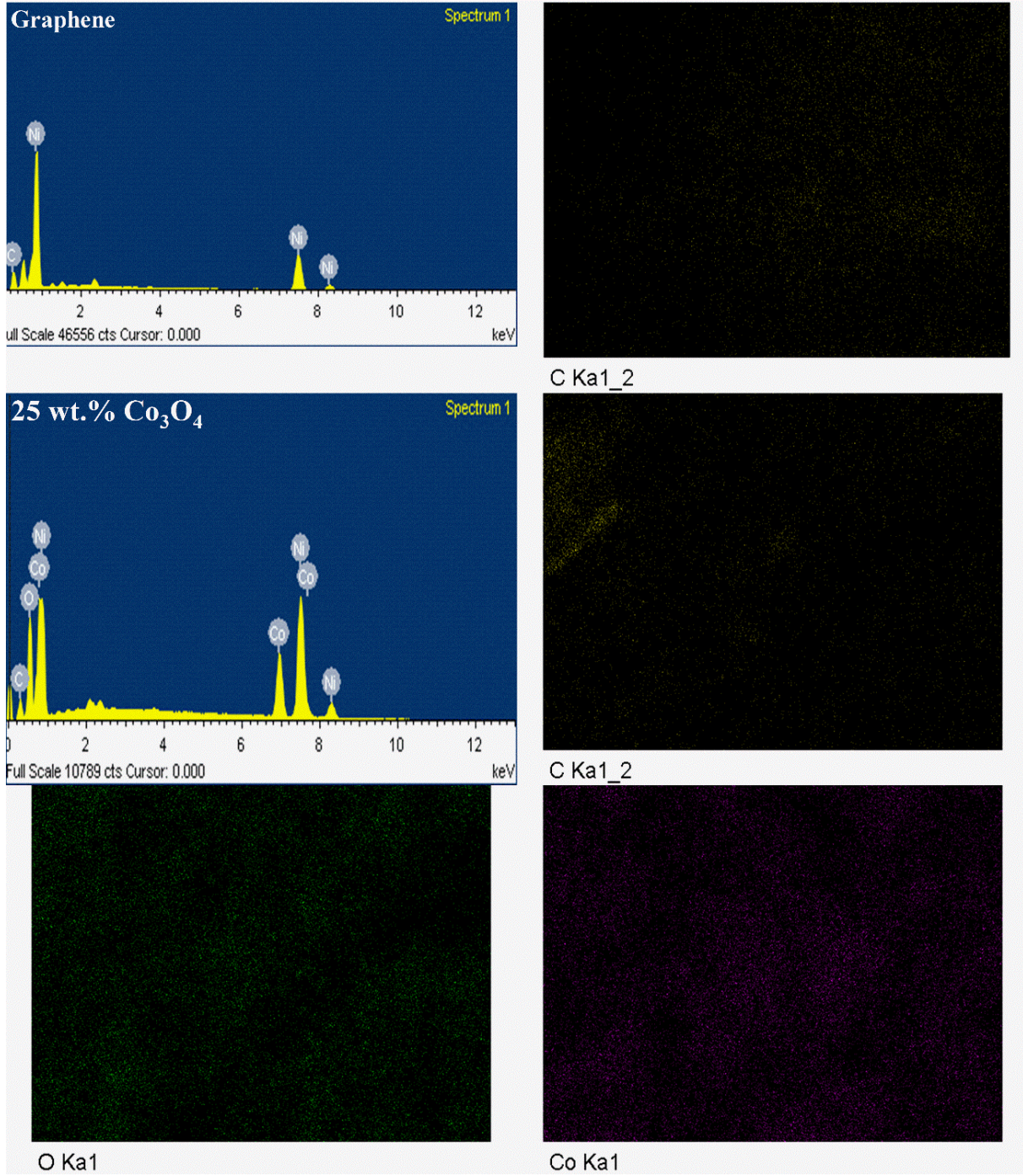


Figure 5. 11: Elemental analysis and the corresponding mapping of graphene/NF and composite with 25 wt.% Co₃O₄/NF

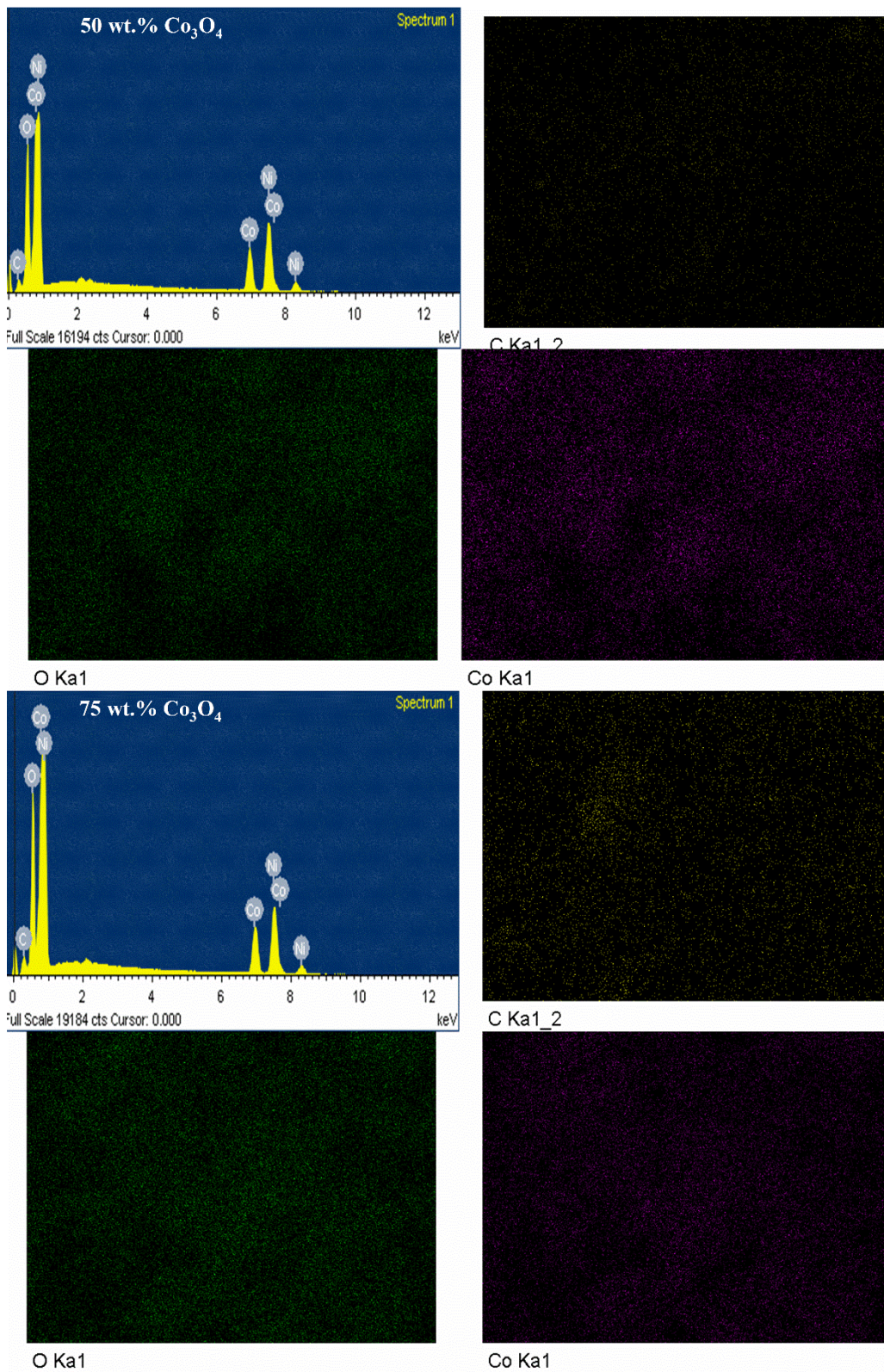


Figure 5. 12: Elemental analysis and the corresponding elemental mapping of Co_3O_4 -Graphene/NF composite with 50, and 75 wt.% Co_3O_4 content.

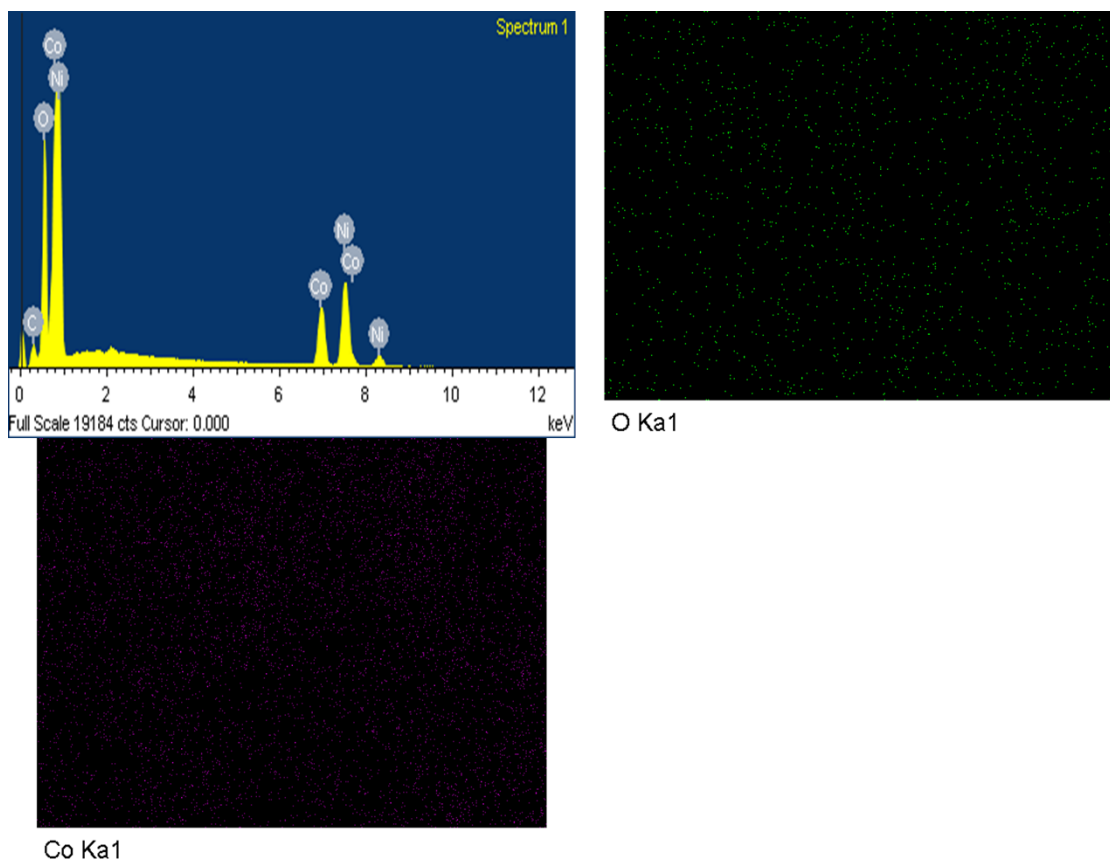


Figure 5.13: Elemental analysis and the corresponding elemental mapping of $\text{Co}_3\text{O}_4/\text{NF}$ thin film.

The EDS spectrum of the deposited composite thin film with 75 wt.% Co_3O_4 content, **Figure 5.12**, revealed C, O, Co, and Ni elements with 21.5, 49, 11, 18.5 at.% with a Co_k/O_k ratio of 22.45. It can be observed that the Co/O ratio for all of the deposited films corresponding to Co_3O_4 -graphene composites is lower than the corresponding pure $\text{Co}_3\text{O}_4/\text{NF}$ demonstrating the increase of Co vacancies either at octahedral (Co^{3+}), tetrahedral (Co^{2+}) or both sites in the spinel structure of Co_3O_4 nanoparticles. Furthermore, the lateral distribution of elements was checked from the corresponding elemental mapping for each composite, illustrating that the deposited films exhibit good film uniformity over the entire scanned area.

5. 2. 4. XPS analysis of the Co_3O_4 -graphene composites thin films

To illustrate the chemical and interfacial electronic states on the Co_3O_4 -graphene hybrid catalyst surfaces, X-ray photoelectron spectroscopy (XPS) was performed for the pure phases and their hybrid catalysts with different Co_3O_4 content (25, 50, and 75 wt.%). The XPS survey spectra in **Figure 5.14** for the pure phase of the nanostructured Co_3O_4 , graphene nanosheets, as well as their hybrid catalyst, reveal

the presence of typical signals corresponding to the metallic phase of Co (i.e. Co 2p, Co 3p, and Co 3s), active oxide states O 1s, as well as, C 1s corresponding to the active states of carbon-related to the graphene nanosheets. For demonstrating the nature of these active states, a high-resolution XPS scan for each case is performed. High-resolution XPS scans of Co 2p correspond to the nanostructured Co_3O_4 and hybrid catalyst with graphene are illustrated in **Figure 5. 15(a)**, which reveal the presence of Co characteristic peaks that belong to Co $2p_{3/2}$ and Co $2p_{1/2}$ accompanied by a few shake-up satellite peaks due to the spin-orbital coupling of these active electronic states. The deconvoluted high-resolution XPS scan of Co $2p_{3/2}$ for the pure phase of Co_3O_4 , **Figure 5. 15(b)**, exhibited two main peaks at 780.5 eV and 781.5 eV, corresponding to the binding energy of Co^{3+} and Co^{2+} , respectively. Meanwhile, the deconvolution of the Co $2p_{1/2}$ band revealed two peaks at 795 eV caused by Co^{3+} states and 797.5 by Co^{2+} states.

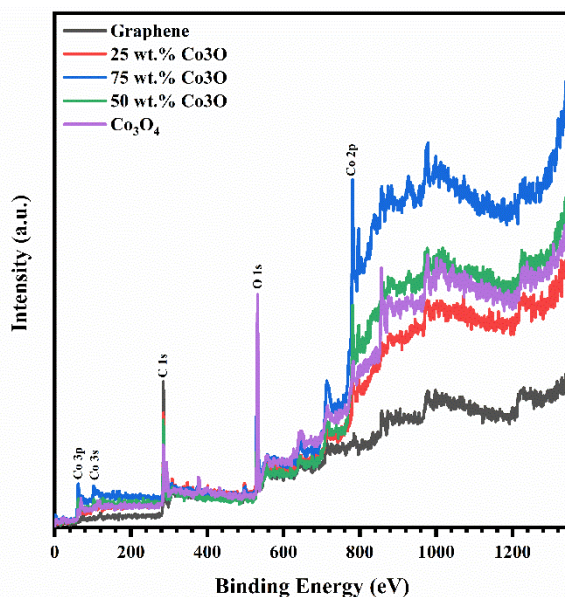


Figure 5. 14: Wide-scan XPS survey spectra of the Nanostructured pure phases of graphene and Co_3O_4 electrocatalysts, and their hybrid catalysts with different Co_3O_4 content.

The average energy separation between the two main spin-orbital states is around 15.25 eV, which is a characteristic value for Co $2p_{3/2}$ and Co $2p_{1/2}$ orbital in Co_3O_4 [188, 189, 233, 234]. It can be observed that the high-resolution XPS scan of Co 2p for all hybrid catalysts revealed a negative shift to a lower value of binding for all electronic states compared with the pure Co_3O_4 phase, whereas the hybrid catalyst with 25 wt.% Co_3O_4 content, **Figure 5. 15(c)**, revealed deconvoluted bands of Co $2p_{3/2}$ at 779.7 eV and 781.1

eV, in addition to deconvoluted bands of Co 2p_{1/2} at 794.8 eV and 796.9 eV with an average spin-orbital energy separation of 15.45 eV.

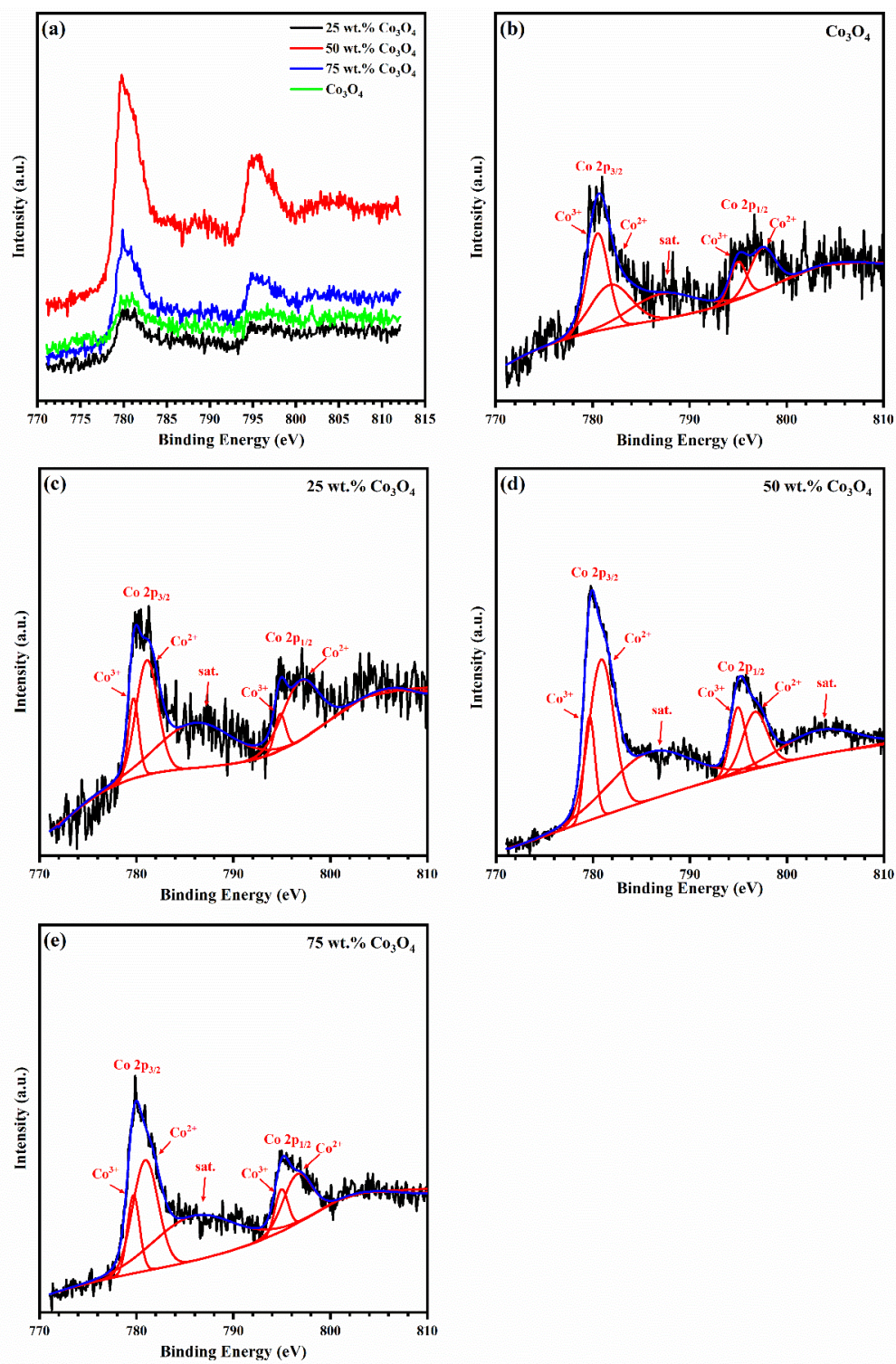


Figure 5. 15: Co 2p XPS spectra of Co₃O₄-graphene composites.

The deconvoluted high-resolution XPS scan of a hybrid catalyst with 50 wt.% Co_3O_4 content in **Figure 5. 15(d)** exhibited split bands Co 2p_{3/2} at 779.65 eV and 780.87 eV, accompanied by split bands of Co 2p_{1/2} at 794.94 eV and 796.7 eV with an average spin-orbital energy separation of 15.44 eV. Moreover, the hybrid catalyst with 75 wt.% Co_3O_4 content in **Figure 5. 15(e)** revealed subbands of Co 2p_{3/2} at 779.7 eV and 780.93 eV, as well as Co 2p_{1/2} subbands at 794.96 eV and 796.6 with an average spin-orbital energy separation of 15.47 eV. It can be observed that the intensity of Co 2p_{3/2} and Co 2p_{1/2} bands was improved in the hybrid catalyst, in which the catalyst with 50 wt.% Co_3O_4 content possessed the highest relative intensity compared with other catalysts. Furthermore, the relative increases of the deconvoluted subband area correspond to the Co^{2+} , as well as the shake-up satellite peaks revealing the improvement of the concentration of the active sites with higher electron-spin states [235-237]. Based on the deconvolution of the high-resolution XPS scan of Co 2p, we can approximate the relative contribution of Co^{3+} and Co^{2+} states in the deposited Co_3O_4 -graphene/NF thin films based on the shared area of each state. The deconvoluted Co 2p_{3/2} XPS scan of Co_3O_4 /NF revealed that 54% of the band area corresponds to a lower spin state of Co^{3+} 2p_{3/2} and 46% is related to a higher spin state Co^{2+} 3p/2. Meanwhile, the deconvolution of the Co 2p_{3/2} XPS scan of the nanostructured Co_3O_4 -graphene/NF hybrid catalyst revealed improvement in the contribution of the high spin state Co^{2+} 2p_{3/2} with area percent ranging from 75 to 78% compared with the lower spin state Co^{3+} 3p/2 with an area percent in the range 22 to 25%. Similar behavior was observed for the second orbital states of Co 2p_{1/2}, in which further improvement was shown in the high spin state (Co^{2+}) compared with the lower spin state (Co^{3+}) in all hybrid catalysts. The observed improvement in the Co^{2+} state contribution compared with Co^{3+} states in the case of all hybrid catalysts, revealed the hybridization with graphene-enhanced the reduction of Co^{3+} to more electrocatalytic active sites of Co^{2+} [234] that accompanied the formation of a high concentration of oxygen vacancies [238, 239]. The role of these active states in the spinel structure Co_3O_4 nanocrystals was theoretically investigated Zhang et al., [240], who revealed that the concentration increase of the high spin Co state (Co^{2+}) at the interface of the working electrode would result in the overall improvement of the electrochemical performance. The observed improvement in the concentration of the high spin state Co^{2+} in the spinel structure of Co_3O_4 during the deposition of Co_3O_4 -graphene thin films compared with the Co_3O_4 /NF thin films can be explained as follows: As mentioned above, thermal aggregation was noticed to have more effect in the case of Co_3O_4 /NF compared with the Co_3O_4 -graphene composites/NF thin films due to the slow dissipation of local thermal heating.

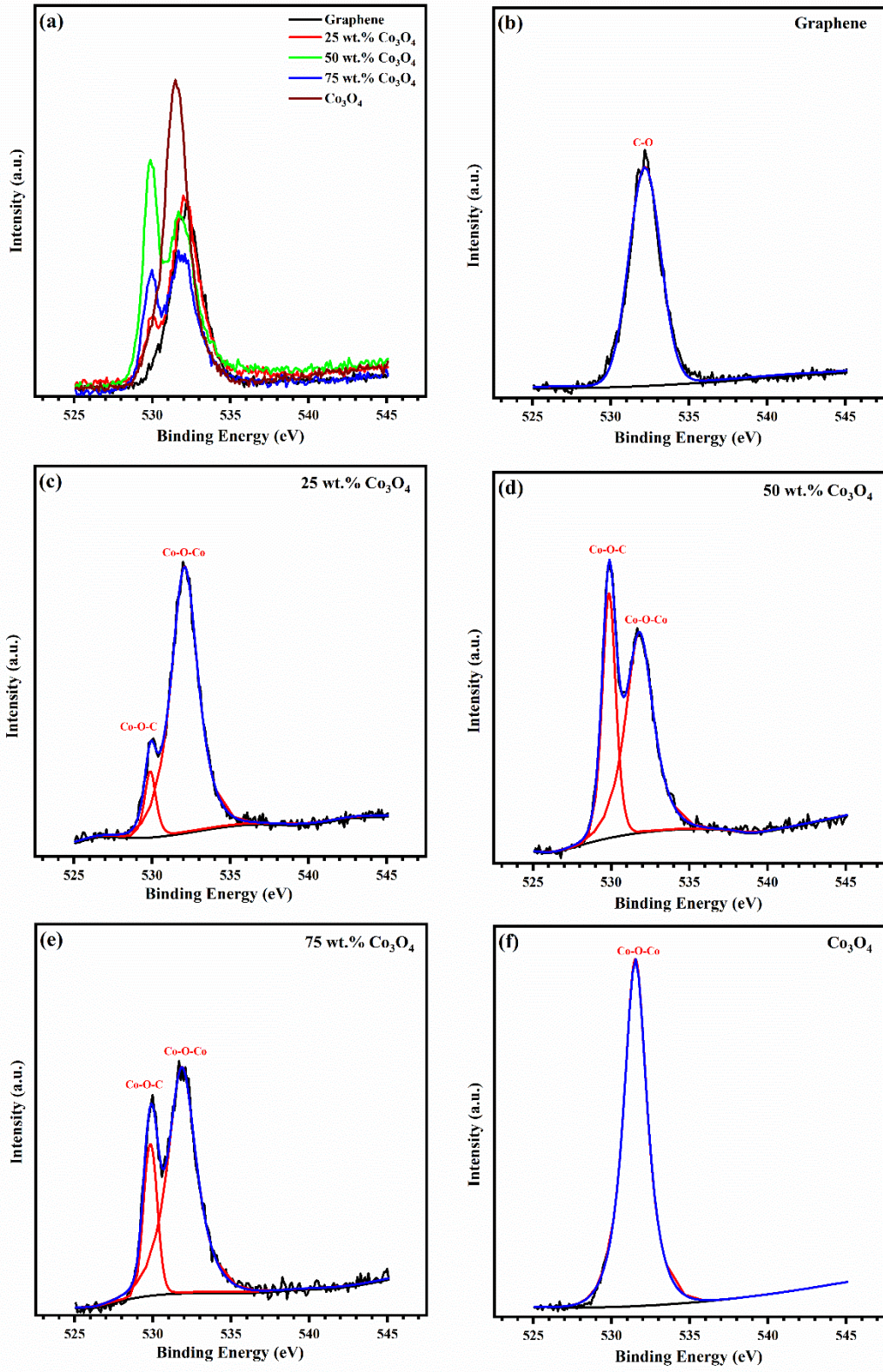


Figure 5. 16: O 1s XPS spectra of Co₃O₄-graphene composites

The excessive local thermal heating due to the successive impact with submicron particles would result in further oxidation of Co^{2+} related to CoO states in the spinel structure to Co^{3+} of the Co_3O_4 , which required a high temperature for oxidation [241]. Meanwhile, the presence of graphene nanosheets in the Co_3O_4 -graphene/NF thin films prevents further heating for the fragmented particles, which reduces the possibility of thermal oxidation of the high spin states of Co^{2+} . This agrees with the obtained results from SEM analysis in the previous section. **Figure 5. 16(a)** illustrates the high-resolution O 1s XPS spectra for the pure phases of graphene/NF and Co_3O_4 /NF, as well as their hybrid catalysts with different Co_3O_4 content (25, 50, and 75 wt.%). The O 1s XPS spectrum in **Figure 5. 16(b)** of the graphene/NF catalyst revealed only one main band centered at a binding energy of 532.18 eV that arose from the existence of some residual oxygen-containing groups at the grain boundaries such as C–O [242]. On the other hand, the O 1s XPS spectrum of the pure Co_3O_4 /NF catalyst in **Figure 5. 16(f)** revealed one main band at 531.5 eV, which is the main characteristic bond (Co–O–Co) of Co_3O_4 -based materials [237, 243]. In the case of Co_3O_4 -graphene hybrid catalysts with 25, 50, and 75 wt.% O 1s XPS spectra, **Figure 5. 16(c–e)** exhibited the evolution of new active bond states corresponding to Co–O–C at 529.86 eV, which demonstrated the improvement of synergy between the Co_3O_4 nanoparticles and the graphene nanosheets in the case of the hybrid catalysts compared with the pure phases of Co_3O_4 /NF and graphene/NF catalysts. The observed new bond states in our hybrid catalyst are in agreement with many previous reports concerning Co_3O_4 graphene-based catalysts [78, 234, 237, 242, 243]. Moreover, it can be observed that the hybrid catalyst with 50 wt.% Co_3O_4 content exhibited the highest intensity of the new bond state, which demonstrates that this hybrid catalyst would possess the highest number of distributed active states at the surface of the working electrode compared with the other hybrid catalysts with 25 and 75 wt.% Co_3O_4 content. In addition, it was observed that the main characteristic O-related bond of the Co_3O_4 spinel structure shown at 531.5 eV for the pure Co_3O_4 /NF was positively shifted to 532, 531.85, and 531.85 eV corresponding to hybrid catalysts with 25, 50, and 75 wt.%, respectively. The observed positive shift of the Co–O bond in the hybrid catalyst may be caused by the strong coupling between the nanostructured Co_3O_4 and graphene nanosheets. A similar positive shift in the Co binding energy was observed in the Co_3O_4 - MoS_2 hybrid catalyst [188, 244].

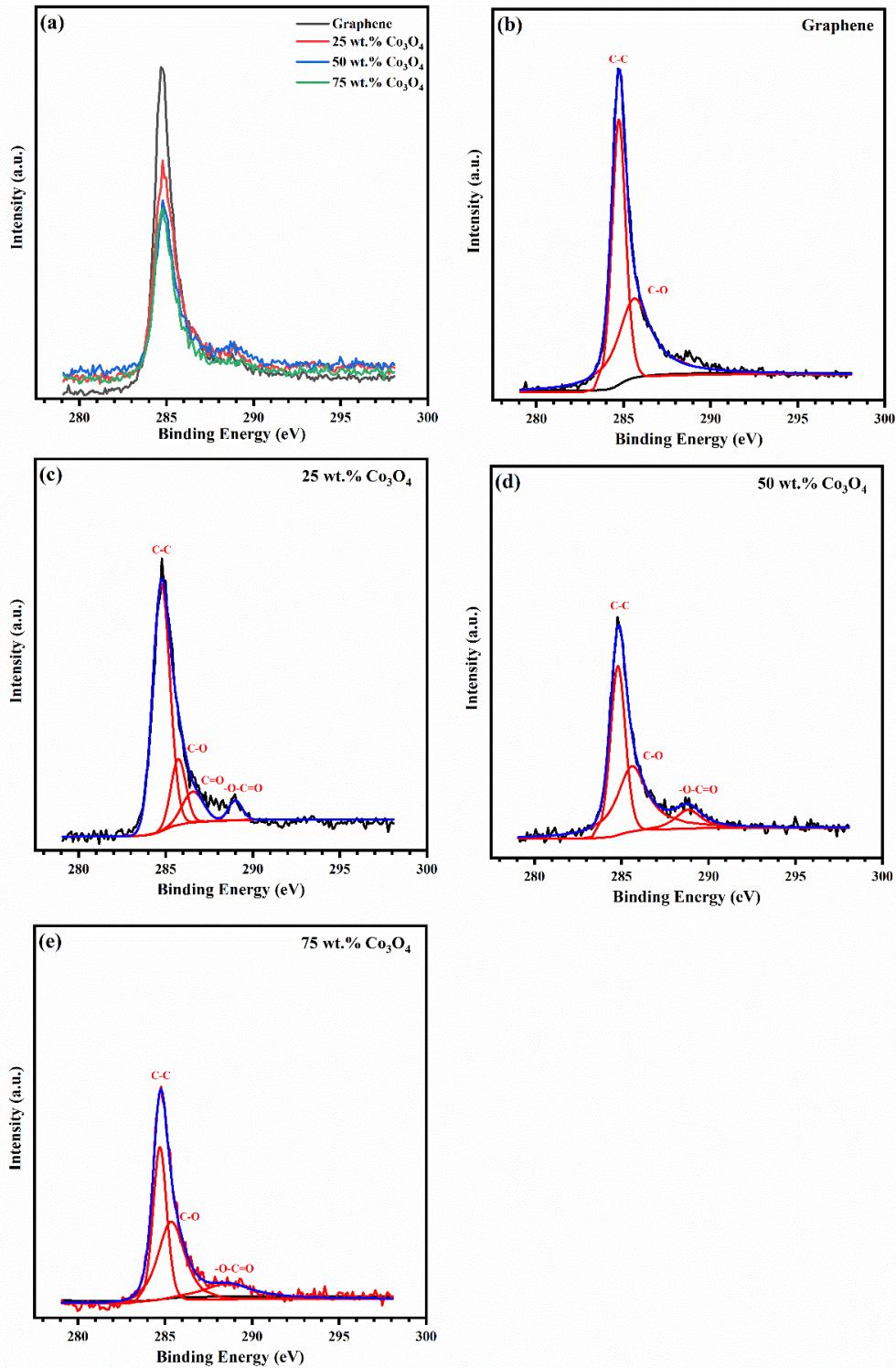


Figure 5. 17: C 1s XPS spectra of Co_3O_4 -graphene composites (a-d)

Figure 5. 17(a) illustrates the high-resolution C 1s XPS spectra of the graphene/NF and the hybrid catalysts with different Co₃O₄ content, in which each spectrum was deconvoluted to identify the origin of the observed bands. The deconvolution of the C 1s XPS spectrum of graphene/NF, **Figure 5. 17(b)**, exhibited main bands at 284.73 eV that considered the main characteristic band caused by the sp²-hybridized carbon (C–C) in the planar graphene sheets [242], as well as, a weak shoulder at 285.73 eV caused by some oxygenated bonds in the C–O bond at the graphene layer boundaries [189]. These characteristic bands were also observed in **Figure 5. 17(c-e)** of the hybrid catalysts with 25, 50, and 75 wt.% Co₃O₄ content in addition to the evolution of the new weak band in the range from 288.6 eV to 288.9 eV corresponding to the new bonded state with oxygen (–O–C=O). This indicated the relative increase in the oxygen-containing functional groups in the hybrid catalysts [189, 245].

5. 2. 5. Electrochemical active surface area

The electrochemical active surface area (ECSA) of the Co₃O₄-graphene hybrid catalysts was estimated from the double-layer capacitance (C_{DL}) region [78]. The applied potential ranges from 0.924 to 1.124 V vs. RHE in 1 M KOH electrolyte, in which no Faradaic reaction is noticed. The C_{DL} values were calculated by the scan-rate-dependence of cyclic voltammetry (CV) plots according to **Eq. 2. 5**. The CV plots of the pure phases of Co₃O₄/NF and graphene/NF, as well as the Co₃O₄-graphene/NF hybrid catalyst at different Co₃O₄ contents (25, 50, and 75 wt.%), were recorded at scan rates of 10, 20, 30, 40, 50, 60, 70, 80, 90 and 100 mV.s⁻¹, as shown in **Figure 5. 18**. Then, a linear relationship based on eq. 5 between ΔJ at 1.024 V vs. RHE and scan rates were plotted for all working electrodes as illustrated in **Figure 5. 19**. The obtained ECSA represented by C_{DL} values were recorded in **Table 5. 1**. The pure phases of Co₃O₄/NF and graphene/NF possessed relatively low ECSA values of 4.32, and 4.6 mF.cm⁻², respectively. Meanwhile, hybrid Co₃O₄-graphene catalysts exhibited higher ECSA, in which the hybrid catalyst with 50 wt.% Co₃O₄ content exhibited the highest ECSA value of 23.12 mF.cm⁻² compared with the other catalysts. Hence, it has a higher concentration of electroactive sites at the interface between the working electrode and the electrolyte. The overpotential (η) values corresponding to the OER and HER were estimated according to **Eq. 2.(2 and 3)** [76]. The electrocatalytic reaction kinetics can be investigated using Tafel analysis, in which the estimated overpotential for either the OER or the HER is drawn on the y-axis vs. the log scale of the produced current according to the Tafel relation given by **Eq. 2. 4** [77]. The estimated slope exhibits the electrocatalytic reaction kinetics of the modified working electrode:

5. 2. 6. Oxygen evolution reaction activity of Co₃O₄-graphene hybrid catalysts

Figure 5. 20(a, b) shows the IR-corrected LSV plots and the corresponding Tafel plots of the Co₃O₄/NF, graphene/NF, as well as their hybrid catalysts at different Co₃O₄ contents (25, 50, and 75 wt.%) in the potential range from 1.2 to 1.8 V vs. RHE to investigate their electrocatalytic activity toward the OER in 1.0 M KOH. It can be observed that all working electrodes exhibit oxidation peaks ranging from 1.34 to 1.36 V. In addition, the bare Ni foam and the nanostructured Co₃O₄/NF thin film have a relatively high OER onset potential ranging from 1.58 to 1.6 V; meanwhile, the pure graphene/NF and Co₃O₄-graphene hybrid catalysts with different Co₃O₄ contents have a lower OER onset potential ranging 1.52 to 1.54 V. The overpotential (η) and the corresponding Tafel slope values of the OER for the pure phases of Co₃O₄/NF, graphene/NF, as well as their hybrid catalysts were estimated according to **Eq. 2. 2** and **Eq. 2. 4**. The charge transfer resistance (R_{ct}) for the OER region at η 300 mV was estimated for each working electrode using the electrochemical impedance spectroscopy (EIS), **Figure 5. 21(a)** and recorded in **Table 5. 1**. The nanostructured Co₃O₄/NF catalyst provides a current density of 10 mA.cm⁻² at a relatively high η of 349 mV, Tafel slope of 77 mV.dec⁻¹, and R_{ct} of 13.5 Ω ; while, the pure graphene/NF catalyst reveals high activity toward the OER that possesses a low η of 283 mV@10 mA.cm⁻², very fast reaction kinetics with very small Tafel slope of 32 mV.dec⁻¹ and small R_{ct} of 2.6 Ω . In the case of the Co₃O₄-graphene hybrid catalysts, it can be observed that increasing graphene content results in a gradual decrease of onset potential, η , and Tafel slope values. This behavior revealed the overall improvement in the electrocatalytic activity toward the OER. Moreover, the hybrid catalyst with 25 wt.% Co₃O₄ content revealed the optimum combination for the OER with a low η of 283 mV@10 mA.cm⁻², superior reaction kinetics with very small Tafel slope of 25 mV.dec⁻¹, and R_{ct} of 3.5 Ω . This behavior can be explained as follows: I) The improvement in the charge transfer resistance with increasing graphene content as illustrated from Nyquist plots of the OER region at overpotential value of 300 mV, **Figure 5. 21(a)**, II) the formation of native structural and interfacial defects such as Co vacancy, O vacancy, as well as edge and heteroatom sites in graphene nanosheets that produce more electrocatalytic active sites [232, 246, 247]. The OER long-term stability @50 mA.cm⁻² was verified for 50 hours in 1.0 M KOH as shown in **Figure 5. 20(c)**.

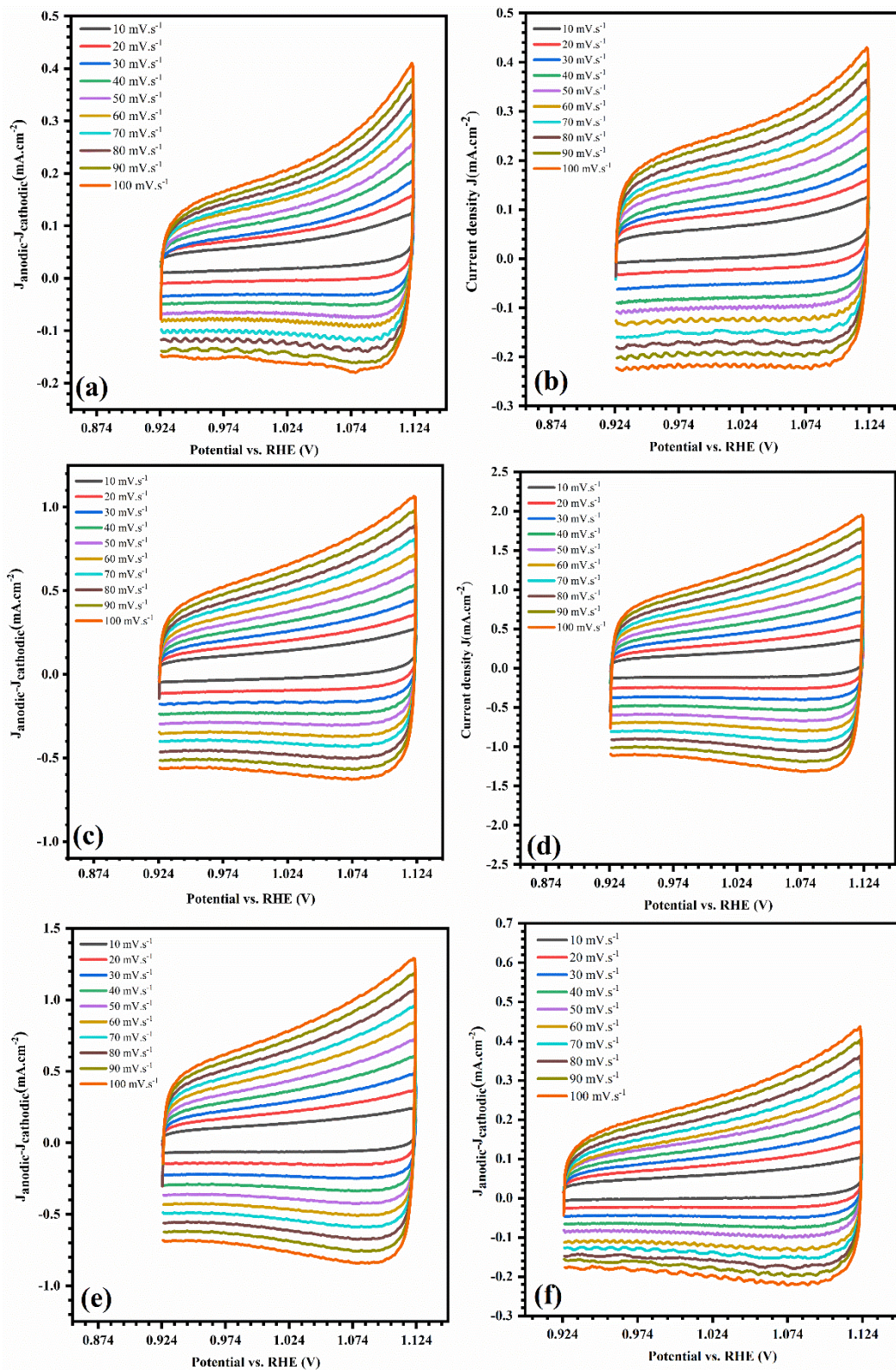


Figure 5. 18: CV plots of Co_3O_4 -composites at different scan ranges in the non-Faradic region from 0 to 0.2 vs. Hg/HgO.

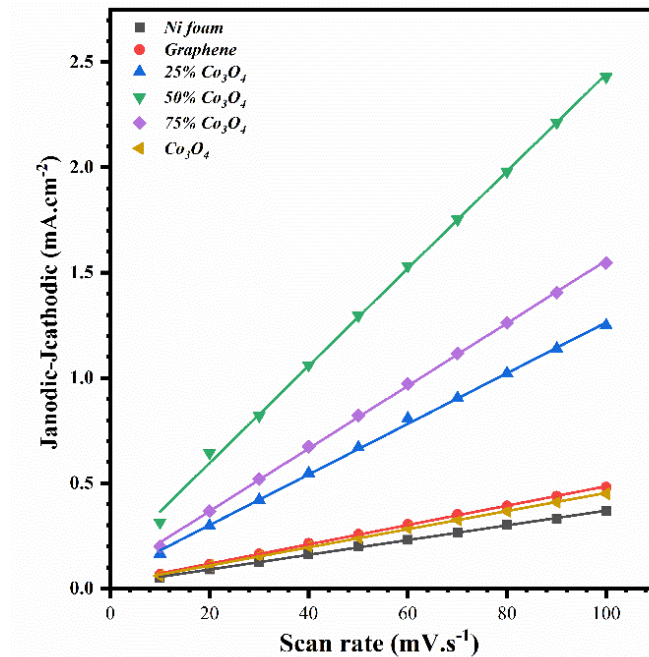


Figure 5.19: Plots of the current density vs. scan rate of Co_3O_4 -graphene composite

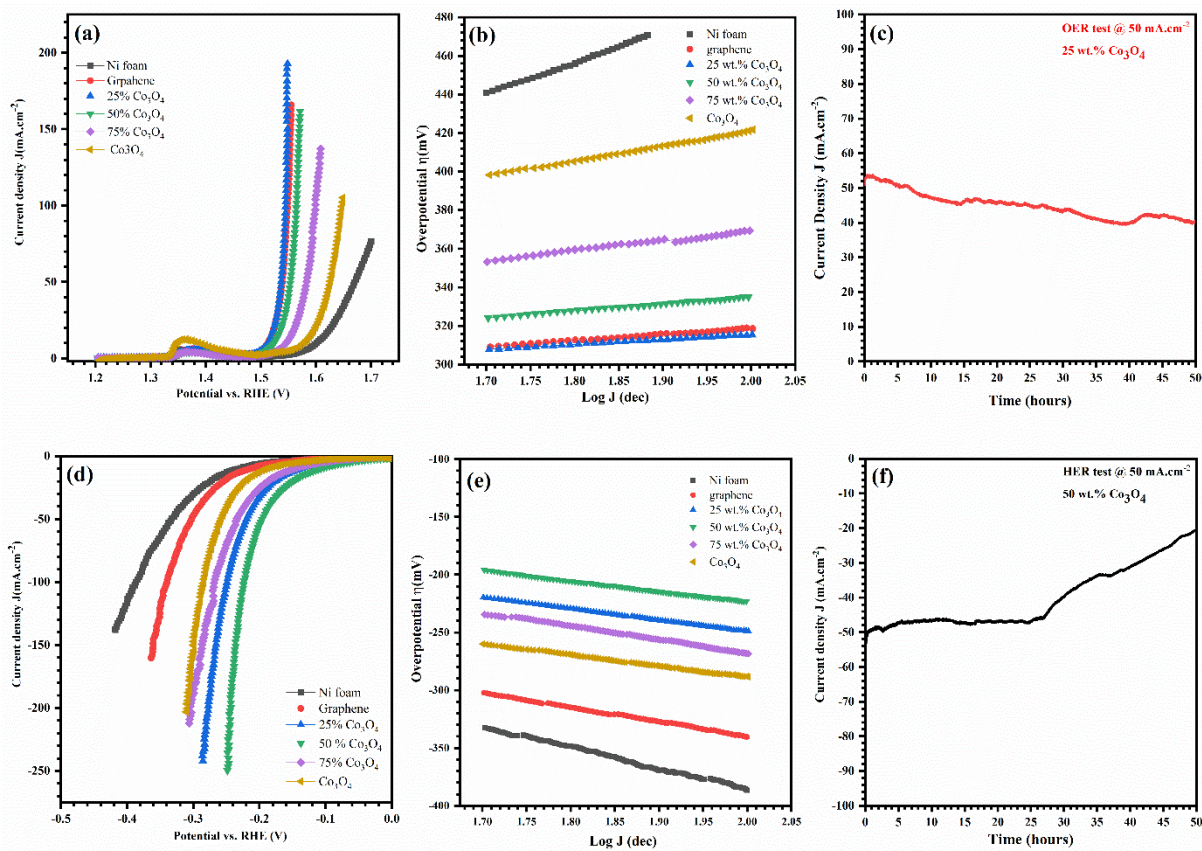


Figure 5.20: LSV, the derived Tafel plot, and the stability test @50 $mA.cm^{-2}$ of OER (a, b, c) and of HER (d, e, f) of Co_3O_4 -graphene hybrid catalysts

5. 2. 7. Hydrogen evolution activity of Co₃O₄-graphene hybrid catalysts

Figure 5. 20(d, e) shows the IR-corrected linear sweep voltammetry and Tafel plots of the pure phases of Co₃O₄/NF, graphene/Ni foam, as well as their composites at different Co₃O₄ content (25, 50, and 75 wt.%) in the potential range from 0 to -0.6 V vs. RHE to investigate the electrocatalytic activity toward the HER in 1.0 M KOH. The overpotential (η) and the corresponding Tafel slope values were calculated according to **Eq. 2. (3 and 4)**, as well as R_{ct} from the Nyquist plots at η_{HER} of 100 mV, **Figure 5. 21(b)** and recorded in **Table 5. 1**. It was noticed that the nanostructured Co₃O₄/NF catalyst reveals relatively high HER activity compared with the pure graphene/NF catalyst, which provides 10 mA.cm⁻² at a relatively lower η of 188 mV, Tafel slope of 97 mV.dec⁻¹, and R_{ct} of 18 Ω . Meanwhile, the pure graphene/NF catalyst provides 10 mA.cm⁻² at a higher η of 213 mV, Tafel slope of 125 mV.dec⁻¹, R_{ct} of 25 Ω . The electrocatalytic activity of Co₃O₄-graphene hybrid catalysts toward the HER in 1.0 M KOH was also investigated at different Co₃O₄ content (25, 50, and 75 wt.% content). It was observed that the combination between the nanostructured Co₃O₄ and graphene nanosheets resulted in an overall improvement in the HER electrocatalytic activity. The estimated η_{HER} , Tafel slope, and R_{ct} values of the hybrid catalysts were recorded in **Table 5. 1**.

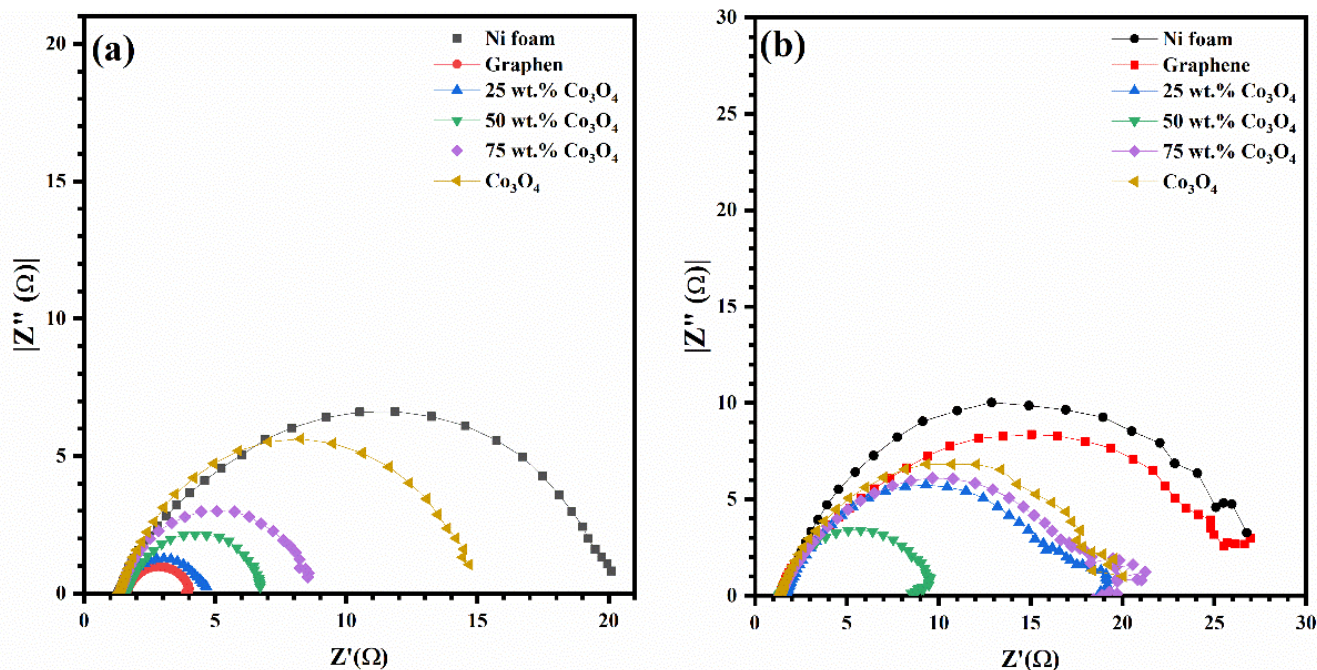


Figure 5. 21: Nyquist plot in 1.0 M KOH of the Co₃O₄-graphene catalysts at an overpotential 300 mV correspond for the (a) OER, and (b) at an overpotential of 100 mV correspond HER

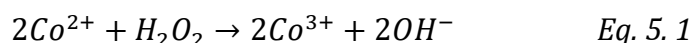
The hybrid catalyst with 50 wt.% Co₃O₄ revealed the best electrocatalytic performance compared with the pure nanostructured Co₃O₄/NF catalyst and graphene nanosheets/NF catalysts, as well as hybrid catalysts with 25, and 75 wt. Co₃O₄ content. It provides 10 mA.cm⁻² at the lowest η of 108 mV, a Tafel slope of 90 mV.dec⁻¹, and a small R_{ct} of 8.3 Ω. Moreover, the observed enhancement in the HER electrocatalytic activity can also be attributed to the improvement in the number of active sites at the interface of the working electrode, in which the catalyst with 50 wt.% content possesses the highest ECSA value of 23.12 mF.cm⁻². Furthermore, the HER long-term stability @50 mA.cm⁻² was verified for nearly 30 hours in 1.0 M KOH as shown in **Figure 5. 20(f)**.

Table 5. 1: Electrocatalytic activity of Co₃O₄-graphene composite/Ni foam for OER and HER

	Composition ratio (wt.%)		Overpotential η (mV)					Tafel slope (mV.dec ⁻¹)	R _{ct} (Ω)	Co ₃ O ₄ (wt.%)	ECSA (mF.cm ⁻²)
	Co ₃ O ₄	Gr	10	20	50	100	150				
OER	Bare Ni Foam		372	398	440	-	-	164	19.5	Ni foam	3.5
	0	100	283	294	310	320	328	32	2.6		
	25	75	283	294	307	315	318	25	3.5	0	4.6
	50	50	295	308	324	335	340	36	5		
	75	25	316	332	353	370	-	50	7.4	25	12.04
	100	0	349	370	398	422	-	77	13.5		
HER	Bare Ni Foam		230	273	333	386		179	25.7	50	23.12
	0	100	213	254	302	340	360	125	25		
	25	75	137	176	219	248	265	99	15.2	75	14.9
	50	50	108	149	195	223	236	90	8.3		
	75	25	147	187	234	269	288	117	17	100	4.32
	100	0	188	223	260	288	305	97	18		

5. 2. 8. H₂O₂ electrochemical sensing by Co₃O₄-graphene hybrid catalysts

Figure 5. 22(a) reveals the cyclic voltammogram (CV) plots of the graphene nanosheets/NF, Co₃O₄ nanoparticles/NF, and their hybrid catalysts at 50 mV.s⁻¹ in 0.1 M NaOH without and with 5 mM H₂O₂. It can be observed that a spontaneous increase in the response current upon the addition of 5 mM H₂O₂ starts from 0 V for the pure Co₃O₄/NF, as well as the hybrid catalysts with 25, 50, and 75 wt.% Co₃O₄ content. This behavior reflects the high reduction tendency of H₂O₂ by the prepared electrocatalyst, which is associated with the redox transition of Co(OH)₂/Co₃O₄ at potential > -0.4 V [215, 219] as illustrated below:



The electrochemical reduction of H_2O_2 reduction by Co_3O_4 -graphene hybrid catalyst in 0.1 M NaOH is further studied by the chronoamperometric measurements at -0.45 V at different H_2O_2 concentrations, **Figure 5. 22(b)**. It can be observed that the $\text{Co}_3\text{O}_4/\text{NF}$ catalyst and the Co_3O_4 -graphene hybrid catalysts with 25, 50, and 75 wt.% Co_3O_4 content reveals a good step response with the gradual increase of H_2O_2 concentration. For the quantitative analysis of the H_2O_2 sensing response characteristics by the Co_3O_4 -graphene hybrid catalyst, the current response behavior for each catalyst was studied as a function of the injected H_2O_2 concentration from the calibration curves, **Figure 5. 23(a-d)**.

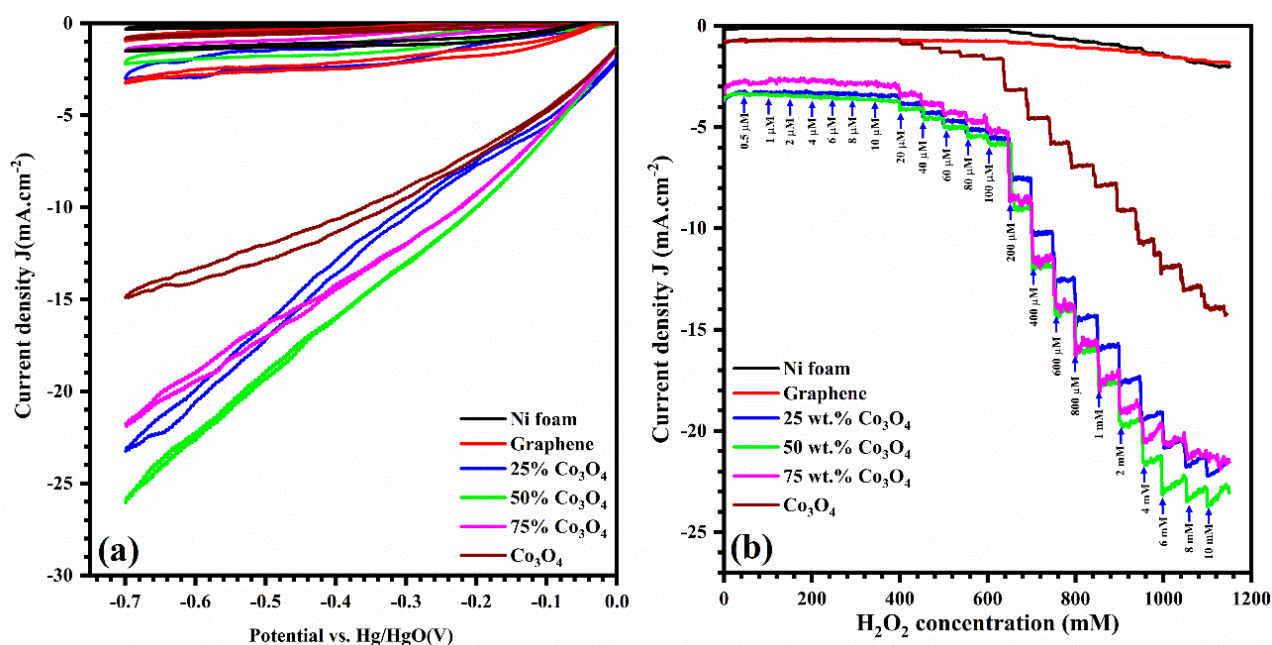


Figure 5. 22: Cyclic voltammogram from 0 to -0.7 vs. Hg/HgO at a scan rate of 50 mV.s^{-1} without and with 5 mM of H_2O_2 in 0.1 M NaOH **(a)** and the corresponding amperometric response at -0.45 V of Co_3O_4 -graphene hybrid catalyst at various Co_3O_4 content.

It was observed that the nanostructured $\text{Co}_3\text{O}_4/\text{NF}$ catalyst exhibits a strong reduction tendency with a very high sensitivity of $7790 \mu\text{A} \cdot \text{mM}^{-1} \cdot \text{cm}^2$, linear detection ranges from $6 \mu\text{M}$ to 1 mM of H_2O_2 , and a low detection limit (LOD) of $0.04 \mu\text{M}$. Moreover, the nanostructured Co_3O_4 -graphene/NF hybrid catalyst revealed a linear detection range from 0.02 to 1 mM of H_2O_2 for all hybrid catalysts, LOD range from 0.14 to $0.3 \mu\text{M}$, and a superior sensitivity of 12424 , 18110 , and $16280 \mu\text{A} \cdot \text{mM}^{-1} \cdot \text{cm}^2$ corresponding to 25, 50, and 75 wt.% Co_3O_4 , respectively. The improvement in the electrocatalytic activity toward the H_2O_2 reduction by the Co_3O_4 -graphene hybrid catalyst can be explained through the provided mechanism based on eq. 6 that is schematically illustrated in **Figure 5. 24**. In the Co_3O_4 -graphene hybrid catalysts, each of the Co_3O_4 nanoparticles and the graphene nanosheets has different contribution in the observed

sensitivity enhancement of H_2O_2 reduction in the alkaline medium that can be further illustrated as follows: The graphene nanosheets have two separate roles that effectively contribute to the observed H_2O_2 improvement by the deposited hybrid catalyst electrodes, the first function is increasing of the high-spin Co species (Co^{2+}) concentration at the interface of the working electrode during the deposition process, which explained in more details in the XPS analysis of the Co_3O_4 -graphene composites; the second role is during the measurement of the electrocatalytic activity of the deposited Co_3O_4 -graphene hybrid catalyst toward the reduction of H_2O_2 species, which the superior electrical conductivity of the graphene nanosheets and the observed synergetic effect between the Co_3O_4 and the graphene plays a vital role in the improvement of the charge transfer kinetics of the hybrid electrode.

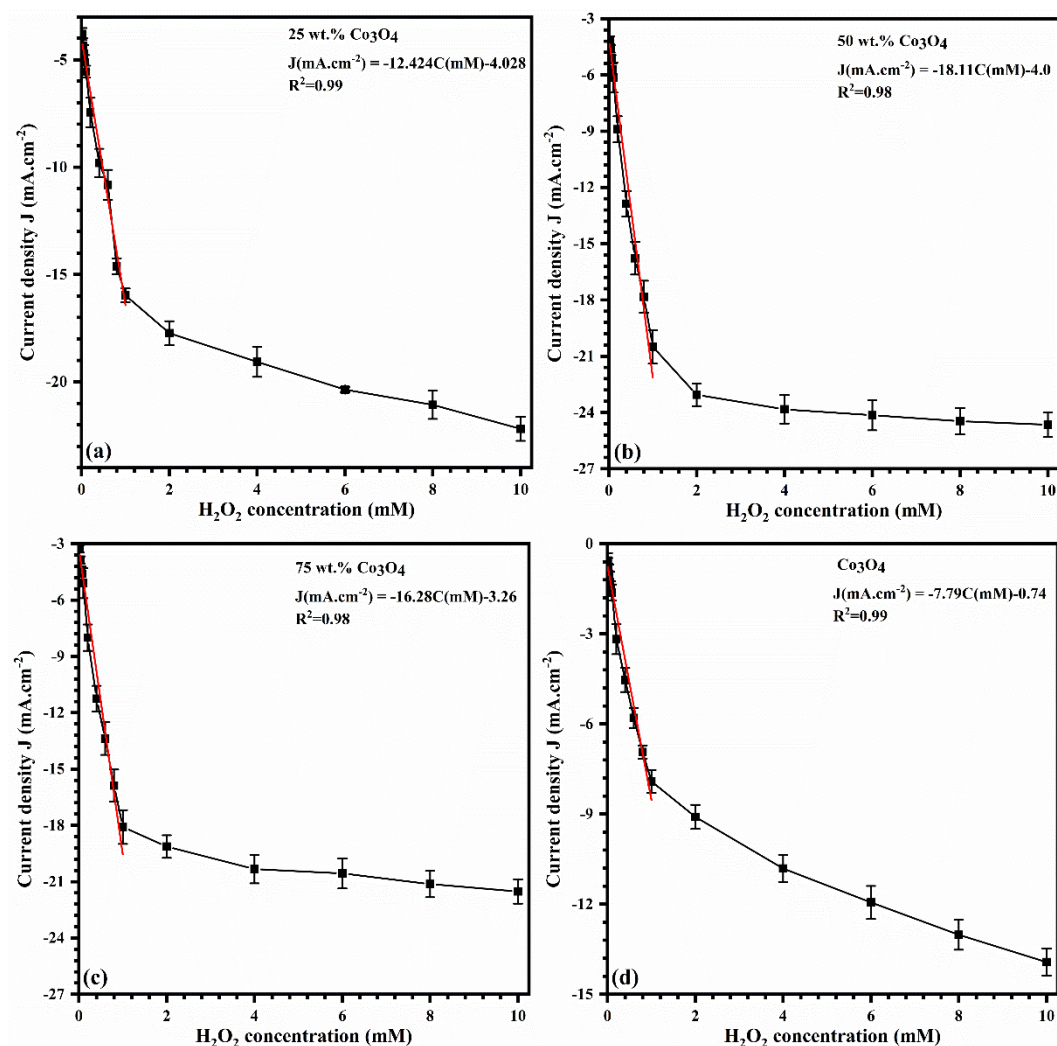


Figure 5. 23: Calibration curves of current-induced response to H_2O_2 concentration by Co_3O_4 -graphene catalyst at different Co_3O_4 contents.

On the other hand, according to **Eq 5. 1**, the detection of H₂O₂ mainly depends on the existence of the high-spin state Co²⁺ of the Co₃O₄ species at the interface of the working electrode, which directly oxidized by the H₂O₂ to the low-spin state (i.e. Co³⁺), **Figure 5. 24**. The hybrid catalysts of Co₃O₄-graphene nanosheets combine multiple functional species that result in an overall enhancement in the electrocatalytic activity toward the H₂O₂ reduction. In the case of the hybrid catalyst, we observed that composites with 50 wt.% Co₃O₄ revealed the optimum combination for H₂O₂ reduction, which can be understood through the above-mentioned mechanism and the related XPS analysis of Co₃O₄-graphene composites at different Co₃O₄ content. As illustrated in the discussion of the Co 2p high-resolution XPS scan, we observed that all hybrid catalysts at Co₃O₄ contents of 25, 50, and 75 wt.% have a relatively large concentration of higher spin state Co²⁺ of the Co₃O₄ spinel structure compared with the lower spin state Co³⁺. The observed improvement in the high spin states Co²⁺ results in an increase of electrocatalytic active states to the H₂O₂ reduction at the interface of the working electrode. The obtained sensitivity of our hybrid catalyst is superior compared with other Co₃O₄-based catalysts fabricated by other techniques, which in comparison with the recently published papers was provided in **Table 5. 2**. Hence, the obtained results revealed that the Co₃O₄-graphene hybrid catalyst is a promising nonenzymatic sensor for the rapid detection of H₂O₂ with superior sensitivity.

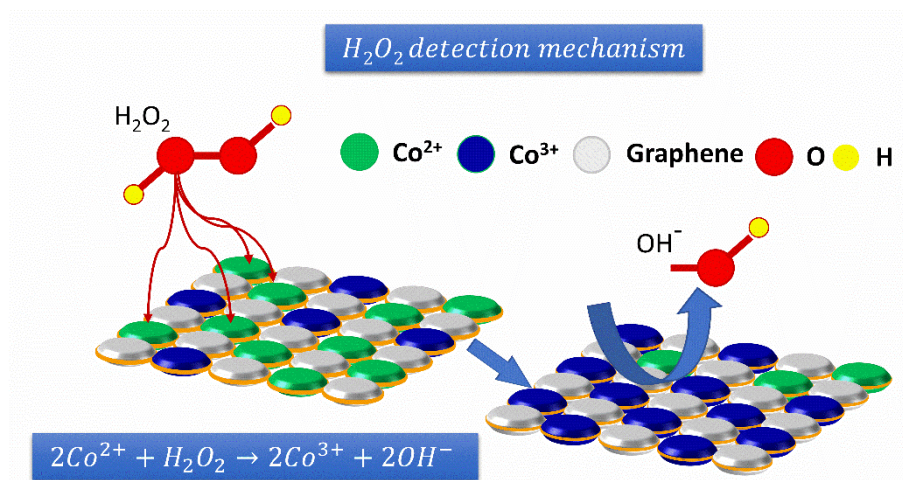


Figure 5. 24: Schematic diagram for illustration the H₂O₂ detection mechanism by the Co₃O₄-Graphene hybrid catalysts

Table 5. 2: Comparison of the electrochemical performance between the present work and recently published work of Co-based nonenzymatic amperometric H_2O_2 sensors

Modified electrode	Potential (V)	Electrolyte	Response time (s)	Sensitivity ($\mu A \cdot mM^{-1} \cdot cm^{-2}$)	Linear range (mM)	LOD (μM)	Ref.
50 wt.% Co_3O_4/NF	-0.45	0.1 M NaOH	2-3	18110	0.02-1	0.14	This work
75 wt.% Co_3O_4/NF				16280		0.16	
25 wt.% Co_3O_4/NF				12424		0.3	
Co_3O_4/NF				7790		0.04	
$NiCo_2O_4/Co_3O_4$	-0.35	0.1 M NaOH	-	303.42	0.02-1.1	0.59 6	[248]
$NiCo_2S_4/rGO$	-0.45	0.1 M NaOH	5	118.5	0.025-11.25	0.19	[249]
Co_3O_4/NPG	-0.3	0.1 M NaOH	2	1338.7	0.02-19.1	6.4	[215]
$Au@C-Co_3O_4$	+0.5	0.1 M PBS (pH 7.4)	-	7553	0.00005-0.1	0.01 9	[216]
Co_3O_4/rGO		0.1 M PB (pH 7.0)		3450	0.00005-0.4	0.01 5	[218]
$MnO_2-Co_3O_4/GO$	+0.5	PBS (PH 7.0)	3	53.65	0.005-1.2	0.8	[250]
Co_3O_4-rGO	-0.19	0.1 M PBS (pH 7.4)	5	1140	0.015-0.675	2.4	[251]
Co_3O_4 hollow sphere	+0.39	0.1 M NaOH	3	979.79	0.0004-2.2	0.10 5	[214]
$Co_3O_4/CNTs$	-0.19					-	
Nanoporous Co_3O_4	-1	0.1 MPBS (pH 7.0)	2	1357	0.2-1.3	200	[252]
Co_3O_4-NWs/CF	-0.48	0.1 M KOH	3	230	0.01-1.05	1.4	[253]
Nafion/ GO/Co_3O_4	0.76	Phosphate (pH 7.4)	4	560	0.001-0.1	0.3	[254]

5.3. Summary

Nanostructured Co_3O_4 -graphene composites with different Co_3O_4 contents (25, 50, and 75 wt.%) were deposited on Ni foam supporting substrate using the NPDS from initial micro-sized particles of Co_3O_4 and graphite powders. The resultant deposited films were investigated for the OER, HER electrocatalytic activity in 1.0 M KOH, as well as H_2O_2 sensing in 0.1 M NaOH. Analysis of the ECSA revealed the hybridization between Co_3O_4 and graphene resulted in an overall enhancement of ECSA. Consequently, the increase in the concentration of the active sites on the surface of the hybrid working electrode was noted. A hybrid catalyst with 50 wt.% Co_3O_4 exhibited the highest ECSA value of 23.2 $mF \cdot cm^{-2}$. The observed enhancement in the electroactive sites at the interface of the nanostructured Co_3O_4 -graphene/NF hybrid catalyst is due to the increase of the high-spin states (Co^{2+}) concentration compared with the pure Co_3O_4/NF catalyst. The graphene/NF, as well as the hybrid catalyst with 25 wt.% Co_3O_4 revealed the highest electrocatalytic activity toward the OER that provided 10 $mA \cdot cm^{-2}$ at an overpotential (η) of 283 mV. On the other hand, a hybrid catalyst with 50 wt.% Co_3O_4 exhibited the highest HER

electrocatalytic activity with a small overpotential of 108 mV to provide $10 \text{ mA}\cdot\text{cm}^{-2}$ in 1.0 M KOH. In the case of H_2O_2 reduction by the nanostructured Co_3O_4 -graphene/NF hybrid catalyst, we found that the pure catalyst of Co_3O_4 /NF revealed a very high reduction tendency toward the H_2O_2 in 0.1 M NaOH, which resulted in an ultra-high sensitivity of $7790 \text{ }\mu\text{A}\cdot\text{mM}^{-1}\cdot\text{cm}^{-2}$ with a linear detection range from $6 \text{ }\mu\text{M}$ to 1 mM and low detection limit of $0.04 \text{ }\mu\text{M}$. Moreover, hybridization with graphene nanosheets in the hybrid catalyst resulted in further improvement of the working electrode sensitivity that reached superior values compared with previously reported papers, in which the hybrid catalyst with 50 wt.% Co_3O_4 revealed the highest sensitivity of $18110 \text{ }\mu\text{A}\cdot\text{mM}^{-1}\cdot\text{cm}^{-2}$.

Chapter 6:

*Facile One-Step Deposition of ZnO-Graphene Nanosheets
Hybrid Photoanodes for Enhanced Photoelectrochemical
Water Splitting*

6.1. Overview

The heterostructure nanocomposites (NCs) between transition metal oxides (TMOs) and two-dimensional (2D) nanomaterials such as graphene nanosheets have recently gained a great deal of interest due to their novel properties compared with the pure phase of either TMOs or the 2D materials. The modification of the formed surface states at the grain boundaries interfaces between the TMO and the graphene nanosheet is mostly accompanied by the variation of various physicochemical properties such as Fermi energy level, charge carrier concentration as well as the fabricated heterostructure electrode work function. The modification of these characteristics due to the synergy improvement between each component in the hybrid NCs results in novel properties and superior performance in energy conversion and storage applications [255-258].

The vast spread of graphene-based energy storage and conversion applications requires a cost-effective technique that is amenable to mass production. However, the common techniques for graphite to graphene reduction have a very long preparation time, high production cost, and a small production yield [259]. It is known that top-down approaches for the graphite-to-graphene transformation are more suitable for mass production such as sonochemical-assisted graphite exfoliation [91], and shear exfoliation [94]. These techniques result in relatively slow graphite-to-graphene transformation rates and produce a secondary waste product because they require stabilizing liquids and need solvent removal. The ball milling approach in the form of dry and wet ball milling has also been used for the exfoliation of graphite to graphene nanosheets of small size. Also, the graphite-to-graphene transformation using the ball milling technique is very slow and requires a very long time (~ 20 h), and sometimes requires waste removal using sonication leading to a decrease in the total production yield [49, 54, 95, 97].

In contrast to the above-mentioned techniques, here we report the direct transformation of graphite micro-sized flakes to graphene nanosheets in a one-step process at room temperature with a very short preparation time using a top-down approach based on the nanoparticle deposition system (NPDS), which is one of the vacuum kinetic spray processes [101, 163, 164]. This spontaneous transformation of graphite to graphene nanosheets was accompanied by the hybridization of the TMOs to produce efficient electrodes that were modified with hybrid NCs for energy storage and conversion applications. In our previous studies, we already fabricated various modified electrodes using the NPDS to produce nanosized TMOs hybrids with 2D materials such as graphene and MoS₂ nanosheets. These modified electrodes revealed

high performance in many electrochemical energy conversion and storage applications such as supercapacitors [260] and electrocatalytic water splitting [261, 262], photocatalytic degradation of organic dyes [263] as well as the nonenzymatic electrochemical sensor of H_2O_2 in an alkaline medium [258, 264].

Nanostructured ZnO is a well-known material that exhibits high performance in many photo-energy conversion and storage applications, such as photocatalysts, photoelectrochemical (PEC) water splitting, and photovoltaics [265-268]. The formation of NCs with carbon-based materials such as graphene nanosheets, reduced graphene oxide (rGO), and carbon nanotubes (CNT) provides an overall enhancement in the charge transfer kinetics. This improvement in the electrochemical reaction kinetics is associated with the enhanced electrocatalytic activity due to the interface reconstruction and synergy improvement between different species in the heterostructure NCs [269]. This, in turn, enhances the related physical and chemical properties that are desired for improving the energy conversion and storage applications [270-273].

The alteration of physical and chemical properties due to the interface reconstruction of ZnO-based hybrid photoanodes can be strongly affected by the fabrication technique. Optimizing the heterostructure constituents and the fabrication conditions can help to achieve the optimum design with improved photo-energy conversion performance. Min et al., [274] prepared a ZnO-graphene heterostructure using the ionic liquid-solvothermal assisted method. The rGO, prepared using the common Hammer technique, was mixed with ZnO powder by stirring, followed by 2 h of ultrasonication, and hydrothermal treatment for 4 h at 160 °C. The obtained composites exhibited a photocurrent of $0.015 \text{ mA} \cdot \text{cm}^{-2}$ @ 0.3 V vs. Ag/AgCl in 1 M NaOH. Yusoff et al., [275] synthesized rGO decorated by Fe_3O_4 -ZnO core-shell structure using the hydrothermal technique. The fabricated heterostructure photoanode revealed a photocurrent of $0.85 \text{ mA} \cdot \text{cm}^{-2}$ @ 1.23 V vs. the reversible hydrogen electrode (RHE) in 0.1 M KOH. Chandrasekaran et al., [276] reported on the evolution of complex structures between the rGO sheets and the triangle-shaped ZnO in the heterostructure photoanodes. The utilized preparation method involved several steps using the hydrothermal technique. The obtained photoanode exhibited a photocurrent of $1.52 \text{ mA} \cdot \text{cm}^{-2}$ @ 1.45 V vs. RHE in 0.1 M NaOH. Khan et al, [271] prepared ZnO/rGO heterostructure photoanode using a combination of sonochemical-assisted calcination at 400 °C for ZnO and the hydrothermal technique for the preparation of rGO according to the Hammer method. This multi-step preparation process consumed a great deal of time of more than 8 h. The fabricated photoanode revealed a maximum photo-response current of $1.55 \text{ mA} \cdot \text{cm}^{-2}$ @ 1 V vs. Ag/AgCl in 0.5 M Na_2SO_4 . Tayebi et al., [273] have synthesized ZnO-

graphene composites in several steps, including the separate preparation of graphene nanosheets using the common Hammer exfoliation technique for graphite micro-sized powder in concentrated sulfuric acid. ZnO was separately prepared using a hydrothermal autoclave at 500 °C and then mixed with the graphene nanosheet by ultrasonication. Finally, the obtained powder was loaded to the substrate using a binder in a separate step. The obtained ZnO-graphene hybrid photoanode exhibited maximum of 0.6 mA·cm⁻² at 0.6 V vs. Ag/AgCl under the visible light irradiation of 100 mwatt·cm⁻² in 0.5 M Na₂SO₄ electrolyte.

The above-mentioned survey concerning the fabrication of ZnO-based heterostructure photoanodes revealed a good electrochemical performance toward the PEC water splitting in a neutral medium. However, these synthetic techniques can only be used on a substrate of small size for research and development purposes and they are not suitable for broad commercial use due to several reasons: a) they do not consider the production cost efficiency because they consume substantial preparation time for producing small size electrodes in several consecutive steps for obtaining the desired nano-sized powder and then uploading it to the holding substrate using a binder; b) other synthetic techniques use dangerous chemicals as a reactant and produce secondary products after chemical reaction as waste, especially the common Hammer exfoliation method; c) it is difficult to scale-up the above-mentioned techniques to produce large devices suitable for commercial applications. In contrast with the previously mentioned techniques, the top-down approach for fabrication of the nanostructured hybrid electrodes using NPDS has various distinctive features such as a) one-step deposition using the vacuum kinetic spray at room temperature; b) no thermal heating that can damage the substrate [277]; c) binder-free; d) no hazardous chemicals or waste [100, 221]; and e) easy fabrication of large-sized depositions in a manner ready for mass production. For example, a 1 m² electrochromic device based on nanostructured WO₃ thin films was fabricated using NPDS [99].

In this work, we deposited nanostructured ZnO-graphene hybrid photoanodes with different graphite contents (25, 50, and 75 wt.%) using a one-step kinetic spray of mixed ZnO and graphite micro-sized powders on titanium (Ti) sheet substrates by the NPDS method. The fabricated electrodes were utilized as photoanodes for PEC water splitting in the alkaline medium. The effect of graphite content on the photogenerated charge carrier separation and kinetics was studied and the optimization of ZnO-graphene hybrid photoanodes for improving PEC water splitting was demonstrated.

6. 2. Results and discussion

6. 2. 1. X-ray diffraction analysis of ZnO-graphene composites

The structural phase of micro-sized ZnO, graphite and mixed micro-sized powders with differing graphite content (25, 50, and 75 wt.%) was identified using the XRD patterns. The XRD pattern of ZnO microparticles in **Figure 6. 1(a)** exhibits several diffraction peaks that belonged to the wurtzite-type hexagonal structure of ZnO (space group: $P6_3mc$, ICDD: 04-008-8198) [278]. The XRD pattern of graphite micro-sized powder reveals two characteristic diffraction peaks at 26.5° and 56.42° attributed to the (002) and (004) crystalline planes of the graphite hexagonal structure (space group $P6_3/mmc$ (ICDD: 00-056-016, PDF 2010) [261, 264]. Furthermore, the XRD patterns of ZnO-graphite mixed micro-sized powder with different graphite content (25, 50, and 75 wt.%) depicts the mixed diffraction peaks belonging to the hexagonal phases of either the bulk structure of ZnO or graphite without the evolution of any other secondary phases caused by the ball milling process.

Figure 6. 1(b) exhibits the XRD patterns of the bare titanium sheet and the deposited thin films of pure ZnO and ZnO-graphene NCs at various graphite contents (25, 50, and 75 wt.%). The XRD pattern of the titanium sheet substrate depicted several characteristic peaks at 40.08° , 52.92° , and 70.56° that represented the (102), (2-11), and (102) crystalline planes of the hexagonal titanium structure (space group: $P6/mmm$), respectively [279, 280]. The XRD pattern of pure ZnO and ZnO-graphene NCs thin film exhibits several diffraction peaks with very small intensities. These peaks were assigned to the wurtzite hexagonal structure of ZnO and were accompanied by multiple intense XRD peaks matching with the titanium substrate. This behavior demonstrated the micro-sized particle fragmentation to a very small crystalline size at the surface of the titanium substrate. Moreover, no detectable XRD peaks were belonging to the hexagonal structure of graphite powder, demonstrating the layer separation of the graphite micro-sized structure to a very short ordering range in the form of graphene nanosheets. This behavior was observed in most of the fabricated heterostructure electrodes produced by the NPDS method [260-262]. The observed low degree of crystallinity in the fabricated electrodes in most cases is accompanied by the evolution of several interfacial structural defects at the grain boundaries that act as electroactive sites for any various electrocatalytic reactions at the semiconductor/electrolyte interface [223].

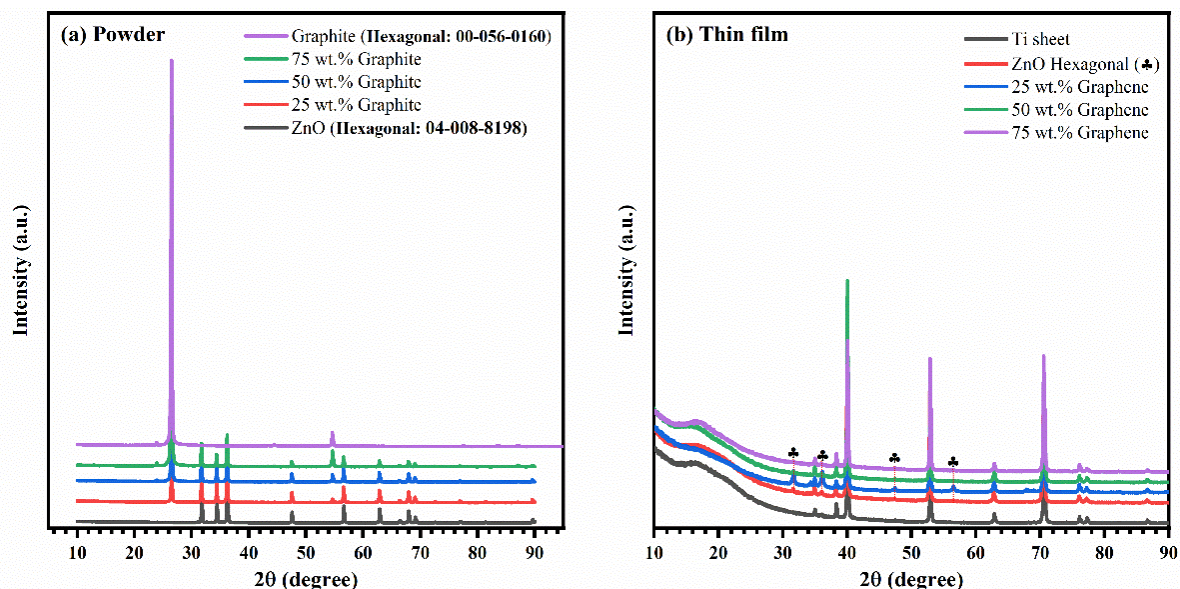


Figure 6. 1: XRD patterns of mixed micro-sized ZnO-graphite powder **(a)** and nano-sized ZnO-graphene thin film deposited on a titanium sheet **(b)**.

6. 2. 2. Surface morphology of ZnO-graphene composites

Figure 6. 2 reveals the FE-SEM images and the corresponding EDS elemental analysis of pure ZnO and mixed ZnO-graphite micro-sized powder with different graphite content (25, 50, and 75 wt.%). The surface morphology of the ZnO and ZnO-graphite mixed powder according to the SEM images exhibits a wide size variation of a multiple layered sheet structure with various size dimensions up to 500 nm. The elemental analysis using the EDS spectra revealed the presence of graphite species (i.e., carbon atoms) for all mixed powders that were used for the deposition of hybrid photoanode fabrication by NPDS. **Figure 6. 3(a, b)** shows the SEM image of the nanosized ZnO thin films on a titanium sheet substrate and the corresponding elemental analysis. The deposited thin film exhibited a mixed morphology of nanorods (width \leq 50 nm and length \leq 200nm) and nanosheets with lateral dimensions \leq 100 nm. The homogenous distribution of ZnO species all over the deposited area on the titanium sheet substrate was demonstrated from the compositional elemental mapping of Zn k_{α} and O k_{α} as shown in **Figure 6. 3(c, d)**. The SEM morphology of the deposited ZnO-graphene NCs with 25, 50, and 75 wt.% graphite content is shown from **Figure 6. 4** to **Figure 6. 6**. The fragmentation of ZnO and graphite micro-sized powder to merged nanosheets with a variable size smaller than 100 nm was observed.

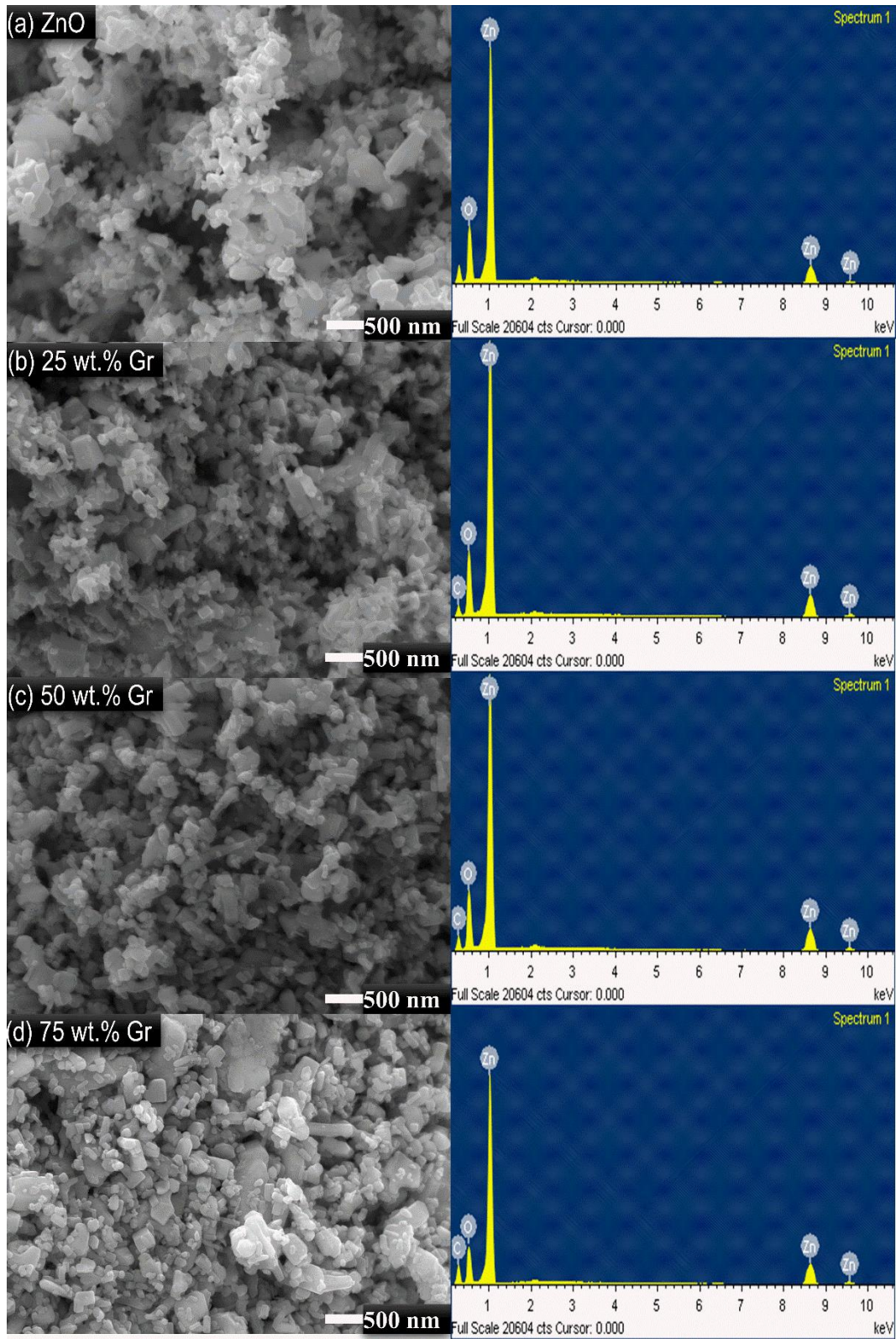


Figure 6. 2: SEM image and the corresponding EDS elemental analysis of pure ZnO powder **(a)**, mixed ZnO-graphite micro-sized powder with 25 wt.% **(b)**, 50 wt.% **(c)**, and 75 wt.% graphite contents **(d)**.

The homogenous distribution of Zn, O and C species on the titanium sheet substrate were also demonstrated for all hybrid NCs through tracking the elemental mapping of Zn k_{α} , O k_{α} , and C k_{α} using the EDS compositional elemental mapping. **Figure 6. 7** reveals the cross-sectional view and corresponding composition elemental mapping (O_k, Zn_K, and C_k) of ZnO-graphene NCs on a titanium sheet substrate with 50 wt.% graphite contents. The elemental analysis mapping in **Figure 6. 7(b-d)** exhibits the homogeneous distribution of ZnO and graphene species across the deposited area. This provided the observed synergy improvement as explained in the XPS analysis discussion. Furthermore, the HR-TEM image in **Figure 6. 8(a, b)** depicts the typical interface between the adjacent nanocrystalline domains of ZnO and graphene nanosheets. It can be observed that on the side of the ZnO, multiple crystalline domains with low-angle grain boundaries are mostly oriented along the preferable (100) crystalline plane of the hexagonal ZnO with an interplanar distance ~ 0.287 nm [281], see **Figure 6. 8(c)**.

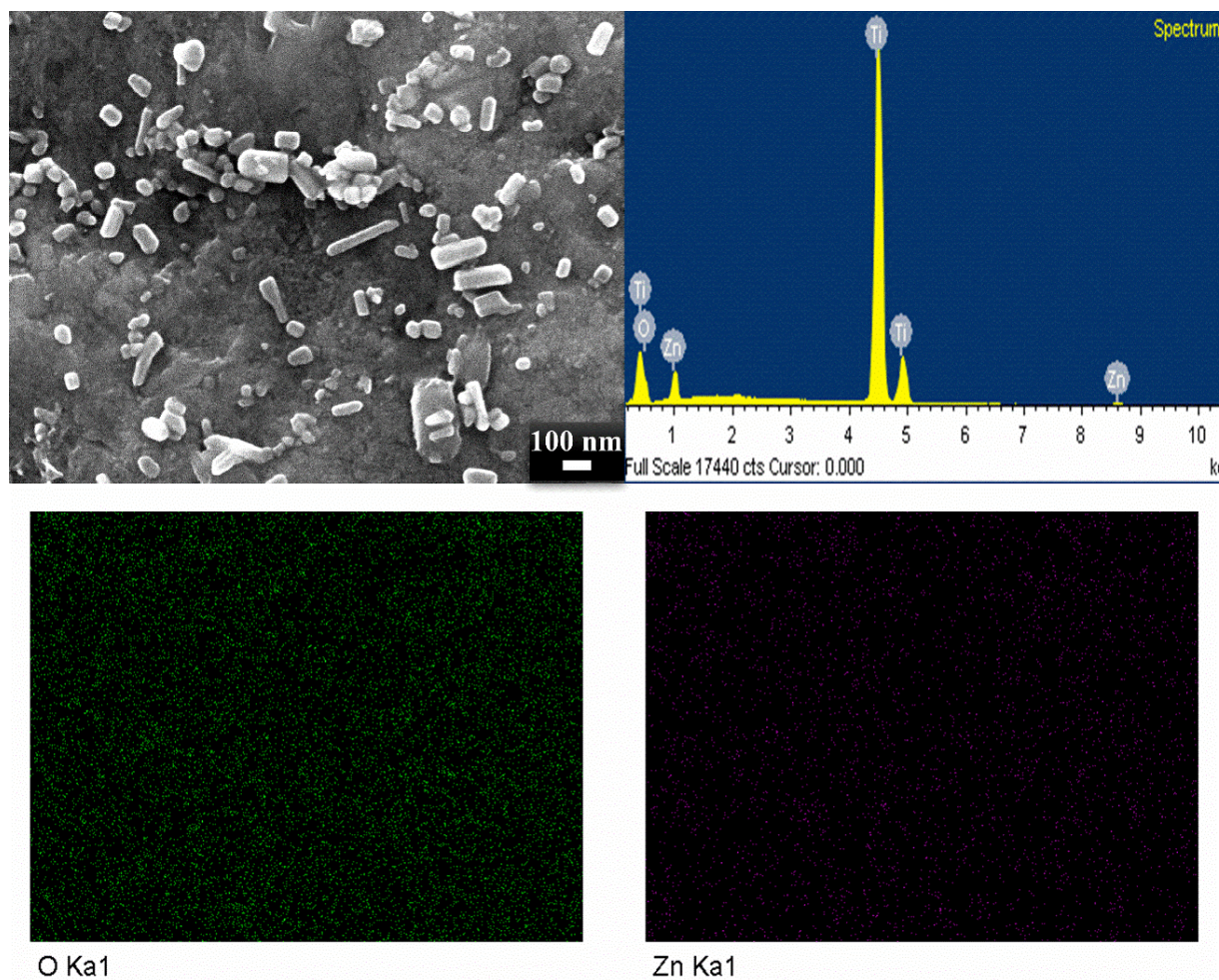


Figure 6. 3: SEM image and the corresponding EDS elemental analysis mapping of ZnO nanosheet thin films on a titanium sheet.

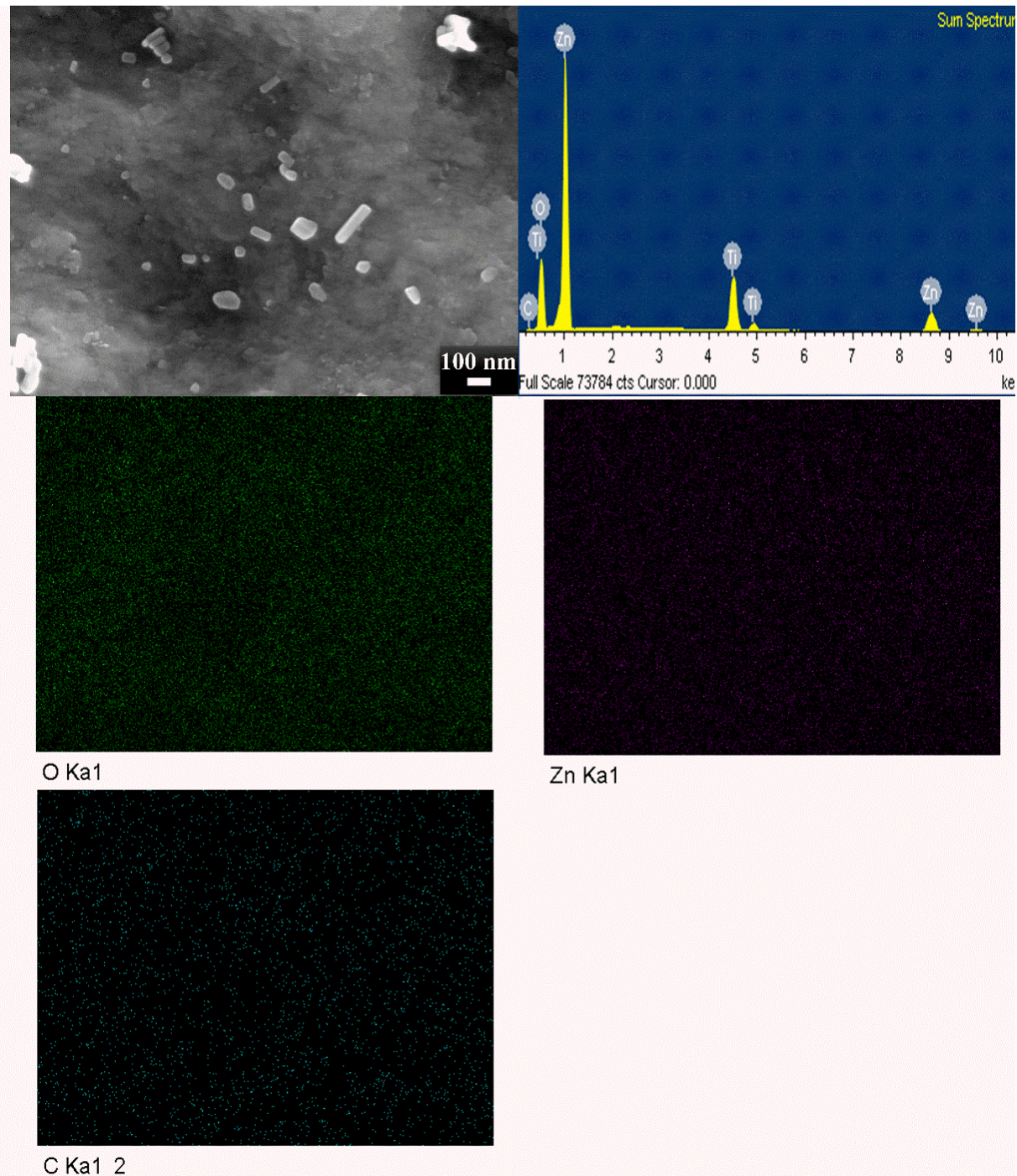


Figure 6. 4: SEM image and the corresponding EDS elemental analysis mapping of the ZnO-graphene NCs thin films with 25 wt.% graphite contents on a titanium sheet.

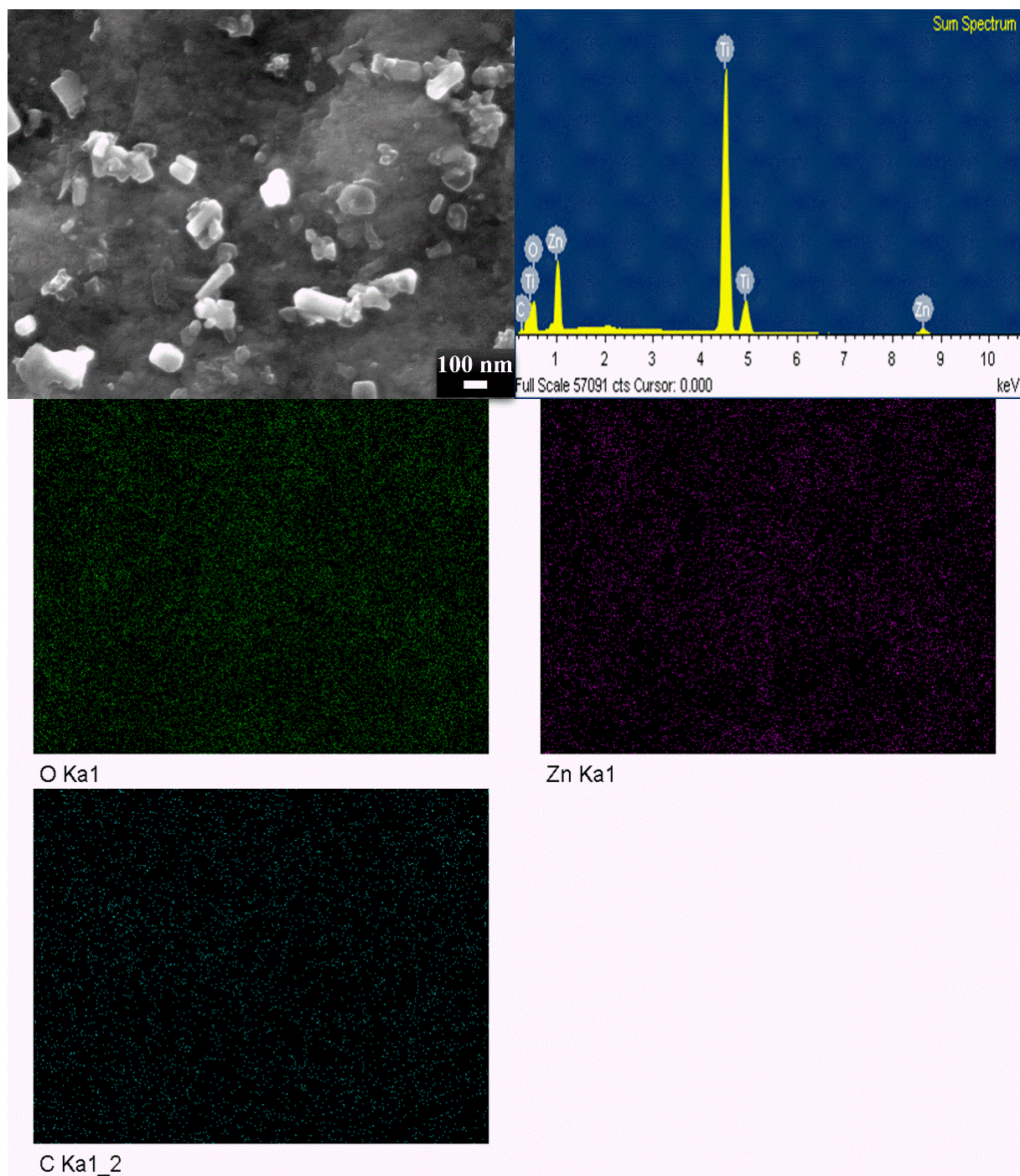


Figure 6. 5: SEM image and the corresponding EDS elemental analysis mapping of ZnO-graphene NCs thin films with 50 wt.% graphite contents on a titanium sheet.

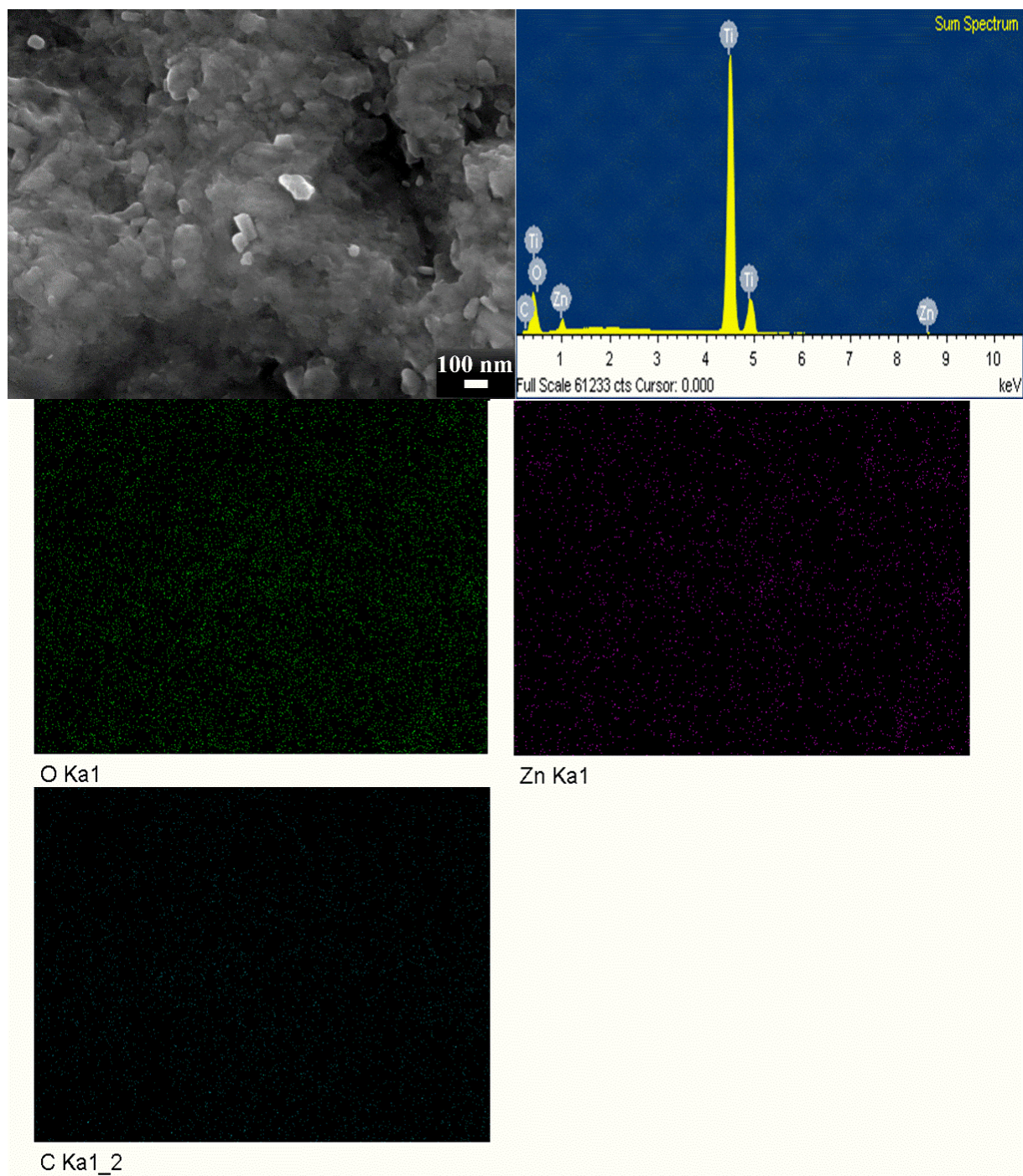


Figure 6. 6: SEM image and the corresponding EDS elemental analysis mapping of the ZnO-graphene NCs thin films with 75 wt.% graphite contents on a titanium sheet.

On the other hand, the observed single crystalline domain with an interplanar distance of 0.22 nm, see **Figure 6. 8(d)**, belongs to the (1120) crystalline plane of the graphene nanosheets. This confirms the transformation of the micro-sized layered structure of graphite powder with a weak van der Waals layer separation of 0.33 nm to small graphene nanosheets [282-284]. The small size of the graphene nanosheets is mostly accompanied by a large concentration of interfacial edge defects that enable the hybridization of graphene nanosheets through the electronic cloud of p-orbitals with the nanosized ZnO crystalline domains. This hybridization is expected to further improve the synergy between ZnO and the graphene species in the deposited hybrid photoanode.

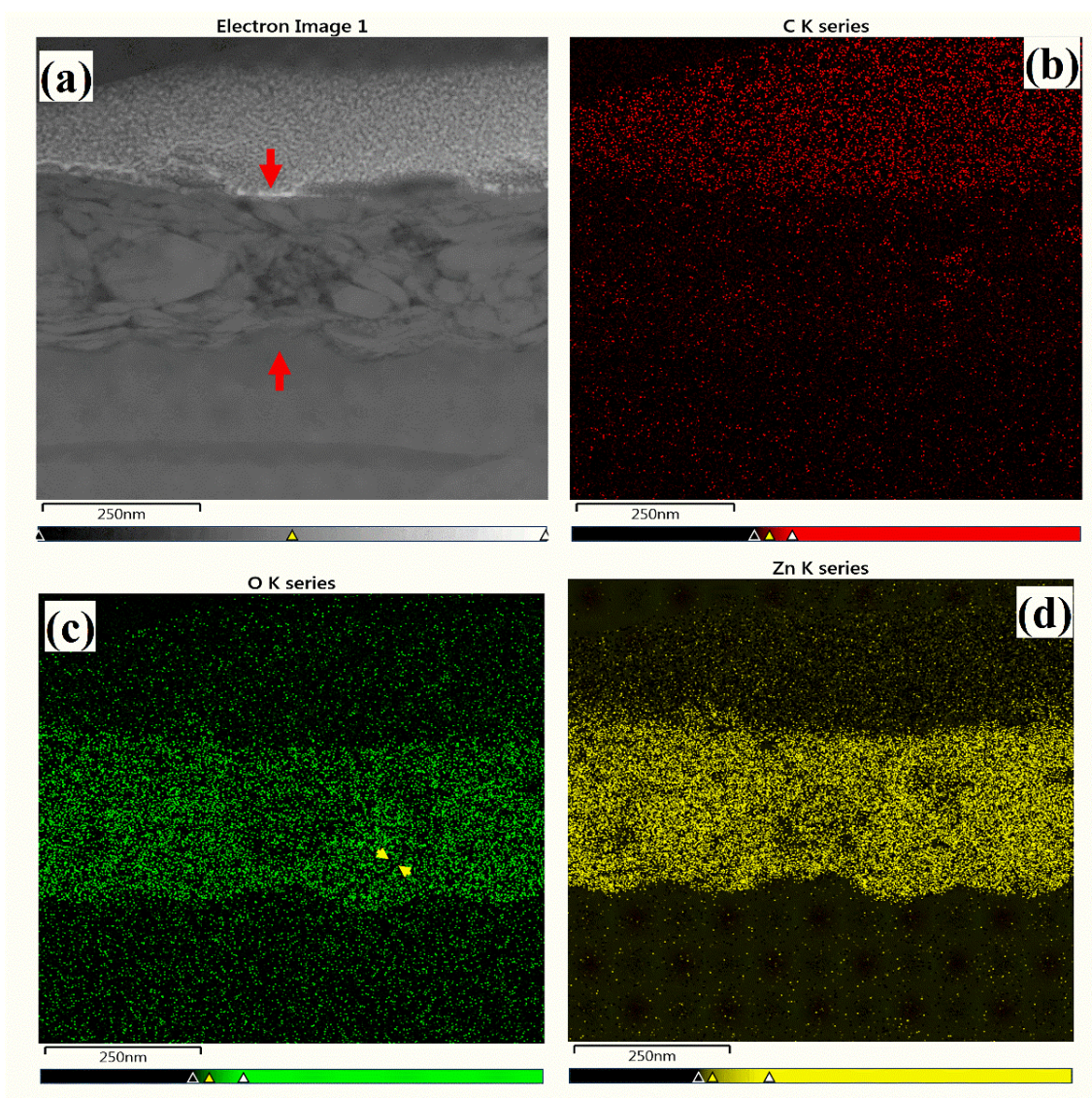


Figure 6. 7: Cross-sectional view (a), and the corresponding EDS elemental analysis mapping (b-d) of ZnO-graphene with 50 wt.% graphite content on titanium sheets.

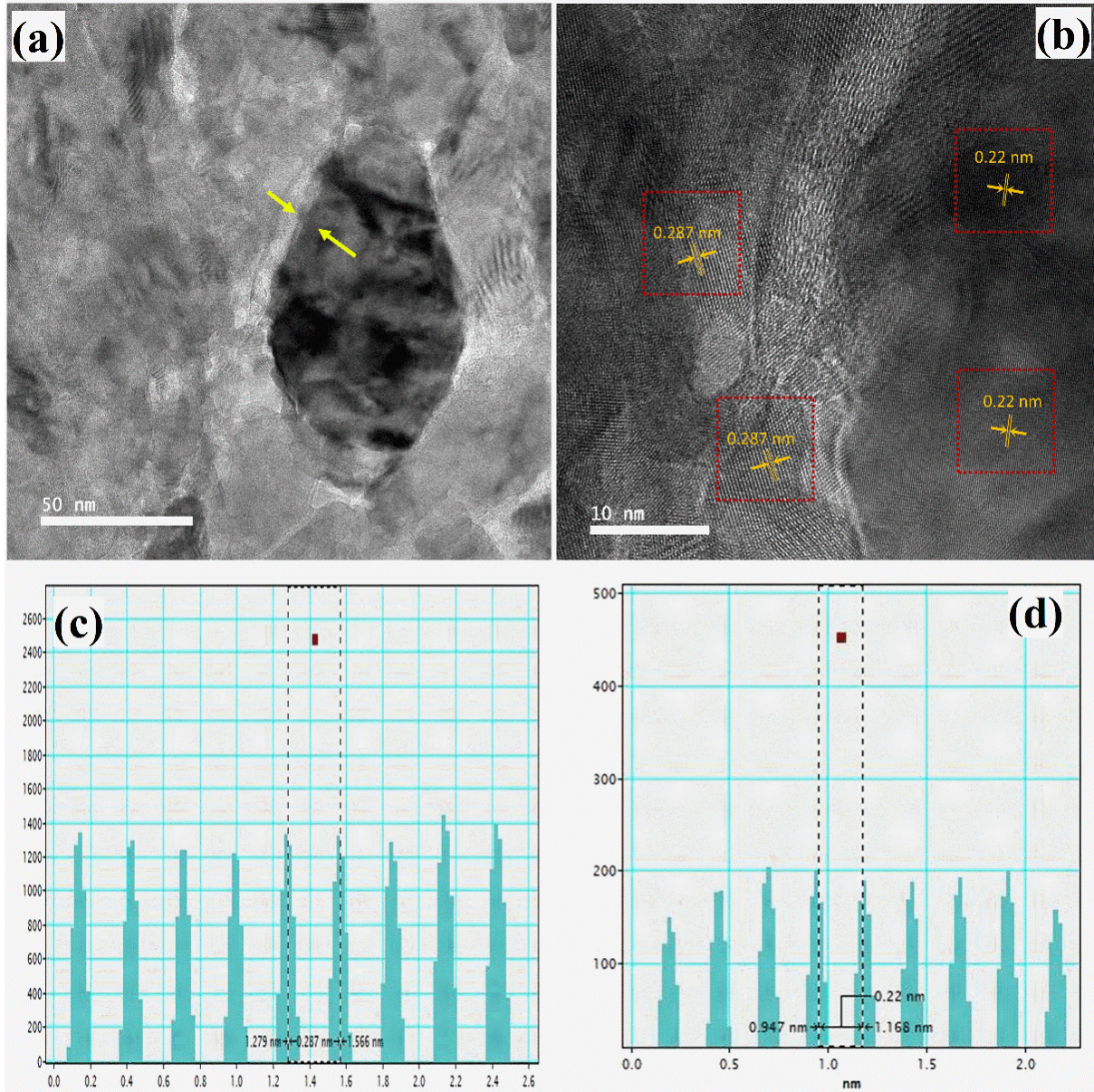


Figure 6. 8: HRTEM image and the corresponding interplanar distance histogram analysis of ZnO-graphene nanosheet thin films on titanium sheets.

6. 2. 3. FTIR and Raman studies on ZnO-graphene composites

Figure 6. 9(a) reveals the FTIR spectrum of ZnO micro-sized powder in the wavenumber range from 650 to 4000 cm^{-1} . Several vibration bands were recognized at 692, 833, 985, 1380, 1510, 1560, and 3400 cm^{-1} . The observed bands at 692 and 833 cm^{-1} are assigned to the induced microstructural modification of the wurtzite-type hexagonal lattice of ZnO [285]. The active vibrations related to the bending and stretching vibration of the adsorbed O–H groups were observed at 1380 and 3400 cm^{-1} , respectively [286]. The vibration bands centered at 985 cm^{-1} , as

well as the overlapped bands ranging from 1510~1560 cm^{-1} , can be attributed to the bending vibrations of the C–H bonds [287] and the asymmetric stretching vibration of the C=O bonds, respectively. These active vibration modes can be originated from the organometallic ionic sources used in the preparation of the ZnO micro-sized powder or from the adsorbed CO_2 at the surface of ZnO powder [278, 288].

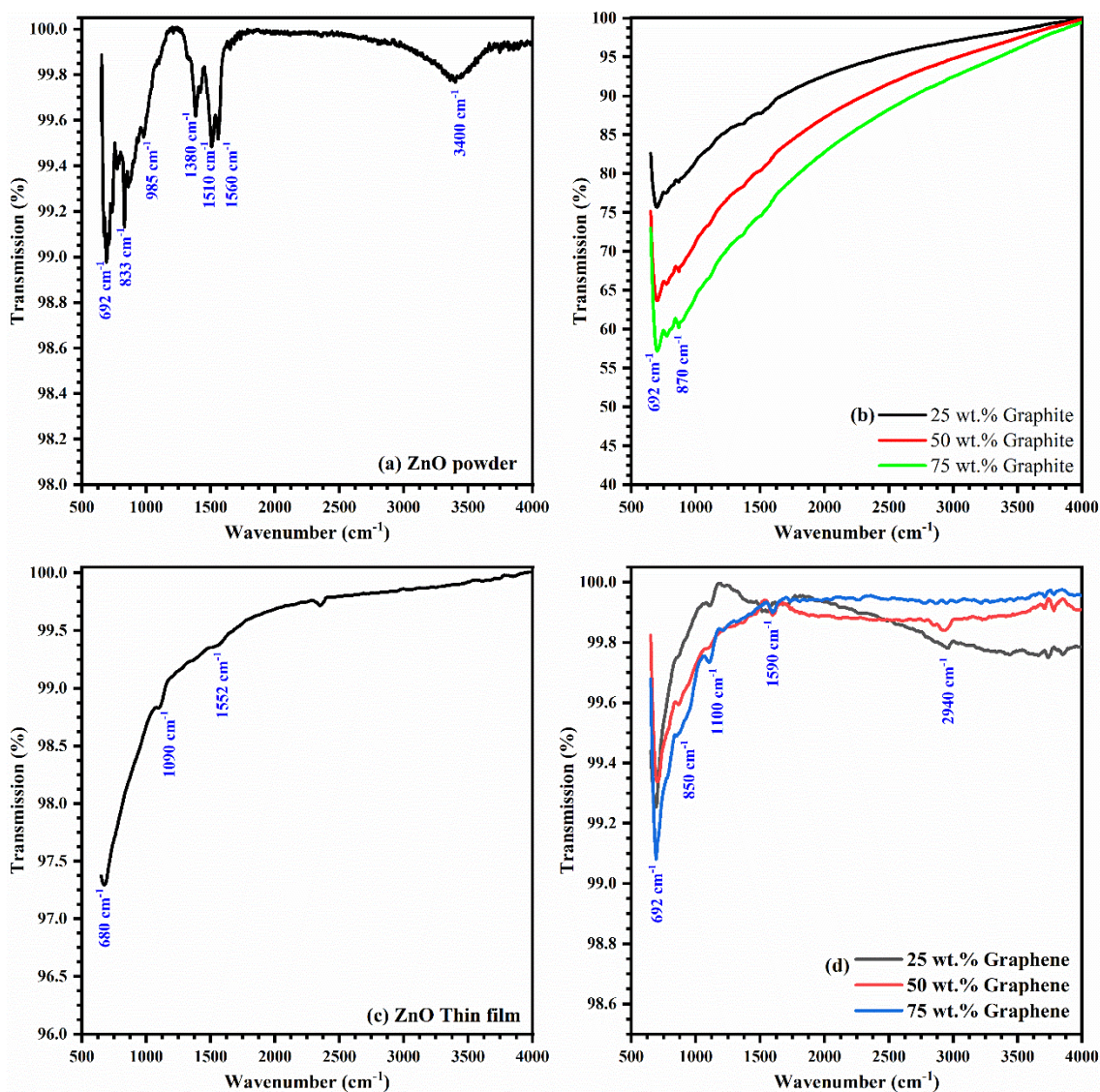


Figure 6. 9: FTIR spectra of ZnO and ZnO-graphite mixed powder (a, b), nanostructured ZnO and ZnO-graphene thin films on a titanium sheet (c, d).

Figure 6. 9(b) demonstrated the FTIR spectra of the ZnO-graphite mixed powder at different graphite contents (25, 50, and 75 wt.%). All mixed powders showed the characteristic lattice vibrations of hexagonal ZnO at 692 and 870 cm^{-1} . These bands showed a wide overlap with other

absorption bands resulting from the bonding between ZnO and the graphite species in the mixed powder, such as C=O and C–O–C bonds [256]. **Figure 6. 9(c, d)** reveals the FTIR spectra of the deposited thin films of ZnO and ZnO-graphene nanosheets with various graphite contents (25, 50, and 75 wt.%) on the titanium sheet substrate. Various active vibration modes were detected related to either ZnO species or other carbon-bonded states in the deposited nanocomposites thin films. By comparing the FTIR spectra of the micro-sized powder and the deposited nanostructured ZnO thin film, we observed the enhancement of the ZnO lattice active vibrations that are induced by the interfacial defects at the crystalline grain boundaries during the deposition process. The layer separation of the graphite crystalline hexagonal structure and the fragmentation to lower domain size resulted in a reduction in the intensity of carbon-related vibrations. Furthermore, a distinguished peak caused by the skeletal vibration of the graphene nanosheets was observed at 1590 cm^{-1} [289]. In addition, the bonding between ZnO and the graphene species through C–O–C bonds was observed at 1100 cm^{-1} [256]. Further investigation into the variation in the active vibrations related to ZnO species, and the direct transformation of layered structure graphite to graphene nanosheets during the deposition process by the NPDS, was performed using micro-Raman spectroscopy as illustrated below.

The micro-Raman spectrum of ZnO powder in the Raman shift range of $200\text{ to }800\text{ cm}^{-1}$, seen in **Figure 6. 10(a)**, reveals multiple active Raman modes at 332 , 379 , and 439 cm^{-1} . The observed active Raman vibrations are related to optical phonons at the Γ -point of the wurtzite-type hexagonal structure of ZnO according to the linear combination of optical phonons ($1A_1+2B_1+1E_1+2E_2$). The A_1 -symmetry mode represents the transverse optical (TO) phonon mode and E_1 refers to the longitudinal optical (LO) phonon mode. The E_2 -symmetry mode is divided into two modes. The low-frequency mode (E_{2L}) refers to the vibration related to oxygen atom whereas the high-frequency mode (E_{2H}) refers to the vibration of the heavy Zn atoms. Besides, two inactive silent Raman modes at low frequency (B_{1L}) and high frequency (B_{1H}) mode can be activated through the incorporation of some interfacial structural defects [290-292]. The active Raman mode at 332 cm^{-1} is mainly attributed to the interference of the optical phonon vibration ($E_{2H}-E_{2L}$) [278, 293]. The first-order vibration corresponding to the polar transverse optical phonon mode with A_1 symmetry was observed with low intensity at 379 cm^{-1} , meanwhile, the non-polar second-order vibration related to the E_{2H} symmetry was observed at 439 cm^{-1} [294]. **Figure 6. 10(b)** shows the micro-Raman spectra of ZnO-graphite mixed micro-sized powder at different

graphite contents (25, 50, and 75 wt.%). The detected vibrations were located at Raman shifts of 332, 439, 1350, 1582, 2720, and 3250 cm^{-1} . By comparing the Raman spectra of the mixed powder with pure ZnO powder, the second-order vibrations of the wurtzite-type hexagonal structure of ZnO were found at Raman shifts of 332 and 439 cm^{-1} . Meanwhile, the first-order polar vibration related to the $A_1(\text{TO})$ symmetry mode was inhibited. Other active Raman vibrations were detected in the case of ZnO-graphite mixed powder that belongs to various graphite species. The characteristic G-band active Raman mode of graphite corresponding to the E_{2g} mode was observed at 1582 cm^{-1} . Whereas the grain boundary related to active vibration corresponding to the D mode was recorded at 1350 cm^{-1} [110]. In addition, other second-order vibrations at 2720 and 3250 cm^{-1} belonged to the 2D and intravalley 2D'-symmetry modes respectively [111, 112]. The intensity ratio (I_D/I_G) between the defect-related active Raman mode D and the main active Raman G modes is of particular interest because it refers to the degree of fragmentation and layer separation of micro-sized graphite powder. When $I_D/I_G > 1$, it represents the transformation of the graphite micro-sized layered structure to the nano-sized graphene nanosheets (i.e., the decrease of domain size in the sp^2 plane) [115].

Figure 6. 10(c) depicts the deconvoluted micro-Raman spectrum of the nanostructured ZnO thin film on the titanium sheet substrate. The Raman spectrum contains three overlapped bands centered at 287, 335, and 518 cm^{-1} . The observed band centered at 335 cm^{-1} refers to the second-order vibrations of the wurtzite-type hexagonal structure of the ZnO. Like the powder, this band has a slight shift to lower wavenumber. However, the other detected Raman modes at 287 and 518 cm^{-1} were not observed in the Raman spectrum of the ZnO micro-sized powder. The observed new vibrations at 287 and 518 cm^{-1} are attributed to the induced activation of the ZnO low-frequency first (B_{1L}) and second-order silent modes ($2B_{1L}$). The activation of silent modes at the Γ -point in the wurtzite-type hexagonal structure of ZnO has been observed in many ZnO-based thin films. This behavior was attributed to the decrease of the crystallinity range and the evolution of a specific interfacial structural defect in the short-order crystalline domain [295-301]. This behavior indicates the fragmentation of the micro-sized ZnO powder with a high degree of crystallinity to a lower size range with a very small domain size. This illustration is supported by the observed absence of XRD peaks in the nano-sized ZnO-based thin films using the NPDS. **Figure 6. 10(d)** exhibits the Raman spectra of ZnO-graphene NCs thin films on titanium sheet substrate with different graphite contents (25, 50, 75 wt.%). All hybrid NCs revealed several active Raman modes

at 305, 567, 1349, 1586, 1620, 2692, and 2940 cm^{-1} . The observed active Raman modes related to the ZnO species are 305 and 567 cm^{-1} corresponding to the first and second-order silent vibration of B_{1L} and $2B_{1L}$, respectively. Furthermore, we observed the shift of these vibrations to a higher Raman shift due to the intergranular hybridization with the graphene nanosheet by comparison with the pure ZnO nanostructured thin film.

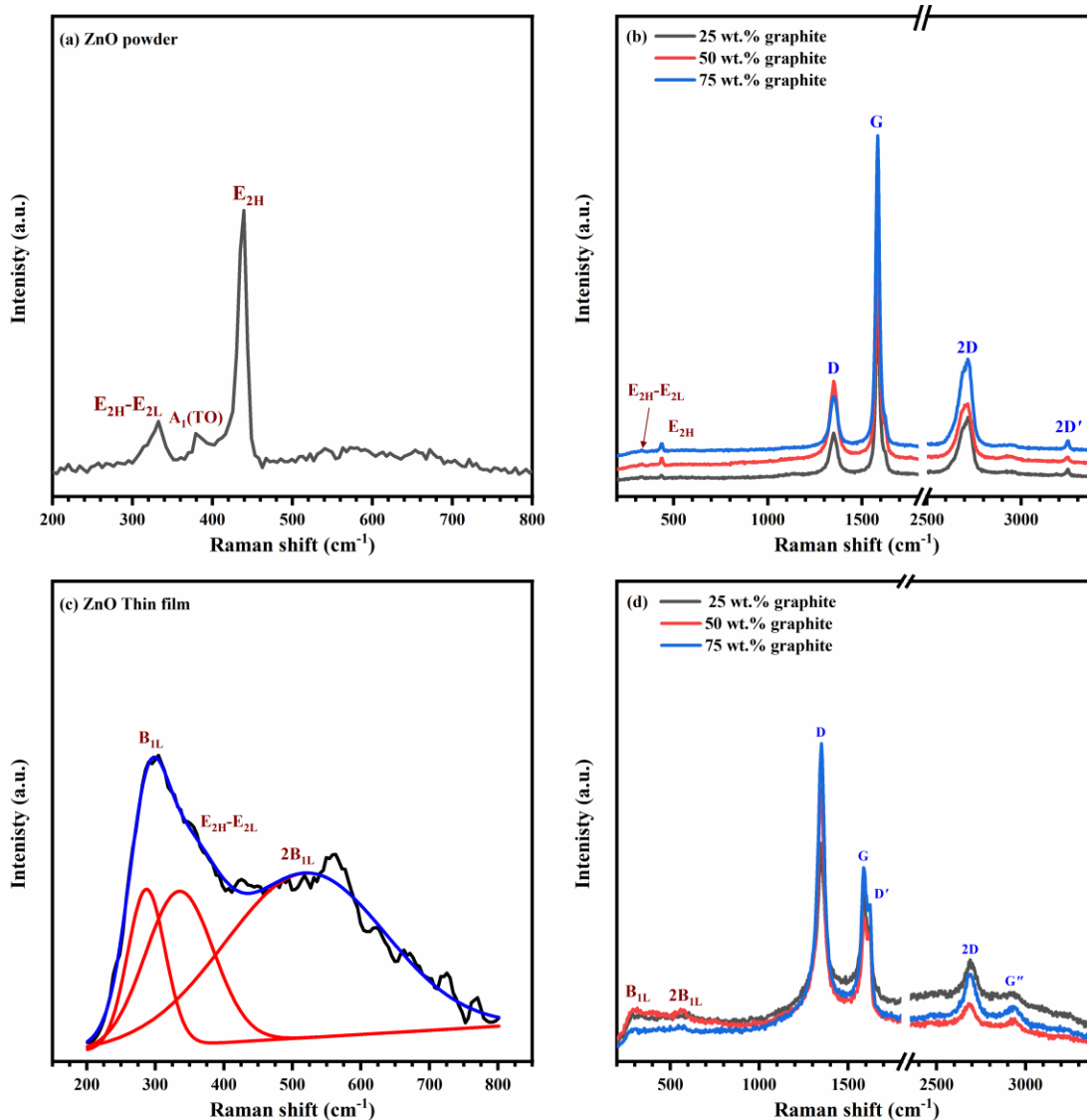


Figure 6. 10: Raman spectra of the ZnO micropowder (a), ZnO-Graphite micro powder mixture (b), nanostructured ZnO thin film (c), and nanostructured ZnO-Graphene thin films on a titanium sheet.

The characteristic active Raman vibrations of the graphene nanosheets at 1349, 1586, and 2692 cm^{-1} were attributed to the same active Raman modes in the graphite microstructure corresponding to the D, G, and second-order 2D vibration mode, respectively. The observed weak

shoulder at 1620 cm^{-1} is attributed to the D'-symmetry mode caused by the displacement of carbon atoms inside the crystal lattice to the surface layer [110, 114]. The graphite-to-graphene phase transformation due to the size reduction and layer separation in the nano-sized ZnO-graphite thin film on titanium sheet substrate were identified from the change in the intensity ratio (I_D/I_G) between the characteristic Raman modes D and G. The layer separation in the micro-sized graphite powder is mainly accompanied by the enhancement of the disorder-related Raman modes (D, G''), whereas the G and 2D bands that distinguish crystallinity or order degree are inhibited. In the case of ZnO-graphite mixed micro-sized powder, the I_D/I_G ratio was 0.65, 0.71, and 0.54 corresponding to the mixed powder with 25, 50, and 75 wt.% graphite content, respectively. After the deposition process using the NPDS, the I_D/I_G ratio was improved to 1.07, 1.2, and 1.24 for hybrid nanocomposites with respective 25, 50, and 75 wt.% graphite content, which depicted the evolution of graphene nanosheets in all the ZnO-graphene NCs/Ti-sheet hybrid photoanodes.

6. 2. 4. Surface bonding characterization of ZnO-graphene NCs

X-ray photoelectron spectroscopy (XPS) was used to identify the interfacial chemical bonding states on the titanium-modified surface with either pure nanosized ZnO or ZnO-graphene NCs on titanium sheets at different graphite contents (25, 50, and 75 wt.%). **Figure 6. 11(a)** shows the XPS survey spectra for the nanosized ZnO/Ti-sheets and ZnO-graphene NCs/Ti-sheet with 25, 50, 75 wt.% graphite contents. The XPS survey spectrum of nanostructured ZnO/Ti-sheet reveals various signals related to the zinc metallic phase (Zn 3d, Zn 3p, Zn 3s, Zn LMM1, Zn KLL, Zn LL M3, Zn 2p_{3/2}, and Zn 2p_{1/2}), and others correspond to oxide bonded states (O 1s, O KLL). The same active states related to ZnO species were also observed in ZnO-graphene hybrid photoanodes as well as the C 1s state referring to the presence of graphene species. For understanding the mutual synergy behavior between the nano-sized ZnO and graphene nanosheets species, the high-resolution XPS scan for each active bonded state (Zn 2p, O 1s, and C1s) was carried out as shown in **Figure 6. 11(b-d)**, and the deconvoluted band was recorded in **Table 6. 1**. **Figure 6. 12** exhibits the Zn 2p high-resolution XPS scan in the binding energy range from 1010 to 1050 eV for the titanium-modified electrodes with the nano-sized ZnO/Ti-sheet and ZnO-graphene NCs/Ti-sheet hybrid photoanodes.

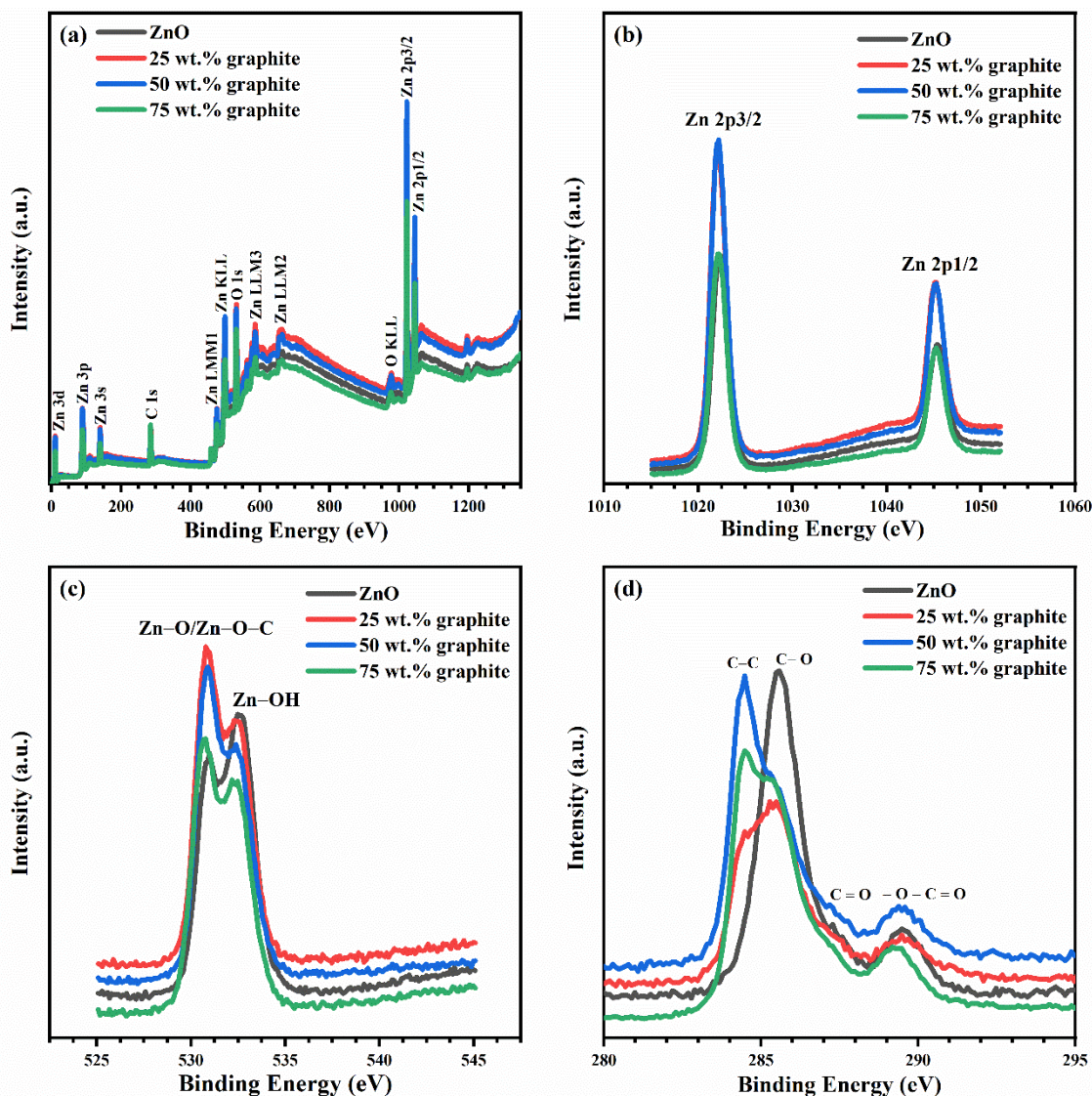


Figure 6. 11: XPS survey spectrum **(a)** and, high-resolution XPS scans of Zn 2p **(b)**, and O 1s **(c)**, and C 1s **(d)** of ZnO-graphene NCs on titanium sheet.

The deconvoluted Zn 2p XPS scan revealed two well-resolved and sharp bands centered at 1022.18, and 1045.28 eV corresponding to Zn 2p_{3/2} and Zn 2p_{1/2}, respectively, with an energy separation of 23.1 eV of the related active bonded Zn-metallic phases [273, 302]. The observed band at low binding energy (1022.18 eV) was attributed to the Zn ions in the nonstoichiometric hexagonal structure of ZnO. Besides, there were no observable peak position changes of Zn 2p_{3/2} and Zn 2p_{1/2} in the case of the ZnO-graphene NCs compared with the pure ZnO phase. The XPS band sharpness of the Zn 2p scan for pure ZnO and hybrid ZnO-graphene photoanodes with different graphite contents demonstrates the presence of Zn ions with the active divalent state (Zn²⁺) [303, 304]. Furthermore, the relative peak intensity was improved in

the case of hybrid NCs with 25 and 50 wt.% graphite contents compared with the pure nano-sized ZnO/Ti-sheet. This refers to the improvement in the concentration of Zn²⁺ active states at the surface of those hybrid NCs thin films.

Table 6. 1: XPS band centers according to the deconvolution of the high-resolution XPS scans of Zn 2p, O 1s, and C 1s of ZnO-graphene nanosheet hybrid photoanodes at different graphite contents (wt.%)

Band	Binding Energy (eV)			
	ZnO	25 wt. % graphite	50 wt. % graphite	75 wt. % graphite
C 1s	-	284.32	284.37	284.36
	285.57	285.43	285.20	285.25
	287.33	287.15	287.24	287.20
	289.52	289.51	289.20	289.23
O 1s	530.82	530.78	530.78	530.62
	532.57	532.44	532.41	532.40
Zn 2p	1022.32	1022.13	1022.17	1022.21
	1045.40	1045.21	1045.26	1045.30

Figure 6. 13(a-d) shows the deconvoluted high-resolution O 1s XPS scan of the nanosized ZnO/Ti-sheet and ZnO-graphene NCs/Ti-sheet with 25, 50, and 75 wt.% graphite content in the binding energy range of 525 to 545 eV. The deconvoluted bands of the high-resolution O 1s XPS scan of the nano-sized ZnO/Ti-sheet exhibit two overlapped bands centered at 530.82 and 532.57 eV. The first band at a lower binding energy (530.82 eV) refers to the divalent state of bonded oxygen anions (O²⁻) in the wurtzite-type hexagonal structure of ZnO [305]. The second peak at higher binding energy (532.57 eV) is ascribed to either the adsorption hydroxyl group at the surface of the nano-sized ZnO [306] or the presence of some reduced Zn ions at the interface of the ZnO grain boundaries that tend to decrease the crystalline domain size [307]. In the case of titanium modified with ZnO-graphene hybrid NCs, the deconvolution of the high-resolution O 1s XPS scan reveals similar band positions with slight variations in the positions of the peaks compared with the pure nano-sized ZnO/Ti-sheet, as summarized in **Table 6. 1**. Furthermore, the incorporation of graphene nanosheets with nano-sized ZnO resulted in the intensity improvement of the first band at lower binding energy compared with the second band at a higher binding energy, **Figure 6. 11(c)**, referring to the improvement of various possible oxygen-related states (Zn–O/O–C). Besides, the intensity of the second band at higher binding energy (~ 532 eV) was gradually decreasing with increasing graphite content in ZnO-graphene NCs/Ti-sheet. This behavior is attributed to the improvement in the hydrophobic tendency in the hybrid NCs as a result of the formation of graphene nanosheets that is mostly accompanied by the enhancement of the charge transfer kinetics in photon energy conversion processes

[308, 309]. This behavior depicts the hybridization and synergy improvement between the graphene and nanostructured ZnO species in the fabricated ZnO-graphene nanosheet hybrid photoanodes [276].

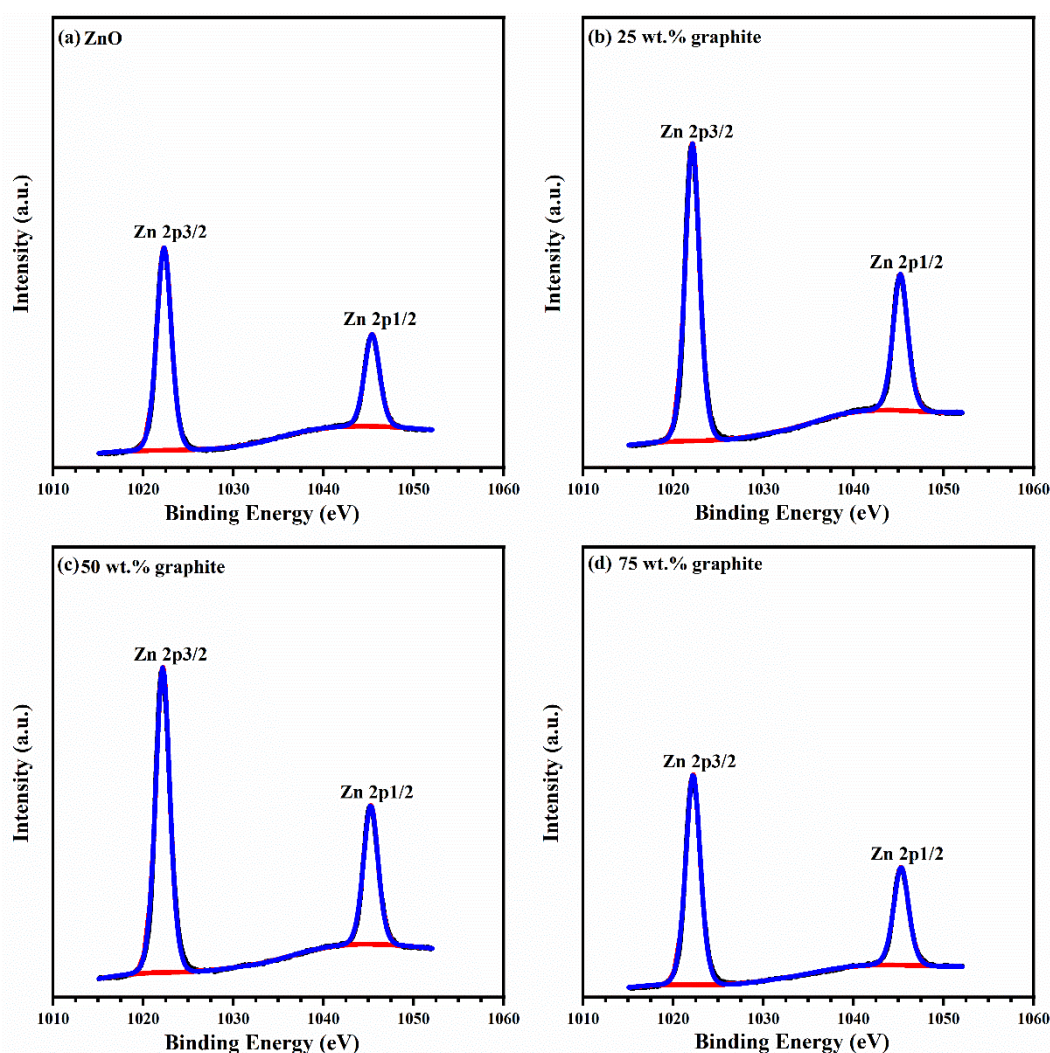


Figure 6. 12: Deconvoluted Zn 2p XPS scan of pure ZnO (a) and ZnO-graphene NCs/Ti-sheet thin films on titanium sheet with 25 wt.% (b), 50 wt.% (c), and 75 wt.% (d) graphite content.

Figure 6. 14 shows the high-resolution C 1s XPS scans of nano-sized ZnO/Ti-sheet and ZnO-graphene NCs/Ti-sheet at different graphite content (25, 50, and 75 wt.%). The deconvoluted C 1s XPS spectrum of the nano-sized ZnO/Ti-sheet in **Figure 6. 14(a)** reveals several bonded states, see **Table 6.1**, which can be attributed to adsorbed CO₂ and structural carbonate species containing C=O [310]. This result is supported by the detected active vibrations in the FTIR spectra of the ZnO micro-sized powder and the corresponding nanosized ZnO/Ti-sheet thin films as shown in **Figure 6. 9**. The deconvolution of the C 1s XPS scans of all hybrid ZnO-graphene NCs/Ti-sheet in **Figure 6. 14(b-d)** exhibits the main band at

284.34 ± 0.02 eV that was caused by the sp²-hybridized carbon (C–C) in the graphene nanosheets [242]. Besides, we observed several oxygenated bonds mostly located at the boundaries of the graphene nanosheets resulting from hybridization with metal-oxide compounds, such as the C–O bond at 285.3 ± 0.2, C=O bond at 287.2 ± 0.05 eV, and –O–C = O at 289.35 ± 0.15 eV [189, 245]. The modifications of ZnO-graphene NCs/Ti-sheet hybrid photoanodes after the end of the PEC water splitting measurements were investigated using the XPS analysis as shown in **Figure 6. 15**.

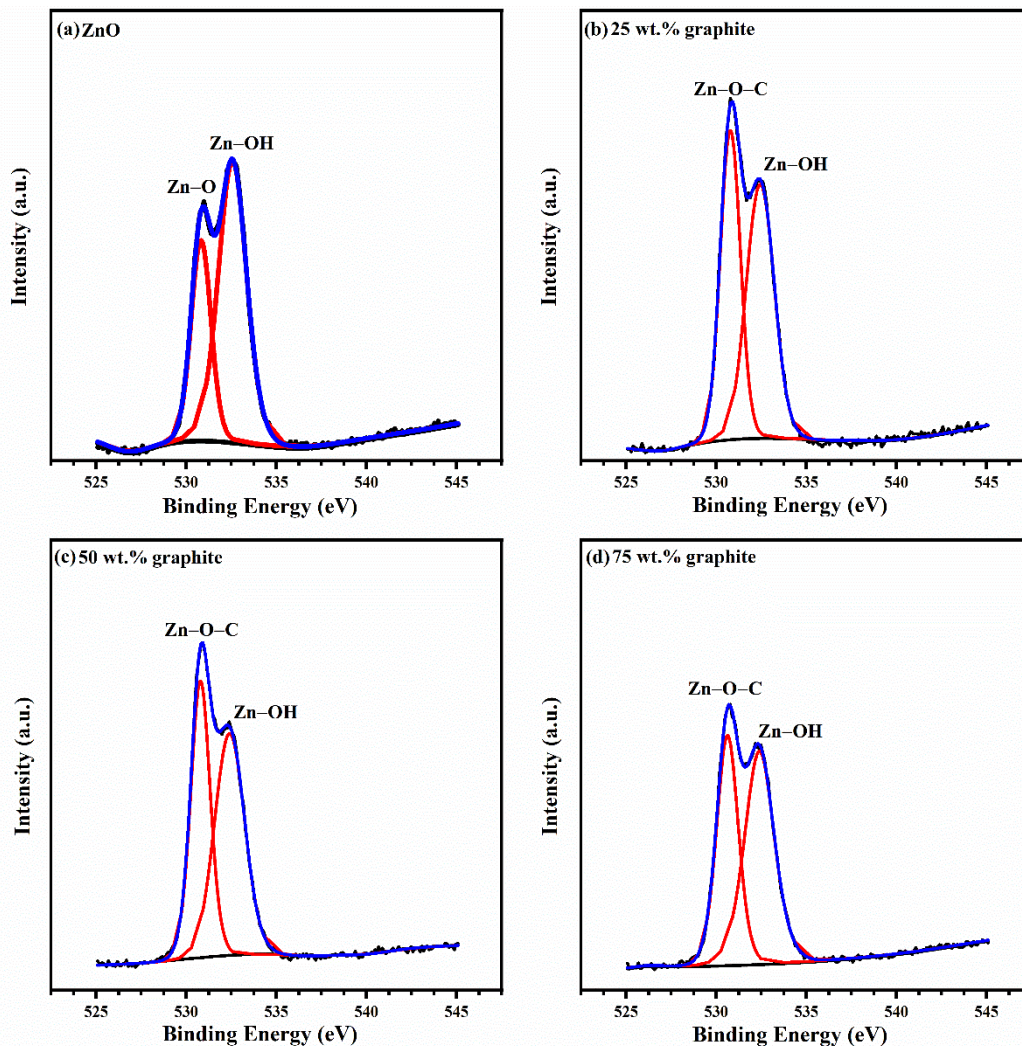


Figure 6. 13: Deconvoluted O 1s XPS scan of pure ZnO **(a)** and ZnO-graphene NCs/Ti-sheet thin films with 25 wt.% **(b)**, 50 wt.% **(c)**, and 75 wt.% **(d)** graphite content.

The XPS survey spectra of ZnO-graphene NCs in **Figure 6. 15(a)** reveals the appearance of some additive active states S 2p, O 1s, and Na 1s that are caused by the adsorption of the used electrolyte

species for the PEC water splitting experiment. Besides, the intensity of Zn 2p active states was strongly inhibited in the case of hybrid NCs at different graphite content.

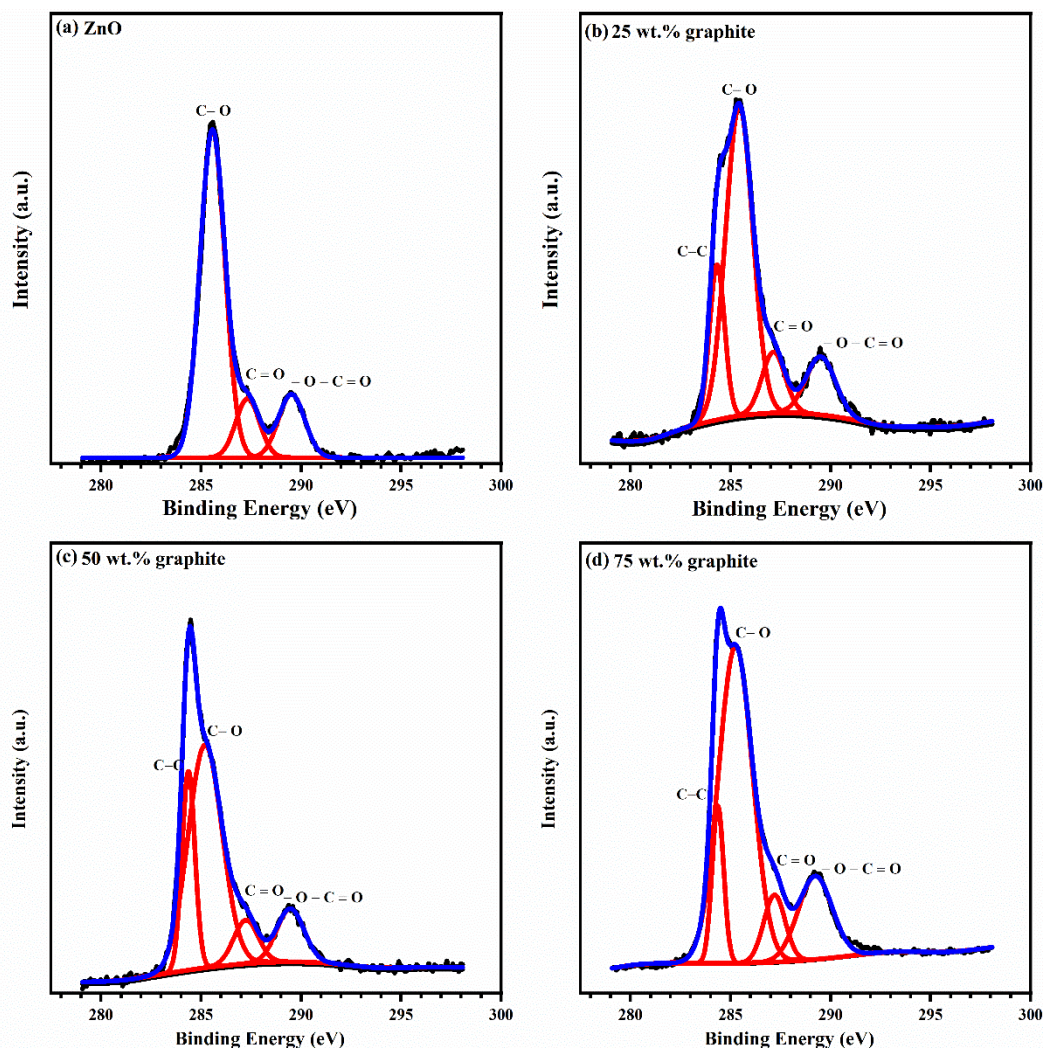


Figure 6. 14: Deconvoluted C 1s XPS scans of nano-sized ZnO/Ti-sheet (a), and ZnO-graphene NCs/Ti-sheet thin films with 25 wt.% (b), 50 wt.% (c), and 75 wt.% (d) graphite content.

To illustrate the photo-induced chemical change on the surface of ZnO-graphene NCs/Ti-sheet, we provide the high-resolution XPS of Zn 2p, O 1s, and C 1s for all photoanodes as shown in **Figure 6. 15 (b-d)**. The position of detected peaks in the high-resolution XPS scan is recorded in **Table 6. 2**. The high-resolution Zn 2p XPS scan in **Figure 6. 15(b)** reveals that the active states characterized by the ZnO species (Zn 2p_{3/2} and Zn 2p_{1/2}) were strongly decreased in the case of ZnO-graphene hybrid NCs/Ti-sheets compared to pure ZnO/Ti-sheets. This behavior is ascribed to the photo-induced dissolution of ZnO species during the PEC water splitting process that is accompanied by the photoinduced formation of

soluble ZnSO₄ species in the Na₂SO₃ solvent for prolonged exposure for light illumination [311, 312]. Furthermore, the improvement in the visible-light harvesting in the case of ZnO-graphene hybrid NCs compared with the nano-sized ZnO make the photo-induced dissolution more observable. Analysis of the O 1s XPS scans in **Figure 6. 15 (c)**, exhibits the disappearance of O 1s peak at low binding energy that distinguishes the hexagonal phase of ZnO. Whereas, the O 1s peaks related to OH adsorption and formation of Zn(OH)₂ species [313] were detected at higher binding energies, see **Table 6. 2**.

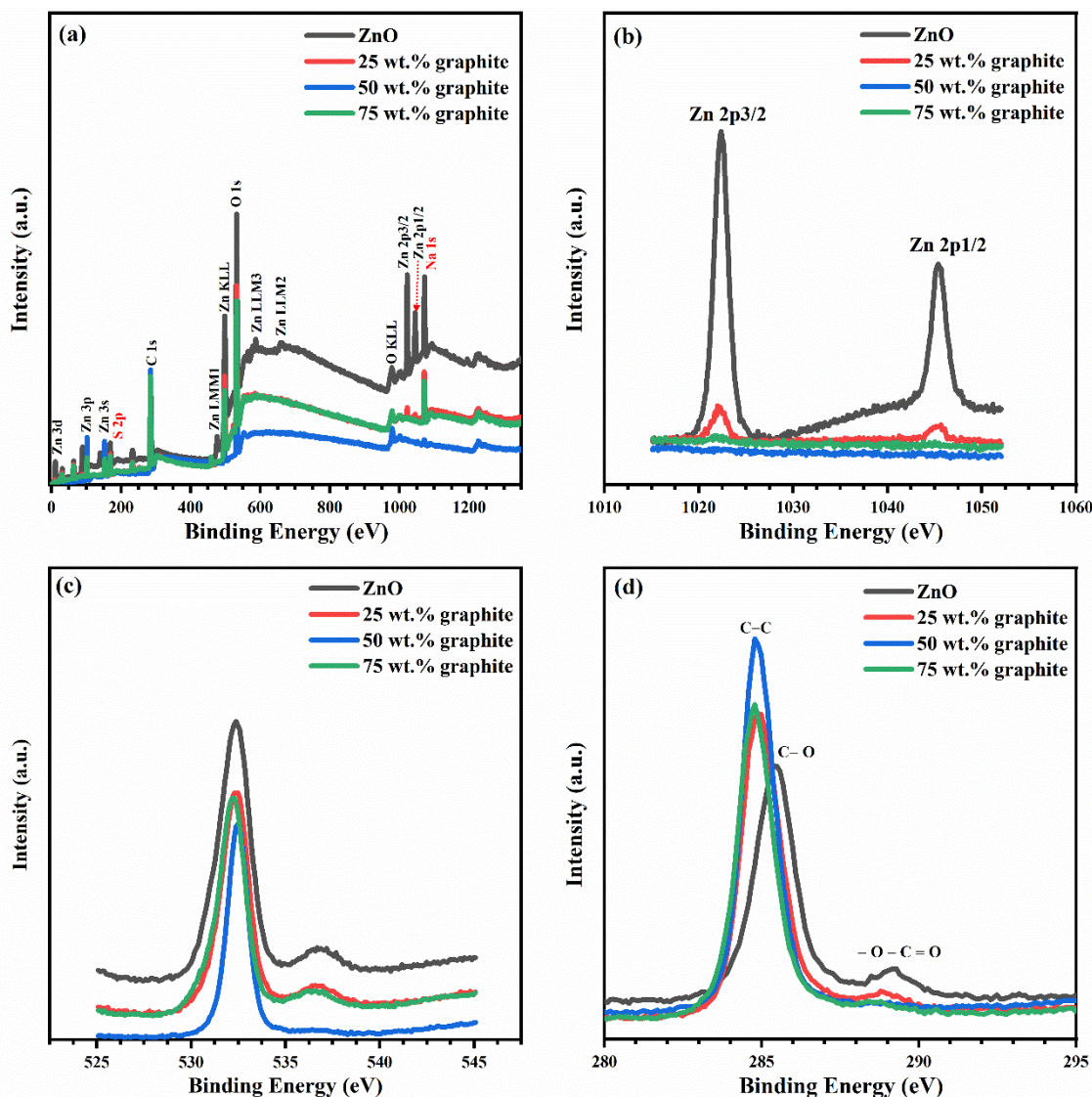


Figure 6. 15: XPS survey spectrum **(a)** and, high-resolution XPS scans of Zn 2p **(b)**, and O 1s **(c)**, and C 1s **(d)** of ZnO-graphene NCs on titanium sheet after the photoelectrochemical water splitting measurements.

Another interesting feature was recognized from the analysis of C 1s high-resolution XPS scan of ZnO-graphene hybrid NCs. The detected peaks in the C 1s scan of the nano-sized ZnO/Ti-sheet photoanode after the PEC experiment exhibit two characteristic peaks related to the CO₂ adsorption as explained before for the nano-sized ZnO/Ti-sheet before the PEC measurements. Moreover, in the case of ZnO-graphene hybrid NCs the intensity of C 1s peaks, **Figure 6. 15(c)**, related to the bonding between carbon and oxygen species was diminished. This behavior can be attributed to either the dissolution of ZnO species or the photocatalytic reduction of graphene nanosheets [314], [315].

Table 6. 2: Analysis of the high-resolution XPS scans of Zn 2p, O 1s, and C1s of ZnO-graphene NCs hybrid photoanodes at different graphite contents (wt.%) after the photoelectrochemical water splitting measurements

Band	Binding Energy (eV)			
	ZnO	25 wt. % graphite	50 wt. % graphite	75 wt. % graphite
C 1s	-	284.88	284.78	284.78
	285.48	-	-	-
	289.28	288.78	-	-
O 1s	532.38	532.38	532.48	532.28
	536.68	536.58	-	-
Zn 2p	1022.38	1022.1	-	-
	1045.38	1045.1	-	-

6. 2. 5. The optical band gap of ZnO-graphene nanosheets photoanodes

Figure 6. 16(a) reveals the diffuse reflectance spectra of titanium modified with nano-sized ZnO/Ti-sheet and ZnO-graphene NCs/Ti-sheet at various graphite contents (25, 50, and 75 wt.%) in the wavelength range from 200 to 800 nm. The recorded diffuse reflectance (R) is related to the material absorption coefficient (α) as described by the Kubelka-Munk function (F) given by **Eq. 6. 1** [316]. Then, the optical bandgap (E_g) of the ZnO-graphene NCs/Ti-sheet hybrid photoanode was estimated by substituting the α from in Tauc's relation for the direct allowed transition described by **Eq. 6. 2** [317].

$$\frac{\alpha}{S} = F = \frac{(1-R)^2}{2 \times R} \quad \text{Eq. 6. 1}$$

$$(\alpha h\nu)^2 = C(h\nu - E_g) \quad \text{Eq. 6. 2}$$

Where S is the scattering coefficient, $h\nu$ is the incident photon energy, and C is the proportionality constant.

The E_g of the ZnO-graphene NCs/Ti-sheet was estimated from the extrapolation of the linear part in the high-energy level with the x-axis according to Tauc's relation, see **Figure 6. 16(b)**. The determined E_g of ZnO-graphene hybrid NCs with 25, 50, and 70 wt.% graphite contents were 2.9, 2.6, and 3.1 eV,

respectively. The obtained values were lower than the nano-sized ZnO-/Ti-sheet. This demonstrated that the incorporation of graphene nanosheets resulted in a decrease in the optical band gap of the ZnO host lattice. This behavior is expected to improve solar radiation light-harvesting in the visible spectral region. **Figure 6. 16(c)** reveals the valence band (VB) level estimation from the XPS survey spectrum of the titanium-modified photoanodes with nano-sized ZnO and ZnO-graphene NCs in the binding energy range from -3 to 6 eV. The VB of the titanium-modified photoanode with the nano-sized ZnO was 2.75 eV, meanwhile, the incorporation of graphene nanosheets results in the negative shift of the VB level to lower binding energy at 2.5 eV for all ZnO-graphene NCs. An illustrative energy band structure diagram for titanium modified with the nanostructured ZnO and ZnO-graphene heterostructured photoanodes is illustrated in **Figure 6. 16(d)**.

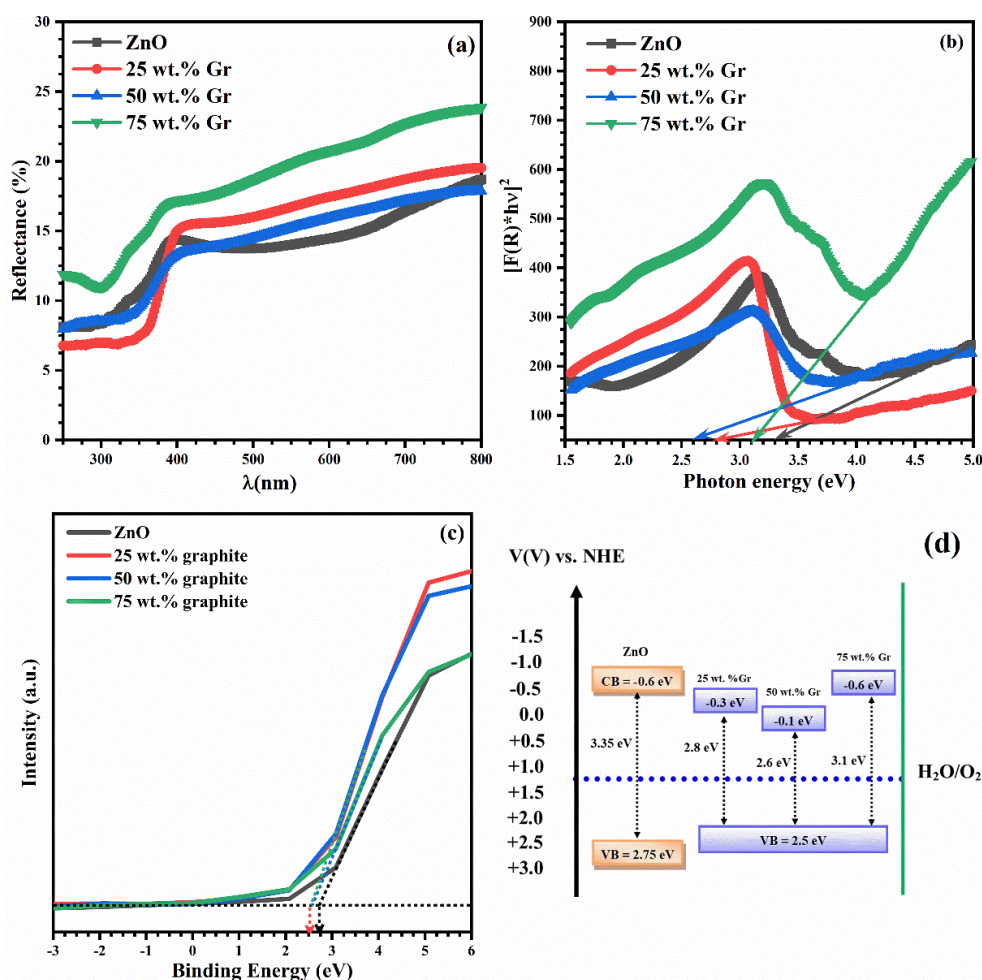


Figure 6. 16: Diffuse reflectance spectra and the corresponding Kubelka-Munk plot **(a, b)**, Valence band estimation from the XPS survey spectrum **(c)**, and demonstrative band structure diagram of ZnO-graphene hybrid photoanodes with different graphite contents **(d)**.

6. 2. 6. Photoluminescence studies on ZnO-graphene nanosheets hybrid photoanodes

Photoluminescence spectroscopy is a powerful tool for examining the behavior of the interfacial structural defects through the identification of various defect-related trapping and recombination centers within the band structure of the used semiconductor material [318]. Nano-sized ZnO materials have various types of structural related defects (interstitials and vacancies) that provide several pathways for radiative recombinations [278, 319]. Hence, we used the PL emission spectra for studying the effect of graphene hybridization with ZnO species on the recombination centers concentration in the hybrid NCs thin films. PL emission spectra of ZnO-graphene NCs/Ti-sheet at different graphite contents (25, 50, 75 wt.%) were scanned at three different excitation wavelengths (λ_{ex}) to detect all possible radiative centers in the band structure of these hybrid NCs as shown in **Figure 6. 17(a-c)**. The high excitation energies at 3.82 and 3.31 eV corresponding to 325 and 375 nm, respectively, were used to examine the band edge and the accompanied excitonic band emission as well as other shallow defect-related emissions. Besides, the lower excitation energy at 2.92 eV corresponding to an λ_{ex} of 425 nm was used to detect other deep defect-related emissions. Based on the recorded PL emission spectra various emission bands in the UV-visible spectral regions were detected at 362, 378, 422, 444, 487, 512, and 520 nm. The origin of the emission centers was identified as illustrated in the schematic band diagram in **Figure 6. 17(d)**. The first UV emission band at 362 nm represents the band edge emission; meanwhile, the second UV emission band could be ascribed to either exciton-related recombination emission or the recombination of shallow trapped electrons at interstitial zinc (Zn_i) species with photogenerated holes [320, 321]. The observed blue emission bands in the range from 420 to 440 nm are mainly ascribed to the recombination of shallow trapped electrons at Zn_i with trapped holes with extended vacancy states related to Zinc (Zn_v) near the top of the valence band. The observed emission bands at a lower energy in the blue-green spectral region could arise from the recombination of trapped electrons with deeper defect states mostly oxygen vacancies (O_v) with either photogenerated holes or trapped holes at Zn_v [318, 322, 323]. The PL emission spectra of ZnO-graphene NCs/Ti-sheet hybrid photoanodes reveal the quenching of PL emission intensity with the addition of graphene nanosheets to the nanostructured ZnO-based hybrid photoanodes at all used excitation energies (band edge and defect -related emission), as shown in **Figure 6. 17(a-c)**. The utilized ZnO-graphene NCs/Ti-sheet hybrid photoanode with 50 wt.% graphite contents exhibited the lowest PL emission intensity. The observed decrease in the PL emission intensity revealed the reduction in the photogenerated electron-hole pair recombination and the improvement of photogenerated electron-hole

pair separation. This, in turn acts to enhance the photoconversion efficiency in the ZnO-graphene NCs/Ti-sheet photoanodes [324, 325].

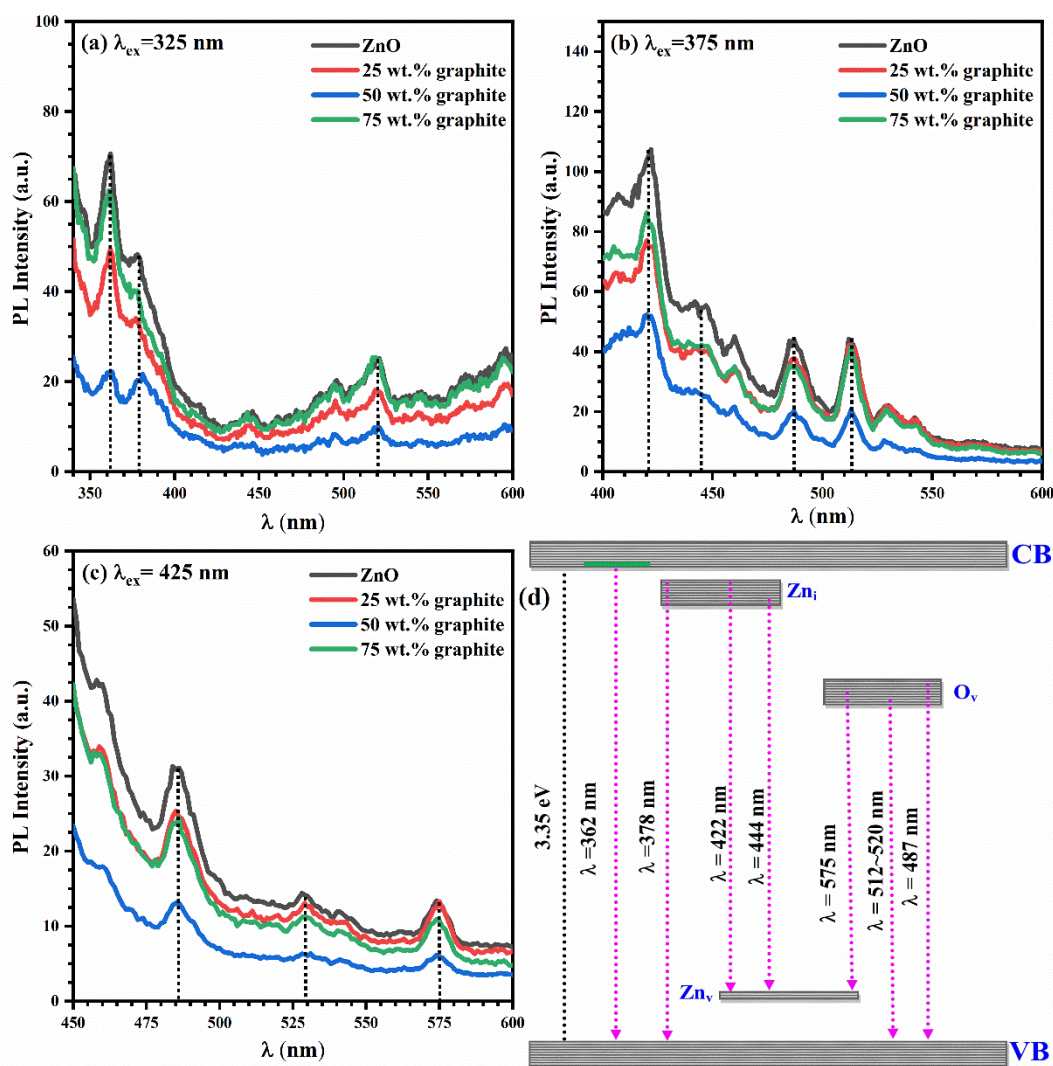


Figure 6.17: Photoluminescence emission spectra of ZnO-graphene hybrid photoanodes at different excitation wavelengths (λ_{ex}) and the corresponding radiative center illustrative band diagram.

6. 2. 7. Photoelectrochemical water splitting measurements

Figure 6.18(a) reveals the photo-response current of a nano-sized ZnO/Ti-sheet and ZnO-graphene NCs hybrid photoanodes with different graphite contents (25, 50, and 75 wt.%) in the potential range from 0.5 to 1.8 V vs. RHE (-0.177 to 1.23 V vs. Hg/HgO). The onset potential of the nano-sized ZnO/Ti-sheet photoanode was 1.024 V vs. RHE, which is negatively shifted with the incorporation of graphene nanosheets.

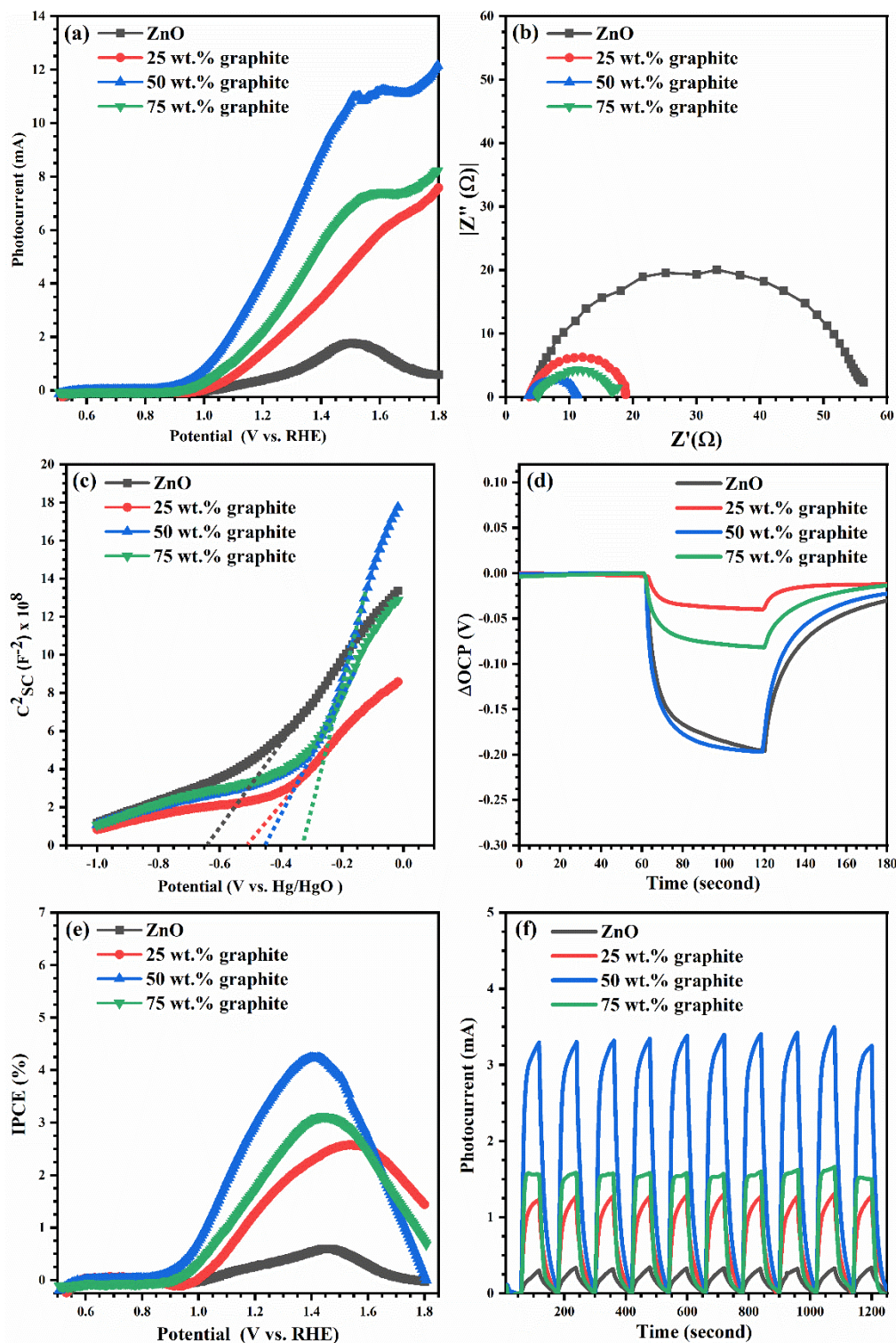


Figure 6. 18: Photocurrent density vs. applied potential (a), Nyquist plot under illumination at 1.23 V vs. RHE (b), Mott-Schottky (M-S) plot in the dark state (c), the change in the open circuit potential (ΔOCP) with light illumination (d), incident photon-to-electron conversion efficiency (IPCE) vs. potential (e), and response current stability for 10 cycles (f) of ZnO-graphene hybrid photoanodes at different graphene contents.

The onset potential of ZnO-graphene nanosheets on Ti-sheet photoanodes was reduced by 25, 428, and 107 mV, which corresponds to hybrid NCs hybrid photoanodes with 25, 50, and 75 wt.% graphite content, respectively. Besides, the measured photocurrent at 1.23 V vs. RHE for NCs hybrid photoanodes was 1.69, 4.73, and 2.53 mA. This revealed the improvement of the hybrid photoanode response current compared with the nano-sized ZnO/Ti-sheet that exhibited a lower photo-response current of 0.469 mA. **Figure 6. 18(b)** reveals the Nyquist plots of ZnO-graphene NCs/Ti-sheet hybrid photoanodes at 1.23 V. vs. RHE under visible light illumination. It can be observed that the incorporation of graphene nanosheets results in an overall improvement in the charge transfer kinetics of the nano-sized ZnO/Ti-sheet photoanodes under visible light illumination. The hybrid photoanode with 50 wt.% graphite contents exhibited the lowest charge transfer resistance (R_{ct}) of 8 Ω compared with the hybrid photoanodes with 25 wt.% graphene contents (15 Ω), and 75 wt.% graphene contents (13 Ω) as well as the pure ZnO/Ti-sheet photoanode with R_{ct} of 52 Ω . This demonstrates the improvement of the photogenerated charge carrier separation with the addition of graphene to the NCs hybrid photoanode. The modification of the flat band potential (V_{fb}) and the donor concentration (N_D) of ZnO/Ti-sheet photoanode with the incorporation of graphene nanosheets was investigated through the Mott-Schottky equation. The interfacial capacitance of the semiconductor electrode (C_{sc}) due to the space-charge layer varied as a function of the electrode potential, which is represented by equation **Eq. 6. 3** [326]:

$$\frac{1}{C_{sc}^2} = \frac{1}{2\epsilon\epsilon_0 A^2 e N_D} \left(V - V_{fb} - \frac{k_B T}{e} \right) \quad \text{Eq. 6. 3}$$

where N_D is the donor concentration (majority carrier concentration, i.e. electron in n-type ZnO semiconductor, ϵ_0 is the vacuum electric permittivity, ϵ is the dielectric constant of ZnO (8.5) [327], V is the anode potential, V_{fb} is the flat band potential, e is the electron charge, k_B is Boltzmann's constant, and T is the absolute temperature.

The Mott-Schottky plots of the nano-sized ZnO and ZnO-graphene NCs hybrid photoanodes with different graphite contents (25, 50, and 75 wt.%) are shown in **Figure 6. 18(c)**. The estimated slopes and x-intercepts provided the desired information for estimating N_D and V_{fb} as illustrated in **Table 6. 3**. We found that graphene nanosheet hybridization with ZnO results in a strong positive shift in V_{fb} . The hybrid photoanode with 50 wt.% graphene content reveals the highest positive shift compared with the pure ZnO/Ti-sheet photoanode. The reduction in V_{fb} and N_D plays an important role in the observed improvement in the PEC water splitting performance. This can be further illustrated as follows: from the basic definition of the flat band potential, it is equal to the electrode bias potential relative to the reference

electrode when the band is flat referring to the consumed external electrical energy for controlling the electrode surface polarization [328]. Hence, the reduction in the V_{fb} demonstrates the improvement the energy conversion efficiency. The variation of N_D in an n-type semiconductor is not directly related to the PEC water splitting because it represents the variation in the majority carrier concentration. The majority of carriers are not directly involved in the PEC reactions at the electrode/electrolyte interface as described by **Eq. 6. 4**. However, the variation in N_D strongly affects the position of Fermi level (E_f) relative to the intrinsic energy level (E_i) at the bandgap center of the modified electrode, as demonstrated by **Eq. 6. 5**. Furthermore, the minority carrier concentration (i.e., holes) within the space-charge layer given by the solution of Poisson's equation, as described by **Eq. 6. 6**, refers to the improvement of the minority carrier concentration (P) within the space charge layer when an E_f shift toward the E_i level [329]. The variation in V_f , N_D , and the associated modification of E_f for ZnO-graphene hybrid photoanodes with varying graphene content is schematically illustrated in **Figure 6. 19**.

$$N_D = n = n_i e^{\left(\frac{E_f - E_i}{k_B T}\right)} \quad \text{Eq. 6. 4}$$

$$E_f = E_i + K T \times \ln \left(\frac{N_D}{n_i}\right) \quad \text{Eq. 6. 5}$$

$$P = n_i e^{\left(-\frac{E_i - E_f}{k_B T}\right)} \quad \text{Eq. 6. 6}$$

The formed space charge layer at the interface between the modified photoanode and the electrolyte plays an important role in the photogenerated charge carrier separation and overall energy conversion performance. According to Kelly et al., [330], the spatial separation at the semiconductor/electrolyte interface between the photogenerated electrons and holes is necessary for observing the PEC response current. They emphasized that the photogenerated electron-hole pairs at the depletion layer are separated by the applied external potential within a very short time (\sim ps) [331], in which the photogenerated electrons drift to the bulk region within the photoanode surface. Meanwhile, the photogenerated holes migrate to the photoanode/electrolyte interface and participate in the PEC water splitting process. Hence, the width of the space charge layer (W_{SCL}) represents an important parameter that is strongly related to the minority carrier lifetime since a large W_{SCL} requires a relatively long carrier lifetime or it would recombine within the bulk region of the semiconductor before reaching the depletion region edge. W_{SCL} can be calculated from the band bending potential ($V - V_{fb}$) at the interface of the utilized photoanode according to **Eq. 6. 7**:

$$W_{SCL} = \sqrt{\frac{2\epsilon\epsilon_0(V-V_{fb})}{eN_D}} \quad \text{Eq. 6. 7}$$

The calculated W_{SCL} for the nano-sized ZnO/Ti-sheet and ZnO-graphene hybrid photoanodes is $< 1\text{nm}$, which is very small compared with the minority carrier diffusion length of ZnO ($\sim 30\text{ nm}$) [332]. The photogenerated electron-hole pair separation is strongly affected by the variation of W_{SCL} . This can be explained in more detail as follows: since the formed space charge layer at the photoanode/electrolyte interface has a built-up localized electric field where the majority carriers (i.e., electrons in an n-type semiconductor) are depleted bulk region of photoanode and away from the photoanode/electrolyte interface. Hence, the photogenerated electron-hole pair recombination rate within the space charge region would be reduced and consequently, the charge carrier separation will be improved [333]. Based on the estimated W_{SCL} values of ZnO-graphene NCs hybrid photoanodes, the incorporation of high graphene nanosheet content (50 and 75 wt.%) resulted in the increase of W_{SCL} compared with the nano-sized ZnO photoanodes, **Table 6. 3**.

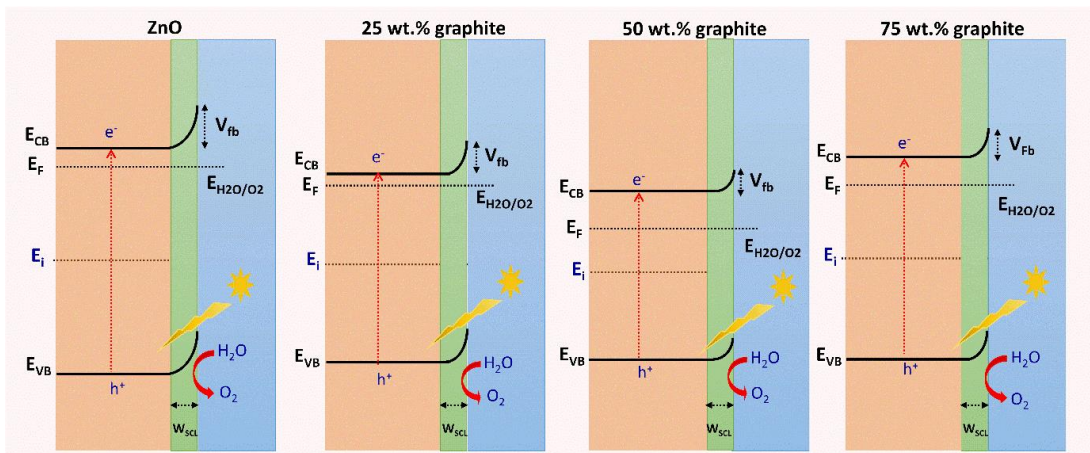


Figure 6. 19: Schematic band diagram to illustrate the effect of graphene on the band structure of ZnO-based photoanodes

This demonstrated that the incorporation of graphene nanosheets not only improves the charge carrier kinetics of ZnO-graphene NCs hybrid photoanodes but also improves the photo-generated carrier separation within the space charge layer at the semiconductor/electrolyte interface. This demonstrated that the photogenerated minority carriers in all fabricated electrodes have a high possibility to reach the photoanode/electrolyte interface and effectively participate in the PEC oxidation of water. The incident photon to current efficiency (IPCE) for ZnO-graphene NCs/Ti-sheet hybrid photoanodes in the presence of external bias voltage was determined according to **Eq. 6. 8** [334]:

$$IPCE(\%) = J_{ph} \frac{(1.23 - (V - V_{ocp}))}{P_{light}} \times 100\% \quad Eq. 6. 8$$

where J_{ph} is the photocurrent density ($\text{mA} \cdot \text{cm}^{-2}$), V is the electrode bias potential, V_{ocp} is the open circuit potential in the electrolyte under the light illumination, and P is the incident light power density ($\text{mW} \cdot \text{cm}^{-2}$).

The change in the open circuit potential (ΔOCP) with light illumination is shown in **Figure 6. 18(d)**, which was used for calculating the IPCE (%) for ZnO-graphene hybrid photoanodes. The estimated IPCE vs. the applied bias potential plots for the nanostructured ZnO photoanode and graphene hybrid electrodes with 25, 50, and 75 wt.% graphite content is shown in **Figure 6. 18(e)**, which demonstrates the improvement of IPCE with graphene hybridization. The hybrid photoanode with 50 wt.% graphite contents revealed the best PEC water oxidation performance with an IPCE of $\sim 4\%$ compared with pure ZnO and other graphene hybrid photoanodes. Furthermore, the photo-response current stability was verified for 10 cycles using chronoamperometric plots for all titanium modified electrodes as shown in **Figure 6. 18(f)**.

Table 6. 3: The estimated donor concentration (N_D), flat band potential (V_{fb}), and width of the space charge layer (W_{scl}) of ZnO-graphene NCs/Ti-sheet hybrid photoanodes at different graphite content.

Electrode	V_{fb} (V)	$N_D \times 10^{27}$ (m^{-3})	W_{scl} (nm) @1.23 V vs. RHE
ZnO	-0.63097	7.35059	0.39
25 wt.% graphite	-0.53126	9.30419	0.33
50 wt.% graphite	-0.36329	3.06452	0.53
75 wt.% graphite	-0.43222	4.87644	0.44

6. 3. Summary

ZnO-graphene NCs hybrid photoanodes were directly deposited in a one-step process on a titanium sheet at room temperature by a vacuum kinetic spray using the NPDS without any chemical treatment or any other post-treatment. The fabricated hybrid ZnO-graphene NCs/Ti-sheet hybrid photoanodes were used to study the PEC water splitting in 0.5 M Na_2SO_3 . The analysis of FTIR and Raman spectra revealed the direct transformation of the micro-sized graphite powder to small domains of graphene nanosheets in the NCs hybrid photoanodes with 25, 50, and 75 wt.% of graphite contents. Furthermore, the fragmentation of the micro particles resulted in the evolution of new active modes that were strongly influenced by the interfacial structural defects. The SEM images exhibited the fragmentation of ZnO and

graphite microparticles to the morphology of a combination of nanorods and nanosheets. The HR-TEM image of ZnO-graphene NCs with 50 wt.% graphite contents exhibited the typical interface between the nanocrystalline domains of ZnO and the graphene nanosheets. This referred to the strong hybridization between ZnO and the graphene species in the fabricated photoanode. The high-resolution O 1s and C 1s XPS scan revealed the evolution of many bonded states (C–O, C=O, and –O–C=O) indicating the synergy improvement between ZnO and graphene species in ZnO-graphene NCs/Ti-sheet hybrid photoanodes. The estimated optical band gap of the nanosized ZnO thin film was 3.35 eV, which was reduced to 2.9, 2.6, and 3.1 eV corresponding to the NCs hybrid photoanode with 25, 50, and 75 wt.% graphite content. This behavior was attributed to the hybridization with graphene nanosheets and the accompanied improvement in the interfacial space charge between the ZnO and graphene boundaries. The PL emission spectra revealed the quenching of emission intensity in the ZnO-graphene NCs/Ti-sheet compared with the nanosized ZnO/Ti-sheet. The hybrid NCs with 50 wt.% graphite contents exhibited the lowest emission intensity. This behavior revealed a decrease in the photogenerated carrier recombination rate, which is associated with charge carrier separation as well as the improvement in the visible light-harvesting efficiency. The analysis of the Mott-Schottky plots revealed a positive shift of the flat band potential, a decrease in the donor concentration, the tuning of hybrid photoanode Fermi energy level, as well as the increase in the width of the space charge layer. This behavior played an important role in the photogenerated electron-hole separation within the space charged layer at the interface between the electrode and the electrolyte and resulted in an overall improvement of PEC water splitting. We found that the incorporation of graphene in ZnO-graphene NCs/Ti-sheet hybrid photoanodes resulted in an improvement of the charge transfer resistance and the associated photo-response current compared with nanosized ZnO/Ti-sheet photoanodes. The ZnO-graphene NCs/Ti-sheet hybrid photoanodes with 25, 50, and 75 wt.% graphite content exhibited a photo-response current @ 1.23 V vs. RHE of 1.69, 4.82, and 2.6 mA·cm⁻², respectively, compared with only 0.47 mA·cm⁻² for the nanosized ZnO/Ti-sheet photoanode. Also, the maximum IPCE for ZnO-graphene NCs/Ti-sheet hybrid photoanodes was shifted to a lower potential relative to ZnO/Ti-sheet. The NCs hybrid photoanode with 50 wt.% graphite contents exhibited the highest efficiency of 4.23 % at the smallest bias potential of 1.4 V vs. RHE. The photocurrent stability was verified for 10 cycles for all fabricated photoanodes. Compared to other preparation techniques of ZnO-graphene NCs/Ti-sheet hybrid photoanodes, the NCs hybrid photoanodes were fabricated using the NPDS method in a very short time with a relatively low cost. Finally, these photoanodes conclusively revealed high-performance toward the PEC water splitting in an alkaline medium.

Chapter 7:

*Room-Temperature Deposition of ZnO-Graphene
Nanocomposite Hybrid Photocatalysts for Improved Visible-
Light-Driven Degradation of Methylene Blue*

7.1. Overview

Nanostructured semiconductor materials are widely used for photocatalytic degradation of organic pollutants because they are highly efficient at mineralization of various types of organic materials at normal ambient conditions. This is of great importance in many commercial applications, such as water purification and self-cleaning [335-339]. Nanostructured ZnO semiconductors with a high exciton binding energy of ~ 60 meV exhibit excellent optoelectronic characteristics [323], which make them a popular material for energy conversion applications such as photovoltaics, photo-electrocatalytic water oxidation, and photocatalytic degradation of organic dyes [265, 266]. ZnO-based photocatalysts have exhibited optimal photocatalytic performance in neutral media, in contrast to TiO₂-based photocatalysts that usually perform better in acidic media. This makes nanostructured ZnO-based materials and their nanocomposites (NCs) widely used for photocatalytic degradation of various types of organic dyes, such as phenol [340], 2-phenylphenol [341], 4-nitrophenol [342], methyl orange [343-345], and methylene blue (MB) [346, 347]. However, ZnO-based material has exhibited low photocatalytic activity due to the high optical bandgap in the UV region [278] as well as the high recombination of photogenerated electron-hole pairs [256].

The formation of nanocomposites between nanostructured semiconductors and graphene species is widely used for photon energy conversion applications. This arises from the overall improvement in the charge transfer kinetics at the semiconductor/solution interface [348-352]. The formation of nanocomposites is accompanied by tuning the interfacial surface states between the nanostructured grain boundaries. Hence, the space-charged layer of the nanosized grains would strongly affect the photogenerated carrier concentration at the semiconductor/electrolyte interface. The tunability of nanocomposite interfacial states makes it possible to improve their performance for energy conversion and storage applications [270-273].

Graphene-based NCs are widely used in wastewater treatment from the contaminating organic dyes through the photocatalytic degradation process. Vinothkannan et al., [353] synthesized reduced graphene oxide (rGO)/Fe₃O₄ hybrid NCs, and the nanosized rGO was prepared by the Hammer process. Besides, chemical precipitation was used for preparing Fe₃O₄ nanoparticles (NPs). The synthesized NCs exhibited high adsorption and photocatalytic degradation efficiency for MB dye molecules under visible light irradiation. However, the fast recombination process of photogenerated electron-hole pairs is the main drawback of Fe₃O₄-based materials. This results in an overall reduction of the solar energy

photoconversion efficiency. On the other hand, ZnO-based materials and NCs are distinguished by long minority carrier lifetime (i.e., holes), and this makes them promising materials for solar energy conversion applications. However, the wide bandgap of ZnO in the UV region restricts the usage of the pure ZnO nanostructure in visible light harvesting and conversion applications [354]. This limitation can be overcome by the formation of hybrid NCs with either lower bandgap materials or graphene nanosheets. Jenita Rani et al., [207] have reported the preparation of rGO/zinc ferrite NCs using a two-step process involving the Hammer technique for reducing graphite micro-sized powder to rGO and solvothermal technique for heterostructure formation with nanosized zinc ferrite and rGO nanosheets. The designed rGO/zinc ferrite NCs photocatalyst with narrow band gap of 1.86 eV exhibited high photocatalytic degradation efficiency toward MB degradation in the presence of H₂O₂ oxidative agent due to the π - π interactions and hydrogen bonding between the rGO and MB dye species. Hsieh et al., [355] prepared Cu-doped ZnO-graphene NCs using a combination of Hammer process and microwave techniques. The incorporated Cu ions in the prepared NCs resulted in the enhancement of visible light harvesting and MB photocatalytic degradation efficiency in H₂O. Ahmad et al., [356] synthesized ZnO-graphene NCs using a combination of the common Hammer technique for graphene preparation and solvothermal technique for hybridization of graphene and ZnO NPs. The prepared NCs exhibited a variety of optical band gap extending from 2.9 to 3.3 eV that depends on the mixing ratio between ZnO and rGO species. The incorporation of graphene nanosheets in ZnO resulted in the improvement of visible light harvesting as well as the enhancement of MB photocatalytic degradation efficiency. Atchudan et al. [357] reported the preparation of rGO decorated with ZnO NPs using several consecutive steps for the incorporation of ZnO species involving thermal refluxing at 65 °C for 24 h that followed by thermal oxidation in the oven at 100 for 5 h. Xue et al. [358] prepared ZnO-rGO NCs using Hummer and Offeman technique to reduce the micro-sized graphite powder to nanostructure rGO and photochemical precipitation technique for ZnO NPs. The synthesized heterostructure ZnO-rGO NCs exhibited high photocatalytic degradation efficiency of MB under UV and visible light irradiation.

The photocatalytic degradation of organic pollutants using nanostructured semiconductor materials has mainly two forms, the dispersed particulate, and the thin film. Nalajala et al. [359] demonstrated that the thin film form is more efficient since 1 mg of nanostructured thin film photocatalysts has the same photocatalytic activity as 25 mg of sample powder photocatalysts. Besides, the removal of the dispersed nanoparticles from the solution after the organic material degradation is very difficult and needs a centrifuge with a very high rotation speed (> 6,000 rpm) to guarantee that all the dispersed powder is

collected. This increases the cost of organic dye removal using a nano-semiconductor powder; hence, thin-film is more suitable for most practical applications.

The widespread of nanosized graphene in various commercial applications concerned with energy conversion and storage has driven the need to find a suitable technology that takes into consideration mass production with high cost-efficiency. There are multiple techniques for graphite-to-graphene transformation, including top-down techniques such as sonochemical-assisted graphite exfoliation [91], shear exfoliation [94], as well as dry- and wet-ball milling [49, 54, 95, 97]. However, these techniques have some restrictions, such as a slow rate of graphite-to-graphene transformation, low production yield, involvement of waste products, and high production cost [259].

In contrast to the above-mentioned techniques, the fabrication of hybrid NCs using the direct deposition by the nanoparticle deposition system (NPDS), which is a vacuum kinetic spray process [101, 163, 164]. This technique takes into consideration the production cost efficiency, which is of great importance for commercial applications related to wastewater treatment because it provides a large deposition area in a short time with a reasonable production cost. Besides, no chemical treatment was involved that make our technique eco-friendly [99, 262]. Here we report on the direct transformation of graphite into graphene nanosheets in a one-step process at room temperature with a very short preparation time, using the NPDS. The instantaneous fragmentation of the 2D layered structure of bulk graphite to graphene nanosheets is usually accompanied by a sharp increase in the localized temperature. This provides a suitable environment for strong bonding between the grains and hybridization between the nanostructured transition metal oxide (TMO) and the formed graphene species in the fabricated nanocomposites thin films. NPDS has been used by our research group to fabricate various functional nanostructured thin films from TMO hybrids with 2D material, such as graphene and MoS₂ nanosheets. Such optimized nanostructured thin films have been utilized in many electrochemical energy conversion and storage applications, such as supercapacitors [260] and electrocatalytic water splitting [261, 262], as well as for non-enzymatic H₂O₂ detection in an alkaline medium [258, 264].

In the present study, we provided an effective and economically viable technique for the fast fabrication of nanosized hybrid photocatalysts using a one-step kinetic spray deposition at room temperature by the NPDS technique. Herein, we directly deposited ZnO-graphene nanocomposites (NCs) hybrid photocatalysts with various graphite contents (25, 50, and 75 wt.%) on nickel foam (NF) porous substrate without any chemical treatment from ZnO and graphite microparticles. Also, we investigated the

dependence of the graphite-to-graphene transformation in the deposited ZnO-graphene NCs/NF heterostructured thin films on the incorporated graphite ratio using various analytical techniques. We also evaluated the effect of graphite content variation on the photocatalytic activity of ZnO-graphene NCs/NF hybrid photocatalysts using the photocatalytic degradation of MB under visible light illumination.

7.2. Results and Discussion

7.2.1. XRD patterns of ZnO-graphene NCs hybrid photocatalysts

Figure 7. 1(a) exhibits XRD patterns of ZnO and graphite micro-sized powder as well as their mixtures with different graphite contents (25, 50, and 75 wt.%). The XRD pattern of ZnO microparticles revealed several characteristic peaks matched with the wurtzite-type hexagonal structure of the ZnO phase (space group: $P6_3mc$, ICDD: 04-008-8198) [278]. In contrast, the XRD pattern of the pure graphite phase depicted two distinct peaks at 26.5° and 56.42° ascribed to the (002) and (004) crystalline planes of the hexagonal graphite phase (space group $P6_3/mmc$ (ICDD: 00-056-016, PDF 2010) [261, 264]. The XRD patterns of ZnO and graphite mixed micro-sized powders with graphite content of 25, 50, and 75 wt.% revealed the presence of ZnO and the graphite species in all composites that were used for the thin film deposition process, without any new secondary phases. **Figure 7. 1(b)** presents the XRD patterns of ZnO thin film as well as ZnO-graphene NCs thin films on NF porous substrate with graphite content of 25, 50, and 75 wt.%.

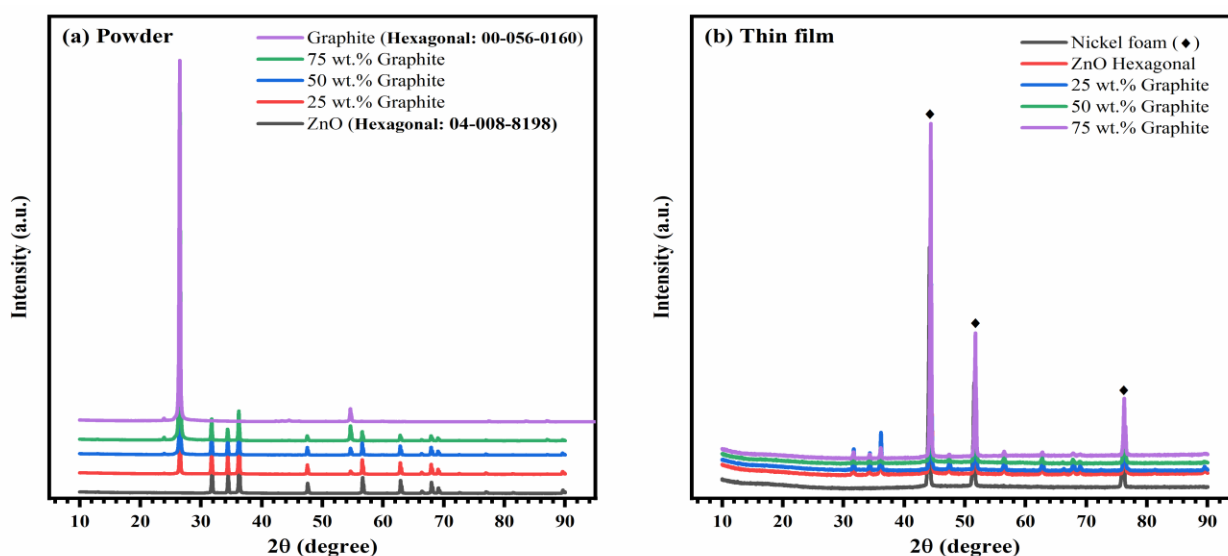


Figure 7. 1: XRD patterns of ZnO-graphite micro-sized powders at different graphite contents **(a)**, and the corresponding deposited nanostructured thin films on the NF porous substrate **(b)**.

All the deposited thin films on the NF substrate exhibited characteristic XRD peaks at 2θ of 44.19° , 51.54° , and 76.09° belonging to the (111), (200), and (220) crystalline planes of the cubic phase of Ni, respectively (ICDD: 00-004-0850) [264]. Additionally, several distinct peaks related to the wurtzite-type hexagonal ZnO phase were detected in the deposited thin films of pure ZnO and all hybrid nanocomposites with graphite content of 25, 50, and 75 wt.%. The detected XRD peak intensity corresponding to the ZnO species was lower than that of the corresponding powder, revealing a decrease in the crystalline domain size due to micro-sized particle fragmentation during the deposition by the NPDS. Furthermore, the characteristic peaks that were matched with the crystalline hexagonal phase of the graphite powder completely disappeared. This behavior revealed the layer separation of the micro-sized graphite powder into a smaller domain size, in the nano-size range. This behavior was observed during the fabrication of various types of graphene-based NCs that were used for energy conversion and storage applications [260-262, 264]. The observed reduction in the crystallite size was associated with the increase of the surface-to-volume ratio and the associated interfacial surface states that act as active sites for various catalytic reactions at the interface between the modified electrocatalyst and the electrolyte [223].

7. 2. 2. Raman studies on ZnO-graphene NCs

The active Raman modes of ZnO micro-sized powder were identified in the Raman shift range from 200 to 800 cm^{-1} as shown in **Figure 7. 2(a)**. Various Raman peaks were depicted at 332 , 379 , and 439 cm^{-1} correspond to the optical phonons at the Γ -point of wurtzite-type hexagonal structure of ZnO. These modes were theoretically explained in the form of mathematical summation of various active and silent optical phonon modes ($1A_1+2B_1+1E_1+2E_2$). The transverse active optical vibration is represented by a single state A_1 -symmetry mode and the active longitudinal vibration is represented by a single state E_1 -symmetry mode. The E_2 -symmetry mode has two active vibrations, the first at the low-frequency side (E_{2L}) is caused by the lighter oxygen atom vibration, and the second at the high-frequency side (E_{2H}) caused by the heavier Zn atoms vibrations. Furthermore, there are some inactive phases in normal conditions called silent low-frequency vibration (B_{1L}) and high-frequency vibration (B_{1H}). These silent modes can be activated as a result of the evolution of special defects at the interfacial grain boundaries [290]. The second-order vibration corresponds to the optical phonon mode ($E_{2H}-E_{2L}$) was observed at 332 cm^{-1} [293, 318]. Whereas the first-order transverse optical phonon mode $A_1(\text{TO})$ was recorded at a higher

Raman shift of 379 cm^{-1} . The active second-order mode caused by the non-polar E_{2H} symmetry mode was observed at 439 cm^{-1} [294]. The micro-Raman spectrum of nanostructured ZnO/NF thin-film in **Figure 7. 2(b)** depicts various active Raman modes at 327 , 378 , 438 , and 571 cm^{-1} . The observed phonons at 327 , 378 and 438 cm^{-1} are corresponding to E_{2H} - E_{2L} , $A_1(\text{TO})$, and E_{2H} symmetry modes as explained in the powder case. The new vibration at 571 cm^{-1} can be attributed to the longitudinal optical phonon A_1 (LO) symmetry mode [360]. The observation of this vibration mode indicates the fragmentation of micro-sized crystalline ZnO particles to a lower size range with high polycrystalline tendency and very small crystalline domain size [292]. This supports the observed low degree of crystallinity of the deposited nanostructured ZnO/NF thin film [361].

Raman spectra of the ZnO-graphite micro-sized powder in **Figure 7. 2(c)** reveals two characteristic bands matching with the wurtzite-type hexagonal structure of ZnO at 332 and 439 cm^{-1} , as well as new active Raman vibration caused by the mixed graphite powder at $1,350$, $1,582$, $2,720$, and $3,250\text{ cm}^{-1}$. The characteristic G-band caused by the E_{2g} -symmetry mode of the bulk structure graphite microcrystals was observed at $1,582\text{ cm}^{-1}$, while the active vibrations related to the D-band that induced by the interfacial grain boundaries was depicted at $1,350\text{ cm}^{-1}$ [110]. Furthermore, the second-order vibrations related to the 2D and intravalley $2D'$ -symmetry modes were recognized at $2,720$ and $3,250\text{ cm}^{-1}$, respectively [111, 112]. The fragmentation and layer separation of the two-dimensional layered structure of graphite microcrystals into small-sized graphene nanosheets were demonstrated from the intensity ratio variation between the D band and the G band (I_D/I_G). When $I_D/I_G < 1$, this depicted the large size of the crystalline domain in the graphite microcrystals, whereas the increase of the I_D/I_G ratio to > 1 referred to the layer separation of the graphite microcrystals and the transformation into small-sized graphene nanosheets [115]. **Figure 7. 2(d)** depicts the micro-Raman spectra of ZnO-graphene NCs/NF hybrid photocatalysts at graphite content of 25, 50, and 75 wt.%. The NCs exhibited multiple active phonon modes at 327 , 433 , 580 , $1,348$, $1,593$, $1,621$, $2,688$, and $2,935\text{ cm}^{-1}$. The detected Raman vibrations at low Raman shift values of 327 , 433 , and 588 cm^{-1} corresponded to E_{2H} - E_{2L} , E_{2H} , and $A_1(\text{LO})$ symmetry phonon modes of the wurtzite-type hexagonal phase of the ZnO [360]. The observed active phonon vibrations at Raman shifts of $1,348$, $1,593$, and $2,688\text{ cm}^{-1}$ had the same origin as explained in the case of graphite powder corresponding to the D, G, and second-order 2D vibration modes, respectively. The weak shoulder at the Raman value $1,621\text{ cm}^{-1}$ is attributed to the D' -vibration

caused by the displacement of carbon atoms from the entire hexagonal graphite host lattice to the interfacial boundaries between the adjacent nano-sized grains [110, 114]. Also, the disorder improvement at the grain boundaries of the graphene nanosheets induced the G'' vibration Raman shift of $2,935\text{ cm}^{-1}$ [112].

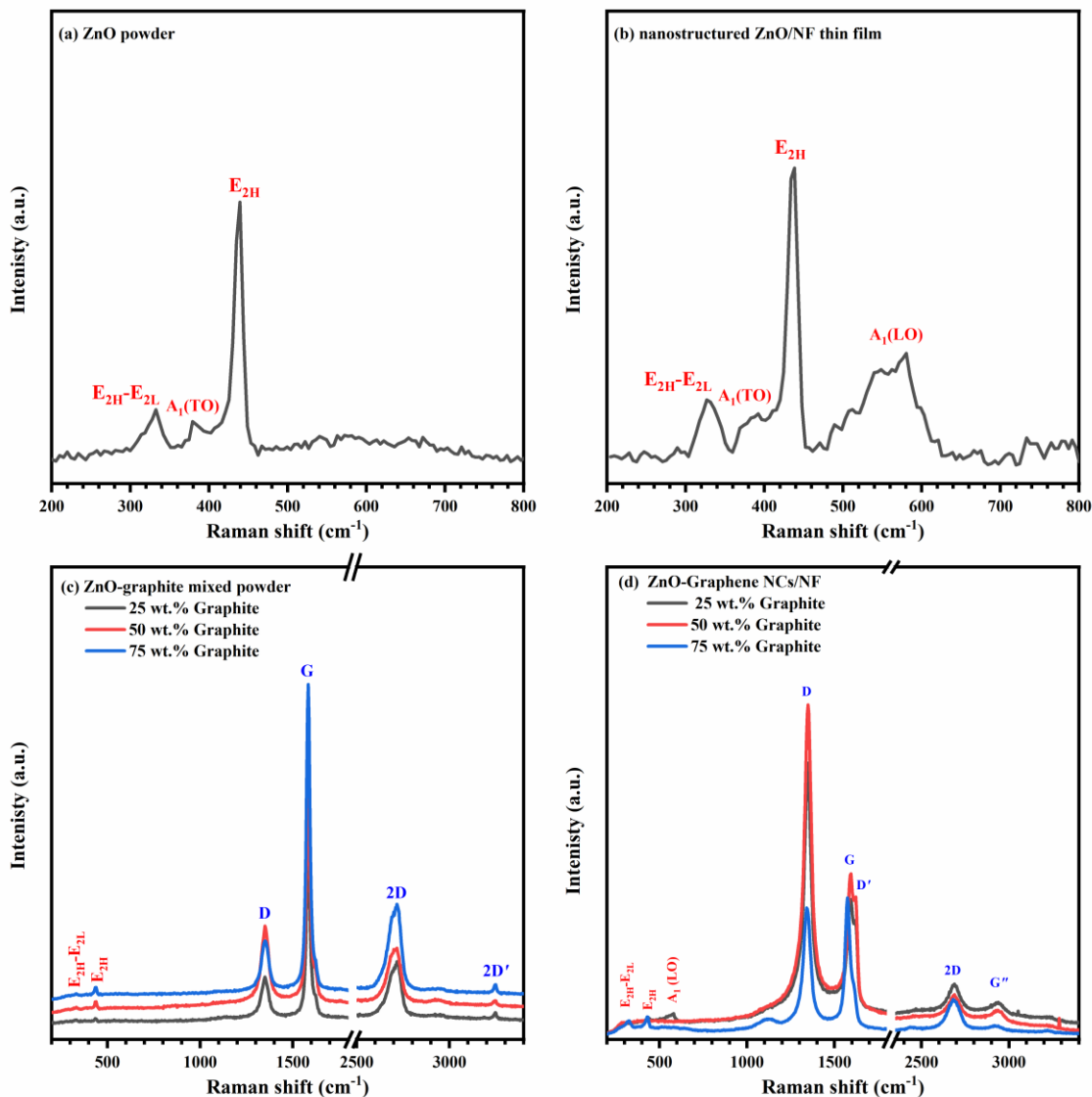


Figure 7. 2: Raman spectra of the ZnO micro-sized powder and the corresponding nanostructured thin film (a, b), ZnO-graphite mixed micro-sized powders, and the corresponding nanostructured thin films (c, d).

The graphite-to-graphene transformation due to the layer separation and micro-sized particle fragmentation in the deposited ZnO-graphene NCs/NF thin films was recognized from the variation in the intensity ratio (I_D/I_G) between the characteristic Raman modes D and G-symmetry modes. In comparing the Raman spectra of the micro-sized mixed powders at different graphite

contents and the corresponding nanostructured thin films, we found an improvement in the I_D/I_G . This intensity ratio was enhanced from 0.65 to 1.6, from 0.71 to 1.7, and from 0.54 to 0.95 for the NCs with graphite contents of 25, 50, and 75 wt.%, respectively. This behavior indicates that the graphite-to-graphene transformation through microparticle fragmentation was highly probable in the hybrid composites with a high content of graphite content of 25 and 50 wt.%. Whereas the degree of graphite-to-graphene transformation was relatively lower in the case of ZnO-graphene with low ZnO content.

7. 2. 3. Surface morphology of ZnO-graphene nanocomposites photocatalysts

The surface morphology and the equivalent compositional elemental analysis of ZnO microparticles and ZnO-graphite mixed micro-sized powder with 25, 50, and 75 wt.% of graphite contents are shown in **Figure 7. 3**. SEM image of ZnO powder revealed aggregated particles with semispherical and flake morphology with a lateral dimension < 500 nm. The relative percentage of flake-like morphology was increased with increasing graphite powder content. This powder was used for the deposition of nanostructured pure ZnO and ZnO-graphene NCs thin films on NF porous substrate using the NPDS without any chemical treatment. **Figure 7. 4(a)** shows SEM images of the deposited nanostructured ZnO/NF thin films, which reveal mixed nanosheets and nanorods morphology with lateral dimensions in the range from < 100 nm to 200 nm. The deposition uniformity of the ZnO/NF thin film is illustrated by the corresponding composition mapping shown in **Figure 7. 5**. The fragmentation of the micro-sized graphite powder into nanosized graphene with various morphology (nanoflakes and nanoflowers) is depicted in SEM images of ZnO-graphene NCs/NF with various graphite contents (25, 50, 75 wt.%); see **Figure 7. 4(b-d)**. The SEM image of hybrid NCs with 25 wt.% graphite content exhibits a relatively low percentage of graphene nanoflakes compared with the main matrix species of ZnO host lattice. Furthermore, increasing the graphite weight percentage in ZnO-graphene NCs up to 50 wt.% resulted in the total transformation to the nanoflakes morphology. This indicated that the main matrix of the hybrid composites was changed from ZnO to graphene species. Further, increase the graphite content up to 75 wt.% exhibited a second morphology change to the nanoflower morphology as illustrated in **Figure 7. 4(d)**. This interesting feature revealed the morphology dependence of ZnO-graphene NCs/NF on the graphite content used during the deposition process by the NPDS. The spatial uniformity of ZnO-graphene NCs/NF thin film on the lateral area of the NF porous substrate was also demonstrated from the corresponding composition mapping as shown in **Figure 7. 6** to **Figure 7. 8**.

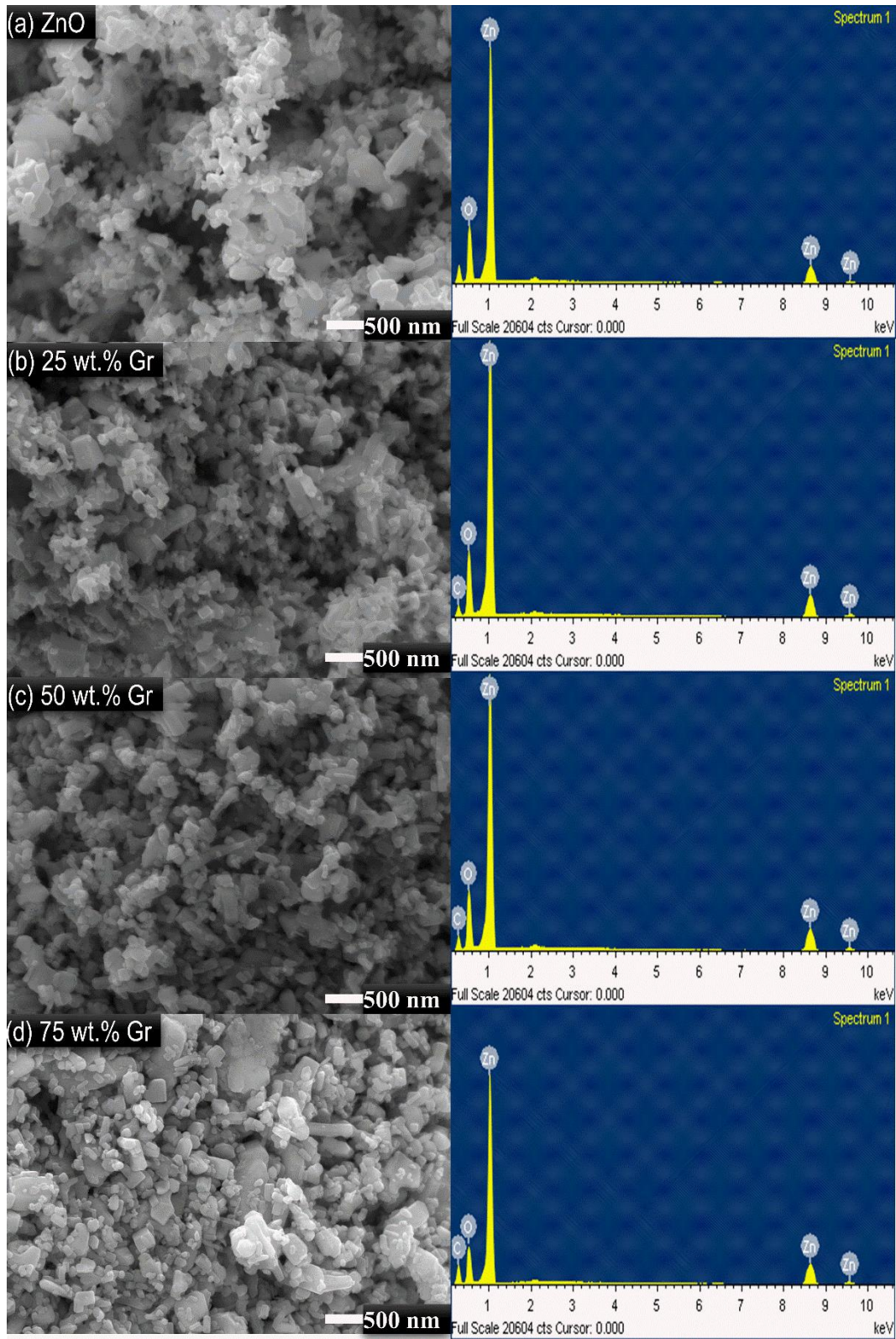


Figure 7. 3: SEM image and the corresponding EDS elemental analysis of pure ZnO powder (a), mixed ZnO-Graphite micro-sized powder with 25 wt.% (b), 50 wt.% (c), and 75 wt.% graphite contents (d).

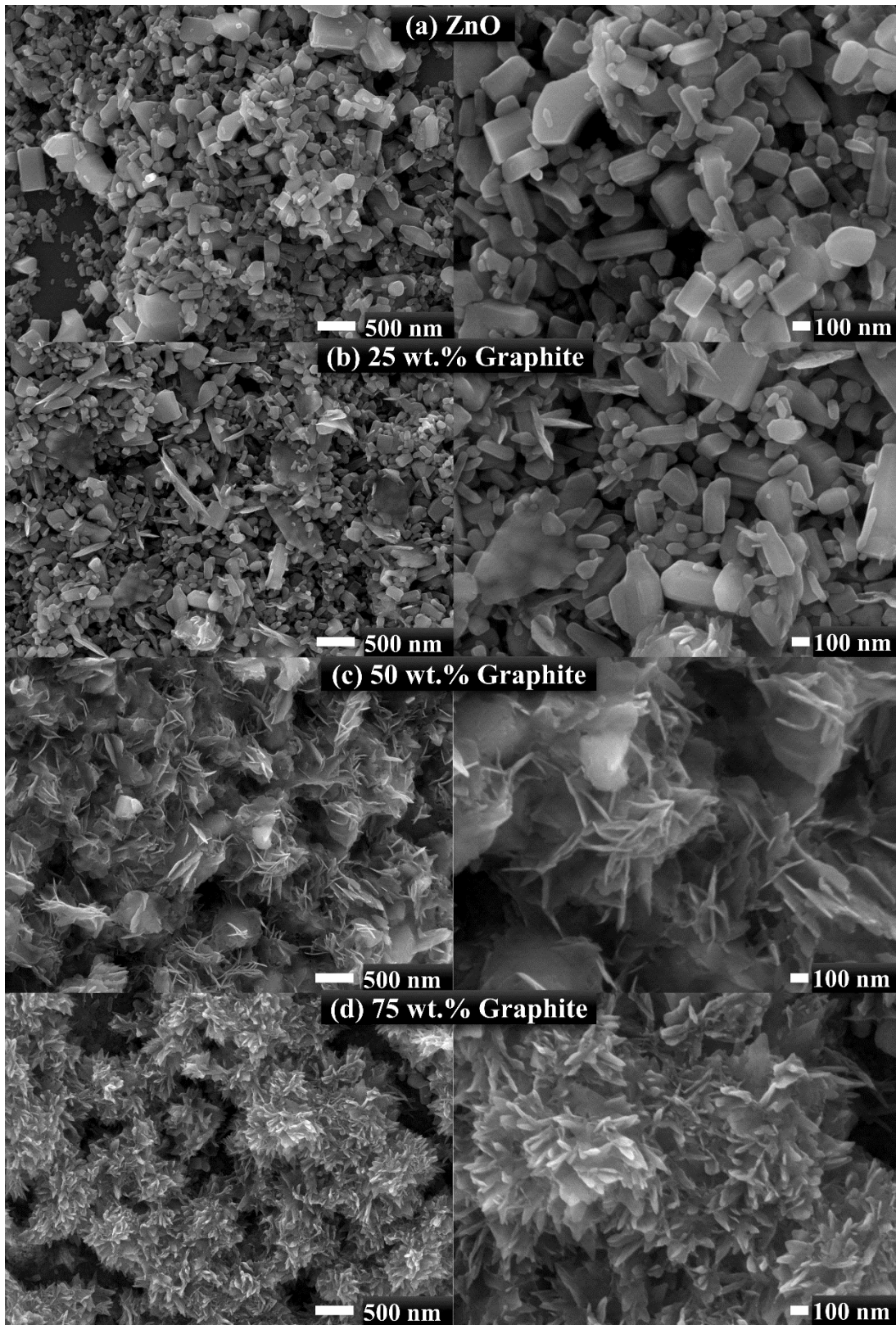


Figure 7. 4: SEM images of nanostructured ZnO/NF thin film (a), and ZnO-graphene NCs/NF thin films at graphite content of 25 wt.% (b), 50 wt.% (c), and 75 wt.% (d)

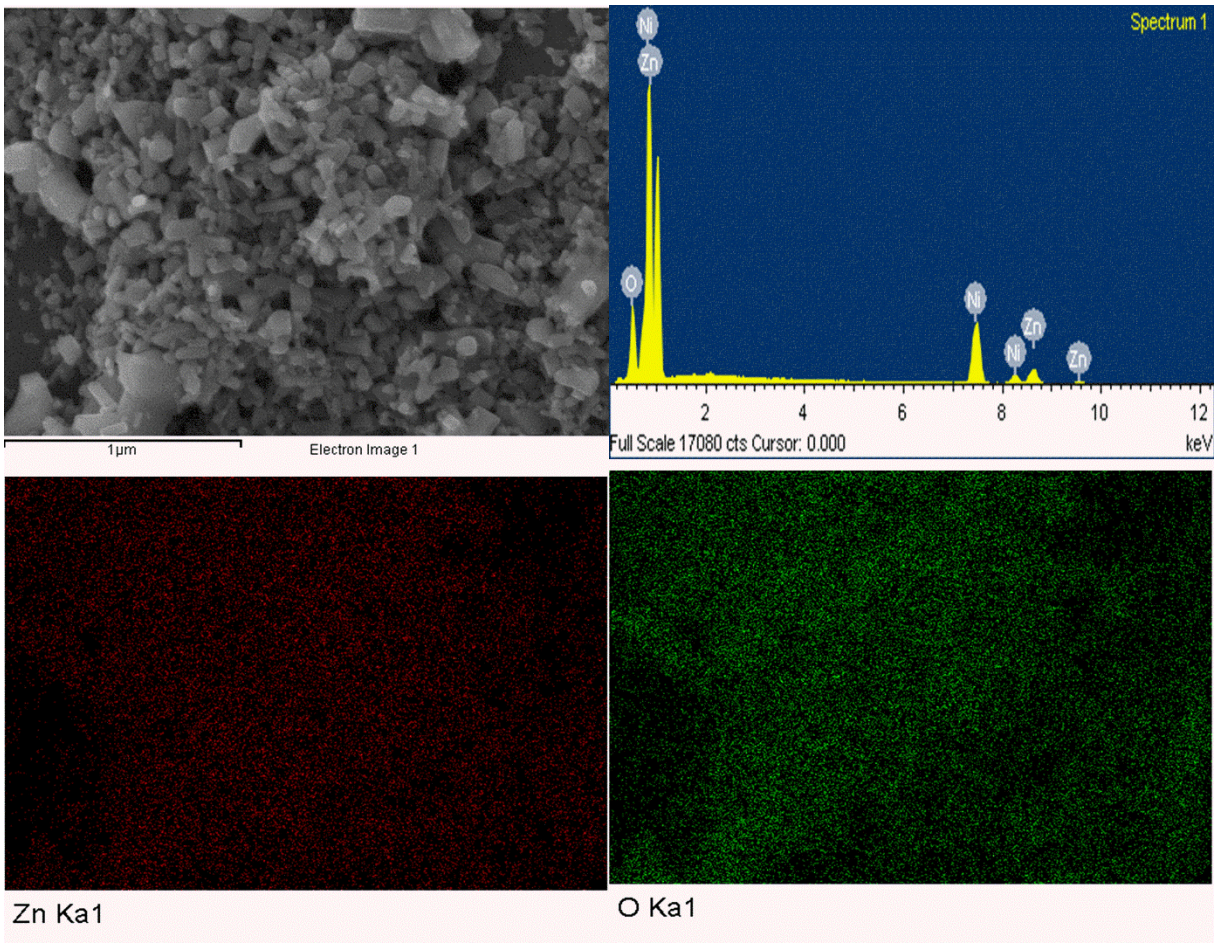


Figure 7. 5: The elemental composition analysis and the corresponding lateral mapping of nanostructured ZnO/NF photocatalyst.

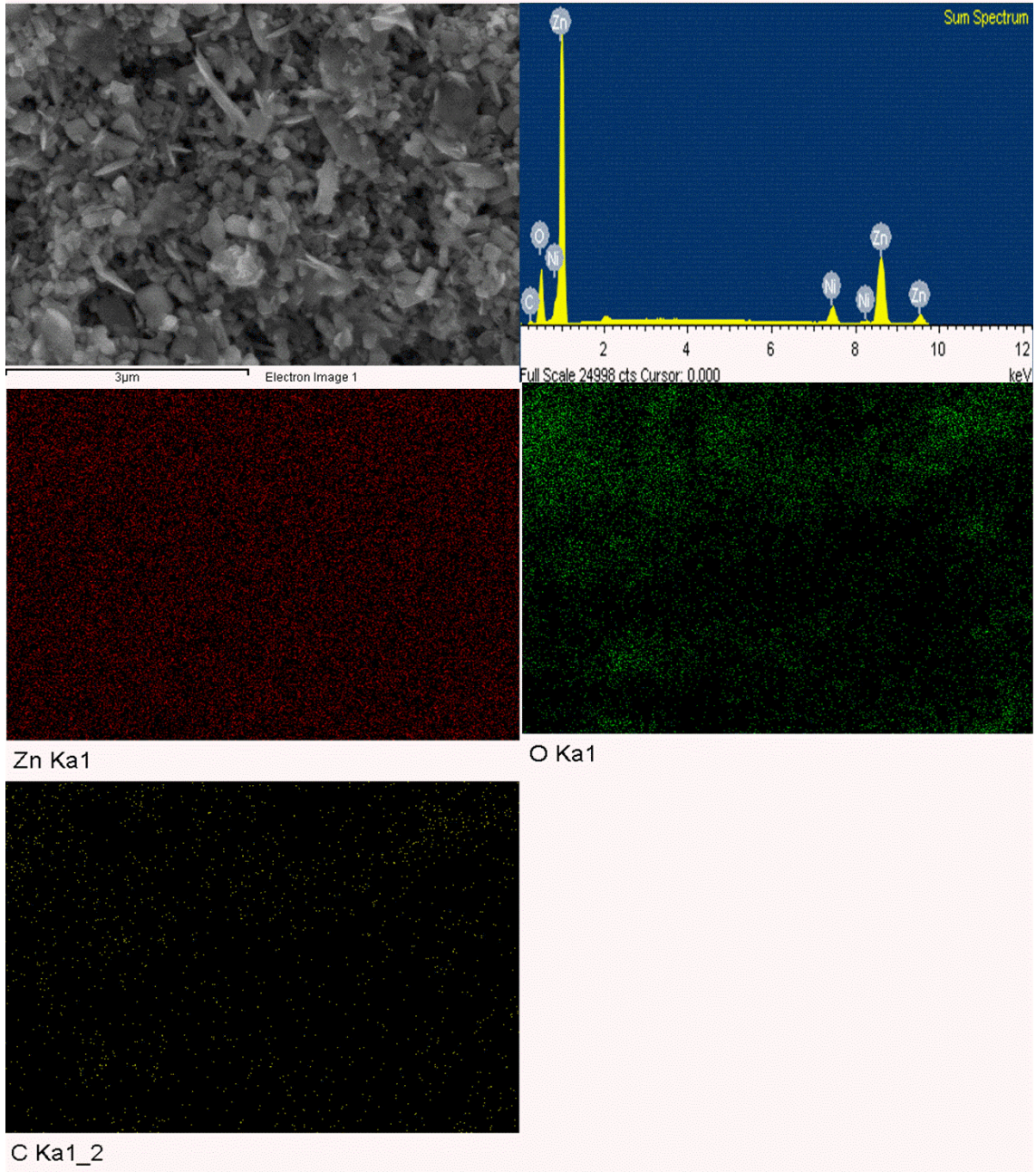


Figure 7. 6: Elemental composition analysis and the corresponding lateral mapping of ZnO-graphene /NF nanocomposites photocatalyst with 25 wt.% graphite contents.

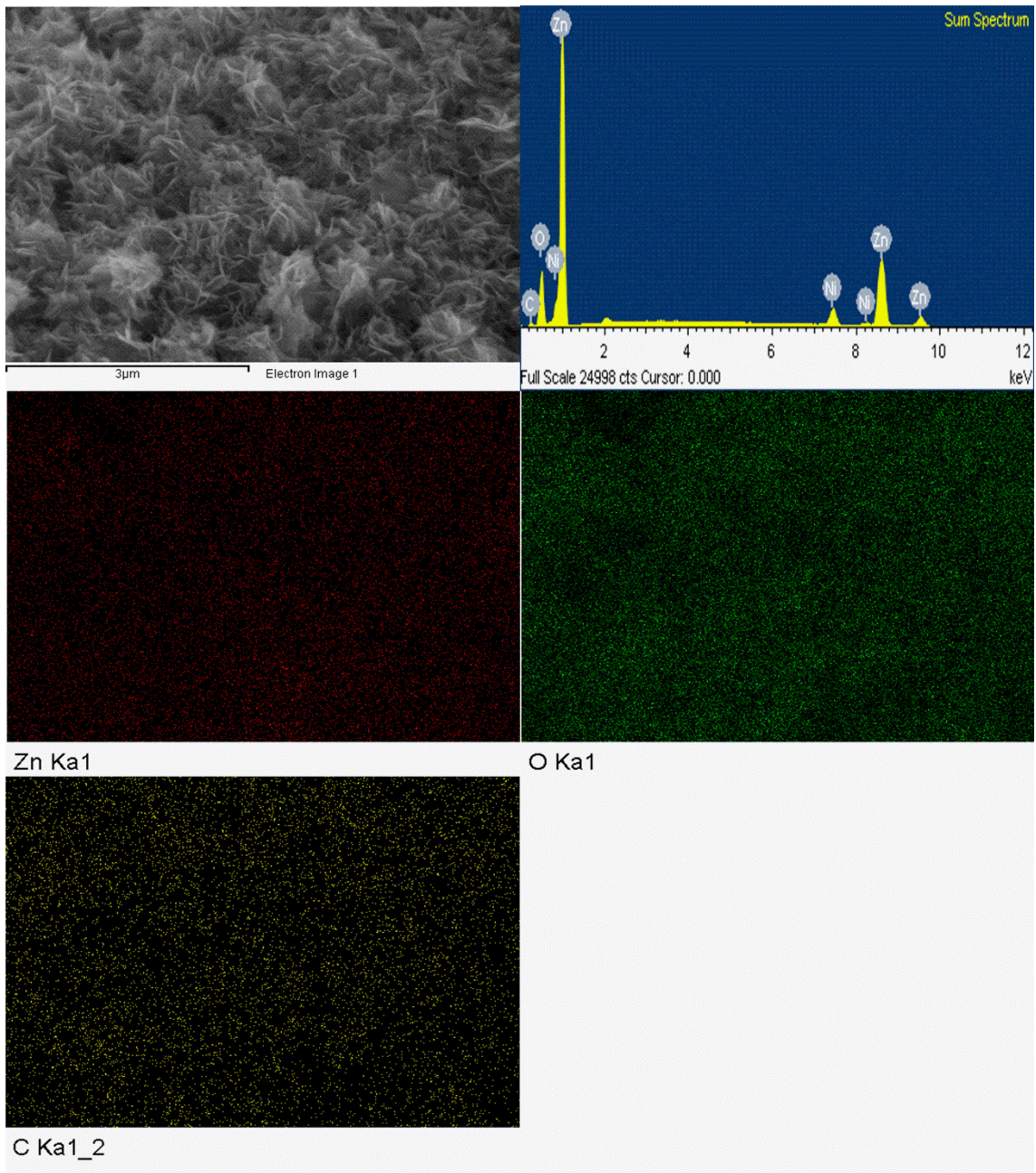


Figure 7. 7: Elemental composition analysis and the corresponding lateral mapping of ZnO-graphene/NF nanocomposites photocatalyst with 50 wt.% graphite contents.

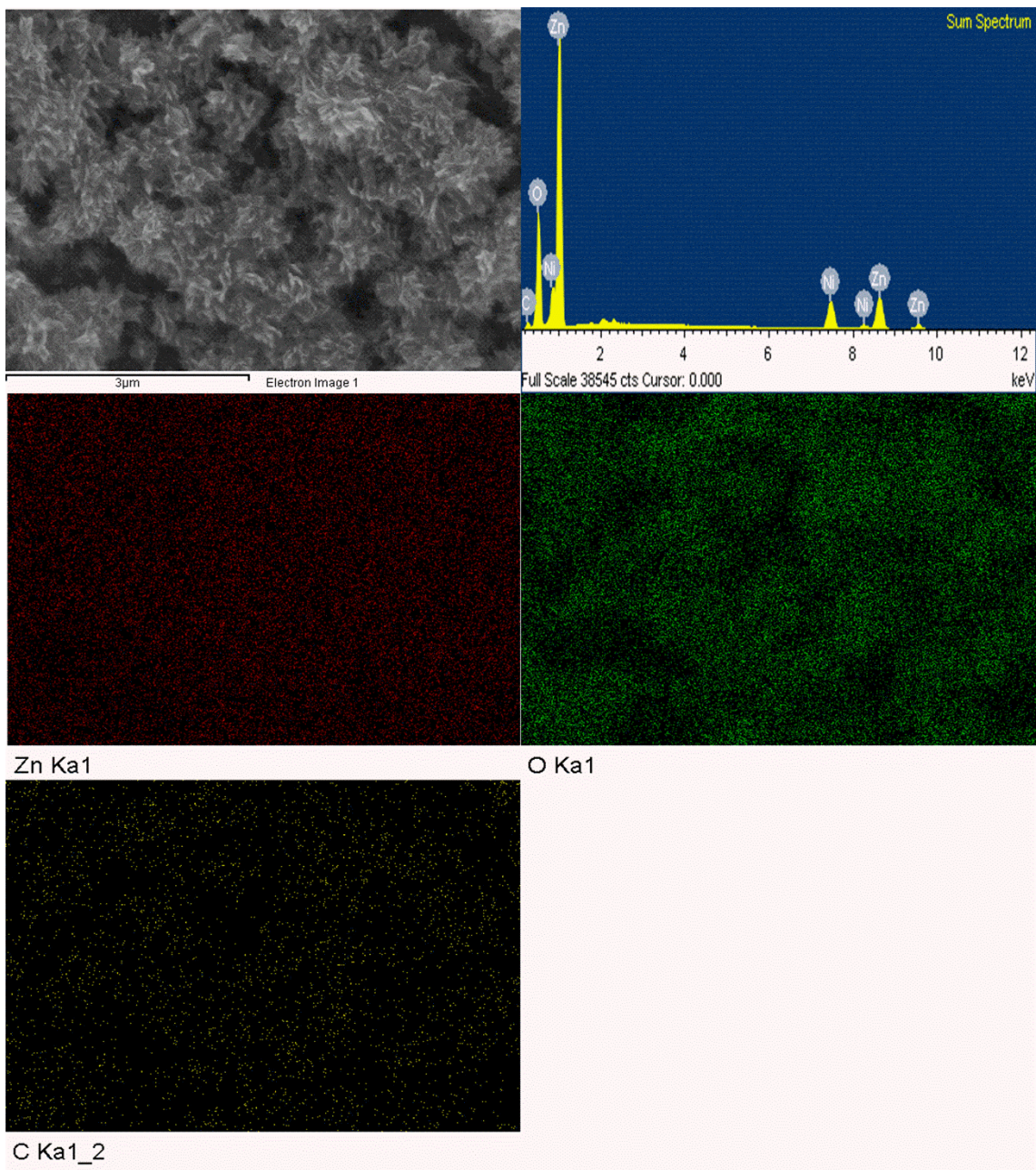


Figure 7. 8: Elemental composition analysis and the corresponding lateral mapping of ZnO-graphene /NF nanocomposites photocatalyst with 75 wt.% graphite contents.

7. 2. 4. Investigation of the surface bonding states on ZnO-graphene NCs/NF hybrid photocatalysts.

The nature of chemical bonding states at the surface of nanostructured ZnO/NF and ZnO-graphene NCs/NF hybrid photocatalysts with various graphite contents (25, 50, and 75 wt.%) were depicted using XPS. **Figure 7. 9(a)** reveals the XPS survey spectra in the binding energy range from -3 to 1,400 eV, in which the survey spectrum of ZnO/NF nanosheets exhibited various typical signals of zinc element (Zn 3d, Zn 3p, Zn 3s, Zn LMM1, Zn KLL, Zn LL M3, Zn 2p_{3/2}, and Zn 2p_{1/2}), and oxygen element (O 1s, O KLL). Also, the carbon signal was detected in all the ZnO-graphene NCs/NF hybrid photocatalysts. The high-resolution XPS scans for Zn 2p, O 1s, and C 1s were further investigated to illustrate the synergy improvement in the case of the NCs hybrid photocatalysts, as demonstrated in **Figure 7. 9(b-d)**.

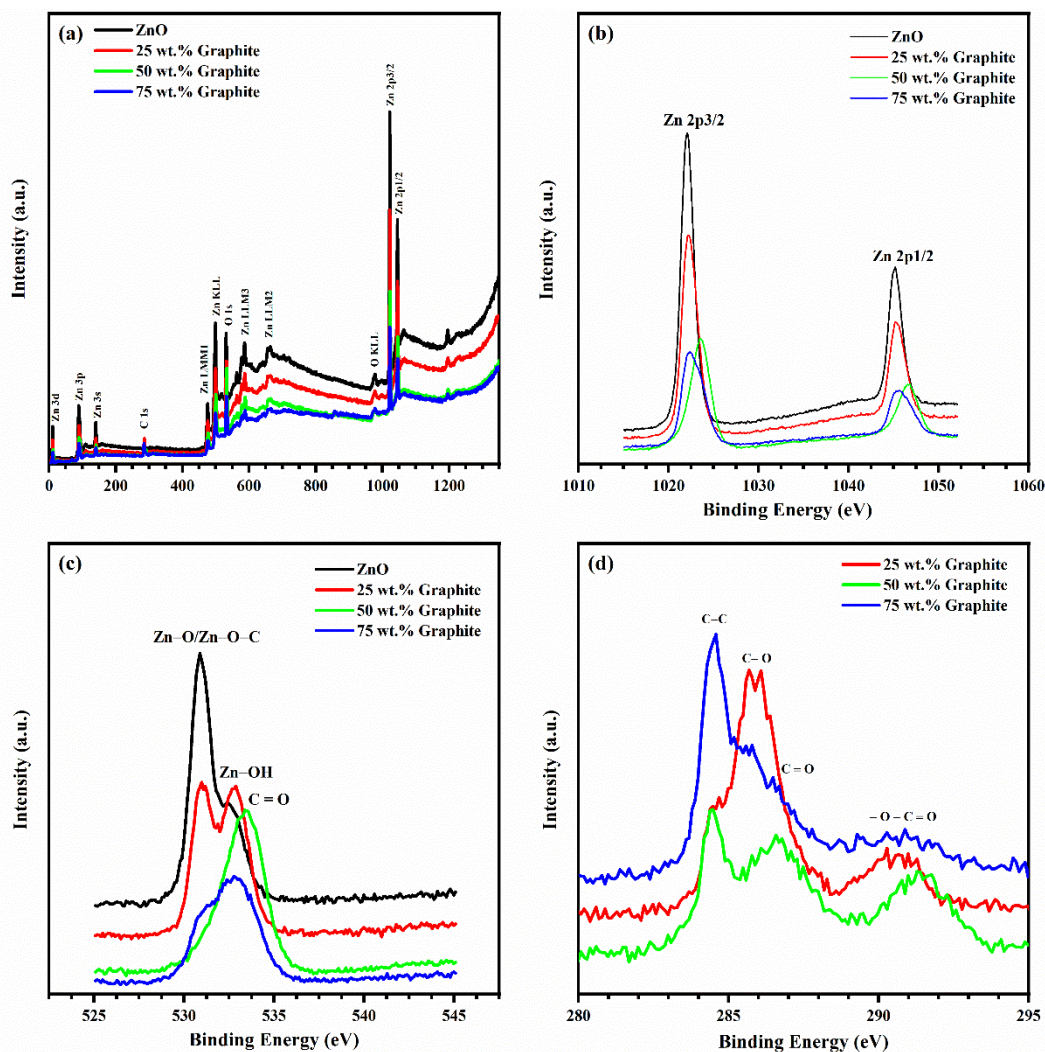


Figure 7. 9: XPS survey spectra (a) and high-resolution XPS scans of Zn 2p(b), O 1s (c), and C 1s (d) of ZnO-graphene NCs/NF hybrid photocatalysts at different graphite contents.

The origin of each XPS band was recognized and recorded in **Table 7. 1**. The Zn 2p high-resolution XPS spectra of nanostructured ZnO/NF and ZnO-graphene NCs/NF were further analyzed using the deconvolution process to estimate the exact positions of the peaks; see **Figure 7. 10**. The deconvoluted spectrum of nanostructured ZnO/NF exhibited two characteristic sub-bands $2p_{3/2}$ and $2p_{1/2}$ at 1,022.1 eV and 1,045.2, respectively. The energy line separation between the maximum of these bands was 23.1 eV, which arose from the divalent ionic state of zinc in the nonstoichiometric phase of the wurtzite-type hexagonal structure of the ZnO [273, 302]. In the ZnO-graphene NCs/NF hybrid photocatalysts, we observed a positive shift in the peak position of Zn 2p sub-bands ($2p_{3/2}$ and $2p_{1/2}$) to higher binding energy compared with the ZnO/NF; see **Table 7. 1**.

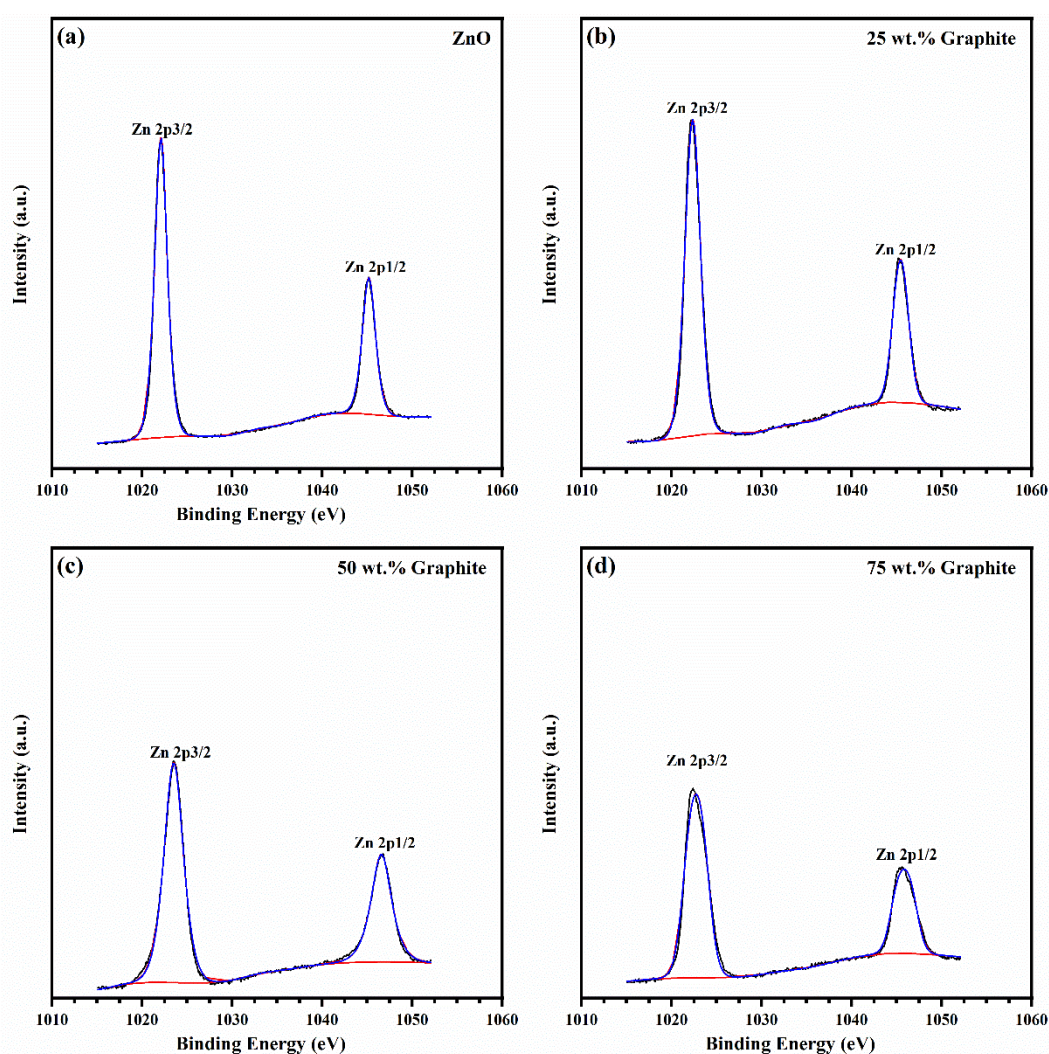


Figure 7. 10: Deconvoluted Zn 2p XPS scans of nanostructured ZnO/NF (a) and ZnO-graphene NCs/NF hybrid photocatalysts with 25 wt.% (b), 50 wt.% (c), and 75 wt.% graphite contents (d).

The NCs hybrid photocatalyst with 50 wt.% graphite contents exhibited the highest energy shift ($\delta = 1.4$ eV) compared with the other hybrid photocatalysts with graphite content of 25 wt.% ($\delta = 0.24$ eV) and 75 wt.% ($\delta = 0.62$ eV). The deconvolution of the O 1s XPS spectrum of ZnO/NF nanosheets in **Figure 7. 11(a)** exhibits the presence of oxygen active states related to the ZnO host lattice at binding energies of 530.91 and 532.67 eV. The observed main peak at 530.91 eV was attributed to the characteristic bonded state in the hexagonal structure of ZnO between the oxygen anion and the Zn cation [305].

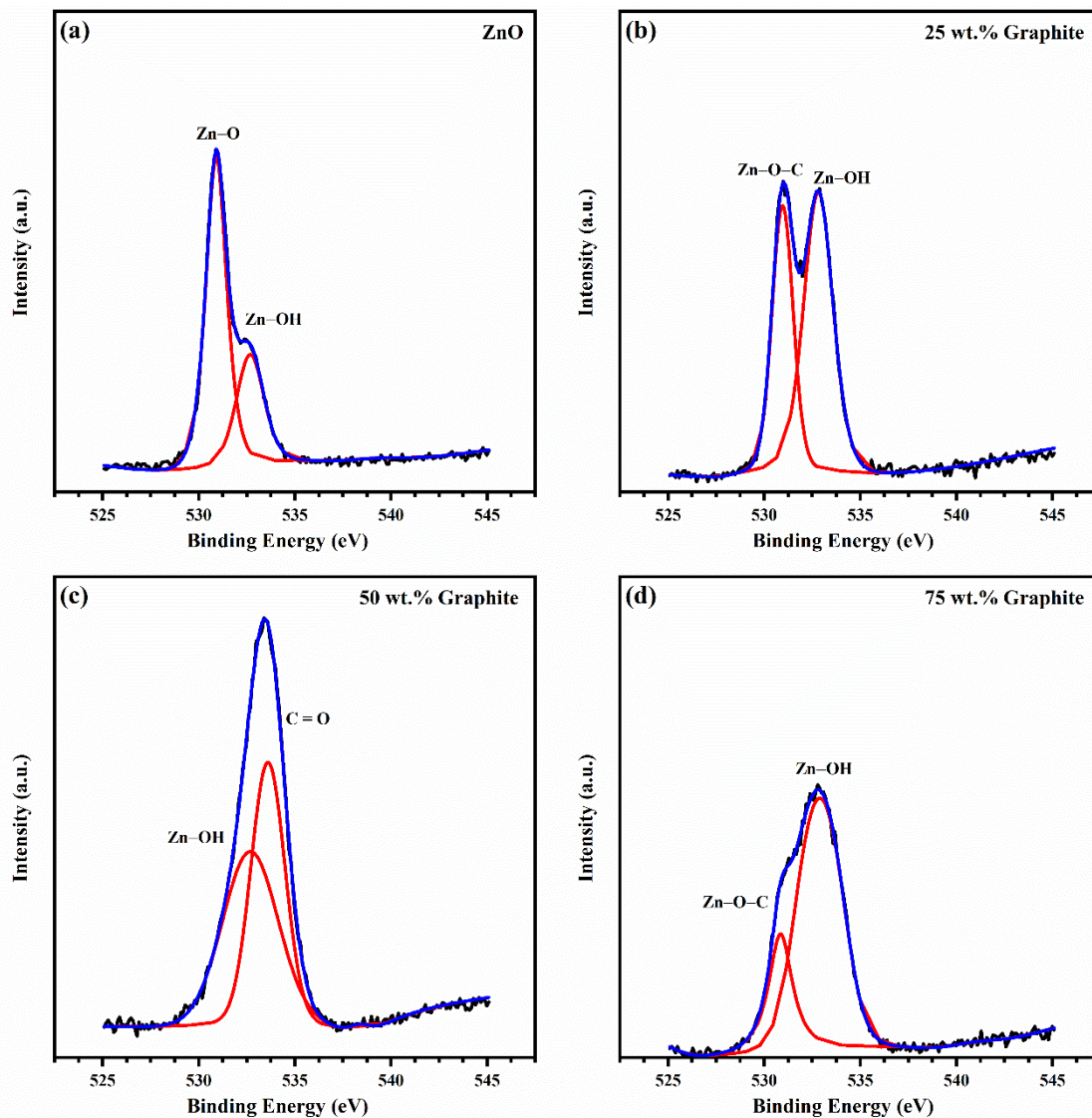


Figure 7. 11: Deconvoluted O 1s XPS scans of nanostructured ZnO/NF (a) and ZnO-graphene NCs/NF hybrid photocatalysts with 25 wt.% (b), 50 wt.% (c), and 75 wt.% (d) graphite content.

On the other hand, the presence of either adsorbed hydroxyl groups or reduced Zn atoms at the grain boundaries of nanostructured ZnO was the main reason for the observed shoulder at the higher binding energy of 532.67 eV [306], [307]. The analysis of high-resolution O 1s XPS spectra by deconvolution of ZnO-graphene NCs/NF hybrid photocatalysts at different graphite contents is shown in **Figure 7. 11(b-d)**. The recognized O 1s sub-band positions in the hybrid photocatalysts with graphite contents of 25 and 75 wt.% were like the pure nanosheets ZnO/NF, with a slight variation in the position of the peak; see **Table 7. 1**. On the other hand, the NCs hybrid photocatalysts with 50 wt.% graphite content exhibited a new band at a higher binding energy of 533.6 eV, corresponding to the C = O bond [357].

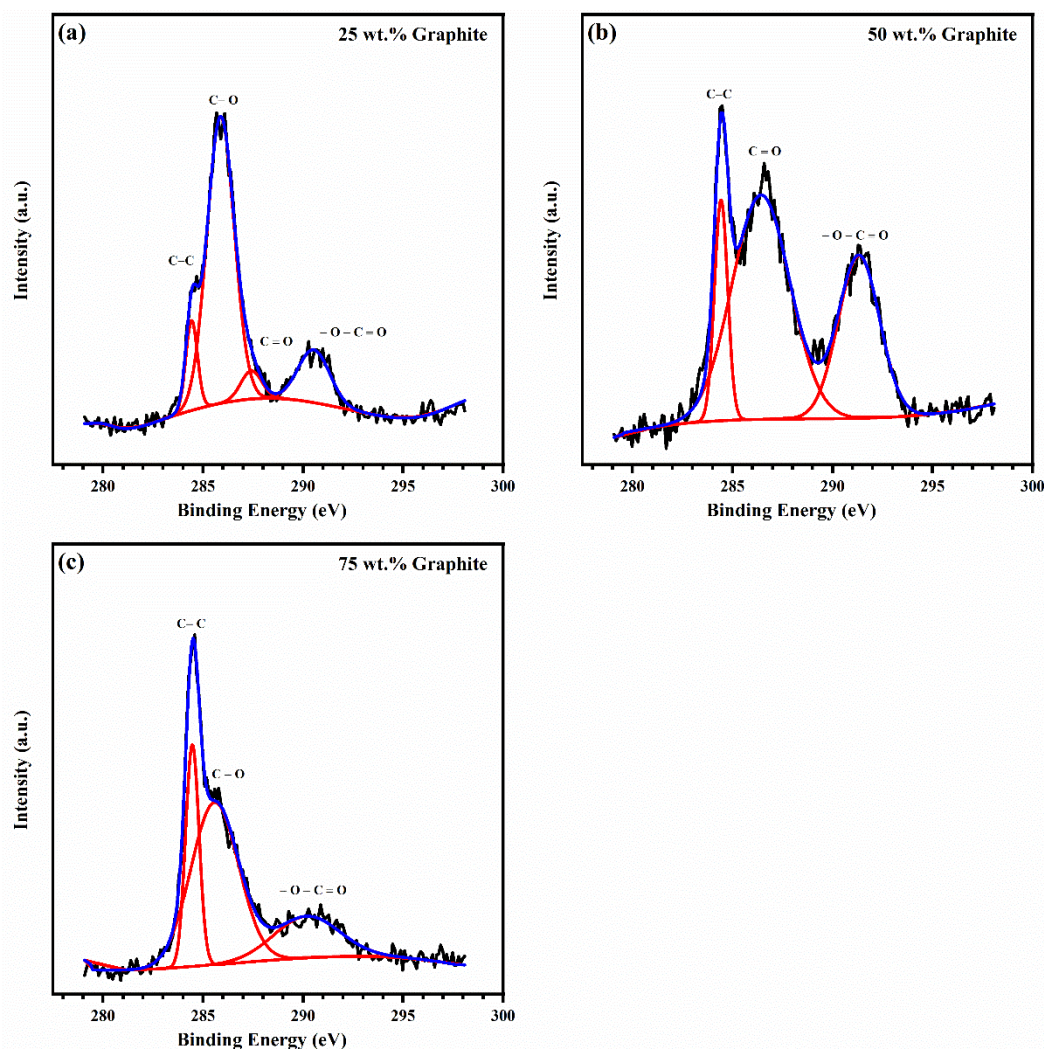


Figure 7. 12: Deconvoluted C 1s XPS scans of ZnO-graphene NCs/NF hybrid photocatalysts with 25 wt.% (a), 50 wt.% (b), and 75 wt.% (c) graphite content.

The deconvoluted spectra of the C 1s scan for the ZnO-graphene NCs/NF heterostructure with 25, 50, and 75 wt.% of graphite contents are shown in **Figure 7. 12(a-c)**. The characteristic C–C bond of graphene nanosheets caused by the sp^2 -hybridization between adjacent carbon atoms was observed at 284.43 ± 0.03 in the ZnO-graphene NCs/NF hybrid photocatalysts. Multiple bonded states between oxygen and the graphene species were detected, such as C–O, C=O, and –O–C=O bonds at 285.72 ± 0.14 , 287.41, and 290.34 ± 0.16 eV, respectively. The NCs hybrid photocatalysts with 50 wt.% graphite content exhibits certain distinct features in some of the oxygenated bonds, such as the negative shift of the C=O bond to lower binding energy, whereas the –O–C = O bond was detected at higher binding energy (291.32 eV) compared with other NCs hybrid photocatalysts. The hybridization between ZnO and the graphene species in the deposited NCs thin films was depicted by either the evolution of new bond states or a noticeable peak position shift. This confirmed the strong synergy between the different species presented in the ZnO-graphene NCS/NF hybrid photocatalysts [276].

Table 7. 1: Deconvoluted high-resolution XPS bands of Zn 2p, O 1s, and C1s scans of ZnO-graphene NCs/NF hybrid photocatalysts at different graphite contents (wt.%)

Band	Binding Energy (eV)			
	ZnO	25 wt.% graphite	50 wt.% graphite	75 wt.% graphite
C 1s	-	284.43	284.42	284.46
	-	285.87	-	285.58
	-	287.41	286.42	-
	-	290.50	291.32	290.17
O 1s	530.91	530.95	-	530.84
	532.67	532.81	532.67	532.88
Zn 2p	-	-	533.60	-
	1,022.10	1,022.34	1,023.52	1,022.72
	1,045.20	1,045.44	1,046.58	1,045.82

7. 2. 5. The optical band gap of ZnO-graphene NCs/NF hybrid photocatalysts

Figure 7. 13(a) exhibits the optical absorbance spectra of ZnO nanosheets/NF and ZnO-graphene NCs/NF hybrid photocatalysts at different graphite contents (25, 50, and 75 wt.%), in the UV-visible region extending from 200 to 800 nm. The optical absorbance spectrum of the ZnO nanosheets/NF reveals the main absorption region in the UV region from 200 to 375 nm and a sharp absorption edge near the UV region at about 390 nm. The excitation with lower energy in the visible region was accompanied by a relatively smaller absorbance that seemed to be independent of excitation light wavelength (λ). In the case of ZnO-graphene NCs/NF hybrid photocatalysts, the main absorption edge was positively shifted to relatively longer wavelengths, and the optical absorbance in the visible region was improved. The optical

band gaps (E_g) of the ZnO nanosheets/NF and the ZnO-graphene NCs/NF were estimated from the corresponding optical absorbance spectra using Tauc's plots as shown in **Figure 7. 13(b)**, based on the following equation [317]:

$$(\alpha h\nu)^2 = C(h\nu - E_g) \quad \text{Eq. 7. 1}$$

where α is the optical absorption coefficient, $h\nu$ is the incident photon energy, and C is the proportionality constant. The estimated E_g of the ZnO nanosheets/NF and ZnO-graphene NCs/NF hybrid photocatalysts with 25, 50, and 75 wt.% graphite contents were 3.18, 3.0, 2.9, and 3.05 eV, respectively.

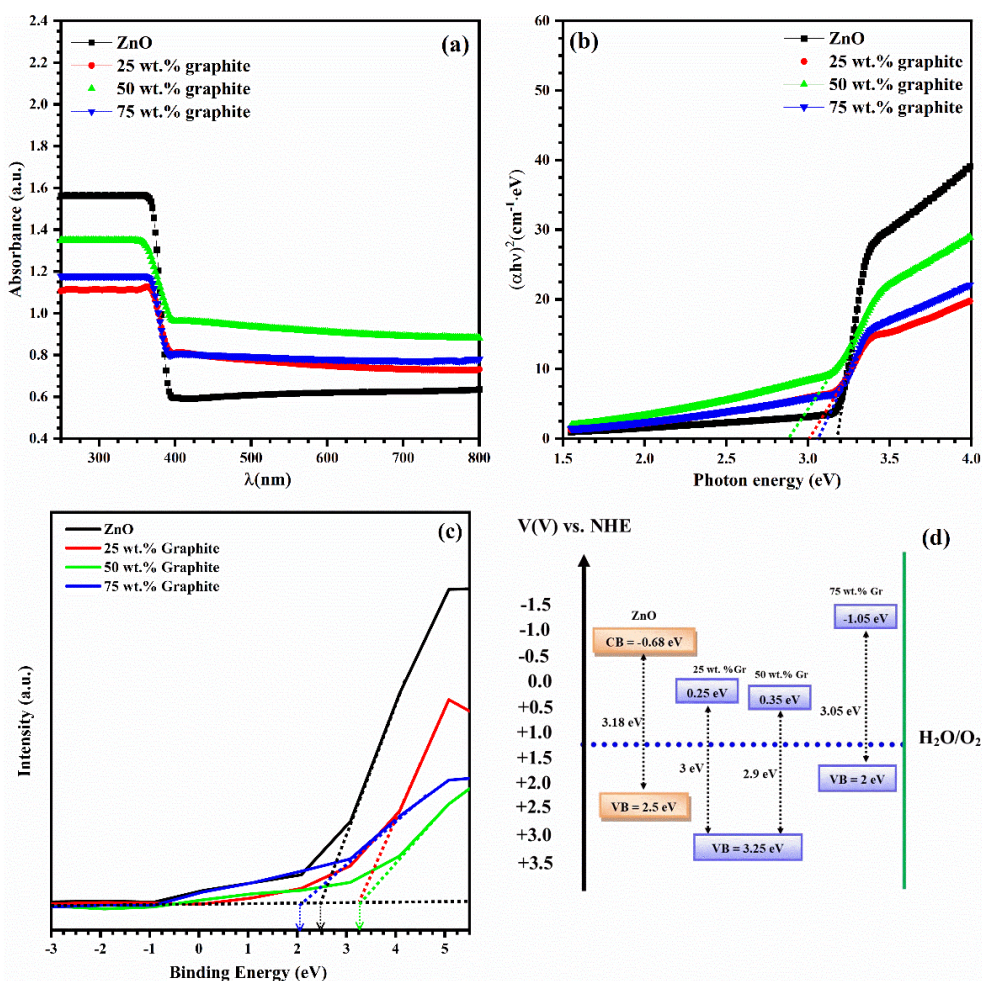


Figure 7. 13: Optical absorbance spectra and the corresponding Tauc plots (a, b), valence band estimation from the XPS survey spectrum (c), and a demonstrative band structure diagram of ZnO-graphene NCs/NF hybrid photocatalysts with different graphite contents.

The observed decrease in the optical band gap of nanostructured ZnO with graphene species incorporation indicated the role of the graphene nanosheets in improving the solar light-harvesting of nanostructured

ZnO thin films. The effect of the graphite content variation on the valence band energy level of the ZnO host lattice was investigated using XPS survey spectra in the binding energy range from -3 to 5 eV, as shown in **Figure 7. 13(c)**. We found that the incorporation of graphene in the NCs hybrid photocatalysts with 25 and 50 wt.% graphite contents resulted in a positive shift of the ZnO host lattice VB from 2.5 to 3.25 eV, while an increase in the graphite content up to 75 wt.% resulted in a negative shift of the ZnO VB to 2 eV. Based on the estimated values of the optical bandgap and the corresponding VB energy levels, the position of the conduction band energy level was estimated for the nanostructured ZnO/NF as well as the NCs/NF hybrid photocatalysts according to the energy band diagram illustrated in **Figure 7. 13(d)**.

7. 2. 6. Photocatalytic activity of ZnO-graphene nanocomposite photocatalysts

Figure 7. 14 reveals the proposed mechanism of MB photocatalytic degradation using ZnO-graphene NCs/NF hybrid photocatalysts. This mechanism can be understood as cumulative effects caused by the synergy improvement between the ZnO and graphene species in the hybrid NCs photocatalysts. The presence of graphene nanosheets in the hybrid NCs photocatalyst is expected to improve the transportation and separation of photogenerated electron-hole pairs at the semiconductor/solution interface. This behavior is ascribed to several possible reasons. The characteristic planar π -bonded structure of carbon arrays with superior electrical conductivity in the graphene nanosheets can improve the transportation of photogenerated electrons [362]. The high surface area of graphene nanosheets can endow a preferable interfacial hybridization with nanostructured ZnO species in the deposited NCs photocatalysts. Hence, the synergy improvement provides transportation pathways for the photogenerated electrons from ZnO to graphene nanosheets according to the known percolation mechanism. This by turn will enhance the photogenerated charge carrier separation and increases the photogenerated electron lifetime [363, 364]. The improvement of ZnO-graphene NCs surface area, as well as the transportation of photogenerated electrons to graphene nanosheets, are expected to improve the cationic dye molecules (MB) adsorption via the spatially localized electrostatic field at the NCs photocatalyst/solution interface [365]. The MB dye molecules would adsorb to the surface of ZnO-graphene NCs hybrid photocatalysts through the electrostatic interaction, hydrogen bond formation, or π - π interaction with graphene nanosheet species [366]. The photocatalytic degradation mechanism of adsorbed MB molecules at the interface of ZnO-graphene NCs photocatalysts can be explained according to the following equations [367]:





The incident light radiation with photon energy ($h\nu$) in the visible light spectral region induces charge carrier excitation within the ZnO bandgap and results in photo-generation of electron-hole pairs. Then the photogenerated holes in the valence band stimulate water splitting at the semiconductor/solution interface as well as the formation of active hydroxide radicals (OH^\bullet). The formed OH^\bullet radicals initiate the MB degradation gradually by increasing the illumination time. According to the illustrated mechanism, the photocatalytic degradation of MB is affected by many parameters related to the utilized nano-sized photocatalyst, such as the optical band, the ability of the photogenerated charge carrier to separate, as well as the reaction rate constant for producing the active OH^\bullet radicals desired for MB degradation. The incorporation of graphene species in the nanostructured ZnO/NF thin film photocatalyst likely affects all of these parameters because it improves the transport and charges separation of photogenerated carriers as well as improving the visible light harvesting; hence, the overall MB degradation process would be improved [368].

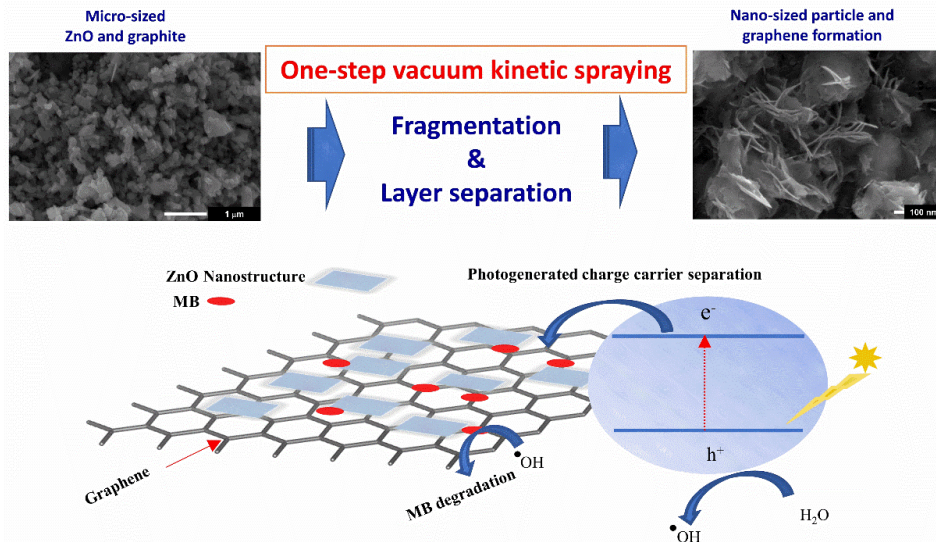


Figure 7. 14: Schematic diagram for ZnO-graphene NCs hybrid photocatalysts formation and MB degradation mechanism under visible light illumination

However, finding the optimal combination of ZnO and graphene species in the fabricated NCs hybrid photocatalyst is important because sometimes a high concentration of graphene can induce surface recombination centers for the photogenerated carriers, resulting in the deterioration of charge separation of the photogenerated carriers and overall inhibition of the MB degradation process [369]. Hence, we

fabricated ZnO-graphene NCs/NF hybrid photocatalysts with different graphite contents (25, 50, 75wt.%) to find the optimal combination for improving the visible light degradation of MB (**Figure 7. 15(a-d)**).

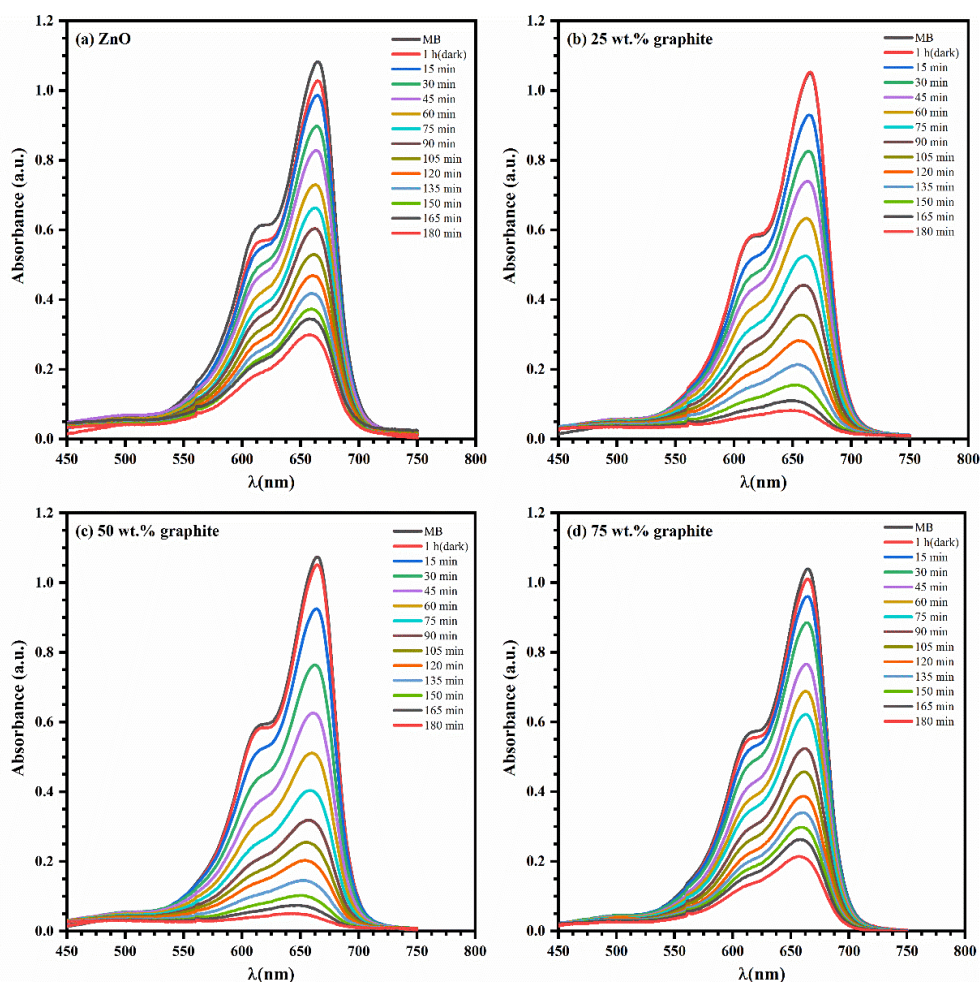


Figure 7. 15: The variation of MB optical absorbance with illumination time in the presence of nanostructured ZnO/NF photocatalyst (a), and ZnO-graphene NCs photocatalysts with 25 (b), 50 (c), and 75 wt.% (d) graphite content under a visible light intensity of $50 \text{ mW}\cdot\text{cm}^{-2}$.

The incorporation of graphene species in the nanostructured ZnO matrix resulted in the improvement of MB degradation, as shown in **Figure 7. 16(a)**. The photocatalytic degradation efficiency (η) of MB correlated with illumination time by ZnO-graphene NCs/NF photocatalysts was evaluated based on the following equation:

$$\eta(\%) = 1 - \frac{c}{c_0} \quad \text{Eq. 7. 6}$$

Figure 7. 16(b) presents the photocatalytic degradation efficiency plots of MB for the ZnO-graphene NCs/NF photocatalysts at different graphite contents. The nanostructured ZnO/NF photocatalyst exhibited

around 72% MB degradation after 3 h of illumination, whereas the NCs photocatalysts with 25, 50, and 75 wt.% graphite contents induced 93%, 98%, and 80% degradation, respectively.

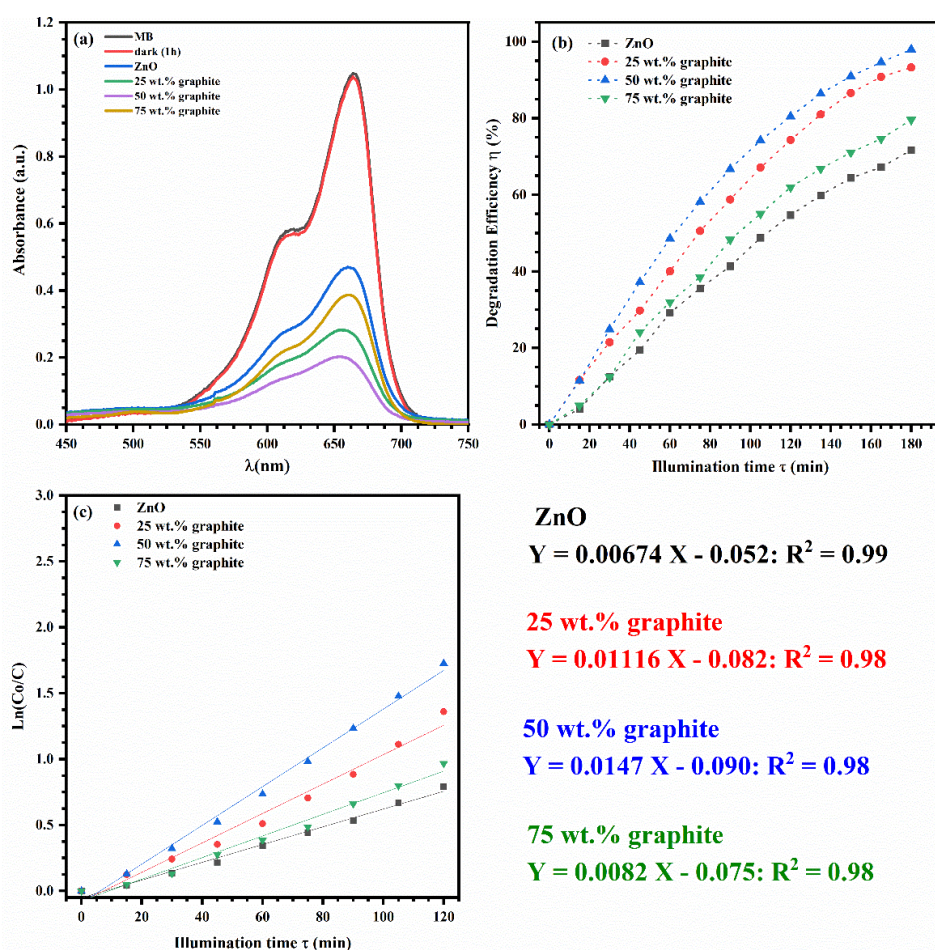


Figure 7. 16: Optical absorbance spectra at 2 h illumination time (a), the photocatalytic degradation efficiency at different illumination times τ (b), and the linear relation of $\ln(C_o/C)$ vs. the illumination time τ (c) of the ZnO-graphene NCs/NF hybrid photocatalysts.

The photocatalytic degradation of MB by the hybrid ZnO-graphene NCs/NF under visible light was evaluated based on the Langmuir–Hinshelwood kinetics expression. In this case, the photocatalytic reaction expresses the pseudo-first-order kinetics as a function between the MB dye concentration (C), and the incident illumination time (τ) [370]:

$$\ln\left(\frac{C_o}{C}\right) = k_a \tau \quad \text{Eq. 7. 7}$$

where C_o is the initial concentration of MB (5 ppm) and k_a refers to the apparent kinetic constant in the linear region.

Figure 7. 16(c) presents $\ln(C/C_0)$ vs. τ plots of the nanostructured ZnO/NF and ZnO-graphene NCs/NF photocatalysts, in which the slope was used to determine k_a according to **Eq. 7**. The estimated k_a values are 0.00674, 0.01116, 0.0147, and 0.0082 min^{-1} corresponding to ZnO/NF and ZnO-graphene NCs/NF with 25, 50, and 75 wt.% graphite contents, respectively.

7.3. Summary

ZnO-graphene NCs/NF hybrid photocatalysts with different graphite contents (25, 50, and 75 wt.%) were directly deposited at room temperature on nickel foam (NF) porous substrate in a one-step vacuum kinetic spray process using the NPDS technique without any post-treatment. The deposited nanostructured thin films resulted from the fragmentation and localized thermal bonding of ZnO and graphite microparticles. The deposited nanostructured ZnO/NF and ZnO-graphene NCs/NF thin films with 25, 50, and 75 wt.% graphite contents were utilized as photocatalysts for MB degradation under visible light illumination. The XRD patterns of the nanostructured thin films revealed the total disappearance of the crystalline planes of the related graphite microcrystalline domains, indicating the layer separation and transformation of the graphene nanosheets. Also, the XRD peak intensity of the crystalline domains related to the ZnO species was strongly inhibited in the deposited nanostructured thin films due to the ZnO particles being reduced to the nano-size range caused by the kinetic-induced particle fragmentation. Raman spectra of the deposited thin films of ZnO nanosheets/NF exhibited the evolution of a new active Raman mode corresponding to A_1 (LO) of the ZnO species induced by the improvement of disorder at the interfacial grain boundaries. This was also observed for the ZnO-graphene NCs/NF thin films with 25, 50, and 75 wt.% graphite contents, in which the disorder-sensitive Raman modes (D, D', and G'') related to the graphite species were noticeably changed compared with the corresponding bulk graphite powder. These results indicated the fragmentation and thinning of the graphite micro-sized particles into nano-sized graphene flakes. The relative fragmentation of graphite microparticles into nano-sized graphene nanoflakes in the NCs thin films was strongly dependent on the ZnO content. The NCs hybrid photocatalysts with high ZnO contents (75 and 50 wt.%) had more micro-sized graphite powder fragmentation into nano-sized graphene flakes compared with the hybrid photocatalyst with 25 wt.% ZnO content. SEM images of the ZnO/NF thin films revealed nanorods and nanosheets morphology. With the addition of 25 wt.% graphite content to the deposited ZnO-graphene NCs/NF thin films, we observed the initiation of morphological transformation into nanoflakes. The increase of graphite content up to 50 wt.% in the NCs thin films was accompanied by the total transformation into nanoflakes morphology.

Furthermore, an increase in the graphite content up to 75 wt.% resulted in a second morphology transformation to nanoflower morphology. This behavior revealed the strong dependence of surface morphology on the ZnO-to-graphite composition ratio. The effect of graphite content variation on the ZnO-graphene NCs/NF surface bonding states was studied using the deconvolution of high-resolution XPS spectra of C 1s, O 1s, and Zn 2p. The deconvoluted Zn 2p spectra of ZnO-graphene NCs/NF exhibited a positive shift of Zn 2p_{3/2} and Zn 2p_{1/2} binding energies to higher values, with energy shifts of 0.24, 1.4, and 0.62 eV corresponding to the NCs hybrid photocatalysts with graphite contents of 25, 50, and 75 wt.%, respectively. The high-resolution C 1s XPS spectra exhibited multiple bonded states between the ZnO and the graphene species in the deposited thin films, such as C–O, C = O, and –O–C = O bonds. Furthermore, the relative intensity of the C = O bonds in the NCs hybrid photocatalysts with 50 wt.% graphite content was noticeably enhanced compared to those with other graphite contents. The O 1s high-resolution spectrum of the NCs hybrid photocatalyst with 50 wt.% graphite content exhibited the evolution of new oxygenated bonded states at 533.6 eV, corresponding to the C = O bond. The observed binding energy shift in some bonded states, as well as the evolution of new bonding states, evidenced the strong hybridization between the ZnO and the graphene species, and the improved synergy in all the fabricated ZnO-graphene NCs/NF hybrid photocatalysts, especially the NCs hybrid photocatalysts with 50 wt.% graphite contents. Our analyses of the UV-visible optical absorbance spectra of ZnO-graphene NCs/NF revealed the improvement of visible light harvesting by decreasing the optical bandgap from the 3.18 eV of nanostructured ZnO/NF to 3.0, 2.9, and 3.05 eV corresponding to the NCs hybrid photocatalysts with 25, 50, and 75 wt.% graphite content, respectively. We also studied the photocatalytic activity of nanostructured ZnO/NF and ZnO-graphene NCs/NF hybrid photocatalysts using MB degradation under visible light illumination of nearly 50 mW·cm⁻². The estimated photocatalytic degradation efficiencies after 3 h of illumination were 72%, 93%, 98%, and 80%, corresponding to nanostructured ZnO/NF and NCs hybrid photocatalysts with 25, 50, and 75 wt.% graphite contents, respectively. The photocatalytic reaction rate constant was evaluated from the time-dependent concentration variation of the characteristic optical absorbance peak at 664 nm. The estimated rate constants were 0.00674, 0.01116, 0.0147, and 0.0082 min⁻¹, corresponding to the nanostructured ZnO/NF and the NCs hybrid photocatalysts with 25, 50, and 75 wt.% graphite contents, respectively. The observed enhancement in the photocatalytic activity of ZnO-graphene NCs/NF was attributed to the improvement of visible light harvesting as well as the synergy between the ZnO and the graphene species in the deposited nanostructured thin films.

Chapter 8:

*Nanosized Co_3O_4 - MoS_2 Heterostructure Electrodes for
Improving the Oxygen Evolution Reaction in an Alkaline
Medium*

8.1. Overview

Nanostructured Co_3O_4 electrocatalysts are widely utilized as efficient anodes for water oxidation in alkaline media [194, 371-373] because they have many advantages such as abundance, low cost, chemical stability, and corrosion resistance [192, 193]. On the other hand, these electrocatalysts have weaknesses related to the chemisorption of oxygen-containing intermediates between the working electrode and the electrolyte that may result in poor electrocatalytic reaction kinetics. This behavior can be modified by the incorporation of metal oxide species and by increasing active site concentrations at the surface of the electrocatalyst [374]. Conway et al., [375] investigated the behavior of oxygen-related surface intermediates in the oxygen evolution reaction (OER) with Co_3O_4 on Ni substrate. They found that the reaction kinetics of the OER depends on the oxidation state of the active sites (i.e., metal ions), as well as the interfacial coverage by oxygen-related intermediates (i.e., OH/O) between the oxide-based electrocatalyst and the electrolyte.

Also, MoS_2 -based electrodes are commonly used for water splitting applications due to their layered structure, electronic band structure [376-378], and the existence of interfacial edge sites that act as electrocatalytic active sites [379]. However, there are a few drawbacks with these materials such as the low concentration of active sites and the high potential barrier required to initiate water dissociation oxidation due to the strong adsorption of the interfacial OH^- group [380]. Many efforts have been made to overcome these restrictions by improving the concentration of the interfacial active centers by activation of the MoS_2 surface [381, 382].

Recently, low dimension interface engineering has provided efficient methods that greatly enhance the electrochemical performance of electrocatalysts. These have included inducing novel interfacial physical and chemical properties that are accompanied by synergistic effects between the various electroactive species at the working electrode surface. The formation of heterostructure electrodes is a powerful way to modify the surface structure of the working electrode that results in high concentrations of interfacial active sites. For example, it was reported that the existence of metallic clusters on the oxide surface is responsible for increasing the OER rate in alkaline media because they improve the adsorption of OH^- and oxygen-containing intermediates [383]. Hence, the fabrication of novel heterostructures that create synergies between electroactive species and increases binding affinities for the oxygen-formed intermediates is very important for improving the overall efficiency of water splitting [384, 385]. Chen et al., [194] fabricated nanostructured Co_3O_4 composites with an organic framework that revealed OER

improvement with a small overpotential (η) 320 mV. Yang et al., [386] have fabricated CoFe@NiFe-LDH nanosheets with core-shell architecture on Ni foam using a hydrothermal process for 6 hours followed by electrodeposition technique. The prepared hybrid electrodes exhibited high electrocatalytic activity toward the OER in an alkaline medium, which provided $10 \text{ mA}\cdot\text{cm}^{-2}$ at a very small η of 190 mV. Xun et al., [387] constructed integrated ternary composites of CoO/Co₃O₄ nanoparticles supported on CoMoO₄ nanorods through a hydrothermal treatment at 120 °C for 12 hours followed by two-step thermal annealing at 400 and 600 °C for 2 hours. The designed ternary hybrid electrode revealed high electrocatalytic activity toward the OER in 1.0 M KOH that provided $10 \text{ mA}\cdot\text{cm}^{-2}$ at a low η of 253 mV. Malik et al., [196] have synthesized a heterostructure of CoPt/ Co(OH)₂ NPs that exhibit good activity toward the OER with a small η value of 334 mV at $10 \text{ mA}\cdot\text{cm}^{-2}$. On the other hand, the evolution of an amorphous region at the interface of a Co-based electrocatalyst also improved the overall OER electrocatalytic activity [195]. Many researchers have shown that the bulk structure does not influence the heterostructure activity toward the water oxidation (i.e. OER). For example, polycrystalline or amorphous nanostructured Co-based materials electrodes revealed higher electrocatalytic activity toward the oxygen evolution reaction compared with the corresponding crystalline electrocatalysts [197]. Moreover, the amorphous heterostructure electrocatalysts are characterized by higher volume and surface confinement of electrocatalytic species compared with crystalline materials [198] as well as a high density of electroactive sites toward the OER at the surface of the electrocatalyst [199, 200]. Based on these interesting features, many researchers reported efficient amorphous heterostructure electrocatalysts based on nanostructured Co₃O₄ [202-205]. Also, the architecture engineering of MoS₂-based heterostructure electrodes has a great role in improving the efficiency of overall water splitting. Si et al. [388] synthesized co-doped MoS₂ nanosheets with Co and Fe through a template confined strategy that improved the electrode active surface area, charge transfer, and concentration of electroactive centers. This resulted in an overall enhancement in the electrocatalytic activity toward overall water splitting. Wei et al. [389] prepared MoS₂-Ni(OH)₂ heterogeneous electrocatalyst on Ni foam. The obtained heterostructure electrode revealed improvement in the interface synergy between the layered structure of MoS₂ nanosheets and the Ni(OH)₂ nanorods that resulted in an enhancement of charge transfer kinetics and overall water splitting efficiency.

One of the promising heterostructure combinations is a nanostructured Co₃O₄-MoS₂ hybrid catalyst. This material possesses several factors that provide high OER activity in an alkaline medium including (1) a high concentration of the active sites due to the thermal equilibrium OH⁻ adsorption on Co species

that can dissociate the H-OH bonds, (2) the free energy (ΔG) value is close to the thermo-neutral potential of water dissociation due to charge transfers from Co_3O_4 to MoS_2 caused by the large difference in electronegativity between S and Co [390], and (3) the existence of antibonding empty states of related Co species (i.e. Co^{2+} , Co^{3+}) that can enhance oxygen intermediates adsorption [391]. Liu et al. [244] prepared nanostructured Co_3O_4 , MoS_2 , and their heterostructure $\text{Co}_3\text{O}_4@\text{MoS}_2$ on carbon cloth (CC) by a hydrothermal reaction in two separate steps, in which the whole preparation process takes more than 24 hours. The obtained electrocatalyst provided $10 \text{ mA}\cdot\text{cm}^{-2}$ at a η of 417, 315, and 269 mV corresponding to MoS_2/CC , $\text{Co}_3\text{O}_4/\text{CC}$, and $\text{Co}_3\text{O}_4@\text{MoS}_2/\text{CC}$, respectively. Muthurasu et al., [210] have synthesized metal-organic framework derived $\text{Co}_3\text{O}_4@\text{MoS}_2$ on Ni foam (NF) using a combination of pyrolysis at 300 °C for 1 h followed by a hydrothermal process for 10 hours at 200 °C. The obtained electrocatalysts revealed high OER electroactivity in 1.0 M KOH that provided $10 \text{ mA}\cdot\text{cm}^{-2}$ at a η of 230 mV and a Tafel slope of $45 \text{ mV}\cdot\text{dec}^{-1}$.

In our previous studies, we fabricated various heterostructures electrodes in the nano-size range with an amorphous or polycrystalline structure that exhibited high efficiency toward various electrochemical applications as oxygen evolution and hydrogen evolution reactions [261], nonenzymatic H_2O_2 sensors [392], and supercapacitors [79] using one of the top-down techniques called the nanoparticle deposition system (NPDS), which is characterized by low-temperature deposition of binder-free ceramic-based thin films in the nano-size range [221, 277]. Unlike other fabrication techniques, our deposition technique (i.e. NPDS) considers the cost-efficiency that is needed for commercializing the electrochemical water splitting applications and its applicability for mass production for real-life commercial applications [100]. Besides, our technique has a very short fabrication time (i.e. one step deposition with minutes) and does not use hazardous chemicals. Moreover, in contrast to all the techniques mentioned above our deposition techniques can be scaled up for large deposition areas as reported by Sung-Ik Park [99] who deposited WO_3 thin films with 1 m^2 geometrical area using NPDS.

8.2. Results and discussion

8.2.1. XRD patterns of Co_3O_4 - MoS_2 composites

The microcrystalline structure of Co_3O_4 , MoS_2 as well as their mixed micro-sized powder with 25, 50, and 75 wt.% MoS_2 content was investigated using the XRD patterns as shown in **Figure 8. 1(a)**. The XRD pattern of Co_3O_4 microparticles revealed several diffraction peaks, which are in good agreement with the face-centered cubic phase of Co_3O_4 (space group: Fd-3m, ICDD: 43-1003) [222]. The XRD

pattern of MoS₂ microparticles exhibited several characteristic peaks with relatively high intensity compared to other peaks with lower intensity at 28.96, 32.62, 33.44, 35.82, 39.4, 44.1, 49.74, 55.94, 58.28, and 60.1° corresponding to (004), (100), (101), (102), (103), (006), (105), (110), and (008), respectively, of bulk MoS₂ hexagonal structure (space group: P6₃/mmc, ICDD: 03-065-1951, PDF 2010). Besides, XRD patterns of the Co₃O₄-MoS₂ mixed micro-sized powder with 25, 50, and 75 wt.% MoS₂ content exhibited the presence of both phases, cubic Co₃O₄, and hexagonal MoS₂ without the presence of any new secondary phases due to the ball milling before the deposition process. **Figure 8. 1(b)** shows XRD patterns of the bare Ni foam (NF) substrate without deposition, the deposited films of MoS₂/NF, Co₃O₄/NF, and their composites thin films with different MoS₂ content (25, 50, and 75 wt.%) on Ni foam. In the case of the bare Ni foam, three main diffraction peaks were observed at 2θ values of 44.19, 51.54, and 76.09° corresponding to the (111), (200), and (220) crystalline planes of the face-centered cubic of pure Ni phase (space groups: Fm-3m, ICDD: 00-004-0850, PDF 2010). It can be observed that the deposited films' XRD patterns of pure phases MoS₂/NF, Co₃O₄/NF, and their hybrid composites revealed only XRD peaks characteristic to the cubic structure Ni foam substrate. However, when we magnified the XRD patterns we found several peaks matched with Co₃O₄ and MoS₂ phases with a very low intensity compared with the background radiation. This behavior is due to the high crystalline nature of the used Ni foam substrate.

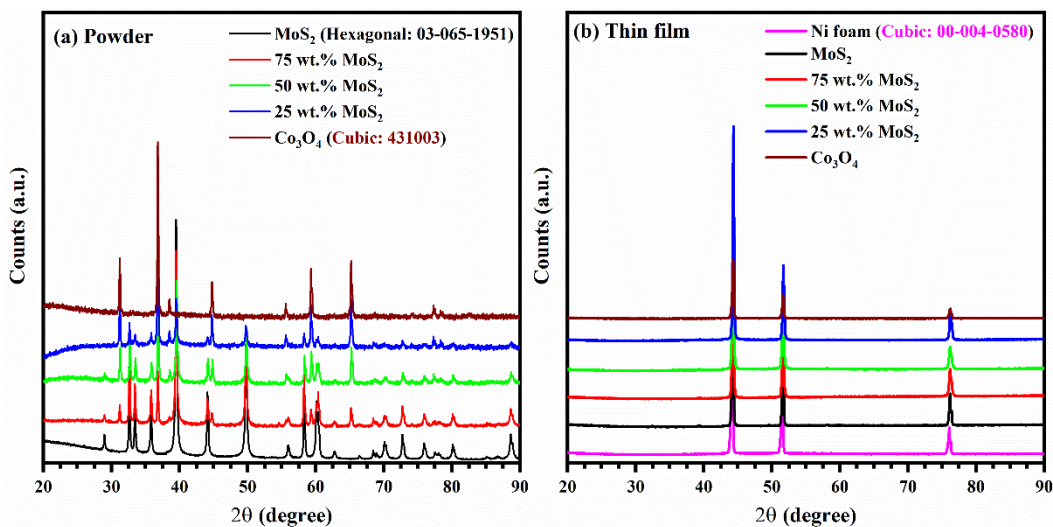


Figure 8. 1: XRD patterns of Co₃O₄-MoS₂ composites in powder form (a) and thin film deposited on Ni foam substrate.

Furthermore, the low intensity of the XRD peaks in all deposited films demonstrated the fragmentation of the initial microparticles to many domains with a very small domain size. This behavior is commonly observed during the deposition of functional semiconductor thin films on a substrate with a

high degree of crystallinity using the NPDS [261]. Moreover, according to Du et al [223], the low degree of crystallinity in Co₃O₄-based heterostructure electrodes is accompanied by a higher concentration of metal oxide interfacial defects that act as an electrocatalytic active center for the oxygen evolution reaction. Hence, the micro-Raman analysis was performed for precise identification of the actual active phases at the surface Co₃O₄-MoS₂ heterostructures electrodes as discussed in the next section.

8. 2. 2. Raman spectra of Co₃O₄-MoS₂ composites

8. 2. 2. 1. Microparticles in powder form

Figure 8. 2(a) shows the Raman spectrum of MoS₂ microparticles that consists of several first-order Raman peaks at Raman shift of 279, 373, and 400 cm⁻¹. Second-order Raman peaks at 447, and 562 cm⁻¹, as well as the linear combination of these active modes at 585 cm⁻¹, were observed (see **Table 8. 1**). The observed active Raman modes matched the 2H-bulk structure of MoS₂, in which the two most intense Raman peaks at 373 and 400 cm⁻¹ correspond to the first-order vibration modes of E¹_{2g}, and A_{1g}, respectively. The observed Raman peaks with small intensities at 279 cm⁻¹ were attributed to the first-order symmetry mode E_{1g} [119-123]. Meanwhile, Raman peaks at 447, 562, and 585 cm⁻¹ were attributed to the second-order vibrations of the longitudinal acoustic (2LA) mode, 2E_{1g}(Γ), and E¹_{2g}(M)+LA(M), respectively [393]. The Raman spectrum of the Co₃O₄ micro powder, **Figure 8. 2(e)**, exhibited various Raman peaks centered at 188, 474, 515, 611, and 679 cm⁻¹ related to either separate or linear combinations of A_{1g}+E_g+3F_{2g} Raman active modes of the Co₃O₄ spinel structure. The observed Raman peak with the highest relative intensity at 679 cm⁻¹ is related to the A_{1g} mode caused by the O⁷_h spectroscopic symmetry of the octahedral site (CoO₆). The lower intensity vibration band correspond to E_g symmetry mode was observed at 474 cm⁻¹. The F_{2g} symmetry mode that matched the tetrahedral sites of CoO₄ caused many vibration modes with various intensities at 192, 515, and 611 cm⁻¹ corresponding to F⁽¹⁾_{2g}, F⁽²⁾_{2g}, and F⁽³⁾_{2g}, respectively [224-226]. Raman spectra of the mixed Co₃O₄-MoS₂ microparticles at various MoS₂ contents (75, 50, 25 wt.%) are shown in **Figure 8. 2(b-d)**. These reveal the same characteristic bands for Co₃O₄ and MoS₂, **Table 8.1**.

8. 2. 2. 2. Nanosized Co₃O₄-MoS₂ thin films

The Raman spectrum of the nanostructured MoS₂ electrode on the porous NF substrate is shown in **Figure 8. 3(a)**, which consists of several characteristic first and second-order symmetry modes related to the MoS₂ phase. The first order vibration modes were observed at 283, 381, and 405 cm⁻¹, and these were attributed to the E_{1g}, E¹_{2g}, and A_{1g} symmetry modes of the MoS₂ phase, respectively. The second-order vibration modes were observed at 451, 570, and 598 cm⁻¹ resulting from the 2LA (M), 2E_{1g}(Γ), and

$E^{1}_{2g}(M)+LA(M)$ symmetry modes, respectively. The active Raman vibration modes for the nanostructured Co_3O_4 thin films were identified as illustrated in **Figure 8. 3(e)**, in which Raman peaks centered at 192, 483, 525, 620, and 690 cm^{-1} belong to various Raman modes ($A_{1g}+E_g+3F_{2g}$) characteristic of Co_3O_4 . The active Raman modes A_{1g} caused by the octahedral site (CoO_6) vibration according to the O^7_h spectroscopic symmetry with the highest relative intensity was observed at 690 cm^{-1} , whereas other characteristic vibration modes with relatively lower intensities corresponding the E_g , $F^{(2)}_{2g}$, and $F^{(2)}_{2g}$ modes were observed at 483, 525, and 620 cm^{-1} . Moreover, another characteristic peak related to the tetrahedral sites of CoO_4 corresponding to the $F^{(3)}_{2g}$ mode of the tetrahedral sites of CoO_4 was observed at a Raman shift of 192 cm^{-1} [224-226]. Raman spectra of the heterostructure composite of Co_3O_4 - MoS_2 are shown in **Figure 8. 3(b-d)** and the identified Raman peaks are tabulated in **Table 8. 2**. All heterostructure composites with various MoS_2 content (75, 50, and 25 wt.%) possessed the same peaks related to either Co_3O_4 or MoS_2 phases. Moreover, overall positive shifts to higher Raman shift values were observed in the nanostructured thin films and the bulk phase for MoS_2 and Co_3O_4 as well as the mixed composites before the deposition due to powder fragmentation, which was accompanied by lattice disorder within the low range crystalline domains [124, 227].

Table 8. 1: Identification of Raman modes in the mixed Co_3O_4 - MoS_2 powder at different MoS_2 contents (wt.%).

Characteristic bands	Raman shift (cm^{-1})				Co_3O_4
	MoS_2	75 wt.% MoS_2	50 wt.% MoS_2	25 wt.% MoS_2	
F_{2g}					188
E_g				474	474
Co_3O_4 F_{2g}		516	516	516	515
F_{2g}				611	611
A_{1g}		684	684	680	679
E_{1g}	279	283	278	278	
E^{1}_{2g}	373	377	377	377	
MoS_2 A_{1g}	400	400	400	400	
2LA(M)	447	447	447	447	
2E _{1g} (Γ)	562	562	562	562	
$E^{1}_{2g}(M)+LA(M)$	585	589	589	589	

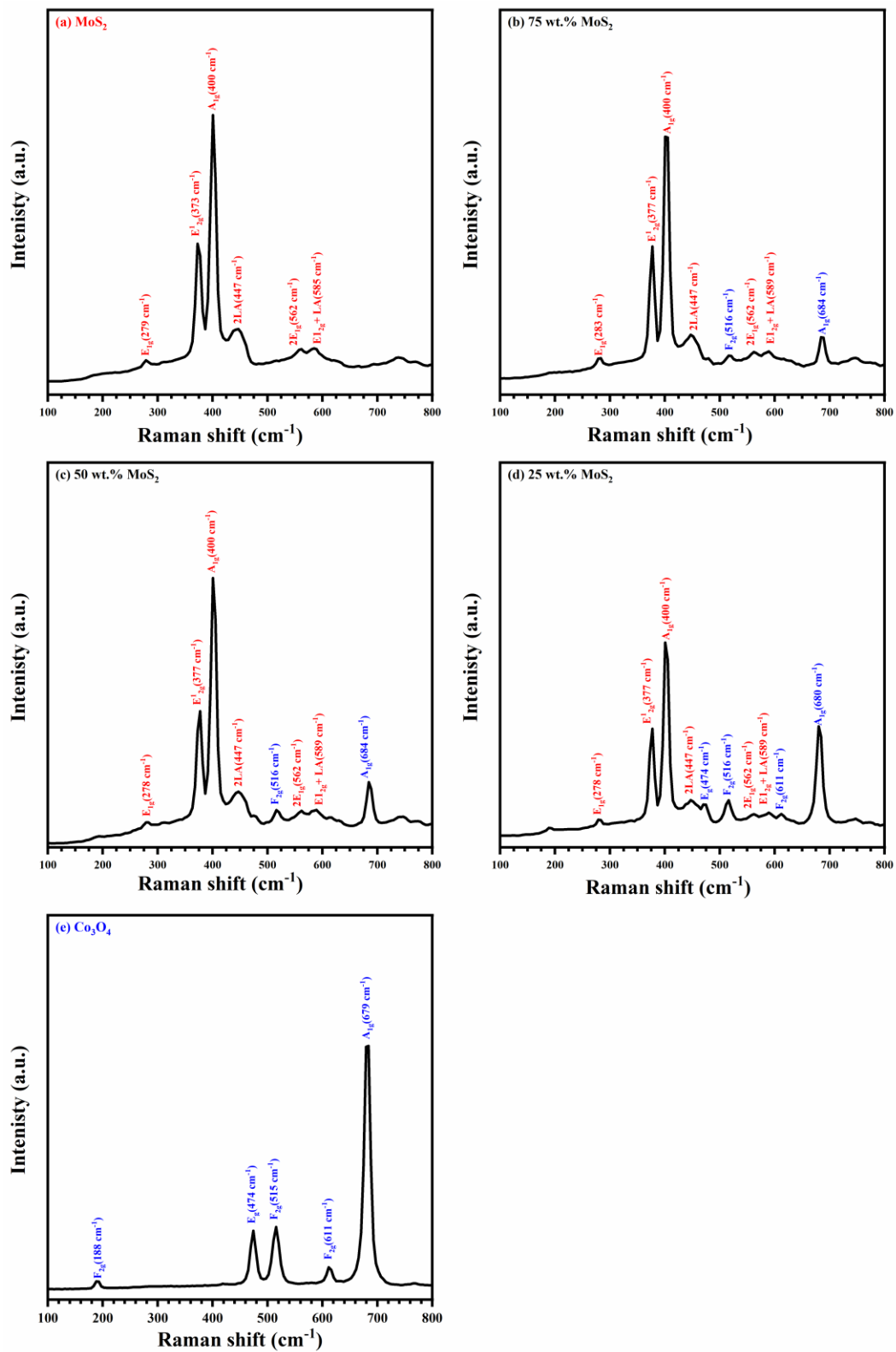


Figure 8. 2: Raman spectra of mixed Co_3O_4 - MoS_2 microparticles at different MoS_2 contents

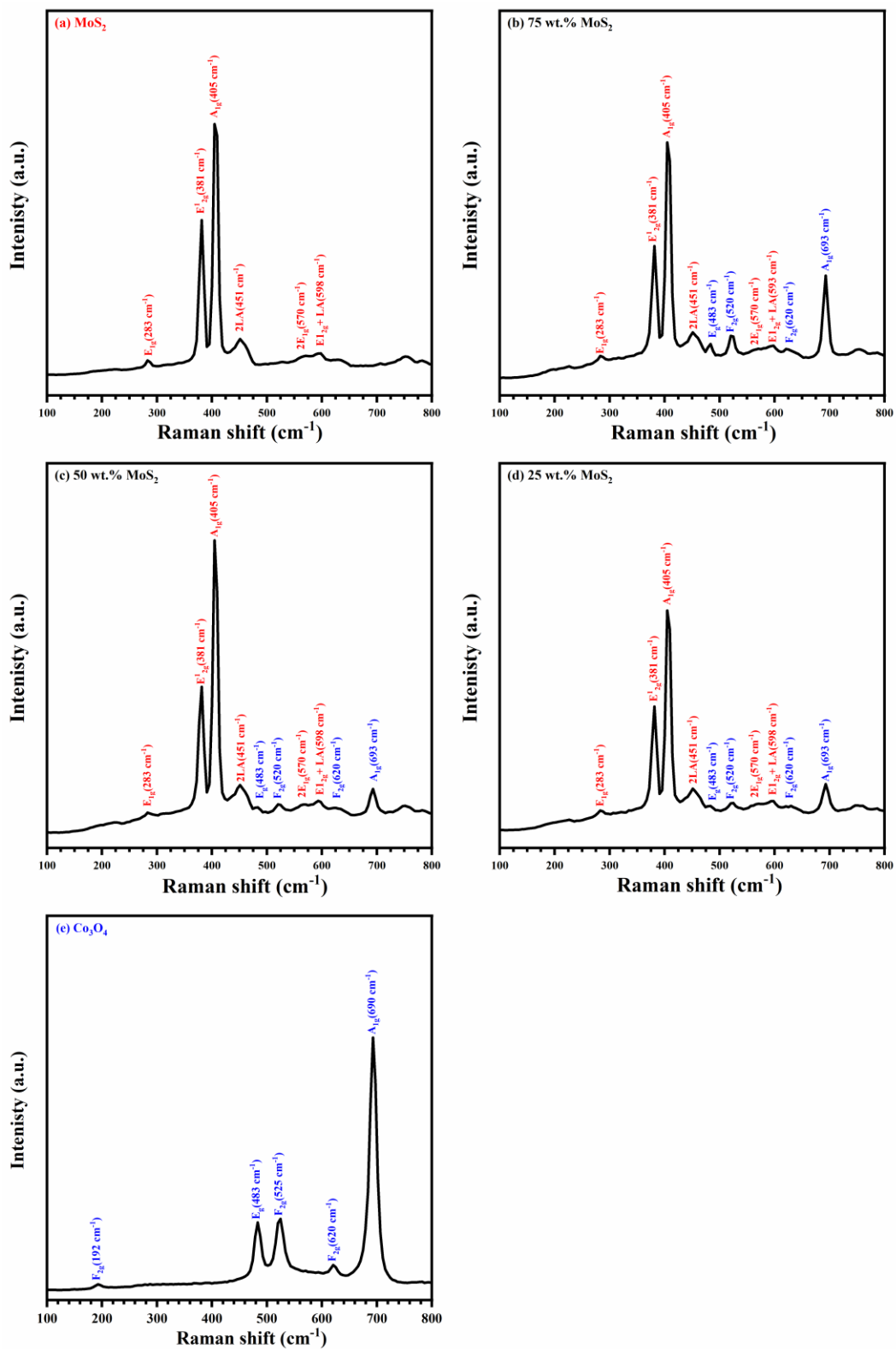


Figure 8. 3: Raman spectra of the MoS₂/NF (a), Co₃O₄-MoS₂ heterostructure composites (b-d), and Co₃O₄/NF (e).

Table 8. 2: Identification of active Raman modes in the nanostructured $\text{Co}_3\text{O}_4\text{-MoS}_2$ heterostructure electrodes at different MoS_2 contents (wt.%)

Characteristic bands	Raman shift (cm^{-1})				
	MoS_2	75 wt.% MoS_2	50 wt.% MoS_2	25 wt.% MoS_2	Co_3O_4
Co_3O_4	F_{2g}				192
	E_g		483	483	483
	F_{2g}		520	520	525
	F_{2g}		620	620	620
	A_{1g}		693	693	690
MoS_2	E_{1g}	283	283	283	283
	E^1_{2g}	381	381	381	381
	A_{1g}	405	405	405	405
	2LA(M)	451	451	451	451
	2E $^1_{1g}$ (Γ)	570	570	570	570
	E $^1_{2g}$ (M)+LA(M)	598	593	593	593

8. 2. 3. Morphology investigation of $\text{Co}_3\text{O}_4\text{-MoS}_2$ composites

8. 2. 3. 1. The initial microparticles

Figure 8. 4(a, b) shows SEM images of MoS_2 microparticles that consist of several multi-layered sheets with variable lengths in the micro-scale range ($0.5 \mu\text{m} \leq \text{sheet diagonal length} \leq 3\mu\text{m}$) stacked together with various orientations. The analysis of Co_3O_4 microparticle SEM images, **Figure 8. 5(e, f)**, revealed the existence of self-aggregated particles with relatively isotropic semispherical shapes with a broad size variation from less than $1 \mu\text{m}$ to $\leq 5 \mu\text{m}$. The aggregation tendency is further illustrated in the magnified SEM image in **Figure 8. 5(f)**. SEM images of $\text{Co}_3\text{O}_4\text{-MoS}_2$ mixed powder with various MoS_2 contents (75, 50, and 25 wt. %), are shown in **Figure 8. 4(c, d)** and **Figure 8. 5(a-d)**. They reveal a mixed sheet and semispherical shape that seemed proportional to the amount of micro powder used for each phase of Co_3O_4 or MoS_2 . The elemental analysis using the EDS spectra for the microparticles of Co_3O_4 and MoS_2 as well as their mixed powders (MoS_2 contents of 25, 50, and 75 wt.%) are shown in **Figure 8. 6**. The EDS spectra of all composite powders exhibited typical signals to O_K , Co_K , S_K , and Mo_L , which represent the existence of Co_3O_4 and MoS_2 species in the mixed powder used for the deposition of the heterostructure $\text{Co}_3\text{O}_4\text{-MoS}_2$ thin films. The contributions of Co_3O_4 and MoS_2 species in the mixed powder are recorded in **Table 8. 3**. In the case of the pure Co_3O_4 powder, the elemental atomic ratio of Co_K/O_K was 0.347, which is smaller than the theoretical value of 0.75 [229]. This is due to the deficiency of Co species caused by a high density of Co-related structural and interfacial defects (i.e., vacancies at either octahedral and or tetrahedral sites in the Co_3O_4 structure) [227]. Moreover, we noticed that the Co_K/O_K in

the mixed powder was further reduced to 0.065, 0.145, and 0.169 corresponding to MoS₂ contents of 25, 50, and 75 wt.%, respectively. This reveals that mixing Co₃O₄ and MoS₂ powder had a strong effect that induced distortion of Co species within the interior crystal lattice of the spinel structure of Co₃O₄.

Table 8. 3: EDS elemental analyses of Co₃O₄-MoS₂ mixed powder

Mixed powder (wt.%)		EDS Elemental analysis (at. %)				
Co ₃ O ₄	MoS ₂	S _K	Mo _L	O _K	Co _K	Co _K /O _K
0	100	67.28	32.72	-	-	-
25	75	30.9	17.2	48.72	3.18	0.065
50	50	24.01	12.29	55.62	8.08	0.145
75	25	20.32	9.76	60.22	10.15	0.169
100	0	-	-	64.77	22.47	0.347

8. 2. 3. 2. Nanosized Co₃O₄-MoS₂ heterostructure electrodes

SEM images of the nanostructured MoS₂/NF thin film in **Figure 8. 7(a, b)** exhibit sheet morphologies with various dimensions in the nano-size range (50 nm ≤ average size ≤ 300 nm) according to the high-resolution SEM image shown in **Figure 8. 7(b)**. Moreover, a denser or more highly packed film layer was also observed, which revealed the possibility of fragmented particles with a lower size range. On the other hand, the surface morphology of the deposited Co₃O₄/NF thin film, **Figure 8. 8(e, f)**, revealed nearly spherical shapes with a relatively wide size distribution that consists mainly of semispherical particles with an average size of less than 100 nm and agglomerated particles with relatively larger sizes. In the case of the heterostructure composites with 75 wt.% MoS₂, we observed that the deposited films, **Figure 8. 7(c, d)**, exhibited nanosheets with dimensions less than 100 nm accompanied by dense packing of the heterostructures particles at the film surface that resulted in merging of particle grain boundaries and overlapping of their spatial coordination. This may reduce the ability to recognize the interlayer grain boundaries. Further increases in the MoS₂ content up 50 wt.% showed different morphology behaviors. SEM images in **Figure 8. 8(a, b)** revealed a lower fragmentation degree of the deposited microparticles compared with other composites. The sizes of the flake morphologies of the deposited grains with various sizes and orientations varied from less than 100 nm to several hundreds of nanometers. The surface morphology of the heterostructure thin film with 25 wt.% MoS₂, **Figure 8. 8(c, d)**, demonstrated a combination of relatively high concentration nanoparticles with sizes less than 100 nm accompanied by a lower contribution of nanosheets with variable sizes up to 200 nm. Moreover, the surfaces of the deposited film seemed to be less packed or less dense (i.e., higher roughness) compared

with the pure phase MoS₂/NF and 25 wt.% MoS₂ composites thin films. There are some common characteristic features shared by all the deposited films including the wide size distribution of the fragmented particles during the deposition process associated with the intersections of particles at grain boundaries. These features can be further illustrated as follows. According to the particle fragmentation mechanism active when using NPDS, particles carried by compressed air are accelerated due to the pressure difference between the inlet and outlet of a converging-diverging nozzle. Thus, the acceleration of the carried microparticles resulted in a change in their kinetic energy.



Figure 8. 4: SEM images of the micro-sized particles of (a, b) MoS₂, and (c, d) composites with 75 wt.% MoS₂ content

The accelerated particles do not all have the same value of kinetic energy, and there is an average kinetic energy value that represents the maximum of the statistical kinetic energy distribution. The amount of kinetic energy each particle has influenced the particle fragmentation degree due to the impact. Hence, it is expected that we would obtain a relatively wide particle size distribution in the deposited films. Moreover, as a result of inelastic collapse upon impact with the substrate, there is a high probability of local thermal heating at the same impact point coordinates within a very short time (in the nanosecond range) that might induce local thermal welding of the grain boundaries resulting in the observed agglomeration in SEM images [230, 231]. A quantitative elemental analysis of the pure phases of Co₃O₄, MoS₂, and their heterostructure thin films from the EDS spectra is illustrated in **Figure 8. 9** to **Figure 8.**

13. The estimated element percentage of Co_3O_4 and MoS_2 species in the nanostructured $\text{Co}_3\text{O}_4\text{-MoS}_2$ heterostructure thin films (i.e., O_K , Co_K , Mo_L , and S_K) are recorded in **Table 8. 4**. The elemental atomic ratio of Co_K/O_K was 0.318 in the case of the $\text{Co}_3\text{O}_4/\text{NF}$ thin-film, which is lower than the corresponding value in the micro powder and still lower than the theoretical value, indicating a significant deficiency in the Co species in the host lattice of bulk Co_3O_4 . The estimated Co_K/O_K values in the case of the heterostructure thin film are 0.3384, 0.367, and 0.188 corresponding to composites with 75, 50, and 25 wt.% MoS_2 , respectively.

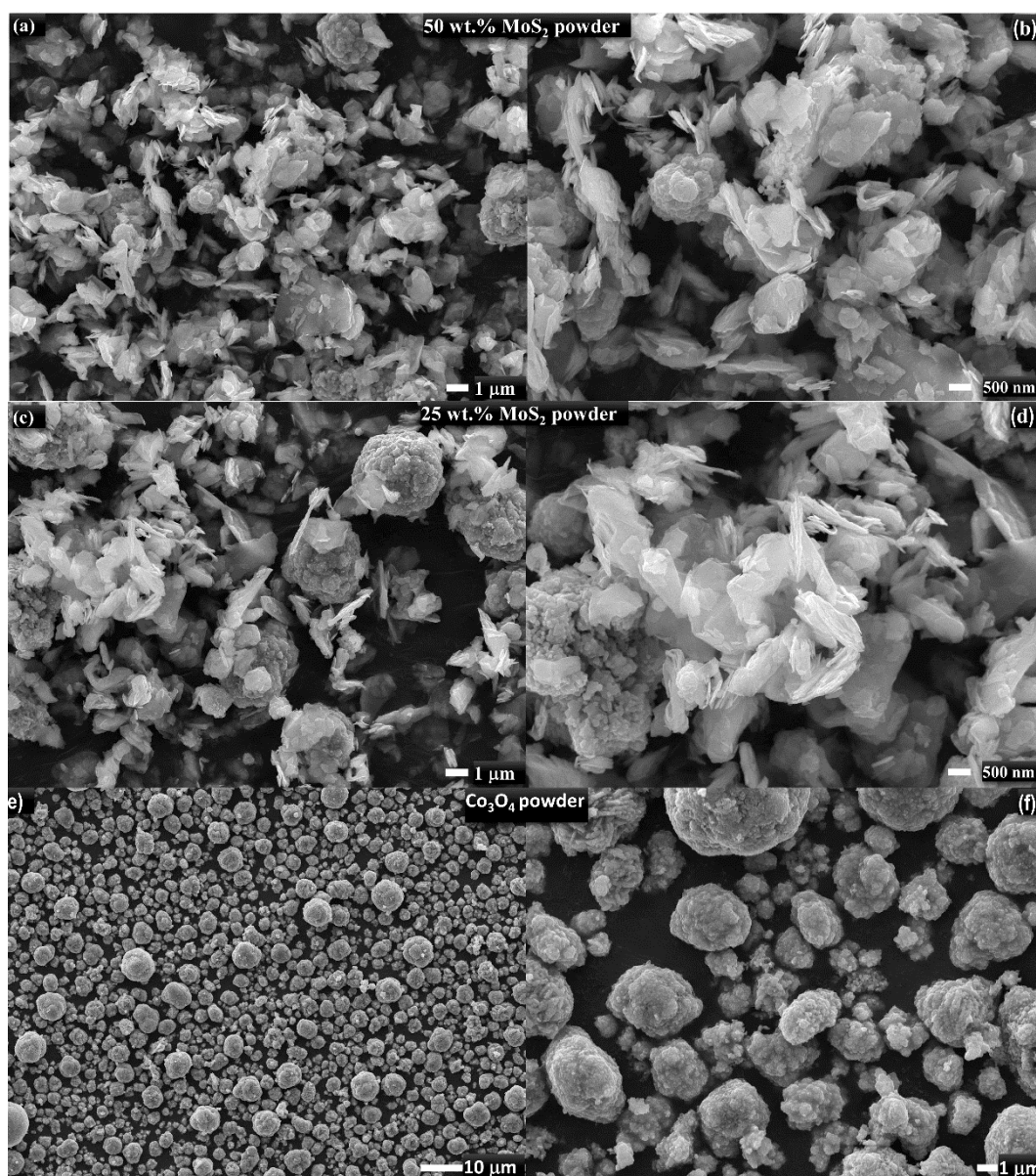


Figure 8. 5: SEM images of the micro-sized particles of composites with (a, b) 50 wt.%, (c, d) 25 wt.% MoS_2 content, and (e, f) pure Co_3O_4 powder

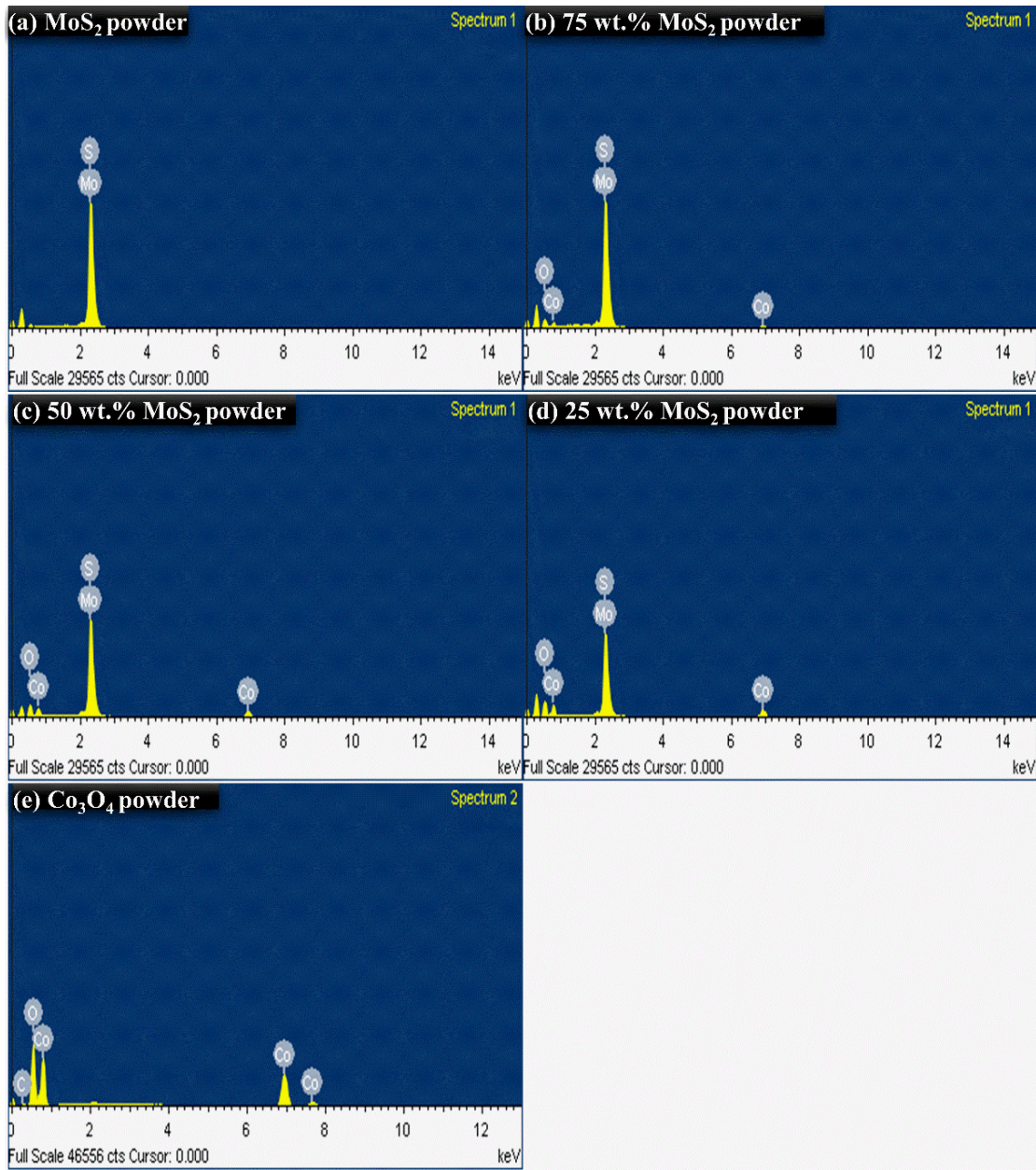


Figure 8. 6: Elemental analyses from the EDS spectra of the used micro-sized powder before deposition of Co₃O₄-MoS₂ composites at different MoS₂ contents

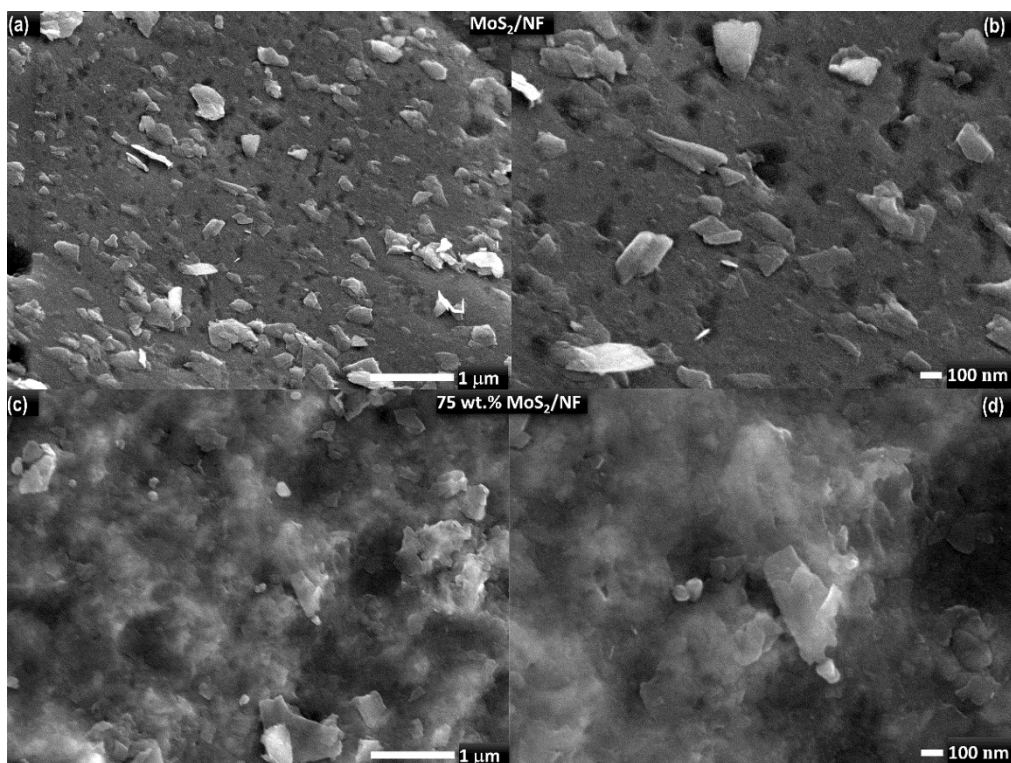


Figure 8. 7: SEM images of pure MoS₂/NF (a, b), and 75 wt.% MoS₂/NF (c, d).

Table 8. 4: EDS elemental analyses of heterostructure composites of Co₃O₄-MoS₂/NF thin films

Composite (wt.%)		EDS Elemental analysis (wt.%)					
Co ₃ O ₄	MoS ₂	Ni _K	S _K	Mo _L	O _K	Co _K	Co _K /O _K
0	100	90.82	6	3.17	-	-	-
25	75	63.41	7.2	3.47	19.43	6.49	0.334
50	50	57.2	8.07	3.5	22.84	8.4	0.367
75	25	35.53	6.37	2.31	47.33	8.46	0.188
100	0	2.96	-	-	73.64	23.41	0.318

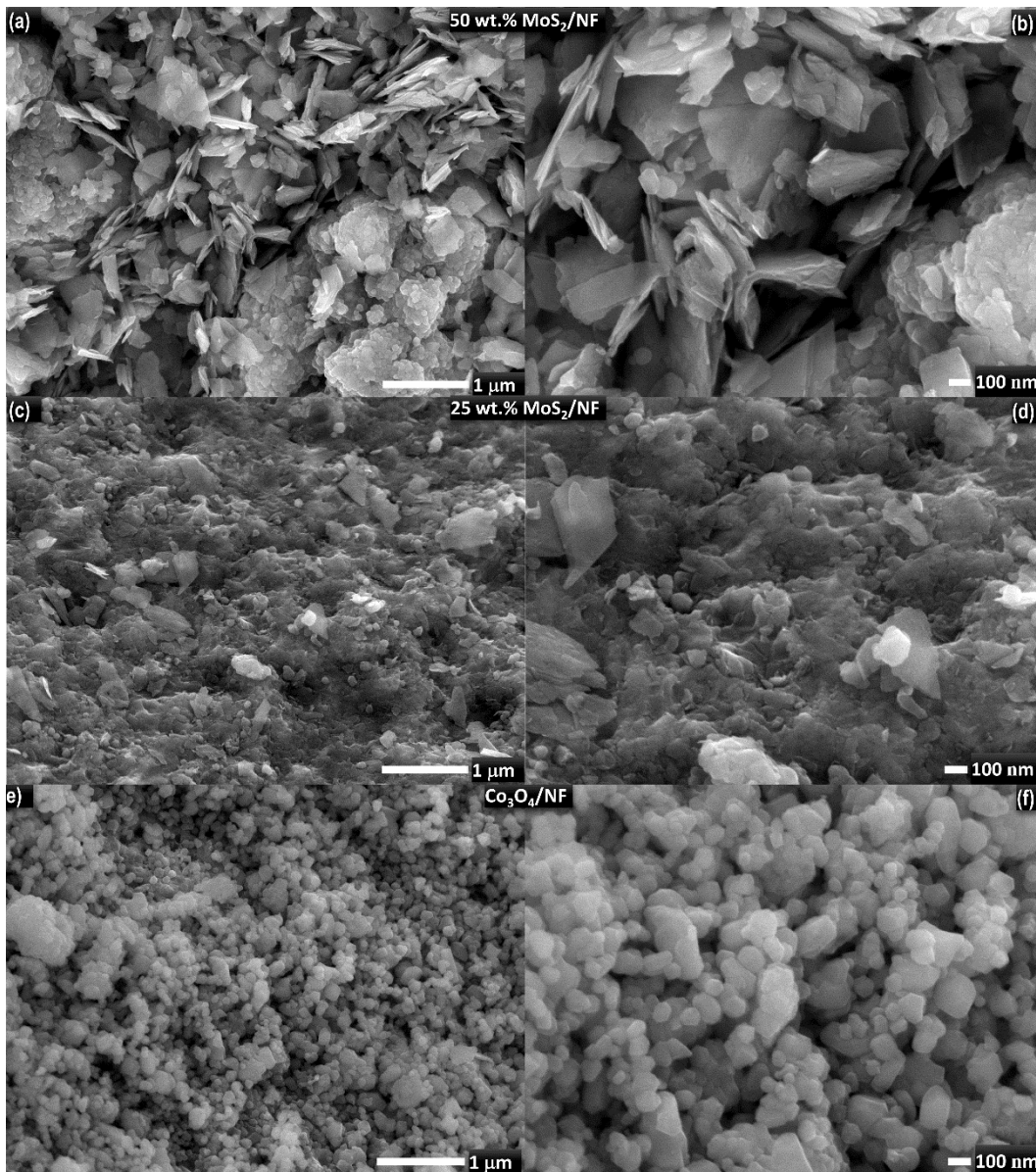


Figure 8. 8: SEM images of composites with 50 wt.% MoS₂/NF (a, b), 25 wt.% MoS₂/NF (c, d), and pure Co₃O₄/NF (e, f).

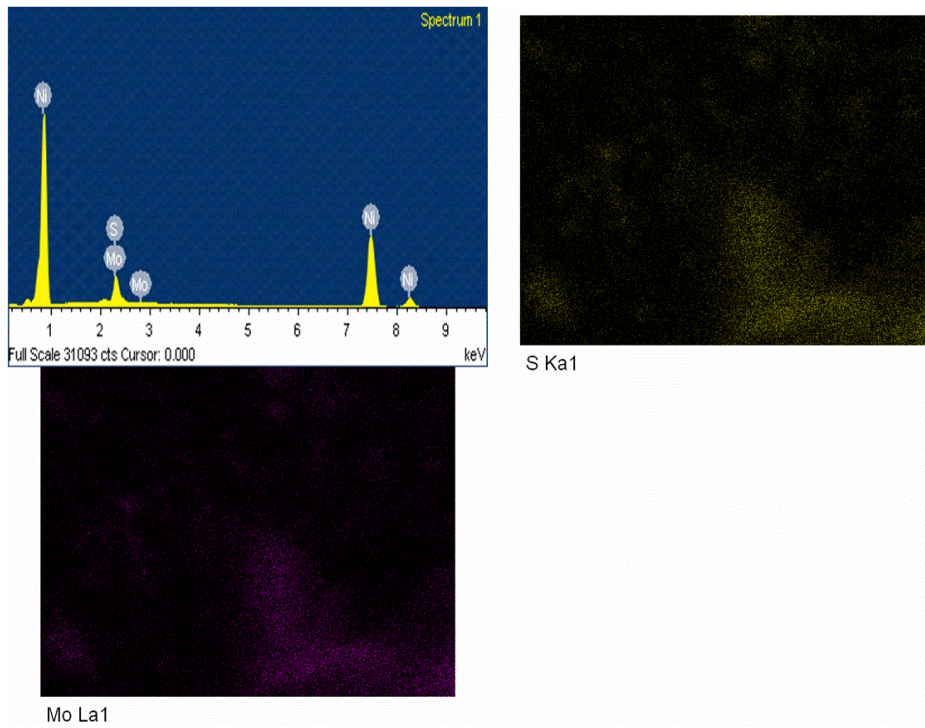


Figure 8. 9: Elemental analysis from EDS spectrum and the corresponding maps of the MoS_2 thin film on the 3D Ni foam substrate.

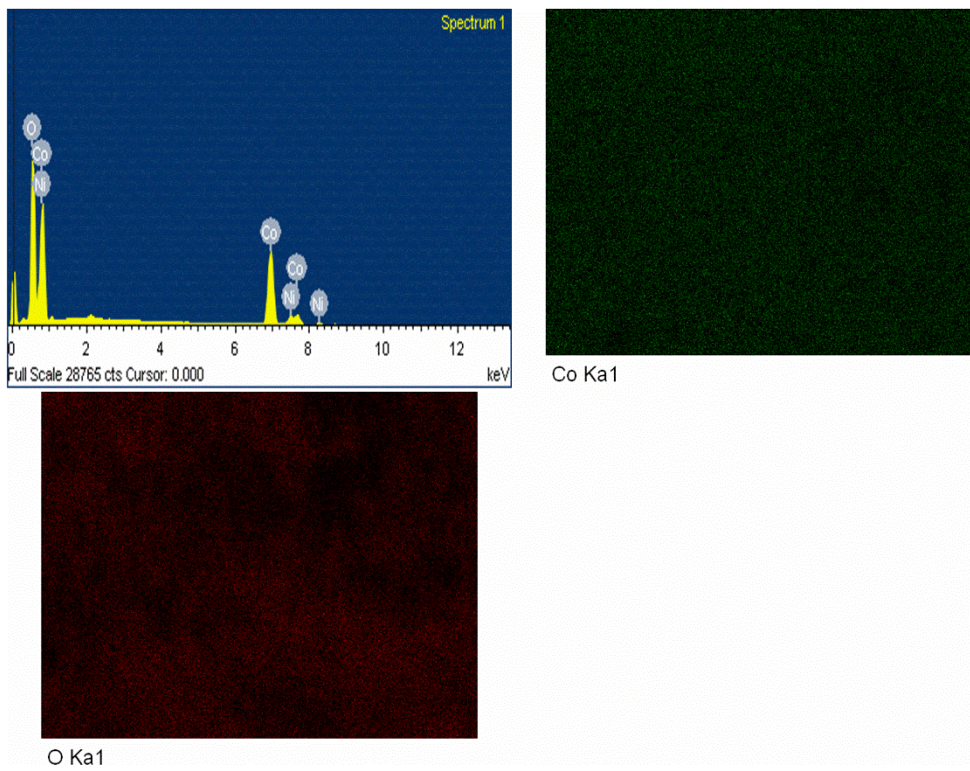


Figure 8. 10: Elemental analysis from EDS spectrum and the corresponding maps of the pure phase Co_3O_4 thin film on the 3D Ni foam substrate.

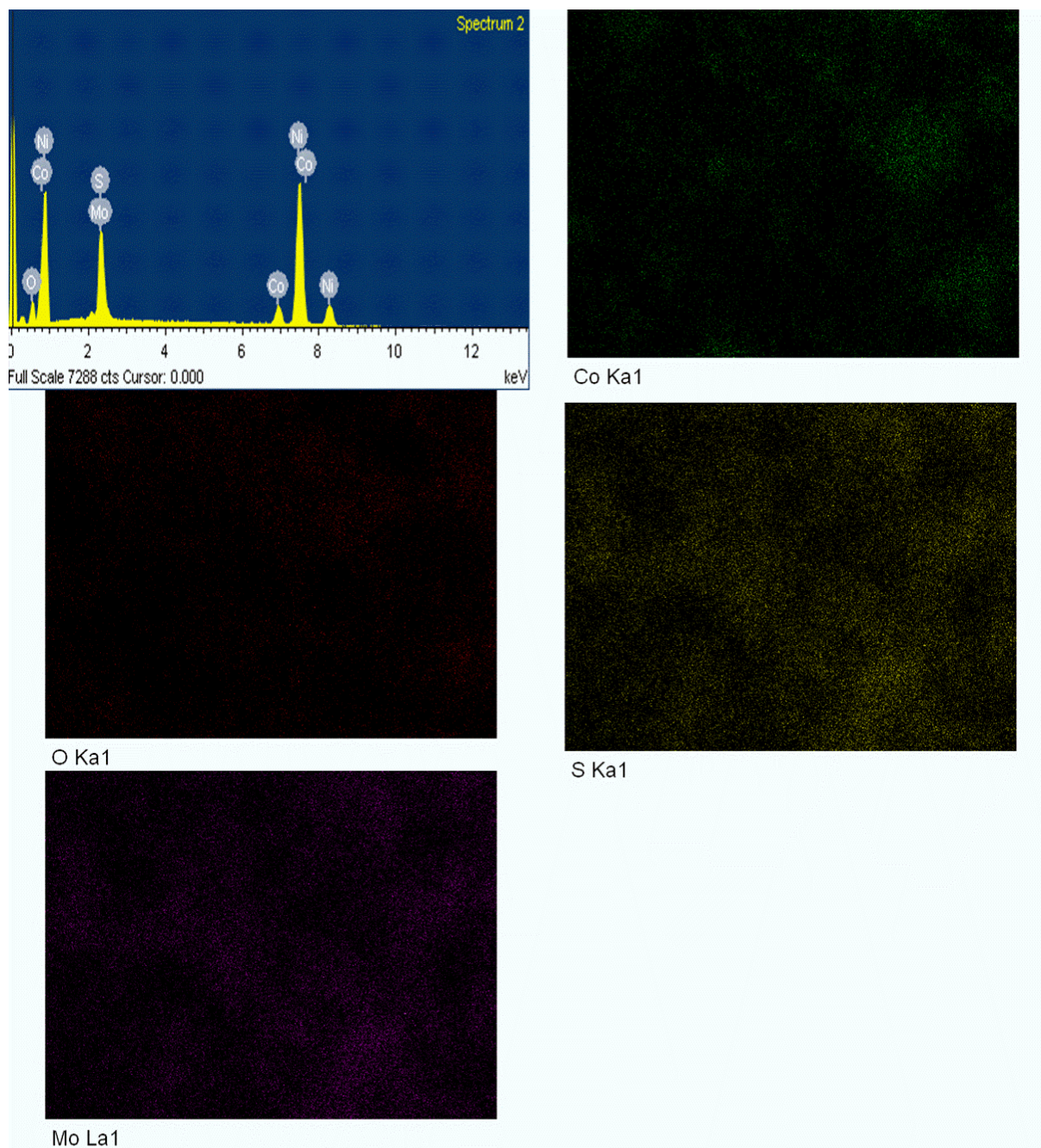


Figure 8. 11: Elemental analysis from EDs spectrum and the corresponding maps of the heterostructure composite with 75 wt.% MoS₂ thin film on the 3D Ni foam substrate.

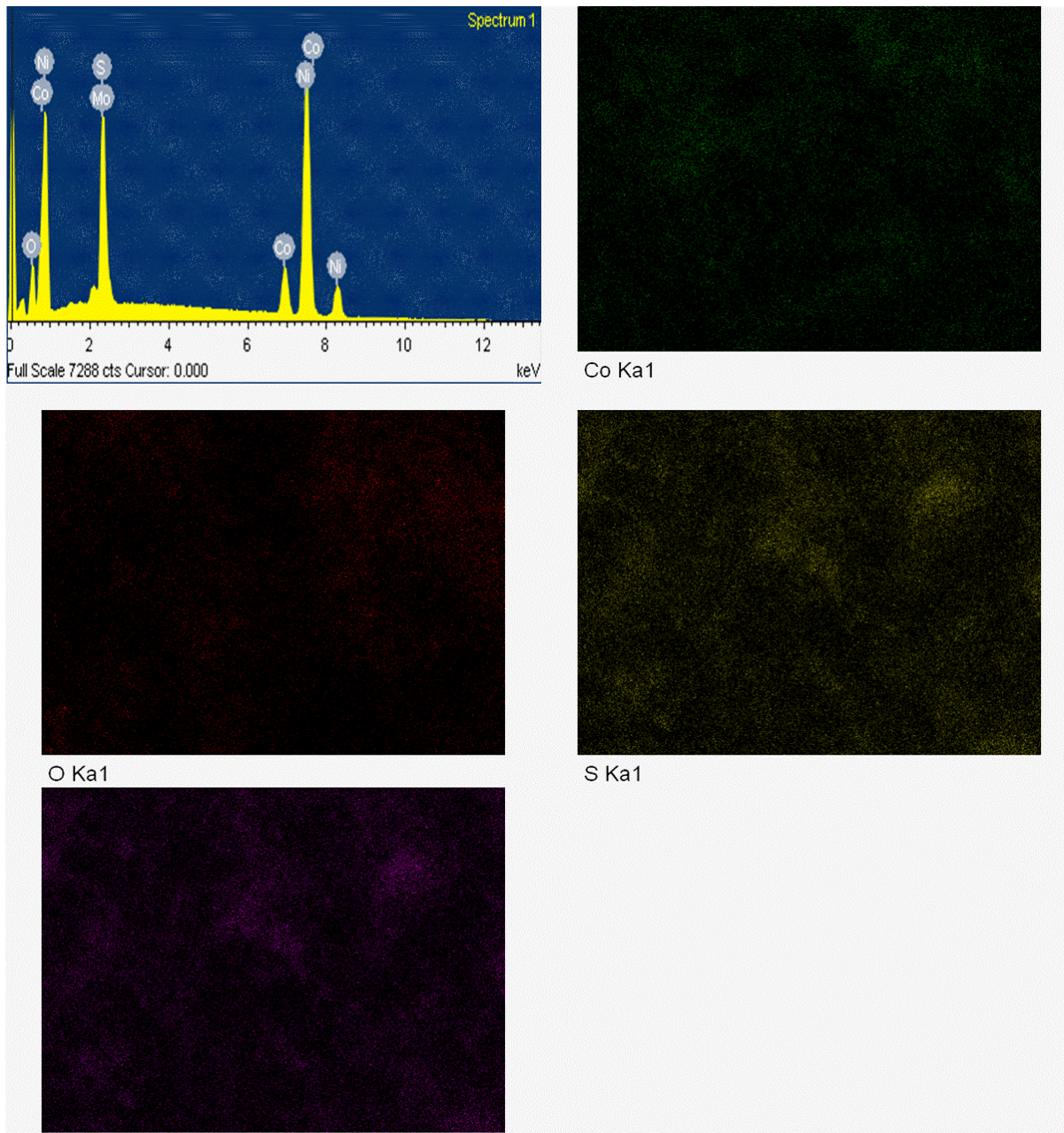


Figure 8. 12: Elemental analysis from the EDS spectrum and the corresponding maps of the heterostructure composite with 50 wt.% MoS₂ thin film on the 3D Ni foam substrate.

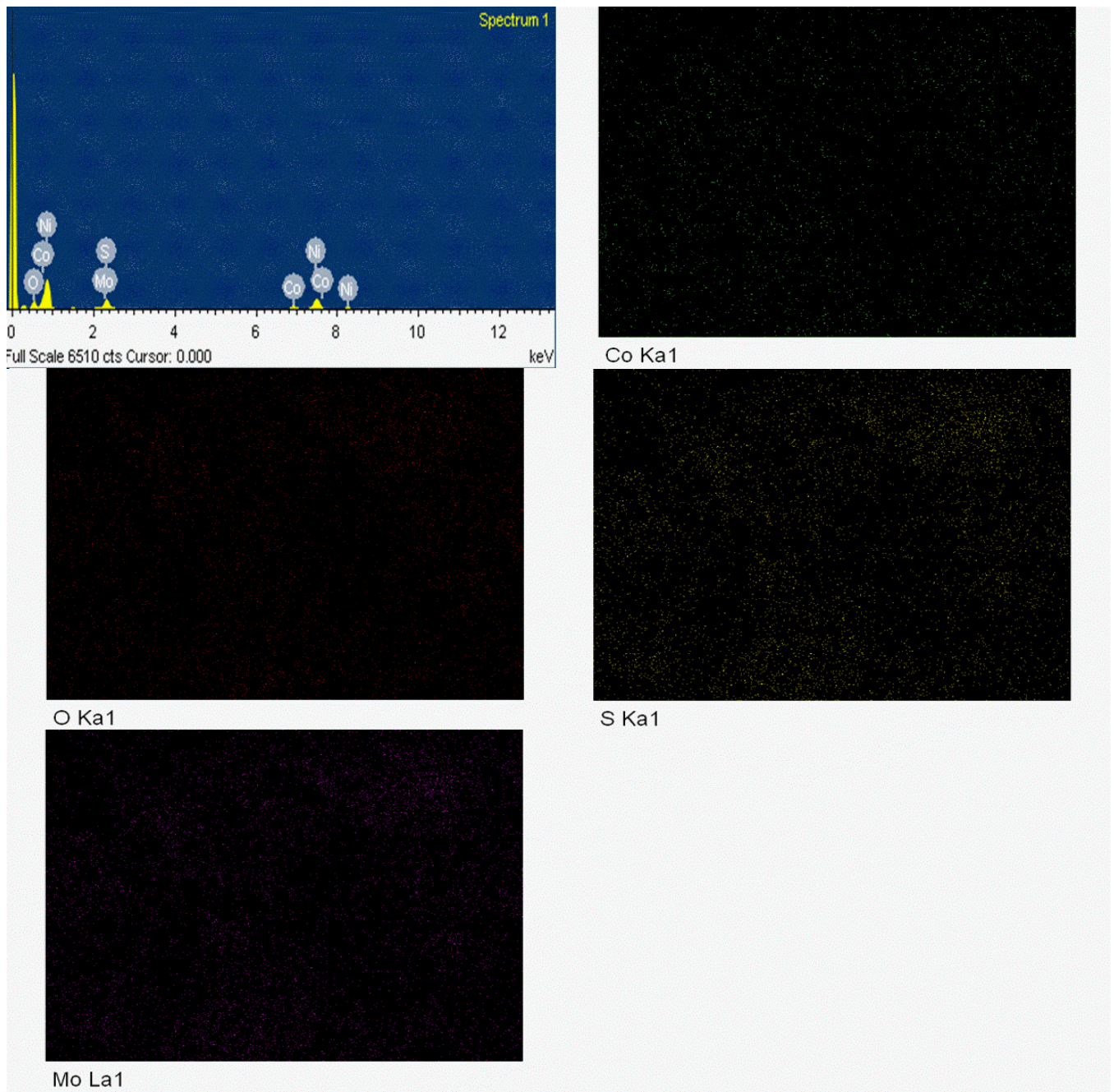


Figure 8. 13: Elemental analysis from EDS spectrum and the corresponding maps of heterostructure composite with 25 wt.% MoS₂ thin film on the 3D Ni foam substrate.

8. 2. 4. Surface bonding states of Co₃O₄-MoS₂ hybrid electrocatalysts

The XPS was utilized to study the characteristics of the interfacial active site of the deposited Co₃O₄-MoS₂ heterostructure electrodes. **Figure 8. 14(a)** reveals the XPS survey scans of the Co₃O₄-MoS₂ heterostructure composites at various MoS₂ contents (25, 50, and 75 wt.%) including the typical signals of S, Mo, O, and Co elements. Moreover, the corresponding high-resolution XPS scans of S 2p, Mo 3d, O 1s, and Co 2p sub electronic bands are illustrated in **Figure 8. 14(b-e)**. **Figure 8. 15(a)** reveals the deconvoluted XPS scan of the S 2p band of the pure phase MoS₂, which consists mainly of two sub-bands centered at 162.25 eV and 163.49 eV, which correspond to S 2p_{3/2} and S 2p_{1/2}. Similar sub-bands were observed in the case of the heterostructure electrodes with MoS₂ content 75, 50, and 25 wt.%, **Figure 8. 15(b-d)**, and the positions of the estimated peaks are recorded in **Table 8. 5**. Peak positions related to both S 2p_{3/2} and S 2p_{1/2} for the heterostructure electrodes are negatively shifted to lower binding energy values, and the observed shift is relatively higher in the case of the S 2p_{1/2} sub-band compared with S 2p_{3/2}. This negative shift may represent an improvement in the electron density at the interface of the MoS₂-based heterostructure electrodes [384, 394]. The deconvoluted high-resolution Mo 3d XPS scan, **Figure 8. 16(a)**, of the pure phase of the MoS₂ electrode, reveals 2 characteristic sub-bands centered at 229.4 and 232.54 eV corresponding to Mo 3d_{5/2} and Mo 3d_{3/2}, respectively. There is also a weak band corresponding to the high oxidation state (Mo⁶⁺) at 236.2 eV [395]. Furthermore, there is a detectable sub-band at 226.57 eV, which is related to the S 2s states that commonly overlap with the high-resolution XPS scan of the Mo 3d states [396]. The deconvoluted Mo 3d XPS scans of the heterostructure composites are shown in **Figure 8. 16(b-d)**. These reveal the same characteristic bands in the MoS₂ phase. Also, all the observed states in the Mo 3d XPS scan were negatively shifted to lower binding energy values with increasing Co₃O₄ content like the case of the S 2p XPS scan. The deconvoluted high-resolution O 1s XPS scan (**Figure 8. 17 (d)**) of the pure Co₃O₄ electrode exhibited one characteristic peak at 531.5 eV that represents the Co–O–Co bond in the cobalt oxide materials. Besides, the O 1s XPS scan of the heterostructure electrodes with different MoS₂ contents, **Figure 8. 17(a-c)**, shows sub-bands peaks position corresponding to the O 1s scan listed in **Table 8. 5**, which revealed positive shifts with increasing MoS₂ content relative to the pure phase of Co₃O₄. Moreover, in the case of heterostructure composites, additional sub-band shoulders were observed at 530.1 and 529.78 eV, corresponding to composites with 50 and 25 wt.% MoS₂, respectively. The deconvoluted Co 2p XPS scan, **Figure 8. 18(d)**, exhibited the presence of cobalt-related peaks (Co 2p_{3/2} at 780.73 eV and Co 2p_{1/2} 796.65 eV) associated with a low-intensity shoulder as a result of the spin-orbital coupling between these electronic sub-bands.

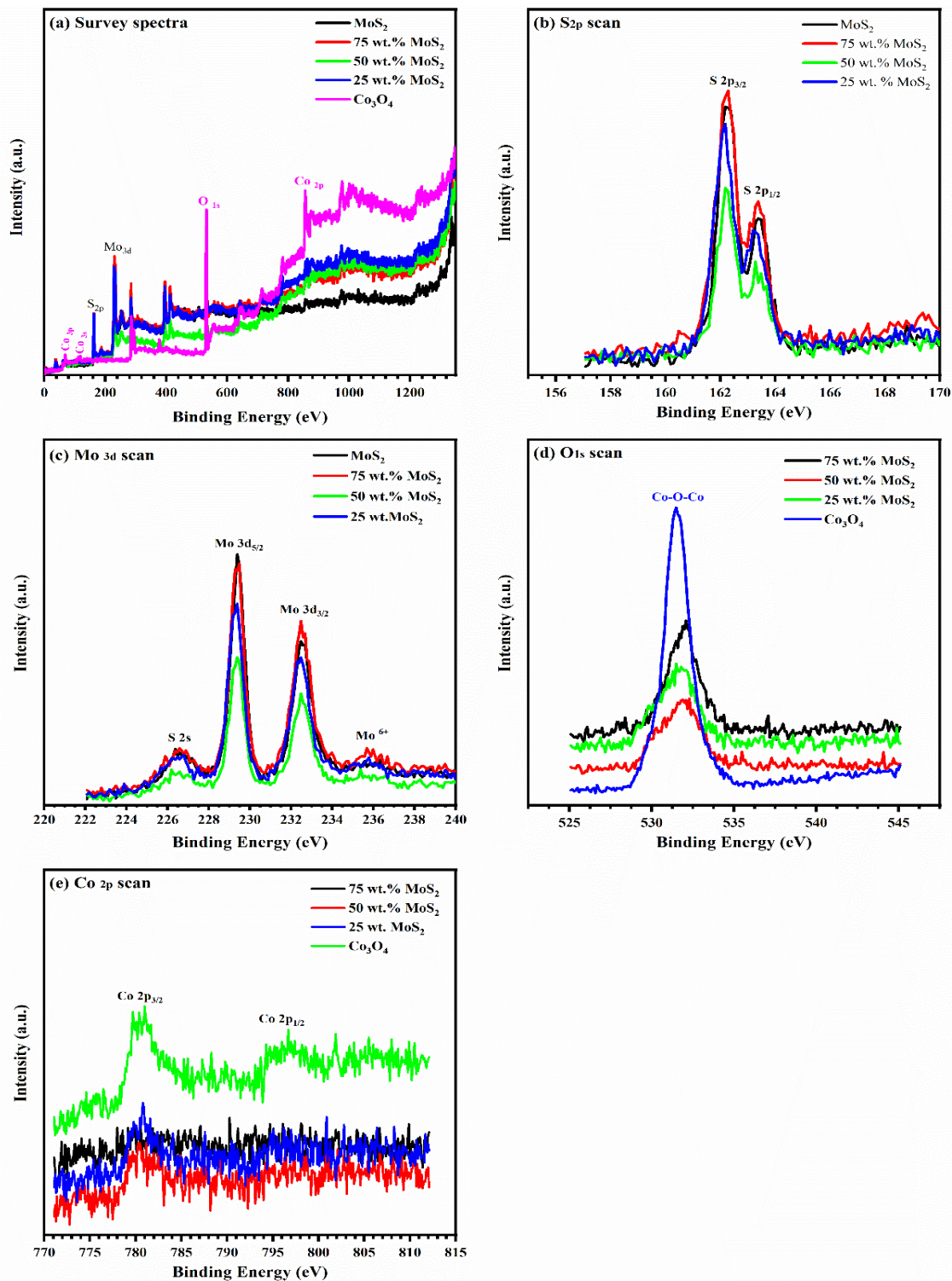


Figure 8. 14: XPS survey spectrum (a) and, high-resolution XPS scans of S 2p (b), and Mo 3d (c), O 1s (d), and Co 2p (e) of Co_3O_4 - MoS_2 heterostructure thin films.

Table 8. 5: XPS peaks positions estimated from the deconvolution of XPS scans of S_{2p} , Mo_{3d} , O_{1s} , Co_{2p} of $Co_3O_4-MoS_2$ heterostructure composites at different MoS_2 contents (wt.%)

Band	Binding Energy (eV)				
	MoS_2	75 wt. % MoS_2	50 wt. % MoS_2	25 wt. % MoS_2	Co_3O_4
S_{2p}	162.25	162.25	162.21	162.11	-
	163.49	163.44	163.4	163.31	-
Mo_{3d}	226.57	226.63	226.47	226.4	-
	229.4	229.4	229.36	229.3	-
	232.54	232.54	232.52	232.45	-
	236.2	236	235.57	235.22	-
O_{1s}	-	531.78	531.92	531.7	531.545
	-	-	530.1	529.78	-
Co_{2p}	-	780.92	780.92	780.88	780.73
	-	797	797	796.11	796.65

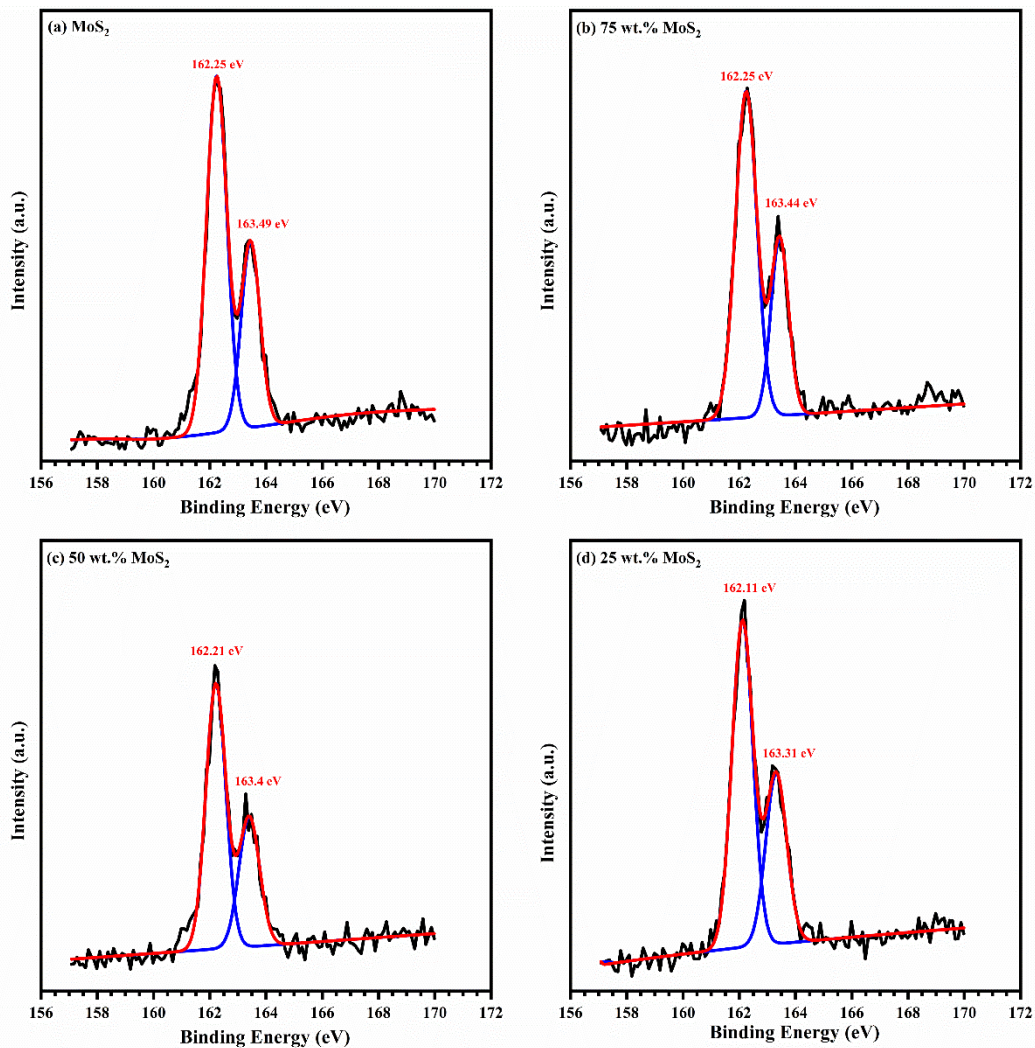


Figure 8. 15: Deconvoluted S_{2p} XPS scan of pure MoS_2 (a), 75 wt.% MoS_2 (b), 50 wt.% MoS_2 (c), and 25 wt.% MoS_2 (d) heterostructure thin films.

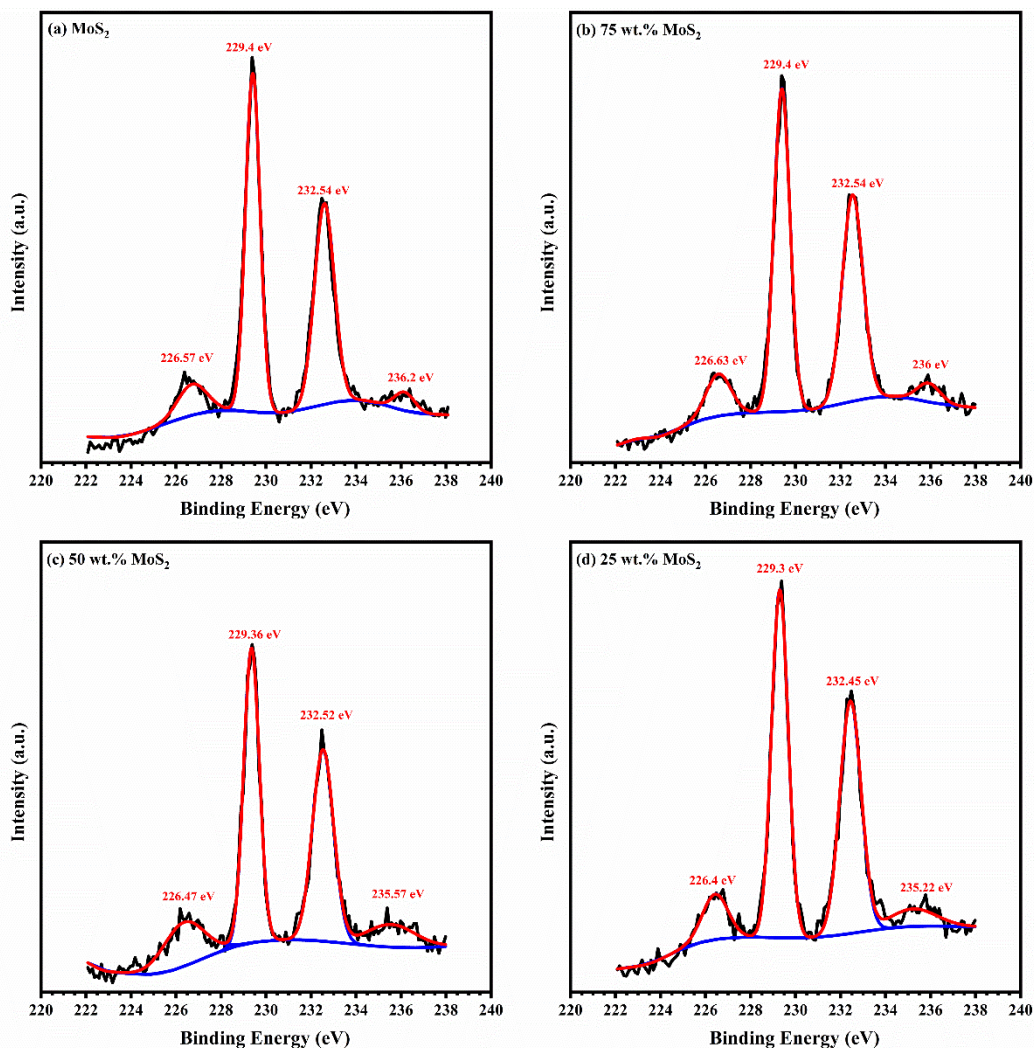


Figure 8. 16: Deconvoluted Mo 3d XPS scan of pure MoS₂ (a), 75 wt.% MoS₂ (b), 50 wt.% MoS₂ (c), and 25 wt.% MoS₂ (d) heterostructure thin films.

Furthermore, the deconvolution of the 2p_{3/2} sub-band exhibited two peaks at 780.5 eV and 781.5 eV that matched with Co³⁺ and Co²⁺ states, respectively. The deconvoluted sub-band of 2p_{1/2} states exhibited Co³⁺ states at 795 eV and Co²⁺ states at 797.5 eV. The average energy separation between the two main spin-orbital states is around 15.25 eV, which is a characteristic value for Co 2p_{3/2} and Co 2p_{1/2} orbital in Co₃O₄ [188, 189, 233, 234]. Moreover, the high-resolution Co 2p XPS scan of the heterostructure electrodes with different MoS₂ contents, **Figure 8. 18(a-c)**, showed a strong overlapping between the high and low spin states that made it difficult to distinguish between them by deconvolution. However, the observed Co 2p states (i.e., 2p_{3/2} or 2p_{1/2}) in all heterostructure electrodes exhibited a positive shift with increasing MoS₂ content compared with the pure phase of Co₃O₄, **Table 8. 5**. The observed positive shift

in the binding energy of Co 2p with increasing MoS₂ content demonstrates the strong coupling between the Co₃O₄ and MoS₂ in the deposited heterostructure films within the nanoscale range [397].

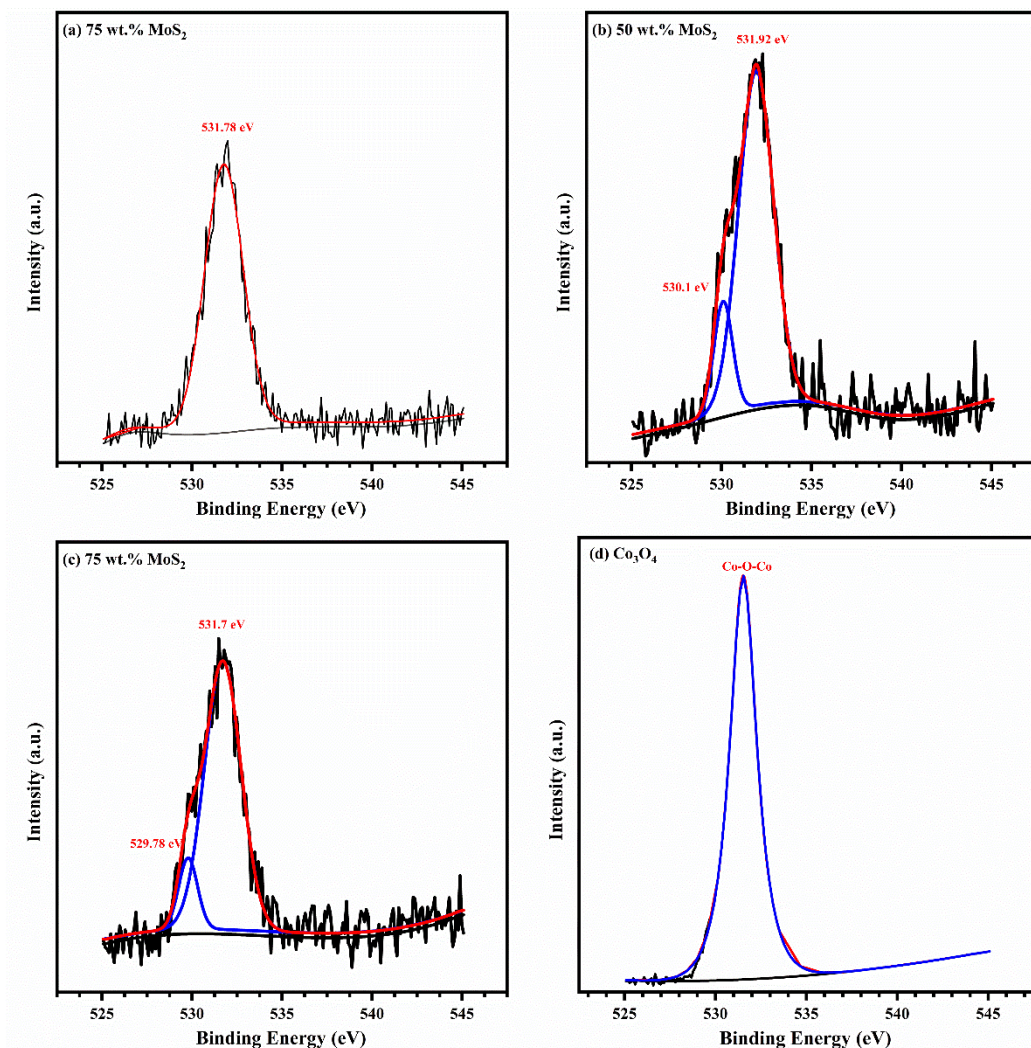


Figure 8. 17: Deconvoluted O 1s XPS scan of 75 wt.% MoS₂ (a), 50 wt.% MoS₂ (b), 25 wt.% MoS₂ (c) heterostructure thin films, and pure Co₃O₄ thin films (d).

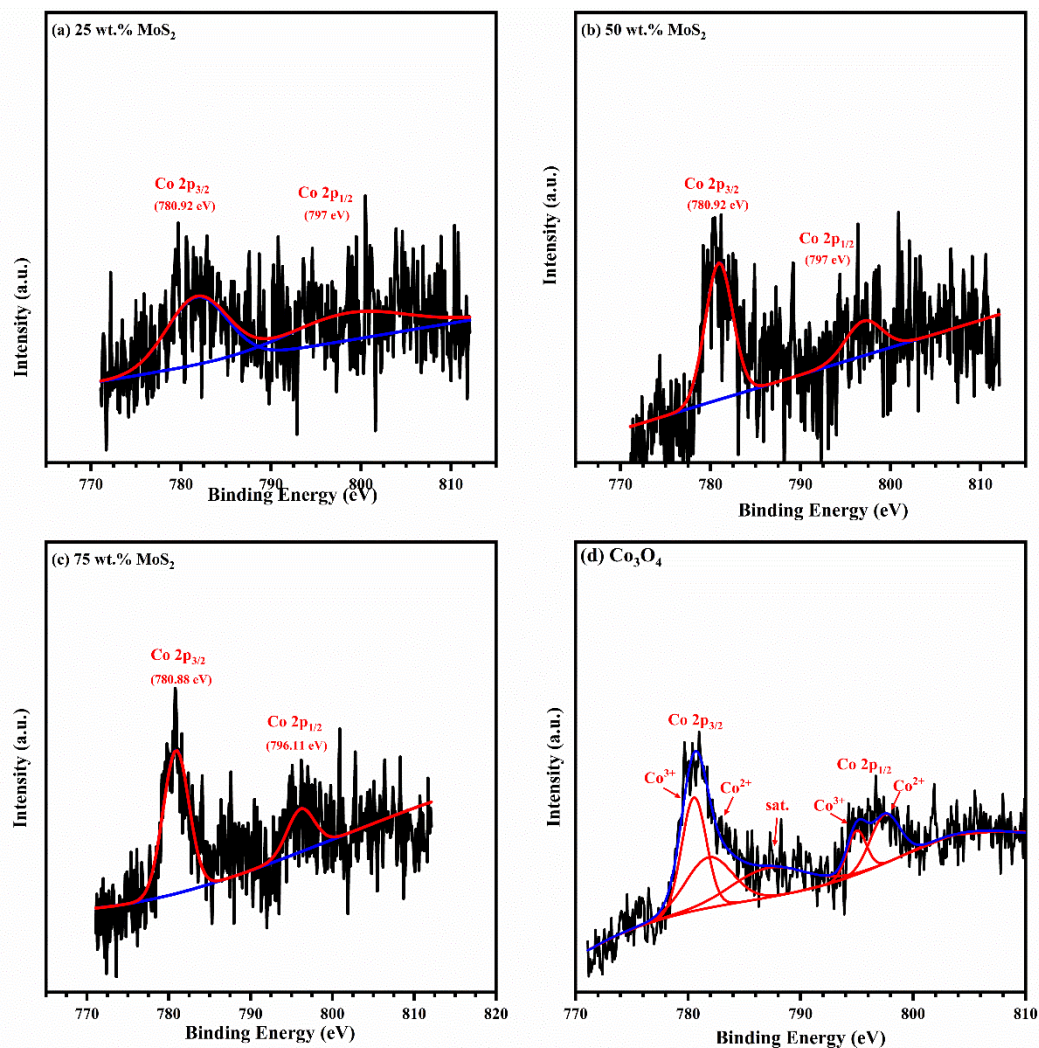


Figure 8. 18: Deconvoluted Co 2p XPS scan of 75 wt.% MoS₂ (a), 50 wt.% MoS₂ (b), 25 wt.% MoS₂ (c) heterostructure thin films, and pure Co₃O₄ thin films (d).

8. 2. 5. Electrochemical active surface area

The electrochemical active surface area (ECSA) of the nanostructured Co₃O₄-MoS₂ heterostructure electrodes was determined using capacitance components corresponding to the double-layer [78] in which the potential was linearly scanned in the non-faradaic range from 0 to 0.1 vs. Hg/HgO in 1.0 M KOH electrolyte. The C_{DL} represents the slope of the linear relationship between the current density (ΔJ) at various scan rates (ν) as described by **Eq. 2. 5**. Cyclic voltammogram plots of the Co₃O₄/NF and MoS₂/NF electrodes, as well as their heterostructure electrocatalysts at various MoS₂ contents (25, 50, and 75 wt.%), were recorded at various scan rates from 10 to 100 mV·s⁻¹, **Figure 8. 19**. A linear between ΔJ at 0.05 vs. Hg/HgO and ν were plotted for all modified electrodes, see **Figure 8. 20(e)**. The obtained C_{DL} values are

recorded in **Table 8. 6**. The estimated ECSA values in terms of C_{DL} of $\text{Co}_3\text{O}_4/\text{NF}$ and MoS_2/NF modified electrodes are 4.32 and 2.9 $\text{mF}\cdot\text{cm}^{-2}$, respectively. Moreover, the modified heterostructure electrodes exhibited improvement in the ECSA with increasing Co_3O_4 content.

8. 2. 6. Electrocatalytic activity of Co_3O_4 - MoS_2 heterogeneous electrodes

Figure 8. 20(a, b) reveals the LSV curves and the Tafel plots of the $\text{Co}_3\text{O}_4/\text{NF}$, MoS_2/NF , and their heterostructure electrocatalysts at various MoS_2 contents (25, 50, and 75 wt.%) in the potential range from 1.2 to 1.8 V vs. RHE to study the OER activity in 1.0 M KOH. As shown, the modified electrode with nanostructured Co_3O_4 had an OER onset potential of 1.6 V. Modified electrodes with the MoS_2 nanosheets and the nanostructured composites with 25, 50, and 75 wt.% MoS_2 content possessed lower onset potentials extending from 1.52 to 1.54 V. The OER overpotential (η) and the associated Tafel slope values were estimated according to **Eq. 2. 2** and **Eq. 2.4**. The OER charge transfer resistance (R_{ct}) at 300 mV was determined from the Nyquist plots as illustrated in **Figure 8. 20(c)** and recorded in **Table 8. 6**. The modified electrodes with Co_3O_4 NPs provided a current density of 10 $\text{mA}\cdot\text{cm}^{-2}$ at an η of 349 mV, a Tafel slope of 77 $\text{mV}\cdot\text{dec}^{-1}$, and an R_{ct} of 13.5 Ω . In contrast, the modified electrode with MoS_2 nanosheets exhibited better OER electrocatalytic activity with a small η of 310 mV at 10 $\text{mA}\cdot\text{cm}^{-2}$, a small Tafel slope of 64 $\text{mV}\cdot\text{dec}^{-1}$, and a small R_{ct} of 5 Ω . Moreover, the modified electrode with the nanostructured Co_3O_4 - MoS_2 composites exhibited higher efficiency and an overall improvement in the OER electrocatalytic activity due to the improvement in the synergy between the various electroactive species at the surface of the hybrid electrocatalysts catalysts, in which increasing MoS_2 content resulted in a reduction of onset potential, η , and Tafel slope values. Moreover, the heterostructure electrocatalysts with 75 wt.% MoS_2 content revealed the best combination for the OER activity with the smallest η value of 298 mV at 10 $\text{mA}\cdot\text{cm}^{-2}$, a very small Tafel slope of 46 $\text{mV}\cdot\text{dec}^{-1}$, and an R_{ct} of 2.5 Ω . This behavior was attributed to the improvement in the charge transfer kinetics. Moreover, the OER long-term stability @50 $\text{mA}\cdot\text{cm}^{-2}$ was verified for 50 hours in 1.0 M KOH as shown in **Figure 8. 20(d)**.

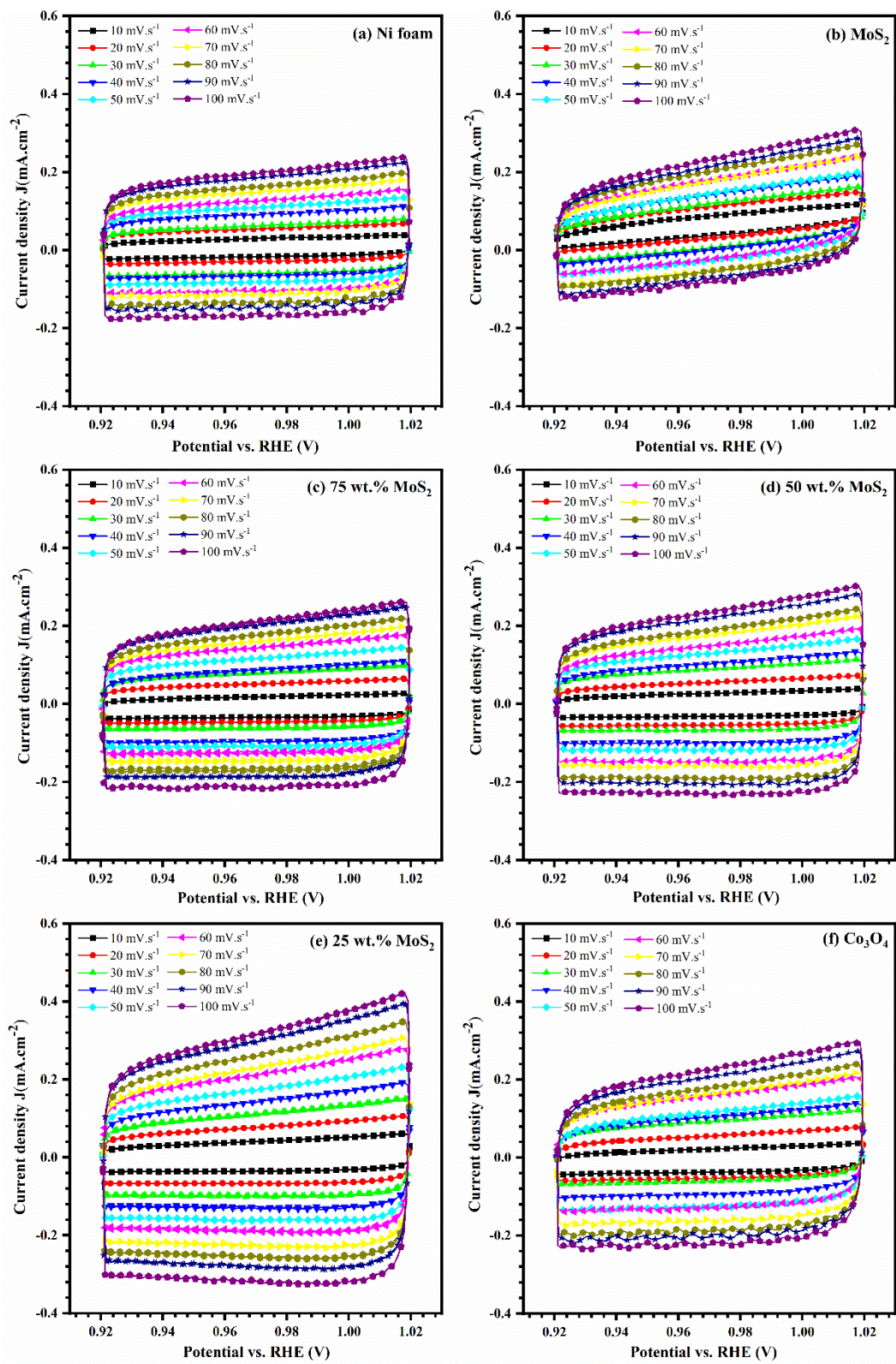


Figure 8. 19: CV plots of $\text{Co}_3\text{O}_4\text{-MoS}_2$ hybrid catalysts at different scan ranges in the non-faradic region from 0.924 to 1.024 vs. RHE (0 to 0.2 vs. Hg/HgO).

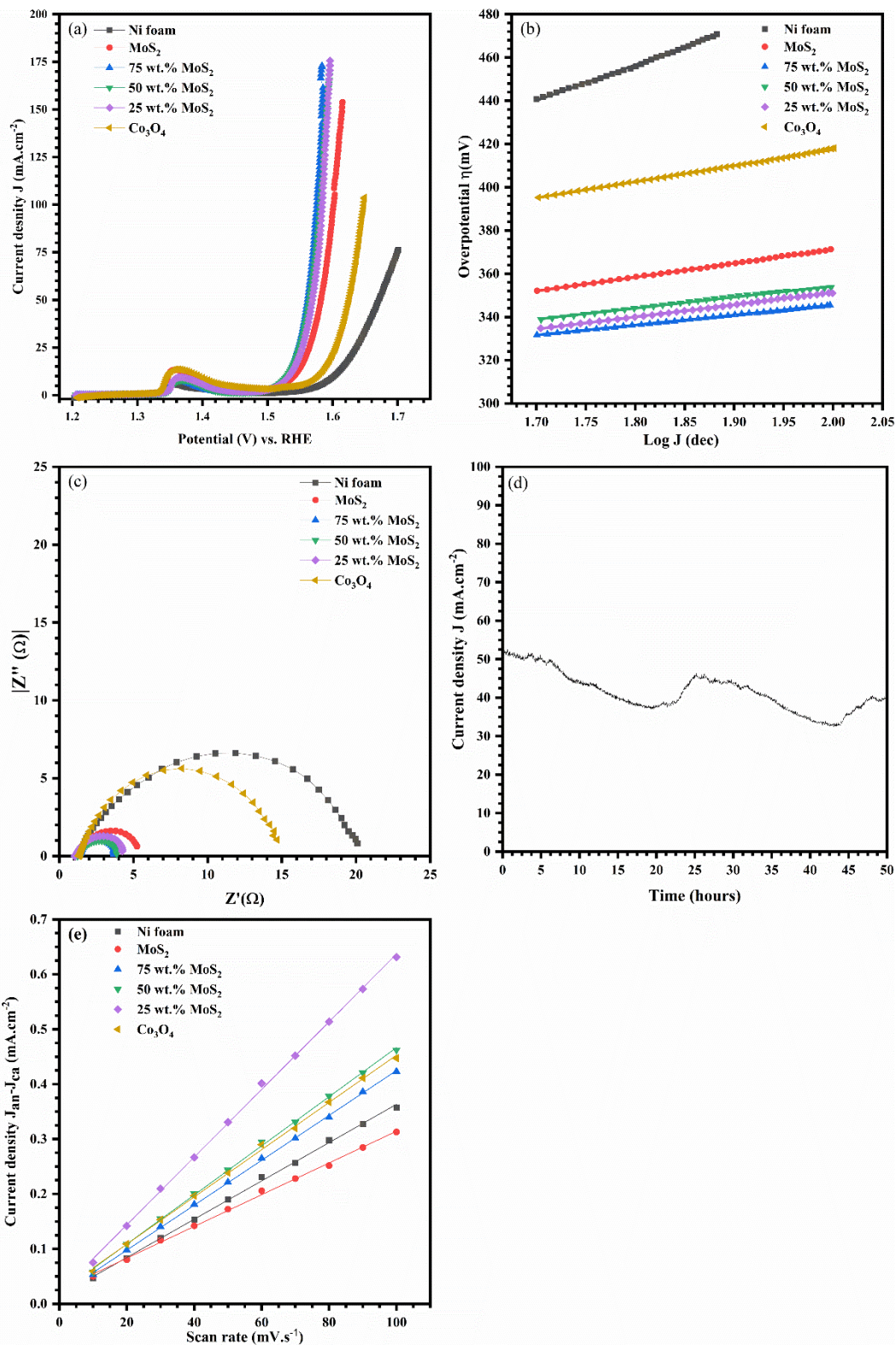


Figure 8.20. OER LSV curves (a), Tafel plots (b), Nyquist plots (c), and stability test at 50 mA.cm⁻² for 50 hours using Co₃O₄-MoS₂ heterostructure electrodes (d), and the current density vs. scan rates plot in the non-faradic region at different MoS₂ contents (e).

Table 8. 6: Values of η , Tafel slope, R_{ct} and ECSA of the modified electrode with Co_3O_4 - MoS_2 composites at various MoS_2 contents.

Composition ratio (wt.%)		Overpotential (mV)					Tafel slope (mV dec ⁻¹)	R_{ct} (W)	ECSA (mF cm ⁻²)	
Co_3O_4	MoS_2	10	20	50	100	150				
Bare Ni Foam		372	398	440	-	-	164	19.5	3.5	
OER	0	100	311	327	352	372	385	64	5	2.9
	25	75	298	312	331	345	353	46	2.5	4.1
	50	50	300	314	334	352	361	51	3	4.47
	75	25	303	318	338	354	363	56	3.5	6.16
	100	0	349	370	398	422	-	77	13.5	4.32

8.3. Summary

Nanosized Co_3O_4 - MoS_2 /Ni foam heterostructure electrodes with various MoS_2 content (25, 50, and 75 wt.%) were fabricated using NPDS from initial powders of Co_3O_4 and MoS_2 microparticles. The obtained nanostructured thin films were utilized to investigate the OER in 1.0 M KOH. The existence of Co_3O_4 and MoS_2 constituents at the surface of the nanostructured Co_3O_4 - MoS_2 thin films at different MoS_2 concentrations was identified by Raman spectra that revealed several characteristic first and second-order Raman vibration mode that belonged to either the pure phase of Co_3O_4 (F_{2g} , E_g , and A_{1g}) or MoS_2 (E_{1g} , A_{1g} , E_{12g} , and LA). By comparing Raman spectra for the corresponding microparticle, we observed a positive spectral shift for all characteristic Raman peaks in the fabricated heterostructure electrodes due to the fragmentation to smaller size ranges. Further investigations of the nature of the active states at the interface of the heterostructure electrodes were performed using XPS. High-resolution XPS scan of Co 2p, O 1s, Mo 3d, and S 2p revealed positive shifts with increasing MoS_2 content, demonstrating synergetic improvement in the nanostructured Co_3O_4 - MoS_2 hybrid electrocatalysts. Linear sweep voltammetry plots of Co_3O_4 - MoS_2 in 1 M KOH revealed that the incorporation of MoS_2 in the heterostructure electrodes led to OER activity enhancement, which the heterostructure electrode with 75 wt.% MoS_2 exhibited an efficient combination with an overpotential of 298 mV at 10 mA·cm⁻², a small Tafel slope of 46 mV·dec⁻¹, and OER stability at 50 mA·cm⁻² for 50 hours.

Chapter 9:

*Facile One-step Deposition of Co_3O_4 - MoS_2 Nanocomposites
using a Vacuum Kinetic Spray Process for Non-Enzymatic
 H_2O_2 Sensing*

9.1. Overview

Accurate and real-time evaluation of hydrogen-peroxide concentrations can serve as a useful tool for the diagnosis of various disease stages [398-400]. Enzymatic biosensors offer efficient and sensitive H_2O_2 detection under certain circumstances [401]. However, high fabrication costs and low recycling reproducibility have restricted the commercialization of enzymatic H_2O_2 detection sensors. Considerable resources have been devoted to developing alternative techniques for non-enzymatic H_2O_2 detection using direct oxidation of H_2O_2 and an electrocatalytic process at the interface between modified electrodes and various metallic or semiconductor nanostructures characterized by a fast response, high stability, and recyclability [402-404]. However, a metallic non-enzymatic biosensor reportedly displayed high electrocatalytic efficiency toward the H_2O_2 detection [405, 406], and high costs continue to restrict the commercial application of metallic-based biosensors. Transition-metal electrocatalysts with high electrocatalytic activity are popular alternatives for metallic electrocatalysts because of their availability and low costs, as well as the chemical stability associated with resistance to corrosion [192, 193, 407]. Co_3O_4 -based materials and composites are promising electrocatalysts for non-enzymatic detection of H_2O_2 , either by oxidation or reduction with effective sensitivity and a wide linear-detection range [216, 217, 248, 392, 408, 409]. The pure phase of nanostructured Co_3O_4 offers a wide surface area and a high concentration of electroactive sites, but poor electrical conductivity and the tendency of the internal grains to aggregate may result in slow charge-transfer kinetics and reduce electrochemical performance [410].

One of the most effective techniques to improve the charge transfer kinetics of nanostructured Co_3O_4 is to assemble hybrid composites with layered structures such as carbon-based or dichalcogenide materials, including MoS_2 . The synergy enhancement between the electroactive species of spinel Co_3O_4 (i.e., Co^{2+} and/or Co^{3+}) and such layered structures increases the electroactive species concentration as well as the development of charge-transfer kinetics, which are accompanied by an overall enhancement in electrochemical performance. In a previous study, we fabricated a hybrid electrocatalyst of Co_3O_4 -graphene nanosheets with superior detection sensitivity to H_2O_2 reduction. The hybrid electrocatalyst was associated with enhanced charge transfer and an increase in electroactive-site concentration due to the high spin state of spinel Co_3O_4 (i.e. Co^{2+}) [392]. Wang et al. [214] prepared nanostructured Co_3O_4 /glassy carbon using pyrolysis, with the results exhibiting a relatively wide linear H_2O_2 detection range of 0.4 μM to 2.2 mM in 0.1 M NaOH and relatively low sensitivity of 120.55 $\mu\text{A}\cdot\text{mM}^{-1}\cdot\text{cm}^{-2}$. Dai et al. [216] synthesized Au@C- Co_3O_4 hybrid electrodes using high-temperature pyrolysis at 450 °C for 4 h as well as

oxidative calcination at 250 °C for 2 h. The modified electrocatalyst achieved a sensitivity toward H₂O₂ reduction of 7553 μA·mM⁻¹·cm⁻² within a small linear detection range of 0.05 to 100 μM. Kong et al. [217] reported preparing Co₃O₄-reduced graphene oxide (rGO) nanostructured composite electrocatalysts using a multi-stage hydrothermal process, with the resulting composite exhibiting relatively high H₂O₂ sensitivity of 1140 μA·mM⁻¹·cm⁻². Kogularasu et al. [218] synthesized polyhedral Co₃O₄-rGO composites electrocatalysts with high activity toward the reduction of H₂O₂, detection sensitivity of 3450 μA·mM⁻¹·cm⁻², and relatively small linear detection range of 0.05 to 400 μM.

In our previous work, we deposited various thin-film semiconductor nanostructures that demonstrated high electrochemical performance for supercapacitor application [79], high electrocatalytic activity toward oxygen and hydrogen evolution reactions in alkaline medium [261, 262], and superior non-enzymatic detection of H₂O₂ reduction in alkaline medium [392] using a nanoparticle deposition system (NPDS), which is a vacuum kinetic spray process. The NPDS involved the deposition of nanostructured ceramic-based materials and their alloys at room temperature without any binders or dangerous chemicals [221, 277]. In contrast with other deposition techniques, the NPDS takes into consideration the cost and fabrication time of the desired electrocatalyst [100]. The NPDS can also be scaled up for large deposition areas, such as those involved in WO₃ thin films with areas of 1×1 m² [99]. Based on a literature survey, nanostructured Co₃O₄-MoS₂ hybrid electrocatalysts have not been previously examined as non-enzymatic sensors for H₂O₂ oxidation. In the present work, we fabricated titanium-modified electrodes with Co₃O₄-MoS₂ nanocomposites (NCs) containing 25, 50, and 75 wt.% Co₃O₄ using a one-step deposition by the NPDS at room temperature without any post-treatment after the deposition process. The results revealed high electrocatalytic activity toward the oxidation of H₂O₂ in an alkaline medium. Compared with the other reported techniques, ours is a simple, one-step process that can rapidly generate composite catalysts with no chemical hazards, and in a manner suitable for scaling up to large-volume production. We also evaluated the electrochemical performance of non-enzymatic detection of H₂O₂ oxidation by Co₃O₄-MoS₂ NC/Ti with different Co₃O₄ contents in an alkaline medium.

9.2. Results and Discussion

9.2.1. XRD analysis of Co₃O₄-MoS₂ composites

The crystal structure of Co₃O₄ and MoS₂ microparticles, and their mixed powder with 25, 50, and 75 wt.% Co₃O₄ content was investigated using the XRD patterns as demonstrated in **Figure**

9. 1(a). The XRD pattern of Co_3O_4 micro-sized powder exhibited several characteristic peaks, which matched with the face-centered cubic structure of spinel Co_3O_4 (space group: Fd-3m , ICDD: 43-1003) [222]. The XRD pattern of MoS_2 micro-sized powder revealed several diffraction peaks at 28.96, 32.62, 33.44, 35.82, 39.4, 44.1, 49.74, 55.94, 58.28, and 60.1 corresponding to (004), (100), (101), (102), (103), (006), (105), (110), and (008), respectively, of bulk MoS_2 hexagonal structure (space group: $\text{P6}_3/\text{mmc}$, ICDD: 03-065-1951, PDF 2010). The XRD patterns of the Co_3O_4 - MoS_2 mixed powder with 25, 50, and 75 wt.% Co_3O_4 content exhibited the presence of both phases, cubic Co_3O_4 , and hexagonal MoS_2 without the evolution of new secondary phases as a result of the ball milling process.

Figure 9. 1(b) revealed the XRD patterns of Co_3O_4 - MoS_2 heterostructure composites thin film on titanium sheet at different Co_3O_4 content (25, 50, and 75 wt.%). The XRD of the bare titanium sheet demonstrated three distinctive peaks located at 40.08, 52.92, and 70.56° correspond to (102), (2-11), and (102) crystalline planes of titanium hexagonal structure (space group: $\text{P6}/\text{mmm}$) [279, 280]. In the case of the deposited thin films of Co_3O_4 , MoS_2 , and their heterostructure composites there are some peaks with a small intensity that matches with the structural phased of deposited material (Co_3O_4 and MoS_2 species) as well as the characteristic peaks of titanium sheet holding substrate. This indicated the particle fragmentation to lower domain sizes at the surface of the deposited films, which is a common behavior in most of the deposited thin films on a crystalline metallic substrate with kinetic spray technique [79, 261, 262]. Besides, the low crystallinity degree observed in Co_3O_4 -based nanostructured composites thin films is mostly accompanied by a large concentration of interfacial surface defect at the grain boundaries that increases with decreasing domain size. This large number of metal oxide surface defects can act as electrocatalytic active sites for many electrochemical applications [223]. Hence, the micro-Raman analysis was performed for precise identification of the actual active phases at the surface Co_3O_4 - MoS_2 NCs thin film on the titanium sheet as discussed in the next section.

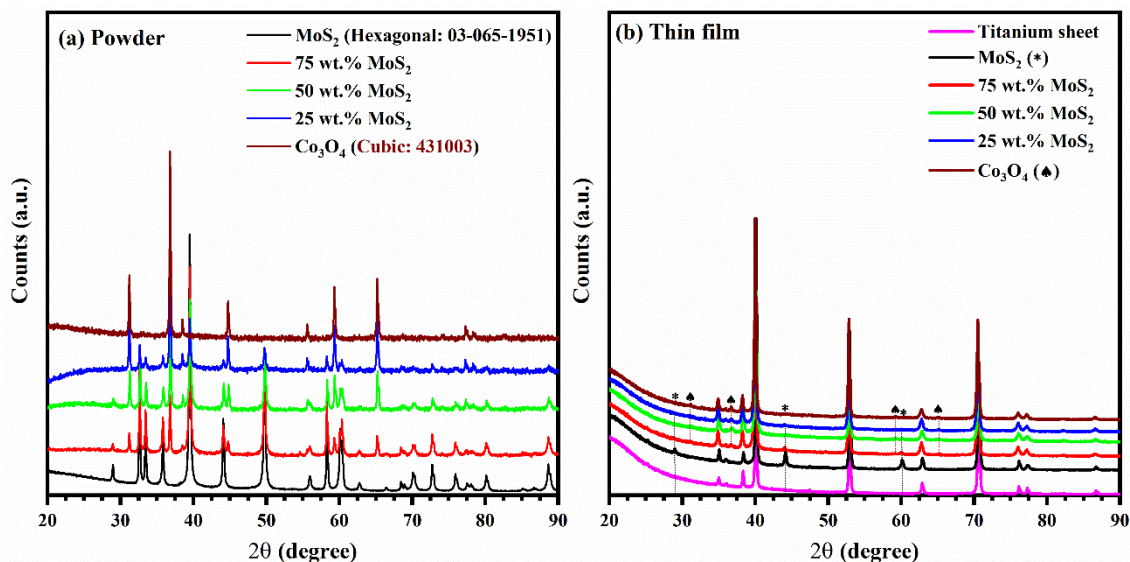


Figure 9. 1: XRD patterns of $\text{Co}_3\text{O}_4\text{-MoS}_2$ composites in powder form (a) and nanostructured thin film deposited on titanium sheet.

9. 2. 2. Surface morphology of $\text{Co}_3\text{O}_4\text{-MoS}_2$ composites

9. 2. 2. 1. $\text{Co}_3\text{O}_4\text{-MoS}_2$ micro-sized powder

The surface morphology of MoS_2 micro-sized powder is shown in **Figure 9. 2(a, b)**, which reveals the layered structure of the micro-sized flakes (0.5–3 μm) with various orientations. The surface morphology of the pure phase Co_3O_4 micro-powder, as shown by SEM in **Figure 9. 3(e, f)** consisted of several aggregated particles with a semispherical morphology that exhibited a range of sizes 0.5 to 5 μm . SEM images of surface morphology of mixed micro-sized powder of $\text{Co}_3\text{O}_4\text{-MoS}_2$ with various Co_3O_4 contents (25, 50, and 75 wt.%) are provided in **Figure 9. 2(c, d)** and **Figure 9. 3(a-d)**. The SEM images revealed mixed morphology of micro-sized flakes and micro-sized spheres for both micro-sized phases of Co_3O_4 and MoS_2 . The measured dimensions had the same size range without any noticeable reduction caused by the ball milling during the mixing process. **Figure 9. 4** depicts energy-dispersive X-ray spectroscopy (EDS) spectra of the micro-sized powder of Co_3O_4 , MoS_2 , and their mixed powder at different Co_3O_4 contents. The EDS spectra of mixed powders displayed characteristic signals corresponding to O_K , Co_K , S_K , and Mo_L , indicating the presence of Co_3O_4 and MoS_2 species in the powder provided for the deposition process using the NPDS. The amounts of each element in the pure phase of Co_3O_4 , MoS_2 as well as their mixed powders were estimated and recorded in **Table 9. 1**. In Co_3O_4 -based materials and composites, the elemental ratio of Co_K/O_K provided useful information about the cation's distribution efficiency with the spinel structure of Co_3O_4 , for which the known theoretical value is 0.75,

and the decrease of this value was correlated with a deficiency in Co species within the bulk lattice and at the interface between the grains of the spinel structure [227, 229]. The Co_K/O_K elemental ratio in the case of Co_3O_4 microparticles is 0.347, which is further decreased in the case of mixed powders with 0.065, 0.145, and 0.169, corresponding to Co_3O_4 contents of 25, 50, and 75 wt.%, respectively. This indicates that powder mixing between Co_3O_4 and the layered structure of the MoS_2 resulted in an increase in the deficiency of cobalt species in the Co_3O_4 spinel structure during the ball-milling process.

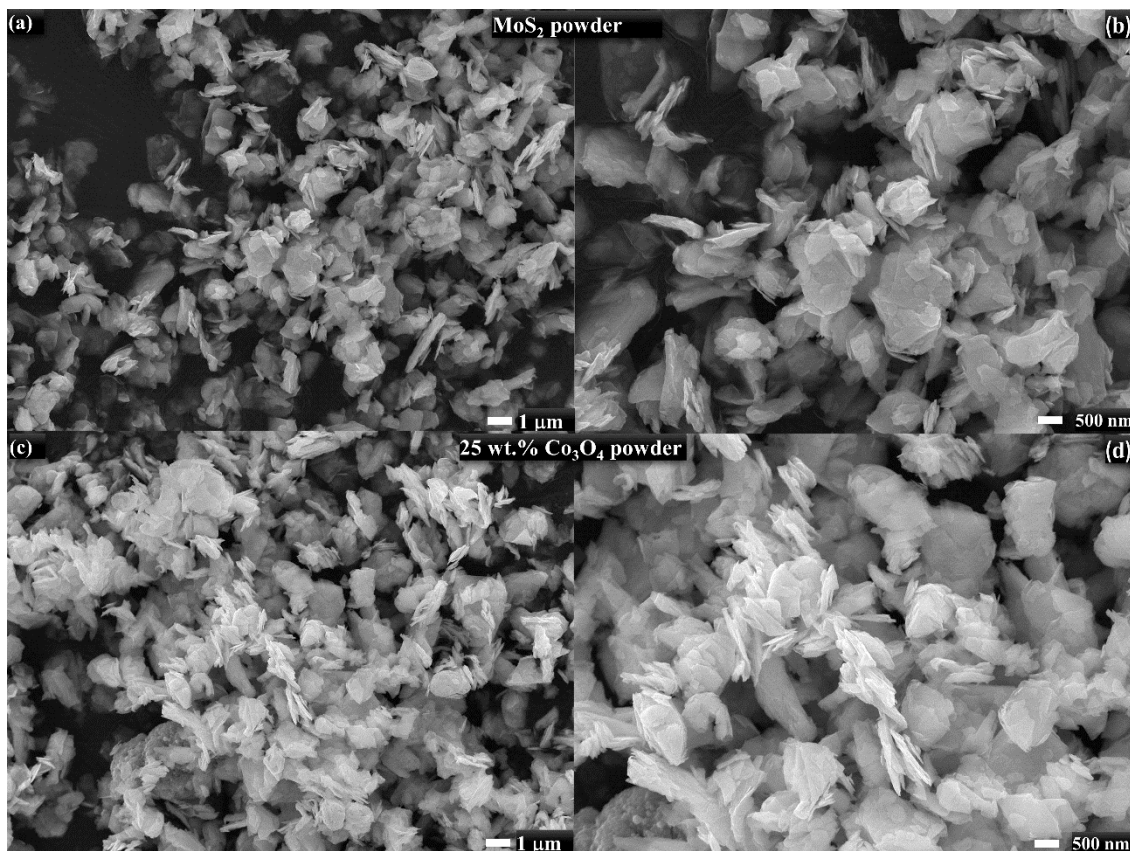


Figure 9. 2: SEM images of micro-sized particles of (a, b) MoS_2 , and (c, d) composites with 25 wt.% Co_3O_4 .

Table 9. 1: EDS elemental analysis of mixed Co_3O_4 - MoS_2 microparticles

Mixed powder (wt.%)		EDS elemental analysis (at. %)				
Co_3O_4	MoS_2	S_K	Mo_L	O_K	Co_K	Co_K/O_K
0	100	67.28	32.72	-	-	-
25	75	30.9	17.2	48.72	3.18	0.065
50	50	24.01	12.29	55.62	8.08	0.145
75	25	20.32	9.76	60.22	10.15	0.169
100	0	-	-	64.77	22.47	0.347

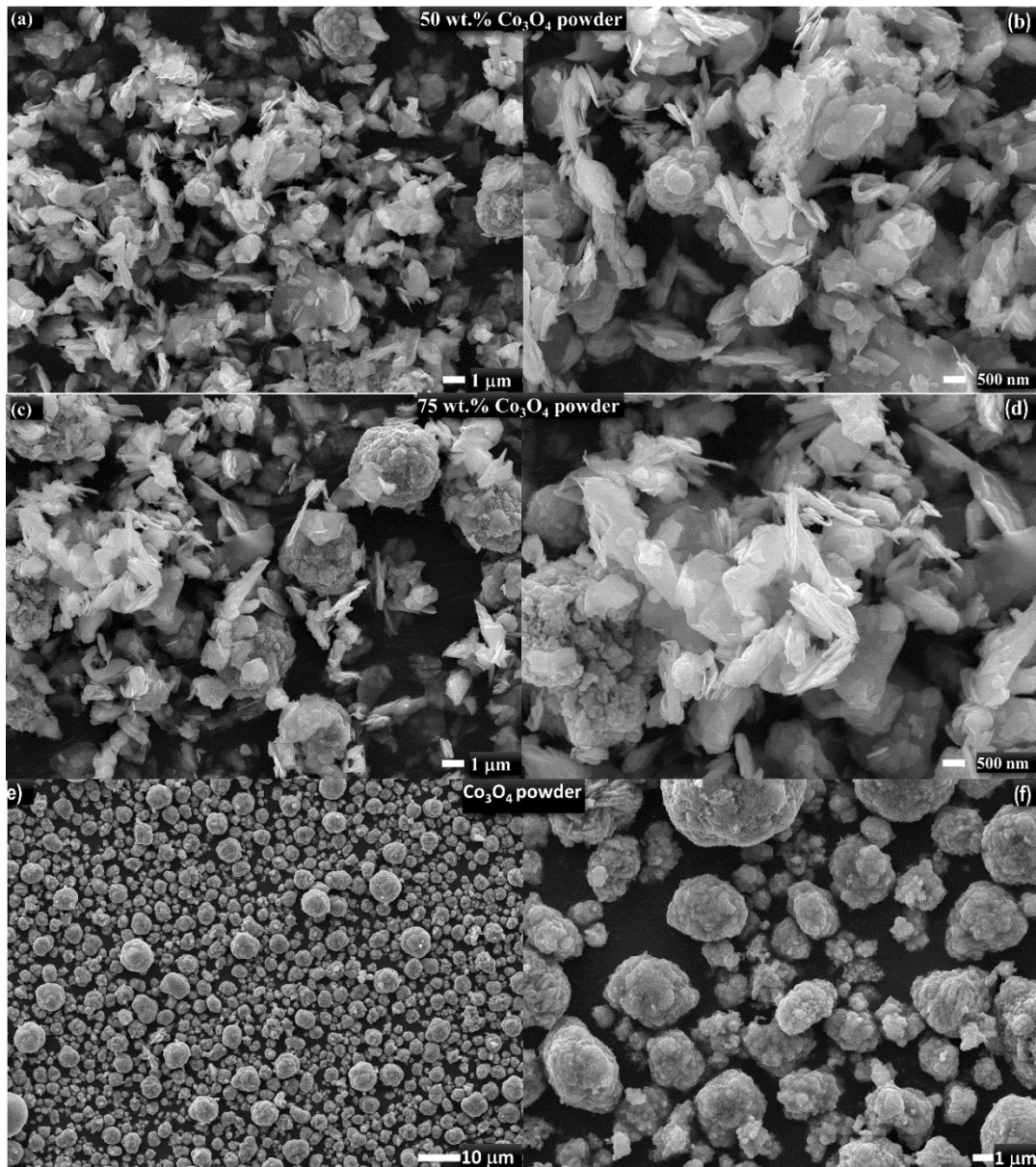


Figure 9. 3: SEM images of micro-sized particles of composites with (a, b) 50 wt.%, (c, d) 75 wt. % Co₃O₄, and (e, f) pure Co₃O₄ powder

Table 9. 2: EDS elemental analysis of nanocomposite Co₃O₄-MoS₂ thin films a titanium sheet.

Composite (wt.%)		EDS elemental analysis (at.%)					
Co ₃ O ₄	MoS ₂	Ti _K	S _K	Mo _L	O _K	Co _K	Co _K /O _K
0	100	43.83	35.99	20.17	-	-	-
25	75	35.04	3.95	2.3	52.23	6.48	0.124
50	50	53.49	1.35	0.65	42.03	2.49	0.059
75	25	33.06	1.63	0.94	31.47	5.51	0.175
100	0	44.19	-	-	52.87	2.94	0.0556

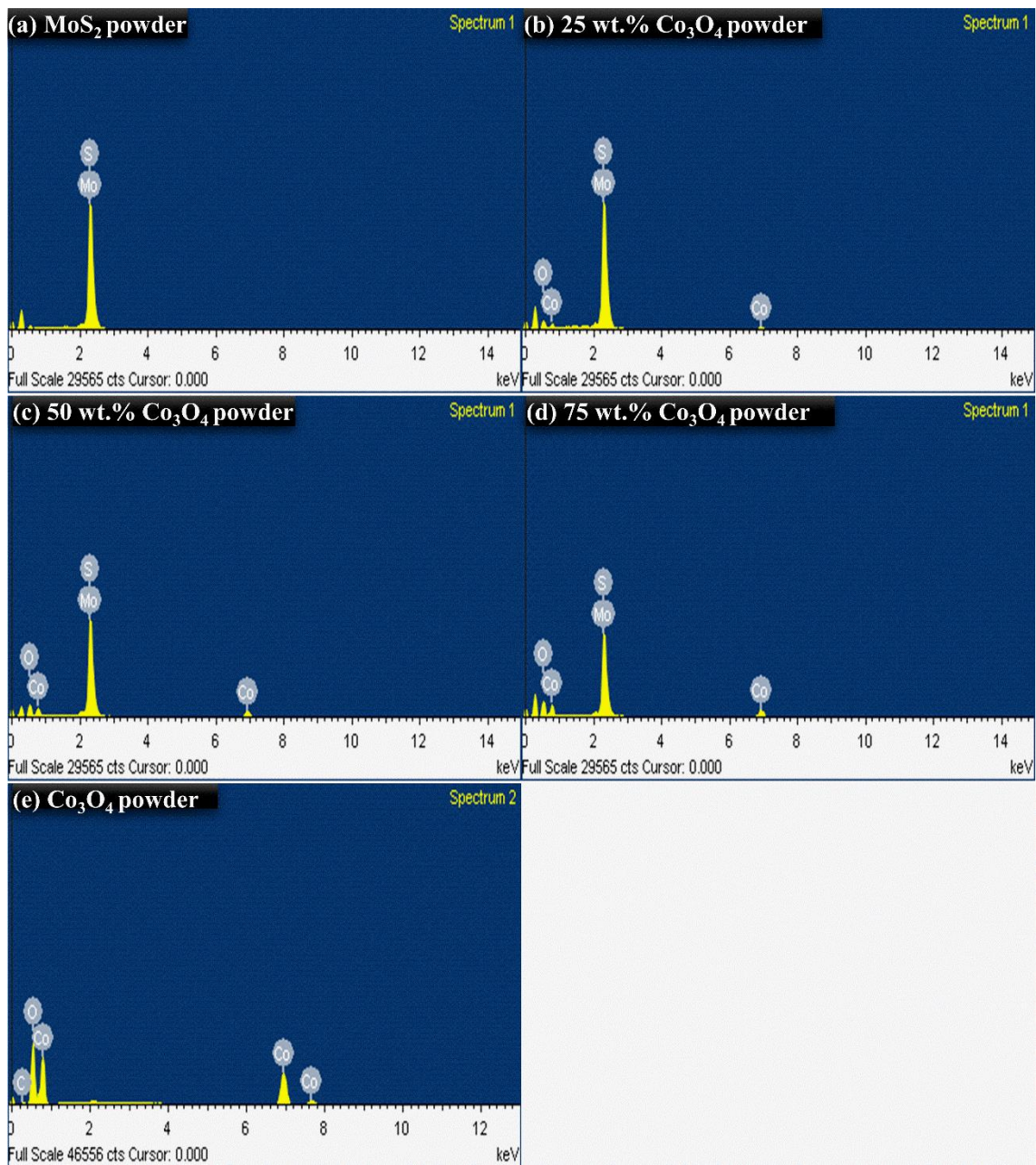


Figure 9. 4: Elemental analysis of EDS spectra of micro-sized powder before deposition of Co_3O_4 - MoS_2 composites at different Co_3O_4 contents.

9. 2. 2. 2. $\text{Co}_3\text{O}_4\text{-MoS}_2$ hybrid composites on titanium sheets

The images of titanium-modified electrodes from high-spatial-resolution SEM of MoS_2 nanosheets are shown in **Figure 9. 5(a, b)** exhibit a sheet morphology with dimensions in the nano-size range (100 nm ~ 500 nm). A layered structure of MoS_2 sheets was observed after the fragmentation of the initial micro-sized flakes to nanosized sheets. **Figure 9. 6(e, f)** depicts SEM images of the titanium-modified electrode with Co_3O_4 nanostructures. The semispherical Co_3O_4 microparticles were completely fragmented to the nano-size range and exhibit a sheet morphology (average lateral length ≤ 100 nm). Comparing SEM images for the pure phase of Co_3O_4 and MoS_2 at the same length scale, the microstructure roughness of the titanium modified electrode with Co_3O_4 nanosheets is expected to be higher than that of layered structured MoS_2 nanosheets. SEM images of the modified titanium electrodes with hybrid nanostructured composites of $\text{Co}_3\text{O}_4\text{-MoS}_2$ at Co_3O_4 contents of 25, 50, and 75 wt.% are shown from **Figure 9. 5(c, d)** to **Figure 9. 6(a, d)**.

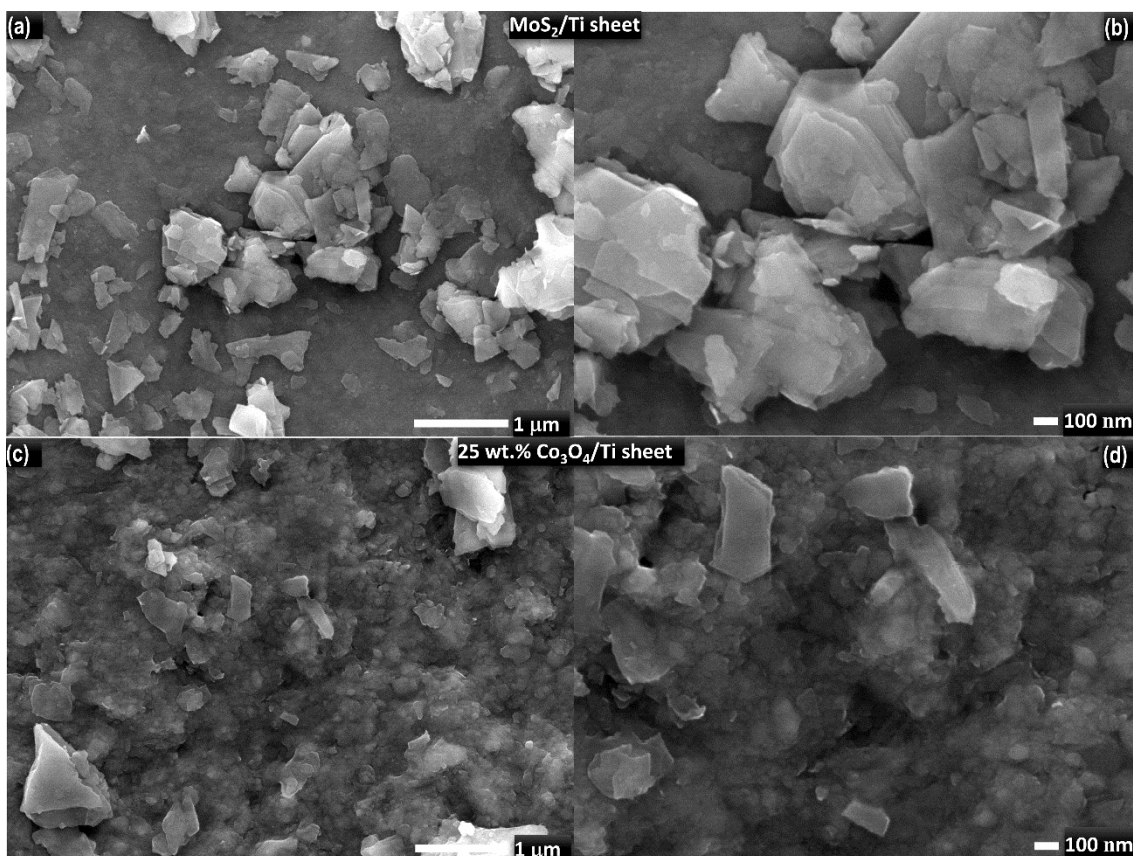


Figure 9. 5: SEM images of MoS_2/Ti (a, b), and 25 wt.% $\text{Co}_3\text{O}_4/\text{Ti}$ (c, d)

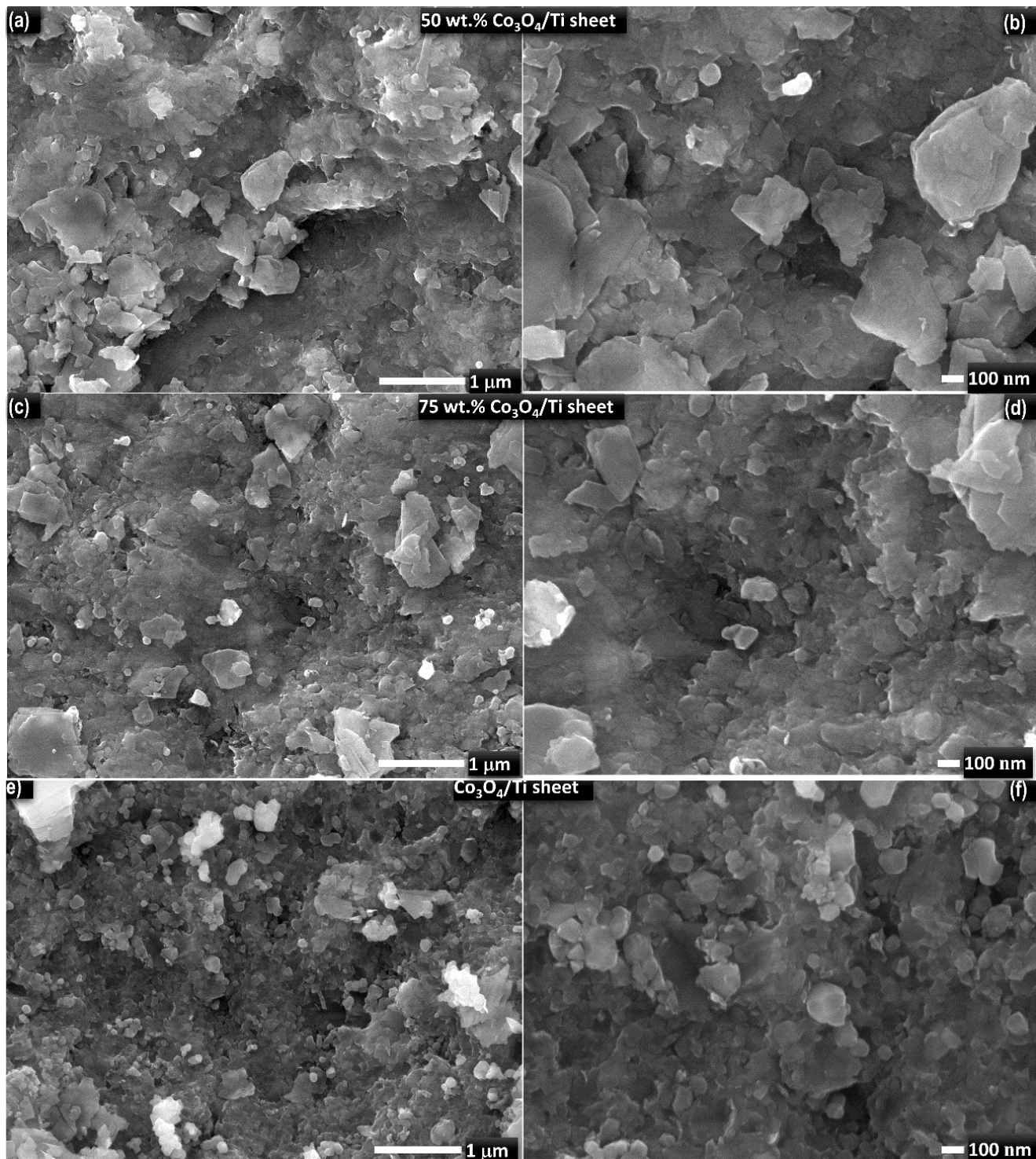


Figure 9. 6: SEM images of composites with 50 wt.% $\text{Co}_3\text{O}_4/\text{Ti}$ (a, b), 75 wt.% $\text{Co}_3\text{O}_4/\text{Ti}$ (c, d), and $\text{Co}_3\text{O}_4/\text{Ti}$ (e, f)

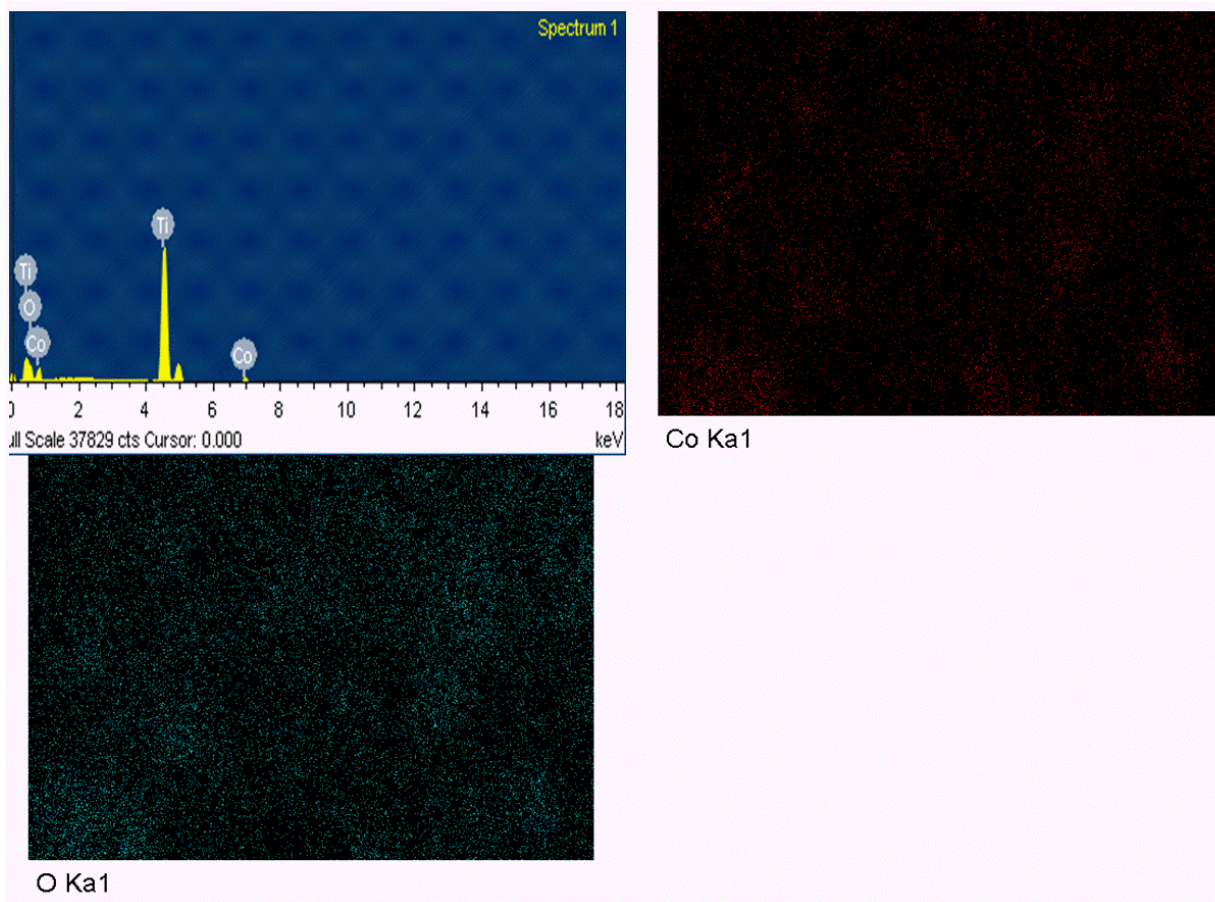


Figure 9. 7: Elemental analysis using EDS spectrum and corresponding mapping of nanostructured Co_3O_4 thin films on a titanium substrate.

The hybrid composites displayed a nanosheet morphology, with a two-size range less than 100 nm expected for Co_3O_4 species and other sheets with dimensions more than 100 nm related to MoS_2 at the surface of the deposited films. The presence of Co_3O_4 helped fragment the MoS_2 layer to a size comparable to MoS_2 -deposited thin films. All titanium modified electrodes with Co_3O_4 - MoS_2 hybrid composites exhibited a wide size distribution of fragmented particles during the deposition process, which was associated with the merging of particle grain boundaries. This can be illustrated in more detail according to the deposition mechanism of the microparticles by the NPDS: First, the microparticles carried by a pressure difference of compressed air and a vacuum acquired kinetic energy through the converging-diverging nozzle outlet. This increase in the kinetic energy of the microparticles can cause an inelastic collapse between the accelerated particles and the hard substrate. Second, local thermal heating is expected due to the inelastic impact between the accelerated powder and the fixed substrate. The heating can lead to the merging of deposited grains and cause the agglomeration in the SEM images [230, 231]. Elemental

EDS analysis and the corresponding mapping of the titanium-modified electrodes with nanostructured Co_3O_4 , MoS_2 as well as their hybrid nanostructured composites are illustrated in **Figure 9. 7** through **Figure 9. 11**. The estimated elemental percentage of Co_3O_4 and MoS_2 (i.e., O_K , Co_K , Mo_L , and S_K) are provided in **Table 9. 2**. Based on the provided microstructure elemental mapping of all deposited thin films we found that both Co_3O_4 and MoS_2 species are distributed homogeneously within the lateral area of the deposited films.

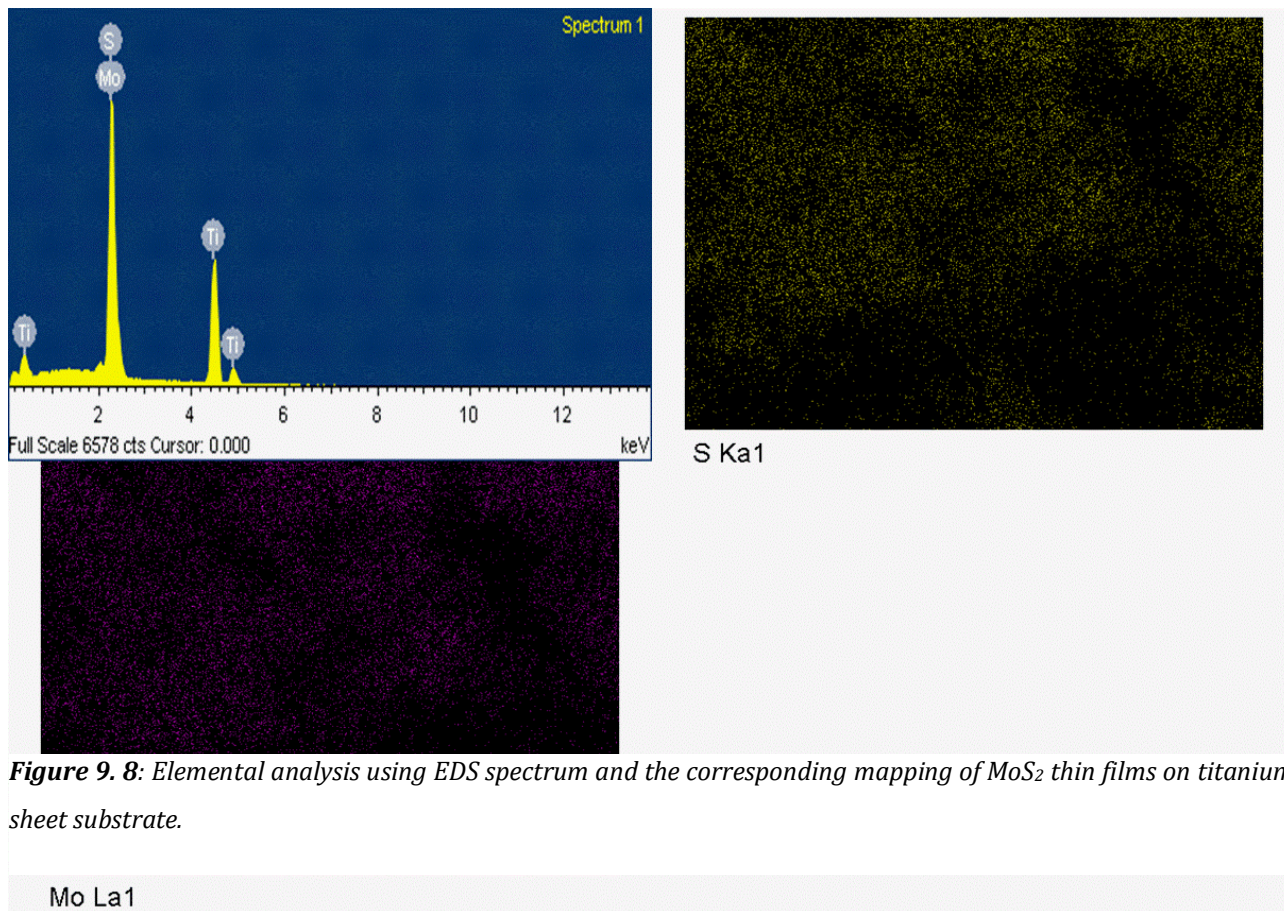


Figure 9. 8: Elemental analysis using EDS spectrum and the corresponding mapping of MoS_2 thin films on titanium sheet substrate.

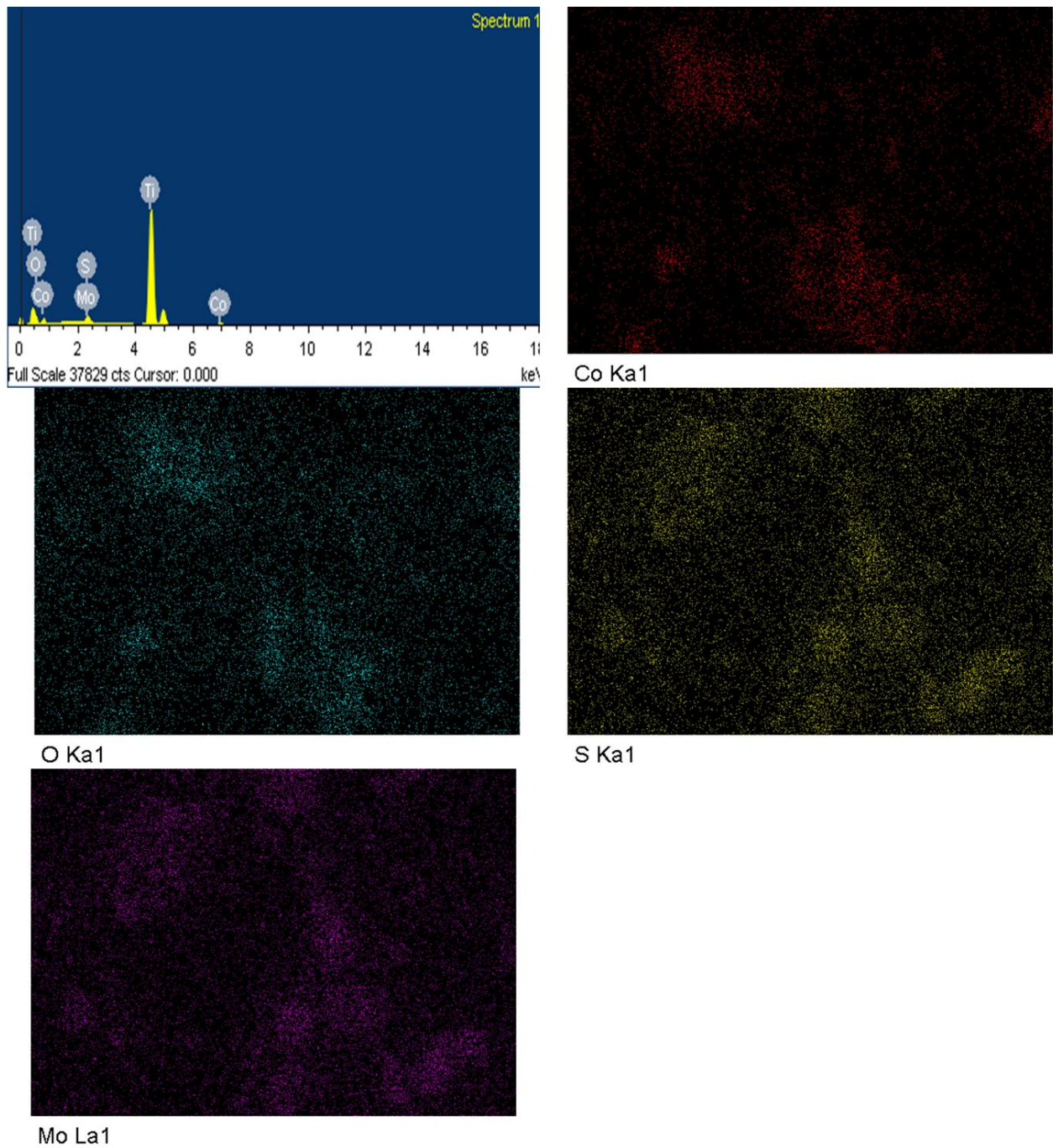


Figure 9. 9: Elemental analysis using EDS spectrum and corresponding mapping of nanocomposites with 25 wt.% Co_3O_4 thin films on a titanium sheet substrate.

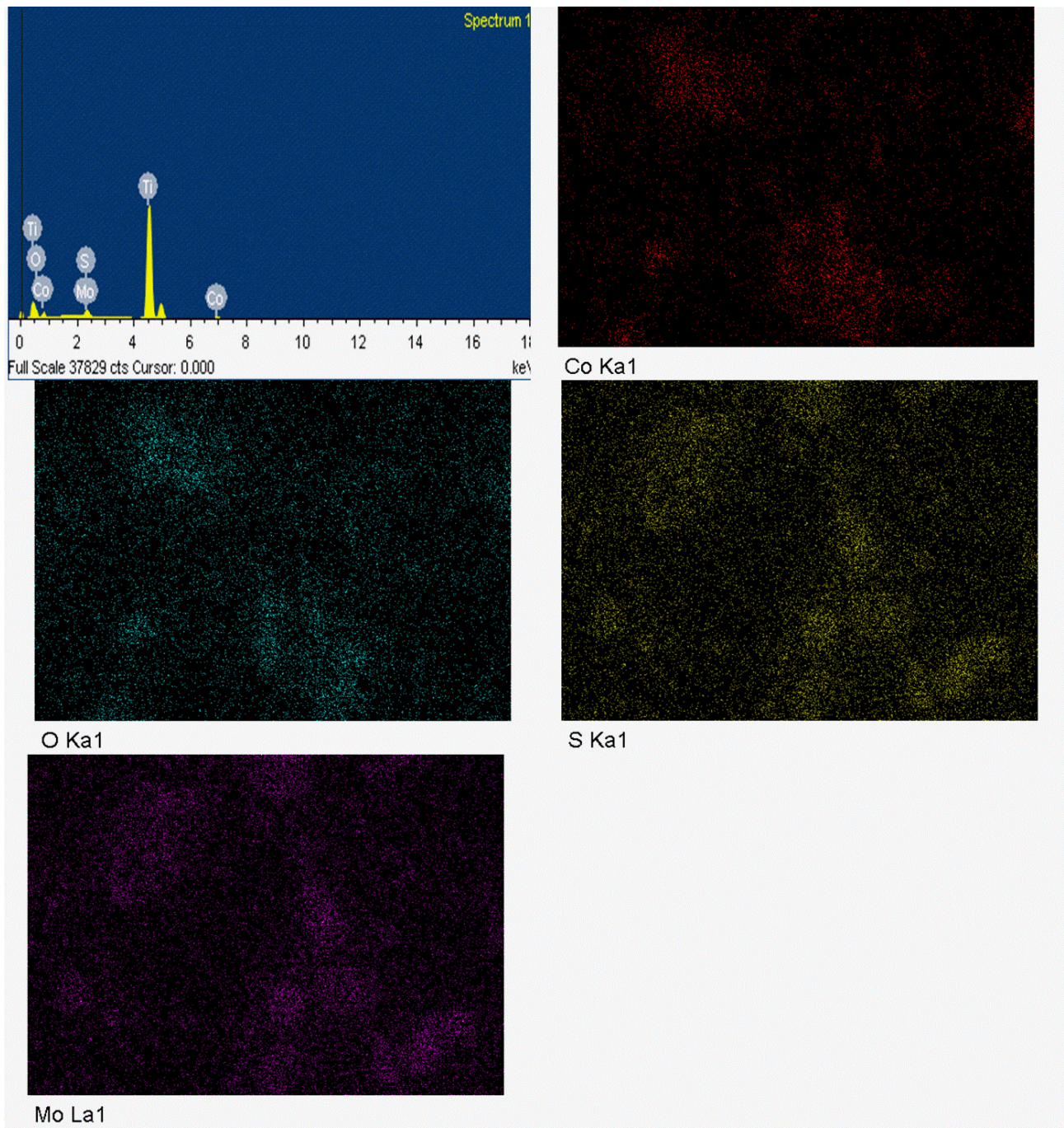


Figure 9. 10: Elemental analysis using EDS spectrum and corresponding mapping of nanocomposite with 50 wt.% Co_3O_4 thin films on a titanium substrate.

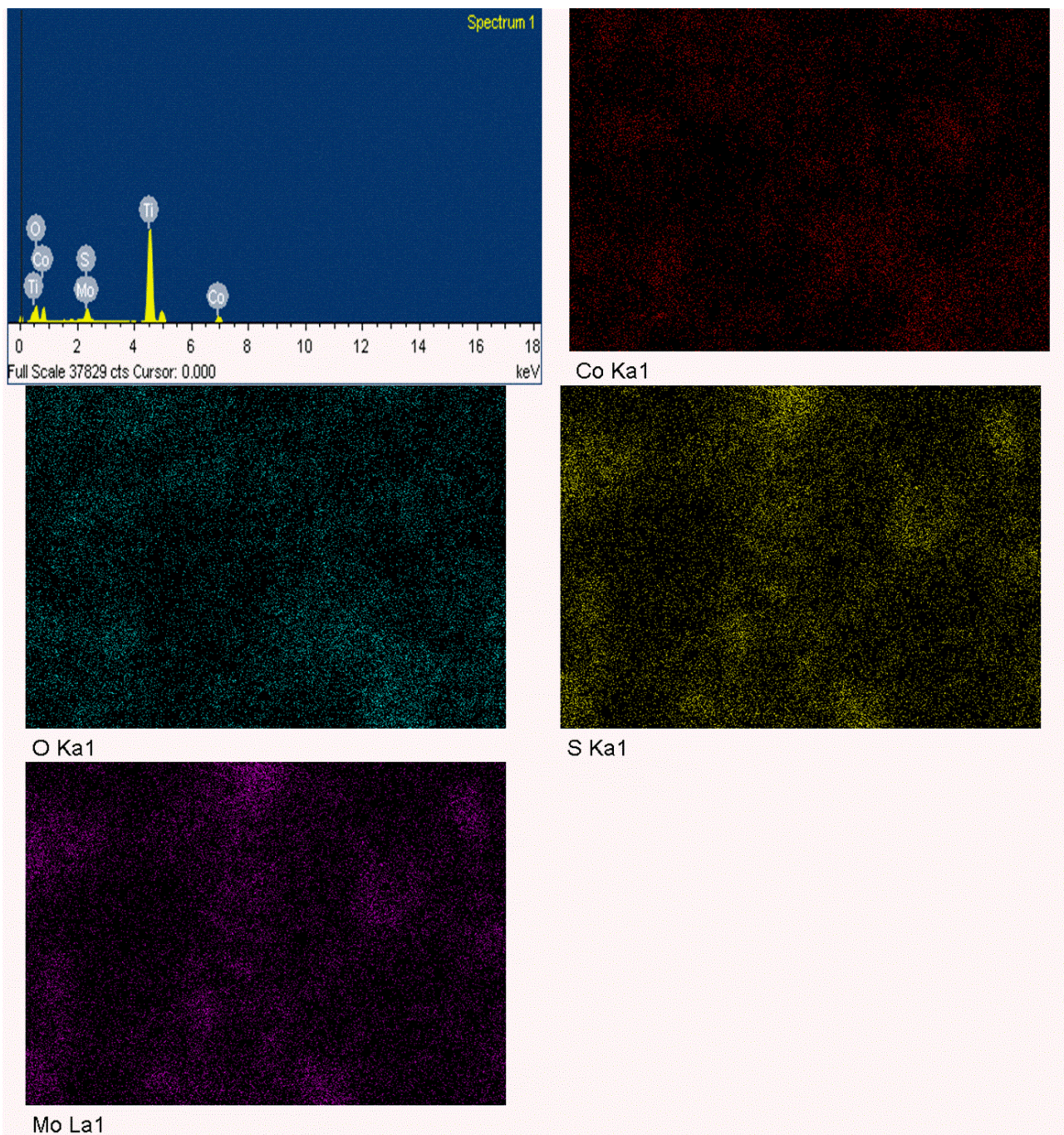


Figure 9. 11: Elemental analysis using EDS spectrum and corresponding mapping of nanocomposite with a 75 wt.% Co_3O_4 thin film on a titanium substrate.

9. 2. 3. Raman studies on Co_3O_4 - MoS_2 heterostructure composites

Micro-structure Raman spectroscopy is a non-destructive surface analysis technique sensitive to localized change at the material surface, with a high spatial resolution in the micro-size range possible by modifying electron-phonon interactions [411]. We employed this technique to distinguish changes due to

the fragmentation of microparticles to the nanometer scale, as well as variations associated with the hetero-structural formation of $\text{Co}_3\text{O}_4\text{-MoS}_2$ NCs.

9.2.3.1. $\text{Co}_3\text{O}_4\text{-MoS}_2$ mixed micro-sized powder

The micro-Raman spectrum of MoS_2 powder in the Raman shift range from 100 to 800 cm^{-1} is illustrated in **Figure 9. 12(a)** and estimated peaks are provided in **Table 9. 3**. The Raman peaks were classified primarily as either first-order symmetry modes at 279, 373, and 400 cm^{-1} or second-order vibrations at 447, and 562 cm^{-1} . These Raman active modes are characterizing by the 2H-layered structure of MoS_2 . The first-order vibration with the highest intensity corresponds to E^{1}_{2g} , and A_{1g} at 373 and 400 cm^{-1} , respectively. A third first-order vibration mode E_{1g} with a very smaller intensity of 279 cm^{-1} [119-123]. However, second-order vibration modes at higher Raman shifts caused by the longitudinal acoustic (2LA) mode, and $2E_{1g}(\Gamma)$ were observed at 447 and 562 cm^{-1} , respectively. Besides, a linear combination between first- and second-order vibration modes ($E^{1}_{2g} [M]+LA[M]$) was observed at a higher Raman shift of 585 cm^{-1} [393]. **Figure 9. 12(e)** depicts the micro-Raman spectrum of pure-phase Co_3O_4 microparticles that consist of several active symmetry modes at shifts of 188, 474, 515, 611, and 679 cm^{-1} . The observed peaks indicate various symmetry modes related to the Co_3O_4 spinel structure. The most intense peak at 679 cm^{-1} is related to the A_{1g} mode caused by the octahedral site (CoO_6). Raman vibration mode with lower intensity at 474 cm^{-1} can be attributed to the E_g symmetry mode.

Table 9. 3: Raman active modes in the $\text{Co}_3\text{O}_4\text{-MoS}_2$ microparticles at different Co_3O_4 content (wt.%).

Characteristic bands	Raman shift (cm^{-1})				
	MoS_2	75 wt.% MoS_2	50 wt.% MoS_2	25 wt.% MoS_2	Co_3O_4
Co_3O_4	F_{2g}				188
	E_g			474	474
	F_{2g}		516	516	515
	F_{2g}				611
	A_{1g}		684	684	680
MoS_2	E_{1g}	279	283	278	278
	E^{1}_{2g}	373	377	377	377
	A_{1g}	400	400	400	400
	2LA(M)	447	447	447	447
	$2E_{1g}(\Gamma)$	562	562	562	562
	$E^{1}_{2g} (M)+LA(M)$	585	589	589	589

The F_{2g} symmetry mode that arose from CoO_4 tetrahedral sites in the spinel structure of Co_3O_4 exhibited active Raman states at 192 cm^{-1} ($F^{(1)}_{2g}$), 515 cm^{-1} ($F^{(2)}_{2g}$), and 611 cm^{-1} ($F^{(3)}_{2g}$) [224-226]. Raman spectra of mixed $\text{Co}_3\text{O}_4\text{-MoS}_2$ microparticles at different Co_3O_4 contents (25, 50, and 75 wt.%)

are illustrated in **Figure 9. 12(b-d)**, which reveals characteristic bands of Co_3O_4 and MoS_2 micro-powder with no noticeable change in Raman peak position, **Table 9. 3**.

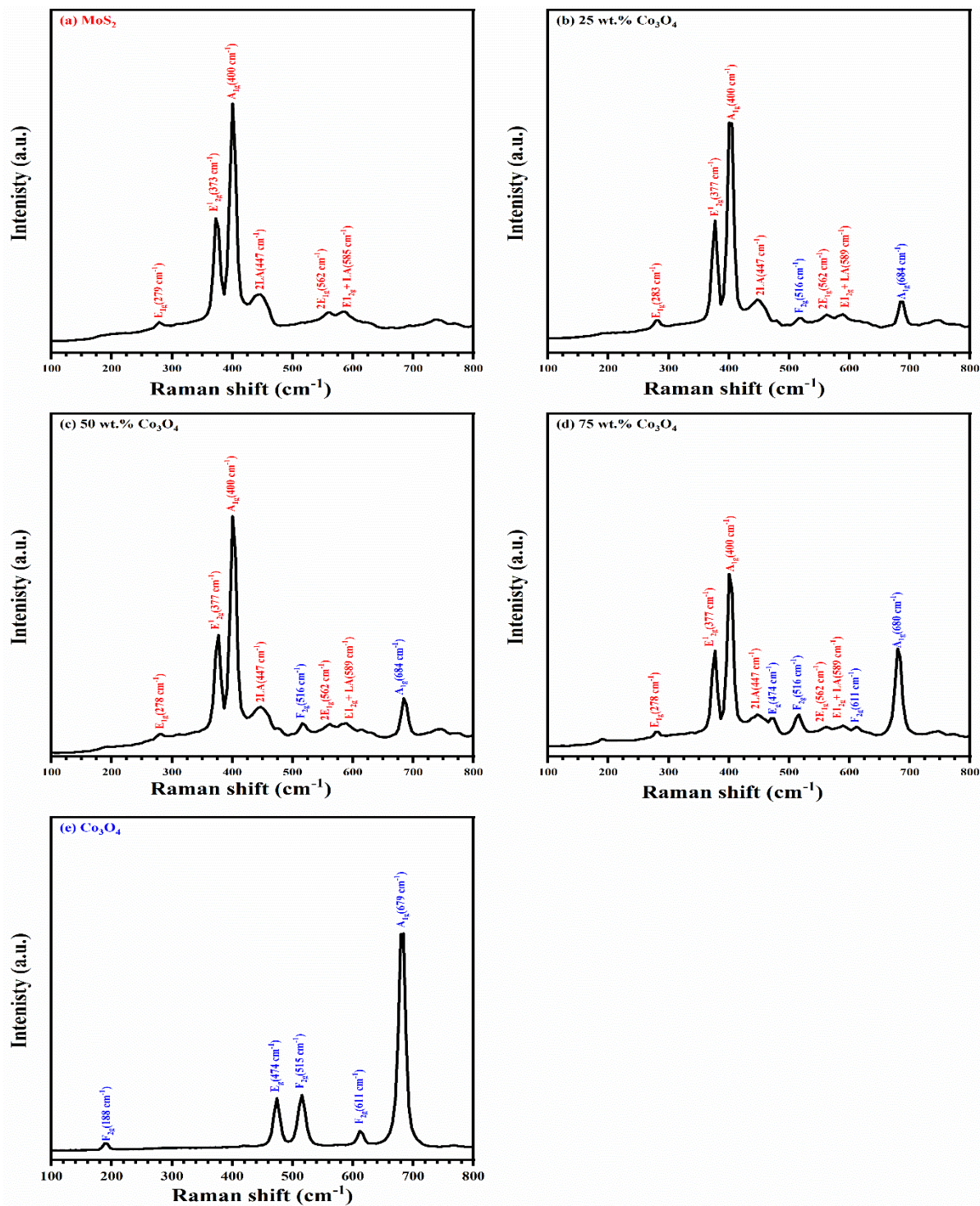


Figure 9. 12: Raman Spectra of mixed Co_3O_4 - MoS_2 micro powders at different Co_3O_4 contents.

The F_{2g} symmetry mode that arose from CoO_4 tetrahedral sites in the spinel structure of Co_3O_4 exhibited active Raman states at 192 cm^{-1} ($F^{(1)}_{2g}$), 515 cm^{-1} ($F^{(2)}_{2g}$), and 611 cm^{-1} ($F^{(3)}_{2g}$) [224-226]. Raman spectra of mixed Co_3O_4 - MoS_2 microparticles at different Co_3O_4 contents (25, 50, and 75 wt.%) are illustrated in **Figure 9. 12(b-d)**, which reveals characteristic bands of Co_3O_4 and MoS_2 micro-powder with no noticeable change in Raman peak position, **Table 9. 3**.

9. 2. 3. 2. Co_3O_4 - MoS_2 hybrid composites on titanium sheet

Figure 9. 13(a) shows the micro-Raman spectrum of the titanium-modified electrode with MoS_2 nanosheets. Several first-order active Raman modes related to the MoS_2 layered structure were detected at 405 , 377 , and 283 cm^{-1} corresponding to the A_{1g} , E^{1}_{2g} , and E_{1g} vibration modes, respectively. Other active modes corresponding to either second-order vibration modes or a linear combination between them were also detected at Raman shifts of 451 , 561 , and 589 cm^{-1} . The micro-Raman spectrum of the modified titanium electrode with Co_3O_4 nanosheets in **Figure 9. 13(e)** shows various Raman peaks at 193 , 483 , 520 , 620 , and 693 cm^{-1} related to the Co_3O_4 phase. The most intense Raman peak related to the first-order A_{1g} symmetry mode due to octahedral (CoO_6) vibration was observed at 693 cm^{-1} . A first-order E_g symmetry mode was observed at 483 cm^{-1} and multiple active Raman modes related to the F_{2g} symmetry mode at evident 193 , 520 , and 620 cm^{-1} [224-226]. **Figure 9. 13(b-d)** depicts micro-Raman spectra of the titanium-modified electrodes with Co_3O_4 - MoS_2 NCs with Co_3O_4 content of 25, 50, and 75 wt.%.

Table 9. 4: Raman peaks of titanium modified electrodes with Co_3O_4 - MoS_2 NCs at different Co_3O_4 contents.

Characteristic bands	Raman shift (cm^{-1})					
	MoS_2	25 wt.% Co_3O_4	50 wt.% Co_3O_4	75 wt.% Co_3O_4	Co_3O_4	
F_{2g}	-	-	-	-	193	
E_g	-	-	-	483	483	
Co_3O_4	F_{2g}	-	525	525	521	520
	F_{2g}	-	630	630	621	620
	A_{1g}	-	693	693	693	693
	E_{1g}	283	283	283	283	-
MoS_2	E^{1}_{2g}	377	381	381	381	-
	A_{1g}	405	405	405	405	-
	2LA(M)	451	451	451	451	-
	2E _{1g} (Γ)	561	566	566	566	-
	E ¹ _{2g} (M)+LA(M)	589	598	593	593	-

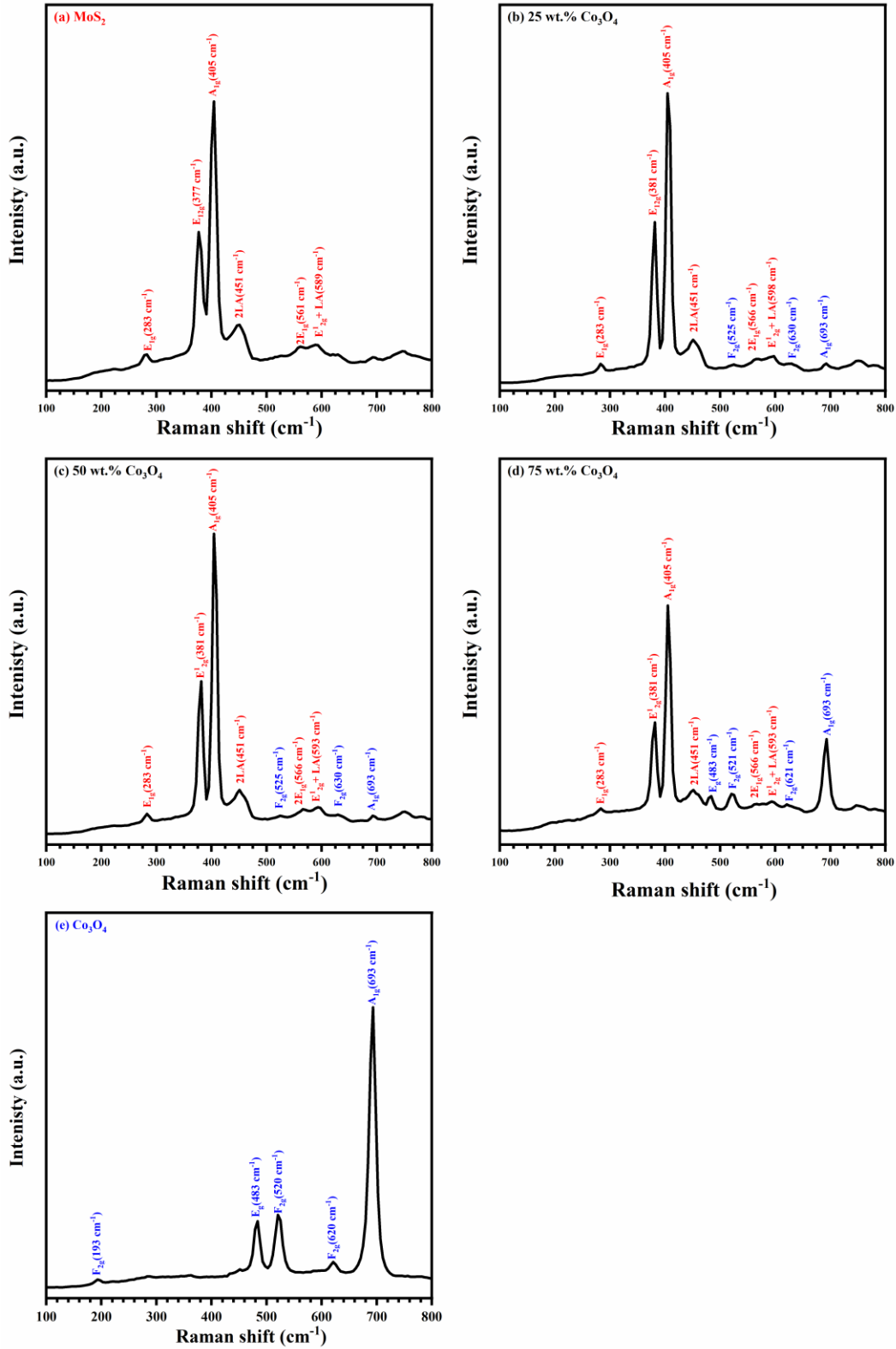


Figure 9.13: Raman spectra of MoS₂ (a), nanocomposites of Co₃O₄-MoS₂ (b-d), and Co₃O₄ (e) nanostructured thin film on titanium sheets.

The recognized active Raman modes related to both phases of Co_3O_4 and MoS_2 are mentioned in **Table 9. 4**. All identified active Raman modes in the deposited thin films of Co_3O_4 - MoS_2 NCs on the titanium sheet substrate exhibited a positive shift in peaks position to a higher value compared with the corresponding micropower. This behavior can be attributed mainly to powder fragmentation and lattice disorder at the nanometer scale [124, 227].

9. 2. 4. XPS studies on Co_3O_4 - MoS_2 nanostructure composites

The origin of electroactive sites at the interface of titanium-modified hybrid electrodes with MoS_2 nanosheets, Co_3O_4 nanosheets, and Co_3O_4 - MoS_2 NCs at different Co_3O_4 contents (25, 50, and 75 wt.%), were investigated in more detail using XPS in a binding-energy range of 0 to 1300 eV. The XPS survey spectra of all modified titanium electrodes in **Figure 9. 14(a)**, reveal the presence of various active states related to sulfur, molybdenum, oxygen, and cobalt. To understand the synergetic behavior of MoS_2 and Co_3O_4 nanosheets in a nanostructured Co_3O_4 - MoS_2 hybrid electrocatalyst, high-resolution XPS scans of S 2p, Mo 3d, O 1s, and Co 2p in the case of the heterostructure electrodes were compared with corresponding pure phases of either MoS_2 or Co_3O_4 nanosheets, as shown in **Figure 9. 14(b-e)**. The deconvolution of a high-resolution S 2p XPS scan of the modified titanium electrode with the pure MoS_2 phase is shown in **Figure 9. 15 (a)**. The S 2p_{3/2} band is evident at 162 eV and the S 2p_{1/2} band is at 163.18 eV. These sub-bands were also detected in modified titanium electrodes with Co_3O_4 - MoS_2 NCs with different Co_3O_4 contents (25, 50, and 75 wt.%) as shown in **Figure 9. 15(b-d)**. The positions of the estimated peaks corresponding to S 2p_{3/2} and S 2p_{1/2} for the individual composites are reported in **Table 9. 5**. In the case of modified titanium electrodes with NCs, an increase in Co_3O_4 content was accompanied by a slight positive shift to higher binding energy values. This behavior indicates the enhancement of interfacial charge-carrier density in the case of nanostructured MoS_2 -modified electrodes [384, 394]. Analysis of a high-resolution Mo 3d XPS scan of the nanostructured MoS_2 /Ti electrode in **Figure 9. 16 (a)** revealed various active states at binding energies of 226.39, 229.19, 232.36, and 235.69 eV. The observed peaks at 229.19 and 232.36 eV represent molybdenum species in the MoS_2 -layered structure corresponding to suborbital states of Mo 3d_{5/2} and Mo 3d_{3/2}, respectively. Another active state related to higher molybdenum oxidation states (Mo^{6+}) was observed at a higher binding-energy value of 235.69 eV [395]. An overlapping peak caused by S_{2s} states is usually reported in high-resolution XPS scans of Mo 3d states at a lower binding energy value of 226.39 eV [396].

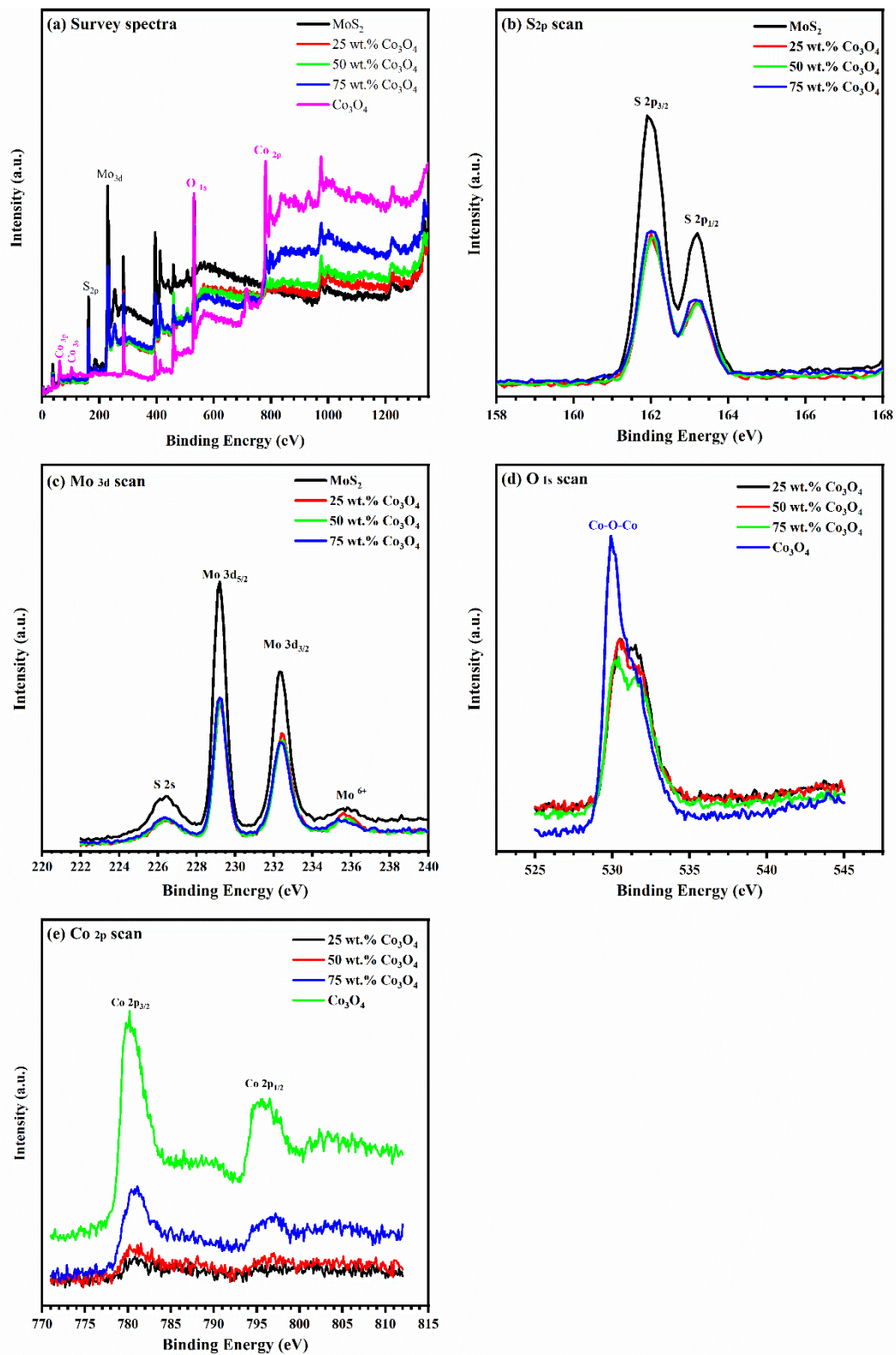


Figure 9.14: XPS survey spectra (a), high-resolution XPS scans of S 2p (b), and Mo 3d (c), O 1s (d), and Co 2p (e) of $\text{Co}_3\text{O}_4\text{-MoS}_2$ nanocomposite thin films

An analysis of the high-resolution Mo 3d XPS scan in the case of the titanium-modified electrode with $\text{Co}_3\text{O}_4\text{-MoS}_2$ NCs is shown in **Figure 9. 16(b-d)**. The results exhibit the same characteristics bands matching the MoS_2 pure phase. A positive shift to a higher binding-energy value was also evident with the incorporation of Co_3O_4 in the heterostructures electrodes, indicating the improvement in the synergy between MoS_2 and Co_3O_4 electroactive species.

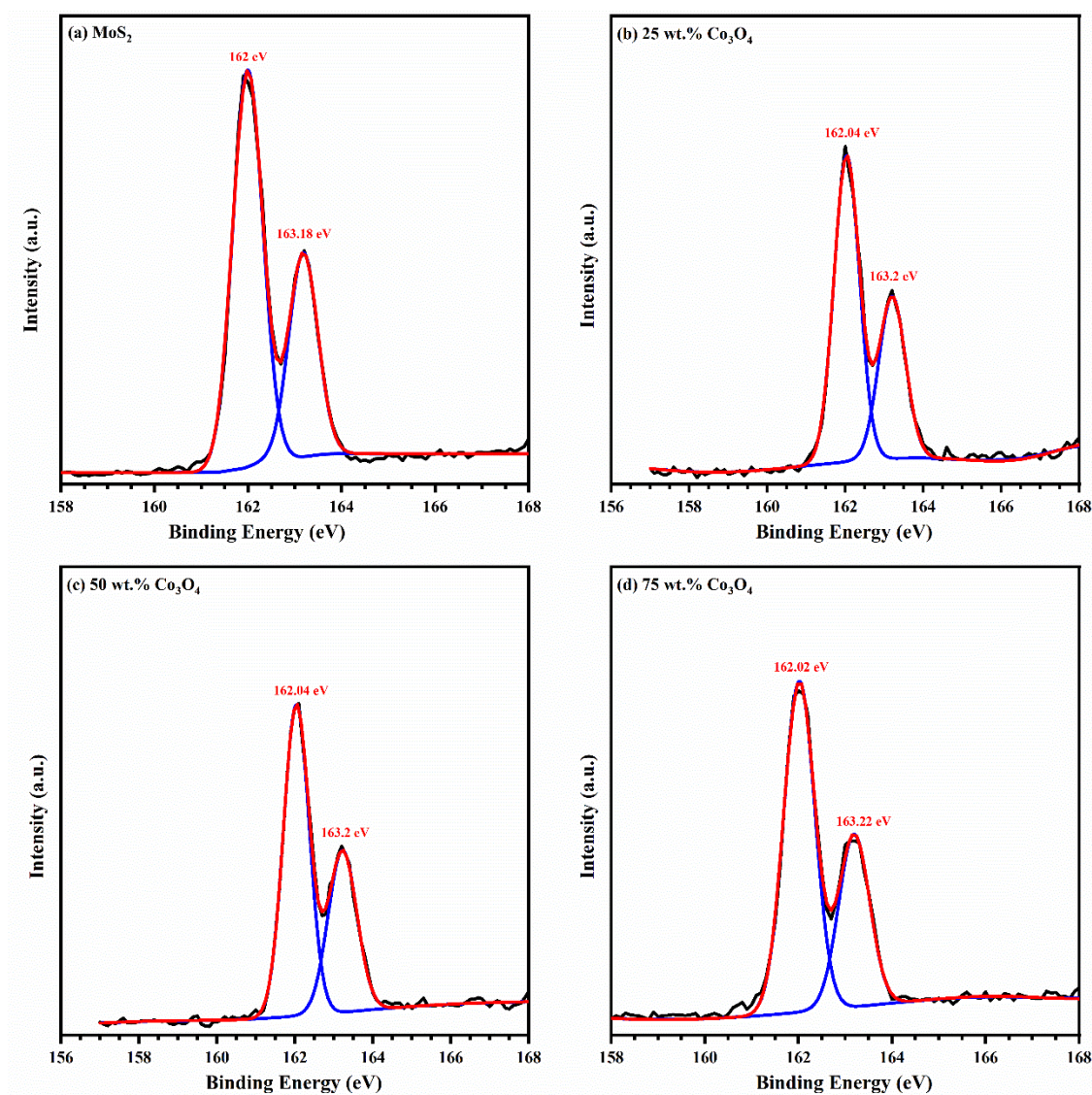


Figure 9. 15: Deconvoluted S 2p XPS scan of pure MoS_2 (a), nanocomposites with 25 wt.% (b), 50 wt.% (c), and 75 wt.% Co_3O_4 (d) thin films.

Figure 9. 17(d) depicts a deconvoluted O 1s XPS scan of the modified titanium electrode with nanostructured Co_3O_4 . The main band at 529.92 eV overlapped with a peaked shoulder at higher binding energy (531.13 eV). High-resolution O 1s XPS scans of the modified titanium electrode with Co_3O_4 - MoS_2 NCs at different Co_3O_4 content are shown in **Figure 9. 17(a-c)**. The results display the same characteristics bands with small variations in peak positions. The intensity ratio between the peak shoulder to the main peak in the O 1s XPS scan was improved in the case of the NC electrocatalyst. This might be caused by the evolution of new metallic bond states (Co-O-Mo).

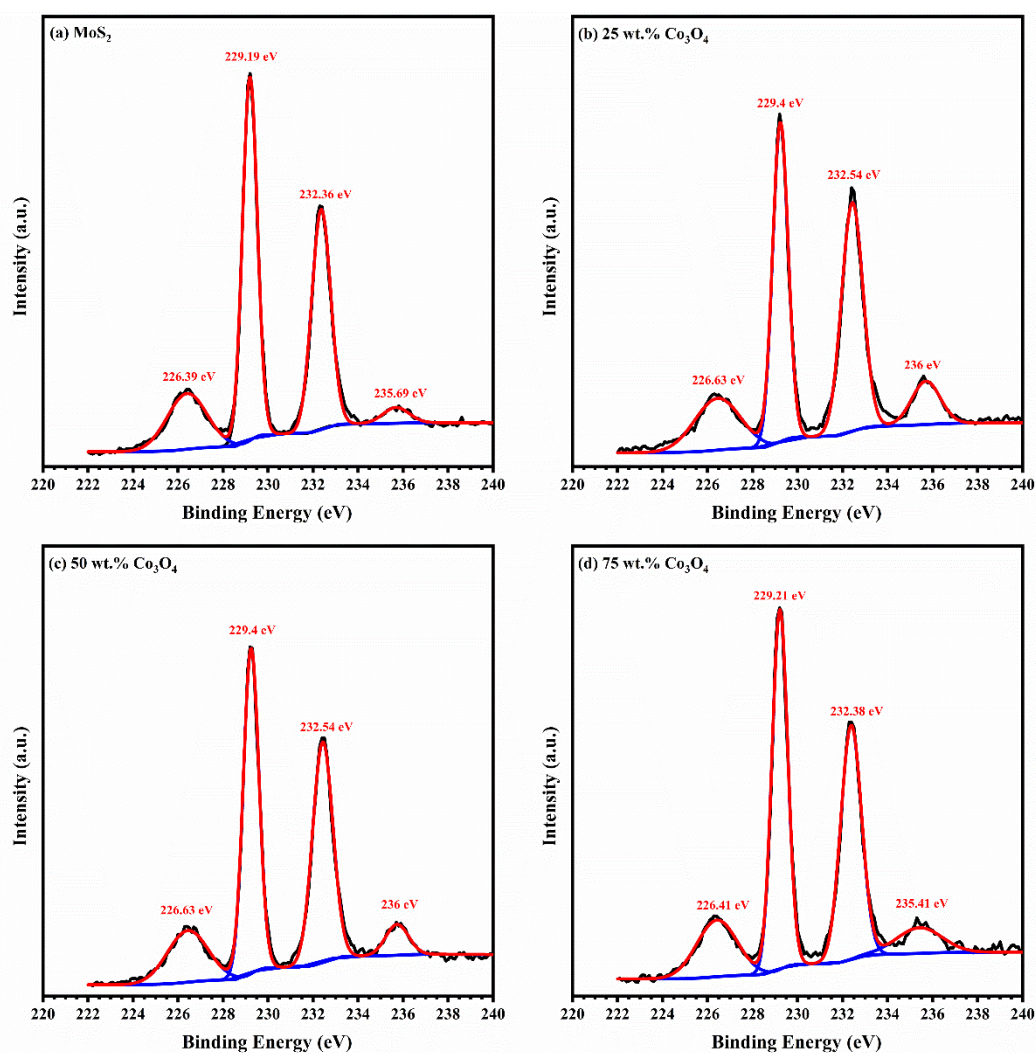


Figure 9. 16: Deconvoluted Mo 3d XPS scan of pure MoS_2 (a), nanocomposites with 25 wt.% (b), 50 wt.% (c), and 75 wt.% Co_3O_4 (d) thin films.

The estimated peak position of O 1s high-resolution XPS scan was tabulated in **Table 9. 5**.The high-resolution Co 2p XPS scans of the modified titanium electrode with nanostructured Co_3O_4 and $\text{Co}_3\text{O}_4\text{-MoS}_2$ hybrid electrocatalysts with 25, 50, and 75 wt.% Co_3O_4 contents are provided in **Figure 9. 18**. Deconvolution was performed to precisely identify the electroactive sites related to cobalt species. The peaks were divided primarily into Co 2p_{3/2} and Co 2p_{1/2} states, as well as secondary satellite peaks caused by spin-orbital interaction of these sub-bands states.

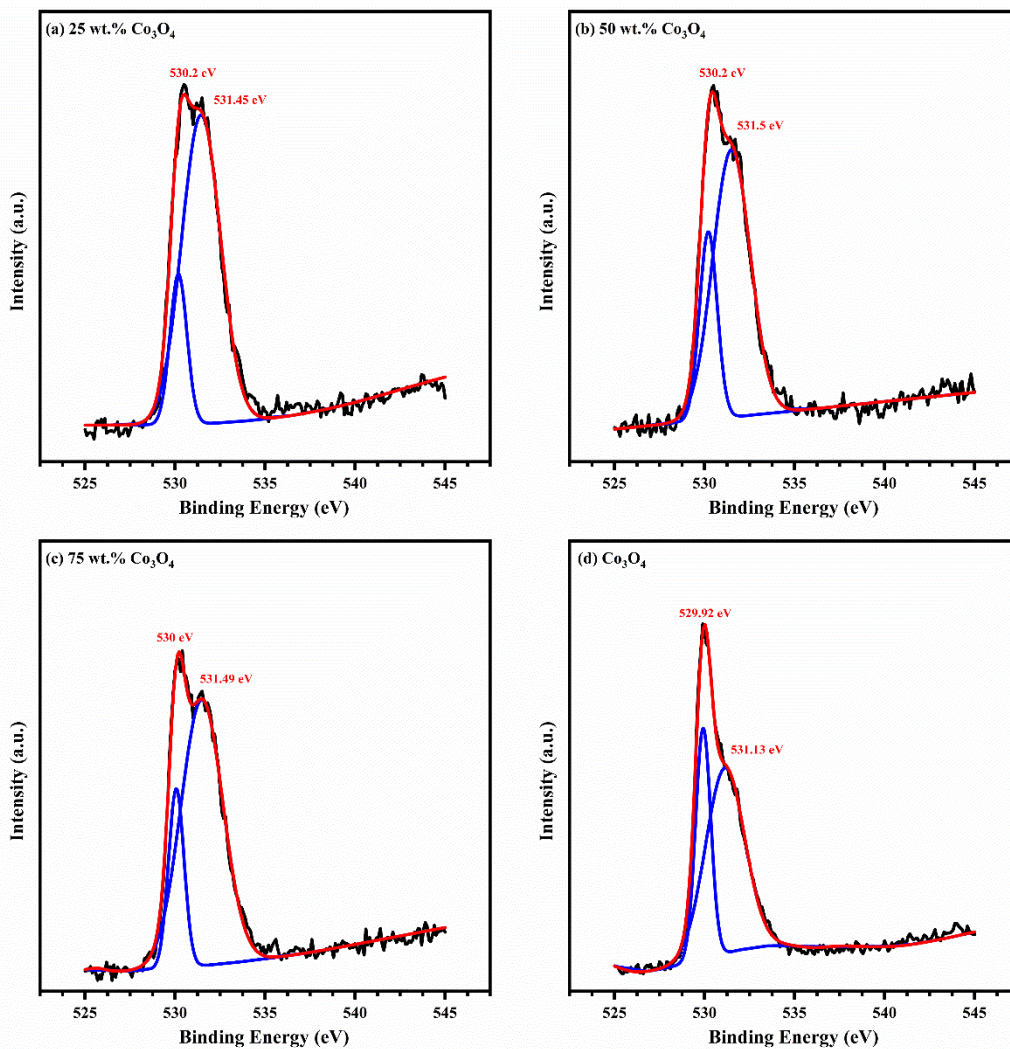


Figure 9. 17: Deconvoluted O 1s XPS scan of nanocomposites with 25 wt.% **(a)**, 50 wt.% **(b)**, 75 wt.% Co_3O_4 **(c)**, and pure Co_3O_4 **(d)** thin films.

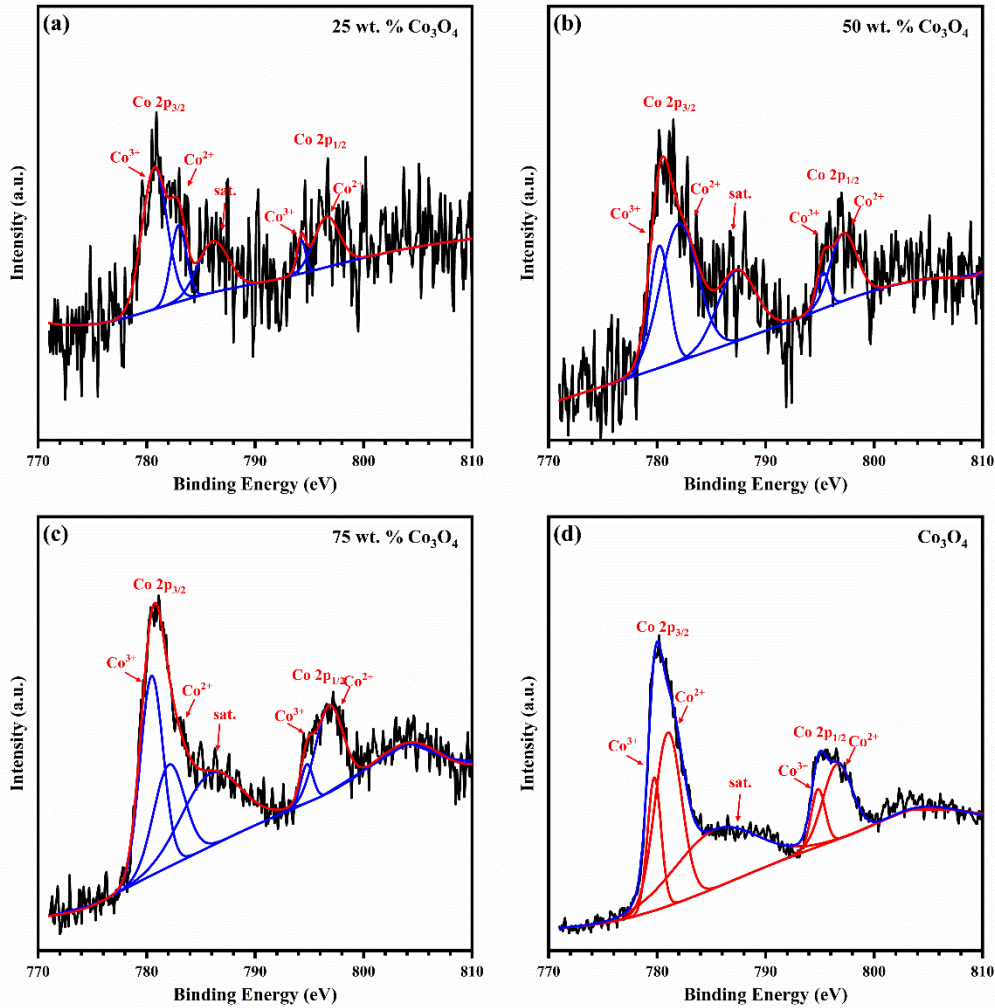


Figure 9.18: Deconvoluted Co 2p XPS scan of nanocomposites with 25 wt.% (a), 50 wt.% (b), 75 wt.% Co₃O₄ (c), and pure nanostructured Co₃O₄ (d) thin films.

Table 9.5: Characteristic peaks of S 2p, Mo 3d, O 1s, and Co 2p deconvoluted XPS scans in nanocomposite Co₃O₄-MoS₂ thin films.

Band	Binding Energy (eV)				
	MoS ₂	25 wt. % Co ₃ O ₄	50 wt. % Co ₃ O ₄	75 wt. % Co ₃ O ₄	Co ₃ O ₄
S 2p	162	162.04	162.04	162.02	-
	163.18	163.2	163.22	163.22	-
	226.39	226.41	226.43	226.44	-
Mo 3d	229.19	229.21	229.24	229.23	-
	232.36	232.38	232.43	232.43	-
	235.69	235.41	235.73	235.7	-
O 1s	-	530.2	530.2	530.00	529.92
	-	531.45	531.5	531.49	531.13
	-	780.72	780.21	780.46	779.74
Co 2p	-	782	782.00	782.07	781.00
	-	786.12	787.30	785.9	785.35
	-	794.24	795.28	794.77	794.83
	-	796.26	797.17	796.82	796.6

Estimated peak positions are reported in **Table 9. 5**. In the case of the modified electrode with nanostructured Co_3O_4 , a high-resolution Co 2p XPS scan revealed peaks related to lower-spin-state Co^{3+} at 779.74 and 794.83 eV, corresponding to Co 2p_{3/2} and Co 2p_{1/2}, respectively. Meanwhile, higher spin states of cobalt species (Co^{2+}) were observed at 781 eV of Co 2p_{3/2} and 796.6 eV of Co 2p_{1/2}. Moreover, the average energy separation between the two main suborbital states was approximately 15.34 eV, matching that of cobalt species in the Co_3O_4 phase [188, 189, 233, 234]. Analysis of Co 2p high-resolution XPS scans corresponding to modified electrodes with nanostructured composites was performed and the estimated sub-orbital peak positions were tabulated in **Table 9. 5**. The detected Co 2p sub-bands in the modified titanium electrode with Co_3O_4 - MoS_2 NCs with Co_3O_4 content of 25, 50, 75 wt.% had the same origin as a pure phase of Co_3O_4 . In a comparison of the modified electrode with pure Co_3O_4 , the positions of the deconvoluted peaks shifted positively to a higher binding-energy value due to strong coupling with MoS_2 species in the hybrid electrocatalysts. This demonstrates the overall improvement of the synergetic effect in all modified electrodes with Co_3O_4 - MoS_2 NCs [397].

9. 2. 5. Electrocatalytic active surface area evaluation

The implicit representation of the electrochemical active surface area (ECSA) of the modified titanium electrode with nanosheets of Co_3O_4 and Co_3O_4 - MoS_2 composites with 25, 50, and 75 wt.% Co_3O_4 and pure MoS_2 were evaluated using the double-layer capacitive current density difference (ΔJ) with a gradual increase in the potential scan rate (ν) in the non-faradaic region [78]. The potential scan rates were 10, 20, 30, 40, 50, 60, 70, 80, 90, and 100 $\text{mV}\cdot\text{s}^{-1}$ in a potential range of 0 to 0.1 against Hg/HgO. The estimated slope according to **Eq. 2. 5** represents the double layer capacitance (C_{DL}). **Figure 9. 19** provides the cyclic voltammetry (CV) curves of Co_3O_4 - MoS_2 /Ti NC electrodes at different Co_3O_4 contents. The derived linear relationship between the current density difference (ΔJ) and the scan rate (ν) is supplied in **Figure 9. 20(a)**. The change in ECSA at different contents of Co_3O_4 is illustrated in **Figure 9. 20(b)**. A gradual increase in Co_3O_4 content in the NCs was accompanied by an increase in the double-layer capacitance, demonstrating an overall improvement in the ECSA. The Co_3O_4 - MoS_2 NC with 75 wt.% Co_3O_4 revealed the highest C_{DL} value of $2.35 \text{ mF}\cdot\text{cm}^{-2}$, compared with pure-phase MoS_2 and Co_3O_4 , as well as other composites with 25 and 50 wt.% Co_3O_4 , which exhibited C_{DL} values of 0.276, 0.423, 0.516, and $1.36 \text{ mF}\cdot\text{cm}^{-2}$, respectively.

9. 2. 6. Electrocatalytic activity of Co₃O₄-MoS₂ NCs toward H₂O₂ oxidation

Figure 9. 21(a-e) depicts CV plots of the modified titanium sheet anode with the nanostructured thin film of MoS₂, Co₃O₄-MoS₂ composites with various Co₃O₄ contents, and Co₃O₄, respectively, at scan rates from 10 to 100 mV·s⁻¹ with increasing steps of 10 mV·s⁻¹ in 0.1 M NaOH. The observed redox peak in the plot of the modified titanium electrode with nanostructured Co₃O₄ and Co₃O₄-MoS₂ related to Co₃O₄ species can be described by the reversible electrochemical conversion of Co₃O₄ to CoOOH according to the following equation [412]:



As shown in **Figure 9. 21(f)**, the linear and systematic variation of the redox-peak current density with a changing scan rate of the utilized working electrodes based on the Co₃O₄-MoS₂ NCs at various Co₃O₄ contents (25, 50, and 75 wt.%) exhibited electrochemical stability of Co₃O₄ species redox reactions as well as controlled diffusion of electrolyte species at the interface of the working electrode [408]. Because H₂O₂ molecules have high activity and a slow decomposition rate, they can be accelerated through the electrocatalytic process at the surface of a metal-oxide electrocatalyst in an alkaline medium with relatively low H₂O₂/O₂ redox potential [216]. Co₃O₄-based materials are widely used as electrocatalysts for H₂O₂ oxidation because of an abundance of electroactive species at their surfaces that can recognize small interruptions induced by an electrochemical reaction at the interface between the electrolyte and the utilized working electrode [212, 213, 264]. **Figure 9. 22(a)** reveals the CV plots of nanostructured MoS₂/Ti, Co₃O₄-MoS₂ NCs/Ti with various Co₃O₄ contents, and Co₃O₄/Ti at a scan rate of 50 mV·s⁻¹ in 0.1 M NaOH without and with 5 mM H₂O₂. In the case of bare titanium electrodes as well as a modified electrode with MoS₂ nanosheets, there would be no significant change in the response in current density to the addition of H₂O₂. Meanwhile, the CV plot of the modified electrode with nanostructured Co₃O₄/Ti revealed a high response current upon the addition of 5 mM H₂O₂, demonstrating that any detectable current response in the modified electrodes with Co₃O₄-MoS₂ NCs would arise from the Co₃O₄ electroactive species.

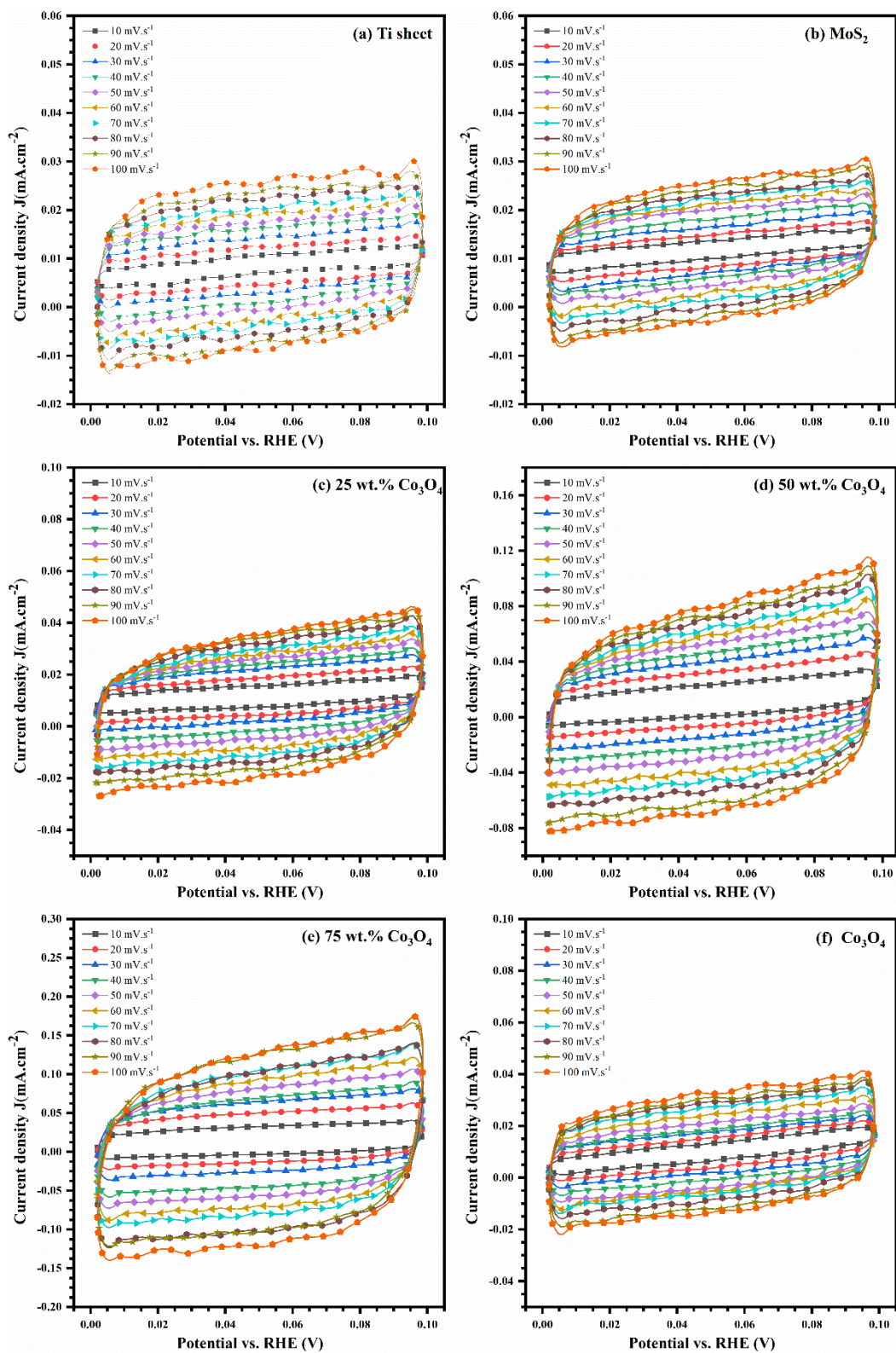


Figure 9. 19: CV plots of $\text{Co}_3\text{O}_4\text{-MoS}_2$ nanocomposites electrodes at different scan range in the non-faradic region from 0.924 to 1.024 vs. RHE (0 to 0.1 vs. Hg/HgO).

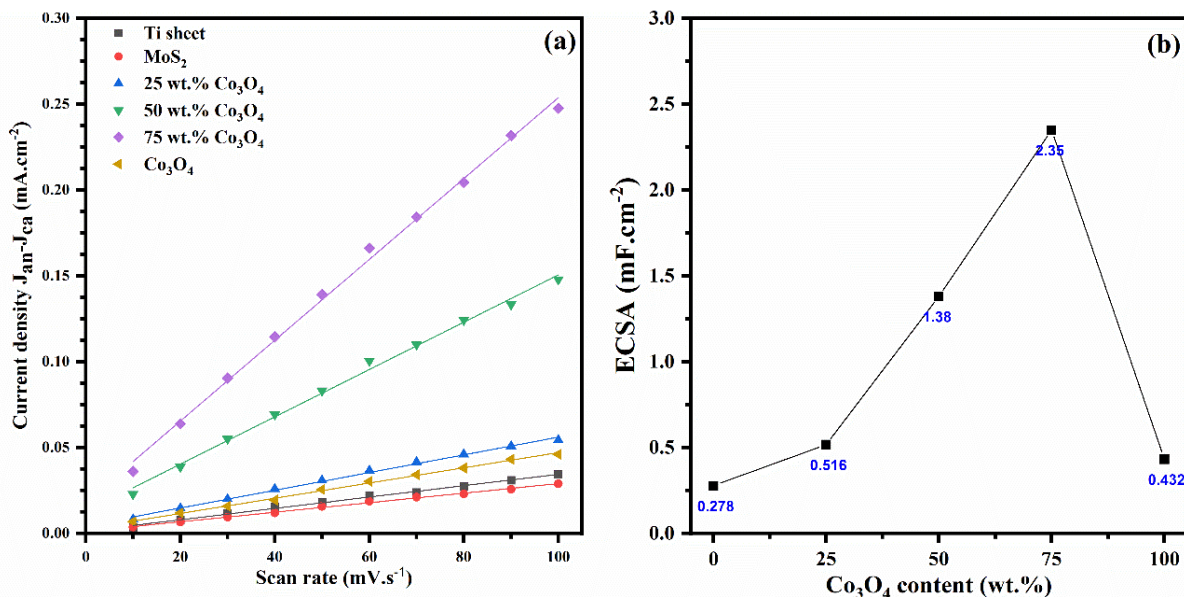
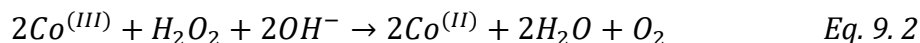


Figure 9.20: Plot of double-layer capacitive current at different scan rates (a) and the corresponding ECSA of Co_3O_4 - MoS_2 NCs in the non-faradic region at different Co_3O_4 contents (b).

The mechanism of H_2O_2 oxidation by Co_3O_4 -based electrocatalysts can be described by an equation provided by Heli et al. [219]:



The oxidation of H_2O_2 is more favorable at electroactive sites with lower spin states related to Co_3O_4 (e.g., Co^{3+}) unlike the case of H_2O_2 reduction in the negative potential regions, in which higher spin states (e.g., Co^{2+}) are more favorable [264, 408]. The combination of MoS_2 nanosheets with Co_3O_4 resulted in an overall improvement in the induced response current caused by H_2O_2 oxidation at the interface of the composites electrode. The response current gradually increased with Co_3O_4 content and the composites with 75 wt.% Co_3O_4 exhibited the greatest change in the response current. Quantitative evaluation of the modified anode's amperometric response was carried out using chronoamperometric curves with the gradual addition of H_2O_2 at various concentrations as shown in **Figure 9.22(b)**. The anodic potential for amperometric detection of H_2O_2 was fixed at +0.6 V for all working electrodes to optimize electrocatalytic sensitivity toward H_2O_2 oxidation in 0.1 M NaOH. The utilized working electrodes responded rapidly to the oxidation of H_2O_2 , producing a steady-state current within 4 s. **Figure 9.22(c)** supplies Nyquist plots of Co_3O_4 - MoS_2 NCs at different Co_3O_4 concentrations in 0.1 M NaOH. The frequency range was from 1 to 10 kHz at a DC potential of 0.5 V and an AC signal with an amplitude of 5 mV in the presence of 5 mM H_2O_2 .

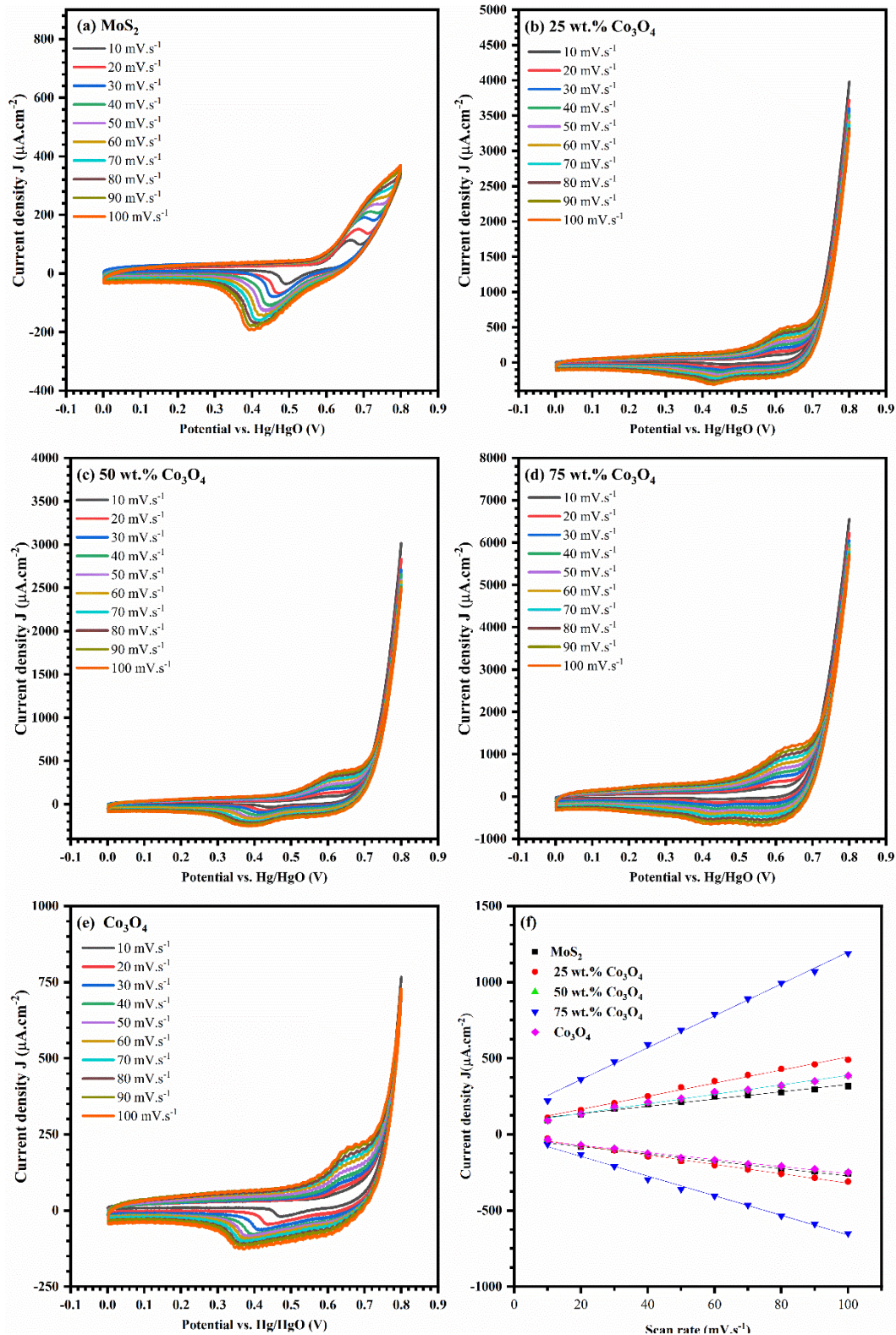


Figure 9. 21: CVs of MoS₂/Ti **(a)**, nanocomposite Co₃O₄-MoS₂ **(b-d)**, and pure nanostructured Co₃O₄/T **(e)** at different scan rates in 0.1 M NaOH. The linear regression of anodic and cathodic peaks vs. scan rate of Co₃O₄ nanocomposite electrodes **(f)**.

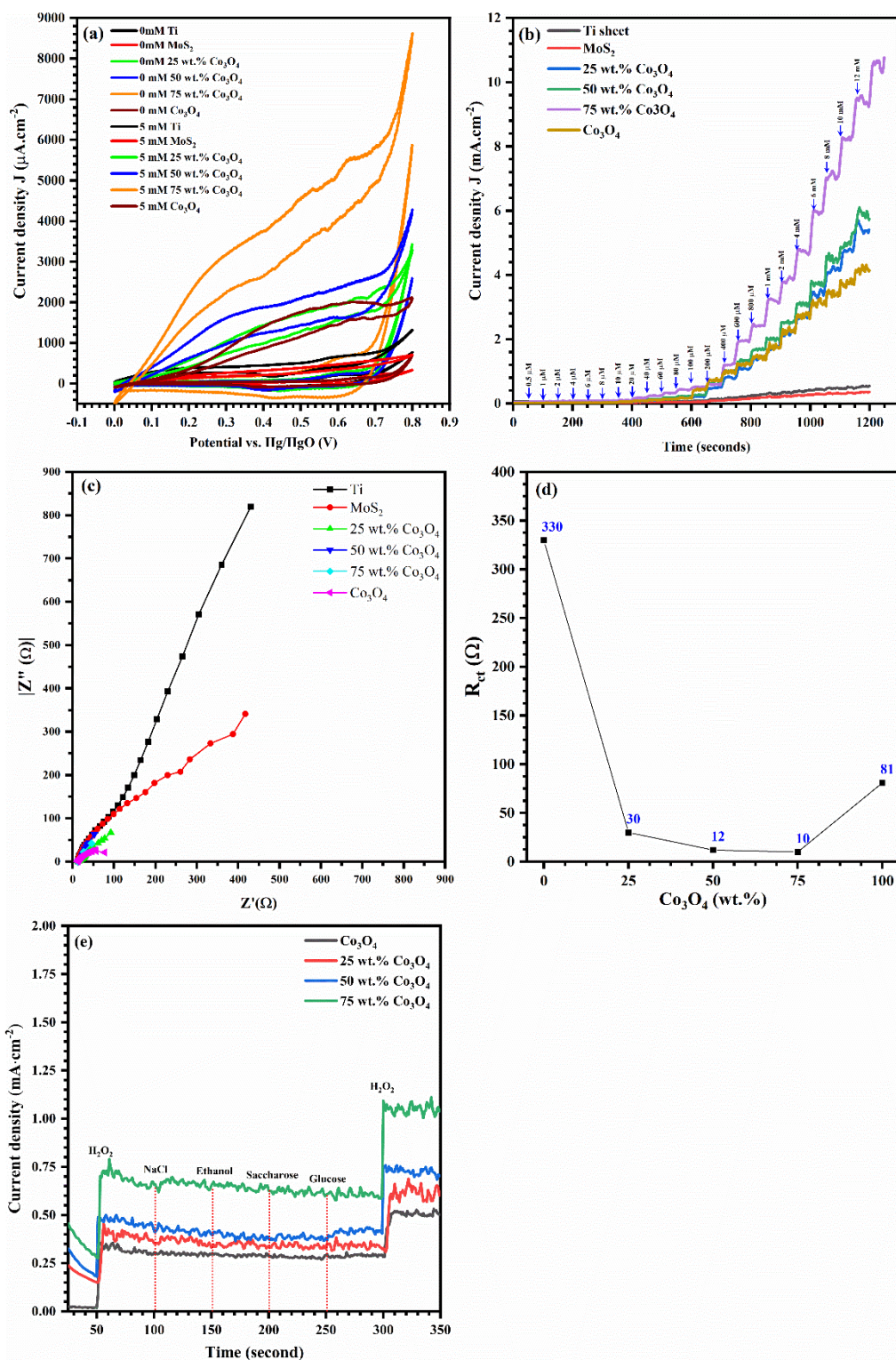


Figure 9. 22: CV curves recorded from 0 to 0.8 vs. Hg/HgO at a scan rate of $50 \text{ mV}\cdot\text{s}^{-1}$ without and with 5 mM of H_2O_2 in 0.1 M NaOH (a), the amperometric response at 0.6 V (b), a Nyquist plot in 0.1 M NaOH at a DC potential of 0.5 V and 5 mM H_2O_2 , and the corresponding behavior of charge-transfer resistance (c, d), oxidation selectivity test using amperometric response at 0.6 V with the addition of 1 mM from H_2O_2 , NaCl, saccharose, and glucose in 0.1 M NaOH (e) of Co_3O_4 - MoS_2 Nanocomposite electrodes at various Co_3O_4 contents

The estimated charge-transfer resistance (R_{ct}) at different Co_3O_4 contents is depicted in **Figure 9. 22(d)**. Increasing the content of Co_3O_4 in the NCs resulted in an overall improvement in the R_{ct} in the presence of H_2O_2 and the composite with 75 wt.% Co_3O_4 exhibited the lowest R_{ct} (10 Ω) accompanied by an overall improvement in detection sensitivity. The oxidation selectivity of titanium modified electrodes with $\text{Co}_3\text{O}_4\text{-MoS}_2$ NCs toward the H_2O_2 in 0.1 M NaOH was investigated for several interfering species, as shown in **Figure 9. 22(e)**, which revealed the amperometric response at oxidation potential of 0.6 V with the successive injection of 1 mM of H_2O_2 , NaCl, ethanol, saccharose, and glucose. It was noticed that the injection of 1 mM H_2O_2 before and after the injection of interfering species was accompanied by a sharp and rapid increase in the response current, meanwhile, the injection of other interfering species induced a very small or negligible response current compared with the H_2O_2 . This result demonstrated the superior selectivity of H_2O_2 oxidation using titanium modified electrodes with $\text{Co}_3\text{O}_4\text{-MoS}_2$ NCs. **Figure 9. 23** exhibited the amperometric calibration curves with the injected concentration of H_2O_2 for titanium modified electrode with the nanostructured Co_3O_4 as well as $\text{Co}_3\text{O}_4\text{-MoS}_2$ NCs with 25, 50, and 75 wt.% Co_3O_4 . All titanium modified electrodes with a wide linear detection range of 20 μM to 1 mM of H_2O_2 oxidation in 0.1 M NaOH. The amperometric-response sensitivity was estimated using the calibration curves between the steady-state response current and the injected H_2O_2 concentration. The linear regression for the modified electrodes at different Co_3O_4 contents can be derived from the following equations:

$$\text{Co}_3\text{O}_4: J(\mu\text{A} \cdot \text{cm}^{-2}) = 1466 C (\text{mM}) + 0.052, \quad R^2 = 0.991 \quad \text{Eq. 9. 3}$$

$$25 \text{ wt. \%Co}_3\text{O}_4: J(\mu\text{A} \cdot \text{cm}^{-2}) = 1587 C (\text{mM}) + 0.122, \quad R^2 = 0.992 \quad \text{Eq. 9. 4}$$

$$50 \text{ wt. \%Co}_3\text{O}_4: J(\mu\text{A} \cdot \text{cm}^{-2}) = 2410 C (\text{mM}) + 0.049, \quad R^2 = 0.994 \quad \text{Eq. 9. 5}$$

$$75 \text{ wt. \%Co}_3\text{O}_4: J(\mu\text{A} \cdot \text{cm}^{-2}) = 3000 C (\text{mM}) + 0.122, \quad R^2 = 0.991 \quad \text{Eq. 9. 6}$$

The estimated slope for each electrode represents its sensitivity to H_2O_2 oxidation. The titanium-modified electrode with nanostructured Co_3O_4 achieved a detection sensitivity of 1466 $\mu\text{A} \cdot \text{mM}^{-1} \cdot \text{cm}^{-2}$. The detection sensitivity to H_2O_2 oxidation was further enhanced in the case of modified electrodes with $\text{Co}_3\text{O}_4\text{-MoS}_2$ NCs with the gradual increase of Co_3O_4 content. The sensitivity of nanocomposites with Co_3O_4 contents of 25, 50, and 75 wt.% were 1587, 2410, and 3000 $\mu\text{A} \cdot \text{mM}^{-1} \cdot \text{cm}^{-2}$, respectively. Furthermore, the lowest detection limit for the H_2O_2 response was in a range of 2 to 5 nM for all working electrodes, revealing the high sensing tendency of the $\text{Co}_3\text{O}_4\text{-MoS}_2$ NCs electrodes. Based on the

estimated electrocatalytic activity of titanium modified electrodes with $\text{Co}_3\text{O}_4\text{-MoS}_2$ NCs toward H_2O_2 oxidation in 0.1 M NaOH in this study, we made a non-enzymatic sensing performance comparison with recent developed Co-based electrocatalysts as illustrated in **Table 9. 6**.

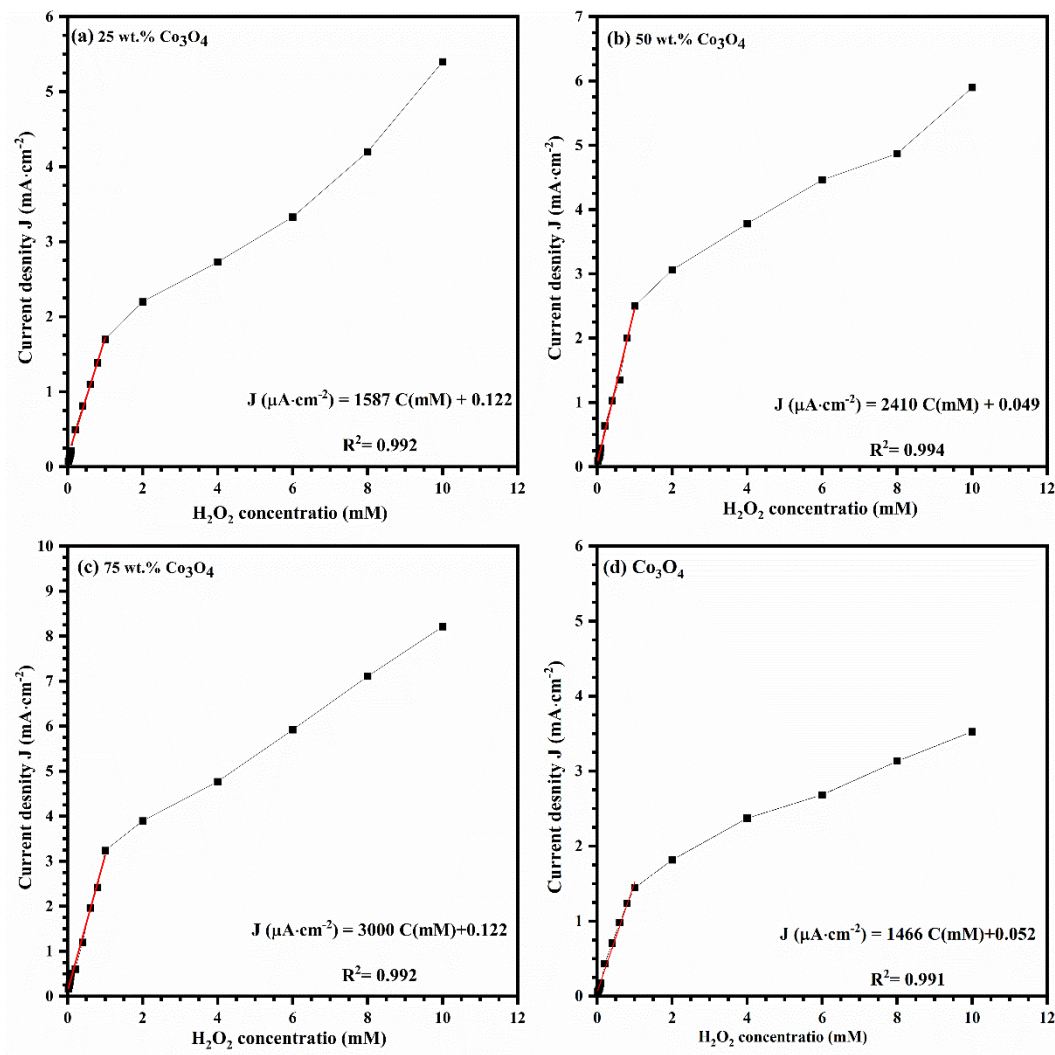


Figure 9. 23: Calibration curves of current-induced response to H_2O_2 concentration by $\text{Co}_3\text{O}_4\text{-MoS}_2$ nanocomposites electrodes at different Co_3O_4 contents.

Table 9. 6: Comparison of electrochemical performance of the present work and recently published work of Co-based nonenzymatic amperometric H_2O_2 sensors.

Modified electrode	Potential (V)	Electrolyte	Response time (s)	Sensitivity ($\mu A \cdot mM^{-1} \cdot cm^{-2}$)	Linear range (mM)	LOD (μM)	Ref.
75 wt.% Co_3O_4/Ti	0.6	0.1 M NaOH	~ 4	3000	0.02-1	0.002~0.005	This work
50 wt.% Co_3O_4/Ti				2410			
25 wt.% Co_3O_4/Ti				1587			
Co_3O_4/Ti				1466			
$NiCo_2O_4/Co_3O_4$	-0.35	0.1 M NaOH	-	303.42	0.02-1.1	0.596	[248]
$NiCo_2S_4/rGO$	-0.45	0.1 M NaOH	5	118.5	0.025-11.25	0.19	[249]
Co_3O_4/NPG	-0.3	0.1 M NaOH	2	1338.7	0.02-19.1	6.4	[408]
$Au@C-Co_3O_4$	+0.5	0.1 M PBS (pH 7.4)	-	7553	0.00005-0.1	0.019	[216]
Co_3O_4/rGO		0.1 M PB (pH 7.0)		3450	0.00005-0.4	0.015	[218]
$MnO_2-Co_3O_4/GO$	+0.5	PBS (PH 7.0)	3	53.65	0.005-1.2	0.8	[250]
Co_3O_4-rGO	-0.19	0.1 M PBS (pH 7.4)	5	1140	0.015-0.675	2.4	[251]
Co_3O_4 hollow sphere	+0.39	0.1 M NaOH	3	979.79	0.0004-2.2	0.105	[214]
$Co_3O_4/CNTs$	-0.19						
Nanoporous Co_3O_4	-1	0.1 MPBS (pH 7.0)	2	1357	0.2-1.3	200	[252]
Co_3O_4-NWs/CF	-0.48	0.1 M KOH	3	230	0.01-1.05	1.4	[253]
Nafion/ GO/Co_3O_4	0.76	Phosphate (pH 7.4)	4	560	0.001-0.1	0.3	[254]

9.3. Summary

$Co_3O_4-MoS_2$ nanocomposite thin films at different Co_3O_4 contents (25, 50, and 75 wt.%) were successfully fabricated at room temperature using an NPDS through one-step deposition from micro-sized powders of Co_3O_4 and MoS_2 . Optimized $Co_3O_4-MoS_2$ NCs/Ti heterostructure electrodes were used as electrocatalysts for non-enzymatic detection of H_2O_2 oxidation in 0.1 M NaOH. The deposited thin-film surface was examined using SEM, Raman spectroscopy, and XPS. The SEM images of the titanium-modified electrodes with $Co_3O_4-MoS_2$ NCs revealed nanosheets with merged grain boundaries, indicating fragmentation of the initial microparticles of Co_3O_4 with a semispherical shape and a multilayer structure of MoS_2 as well as interfacial bonding between Co_3O_4 and MoS_2 species in the deposited films. Increasing Co_3O_4 content resulted in further fragmentation of MoS_2 layers to a lower size range. Analysis of Raman spectra of titanium-modified electrodes with nanostructured Co_3O_4 , MoS_2 nanosheets, and their composites at different Co_3O_4 contents, revealed a positive shift to higher values compared with the corresponding composites in the bulk phase due to the fragmentation to the nano-size range. A synergy effect improvement between various electroactive species at the surface of the titanium-modified

electrodes with $\text{Co}_3\text{O}_4\text{-MoS}_2$ NCs was evident in a high-resolution XPS analysis of the various active state, including S 2p, Mo 3d, O 1s, and Co 2p at the deposited thin-film surfaces. Incorporation of Co_3O_4 in hybrid $\text{Co}_3\text{O}_4\text{-MoS}_2$ NCs was accompanied by a positive shift in binding-energy for MoS_2 -related active states (i.e., S 2p, and Mo 3d) compared with the titanium-modified electrode with pure MoS_2 nanosheets. Modified titanium electrodes with $\text{Co}_3\text{O}_4\text{-MoS}_2$ NCs exhibited a relative improvement in the low spin states (Co^{3+}) related to cobalt species compared with the modified titanium electrode with pure Co_3O_4 nanosheets, which have more preferable electroactive sites for H_2O_2 at high spin states (Co^{2+}). The modified electrodes with 75 wt.% Co_3O_4 supplied the highest contribution from a low spin state (Co^{3+}) compared with other composites. The electrochemical surface area for all titanium-modified electrodes was evaluated using the double-layer capacitance in the non-faradic region, and the modified titanium electrode with pure Co_3O_4 nanosheets achieved a relatively high ECSA of $0.432 \text{ mF}\cdot\text{cm}^{-2}$ compared with pure MoS_2 nanosheets ($0.276 \text{ mF}\cdot\text{cm}^{-2}$). Furthermore, titanium-modified electrodes with $\text{Co}_3\text{O}_4\text{-MoS}_2$ NCs Co_3O_4 contents of at 25, 50, and 75 wt.% exhibited a higher ECSA compared with the pure phase of Co_3O_4 and MoS_2 , and the composite with 75 wt.% Co_3O_4 had the highest ECSA ($2.35 \text{ mF}\cdot\text{cm}^{-2}$) indicating a gradual improvement in the concentration of electrocatalytic active sites with gradual incorporation of Co_3O_4 . The electrochemical performance of titanium-modified heterostructure electrodes with $\text{Co}_3\text{O}_4\text{-MoS}_2$ NCs toward the H_2O_2 oxidation was evaluated using electrochemical impedance spectroscopy, cyclic voltammetry, and chronoamperometric plots in the presence of H_2O_2 . The CV plots of $\text{Co}_3\text{O}_4\text{-MoS}_2$ NCs/Ti sheets at $50 \text{ mV}\cdot\text{s}^{-1}$ revealed a high response current at the Co_3O_4 oxidation peak with the addition of $5 \text{ mM H}_2\text{O}_2$, and the gradual addition of Co_3O_4 was accompanied by enhancement of the response current and charge-transfer kinetics. Detection sensitivity of H_2O_2 was obtained by analyzing the amperometric response with the sequenced addition of H_2O_2 at various concentrations in 0.1 M NaOH . We found that all titanium-modified electrodes have a wide detection range from $20 \text{ }\mu\text{M}$ to 1 mM with a $2\sim 5 \text{ nM}$ limit of detection. The obtained H_2O_2 sensitivity values were 1446, 1587, 2410, and $3000 \text{ }\mu\text{A}\cdot\text{mM}^{-1}\cdot\text{cm}^{-2}$, corresponding to titanium-modified electrodes with nanostructured Co_3O_4 and $\text{Co}_3\text{O}_4\text{-MoS}_2$ NCs with 25, 50, and 75 wt.% Co_3O_4 , respectively. Furthermore, the oxidation selectivity of titanium modified electrodes with $\text{Co}_3\text{O}_4\text{-MoS}_2$ NCs toward the H_2O_2 in 0.1 M NaOH was investigated for several interfering species such as NaCl, ethanol, saccharose, and glucose, which revealed high H_2O_2 oxidation selectivity compared with other interfering species.

Chapter 10:

*Heterostructured Mn₃O₄-2D Materials Nanosheets: One-Step
Vacuum Kinetic Spray Deposition and Non-Enzymatic H₂O₂
Sensing*

10. 1. Overview

The applicability of nanomaterial (NM) engineering enables the research community to improve the performance of various technological applications. The high surface-to-volume ratio of NMs makes their physical properties incredibly sensitive to size, morphology, composition, and surface state defects. The design of novel heterostructure interfaces is widely used for improving the charge transport properties within the space-charged layer on the surface of NMs. NMs with an anisotropic morphology, like nanorods or nanosheets, have attracted much attention in various electrochemical fields related to energy storage and conversion, as well as non-enzymatic biosensor applications [413-415].

Nanostructured electrocatalysts based on transition metal oxides (TMOs) are characterized by their low cost, chemical stability, resistance to corrosion, and high electrocatalytic activity. These materials are considered as a promising alternative to expensive noble-metal-based electrocatalysts [192, 193, 407]. This makes nano-sized TMOs and their composites widely used in practical applications. One of the most interesting structural configurations is the spinel phase of magnetic nanoparticles, such as Co_3O_4 and Mn_3O_4 . This phase is characterized by the presence of several oxidation states that are spatially distributed in different lattice sites in the spinel structure (i.e., octahedral, or tetrahedral). These active states serve as electroactive sites for various electrocatalytic redox reactions. Chen et al. [416] demonstrated that using a nano-sized spinel structure containing mixed phases of cobalt and manganese oxide with various oxidation states (i.e., Co^{2+} , Co^{3+} , Mn^{3+} , and Mn^{4+}) improved H_2O_2 electrocatalytic reduction. Manganese oxides with different forms (i.e., MnO_2 , Mn_2O_3 , and Mn_3O_4) are attractive materials with a diversity of electroactive sites on their surfaces that exhibit high activity in various electrochemical applications [417-420]. Additionally, the presence of multivalent states of manganese (i.e., Mn^{3+} and Mn^{4+}) in catalysts has a profound effect on the H_2O_2 dissociation rate [421]. However, it is known that TMO-based nanomaterials suffer from poor electrical conductivity and small surface areas due to their intrinsic aggregation tendency. These materials also show sluggish charge transport kinetics. This would cause low electrochemical performance in the case of modified electrodes with only TMOs [410, 422]. Wang et al. [423] prepared aggregated octahedral Mn_3O_4 particles with micro-sized domains using a solvothermal technique. Then, the obtained powder was bonded to a glassy carbon substrate. This whole process takes more than 15 h. The fabricated electrode revealed a wide linear detection range from 5 μM to 17 mM H_2O_2 . However, the estimated detection sensitivity was very small (about 5.74 $\mu\text{A} \cdot \text{mM}^{-1} \cdot \text{cm}^{-2}$). Another attempt for improving the electrocatalytic activity through the formation of an $\text{Mn}_3\text{O}_4/\text{Co}_3\text{O}_4$ heterostructure was performed by

Wu et al. [424]. They synthesized $\text{Mn}_3\text{O}_4\text{-MnCo}_2\text{O}_4$ NCs by a solvothermal precipitation method. The fabricated heterostructure electrode exhibited a wide linear detection range from 0.1 μM to around 1.2 mM H_2O_2 at a high oxidation potential of 0.8 V. However, the determined sensitivity for the amperometric response was very small ($34.5 \mu\text{A}\cdot\text{mM}^{-1}\cdot\text{cm}^{-2}$).

The electrocatalytic performance of TMOs can be markedly improved by forming a heterostructure with other functional materials. A common way to improve the charge transfer kinetics at the electrode/electrolyte interface is to form a heterostructure with two-dimensional (2D) materials, such as graphene or MoS_2 . Graphene nanosheets, which are an sp^2 -hybridized carbon array, are the most widely used form of 2D materials. Graphene nanosheets exhibit outstanding surface area, superior electrical and thermal conductivities, and very high mechanical strength [425, 426]. MoS_2 nanosheets are also widely used for improving charge transportation as an alternative to graphene nanosheets because they show very high in-plane charge carrier mobilities [427]. This makes 2D-material nanosheets the optimum choice for improving the charge transport properties of TMO-based catalysts. The expected improvement in the electrocatalytic activity would result from the synergy improvement at the formed heterostructure interfaces [428-430].

The interfacial dislocation and lattice mismatch between heterogeneous compounds still represents a great challenge for researchers. An optimized technique is needed for assembling the different primary building grains in heterostructure composites [431]. Li et al. [432] synthesized heterostructured $\text{MnO-Mn}_3\text{O}_4$ @reduced graphene oxide (rGO) composites in several consecutive but separate steps, in which the rGO was separately prepared through sonication and solvothermal treatment followed by adding the manganese precursor at high calcination temperatures ranging from 400 to 600 $^\circ\text{C}$. This fabrication process takes more than 28 h and the product is in a powder form, which is then mixed with a binder so it can adhere to the electrode surface. This electrode has a wide linear range for H_2O_2 reduction, but shows a very small detection sensitivity of $274.15 \mu\text{A}\cdot\text{mM}^{-1}\cdot\text{cm}^{-2}$. Li et al. [250] prepared a binary $\text{MnO}_2\text{-Co}_3\text{O}_4$ @rGO nanocomposite (NC) by an electrochemical process in the potential range from 0 to -1.5 V, in which the purchased rGO was electrochemically reduced on glassy carbon followed by electrodeposition of $\text{MnO}_2\text{-Co}_3\text{O}_4$ on the modified electrode surface. The fabricated electrode was used for H_2O_2 detection at a high oxidation potential of 0.5 V in 0.1 M phosphate-buffered saline (PBS). The optimized electrode revealed a very small sensitivity of $53.65 \mu\text{A}\cdot\text{mM}^{-1}\cdot\text{cm}^{-2}$ with a wide linear detection range of H_2O_2 extending from 0.1 μM to 1.2 mM. Zeng et al. [433] prepared heterostructure NCs of

Mn₃O₄-MnO₂@graphene using hydrothermal techniques in multiple separate steps. The fabrication process for separate phases and NCs takes more than two days. The obtained hybrid NCs were utilized for H₂O₂ reduction in 0.1 M NaOH, which exhibited high sensitivity (1443 μA·mM⁻¹·cm⁻²) in a relatively wide linear range from 1 to 200 μM H₂O₂.

Recently, we fabricated various heterostructure composites from spinel Co₃O₄ and either graphene nanosheets or MoS₂ nanosheets by using a nanoparticle deposition system (NPDS). The Co₃O₄-graphene hybrid NCs were utilized for H₂O₂ reduction. Alternatively, H₂O₂ oxidation was investigated with Co₃O₄-MoS₂ hybrid NCs. In both cases, the hybridization between spinel Co₃O₄ and the 2D material nanosheets improved the non-enzymatic detection sensitivity of H₂O₂ in an alkaline medium [258, 264]. Furthermore, we also fabricated other hybrid NCs for energy conversion and storage applications in our recently published works [260, 262, 263]. The spontaneous fragmentation of TMOs and the mechanical exfoliation of 2D materials in the hybrid NCs upon the impact of micron powder with the substrate are expected to dramatically increase the localized pressure and temperature. This adiabatic increase in the localized thermodynamics parameters is saturated within a few nanoseconds and provides enough bonding energy between the nano-sized domains of the deposited thin films [100]. Moreover, the deposition by the NPDS process has many advantages. For example, there is no need to use dangerous chemicals, the process does not use any external binders, the cost and fabrication time required to make the desired electrocatalyst are low [221, 277], and the process can be used to produce large samples [99].

A comparison between different hybrid materials consisting of 2D material nanosheets and Mn₃O₄ nanorods, made via a single-step fabrication process, has not been reported in the literature. To clearly understand the role of various synergy routes between the 2D material nanosheets and Mn₃O₄ on the non-enzymatic detection of H₂O₂ reduction, we fabricated modified electrodes with Mn₃O₄ nanorods as well as hybrid NCs with MoS₂ and graphene nanosheets. This was done using a one-step, simple, and cost-effective vacuum kinetic process via by the NPDS at room temperature within a very short time span (as compared with other techniques). The obtained results showed that the incorporation of 2D material nanosheets strongly enhanced the electrocatalytic activity toward the reduction of H₂O₂ in 0.1 M NaOH.

10. 2. Results and Discussion

10. 2. 1. XRD analysis of Mn₃O₄-2D-layered materials composites

Figure 10. 1(a) reveals the XRD patterns of the Mn₃O₄, MoS₂, graphite, Mn₃O₄- composites with either graphite or MoS₂ micron powder. The XRD pattern of the MoS₂ micron powder

exhibits multiple XRD peaks at 14.38, 28.96, 32.62, 33.44, 35.82, 39.4, 44.1, 49.74, 55.94, 58.28, and 60.1° 2θ, corresponding to the (002), (004), (100), (101), (102), (103), (006), (105), (110), and (008) planes, respectively, of the hexagonal phase of micro-crystalline MoS₂ (P6₃/mmc, Ref. card no.: 00-037-1492, PDF 2010). The XRD plot of the micron graphite powder shows the most intense peaks at 26.52° and 54.62° 2θ, corresponding to the (002) and (004) crystalline planes, respectively, of the hexagonal phase of bulk graphite (P6₃/MMC, a = 2.643 Å and c = 6.714 Å Ref. card no.: 00-056-016, PDF 2010).

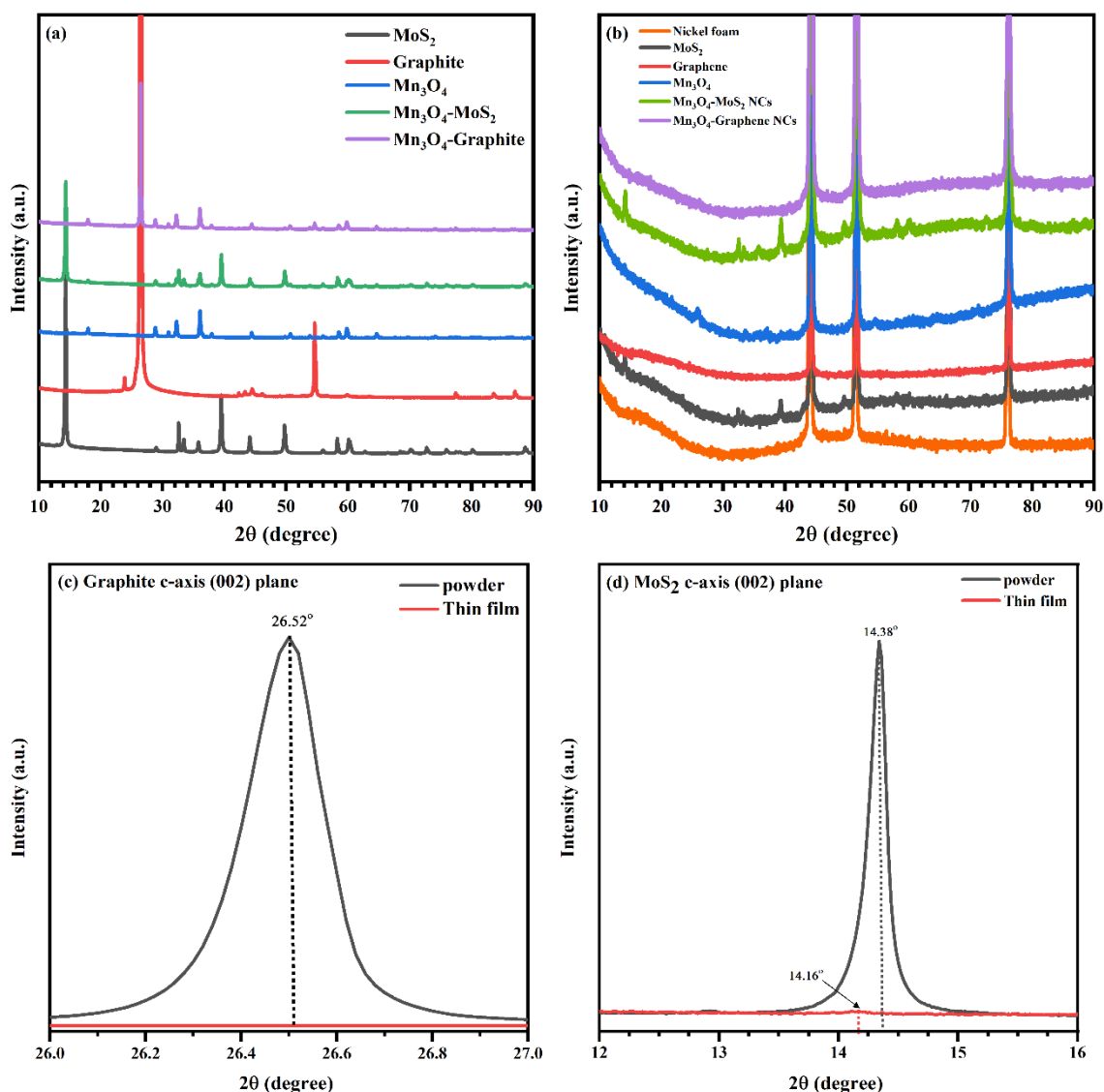


Figure 10. 1: XRD patterns of Mn₃O₄-2D material composites in powder form **(a)** and corresponding nano-sized film on the NF porous substrate **(b)**. Magnified XRD peak related to the c-axis of the (002) plane in the powder and deposited thin films with graphite **(c)** and MoS₂ **(d)**.

Furthermore, another XRD peak with a smaller intensity was observed at a lower 2θ of 23.92° due to the edge oxidation of long-order graphite crystalline domains [105]. The XRD pattern of the micro-sized Mn_3O_4 powder reveals several diffraction peaks at $17.96, 28.84, 30.96, 32.26, 36.06, 37.97, 44.4, 50.66, 53.84, 55.96, 58.52,$ and $59.8^\circ 2\theta$, corresponding to the (101), (112), (200), (103), (211), (004), (220), (105), (312), (303), (321) and, (224) planes, respectively, of the tetragonal Mn_3O_4 structure ($141/\text{amd}$, Ref. card no.: 00-002-1062, PDF 2010). The XRD patterns of the micro-sized powder of Mn_3O_4 mixed with either MoS_2 or graphite powder exhibited the presence of all phases without the evolution of any secondary phases. Here, mixing was carried out via the ball milling processing before deposition. **Figure 10. 1(b)** shows the XRD patterns of the deposited MoS_2 , graphite, Mn_3O_4 , and their composites thin films on NF porous substrates. It can be observed that the XRD patterns of all deposited thin films show three main diffraction peaks at $44.19, 51.54,$ and $76.09^\circ 2\theta$. These peaks match with the (111), (200), and (220) planes of the cubic nickel foam phase (Fm-3m space group, Ref. card no. 00-004-0850, PDF 2010). The mechanism of size reduction caused by the micron particles impacting with the hard substrate has two main possibilities. The first is the fragmentation of the micron crystalline domains into nano-sized crystalline domains with very short-order range as a result of the high impact velocity of the accelerated micron powder on the hard substrate. This behavior was recognized by comparing the intensity of all XRD peaks of the micro-sized particles with the corresponding peaks after the deposition process by the NPDS. The second potential mechanism of size reduction is mechanical exfoliation and interlayer separation of the layered material (i.e., graphite or MoS_2), which can be further illustrated as follows. In **Figure 10. 1(c, d)** the XRD peak corresponding to the c-axis along the (002) crystalline plane of the hexagonal layered structure of graphite and MoS_2 is magnified for the micro-sized material and the corresponding thin film. In the case of the graphite/NF thin film, the XRD peak corresponding to the (002) crystalline plane vanished, demonstrating the interlayer separation and layer thinning of the stacked graphite layers. A similar behavior was observed in the case of MoS_2/NF . However, the XRD peak did not disappear because of the relatively strong interlayer interaction, as compared with the hexagonal graphite phase. The detected XRD peak position of MoS_2/NF was slightly shifted to a lower diffraction angle ($14.16^\circ 2\theta$) compared with the corresponding MoS_2 micron powder ($14.38^\circ 2\theta$). This peak shift indicated an increase in the interplanar distance after the stacked-layer separation during the deposition process by the NPDS. This behavior was also observed for Mn_3O_4 -based composites with layered

materials. This reveals the successful mechanical exfoliation of the layered materials using the vacuum kinetic process of the NPDS.

10. 2. 2. Investigation of the surface structural phase of Mn₃O₄-2D materials hybrid composites

The changes in the structural phases at the surface of the micro-sized powder and the corresponding deposited thin films are identified using the inelastic phonon scattering results obtained by Raman spectroscopy, which are very sensitive to the spatial variations of the material surface. The micro-Raman spectrum provides highly localized scanning control within the micro-size range [411]. Since the deposition of ceramic-based NCs by the NPDS is mostly accompanied by size reduction due to the fracture of the micron powder into the nano-size range, various disorder-related modes are expected to be enhanced. This behavior is associated with multiple variations in the related Raman symmetry modes, which can provide valuable information about the corresponding surface structural phase after the deposition process. Therefore, we used micro-Raman spectroscopy to compare the surface states of the micron powders and the deposited thin films of pure phases of Mn₃O₄, MoS₂, graphite, and their composites. The identified Raman peaks for all phases are recorded in **Table 10. 1**. Raman spectra of MoS₂ micron powder and the deposited thin film on NF porous substrate are shown in **Figure 10. 2(a)**. The micro-Raman spectrum of the MoS₂ micron powder revealed several Raman peaks at 279, 372, 400, 442, and 557 cm⁻¹. The fundamental first-order vibrations at 372 and 400 cm⁻¹ are attributed to the Mo-S bond vibrations, where the in-plane vibrations correspond to the E¹_{2g} symmetry mode and the out-of-plane vibrations correspond to the A_{1g} symmetry mode. Here, the difference in the first-order peak positions is 28 cm⁻¹. The small Raman peak at 279 cm⁻¹ is caused by the first-order vibration of the E_{1g} symmetry mode. The illustrated first-order vibration indicates the layered hexagonal structure of the bulk MoS₂ phase [120-123]. The second-order Raman peaks observed at higher Raman shift values of 442, 557, and 585 cm⁻¹ are ascribed to the symmetry modes of the longitudinal acoustic (2LA), 2E_{1g}(Γ), and their linear combinations, respectively [393]. The micro-Raman spectrum of the nano-sized MoS₂ thin film on the NF porous substrate exhibits active vibrations that are matched with the micron MoS₂ powder. However, the detected Raman peaks were upshifted to a higher wavenumber, as shown in **Table 10. 1**. This behavior is related to the lattice disorder improvement at the interfacial grain boundaries [124]. Furthermore, the peak position difference between the fundamental first-order E¹_{2g} and A_{1g} symmetry modes was reduced to 23 cm⁻¹. The observed spectral shift of all Raman peaks to higher values and the decrease of the fundamental Raman peak difference has two significant meanings. The first is related to the size reduction

due to the micron powder fragmentation, while the second is related to the spontaneous mechanical exfoliation of stacked MoS₂ layers [119, 434]. This behavior is expected to arise from the high-velocity impact between the powder and the hard substrate during the deposition by the NPDS.

Figure 10. 2(b) reveals the micro-Raman spectra of the graphite micron particles and the deposited thin films on the NF porous substrate. The micron powder shows various Raman peaks at 1345, 1575, 2709, and 3231 cm⁻¹. The first Raman peak at 1345 cm⁻¹ corresponds to the first-order D symmetry mode of the hexagonal phase of bulk layered graphite. This vibration is induced by grain boundary edge defects. The Raman peak related to the G band of the hexagonal phase of bulk crystalline graphite at 1575 cm⁻¹ is attributed to the first-order vibration caused by the E_{2g} mode. The intensity of the G band of the bulk graphite phase is strongly affected by the alteration of the ordering range (i.e., the crystallinity degree) [110]. The observed Raman peaks at higher Raman shift values of 2709 and 3231 cm⁻¹ are ascribed to the second-order vibrations related to the 2D intervalley and 2D' symmetry modes, respectively [111, 112]. The micro-Raman spectrum of the graphite thin films on the NF porous substrate exhibits multiple Raman peaks centered at 1354, 1592, 1624, 2701, and 2942 cm⁻¹. The observed Raman peaks at 1354 and 1592 cm⁻¹ represent the first-order symmetry modes of the D and G bands, respectively. Moreover, the Raman peak positions of these bands were upshifted to higher values compared with the corresponding positions in the micron powder. Meanwhile, the second-order 2D symmetry mode at 2701 cm⁻¹ exhibited a downshift compared with the corresponding position in the micron graphite powder. The observed alteration of Raman peak positions of either first- or second-order symmetry modes indicates the enhancement of interfacial surface defects due to the fragmentation of the micron powder by the high-velocity impact with the hard substrate. This behavior is further verified by the observation of other disorder-related modes in the deposited graphite thin films at 1619 and 2936 cm⁻¹. The first disorder-related mode at 1619 cm⁻¹ is due to the translational movement of carbon atoms from bulk lattice sites into the crystalline domain surface. The small band at 2936 cm⁻¹ is induced by the disorder-related G'' band [113, 114]. The layered material exfoliation is another interesting feature that is expected to be caused by the high-velocity impact of the micron powder [101]. The interlayer separation and reduction of graphite stacked layers into small graphene nanosheets can be identified based on the enhanced disorder-related D band and the reduced crystallinity-related G band. This can be recognized by looking at the intensity ratio between the D and G band peaks (I_D/I_G). In the case of the micron graphite powder, the I_D/I_G ratio

is 0.187, which is sharply increased in the case of the nanostructured thin film to 1.4. The observed improvement in the I_D/I_G ratio is caused by the fragmentation and interlayer separation of the micron-crystalline domains in the graphite powder to a few graphene layers. This is mostly accompanied by the presence of a high concentration of edge defects [115]. The reported I_D/I_G ratio of 1.42 is higher than the values in other reports that investigated graphite exfoliation with other techniques [116-118]. This demonstrates the successful exfoliation of the layered graphite hexagonal structure into small graphene nanosheets via one step with the NPDS.

Figure 10. 2(c) depicts the micro-Raman spectra of the Mn_3O_4 micron powder and the corresponding thin film on the NF porous substrate. The micron powder exhibits Raman peaks at 314, 370, and 654 cm^{-1} , which are related to the bulk tetragonal phase of spinel Mn_3O_4 [435, 436]. The phonons detected at relatively low wavenumber values of 314 and 370 cm^{-1} are attributed to the E_g and T_{2g} symmetry modes, respectively. The most intense peak at 654 cm^{-1} corresponds to the A_{1g} symmetry mode that is caused by the stretching vibration of the Mn-O bond in the spinel structure of Mn_3O_4 [437]. The observed active vibration bands, with a negligible intensity at 476 and 558 cm^{-1} , are caused by either asymmetric stretching or out-of-plane bending of oxygen bonds (Mn-O-Mn) in the α - Mn_2O_3 phase [438, 439]. Another probable cause for this weak band is the presence of some divalent Mn^{2+} oxides [440]. The Raman spectrum of the nano-sized Mn_3O_4 /NF thin film shows the same active vibration with lower intensity compared with the corresponding Raman peaks of the micron powder. Additionally, there is a downshift for all Raman peak positions, which is attributed to an improvement in the surface state defects associated with the reduction of the crystalline domain size [441]. The change in the micro-Raman spectrum of the Mn_3O_4 - MoS_2 composite micron powder after deposition on the NF porous substrate is illustrated in **Figure 10. 2(d)**. The Raman spectrum of the Mn_3O_4 - MoS_2 mixed micron powder reveals various active vibrations related to Mn_3O_4 or MoS_2 pure phases, as shown in **Table 10. 1**. However, the observed Raman peaks in the mixed powder related to the MoS_2 phase exhibit spectral upshifting to higher wavenumbers compared with the pure phase of the MoS_2 micron powder. This change may arise from the alteration of the interfacial polarization at the grain boundaries of the formed heterostructure composite during the mixing process carried out via ball milling. Furthermore, the Raman spectrum of the deposited Mn_3O_4 - MoS_2 NCs/NF thin films exhibited the same active vibrations, but with further upshifting in the Raman peak positions. Alternatively, the active vibration related to the Mn_3O_4 phase is slightly shifted to a lower wavenumber value.

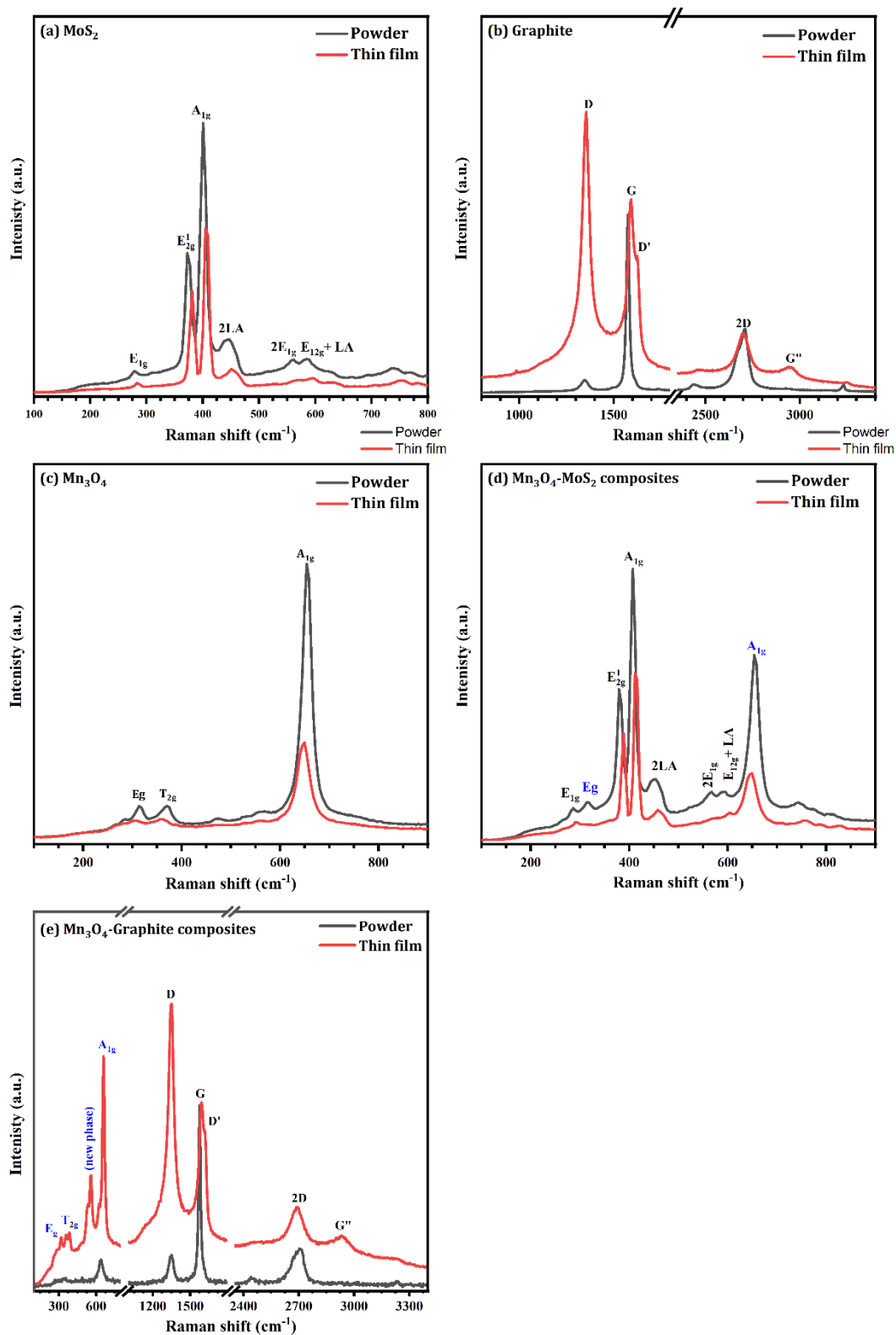


Figure 10. 2: Raman spectra of the micro-sized powder and the corresponding thin films of MoS_2 (a), graphite (b), Mn_3O_4 (c), Mn_3O_4 - MoS_2 (d), and Mn_3O_4 -graphite (e) composites.

The variation in the Raman peak positions is strongly correlated with the spatial localization of interfacial surface states, which can be tuned by the kinetic-induced size reduction through fragmentation of the micron powder or mechanical exfoliation of the stacked layers by the NPDS. In the case of Mn_3O_4 -graphite composites micron powder, the Raman spectrum in **Figure 10. 2 (e)** demonstrates the presence of Mn_3O_4 and graphite species in the mixed powder. The Raman spectrum of the deposited Mn_3O_4 -graphite NCs/NF shows the improvement of disorder-related modes and the inhibition of bulk crystalline modes. The I_D/I_G ratio corresponding to the graphite species in the NC thin film is 1.34, which is higher than the ratio of the corresponding powder (0.8). This shows that the interlayer separation of the layered graphite micron powder is smaller, taking the form of graphene nanosheets. All first-order Raman peaks related to either Mn_3O_4 or graphite species exhibit upshifting to higher values compared with the corresponding peak positions of the mixed micron powder. Meanwhile, the peak position of the second-order 2D symmetry mode at 2692 cm^{-1} exhibited a stronger downshift compared with the corresponding peak position in the micron graphite powder. Furthermore, a new disorder-sensitive vibration is detected at 1615 and 2932 cm^{-1} . This indicates a reduction in the crystalline domain size to the nano-size range, which is accompanied by an improvement in the interfacial defects at the crystalline domain boundaries.

Table 10. 1: Raman active vibrations peaks of Mn_3O_4 -2D materials composites in the form of powder (P) and the corresponding thin film (TF) on NF porous substrate.

Raman Shift (cm^{-1})	Characteristic Raman symmetry modes												
	Phase	MoS ₂				Graphite				Mn ₃ O ₄			
		E _{1g}	E ¹ _{2g}	A _{1g}	2LA	2E _{1g}	D	G	2D	G''	E _g	T _{2g}	A _{1g}
MoS ₂ (P)	279	372	400	442	557								
MoS ₂ (TF)	283	381	404	451	566								
Graphite (P)						1345	1575	2710	-				
Graphite (TF)						1354	1592	2701	2942				
Mn ₃ O ₄ (P)										314	370	654	
Mn ₃ O ₄ (TF)										309	356	649	
Mn ₃ O ₄ -MoS ₂ (P)	285	379	407	453	563					314	-	654	
Mn ₃ O ₄ -MoS ₂ (TF)	290	388	411	459	-					-	-	649	
Mn ₃ O ₄ -graphite (P)						1345	1574	2703	-	305	-	640	
Mn ₃ O ₄ -graphite (TF)						1349	1590	2692	2940	318	375	658	

10. 2. 3. Surface morphology of Mn_3O_4 -2D materials composites

Investigating the surface morphology using SEM images can visually demonstrate the grain size alteration during the deposition process by the NPDS, which can be performed through either kinetic-induced fragmentation of the micron powder or mechanical exfoliation of the mixed layered materials by

spontaneous interlayer separation. **Figure 10. 3(a-c)** show SEM images of the MoS₂ micron powder and the corresponding thin film on the NF substrate, in which the micro-sized powder exhibits stacked flake layers with a wide size distribution extending from less than 1 μm to several μm. The deposited MoS₂/NF thin film shows very thin grains with nanosheet morphology. The observed nanosheets exhibit a wide size distribution with an average size less than 200 nm. Also, the SEM morphology of the graphite micron powder and the corresponding thin films in **Figure 10. 3(d-f)** exhibit the size reduction of the micro flake graphite powder (variable grain sizes ≤ 10 μm) to very small and thin nanosheets with a grain size less than 200 nm. The surface morphology of the micron Mn₃O₄ powder in **Figure 10. 3 (g)** reveals large semi-spherical agglomerates with a lateral size ≤ 5 μm. Moreover, the observed aggregates feature micron rods with various orientations. After the fragmentation process, these micron rods become nanorods (length < 500 nm, width < 50 nm) in the nano-sized Mn₃O₄/NF thin films, as shown in **Figure 10. 3(h, i)**. **Figure 10. 4(a-c)** demonstrate the surface morphology of the mixed Mn₃O₄-MoS₂ micron powder and the corresponding thin film on the NF substrate. The micro mixed powder exhibits a micro flake morphology, which is transformed into small nanosheets with an average size less than 200 nm after the deposition process. In the case of the Mn₃O₄-graphite micron powder, the SEM morphology in **Figure 10. 4(d)** shows semi-spherical agglomerates related to the Mn₃O₄ species and the micron flakes correspond to the graphite powder with the same range observed in the case of the pure phases. Furthermore, the SEM morphology of the Mn₃O₄-graphene NCs/NF thin films in **Figure 10. 4(e, f)** illustrate the fragmentation of micron powder into small nanorods and nanosheets. The elemental compositional analyses of the micron powder of Mn₃O₄, MoS₂, graphite, and their mixed phases are illustrated in **Figure 10. 5**. The homogeneity of compositional distribution after the deposition process on the NF porous substrate for the pure phases and their hybrid NCs is illustrated using EDS elemental mapping with micro-sized spatial resolution as shown from **Figure 10. 6** to **Figure 10. 8**.

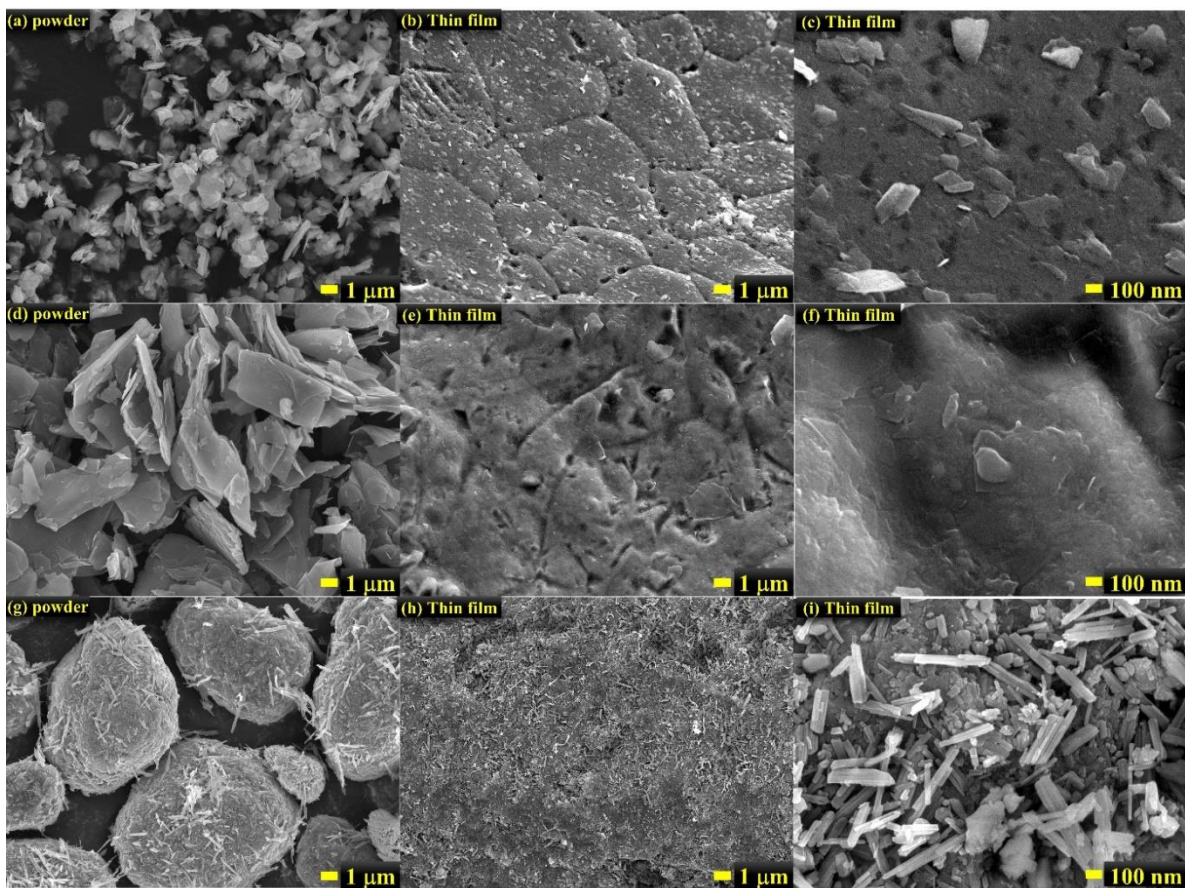


Figure 10. 3: SEM images of the micro-sized powders and the deposited nano-sized thin films on the NF porous substrate: MoS₂ (a-c), graphite (d-f), and Mn₃O₄ (g-i)

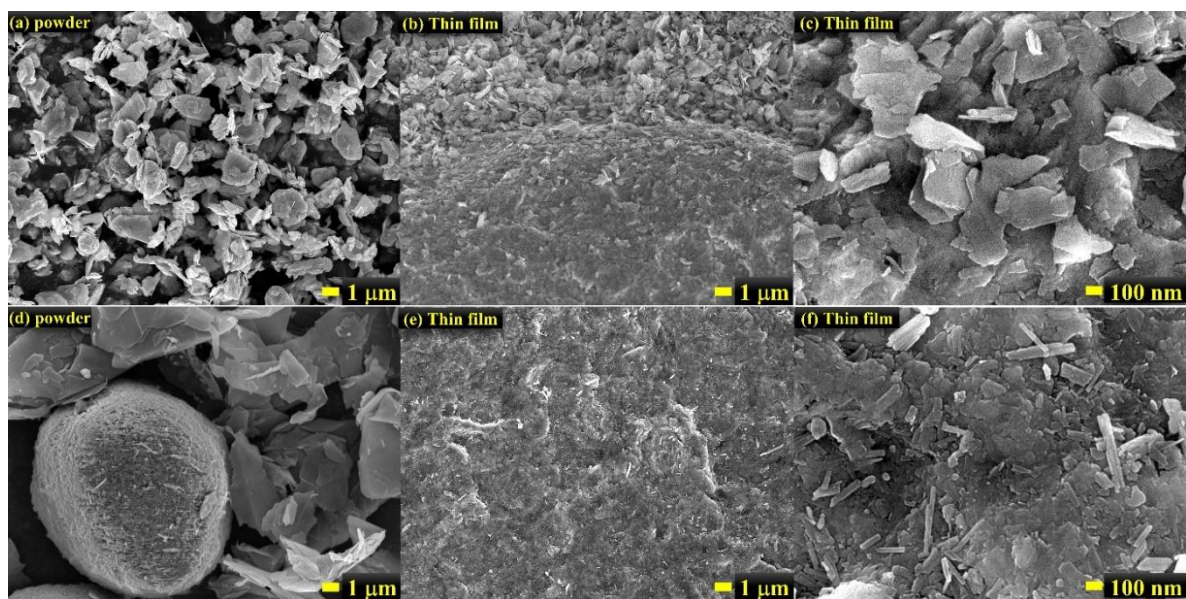


Figure 10. 4: SEM images of the micro-sized powders and the deposited nano-sized thin films on the NF porous substrate: Mn₃O₄-MoS₂ (a-d), and Mn₃O₄-graphite (d-f) composites.

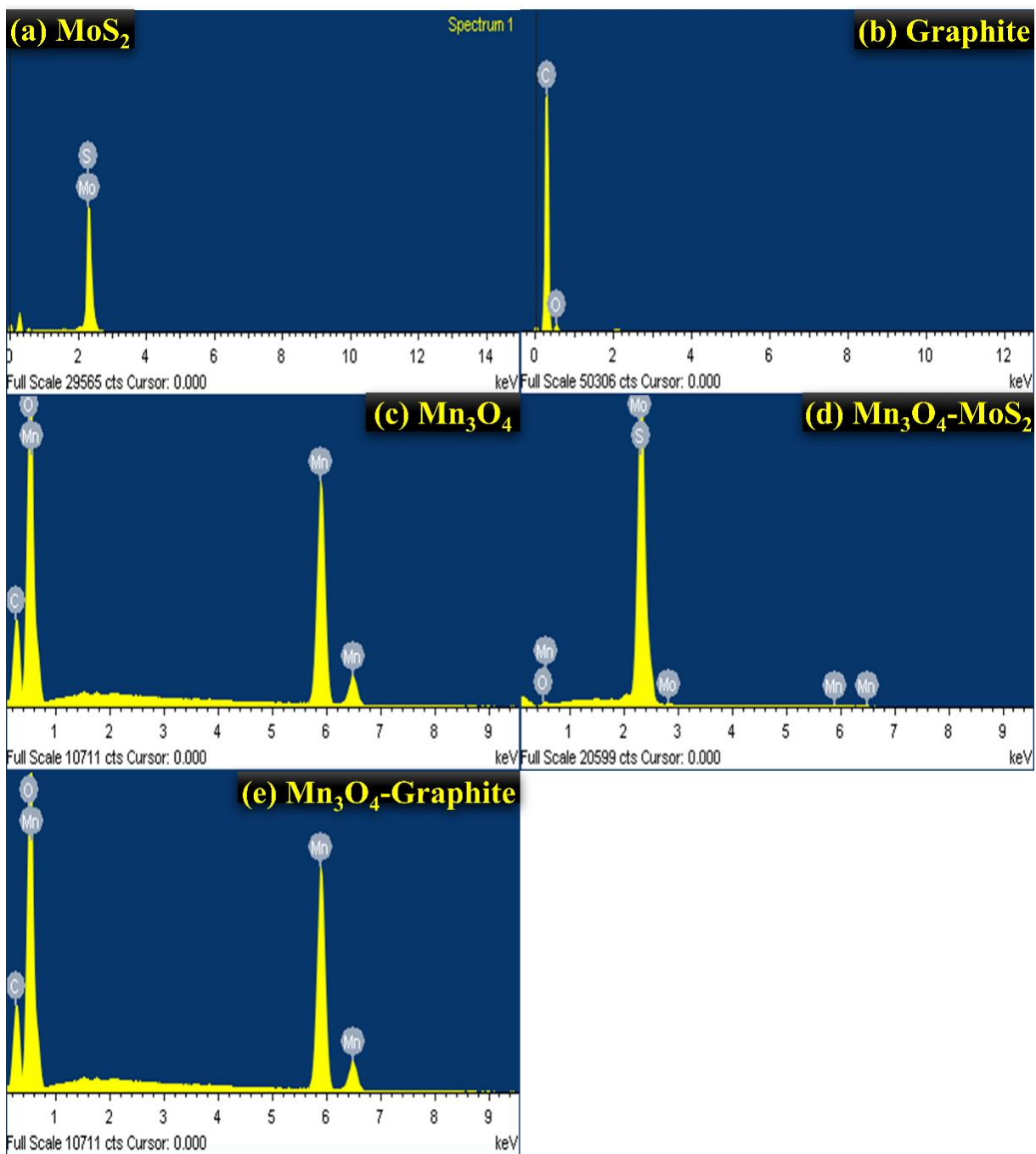


Figure 10. 5: Micron powder EDS elemental composition analysis of MoS₂ **(a)**, graphite **(b)**, Mn₃O₄ **(c)**, Mn₃O₄-MoS₂ composite **(d)**, and Mn₃O₄-graphite composite **(e)**.

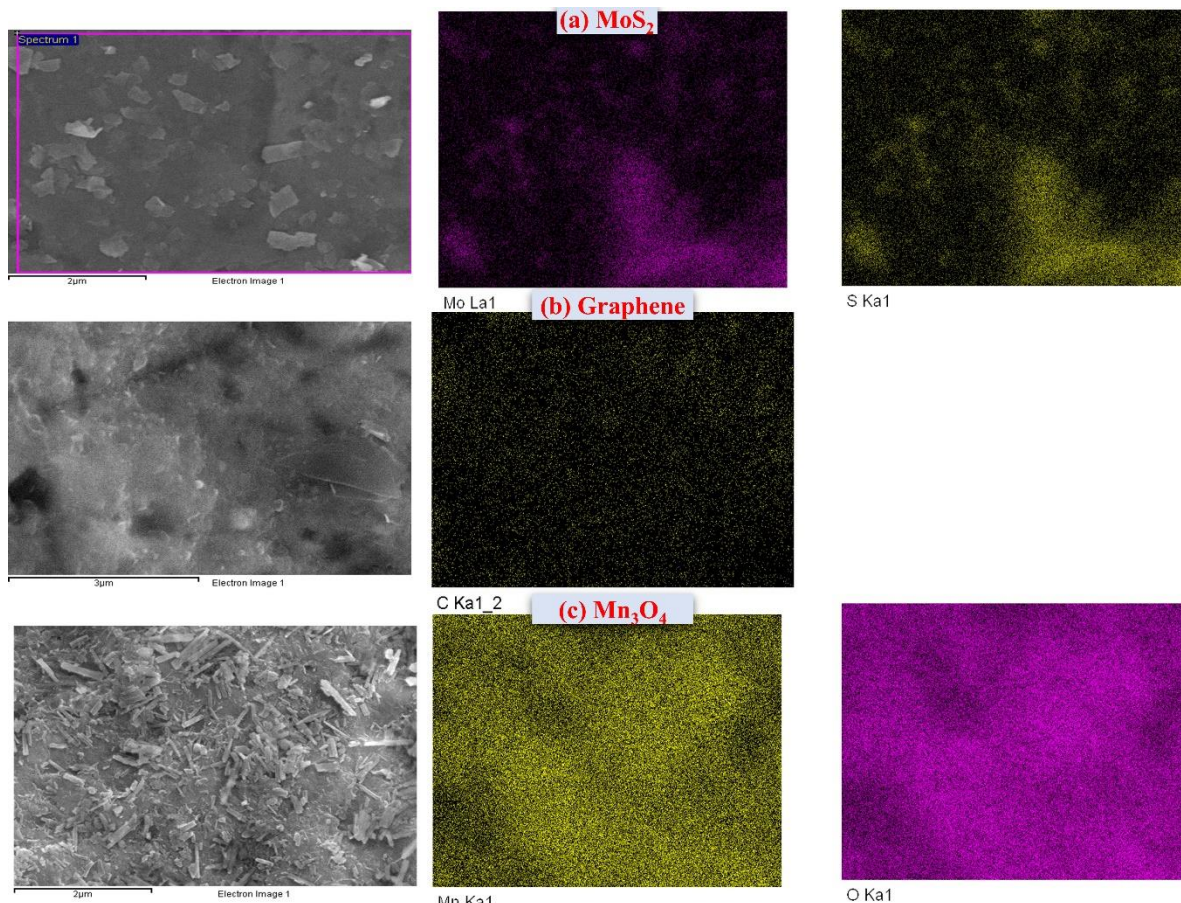


Figure 10. 6: EDS elemental mapping analysis of MoS_2 (a), graphene (b), and Mn_3O_4 (c) thin films on the NF porous substrate.

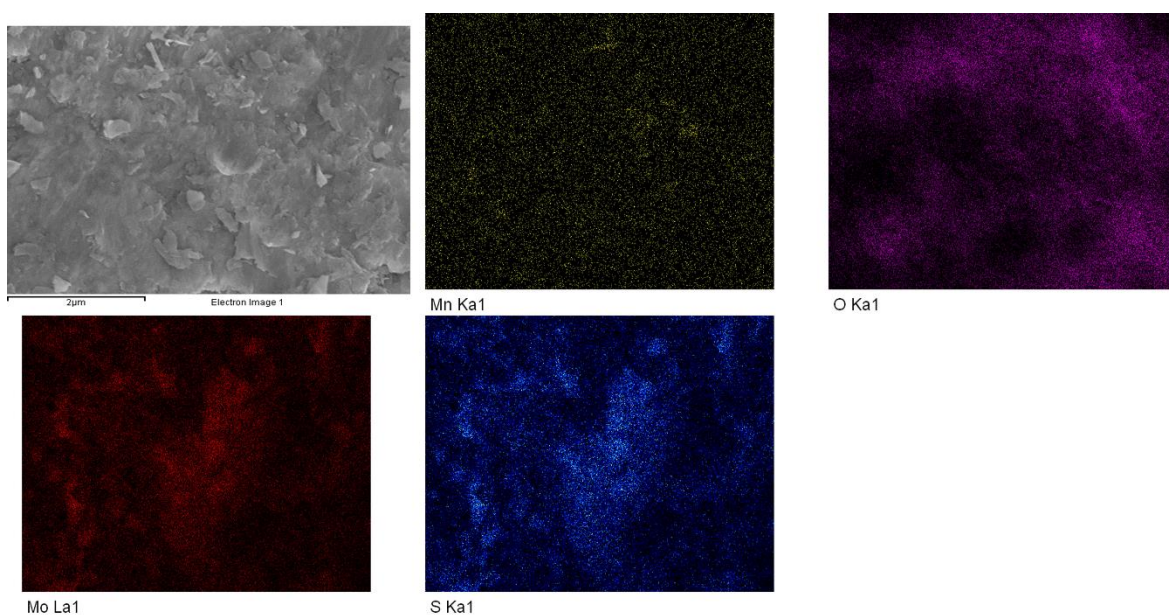


Figure 10. 7: EDS elemental mapping analysis of Mn_3O_4 - MoS_2 NCs on the NF porous substrate.

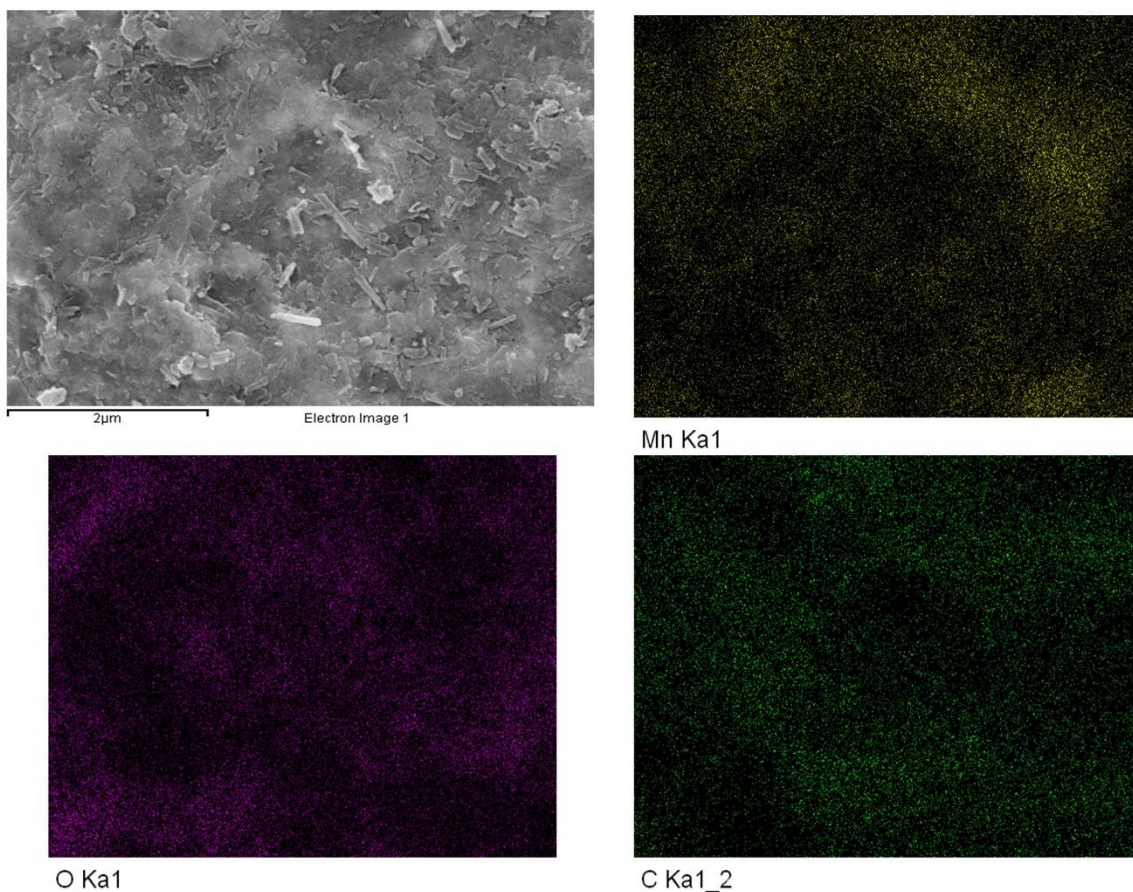


Figure 10. 8: EDS elemental mapping analysis of Mn_3O_4 -graphene NCs on the NF porous substrate.

10. 2. 4. XPS studies on Mn_3O_4 -2D materials composites

The valence and core chemical states on the surface of Mn_3O_4 -based NCs with 2D materials (i.e., MoS_2 and graphene) were examined using XPS. The survey scans in **Figure 10. 9(a)** show that all of the detected chemical states are related to either Mn_3O_4 , MoS_2 , or graphene species in the deposited nano-sized thin films. To demonstrate the hybridization between the nano-sized Mn_3O_4 and the 2D material nanosheets in the hybrid NCs, high-resolution XPS spectra of S 2p, Mo 3d, C 1s, O 1s, and Mn 2p were examined as shown in **Figure 10. 9(b-f)**. For accurate evaluation of the peak position centers, a fitting process was performed for all high-resolution XPS scans as demonstrated from **Figure 10. 10** to **Figure 10. 14**. The estimated peak positions are recorded in **Table 10. 2**. The detected phases in the NCs were compared with the corresponding pure phases to recognize the synergy developed between the Mn_3O_4 and 2D material nanosheet species. The fitting of the high-resolution S 2p and Mo 3d scans for the pure MoS_2 phase and Mn_3O_4 - MoS_2 hybrid NCs are shown in **Figure 10. 10** and **Figure 10. 11**.

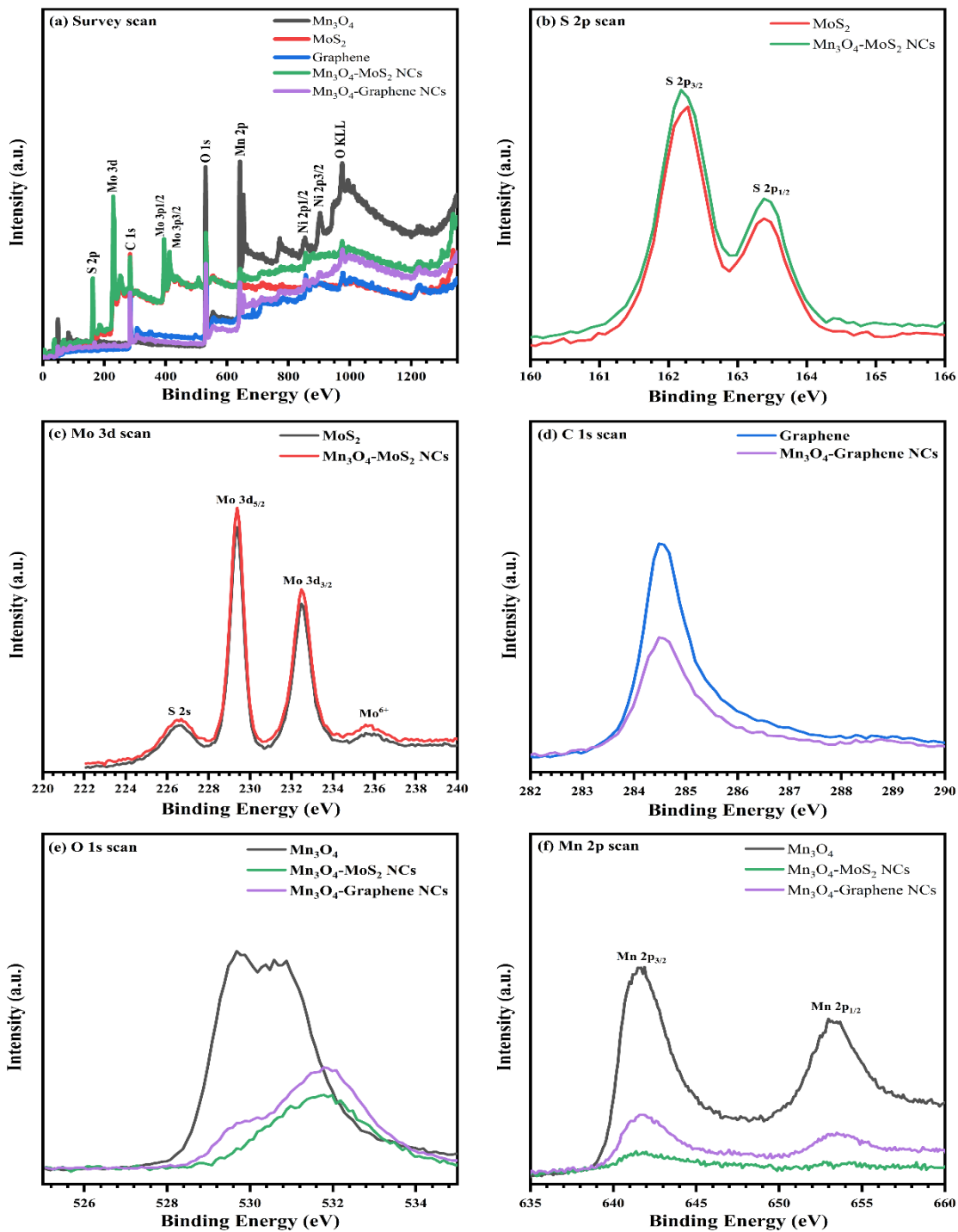


Figure 10. 9: XPS survey spectra (a) and high resolution XPS scans of S 2p (b), Mo 3d (c), C 1s (d), O 1s (e), and Mn 2p (f) of $\text{Mn}_3\text{O}_4\text{-2D}$ material NCs/NF thin films

The deconvoluted S 2p scan of the MoS₂ nanosheets exhibits a double degenerate state at 162.2 and 163.39 eV. Besides, the deconvoluted Mo 3d scan exhibits several states at 226.48, 229.36, 232.5, and 235.95 eV, respectively. These subbands were at almost the same positions in the case of Mn₃O₄-MoS₂ hybrid NCs, as shown in **Table 10. 2**. The detected subbands of Mo 3d at 229.36 and 232.5 eV are related to the valence Mo states in the layered hexagonal structure of MoS₂ and correspond to the spin-degenerate states of the 3d sublevels (5/2 and 3/2). Furthermore, the secondary subbands with relatively low intensity at the higher binding energy side at 235.95 eV are attributed to the oxidation of the Mo core state (Mo⁶⁺) [395]. Another core state is observed at the lower binding energy side of 226.48 eV, which is caused by the S 2s states is observed [396]. The deconvolution of C 1s XPS scans of the pure graphene nanosheets and the Mn₃O₄-graphene hybrid NCs are shown in **Figure 10. 12(a, b)**, where the fitted C 1s scan of the pure graphene nanosheets reveals the main transition state at 284.53 eV; this is caused by the in-plane sp²-hybridized carbon bond in the graphene nanosheets [242]. Moreover, other secondary subbands with small intensities are detected at 284.69 and 287.32 eV; these correspond to oxygenated bonds (i.e., C-O and C=O) at the graphene nanosheets grain boundaries [189]. Similar bands were observed with slight variation in the deconvoluted peaks of Mn₃O₄-graphene hybrid NCs as shown in **Table 10. 2**.

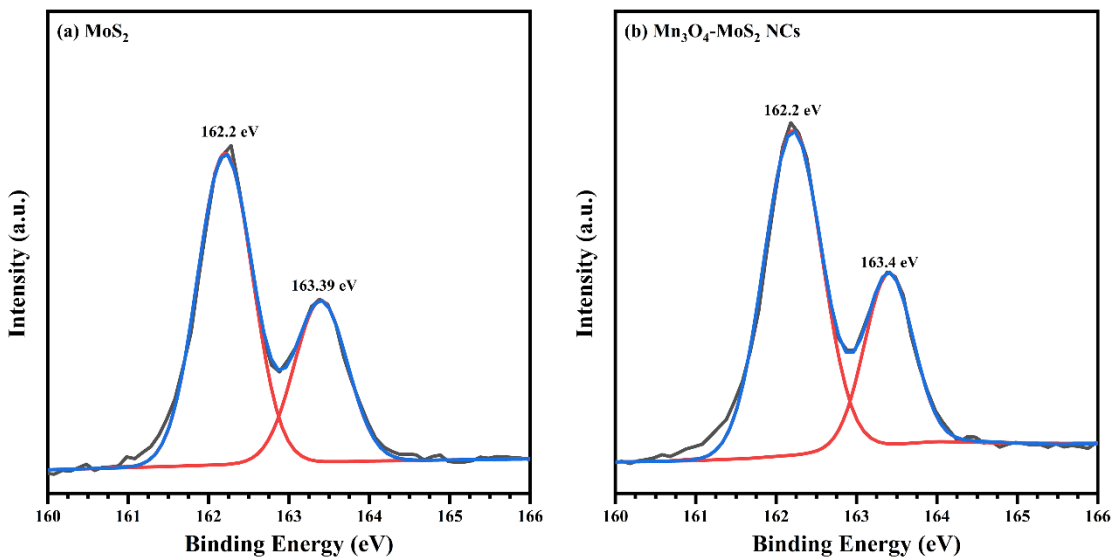


Figure 10. 10: High-resolution S 2p scan of MoS₂ (a) and Mn₃O₄-MoS₂ NC (b) thin films

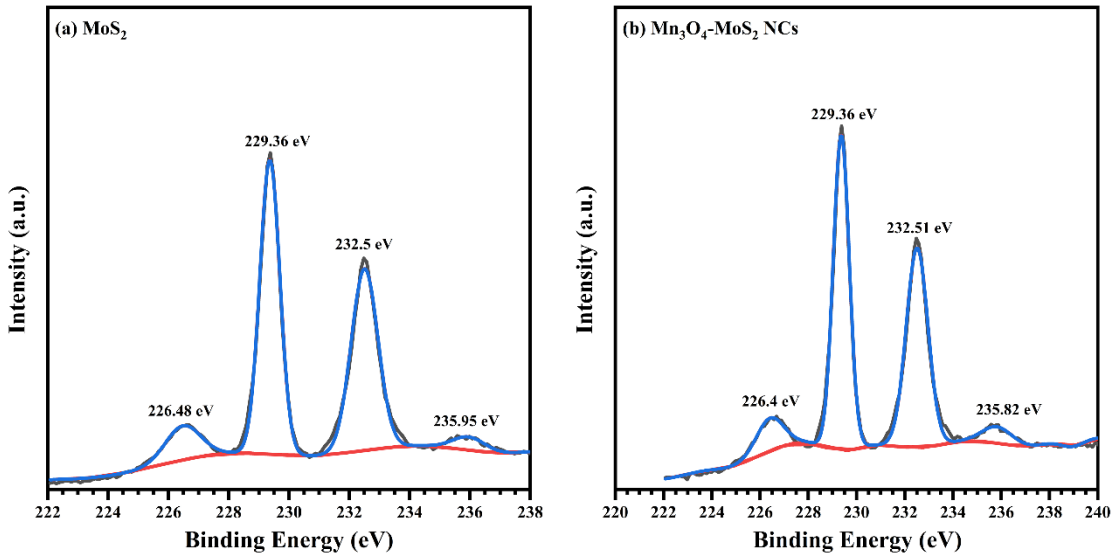


Figure 10.11: High-resolution Mo 3d scan of MoS₂ (a) and Mn₃O₄-MoS₂ NC (b) thin films

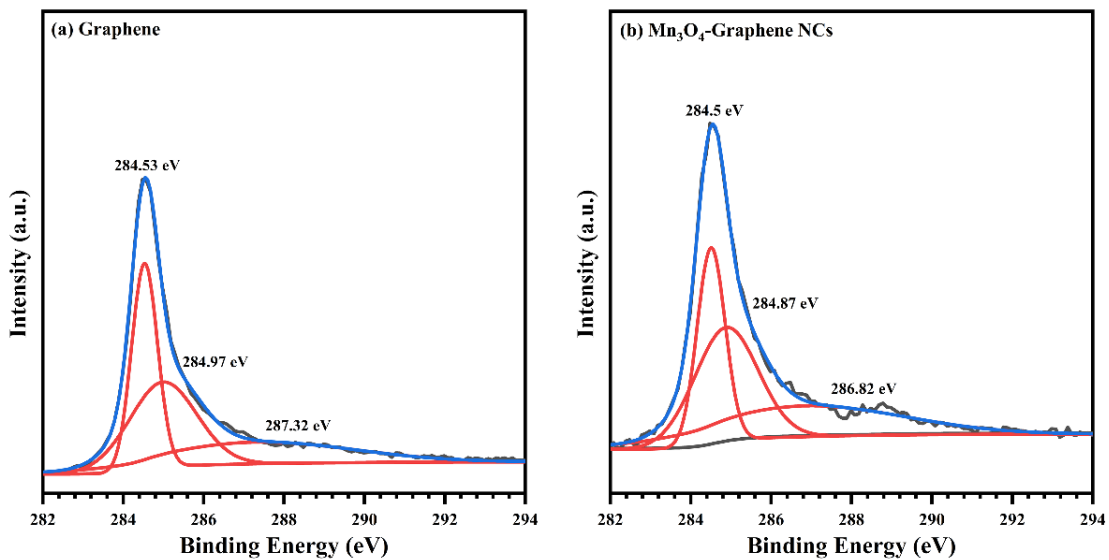


Figure 10.12: High-resolution C 1s scan of graphene (a) and Mn₃O₄-graphene NC (b) thin films

The high-resolution O 1s XPS scans of the pure Mn₃O₄, Mn₃O₄-MoS₂ NCs, and Mn₃O₄-graphene NCs are shown in **Figure 10.9(e)**. The deconvoluted O 1s spectra are shown in **Figure 10.13(a-c)**. The resolved O 1s spectrum of the nano-sized Mn₃O₄ in **Figure 10.13(a)** consists of two overlapped subbands at 529.51 and 530.76 eV. The first band is attributed to the bonded oxygen in the spinel structure of the Mn₃O₄ tetragonal phase.

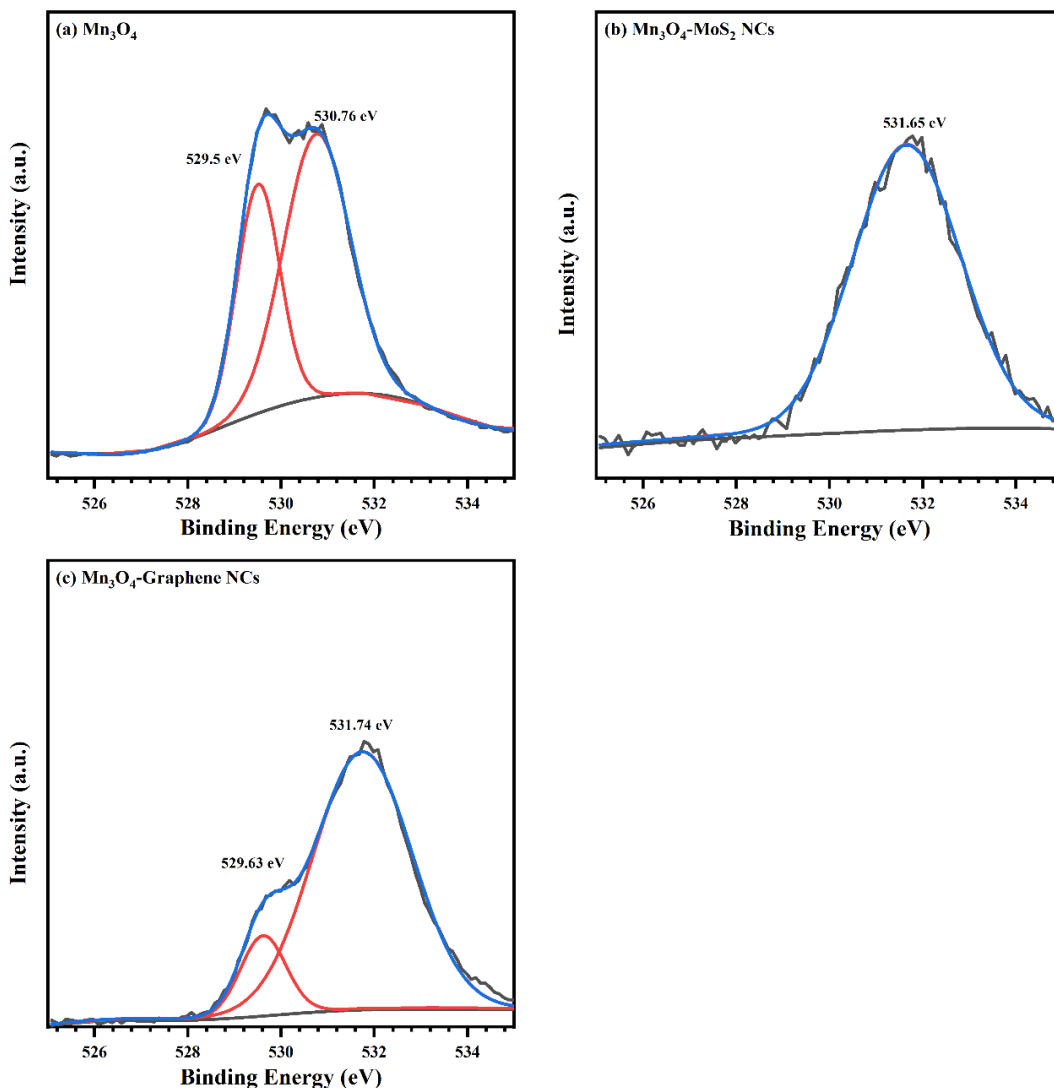


Figure 10. 13: High-resolution O 1s scan of Mn₃O₄ (a) Mn₃O₄-MoS₂ NC (b), and Mn₃O₄-graphene NC (c) thin films

The second band, centered at 530.76 eV, can be attributed to the oxygen species adsorbed through physical or chemical processes [442, 443]. The deconvolution of the O 1s scan of the Mn₃O₄-MoS₂ hybrid NCs in **Figure 10. 13(b)** reveals a new oxygen bonded state at 531.65 eV. This band, which was not observed in the O 1s scan of the pure Mn₃O₄ phase, is attributed to the synergy improvement in the heterostructure NCs through the formation of interfacial S–O bond states at the Mn₃O₄ grain boundaries with the MoS₂ nanosheets [444, 445]. In the case of the Mn₃O₄-graphene hybrid NCs, the deconvoluted O 1s scan in **Figure 10. 13(c)** exhibits two overlapped bands at 529.62 and 531.75 eV. The first band is a characteristic band of bonded oxygen in the lattice of the spinel Mn₃O₄ phase. The second band at 531.75 eV is ascribed to the evolution of new interfacial oxygen bonded states (O–C) with the graphene nanosheets in the hybrid

NCs. This may indicate the synergy improvement between the Mn_3O_4 and graphene species in the hybrid NCs [446, 447]. The high-resolution Mn 2p spectra for the nano-sized Mn_3O_4 , $\text{Mn}_3\text{O}_4\text{-MoS}_2$ NCs, and $\text{Mn}_3\text{O}_4\text{-graphene}$ NCs are illustrated in **Figure 10. 9(f)**. The deconvolution results for Mn 2p subbands for the pure Mn_3O_4 phase, as well as the hybrid NCs, are shown in **Figure 10. 14(a-c)** and the estimated peak positions are recorded in **Table 10. 2**. The Mn 2p spectrum in Mn_3O_4 reveals double-degenerate spin-orbital lines at 641.5 and 653.3 eV corresponding to Mn 2p_{3/2} and Mn 2p_{1/2}, respectively. The binding energy separation is 11.8 eV, which distinguishes the Mn ions in the spinel structure of Mn_3O_4 [448, 449].

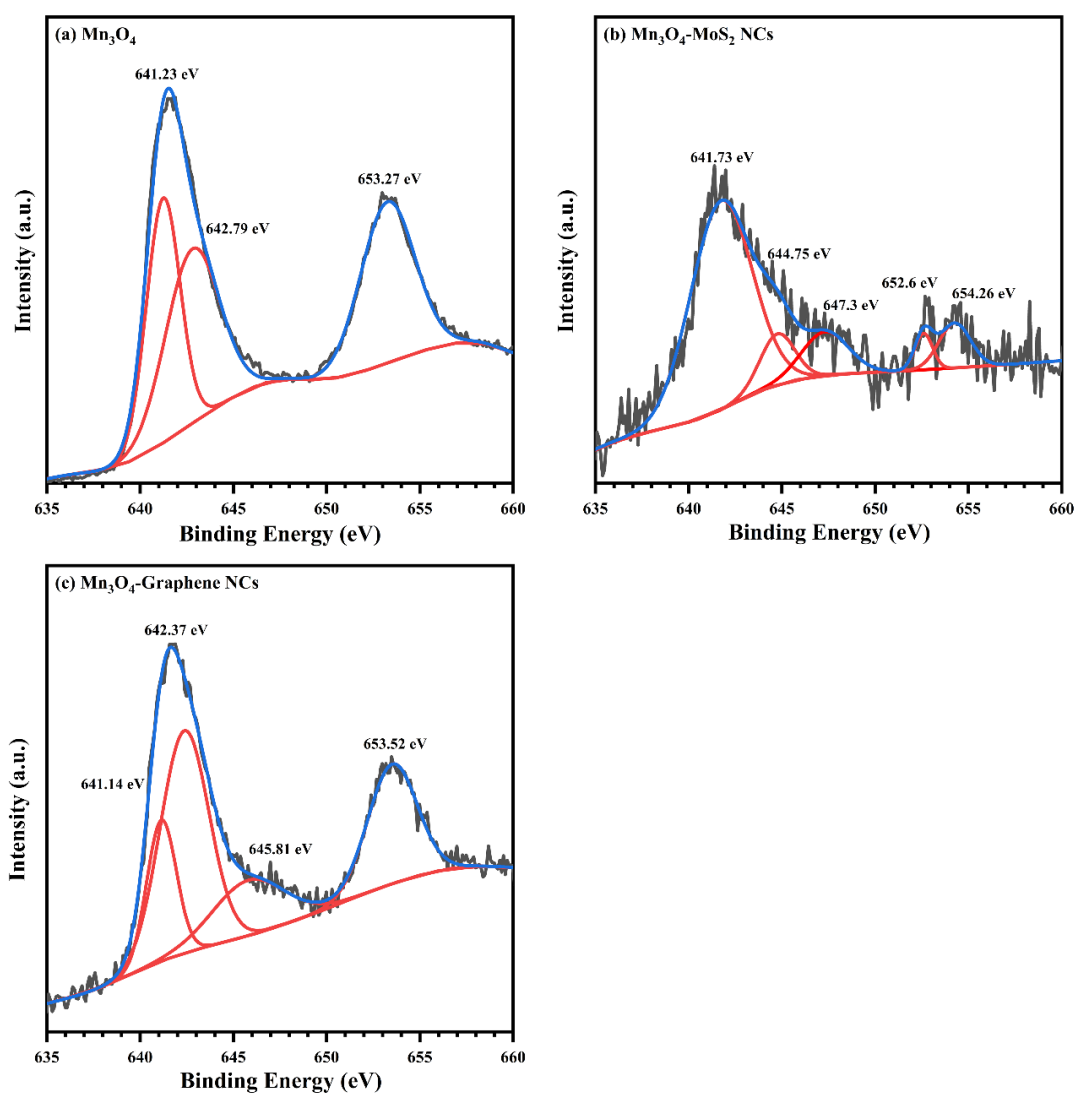


Figure 10. 14: High-resolution Mn 2p scan of Mn_3O_4 (a) $\text{Mn}_3\text{O}_4\text{-MoS}_2$ NC (b), and $\text{Mn}_3\text{O}_4\text{-graphene}$ NC (c) thin films

Table 10. 2: Characteristic peaks of S 2p, Mo 3d, C 1s, O 1s, and Mn 2p deconvoluted XPS scans in Mn₃O₄-2D material NC thin films.

Band	Binding Energy (eV)				
	MoS ₂	Graphene	Mn ₃ O ₄	Mn ₃ O ₄ -MoS ₂ NCs	Mn ₃ O ₄ -Graphene NCs
C 1s		284.53			284.50
		284.69			284.88
		287.32			286.82
S 2p	162.2			162.21	
	163.39			163.4	
Mo 3d	226.48			226.41	
	229.36			229.37	
	232.50			232.51	
	235.95			235.82	
O 1s			529.51		529.62
			530.76		-
			-	531.65	531.75
Mn 2p			641.23	641.73	641.14
			642.79	-	642.37
			-	644.75	645.8
				647.30	
			653.27	652.60	653.52
			-	654.26	-

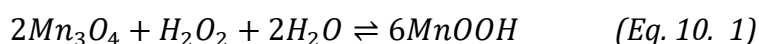
The Mn 2p spin-orbital lines in the Mn₃O₄-graphene NCs are observed at 641.68 and 653.48 with an energy separation of 11.8 eV. Also, the Mn 2p spin-orbital lines in Mn₃O₄-MoS₂ NCs are observed at 641.76 and 653.5 eV with an energy separation of 11.74 eV. This demonstrates the presence of Mn₃O₄ active species at the surface of all hybrid NC thin films. Furthermore, each subband of Mn 2p (3/2 and 1/2) was deconvoluted into a pair of doublets, which can be used to qualitatively recognize the relative concentration of internal oxidation states (i.e., Mn³⁺ and Mn²⁺). The estimated subband positions are recorded in **Table 10. 2**. The deconvolution of the Mn 2p_{3/2} band of the nano-sized Mn₃O₄ exhibits two overlapped subbands centered at 641.23 and 642.79 eV, which correspond to Mn³⁺ and Mn²⁺, respectively. The relative contribution of Mn²⁺/Mn³⁺ in the spinel structure based on the area of the subbands is 1.15. In the case of the Mn₃O₄-MoS₂ hybrid NCs, Mn²⁺ was not identified for Mn 2p_{3/2}, but a new state was detected at 644.75 eV. This new band corresponds to the higher oxidation state of manganese species (Mn⁴⁺) [450]. Additionally, the deconvoluted Mn 2p_{1/2} band exhibits overlapped subbands centered at 652.6 and 654.26 eV, corresponding to Mn³⁺ and Mn²⁺, respectively. Moreover, other satellite peaks are observed at 644.75 and 647.3 eV. The deconvoluted Mn 2p_{3/2} subbands of the Mn₃O₄-graphene hybrid

NCs were observed at 641.14 and 642.37 eV, corresponding to Mn³⁺ and Mn²⁺, respectively. It can be observed that the position of the fitted peak of the Mn₃O₄-graphene hybrid NCs reveals a slight downshift to the lower binding energy side, as compared to the pure phase of Mn₃O₄. The Mn²⁺/Mn³⁺ ratio revealed more than a two-fold enhancement, reaching 2.65. Furthermore, a new shake-up satellite band is observed at 645.8 eV. These results demonstrate the synergy improvement in the graphene-based hybrid NCs, as well as the role of graphene nanosheets in the transformation of Mn³⁺ species into Mn²⁺ to form more electrocatalytic active sites [432, 433, 451].

10. 2. 5. Electrocatalytic activity of Mn₃O₄-2D materials toward H₂O₂ reduction

It is known that H₂O₂ molecules have high activity when they react with other materials. However, they exhibit a slow dissociation rate. The dissociation kinetics of H₂O₂ by reduction or oxidation can be enhanced by electrochemical processes on modified electrode surfaces with nano-sized, transition metal-based electrocatalysts [216]. Nano-sized Mn₃O₄-based electrocatalysts are widely used for non-enzymatic electrochemical applications due to the abundance of various electroactive sites at their surfaces, which can detect small variations that are caused by electrocatalytic processes at the electrode/electrolyte interface [452-456].

Figure 10. 15(a) exhibits the CV curves using a 50 mV·s⁻¹ scan rate and modified working electrodes with Mn₃O₄ nanorods, MoS₂ nanosheets, graphene nanosheets, and their hybrid NCs before and after the injection of 5 mM H₂O₂ in 0.1 M NaOH. It can be observed that the addition of H₂O₂ results in an improvement in the electrocatalytic reduction response current for the pure Mn₃O₄ phase, as well as their hybrid NCs with either MoS₂ or graphene nanosheets. Furthermore, a clear reduction peak is observed near -0.4 V in the case of Mn₃O₄-graphene hybrid NCs. The suggested electrocatalytic reduction mechanism of H₂O₂ by Mn₃O₄-based electrocatalysts was described in earlier reports [433, 457] according to the following equation:



The observed improvement in the reduction response current in the Mn₃O₄-2D material hybrid NCs can be ascribed to the following aspects: (a) the hybridization between the Mn₃O₄ nanorods and either MoS₂ or graphene nanosheets is expected to improve the charge transfer kinetics at the electrode/electrolyte interface; (b) the formation of hybrid NCs with 2D-material nanosheets is associated with variations in the manganese species oxidation states, which is accompanied by the evolution of more

electrocatalytic active sites and an improvement in the redox reactions at the electrode /electrolyte interface (this explanation is supported by the XPS and Raman results); and (c) the heterostructured interface surface between Mn_3O_4 and the 2D material nanosheets would modify the internal local field at the surface grain boundaries, which would further enhance the mobility of the charged carriers produced by the redox reactions [432, 458]. To demonstrate the improvement in the electrocatalytic reduction of H_2O_2 on the working electrode surface, the real-time detection of the H_2O_2 concentration in 0.1 M NaOH was investigated using the CA technique. A typical CA measurement involves the gradual injection of H_2O_2 at -0.4 V for all working electrodes, as shown in **Figure 10. 16(a)**. It can be observed that the bare NF electrode and NF-modified electrodes with MoS_2 and graphene nanosheets have negligible electrocatalytic reduction for H_2O_2 for all H_2O_2 concentrations. Alternatively, spontaneous electrocatalytic reduction of H_2O_2 was observed in the case of NF-modified working electrodes with Mn_3O_4 nanorods, Mn_3O_4 - MoS_2 hybrid NCs, and Mn_3O_4 -graphene hybrid NCs. The average time to reach a steady-state current for Mn_3O_4 -based working electrodes is around 4 s. The CA calibration curves with the injected H_2O_2 concentration are shown in **Figure 10. 16(c-d)**.

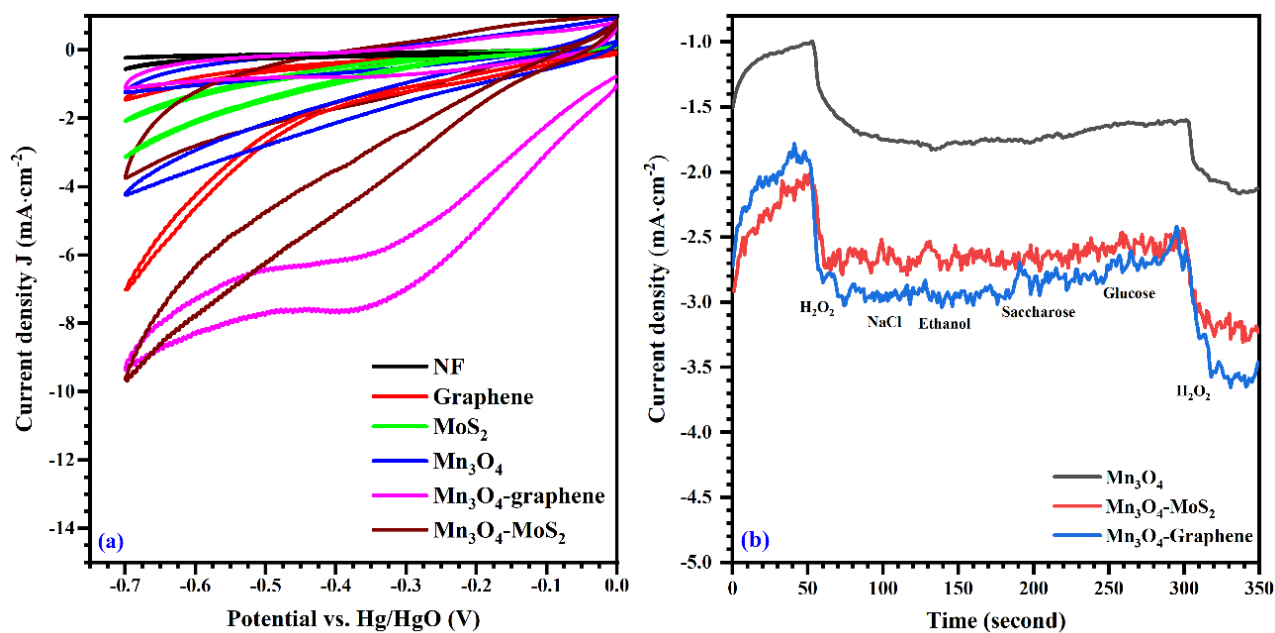


Figure 10. 15: CV plots measured from 0 to -0.7 V vs. Hg/HgO at a scan rate of 50 mV.s⁻¹ without and with 5 mM H_2O_2 in 0.1 M NaOH **(a)**. Electrocatalytic reduction selectivity test using the amperometric response at -0.4 V with the addition of 1 mM H_2O_2 , NaCl, saccharose, and glucose **(b)** for the pure Mn_3O_4 phase and Mn_3O_4 NCs with MoS_2 and graphene nanosheets.

The estimated linear detection range in 0.1 M NaOH extends from 0.2 to 1 mM with a variable limit of detection (LOD) ranging from 18 to 80 μM . The electrocatalytic reduction sensitivity for the Mn_3O_4 nanorods, $\text{Mn}_3\text{O}_4\text{-MoS}_2\text{NCs}$, and $\text{Mn}_3\text{O}_4\text{-graphene NCs}$ was estimated from the amperometric response in the linear detection range. The linear regression for the modified electrodes with pure Mn_3O_4 and its composites is described by the following equations:

$$\text{Mn}_3\text{O}_4: J(\mu\text{A} \cdot \text{cm}^{-2}) = -2320 C (\text{mM}) - 1260, \quad R^2 = 0.98 \quad (\text{Eq. 10. 2})$$

$$\text{Mn}_3\text{O}_4 - \text{MoS}_2 \text{ NCs} : J(\mu\text{A} \cdot \text{cm}^{-2}) = -3220 C (\text{mM}) - 2190, \quad R^2 = 0.99 \quad (\text{Eq. 10. 3})$$

$$\text{Mn}_3\text{O}_4 - \text{graphene NCs}: J(\mu\text{A} \cdot \text{cm}^{-2}) = -5400 C (\text{mM}) - 2280, \quad R^2 = 0.99 \quad (\text{Eq. 10. 4})$$

The slope for the linear detection range refers to the electrocatalytic sensitivity to H_2O_2 reduction. The working electrode modified with Mn_3O_4 nanorods exhibits a high reduction sensitivity of $2320 \mu\text{A} \cdot \text{mM}^{-1} \cdot \text{cm}^{-2}$ towards H_2O_2 , which is further improved upon the incorporation of 2D material nanosheets. The electrocatalytic reduction sensitivity values of the modified electrode with $\text{Mn}_3\text{O}_4\text{-MoS}_2$ NCs and $\text{Mn}_3\text{O}_4\text{-graphene}$ nanosheets are 3220 and $5400 \mu\text{A} \cdot \text{mM}^{-1} \cdot \text{cm}^{-2}$, respectively. These results reveal that the working electrodes based on $\text{Mn}_3\text{O}_4\text{-2D}$ material hybrid NCs fabricated by the NPDS are suitable for non-enzymatic electrochemical sensing of H_2O_2 . These materials demonstrate very high sensitivity compared with other Mn_3O_4 -based electrocatalysts and a wide linear detection range, as demonstrated by comparing these results with recent studies (**Table 10. 3**).

Table 10. 3: Comparison of the electrochemical performance between the present work and the recently published work of Mn_3O_4 -based nonenzymatic amperometric H_2O_2 sensors.

Modified electrode	Potential (V)	Electrolyte	Sensitivity ($\mu\text{A} \cdot \text{mM}^{-1} \cdot \text{cm}^{-2}$)	Linear range (mM)	LOD (μM)	Ref.
$\text{Mn}_3\text{O}_4/\text{NF}$			2320		18	This work
$\text{Mn}_3\text{O}_4\text{-MoS}_2 \text{ NCs}/\text{NF}$	-0.4	0.1 M NaOH	3220	0.2-1	80	
$\text{Mn}_3\text{O}_4\text{-graphene NCs}/\text{NF}$			5400		28	
$\text{MnO-Mn}_3\text{O}_4@\text{rGO}$	-0.45	0.2 M NaOH	274.15	0.004-17	0.1	[432]
$\text{MnO}_2\text{-Co}_3\text{O}_4@\text{graphene}$	+0.5	0.1 M PBS	53.65	0.005-1.2	0.8	[250]
$\text{Mn}_3\text{O}_4\text{-MnCo}_2\text{O}_4 \text{ NCs}$	+0.8	0.1 M PBS	34.5	0.0001-1.2	0.02	[424]
$\text{Mn}_3\text{O}_4\text{-MnO}_2@\text{graphene}$	-0.4	0.1 M NaOH	1443	0.001-0.2	0.16	[433]
$\text{Mn}_3\text{O}_4 \text{ OSMs}$	+0.75	0.1 M PBS	5.74	0.005-17	1.5	[423]
$\text{Mn}_3\text{O}_4@\text{graphene}$	+0.36	0.1 M PBS	-	1-10	250	[452]
$\text{Mn}_3\text{O}_4/3\text{DGF}$	0	0.1 M NaOH	1030	0.002-6.5	10	[459]

The reduction selectivity of NF-modified electrodes with pure Mn_3O_4 and Mn_3O_4 -2D material nanosheets toward H_2O_2 in 0.1 M NaOH was investigated for several interfering species, as shown in **Figure 10.15(b)**. The utilized working electrodes exhibited a spontaneous amperometric reduction current upon the addition of 1 mM H_2O_2 at -0.4 V, whereas the addition of other interfering species, such as NaCl, ethanol, saccharose, and glucose (1 mM), does not produce a sizeable reduction current. This behavior was confirmed by adding 1 mM H_2O_2 for a second time after the interfering solution, which also produced a large reduction time. These results confirm the high selectivity of the fabricated Mn_3O_4 -2D material hybrid NCs toward H_2O_2 reduction in an alkaline medium.

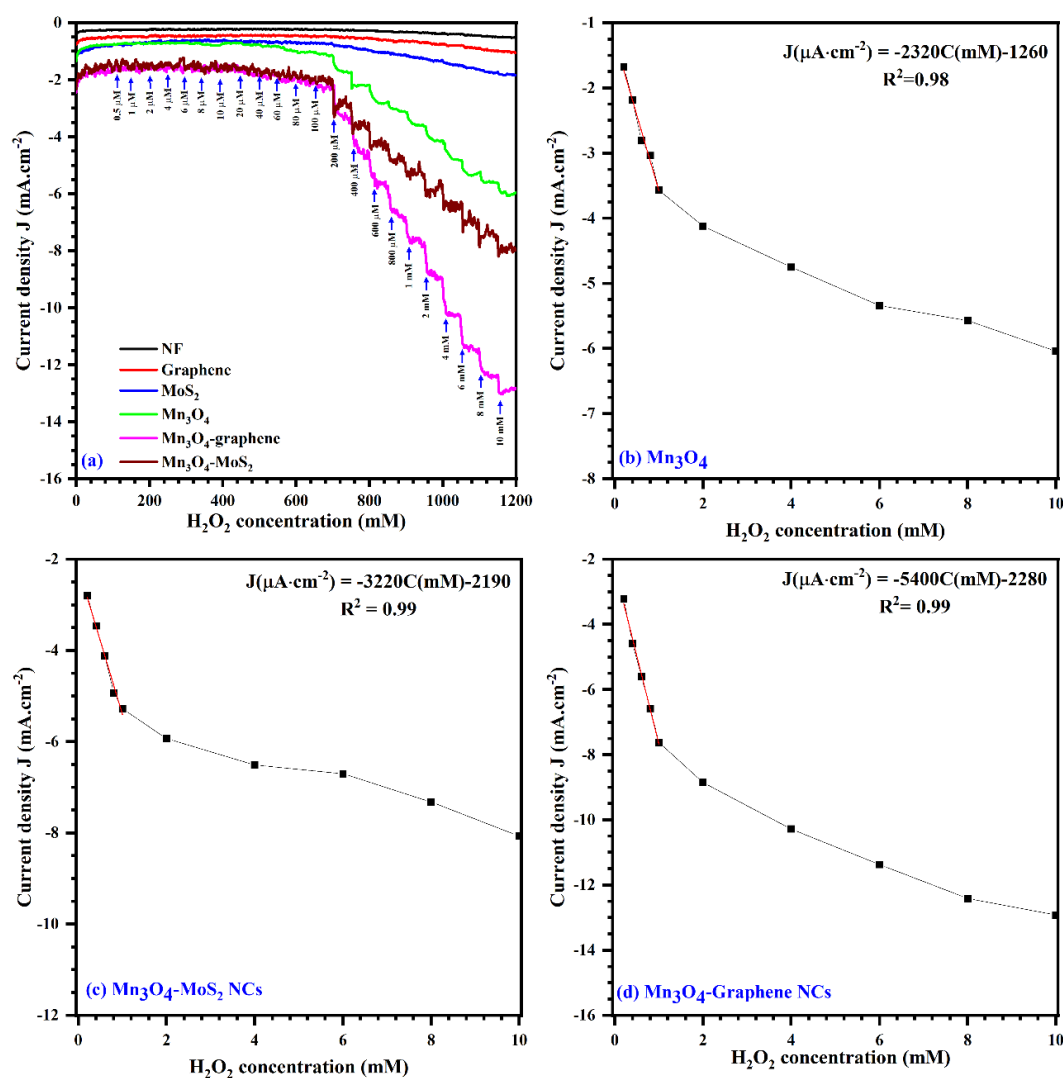


Figure 10.16: Chronoamperometric response at -0.4 V (a). The calibration curves of the current induced response with increasing H_2O_2 concentration by the pure Mn_3O_4 phase (b) and Mn_3O_4 NCs with MoS_2 (c) and graphene nanosheets (d).

10.3. Summary

Mn₃O₄-2D material (MoS₂ or graphene) hybrid NC thin films were successfully deposited on NF substrates at room temperature with one step using the NPDS. The deposited Mn₃O₄, Mn₃O₄-MoS₂ hybrid NCs, and Mn₃O₄-graphene hybrid NCs were used as electrocatalysts for non-enzymatic detection of H₂O₂ reduction in 0.1 M NaOH. The deposited nanostructured thin films were examined using XRD, SEM, and Raman and XPS spectroscopy. XRD patterns of the deposited thin films showed a reduction in the crystalline domain size due to fragmentation and interlayer separation of the micron powder, which was further confirmed by analyzing the surface morphology via SEM. SEM images of the deposited Mn₃O₄ thin films revealed a nanorod morphology, whereas the deposited thin films of MoS₂ and graphene consisted of nanosheets. The SEM images of Mn₃O₄-MoS₂ and Mn₃O₄-graphene hybrid NCs demonstrated mixed nanosheet and nanorod morphologies. This indicated the occurrence of micron powder fragmentation and mechanical exfoliation of the 2D material stacked layers. Comparing the Raman spectra of the micron powders with the spectra of the corresponding deposited nano-sized thin films demonstrated the size-dependent changes of the related Raman symmetry modes, in which all active Raman vibrations in the deposited thin films exhibited upshifting to higher values. Furthermore, the disorder-related modes were strongly enhanced compared with the crystalline modes. This is observed in the case of the deposited graphite thin film, indicating the successful exfoliation of the graphite layered structure into smaller nanosheets via the one-step, vacuum kinetic process. Another interesting feature was noticed in the case of Mn₃O₄-graphene hybrid NCs, where a new phase related to the Mn₂O₃ phase was detected. This indicated the hybridization between the nano-sized Mn₃O₄ and the formed graphene nanosheets, where the formation of graphene nanosheets in the hybrid NCs was accompanied by the reduction of manganese states from lower-spin states to higher-spin states. These states can provide more electroactive sites on the surfaces of hybrid NCs. The high-resolution XPS scans of S 2p, Mo 3d, C 1s, O 1s, and Mn 2p were provided to further demonstrate the synergy between the Mn₃O₄ and MoS₂ or graphene nanosheets in the hybrid NCs. We found no observable changes in the high-resolution XPS scans of S 2p, Mo 3d, or C 1s, but the O 1s and Mn 2p scans were strongly affected. New oxygen-bonded states were detected around 531.65 and 531.75 eV in the Mn₃O₄ hybrid NCs with MoS₂ and graphene nanosheets, respectively. The high-resolution XPS scan of Mn 2p demonstrated that the concentration of higher-spin states (Mn²⁺) relative to the concentration of lower-spin states (Mn³⁺) in the spinel structure of Mn₃O₄ was greatly enhanced in the case of Mn₃O₄-graphene hybrid NCs. Additionally, the formation of hybrid NCs with MoS₂ nanosheets resulted in the evolution of a higher oxidation state (Mn⁴⁺) related to the spinel

phase of Mn_3O_4 . This behavior illustrated the synergy improvement between the Mn_3O_4 and the 2D material nanosheets in the deposited hybrid NCs. The electrocatalytic activity of Mn_3O_4 -2D material hybrid NCs/NF toward H_2O_2 reduction was initially recognized based on CV plots at $50 \text{ mV} \cdot \text{s}^{-1}$, in the absence or presence of $5 \text{ mM H}_2\text{O}_2$ in 0.1 M NaOH . The nano-sized heterostructure electrodes of Mn_3O_4 -2D material nanosheets revealed improvements in the reduction response current compared with the modified electrode that only contained nano-sized Mn_3O_4 . Furthermore, the hybrid NCs with graphene exhibited the highest reduction current compared with the other electrodes. The electrode sensitivity toward H_2O_2 reduction was investigated by analyzing the amperometric response while gradually increasing the H_2O_2 concentration. All fabricated electrodes showed a wide linear detection range from 0.2 to $1 \text{ mM H}_2\text{O}_2$. The estimated reduction sensitivity values of 2320 , 3220 , and $5400 \mu\text{A} \cdot \text{mM}^{-1} \cdot \text{cm}^{-2}$ correspond to the modified electrodes with Mn_3O_4 nanorods, Mn_3O_4 - MoS_2 nanosheets, and Mn_3O_4 -graphene nanosheets, respectively. Moreover, the reduction selectivity to H_2O_2 with other interfering species was examined for all of the fabricated electrodes. These results show the successful fabrication of heterostructured electrodes of Mn_3O_4 -2D material NCs using a simple, room-temperature, one-step vacuum kinetic process by the NPDS. These materials also showed higher detection sensitivity toward the non-enzymatic detection of H_2O_2 as compared with Mn_3O_4 -based electrocatalysts fabricated by other techniques.

Chapter 11: Conclusions

The conventional techniques for producing 2D NMs through the mechanical exfoliation of micron powder require several sequenced steps that mainly occurred in the presence of organic solvents. This takes a long fabrication time and needs further cleaning from waste products. This is a key issue that restricts the mass production of 2D NMs. Hence, the fabrication cost for the commercial applications related to 2D NMs would be so high. The NPDS was successfully used for mechanical exfoliation of graphene nanosheets from the graphite micron power in a simple one-step process at room temperature in a very short time. So, we tried to investigate the mechanical exfoliation of other layered materials with similar hexagonal structural phases such as MoS₂ and BN using the same deposition conditions. Then, we examined the applicability of hybrid NCs formation between layered materials (i.e., graphite and MoS₂) with various TMs compounds in one step process at room temperature using the NPDS. This would dramatically decrease the fabrication time and save a lot of labor work. So, the production cost efficiency is expected to be strongly improved.

The deposited nano-sized thin films of pure 2D materials (i.e., graphene, MoS₂, and BN) and their hybrid NCs with various TMs compounds (i.e., Ni(OH)₂, Co₃O₄, Mn₃O₄, and ZnO) were characterized using several surface scanning techniques such XRD patterns, SEM and HRTEM images. The obtained results indicated the micron particle fragmentation to small nanosized sheets as well as successful mechanical exfoliation of layered materials to small size nanosheets either in the case of pure 2D NMs these films or their hybrid NCs. Besides, the hybridization between the 2D NMs and the TMs species was recognized from well-resolved spectroscopic techniques such as micron-Raman and XPS spectroscopy, which indicated the successful interfacial bonding (i.e., synergy improvement) in either graphene or MoS₂-based hybrid NCs. The fabricated hybrid NCs were utilized for energy conversion through various water splitting routes (i.e., electrocatalysis, photocatalysis, and photo-electrocatalysis) and non-enzymatic H₂O₂ detection in an alkaline medium. The optimum performance of modified electrodes with hybrid NCs is strongly sensitive to the initial composition ratio between TMs and layered materials. So, the effect of composition on the performance of the fabricated electrode toward various applications was investigated as illustrated below.

The fabricated heterostructured electrodes were utilized in several applications related to energy conversion and sensing in the alkaline medium, which the fabricated hybrid NCs was classified according to the desired application as follows:

- Electrocatalytic water splitting in an alkaline medium.

Graphene-based hybrid NCs with Ni(OH)₂ and spinel Co₃O₄ were deposited on nickel foam porous substrates at different graphite content. The fabricated heterostructure electrodes were used to study the electrocatalytic water splitting half reactions the oxygen evolution reactions (OER) and the hydrogen evolution reaction (HER) in 1.0 M KOH. All fabricated electrodes exhibited strong synergy between graphene nanosheets and either Ni(OH)₂ or Co₃O₄ species. Besides, the graphene nanosheets have improved the concentration of high spin states (Co²⁺) in the case of nano-sized spinel Co₃O₄. The electrocatalytic activity toward the OER and the HER was strongly affected by the initial concentration of graphite content. The graphene hybrid NCs with either Ni(OH)₂ or Co₃O₄ that has graphite content ranging from 75~80 wt.% exhibited the highest electrocatalytic activity toward the OER. Meanwhile, the optimum composition for the HER is different depending on the type of TMs. Ni(OH)₂-graphene hybrid NCs with 25 wt.% graphite content exhibit the highest activity toward the HER in 1.0 M KOH. Meanwhile, stoichiometric Co₃O₄-graphene hybrid NCs with initial graphite content of 50 wt.% exhibited the highest activity toward the HER.

Co₃O₄-MoS₂ hybrid NCs was deposited on nickel foam porous substrate at different MoS₂ content. The modified electrodes with pure phases of Co₃O₄ nanoparticles, and MoS₂ nanosheets, and their hybrid NCs were utilized for water splitting 1.0 M KOH. The synergy improvement between Co₃O₄ and MoS₂ species in the hybrid NCs resulted in the overall enhancement of electrocatalytic activity toward the OER in 1.0 M KOH, which hybrid NCs with high MoS₂ content (75 wt.%) exhibited the highest electrocatalytic activity toward the OER.

Based on our finding, the fabrication of hybrid electrodes using a vacuum kinetic spray approach at a high concentration of 2D NMs (either graphene or MoS₂ nanosheets) is strongly recommended for improving the electrocatalytic water oxidation (i.e., OER) in an alkaline medium.

➤ Photocatalytic and Photo-electrocatalytic water splitting.

ZnO-graphene hybrid NCs were deposited at different graphite content on nickel foam porous substrate and titanium sheet flat substrate. Hybrid NCs on nickel foam substrate was utilized for the methylene blue degradation induced by photocatalytic water splitting under visible light illumination. Whereas the hybrid NCs at flat titanium sheets were utilized for the photo-electrocatalytic water splitting in an alkaline medium under visible light illumination. All hybrid NCs exhibited successful mechanical exfoliation of graphite species to small size graphene nanosheets. Besides, the hybrid NCs exhibited a

strong synergy improvement between ZnO and graphene species. The hybridization between ZnO and graphene resulted in the improvement of visible harvesting efficiency and enhancement of both photogenerated carrier transfer kinetics and separations. This was accompanied by the enhancement of both photocatalytic degradation of methylene blue and the response photocurrent under visible light illumination. The ZnO-graphene hybrid NCs with an initial stoichiometric ratio (i.e., 50 wt.%) revealed the highest performance compared with other photoanodes.

➤ Non-enzymatic H₂O₂ detection in alkaline medium.

Several hybrid NCs between 2D NMs (graphene and MoS₂ nanosheets) and spinel structure of Co₃O₄ and Mn₃O₄ were directly deposited in one step by the NPDS at room temperature. The modified electrodes with hybrid NCs exhibited high electrocatalytic activity toward the non-enzymatic H₂O₂ reduction and oxidation in an alkaline medium as illustrated below:

Co₃O₄-graphene hybrid NCs was deposited on nickel foam porous substrate at different graphite content that used to investigate the electrocatalytic reduction of H₂O₂ in 0.1 M NaOH. The modified electrodes with Co₃O₄-graphene hybrid NCs exhibited strong improvement in the electrocatalytic reduction current compared with the pure nano-sized Co₃O₄ phase. The hybrid NCs with an initial composition ratio of 50 wt.% graphite content exhibited superior electrocatalytic reduction sensitivity toward H₂O₂ compared with Co₃O₄-based electrodes fabricated by other conventional techniques.

Mn₃O₄-based NCs with graphene and MoS₂ nanosheets were deposited on nickel foam substrate. The deposited thin films have an initial stoichiometric composition ratio between Mn₃O₄ and the layered materials (i.e., graphite or MoS₂). In this study, we tried to investigate the effect of synergy with different routes between 2D NMs and the spinel structural phase of Mn₃O₄. In both cases, Mn₃O₄-2D hybrid NCs revealed strong hybridization between Mn₃O₄ and either graphene or MoS₂ nanosheets that associated with an improvement in the electrocatalytic activity toward H₂O₂ reduction in 0.1 M NaOH compared with pure Mn₃O₄ phase. Besides, Mn₃O₄-graphene hybrid NCs exhibited the highest sensitivity compared with other electrodes.

Co₃O₄-MoS₂ hybrid NCs at various MoS₂ content were directly deposited in one step by the NPDS on a flat titanium sheet. The fabricated heterostructure electrodes were used to investigate the electrocatalytic oxidation of H₂O₂ in 0.1 M NaOH. The modified electrodes with Co₃O₄-MoS₂ hybrid NCs

exhibited strong improvement in the electrocatalytic oxidation current compared with the pure nano-sized Co_3O_4 phase. The hybrid NCs with low MoS_2 content (25 wt.%) exhibited high electrocatalytic oxidation sensitivity toward H_2O_2 compared with Co_3O_4 -based electrodes fabricated by other conventional techniques.

Finally, the major finding of these studies is the ability of layered materials exfoliation and hybrid NCs formation with various functional nano-sized materials in one-step deposition process by the NPDS according to the vacuum kinetic spray mechanism. Besides, fabricated heterostructured electrodes exhibited high the performance in various electrochemical applications. This indicate the applicability of using the NPDS technique as single process for fabrication of efficient 2D NMs hybrid electrodes with high cost efficiency compared with other conventional technique.

References

1. Dong, Q.Q., et al., *Efficient approach to iron/nitrogen co-doped graphene materials as efficient electrochemical catalysts for the oxygen reduction reaction. Journal of Materials Chemistry A*, 2015. **3**(15): p. 7767-7772.
2. Zhang, H., *Ultrathin Two-Dimensional Nanomaterials. ACS Nano*, 2015. **9**(10): p. 9451-69.
3. Zhang, P., et al., *Two-dimensional materials for miniaturized energy storage devices: from individual devices to smart integrated systems. Chem Soc Rev*, 2018. **47**(19): p. 7426-7451.
4. Zheng, C.N., et al., *The art of two-dimensional soft nanomaterials. Science China-Chemistry*, 2019. **62**(9): p. 1145-1193.
5. Zhu, J., et al., *Two-Dimensional Porous Polymers: From Sandwich-like Structure to Layered Skeleton. Acc Chem Res*, 2018. **51**(12): p. 3191-3202.
6. Zhuang, X., et al., *Two-dimensional soft nanomaterials: a fascinating world of materials. Adv Mater*, 2015. **27**(3): p. 403-27.
7. Chabot, V., et al., *A review of graphene and graphene oxide sponge: material synthesis and applications to energy and the environment. Energy & Environmental Science*, 2014. **7**(5): p. 1564-1596.
8. Rout, C.S., D. Late, and H. Morgan, *Fundamentals and sensing applications of 2D materials*. 2019: Woodhead Publishing.
9. Schneemann, A., et al., *2D framework materials for energy applications. Chemical Science*, 2021. **12**(5): p. 1600-1619.
10. Zhang, K., et al., *Two dimensional hexagonal boron nitride (2D-hBN): synthesis, properties and applications. Journal of Materials Chemistry C*, 2017. **5**(46): p. 11992-12022.
11. Hassan, M., et al., *High performance pliable supercapacitor fabricated using activated carbon nanospheres intercalated into boron nitride nanoplates by pulsed laser ablation technique. Arabian Journal of Chemistry*, 2020. **13**(8): p. 6696-6707.
12. Kwon, I.S., et al., *Ruthenium Nanoparticles on Cobalt-Doped 1T' Phase MoS₂ Nanosheets for Overall Water Splitting. Small*, 2020. **16**(13): p. 2000081.
13. Song, F., et al., *High energy density supercapacitors based on porous mSiO₂@ Ni₃S₂/NiS₂ promoted with boron nitride and carbon. Chemical Engineering Journal*, 2020. **390**: p. 124561.
14. Sun, A., et al., *Enhanced energy storage performance from Co-decorated MoS₂ nanosheets as supercapacitor electrode materials. Ceramics International*, 2018. **44**(11): p. 13434-13438.
15. Wei, S., et al., *Iridium-triggered phase transition of MoS₂ nanosheets boosts overall water splitting in alkaline media. ACS Energy Letters*, 2018. **4**(1): p. 368-374.
16. Le, T.H., et al., *Exfoliation of 2D Materials for Energy and Environmental Applications. Chemistry*, 2020. **26**(29): p. 6360-6401.
17. Jahangir, I., et al., *Richardson constant and electrostatics in transfer-free CVD grown few-layer MoS₂/graphene barristor with Schottky barrier modulation > 0.6 eV. Applied Physics Letters*, 2017. **111**(14): p. 142101.

18. Kwon, I.S., et al., Ruthenium Nanoparticles on Cobalt-Doped 1T' Phase MoS₂ Nanosheets for Overall Water Splitting. *Small*, 2020. **16**(13): p. 2000081.
19. Narula, U., C.M. Tan, and C.S. Lai, Growth Mechanism for Low Temperature PVD Graphene Synthesis on Copper Using Amorphous Carbon. *Scientific Reports*, 2017. **7**(1): p. 1-13.
20. Sun, A.K., et al., Enhanced energy storage performance from Co-decorated MoS₂ nanosheets as supercapacitor electrode materials. *Ceramics International*, 2018. **44**(11): p. 13434-13438.
21. Novoselov, K.S., et al., Electric field effect in atomically thin carbon films. *Science*, 2004. **306**(5696): p. 666-9.
22. Novoselov, K.S., et al., Two-dimensional atomic crystals. *Proc Natl Acad Sci U S A*, 2005. **102**(30): p. 10451-3.
23. Dresselhaus, M.S. and P.T. Araujo, *Perspectives on the 2010 nobel prize in physics for graphene*. 2010, ACS Publications.
24. Jayasena, B. and S. Subbiah, A novel mechanical cleavage method for synthesizing few-layer graphenes. *Nanoscale Res Lett*, 2011. **6**(1): p. 95.
25. Liu, H., et al., Production of mono- to few-layer MoS₂ nanosheets in isopropanol by a salt-assisted direct liquid-phase exfoliation method. *J Colloid Interface Sci*, 2018. **515**: p. 27-31.
26. Ramakrishna Matte, H., et al., MoS₂ and WS₂ analogues of graphene. *Angewandte Chemie International Edition*, 2010. **49**(24): p. 4059-4062.
27. Rao, C.N.R., U. Maitra, and U.V. Waghmare, Extraordinary attributes of 2-dimensional MoS₂ nanosheets. *Chemical Physics Letters*, 2014. **609**: p. 172-183.
28. Hernandez, Y., et al., High-yield production of graphene by liquid-phase exfoliation of graphite. *Nat Nanotechnol*, 2008. **3**(9): p. 563-8.
29. Jawaid, A., et al., Mechanism for Liquid Phase Exfoliation of MoS₂. *Chemistry of Materials*, 2016. **28**(1): p. 337-348.
30. Shi, H.Y., et al., Polyethylenimine-assisted exfoliation of h-BN in aqueous media for anticorrosive reinforcement of waterborne epoxy coating. *Progress in Organic Coatings*, 2020. **142**: p. 105591.
31. Yuan, Y.X., R.Q. Li, and Z.H. Liu, Establishing Water-Soluble Layered WS₂ Nanosheet as a Platform for Biosensing. *Analytical Chemistry*, 2014. **86**(7): p. 3610-3615.
32. Bourlinos, A.B., et al., Aqueous-phase exfoliation of graphite in the presence of polyvinylpyrrolidone for the production of water-soluble graphenes. *Solid State Communications*, 2009. **149**(47-48): p. 2172-2176.
33. Khan, U., et al., Size selection of dispersed, exfoliated graphene flakes by controlled centrifugation. *Carbon*, 2012. **50**(2): p. 470-475.
34. Yi, M., et al., A mixed-solvent strategy for facile and green preparation of graphene by liquid-phase exfoliation of graphite. *Journal of Nanoparticle Research*, 2012. **14**(8): p. 1-9.
35. Zhou, X., et al., Dispersion of graphene sheets in ionic liquid [bmim][PF₆] stabilized by an ionic liquid polymer. *Chem Commun (Camb)*, 2010. **46**(3): p. 386-8.

36. Lin, L.X., et al., *Surface Energy Engineering in the Solvothermal Deoxidation of Graphene Oxide. Advanced Materials Interfaces*, 2014. **1**(3): p. 1300078.
37. Cravotto, G. and P. Cintas, *Sonication-assisted fabrication and post-synthetic modifications of graphene-like materials. Chemistry*, 2010. **16**(18): p. 5246-59.
38. Polyakova, E.Y., et al., *Scanning Tunneling Microscopy and X-ray Photoelectron Spectroscopy Studies of Graphene Films Prepared by Sonication-Assisted Dispersion. Acs Nano*, 2011. **5**(8): p. 6102-6108.
39. Yi, M., et al., *Water can stably disperse liquid-exfoliated graphene. Chemical Communications*, 2013. **49**(94): p. 11059-11061.
40. Asakura, Y., et al., *Effects of ultrasonic frequency and liquid height on sonochemical efficiency of large-scale sonochemical reactors. Ultrason Sonochem*, 2008. **15**(3): p. 244-50.
41. Sutkar, V.S. and P.R. Gogate, *Design aspects of sonochemical reactors: Techniques for understanding cavitation activity distribution and effect of operating parameters. Chemical Engineering Journal*, 2009. **155**(1-2): p. 26-36.
42. Yi, M. and Z.G. Shen, *A review on mechanical exfoliation for the scalable production of graphene. Journal of Materials Chemistry A*, 2015. **3**(22): p. 11700-11715.
43. Antisari, M.V., et al., *Low energy pure shear milling: A method for the preparation of graphite nano-sheets. Scripta Materialia*, 2006. **55**(11): p. 1047-1050.
44. Milev, A., et al., *X-ray diffraction line profile analysis of nanocrystalline graphite. Materials Chemistry and Physics*, 2008. **111**(2-3): p. 346-350.
45. Borah, M., et al., *Few layer graphene derived from wet ball milling of expanded graphite and few layer graphene based polymer composite. Materials Focus*, 2014. **3**(4): p. 300-309.
46. Leon, V., et al., *Exfoliation of graphite with triazine derivatives under ball-milling conditions: preparation of few-layer graphene via selective noncovalent interactions. ACS Nano*, 2014. **8**(1): p. 563-71.
47. Janot, R. and D. Guerard, *Ball-milling: the behavior of graphite as a function of the dispersal media. Carbon*, 2002. **40**(15): p. 2887-2896.
48. Knieke, C., et al., *Scalable production of graphene sheets by mechanical delamination. Carbon*, 2010. **48**(11): p. 3196-3204.
49. Zhao, W.F., et al., *Preparation of graphene by exfoliation of graphite using wet ball milling. Journal of Materials Chemistry*, 2010. **20**(28): p. 5817-5819.
50. Yao, Y.G., et al., *Large-scale production of two-dimensional nanosheets. Journal of Materials Chemistry*, 2012. **22**(27): p. 13494-13499.
51. Aparna, R., et al., *An effective route to produce few-layer graphene using combinatorial ball milling and strong aqueous exfoliants. Journal of Renewable and Sustainable Energy*, 2013. **5**(3): p. 033123.
52. Del Rio-Castillo, A.E., et al., *Selective suspension of single layer graphene mechanochemically exfoliated from carbon nanofibres. Nano Research*, 2014. **7**(7): p. 963-972.

53. Damm, C., T.J. Nacken, and W. Peukert, Quantitative evaluation of delamination of graphite by wet media milling. *Carbon*, 2015. **81**: p. 284-294.
54. Lv, Y.Y., et al., Synthesis of graphene nanosheet powder with layer number control via a soluble salt-assisted route. *Rsc Advances*, 2014. **4**(26): p. 13350-13354.
55. Lin, T.Q., et al., Scotch-tape-like exfoliation of graphite assisted with elemental sulfur and graphene-sulfur composites for high-performance lithium-sulfur batteries. *Energy & Environmental Science*, 2013. **6**(4): p. 1283-1290.
56. Jeon, I.Y., et al., Large-Scale Production of Edge-Selectively Functionalized Graphene Nanoplatelets via Ball Milling and Their Use as Metal-Free Electrocatalysts for Oxygen Reduction Reaction. *Journal of the American Chemical Society*, 2013. **135**(4): p. 1386-1393.
57. Lee, J., C. Shim, and B. Lee, Graphene in edge-carboxylated graphite by ball milling and analyses using finite element method. *Int. J. Mater. Sci. Appl*, 2013. **2**(6): p. 209.
58. Masjedi-Arani, M., et al., CdSnO₃-graphene nanocomposites: Ultrasonic synthesis using glucose as capping agent and characterization for electrochemical hydrogen storage. *Ultrasonics Sonochemistry*, 2020. **61**: p. 104840.
59. Li, D.Q., et al., Influence of morphology and interfacial interaction of TiO₂-Graphene nanocomposites on the visible light photocatalytic performance. *Journal of Solid State Chemistry*, 2020. **286**: p. 121301.
60. Barakat, M.A., et al., Design of ternary Ni(OH)₂/graphene oxide/TiO₂ nanocomposite for enhanced photocatalytic degradation of organic, microbial contaminants, and aerobic digestion of dairy wastewater. *Journal of Cleaner Production*, 2020. **258**: p. 120588.
61. Duan, Y., et al., Efficient and inexpensive MPCVD method to synthesize Co₃O₄/MoS₂ heterogeneous composite materials with high stability for supercapacitors. *Journal of Materials Research and Technology-Jmr&T*, 2021. **10**: p. 953-959.
62. Wang, X., et al., 3D Nest-Like Architecture of Core-Shell CoFe₂O₄@1T/2H-MoS₂ Composites with Tunable Microwave Absorption Performance. *ACS Appl Mater Interfaces*, 2020. **12**(9): p. 11252-11264.
63. Kumar, R., et al., Microwave-assisted synthesis of Mn₃O₄-Fe₂O₃/Fe₃O₄@rGO ternary hybrids and electrochemical performance for supercapacitor electrode. *Diamond and Related Materials*, 2020. **101**: p. 107622.
64. Akedo, J., Aerosol deposition of ceramic thick films at room temperature: densification mechanism of ceramic layers. *Journal of the American Ceramic Society*, 2006. **89**(6): p. 1834-1839.
65. Kim, H.J., C.H. Lee, and S.Y. Hwang, Fabrication of WC-Co coatings by cold spray deposition. *Surface & Coatings Technology*, 2005. **191**(2-3): p. 335-340.
66. Pfeiffer, T., et al., Plasmonic nanoparticle films for solar cell applications fabricated by size-selective aerosol deposition. *Energy Procedia*, 2014. **60**: p. 3-12.
67. Kim, M.S., et al., Dry-spray deposition of TiO₂ for a flexible dye-sensitized solar cell (DSSC) using a nanoparticle deposition system (NPDS). *J Nanosci Nanotechnol*, 2012. **12**(4): p. 3384-8.

68. Chun, D.-M. and S.-H. Ahn, Deposition mechanism of dry sprayed ceramic particles at room temperature using a nano-particle deposition system. *Acta Materialia*, 2011. **59**(7): p. 2693-2703.
69. Akedo, J., Room temperature impact consolidation (RTIC) of fine ceramic powder by aerosol deposition method and applications to microdevices. *Journal of Thermal Spray Technology*, 2008. **17**(2): p. 181-198.
70. Chun, D.-M., et al., Effect of stand-off distance for cold gas spraying of fine ceramic particles (< 5 μm) under low vacuum and room temperature using nano-particle deposition system (NPDS). *Surface and Coatings Technology*, 2012. **206**(8-9): p. 2125-2132.
71. Schmidt, T., et al., Development of a generalized parameter window for cold spray deposition. *Acta Materialia*, 2006. **54**(3): p. 729-742.
72. Papyrin, A., et al., *Cold spray technology*. 2006: Elsevier.
73. Pattison, J., et al., Standoff distance and bow shock phenomena in the Cold Spray process. *Surface and Coatings Technology*, 2008. **202**(8): p. 1443-1454.
74. Chun, D.-M., et al., Nano/micro particle beam for ceramic deposition and mechanical etching. *Physica Scripta*, 2010. **2010**(T139): p. 014047.
75. Tang, C., et al., NiSe Nanowire Film Supported on Nickel Foam: An Efficient and Stable 3D Bifunctional Electrode for Full Water Splitting. *Angew Chem Int Ed Engl*, 2015. **54**(32): p. 9351-5.
76. Li, X.M., et al., Nanostructured catalysts for electrochemical water splitting: current state and prospects. *Journal of Materials Chemistry A*, 2016. **4**(31): p. 11973-12000.
77. Smith, R.D., et al., Water oxidation catalysis: electrocatalytic response to metal stoichiometry in amorphous metal oxide films containing iron, cobalt, and nickel. *J Am Chem Soc*, 2013. **135**(31): p. 11580-6.
78. Li, Y., et al., Ultrathin Co₃O₄ Nanomeshes for the Oxygen Evolution Reaction. *Acs Catalysis*, 2018. **8**(3): p. 1913-1920.
79. Mohammed, M.M.M., A.G. Abd-Elrahim, and D.M. Chun, One-step deposition of a Ni(OH)₂-graphene hybrid prepared by vacuum kinetic spray for high energy density hybrid supercapacitor. *Materials Chemistry and Physics*, 2020. **244**: p. 122701.
80. Wang, Z.G., et al., Enhanced power density of a supercapacitor by introducing 3D-interfacial graphene. *New Journal of Chemistry*, 2020. **44**(31): p. 13377-13381.
81. Gupta, H., et al., High performance supercapacitor based on 2D-MoS₂ nanostructures. *Materials Today: Proceedings*, 2020. **26**: p. 20-24.
82. Li, Q., et al., Flexible high-temperature dielectric materials from polymer nanocomposites. *Nature*, 2015. **523**(7562): p. 576-9.
83. Liu, F.H., et al., High-Energy-Density Dielectric Polymer Nanocomposites with Trilayered Architecture. *Advanced Functional Materials*, 2017. **27**(20): p. 1606292.
84. Taha-Tijerina, J., et al., Electrically Insulating Thermal Nano-Oils Using 2D Fillers. *Acs Nano*, 2012. **6**(2): p. 1214-1220.
85. Pakdel, A., Y. Bando, and D. Golberg, Nano boron nitride flatland. *Chem Soc Rev*, 2014. **43**(3): p. 934-59.

86. Zhang, J., et al., *Observation of Strong Interlayer Coupling in MoS₂/WS₂ Heterostructures*. *Adv Mater*, 2016. **28**(10): p. 1950-6.
87. Jung, J.H., C.H. Park, and J. Ihm, *A Rigorous Method of Calculating Exfoliation Energies from First Principles*. *Nano Lett*, 2018. **18**(5): p. 2759-2765.
88. Bhimanapati, G.R., D. Kozuch, and J.A. Robinson, *Large-scale synthesis and functionalization of hexagonal boron nitride nanosheets*. *Nanoscale*, 2014. **6**(20): p. 11671-5.
89. Lin, H.C., et al., *Rapid and highly efficient chemical exfoliation of layered MoS₂ and WS₂*. *Journal of Alloys and Compounds*, 2017. **699**: p. 222-229.
90. Liu, M.J., et al., *One-step chemical exfoliation of graphite to similar to 100% few-layer graphene with high quality and large size at ambient temperature*. *Chemical Engineering Journal*, 2019. **355**: p. 181-185.
91. Buzaglo, M., et al., *Critical parameters in exfoliating graphite into graphene*. *Physical Chemistry Chemical Physics*, 2013. **15**(12): p. 4428-4435.
92. Coleman, J.N., et al., *Two-dimensional nanosheets produced by liquid exfoliation of layered materials*. *Science*, 2011. **331**(6017): p. 568-71.
93. Novoselov, K.S., et al., *Two-dimensional gas of massless Dirac fermions in graphene*. *Nature*, 2005. **438**(7065): p. 197-200.
94. Paton, K.R., et al., *Scalable production of large quantities of defect-free few-layer graphene by shear exfoliation in liquids*. *Nat Mater*, 2014. **13**(6): p. 624-30.
95. Kumar, G.R., et al., *Shear-force-dominated dual-drive planetary ball milling for the scalable production of graphene and its electrocatalytic application with Pd nanostructures*. *Rsc Advances*, 2016. **6**(24): p. 20067-20073.
96. Zhu, W.S., et al., *Controlled Gas Exfoliation of Boron Nitride into Few-Layered Nanosheets*. *Angewandte Chemie-International Edition*, 2016. **55**(36): p. 10766-10770.
97. Posudievsky, O.Y., et al., *High yield of graphene by dispersant-free liquid exfoliation of mechanochemically delaminated graphite*. *Journal of Nanoparticle Research*, 2013. **15**(11): p. 2046.
98. Chen, S., et al., *Simultaneous Production and Functionalization of Boron Nitride Nanosheets by Sugar-Assisted Mechanochemical Exfoliation*. *Adv Mater*, 2019. **31**(10): p. e1804810.
99. Park, S.-I., *Fabrication of Electrochromic Device Using Nano-particle Deposition System and Its Response Time Modeling for Large-area (1m² Class) Application*. 2018, Dept. of Mechanical Aerospace Engineering, Seoul National University.
100. Chun, D.M. and S.H. Ahn, *Deposition mechanism of dry sprayed ceramic particles at room temperature using a nano-particle deposition system*. *Acta Materialia*, 2011. **59**(7): p. 2693-2703.
101. Nasim, M., et al., *Deposition mechanism of graphene flakes directly from graphite particles in the kinetic spray process studied using molecular dynamics simulation*. *Computational Materials Science*, 2019. **169**: p. 109091.
102. Elton, L. and D.F. Jackson, *X-ray diffraction and the bragg law*. *American Journal of Physics*, 1966. **34**(11): p. 1036-1038.

103. Patterson, A., *The Scherrer formula for X-ray particle size determination*. *Physical review*, 1939. **56**(10): p. 978.
104. Osman, M.A., A.G. Abd-Elrahim, and A.A. Othman, *Identification of trapping and recombination levels, structure, morphology, photoluminescence and optical absorption behavior of alloyed ZnxCd1-xS quantum dots*. *Journal of Alloys and Compounds*, 2017. **722**: p. 344-357.
105. Kaniyoor, A., et al., *Wrinkled Graphenes: A Study on the Effects of Synthesis Parameters on Exfoliation-Reduction of Graphite Oxide*. *Journal of Physical Chemistry C*, 2011. **115**(36): p. 17660-17669.
106. Kaniyoor, A., T.T. Baby, and S. Ramaprabhu, *Graphene synthesis via hydrogen induced low temperature exfoliation of graphite oxide*. *Journal of Materials Chemistry*, 2010. **20**(39): p. 8467-8469.
107. Gao, Y.J., et al., *Reduced graphene oxide as a catalyst for hydrogenation of nitrobenzene at room temperature*. *Chemical Communications*, 2011. **47**(8): p. 2432-2434.
108. Thangasamy, P. and M. Sathish, *Supercritical fluid processing: a rapid, one-pot exfoliation process for the production of surfactant-free hexagonal boron nitride nanosheets*. *Crystengcomm*, 2015. **17**(31): p. 5895-5899.
109. Lei, W.W., et al., *Boron nitride colloidal solutions, ultralight aerogels and freestanding membranes through one-step exfoliation and functionalization*. *Nature Communications*, 2015. **6**(1): p. 1-8.
110. Wang, H.Q., et al., *Microstructural evolution and oxidation resistance of polyacrylonitrile-based carbon fibers doped with boron by the decomposition of B4C*. *Carbon*, 2013. **56**: p. 296-308.
111. Vidano, R., et al., *Observation of Raman band shifting with excitation wavelength for carbons and graphites*. *Solid State Communications*, 1981. **39**(2): p. 341-344.
112. Ferrari, A.C., *Raman spectroscopy of graphene and graphite: Disorder, electron-phonon coupling, doping and nonadiabatic effects*. *Solid State Communications*, 2007. **143**(1-2): p. 47-57.
113. Endo, M., et al., *Scanning tunneling microscope study of boron-doped highly oriented pyrolytic graphite*. *Journal of Applied Physics*, 2001. **90**(11): p. 5670-5674.
114. Liu, Z.J., et al., *Graphite blocks with high thermal conductivity derived from natural graphite flake*. *Carbon*, 2008. **46**(3): p. 414-421.
115. Min, S.D., et al., *Synthesis of Ni(OH)₂/RGO pseudocomposite on nickel foam for supercapacitors with superior performance*. *Journal of Materials Chemistry A*, 2015. **3**(7): p. 3641-3650.
116. Badri, M.A.S., et al., *Green synthesis of few-layered graphene from aqueous processed graphite exfoliation for graphene thin film preparation*. *Materials Chemistry and Physics*, 2017. **193**: p. 212-219.
117. Parab, A.D., et al., *Molecular-Level Insights into Biologically Driven Graphite Exfoliation for the Generation of Graphene in Aqueous Media*. *Journal of Physical Chemistry C*, 2020. **124**(3): p. 2219-2228.
118. Parvez, K., et al., *Exfoliation of Graphite into Graphene in Aqueous Solutions of Inorganic Salts*. *Journal of the American Chemical Society*, 2014. **136**(16): p. 6083-6091.
119. Frey, G.L., et al., *Raman and resonance Raman investigation of MoS₂ nanoparticles*. *Physical Review B*, 1999. **60**(4): p. 2883.

120. Najmaei, S., et al., Thermal effects on the characteristic Raman spectrum of molybdenum disulfide (MoS₂) of varying thicknesses. *Applied Physics Letters*, 2012. **100**(1): p. 013106.
121. Chen, J. and C. Wang, Second order Raman spectrum of MoS₂. *Solid State Communications*, 1974. **14**(9): p. 857-860.
122. Sekine, T., et al., Dispersive Raman Mode of Layered Compound 2h-MoS₂ under the Resonant Condition. *Journal of the Physical Society of Japan*, 1984. **53**(2): p. 811-818.
123. Wieting, T. and J. Verble, Infrared and Raman Studies of Long-Wavelength Optical Phonons in Hexagonal Mo S₂. *Physical Review B*, 1971. **3**(12): p. 4286.
124. Gouadec, G. and P. Colomban, Raman Spectroscopy of nanomaterials: How spectra relate to disorder, particle size and mechanical properties. *Progress in Crystal Growth and Characterization of Materials*, 2007. **53**(1): p. 1-56.
125. Cai, Q., et al., Raman signature and phonon dispersion of atomically thin boron nitride. *Nanoscale*, 2017. **9**(9): p. 3059-3067.
126. Li, L.H., et al., Strong oxidation resistance of atomically thin boron nitride nanosheets. *ACS Nano*, 2014. **8**(2): p. 1457-62.
127. Gorbachev, R.V., et al., Hunting for monolayer boron nitride: optical and Raman signatures. *Small*, 2011. **7**(4): p. 465-8.
128. Zou, X. and Y. Zhang, Noble metal-free hydrogen evolution catalysts for water splitting. *Chem Soc Rev*, 2015. **44**(15): p. 5148-80.
129. Rao, Y., et al., Hydrotalcite-like Ni(OH)₂ Nanosheets in Situ Grown on Nickel Foam for Overall Water Splitting. *ACS Appl Mater Interfaces*, 2016. **8**(49): p. 33601-33607.
130. Feng, L.L., et al., High-index faceted Ni₃S₂ nanosheet arrays as highly active and ultrastable electrocatalysts for water splitting. *J Am Chem Soc*, 2015. **137**(44): p. 14023-6.
131. Wu, Y.Y., et al., Overall Water Splitting Catalyzed Efficiently by an Ultrathin Nanosheet-Built, Hollow Ni₃S₂-Based Electrocatalyst. *Advanced Functional Materials*, 2016. **26**(27): p. 4839-4847.
132. Ni, S.B., et al., The investigation of Ni(OH)₂/Ni as anodes for high performance Li-ion batteries. *Journal of Materials Chemistry A*, 2013. **1**(5): p. 1544-1547.
133. Hu, B.L., et al., Fabrication of Ni(OH)₂ nanoflakes array on Ni foam as a binder-free electrode material for high performance supercapacitors. *Electrochimica Acta*, 2013. **107**: p. 339-342.
134. Chen, S., et al., Three-dimensional N-doped graphene hydrogel/NiCo double hydroxide electrocatalysts for highly efficient oxygen evolution. *Angew Chem Int Ed Engl*, 2013. **52**(51): p. 13567-70.
135. Louie, M.W. and A.T. Bell, An investigation of thin-film Ni-Fe oxide catalysts for the electrochemical evolution of oxygen. *J Am Chem Soc*, 2013. **135**(33): p. 12329-37.
136. Du, X., G. Ma, and X. Zhang, Experimental and theoretical understanding on electrochemical activation processes of nickel selenide for excellent water splitting performance: comparing the electrochemical performances with M-NiSe (M= Co, Cu, and V). *ACS Sustainable Chemistry & Engineering*, 2019.

137. Wang, L., et al., *Optimizing the Volmer Step by Single-Layer Nickel Hydroxide Nanosheets in Hydrogen Evolution Reaction of Platinum*. *Acs Catalysis*, 2015. **5**(6): p. 3801-3806.
138. Subbaraman, R., et al., *Enhancing hydrogen evolution activity in water splitting by tailoring Li(+)-Ni(OH)(2)-Pt interfaces*. *Science*, 2011. **334**(6060): p. 1256-60.
139. Gao, M., et al., *Efficient water oxidation using nanostructured α -nickel-hydroxide as an electrocatalyst*. *Journal of the American Chemical Society*, 2014. **136**(19): p. 7077-7084.
140. Lee, J., G.H. Lim, and B. Lim, *Nanostructuring of metal surfaces by corrosion for efficient water splitting*. *Chemical Physics Letters*, 2016. **644**: p. 51-55.
141. Kong, X., et al., *Free-Standing Holey Ni(OH)₂ Nanosheets with Enhanced Activity for Water Oxidation*. *Small*, 2017. **13**(26).
142. Du, X.Q., et al., *Controlled synthesis of Ni(OH)(2)/Ni₃S₂ hybrid nanosheet arrays as highly active and stable electrocatalysts for water splitting*. *Journal of Materials Chemistry A*, 2018. **6**(16): p. 6938-6946.
143. Xu, Q.C., et al., *Heterogeneous interface engineered atomic configuration on ultrathin Ni(OH)(2)/Ni₃S₂ nanoforests for efficient water splitting*. *Applied Catalysis B-Environmental*, 2019. **242**: p. 60-66.
144. Trotochaud, L., et al., *Solution-cast metal oxide thin film electrocatalysts for oxygen evolution*. *Journal of the American Chemical Society*, 2012. **134**(41): p. 17253-17261.
145. Klaus, S., et al., *Effects of Fe Electrolyte Impurities on Ni(OH)(2)/NiOOH Structure and Oxygen Evolution Activity*. *Journal of Physical Chemistry C*, 2015. **119**(13): p. 7243-7254.
146. Wang, H., et al., *Ni(OH)₂ nanoplates grown on graphene as advanced electrochemical pseudocapacitor materials*. *J Am Chem Soc*, 2010. **132**(21): p. 7472-7.
147. Fang, D.L., et al., *Homogeneous growth of nano-sized beta-Ni(OH)(2) on reduced graphene oxide for high-performance supercapacitors*. *Electrochimica Acta*, 2012. **81**: p. 321-329.
148. Ede, S.R., et al., *One step synthesis of Ni/Ni(OH)(2) nano sheets (NSs) and their application in asymmetric supercapacitors*. *Rsc Advances*, 2017. **7**(10): p. 5898-5911.
149. Wang, L.Q., et al., *Three-dimensional Ni(OH)(2) nanoflakes/graphene/nickel foam electrode with high rate capability for supercapacitor applications*. *International Journal of Hydrogen Energy*, 2014. **39**(15): p. 7876-7884.
150. Lee, J.W., et al., *Non-aqueous approach to the preparation of reduced graphene oxide/ α -Ni(OH)₂ hybrid composites and their high capacitance behavior*. *Chem Commun (Camb)*, 2011. **47**(22): p. 6305-7.
151. Jiang, L., et al., *Ni(OH)(2)/CoO/reduced graphene oxide composites with excellent electrochemical properties*. *Journal of Materials Chemistry A*, 2013. **1**(3): p. 478-481.
152. Chen, X., et al., *One-pot hydrothermal synthesis of reduced graphene oxide/carbon nanotube/ α -Ni(OH)(2) composites for high performance electrochemical supercapacitor*. *Journal of Power Sources*, 2013. **243**: p. 555-561.
153. Subramanya, B., et al., *Novel Co-Ni-graphene composite electrodes for hydrogen production*. *Rsc Advances*, 2015. **5**(59): p. 47398-47407.

154. Huang, Y.G., et al., *The effect of graphene for the hydrogen evolution reaction in alkaline medium. International Journal of Hydrogen Energy*, 2016. **41**(6): p. 3786-3793.
155. Xue, Y., et al., *Anchoring zero valence single atoms of nickel and iron on graphdiyne for hydrogen evolution. Nat Commun*, 2018. **9**(1): p. 1460.
156. Xing, C., et al., *Fluorographdiyne: A Metal-Free Catalyst for Applications in Water Reduction and Oxidation. Angew Chem Int Ed Engl*, 2019. **58**(39): p. 13897-13903.
157. Long, X., et al., *A strongly coupled graphene and FeNi double hydroxide hybrid as an excellent electrocatalyst for the oxygen evolution reaction. Angew Chem Int Ed Engl*, 2014. **53**(29): p. 7584-8.
158. Tang, D., et al., *Carbon quantum dot/NiFe layered double-hydroxide composite as a highly efficient electrocatalyst for water oxidation. ACS Appl Mater Interfaces*, 2014. **6**(10): p. 7918-25.
159. Chun, D.M., et al., *Nano-particle deposition system (NPDS): Low energy solvent-free dry spray process for direct patterning of metals and ceramics at room temperature. International Journal of Precision Engineering and Manufacturing*, 2012. **13**(7): p. 1107-1112.
160. Chun, D.M., et al., *Nano/micro particle beam for ceramic deposition and mechanical etching. Physica Scripta*, 2010. **T139**(T139): p. 014047.
161. Kim, K., et al., *Investigation of Varying Particle Sizes of Dry-Deposited WO₃ Particles in Relation to Performance of Electrochromic Cell. International journal of precision engineering and manufacturing-green technology*, 2018. **5**(3): p. 409-414.
162. Kim, M.S., et al., *Dry-Spray Deposition of TiO₂ for a Flexible Dye-Sensitized Solar Cell (DSSC) Using a Nanoparticle Deposition System (NPDS). Journal of Nanoscience and Nanotechnology*, 2012. **12**(4): p. 3384-3388.
163. Al Nasim, M.N.E.A. and D.-M. Chun, *Substrate-dependent deposition behavior of graphite particles dry-sprayed at room temperature using a nano-particle deposition system. Surface and Coatings Technology*, 2017. **309**: p. 172-178.
164. Al Nasim, M.N.E.A. and D.-M. Chun, *Formation of few-layer graphene flake structures from graphite particles during thin film coating using dry spray deposition method. Thin Solid Films*, 2017. **622**: p. 34-40.
165. Hong, S.T., et al., *Combination of nano-particle deposition system and friction stir spot welding for fabrication of carbon/aluminum metal matrix composite joints of dissimilar aluminum alloys. Cirp Annals-Manufacturing Technology*, 2017. **66**(1): p. 261-264.
166. Hossain, S., et al., *Photocatalytic performance of few-layer Graphene/WO₃ thin films prepared by a nano-particle deposition system. Materials Chemistry and Physics*, 2019. **226**: p. 141-150.
167. Mohammed, M.M.M. and D.M. Chun, *Electrochemical Performance of Few-Layer Graphene Nano-Flake Supercapacitors Prepared by the Vacuum Kinetic Spray Method. Coatings*, 2018. **8**(9): p. 302.
168. Mohammed, M.M.M. and D.-M. Chun, *All-Solid-State Supercapacitor Based on MoS₂-Graphite Composite Prepared by the Vacuum Kinetic Spray Method. Journal of Thermal Spray Technology*, 2019. **28**(5): p. 963-973.

169. Mohammed, M.M.M. and D.M. Chun, Deposition of Ni(OH)₂ on nickel substrate using vacuum kinetic spray and its application to high-performance supercapacitor. *Journal of Materials Science-Materials in Electronics*, 2019. **30**(18): p. 17481-17490.
170. Bernard, M., et al., Structural defects and electrochemical reactivity of β-Ni (OH)₂. *Journal of Power Sources*, 1996. **63**(2): p. 247-254.
171. Warad, H.C., et al., Luminescent nanoparticles of Mn doped ZnS passivated with sodium hexametaphosphate. *Science and Technology of Advanced Materials*, 2005. **6**(3-4): p. 296-301.
172. Johnston, C. and P. Graves, In situ Raman spectroscopy study of the nickel oxyhydroxide electrode (NOE) system. *Applied spectroscopy*, 1990. **44**(1): p. 105-115.
173. Cornilsen, B.C., P.J. Karjala, and P.L. Loyselle, Structural Models for Nickel Electrode Active Mass. *Journal of Power Sources*, 1988. **22**(3-4): p. 351-357.
174. Hall, D.S., et al., Nickel hydroxides and related materials: a review of their structures, synthesis and properties. *Proc Math Phys Eng Sci*, 2015. **471**(2174): p. 20140792.
175. Yan, J., et al., Advanced Asymmetric Supercapacitors Based on Ni(OH)₂/Graphene and Porous Graphene Electrodes with High Energy Density. *Advanced Functional Materials*, 2012. **22**(12): p. 2632-2641.
176. Yan, J., et al., Fabrication and electrochemical performances of hierarchical porous Ni(OH)₂ nanoflakes anchored on graphene sheets. *Journal of Materials Chemistry*, 2012. **22**(23): p. 11494-11502.
177. Wu, Z., et al., Electrostatic induced stretch growth of homogeneous beta-Ni(OH)₂ on graphene with enhanced high-rate cycling for supercapacitors. *Sci Rep*, 2014. **4**: p. 3669.
178. Weidler, N., et al., X-ray Photoelectron Spectroscopic Investigation of Plasma-Enhanced Chemical Vapor Deposited NiO_x, NiO_x(OH)_y, and CoNiO_x(OH)_y: Influence of the Chemical Composition on the Catalytic Activity for the Oxygen Evolution Reaction. *The Journal of Physical Chemistry C*, 2017. **121**(12): p. 6455-6463.
179. Grosvenor, A.P., et al., New interpretations of XPS spectra of nickel metal and oxides. *Surface Science*, 2006. **600**(9): p. 1771-1779.
180. Longo, A., et al., Graphene oxide prepared by graphene nanoplatelets and reduced by laser treatment. *Nanotechnology*, 2017. **28**(22): p. 224002.
181. Diaz-Terán, J., et al., Study of chemical activation process of a lignocellulosic material with KOH by XPS and XRD. *Microporous and mesoporous materials*, 2003. **60**(1-3): p. 173-181.
182. Ganguly, A., et al., Probing the Thermal Deoxygenation of Graphene Oxide Using High-Resolution In Situ X-ray-Based Spectroscopies. *Journal of Physical Chemistry C*, 2011. **115**(34): p. 17009-17019.
183. Xu, Y., et al., Engineering Ni(OH)₂ Nanosheet on CoMoO₄ Nanoplate Array as Efficient Electrocatalyst for Oxygen Evolution Reaction. *Acs Sustainable Chemistry & Engineering*, 2018. **6**(12): p. 16086-16095.
184. Bronoel, G. and J. Reby, Mechanism of oxygen evolution in basic medium at a nickel electrode. *Electrochimica Acta*, 1980. **25**(7): p. 973-976.
185. Shinagawa, T., A.T. Garcia-Esparza, and K. Takanabe, Insight on Tafel slopes from a microkinetic analysis of aqueous electrocatalysis for energy conversion. *Sci Rep*, 2015. **5**: p. 13801.

186. Vilekar, S.A., I. Fishtik, and R. Datta, *Kinetics of the Hydrogen Electrode Reaction. Journal of the Electrochemical Society*, 2010. **157**(7): p. B1040-B1050.
187. Skúlason, E., et al., *Modeling the electrochemical hydrogen oxidation and evolution reactions on the basis of density functional theory calculations. The Journal of Physical Chemistry C*, 2010. **114**(42): p. 18182-18197.
188. Du, X.Q., H. Su, and X.S. Zhang, *Metal-Organic Framework-Derived Cu-Doped Co₉S₈ Nanorod Array with Less Low-Valence Co Sites as Highly Efficient Bifunctional Electrodes for Overall Water Splitting. ACS Sustainable Chemistry & Engineering*, 2019. **7**(19): p. 16917-16926.
189. Liu, Z.B., et al., *Graphite-graphene architecture stabilizing ultrafine Co₃O₄ nanoparticles for superior oxygen evolution. Carbon*, 2018. **140**: p. 17-23.
190. Fujimura, T., et al., *Analysis of the effect of surface wettability on hydrogen evolution reaction in water electrolysis using micro-patterned electrodes. Electrochemistry Communications*, 2019. **101**: p. 43-46.
191. Ranjani, M., et al., *Ni-Co alloy nanostructures anchored on mesoporous silica nanoparticles for non-enzymatic glucose sensor applications. Rsc Advances*, 2015. **5**(71): p. 57804-57814.
192. Deng, X.H. and H. Tuysuz, *Cobalt-Oxide-Based Materials as Water Oxidation Catalyst: Recent Progress and Challenges. ACS Catalysis*, 2014. **4**(10): p. 3701-3714.
193. Li, X.Y., et al., *Cobalt nanoparticles embedded in porous N-rich carbon as an efficient bifunctional electrocatalyst for water splitting. Journal of Materials Chemistry A*, 2016. **4**(9): p. 3204-3209.
194. Chen, T., et al., *Aldehyde reduced Co₃O₄ to form oxygen vacancy and enhance the electrochemical performance for oxygen evolution reaction and supercapacitor. Nanotechnology*, 2019.
195. Yu, X.G., et al., *Microstructural Engineering of Heterogeneous P-S-Co Interface for Oxygen and Hydrogen Evolution. Chemelectrochem*, 2019. **6**(14): p. 3708-3713.
196. Malik, B., et al., *Magnetic CoPt nanoparticle-decorated ultrathin Co(OH)₂ nanosheets: an efficient bifunctional water splitting catalyst. Catalysis Science & Technology*, 2017. **7**(12): p. 2486-2497.
197. Indra, A., et al., *Unification of catalytic water oxidation and oxygen reduction reactions: amorphous beat crystalline cobalt iron oxides. J Am Chem Soc*, 2014. **136**(50): p. 17530-6.
198. Anantharaj, S. and S. Noda, *Amorphous Catalysts and Electrochemical Water Splitting: An Untold Story of Harmony. Small*, 2020. **16**(2): p. e1905779.
199. Liu, J., et al., *The Flexibility of an Amorphous Cobalt Hydroxide Nanomaterial Promotes the Electrocatalysis of Oxygen Evolution Reaction. Small*, 2018. **14**(17): p. e1703514.
200. Tsuji, E., et al., *Electrocatalytic activity of amorphous RuO₂ electrode for oxygen evolution in an aqueous solution. Electrochimica Acta*, 2011. **56**(5): p. 2009-2016.
201. Bergmann, A., et al., *Reversible amorphization and the catalytically active state of crystalline Co₃O₄ during oxygen evolution. Nat Commun*, 2015. **6**: p. 8625.
202. Klingan, K., et al., *Water oxidation by amorphous cobalt-based oxides: volume activity and proton transfer to electrolyte bases. ChemSusChem*, 2014. **7**(5): p. 1301-10.

203. Risch, M., et al., *Water Oxidation by Electrodeposited Cobalt Oxides—Role of Anions and Redox-Inert Cations in Structure and Function of the Amorphous Catalyst*. *ChemSusChem*, 2012. **5**(3): p. 542-549.
204. Risch, M., et al., *Water oxidation by amorphous cobalt-based oxides: in situ tracking of redox transitions and mode of catalysis*. *Energy & Environmental Science*, 2015. **8**(2): p. 661-674.
205. Suryanto, B.H., X. Lu, and C. Zhao, *Layer-by-layer assembly of transparent amorphous Co₃O₄ nanoparticles/graphene composite electrodes for sustained oxygen evolution reaction*. *Journal of Materials Chemistry A*, 2013. **1**(41): p. 12726-12731.
206. Kumar, G.G., G. Amala, and S.M. Gowtham, *Recent advancements, key challenges and solutions in non-enzymatic electrochemical glucose sensors based on graphene platforms*. *Rsc Advances*, 2017. **7**(59): p. 36949-36976.
207. Rani, G.J. and M.J. Rajan, *Reduced graphene oxide/ZnFe₂O₄ nanocomposite as an efficient catalyst for the photocatalytic degradation of methylene blue dye*. *Research on Chemical Intermediates*, 2017. **43**(4): p. 2669-2690.
208. Salamon, J., et al., *One-pot synthesis of magnetite nanorods/graphene composites and its catalytic activity toward electrochemical detection of dopamine*. *Biosens Bioelectron*, 2015. **64**: p. 269-76.
209. Liang, Y., et al., *Co₃O₄ nanocrystals on graphene as a synergistic catalyst for oxygen reduction reaction*. *Nature materials*, 2011. **10**(10): p. 780.
210. Ma, T.Y., et al., *Metal-organic framework derived hybrid Co₃O₄-carbon porous nanowire arrays as reversible oxygen evolution electrodes*. *J Am Chem Soc*, 2014. **136**(39): p. 13925-31.
211. Fiaz, M., et al., *One pot solvothermal synthesis of Co₃O₄@ UiO-66 and CuO@ UiO-66 for improved current density towards hydrogen evolution reaction*. *Materials Chemistry and Physics*, 2019: p. 122320.
212. Chen, J., X.F. Wu, and A. Selloni, *Electronic structure and bonding properties of cobalt oxide in the spinel structure*. *Physical Review B*, 2011. **83**(24): p. 245204.
213. Elhag, S., et al., *Dopamine wide range detection sensor based on modified Co₃O₄ nanowires electrode*. *Sensors and Actuators B-Chemical*, 2014. **203**: p. 543-549.
214. Wang, M., et al., *Highly sensitive H₂O₂ sensor based on Co₃O₄ hollow sphere prepared via a template-free method*. *Electrochimica Acta*, 2015. **182**: p. 613-620.
215. Pei, Y.J., et al., *Ultrafast one-pot anodic preparation of Co₃O₄/nanoporous gold composite electrode as an efficient nonenzymatic amperometric sensor for glucose and hydrogen peroxide*. *Analytica Chimica Acta*, 2019. **1059**: p. 49-58.
216. Dai, H., et al., *High-performance electrochemical biosensor for nonenzymatic H₂O₂ sensing based on Au@C-Co₃O₄ heterostructures*. *Biosens Bioelectron*, 2018. **118**: p. 36-43.
217. Kong, L., et al., *Interconnected 1D Co₃O₄ nanowires on reduced graphene oxide for enzymeless H₂O₂ detection*. *Nano Research*, 2015. **8**(2): p. 469-480.
218. Kogularasu, S., et al., *3D graphene oxide-cobalt oxide polyhedrons for highly sensitive non-enzymatic electrochemical determination of hydrogen peroxide*. *Sensors and Actuators B: Chemical*, 2017. **253**: p. 773-783.

219. Heli, H. and J. Pishahang, Cobalt oxide nanoparticles anchored to multiwalled carbon nanotubes: Synthesis and application for enhanced electrocatalytic reaction and highly sensitive nonenzymatic detection of hydrogen peroxide. *Electrochimica Acta*, 2014. **123**: p. 518-526.
220. Chun, D.M., et al., TiO₂ coating on metal and polymer substrates by nano-particle deposition system (NPDS). *CIRP Annals*, 2008. **57**(1): p. 551-554.
221. Chun, D.M., et al., A nano-particle deposition system for ceramic and metal coating at room temperature and low vacuum conditions. *International Journal of Precision Engineering and Manufacturing*, 2008. **9**(1): p. 51-53.
222. Zhong, H.H., et al., Surfactant-Assisted Fabrication of Cubic Cobalt Oxide Hybrid Hollow Spheres as Catalysts for the Oxygen Reduction Reaction. *Chemelectrochem*, 2018. **5**(16): p. 2192-2198.
223. Du, S., et al., Co₃O₄ nanosheets as a high-performance catalyst for oxygen evolution proceeding via a double two-electron process. *Chem Commun (Camb)*, 2016. **52**(40): p. 6705-8.
224. Du, S., et al., Co₃O₄ nanosheets as a high-performance catalyst for oxygen evolution proceeding via a double two-electron process. *Chemical Communications*, 2016. **52**(40): p. 6705-6708.
225. Zhao, Y., et al., Micro-/nano-structured hybrid of exfoliated graphite and Co₃O₄ nanoparticles as high-performance anode material for Li-ion batteries. *Electrochimica Acta*, 2016. **213**: p. 98-106.
226. Jiang, J. and L.C. Li, Synthesis of sphere-like Co₃O₄ nanocrystals via a simple polyol route. *Materials Letters*, 2007. **61**(27): p. 4894-4896.
227. Gawali, S.R., et al., Role of cobalt cations in short range antiferromagnetic Co₃O₄ nanoparticles: a thermal treatment approach to affecting phonon and magnetic properties. *Scientific reports*, 2018. **8**(1): p. 1-12.
228. Abd-Elrahim, A., M.M. Mohammed, and D.-M. Chun, Composition dependent electrocatalytic activity of Ni(OH)₂-graphene hybrid catalyst deposited by one-step vacuum kinetic spray technique. *Materials Chemistry and Physics*, 2020: p. 122675.
229. George, G. and S. Anandhan, Structural characterization of nano-crystalline Co₃O₄ ultra-fine fibers obtained by sol-gel electrospinning. *Journal of sol-gel science and technology*, 2013. **67**(2): p. 256-266.
230. Mamalis, A.G., I.N. Vottea, and D.E. Manolakos, On the modelling of the compaction mechanism of shock compacted powders. *Journal of Materials Processing Technology*, 2001. **108**(2): p. 165-178.
231. Chen, X., et al., Explosive compact-coating of tungsten-copper alloy to a copper surface. *Materials Research Express*, 2017. **4**(3): p. 036502.
232. George, G. and S. Anandhan, Structural characterization of nano-crystalline Co₃O₄ ultra-fine fibers obtained by sol-gel electrospinning. *Journal of Sol-Gel Science and Technology*, 2013. **67**(2): p. 256-266.
233. Li, J., et al., Effect of TiO₂ crystal structure on the catalytic performance of Co₃O₄/TiO₂ catalyst for low-temperature CO oxidation. *Catalysis Science & Technology*, 2014. **4**(5): p. 1268-1275.
234. Muthurasu, A., S.V.S. Mers, and V. Ganesh, Nitrogen doped graphene quantum dots (N-GQDs)/Co₃O₄ composite material as an efficient bi-functional electrocatalyst for oxygen, evolution and-oxygen reduction reactions. *International Journal of Hydrogen Energy*, 2018. **43**(9): p. 4726-4737.

235. Wang, H.Y., et al., *In Operando Identification of Geometrical-Site-Dependent Water Oxidation Activity of Spinel Co₃O₄*. *J Am Chem Soc*, 2016. **138**(1): p. 36-9.
236. Yuan, H.L., et al., *Low-Temperature Preparation of Superparamagnetic CoFe₂O₄ Microspheres with High Saturation Magnetization*. *Nanoscale Res Lett*, 2010. **5**(11): p. 1817-1821.
237. Li, A., et al., *Graphene supported atomic Co/nanocrystalline Co₃O₄ for oxygen evolution reaction*. *Electrochimica Acta*, 2018. **276**: p. 153-161.
238. Jiang, Y., et al., *A cobalt-nitrogen complex on N-doped three-dimensional graphene framework as a highly efficient electrocatalyst for oxygen reduction reaction*. *Nanoscale*, 2014. **6**(24): p. 15066-72.
239. Tüysüz, H., et al., *Mesoporous Co₃O₄ as an electrocatalyst for water oxidation*. *Nano Research*, 2013. **6**(1): p. 47-54.
240. Zhang, L., et al., *Roughening of windmill-shaped spinel Co₃O₄ microcrystals grown on a flexible metal substrate by a facile surface treatment to enhance their performance in the oxidation of water*. *RSC Advances*, 2014. **4**(82): p. 43357-43365.
241. Barakat, N.A.M., et al., *Synthesis and optical properties of two cobalt oxides (CoO and Co₃O₄) nanofibers produced by electrospinning process*. *Journal of Physical Chemistry C*, 2008. **112**(32): p. 12225-12233.
242. Zhang, J.H., et al., *Facile synthesis of hollow Co₃O₄-embedded carbon/reduced graphene oxides nanocomposites for use as efficient electrocatalysts in oxygen evolution reaction*. *Electrochimica Acta*, 2019. **300**: p. 123-130.
243. Xu, J.M., et al., *Co₃O₄ nanocubes homogeneously assembled on few-layer graphene for high energy density lithium-ion batteries*. *Journal of Power Sources*, 2015. **274**: p. 816-822.
244. Liu, J., et al., *Mutually beneficial Co₃O₄@MoS₂ heterostructures as a highly efficient bifunctional catalyst for electrochemical overall water splitting*. *Journal of Materials Chemistry A*, 2018. **6**(5): p. 2067-2072.
245. Hou, Y., et al., *Vertically oriented cobalt selenide/NiFe layered-double-hydroxide nanosheets supported on exfoliated graphene foil: an efficient 3D electrode for overall water splitting*. *Energy & Environmental Science*, 2016. **9**(2): p. 478-483.
246. Hu, L.S., et al., *Direct anodic exfoliation of graphite onto high-density aligned graphene for large capacity supercapacitors*. *Nano Energy*, 2017. **34**: p. 515-523.
247. Parvez, K., et al., *One-step electrochemical synthesis of nitrogen and sulfur co-doped, high-quality graphene oxide*. *Chem Commun (Camb)*, 2016. **52**(33): p. 5714-7.
248. Chen, D.Z., et al., *Synergistic coupling of NiCo₂O₄ nanorods onto porous Co₃O₄ nanosheet surface for trifunctional glucose, hydrogen-peroxide sensors and supercapacitor*. *Electrochimica Acta*, 2020. **330**: p. 135326.
249. Wang, M., et al., *A novel H₂O₂ electrochemical sensor based on NiCo₂S₄ functionalized reduced graphene oxide*. *Journal of Alloys and Compounds*, 2019. **784**: p. 827-833.
250. Li, S.J., et al., *Electrochemical Synthesis of a Binary Mn-Co Oxides Decorated Graphene Nanocomposites for Application in Nonenzymatic H₂O₂ Sensing*. *International Journal of Electrochemical Science*, 2017. **12**(7): p. 6566-6576.

251. Kong, L., et al., *Interconnected 1D Co₃O₄ nanowires on reduced graphene oxide for enzymeless H₂O₂ detection.* *Nano Research*, 2015. **8**(2): p. 469-480.
252. Cao, G.S., et al., *ELECTROCHEMICAL Co₃O₄ NANOPOROUS THIN FILMS SENSOR FOR HYDROGEN PEROXIDE DETECTION.* *Nano*, 2014. **9**(4): p. 1450047.
253. Liu, M., S. He, and W. Chen, *Co₃O₄ nanowires supported on 3D N-doped carbon foam as an electrochemical sensing platform for efficient H₂O₂ detection.* *Nanoscale*, 2014. **6**(20): p. 11769-76.
254. Ensafi, A.A., M. Jafari-Asl, and B. Rezaei, *A novel enzyme-free amperometric sensor for hydrogen peroxide based on Nafion/exfoliated graphene oxide-Co₃O₄ nanocomposite.* *Talanta*, 2013. **103**: p. 322-9.
255. Azadmanjiri, J., et al., *Graphene-supported 2D transition metal oxide heterostructures.* *Journal of Materials Chemistry A*, 2018. **6**(28): p. 13509-13537.
256. Chen, X.G., et al., *Fabrication of sandwich-structured ZnO/reduced graphite oxide composite and its photocatalytic properties.* *Journal of Materials Science*, 2010. **45**(4): p. 953-960.
257. Han, W.J., et al., *Synthesis of CdS/ZnO/graphene composite with high-efficiency photoelectrochemical activities under solar radiation.* *Applied Surface Science*, 2014. **299**: p. 12-18.
258. Abd-Elrahim, A.G. and D.-M. Chun, *Facile one-step deposition of Co₃O₄-MoS₂ nanocomposites using a vacuum kinetic spray process for non-enzymatic H₂O₂ sensing.* *Surfaces and Interfaces*, 2020. **21**: p. 100748.
259. Buzaglo, M., et al., *Graphite-to-Graphene: Total Conversion.* *Adv Mater*, 2017. **29**(8): p. 1603528.
260. Mohammed, M.M.M., A.G. Abd-Elrahim, and D.M. Chun, *One-step deposition of a Ni(OH)₂-graphene hybrid prepared by vacuum kinetic spray for high energy density hybrid supercapacitor.* *Materials Chemistry and Physics*, 2020. **244**: p. 122701.
261. Abd-Elrahim, A.G., M.M.M. Mohammed, and D.M. Chun, *Composition dependent electrocatalytic activity of Ni(OH)₂-graphene hybrid catalyst deposited by one-step vacuum kinetic spray technique.* *Materials Chemistry and Physics*, 2020. **244**: p. 122675.
262. Abd-Elrahim, A.G. and D.-M. Chun, *Nanosized Co₃O₄-MoS₂ heterostructure electrodes for improving the oxygen evolution reaction in an alkaline medium.* *Journal of Alloys and Compounds*, 2021. **853**: p. 156946.
263. Abd-Elrahim, A.G. and D.-M. Chun, *Room-temperature deposition of ZnO-graphene nanocomposite hybrid photocatalysts for improved visible-light-driven degradation of methylene blue.* *Ceramics International*, 2021. **47**(9): p. 12812-12825.
264. Abd-Elrahim, A.G. and D.M. Chun, *Fabrication of efficient nanostructured Co₃O₄-Graphene bifunctional catalysts: Oxygen evolution, hydrogen evolution, and H₂O₂ sensing.* *Ceramics International*, 2020. **46**(15): p. 23479-23498.
265. Angaiah, S., et al., *A facile polyvinylpyrrolidone assisted solvothermal synthesis of zinc oxide nanowires and nanoparticles and their influence on the photovoltaic performance of dye sensitized solar cell.* *ES Energy & Environment*, 2019. **4**(2): p. 59-65.

266. Chaudhary, D., et al., ZnO nanoparticles decorated multi-walled carbon nanotubes for enhanced photocatalytic and photoelectrochemical water splitting. *Journal of Photochemistry and Photobiology A: Chemistry*, 2018. **351**: p. 154-161.
267. Ong, C.B., L.Y. Ng, and A.W. Mohammad, A review of ZnO nanoparticles as solar photocatalysts: synthesis, mechanisms and applications. *Renewable and Sustainable Energy Reviews*, 2018. **81**: p. 536-551.
268. Rathnasamy, R., et al., Green synthesis of ZnO nanoparticles using *Carica papaya* leaf extracts for photocatalytic and photovoltaic applications. *Journal of Materials Science: Materials in Electronics*, 2017. **28**(14): p. 10374-10381.
269. Qurashi, A., K.S. Subrahmanyam, and P. Kumar, Nanofiller graphene-ZnO hybrid nanoarchitecture: optical, electrical and optoelectronic investigation. *Journal of Materials Chemistry C*, 2015. **3**(45): p. 11959-11964.
270. Fávero, V.O., et al., Layer-by-layer nanostructured supercapacitor electrodes consisting of ZnO nanoparticles and multi-walled carbon nanotubes. *Journal of materials science*, 2018. **53**(9): p. 6719-6728.
271. Khan, I., et al., Sonochemical assisted synthesis of RGO/ZnO nanowire arrays for photoelectrochemical water splitting. *Ultrason Sonochem*, 2017. **37**: p. 669-675.
272. Ma, T.Y., et al., Al₂O₃-doped ZnO coating of carbon nanotubes as cathode material for lithium-sulfur batteries. *Journal of Power Sources*, 2018. **398**: p. 75-82.
273. Tayebi, M., et al., Photocorrosion suppression and photoelectrochemical (PEC) enhancement of ZnO via hybridization with graphene nanosheets. *Applied Surface Science*, 2020. **502**: p. 144189.
274. Min, Y.L., et al., Ionic liquid assisting synthesis of ZnO/graphene heterostructure photocatalysts with tunable photoresponse properties. *Diamond and Related Materials*, 2012. **26**: p. 32-38.
275. Yusoff, N., et al., Core-shell Fe₃O₄-ZnO nanoparticles decorated on reduced graphene oxide for enhanced photoelectrochemical water splitting. *Ceramics International*, 2015. **41**(3): p. 5117-5128.
276. Chandrasekaran, S., et al., Exploring complex structural evolution of graphene oxide/ZnO triangles and its impact on photoelectrochemical water splitting. *Chemical Engineering Journal*, 2016. **290**: p. 465-476.
277. Chun, D.M., et al., TiO₂ coating on metal and polymer substrates by nano-particle deposition system (NPDS). *Cirp Annals-Manufacturing Technology*, 2008. **57**(1): p. 551-554.
278. Othman, A.A., et al., Influence of Cu doping on structural, morphological, photoluminescence, and electrical properties of ZnO nanostructures synthesized by ice-bath assisted sonochemical method. *Journal of Alloys and Compounds*, 2016. **683**: p. 399-411.
279. Yang, B., et al., Preparation of bioactive titanium metal via anodic oxidation treatment. *Biomaterials*, 2004. **25**(6): p. 1003-1010.
280. Zhang, Y.-y., et al., Electrochemical deposition of hydroxyapatite coatings on titanium. *Transactions of Nonferrous Metals Society of China*, 2006. **16**(3): p. 633-637.
281. Othman, A.A., et al., Mn-doped ZnO nanocrystals synthesized by sonochemical method: Structural, photoluminescence, and magnetic properties. *Materials Science and Engineering B-Advanced Functional Solid-State Materials*, 2017. **219**: p. 1-9.
282. Dahal, A. and M. Batzill, Graphene-nickel interfaces: a review. *Nanoscale*, 2014. **6**(5): p. 2548-62.

283. Lei, Y., et al., Photoelectric properties of SnO₂ decorated by graphene quantum dots. *Materials Science in Semiconductor Processing*, 2019. **102**: p. 104582.
284. Lei, Y., et al., Enhanced photoelectric performance of CdSe by graphene quantum dot modification. *Materials Research Express*, 2018. **6**(1): p. 015906.
285. Raja, K., P.S. Ramesh, and D. Geetha, Structural, FTIR and photoluminescence studies of Fe doped ZnO nanopowder by co-precipitation method. *Spectrochim Acta A Mol Biomol Spectrosc*, 2014. **131**: p. 183-8.
286. Reddy, A.J., et al., Structural, optical and EPR studies on ZnO:Cu nanopowders prepared via low temperature solution combustion synthesis. *Journal of Alloys and Compounds*, 2011. **509**(17): p. 5349-5355.
287. Li, X., et al., Synthesis and morphology control of ZnO nanostructures in microemulsions. *J Colloid Interface Sci*, 2009. **333**(2): p. 465-73.
288. Ali, R.N., et al., Band gap engineering of transition metal (Ni/Co) codoped in zinc oxide (ZnO) nanoparticles. *Journal of Alloys and Compounds*, 2018. **744**: p. 90-95.
289. Nethravathi, C. and M. Rajamathi, Chemically modified graphene sheets produced by the solvothermal reduction of colloidal dispersions of graphite oxide. *Carbon*, 2008. **46**(14): p. 1994-1998.
290. Musa, I., N. Qamhieh, and S.T. Mahmoud, Synthesis and length dependent photoluminescence property of zinc oxide nanorods. *Results in Physics*, 2017. **7**: p. 3552-3556.
291. Calleja, J. and M. Cardona, Resonant raman scattering in ZnO. *Physical Review B*, 1977. **16**(8): p. 3753.
292. Tripathi, N., K. Vijayarangamuthu, and S. Rath, A Raman spectroscopic study of structural evolution of electrochemically deposited ZnO films with deposition time. *Materials Chemistry and Physics*, 2011. **126**(3): p. 568-572.
293. Arguello, C., D.L. Rousseau, and S.d.S. Porto, First-order Raman effect in wurtzite-type crystals. *Physical Review*, 1969. **181**(3): p. 1351.
294. Iqbal, J., et al., Synthesis as well as Raman and optical properties of Cu-doped ZnO nanorods prepared at low temperature. *Ceramics International*, 2014. **40**(1): p. 2091-2095.
295. Bundesmann, C., et al., Raman scattering in ZnO thin films doped with Fe, Sb, Al, Ga, and Li. *Applied Physics Letters*, 2003. **83**(10): p. 1974-1976.
296. Serrano, J., et al., Pressure dependence of the lattice dynamics of ZnO: An ab initio approach. *Physical Review B*, 2004. **69**(9): p. 094306.
297. Reuss, F., et al., Optical investigations on the annealing behavior of gallium- and nitrogen-implanted ZnO. *Journal of Applied Physics*, 2004. **95**(7): p. 3385-3390.
298. Wang, Y.G., et al., Observations of nitrogen-related photoluminescence bands from nitrogen-doped ZnO films. *Journal of Crystal Growth*, 2003. **252**(1-3): p. 265-269.
299. Kaschner, A., et al., Nitrogen-related local vibrational modes in ZnO : N. *Applied Physics Letters*, 2002. **80**(11): p. 1909-1911.
300. Wang, X.Q., et al., Nitrogen doped ZnO film grown by the plasma-assisted metal-organic chemical vapor deposition. *Journal of Crystal Growth*, 2001. **226**(1): p. 123-129.

301. Tzolov, M., et al., *Modification of the structure of ZnO : Al films by control of the plasma parameters. Thin Solid Films*, 2001. **396**(1-2): p. 274-279.
302. Zhou, X., T.J. Shi, and H.O. Zhou, *Hydrothermal preparation of ZnO-reduced graphene oxide hybrid with high performance in photocatalytic degradation. Applied Surface Science*, 2012. **258**(17): p. 6204-6211.
303. Al-Gaashani, R., et al., *XPS and optical studies of different morphologies of ZnO nanostructures prepared by microwave methods. Ceramics International*, 2013. **39**(3): p. 2283-2292.
304. Morozov, I.G., et al., *Structural, optical, XPS and magnetic properties of Zn particles capped by ZnO nanoparticles. Journal of Alloys and Compounds*, 2015. **633**: p. 237-245.
305. Das, J., et al., *Micro-Raman and XPS studies of pure ZnO ceramics. Physica B-Condensed Matter*, 2010. **405**(10): p. 2492-2497.
306. Zhou, H. and Z. Li, *Synthesis of nanowires, nanorods and nanoparticles of ZnO through modulating the ratio of water to methanol by using a mild and simple solution method. Materials chemistry and physics*, 2005. **89**(2-3): p. 326-331.
307. Tak, Y., D. Park, and K. Yong, *Characterization of ZnO nanorod arrays fabricated on Si wafers using a low-temperature synthesis method. Journal of Vacuum Science & Technology B: Microelectronics and Nanometer Structures Processing, Measurement, and Phenomena*, 2006. **24**(4): p. 2047-2052.
308. Sharma, R., et al., *ZnO anchored graphene hydrophobic nanocomposite-based bulk heterojunction solar cells showing enhanced short-circuit current. Journal of Materials Chemistry C*, 2014. **2**(38): p. 8142-8151.
309. Hu, D., et al., *Polymer solution-assisted assembly of hierarchically nanostructured ZnO onto 2D neat graphene sheets with excellent photocatalytic performance. Journal of Alloys and Compounds*, 2020. **843**: p. 156030.
310. Alshammari, A.S., et al., *Visible-light photocatalysis on C-doped ZnO derived from polymer-assisted pyrolysis. RSC advances*, 2015. **5**(35): p. 27690-27698.
311. Dworschak, D., C. Brunnhofer, and M. Valtiner, *Photocorrosion of ZnO Single Crystals during Electrochemical Water Splitting. ACS Appl Mater Interfaces*, 2020. **12**(46): p. 51530-51536.
312. Gomathisankar, P., et al., *Photocatalytic Hydrogen Production from Aqueous Na₂S + Na₂SO₃ Solution with B-Doped ZnO. Acs Sustainable Chemistry & Engineering*, 2013. **1**(8): p. 982-988.
313. Kotsis, K. and V. Staemmler, *Ab initio calculations of the O1s XPS spectra of ZnO and Zn oxo compounds. Phys Chem Chem Phys*, 2006. **8**(13): p. 1490-8.
314. Akhavan, O., *Photocatalytic reduction of graphene oxides hybridized by ZnO nanoparticles in ethanol. Carbon*, 2011. **49**(1): p. 11-18.
315. Akhavan, O., et al., *Photodegradation of Graphene Oxide Sheets by TiO₂ Nanoparticles after a Photocatalytic Reduction. Journal of Physical Chemistry C*, 2010. **114**(30): p. 12955-12959.
316. Christy, A.A., O.M. Kvalheim, and R.A. Velapoldi, *Quantitative analysis in diffuse reflectance spectrometry: a modified Kubelka-Munk equation. Vibrational Spectroscopy*, 1995. **9**(1): p. 19-27.
317. Dolgonos, A., T.O. Mason, and K.R. Poeppelmeier, *Direct optical band gap measurement in polycrystalline semiconductors: A critical look at the Tauc method. Journal of Solid State Chemistry*, 2016. **240**: p. 43-48.

318. Othman, A., et al., Mn-doped ZnO nanocrystals synthesized by sonochemical method: Structural, photoluminescence, and magnetic properties. *Materials Science and Engineering: B*, 2017. **219**: p. 1-9.
319. Othman, A.A., et al., Sonochemically synthesized ZnO nanosheets and nanorods: Annealing temperature effects on the structure, and optical properties. *Ceramics International*, 2017. **43**(1): p. 527-533.
320. Mazhdi, M., et al., A study on optical, photoluminescence and thermoluminescence properties of ZnO and Mn doped-ZnO nanocrystalline particles. *Optik*, 2013. **124**(20): p. 4128-4133.
321. Bylander, E., Surface effects on the low-energy cathodoluminescence of zinc oxide. *Journal of Applied Physics*, 1978. **49**(3): p. 1188-1195.
322. Zeng, H.B., et al., Blue Luminescence of ZnO Nanoparticles Based on Non-Equilibrium Processes: Defect Origins and Emission Controls. *Advanced Functional Materials*, 2010. **20**(4): p. 561-572.
323. Othman, A., et al., Sonochemically synthesized ZnO nanosheets and nanorods: Annealing temperature effects on the structure, and optical properties. *Ceramics International*, 2017. **43**(1): p. 527-533.
324. Wang, J., et al., Insight into charge carrier separation and solar-light utilization: rGO decorated 3D ZnO hollow microspheres for enhanced photocatalytic hydrogen evolution. *Journal of Colloid and Interface Science*, 2020. **564**: p. 322-332.
325. Park, C., J. Lee, and W.S. Chang, Geometrical Separation of Defect States in ZnO Nanorods and Their Morphology-Dependent Correlation between Photoluminescence and Photoconductivity. *Journal of Physical Chemistry C*, 2015. **119**(29): p. 16984-16990.
326. Hankin, A., et al., Flat band potential determination: avoiding the pitfalls. *Journal of Materials Chemistry A*, 2019. **7**(45): p. 26162-26176.
327. Coli, G. and K.K. Bajaj, Excitonic transitions in ZnO/MgZnO quantum well heterostructures. *Applied Physics Letters*, 2001. **78**(19): p. 2861-2863.
328. Cendula, P., et al., Calculation of the energy band diagram of a photoelectrochemical water splitting cell. *The Journal of Physical Chemistry C*, 2014. **118**(51): p. 29599-29607.
329. Covington, D. and D. Ray, Effect of surface regions on the electrical conductivity of extrinsic semiconductor films. *Journal of Applied Physics*, 1974. **45**(6): p. 2616-2620.
330. Kelly, J. and D. Vanmaekelbergh, Charge carrier dynamics in nanoporous photoelectrodes. *Electrochimica acta*, 1998. **43**(19-20): p. 2773-2780.
331. Schwarzburg, K. and F. Willig, Modeling of electrical transients in the semiconductor/electrolyte cell for photogeneration of charge carriers in the bulk. *Journal of Physical Chemistry B*, 1997. **101**(14): p. 2451-2458.
332. Willardson, R.K. and A.C. Beer, *Semiconductors and semimetals*. 1977: Academic press.
333. Jiang, C., et al., Photoelectrochemical devices for solar water splitting - materials and challenges. *Chem Soc Rev*, 2017. **46**(15): p. 4645-4660.
334. Chen, H.M., et al., Nano-architecture and material designs for water splitting photoelectrodes. *Chemical Society Reviews*, 2012. **41**(17): p. 5654-5671.

335. Fujishima, A., X. Zhang, and D.A. Tryk, *Heterogeneous photocatalysis: From water photolysis to applications in environmental cleanup*. *International Journal of Hydrogen Energy*, 2007. **32**(14): p. 2664-2672.
336. Komeily-Nia, Z., et al., *Smart photoactive soft materials for environmental cleaning and energy production through incorporation of nanophotocatalyst on polymers and textiles*. *Polymers for Advanced Technologies*, 2019. **30**(2): p. 235-253.
337. Magdalane, C.M., et al., *Self-cleaning mechanism of synthesized SnO₂/TiO₂ nanostructure for photocatalytic activity application for waste water treatment*. *Surfaces and Interfaces*, 2019. **17**: p. 100346.
338. Upadhyay, R.K., N. Soin, and S.S. Roy, *Role of graphene/metal oxide composites as photocatalysts, adsorbents and disinfectants in water treatment: a review*. *Rsc Advances*, 2014. **4**(8): p. 3823-3851.
339. Youssef, Z., et al., *Dye-sensitized nanoparticles for heterogeneous photocatalysis: Cases studies with TiO₂, ZnO, fullerene and graphene for water purification*. *Dyes and Pigments*, 2018. **159**: p. 49-71.
340. Vaiano, V., et al., *Enhanced photocatalytic removal of phenol from aqueous solutions using ZnO modified with Ag*. *Applied Catalysis B-Environmental*, 2018. **225**: p. 197-206.
341. Khodja, A.A., et al., *Photocatalytic degradation of 2-phenylphenol on TiO₂ and ZnO in aqueous suspensions*. *Journal of Photochemistry and Photobiology a-Chemistry*, 2001. **141**(2-3): p. 231-239.
342. Divband, B., et al., *Synthesis of Ag/ZnO nanostructures by different methods and investigation of their photocatalytic efficiency for 4-nitrophenol degradation*. *Applied Surface Science*, 2013. **284**: p. 80-86.
343. Chen, C., et al., *Investigation of photocatalytic degradation of methyl orange by using nano-sized ZnO catalysts*. *Advances in Chemical Engineering and Science*, 2011. **1**(01): p. 9.
344. Acedo-Mendoza, A.G., et al., *Photodegradation of methylene blue and methyl orange with CuO supported on ZnO photocatalysts: The effect of copper loading and reaction temperature*. *Materials Science in Semiconductor Processing*, 2020. **119**: p. 105257.
345. Wang, L., et al., *Enhanced photocatalytic degradation of methyl orange by porous graphene/ZnO nanocomposite*. *Environ Pollut*, 2019. **249**: p. 801-811.
346. El-Shazly, A., et al., *Nanostructured ZnO photocatalysts prepared via surfactant assisted Co-Precipitation method achieving enhanced photocatalytic activity for the degradation of methylene blue dyes*. *Journal of environmental chemical engineering*, 2016. **4**(3): p. 3177-3184.
347. Adeleke, J.T., et al., *Photocatalytic degradation of methylene blue by ZnO/NiFe₂O₄ nanoparticles*. *Applied Surface Science*, 2018. **455**: p. 195-200.
348. Fu, Y.S., X.Q. Sun, and X. Wang, *BiVO₄-graphene catalyst and its high photocatalytic performance under visible light irradiation*. *Materials Chemistry and Physics*, 2011. **131**(1-2): p. 325-330.
349. Li, Q., et al., *CdS/Graphene Nanocomposite Photocatalysts*. *Advanced Energy Materials*, 2015. **5**(14): p. 1500010.
350. Raizada, P., A. Sudhaik, and P. Singh, *Photocatalytic water decontamination using graphene and ZnO coupled photocatalysts: A review*. *Materials Science for Energy Technologies*, 2019. **2**(3): p. 509-525.
351. Williams, G., B. Seger, and P.V. Kamat, *TiO₂-graphene nanocomposites. UV-assisted photocatalytic reduction of graphene oxide*. *ACS Nano*, 2008. **2**(7): p. 1487-91.

352. Xu, T.G., et al., Significantly enhanced photocatalytic performance of ZnO via graphene hybridization and the mechanism study. *Applied Catalysis B-Environmental*, 2011. **101**(3-4): p. 382-387.
353. Vinothkannan, M., et al., One-pot green synthesis of reduced graphene oxide (RGO)/Fe₃O₄ nanocomposites and its catalytic activity toward methylene blue dye degradation. *Spectrochimica Acta Part a-Molecular and Biomolecular Spectroscopy*, 2015. **136**: p. 256-264.
354. Ma, M., et al., Engineering the photoelectrochemical behaviors of ZnO for efficient solar water splitting. *Journal of Semiconductors*, 2020. **41**(9): p. 091702.
355. Hsieh, S.H. and J.M. Ting, Characterization and photocatalytic performance of ternary Cu-doped ZnO/Graphene materials. *Applied Surface Science*, 2018. **427**: p. 465-475.
356. Ahmad, M., et al., A facile one-step approach to synthesizing ZnO/graphene composites for enhanced degradation of methylene blue under visible light. *Applied Surface Science*, 2013. **274**: p. 273-281.
357. Atchudan, R., et al., Facile synthesis of zinc oxide nanoparticles decorated graphene oxide composite via simple solvothermal route and their photocatalytic activity on methylene blue degradation. *Journal of Photochemistry and Photobiology B-Biology*, 2016. **162**: p. 500-510.
358. Xue, B. and Y. Zou, High photocatalytic activity of ZnO-graphene composite. *J Colloid Interface Sci*, 2018. **529**: p. 306-313.
359. Nalajala, N., et al., Why the thin film form of a photocatalyst is better than the particulate form for direct solar-to-hydrogen conversion: a poor man's approach. *Rsc Advances*, 2019. **9**(11): p. 6094-6100.
360. Ye, J.D., et al., Raman study of lattice dynamic behaviors in phosphorus-doped ZnO films. *Applied Physics Letters*, 2006. **88**(10): p. 101905.
361. Cao, B.Q., et al., Morphology evolution and photoluminescence properties of ZnO films electrochemically deposited on conductive glass substrates. *Journal of Applied Physics*, 2006. **99**(7): p. 073516.
362. Lu, D.B., et al., Synthesis of magnetic ZnFe₂O₄/graphene composite and its application in photocatalytic degradation of dyes. *Journal of Alloys and Compounds*, 2013. **579**: p. 336-342.
363. Dembele, K.T., et al., Graphene below the percolation threshold in TiO₂ for dye-sensitized solar cells. *Journal of Materials Chemistry A*, 2015. **3**(6): p. 2580-2588.
364. Huang, C.Y., et al., p-GaN/n-ZnO nanorods: the use of graphene nanosheets composites to increase charge separation in self-powered visible-blind UV photodetectors. *Nanotechnology*, 2018. **29**(44): p. 445201.
365. Meidanchi, A. and O. Akhavan, Superparamagnetic zinc ferrite spinel-graphene nanostructures for fast wastewater purification. *Carbon*, 2014. **69**: p. 230-238.
366. Bai, S., et al., One-pot solvothermal preparation of magnetic reduced graphene oxide-ferrite hybrids for organic dye removal. *Carbon*, 2012. **50**(6): p. 2337-2346.
367. Abdellah, M.H., et al., Photocatalytic decolorization of methylene blue using TiO₂/UV system enhanced by air sparging. *Alexandria Engineering Journal*, 2018. **57**(4): p. 3727-3735.
368. Zhang, H., et al., P25-Graphene Composite as a High Performance Photocatalyst. *Acs Nano*, 2010. **4**(1): p. 380-386.

369. Liu, X.J., et al., Microwave-assisted synthesis of ZnO-graphene composite for photocatalytic reduction of Cr(VI). *Catalysis Science & Technology*, 2011. **1**(7): p. 1189-1193.
370. Fatimah, I., S.B. Wang, and D. Wulandari, ZnO/montmorillonite for photocatalytic and photochemical degradation of methylene blue. *Applied Clay Science*, 2011. **53**(4): p. 553-560.
371. Zhou, X., et al., Ultrathin porous Co₃O₄ nanoplates as highly efficient oxygen evolution catalysts. *Journal of Materials Chemistry A*, 2015. **3**(15): p. 8107-8114.
372. Guan, C., et al., Hollow Co₃O₄ Nanosphere Embedded in Carbon Arrays for Stable and Flexible Solid-State Zinc-Air Batteries. *Adv Mater*, 2017. **29**(44): p. 1704117.
373. Liang, Y., et al., Co(3)O(4) nanocrystals on graphene as a synergistic catalyst for oxygen reduction reaction. *Nat Mater*, 2011. **10**(10): p. 780-6.
374. Conway, B.E. and T.C. Liu, Characterization of Electrocatalysis in the Oxygen Evolution Reaction at Platinum by Evaluation of Behavior of Surface Intermediate States at the Oxide Film. *Langmuir*, 1990. **6**(1): p. 268-276.
375. Conway, B. and T. Liu, Behaviour of surface intermediate states in anodic O₂ evolution electrocatalysis at Co₃O₄ on Ni and Ti substrates. *Berichte der Bunsengesellschaft für physikalische Chemie*, 1987. **91**(4): p. 461-469.
376. Lukowski, M.A., et al., Enhanced hydrogen evolution catalysis from chemically exfoliated metallic MoS₂ nanosheets. *J Am Chem Soc*, 2013. **135**(28): p. 10274-7.
377. Wu, Z.X., et al., Facile preparation of carbon sphere supported molybdenum compounds (P, C and S) as hydrogen evolution electrocatalysts in acid and alkaline electrolytes. *Nano Energy*, 2017. **32**: p. 511-519.
378. Yu, M.H., et al., Engineering Thin MoS₂ Nanosheets on TiN Nanorods: Advanced Electrochemical Capacitor Electrode and Hydrogen Evolution Electrocatalyst. *Acs Energy Letters*, 2017. **2**(8): p. 1862-1868.
379. Yan, K. and Y. Lu, Direct Growth of MoS₂ Microspheres on Ni Foam as a Hybrid Nanocomposite Efficient for Oxygen Evolution Reaction. *Small*, 2016. **12**(22): p. 2975-81.
380. Zhang, J., et al., Engineering water dissociation sites in MoS₂ nanosheets for accelerated electrocatalytic hydrogen production. *Energy & Environmental Science*, 2016. **9**(9): p. 2789-2793.
381. Li, H., et al., Activating and optimizing MoS₂ basal planes for hydrogen evolution through the formation of strained sulphur vacancies. *Nature materials*, 2016. **15**(1): p. 48-53.
382. Dai, X., et al., Co-Doped MoS₂ Nanosheets with the Dominant CoMoS Phase Coated on Carbon as an Excellent Electrocatalyst for Hydrogen Evolution. *ACS Appl Mater Interfaces*, 2015. **7**(49): p. 27242-53.
383. Jiao, L., et al., Metal-Organic Frameworks as Platforms for Catalytic Applications. *Adv Mater*, 2018. **30**(37): p. e1703663.
384. Zhang, J., et al., Interface engineering of MoS₂/Ni₃S₂ heterostructures for highly enhanced electrochemical overall-water-splitting activity. *Angewandte Chemie International Edition*, 2016. **55**(23): p. 6702-6707.
385. Yan, Y., et al., A review on noble-metal-free bifunctional heterogeneous catalysts for overall electrochemical water splitting. *Journal of Materials Chemistry A*, 2016. **4**(45): p. 17587-17603.

386. Yang, R., et al., Synergistic coupling of CoFe-LDH arrays with NiFe-LDH nanosheet for highly efficient overall water splitting in alkaline media. *Applied Catalysis B: Environmental*, 2019. **253**: p. 131-139.
387. Xun, S., et al., MOF-derived cobalt oxides nanoparticles anchored on CoMoO₄ as a highly active electrocatalyst for oxygen evolution reaction. *Journal of Alloys and Compounds*, 2019. **806**: p. 1097-1104.
388. Si, C., et al., Co₃[Fe(CN)₆]₂ nanocube derived architecture of Co, Fe co-doped MoS₂ nanosheets for efficient water electrolysis. *Electrochimica Acta*, 2019. **309**: p. 116-124.
389. Wei, C., et al., MoS₂ nanosheets decorated Ni(OH)₂ nanorod array for active overall water splitting. *Journal of Alloys and Compounds*, 2019. **796**: p. 86-92.
390. Wang, J.S., et al., The mechanism of hydrogen adsorption on transition metal dichalcogenides as hydrogen evolution reaction catalyst. *Physical Chemistry Chemical Physics*, 2017. **19**(15): p. 10125-10132.
391. Wang, J.S., et al., Synergistic effect of two active sites on cobalt oxides towards electrochemical water-oxidation. *Nano Energy*, 2017. **42**: p. 98-105.
392. Abd-Elrahim, A.G. and D.-M. Chun, Fabrication of efficient nanostructured Co₃O₄-Graphene bifunctional catalysts: Oxygen evolution, hydrogen evolution, and H₂O₂ sensing. *Ceramics International*, 2020.
393. Stacy, A.M. and D.T. Hodul, Raman-Spectra of I_{vb} and V_{ib} Transition-Metal Disulfides Using Laser Energies near the Absorption Edges. *Journal of Physics and Chemistry of Solids*, 1985. **46**(4): p. 405-409.
394. Muthurasu, A., V. Maruthapandian, and H.Y. Kim, Metal-organic framework derived Co₃O₄/MoS₂ heterostructure for efficient bifunctional electrocatalysts for oxygen evolution reaction and hydrogen evolution reaction. *Applied Catalysis B: Environmental*, 2019. **248**: p. 202-210.
395. Yang, Y.Q., et al., MoS₂-Ni₃S₂ Heteronanorods as Efficient and Stable Bifunctional Electrocatalysts for Overall Water Splitting. *Acs Catalysis*, 2017. **7**(4): p. 2357-2366.
396. Xiong, X., et al., Flexible membranes of MoS₂/C nanofibers by electrospinning as binder-free anodes for high-performance sodium-ion batteries. *Scientific reports*, 2015. **5**(1): p. 1-6.
397. Liu, J., et al., Mutually beneficial Co₃O₄@MoS₂ heterostructures as a highly efficient bifunctional catalyst for electrochemical overall water splitting. *Journal of Materials Chemistry A*, 2018. **6**(5): p. 2067-2072.
398. Chen, W., et al., Recent advances in electrochemical sensing for hydrogen peroxide: a review. *Analyst*, 2012. **137**(1): p. 49-58.
399. Kim, M.I., et al., A highly efficient electrochemical biosensing platform by employing conductive nanocomposite entrapping magnetic nanoparticles and oxidase in mesoporous carbon foam. *Advanced Functional Materials*, 2011. **21**(15): p. 2868-2875.
400. Wu, P., et al., Electrochemical measurement of the flux of hydrogen peroxide releasing from RAW 264.7 macrophage cells based on enzyme-attapulgite clay nanohybrids. *Biosensors and Bioelectronics*, 2011. **26**(10): p. 4012-4017.
401. Zhai, D., et al., Highly sensitive glucose sensor based on Pt nanoparticle/polyaniline hydrogel heterostructures. *ACS nano*, 2013. **7**(4): p. 3540-3546.
402. Chen, A. and S. Chatterjee, Nanomaterials based electrochemical sensors for biomedical applications. *Chemical Society Reviews*, 2013. **42**(12): p. 5425-5438.

403. Wei, H. and E. Wang, *Nanomaterials with enzyme-like characteristics (nanozymes): next-generation artificial enzymes. Chemical Society Reviews*, 2013. **42**(14): p. 6060-6093.
404. Wu, J., et al., *Nanomaterials with enzyme-like characteristics (nanozymes): next-generation artificial enzymes (II). Chemical Society Reviews*, 2019. **48**(4): p. 1004-1076.
405. Hsu, M.-S., et al., *Gold nanostructures on flexible substrates as electrochemical dopamine sensors. ACS applied materials & interfaces*, 2012. **4**(10): p. 5570-5575.
406. Jirkovský, J.S., et al., *Single atom hot-spots at Au-Pd nanoalloys for electrocatalytic H₂O₂ production. Journal of the American Chemical Society*, 2011. **133**(48): p. 19432-19441.
407. Xiong, X., et al., *Ni₂P nanosheets array as a novel electrochemical catalyst electrode for non-enzymatic H₂O₂ sensing. Electrochimica Acta*, 2017. **253**: p. 517-521.
408. Pei, Y., et al., *Ultrafast one-pot anodic preparation of Co₃O₄/nanoporous gold composite electrode as an efficient nonenzymatic amperometric sensor for glucose and hydrogen peroxide. Anal Chim Acta*, 2019. **1059**: p. 49-58.
409. Brandt, R.E., et al., *Identifying defect-tolerant semiconductors with high minority-carrier lifetimes: beyond hybrid lead halide perovskites. Mrs Communications*, 2015. **5**(2): p. 265-275.
410. Jiang, J., et al., *Recent advances in metal oxide-based electrode architecture design for electrochemical energy storage. Advanced materials*, 2012. **24**(38): p. 5166-5180.
411. Arif, A.F.M., K.S. Al-Athel, and J. Mostaghimi, *3.4 Residual Stresses in Thermal Spray Coating, in Comprehensive Materials Finishing, M.S.J. Hashmi, Editor. 2017, Elsevier: Oxford. p. 56-70.*
412. Zhang, E., et al., *Porous Co₃O₄ hollow nanododecahedra for nonenzymatic glucose biosensor and biofuel cell. Biosensors and Bioelectronics*, 2016. **81**: p. 46-53.
413. Abd-Elrahim, A.G. and D.-M. Chun, *Facile one-step deposition of ZnO-graphene nanosheets hybrid photoanodes for enhanced photoelectrochemical water splitting. Journal of Alloys and Compounds*, 2021: p. 159430.
414. Prakash, N.G., et al., *High performance one dimensional α -MoO₃ nanorods for supercapacitor applications. Ceramics International*, 2018. **44**(8): p. 9967-9975.
415. Swathi, S., et al., *Water-splitting application of orthorhombic molybdate α -MoO₃ nanorods. Ceramics International*, 2020. **46**(14): p. 23218-23222.
416. Kuo, C.C., W.J. Lan, and C.H. Chen, *Redox preparation of mixed-valence cobalt manganese oxide nanostructured materials: highly efficient noble metal-free electrocatalysts for sensing hydrogen peroxide. Nanoscale*, 2014. **6**(1): p. 334-41.
417. Zhang, X., et al., *Highly efficient Mn₂O₃ catalysts derived from Mn-MOFs for toluene oxidation: The influence of MOFs precursors. Molecular Catalysis*, 2020. **482**: p. 110701.
418. Yang, X., et al., *Enhancement effect of acid treatment on Mn₂O₃ catalyst for toluene oxidation. Catalysis Today*, 2019. **327**: p. 254-261.
419. Yang, R., et al., *MnO₂ -Based Materials for Environmental Applications. Adv Mater*, 2021. **33**(9): p. e2004862.

420. Chu, Y., et al., *Embedding MnO@ Mn₃O₄ Nanoparticles in an N-Doped-Carbon Framework Derived from Mn-Organic Clusters for Efficient Lithium Storage*. *Advanced Materials*, 2018. **30**(6): p. 1704244.
421. Parida, K., S. Kanungo, and B. Sant, *Studies on chemically precipitated Mn (IV) oxides*. *Electrochim Acta*, 1981. **26**(2): p. 435-443.
422. Abbasi, A.Z., et al., *Magnetic Capsules for NMR Imaging: Effect of Magnetic Nanoparticles Spatial Distribution and Aggregation*. *Journal of Physical Chemistry C*, 2011. **115**(14): p. 6257-6264.
423. Wang, L., et al., *Non-enzymatic electrochemical sensors for the detection of H₂O₂ based on Mn₃O₄ octahedron submicrostructures*. *Micro & Nano Letters*, 2014. **9**(10): p. 736-740.
424. Wu, Z.L., et al., *Binary cobalt and manganese oxides: Amperometric sensing of hydrogen peroxide*. *Sensors and Actuators B-Chemical*, 2017. **253**: p. 949-957.
425. Allen, M.J., V.C. Tung, and R.B. Kaner, *Honeycomb carbon: a review of graphene*. *Chem Rev*, 2010. **110**(1): p. 132-45.
426. Geim, A.K. and K.S. Novoselov, *The rise of graphene, in Nanoscience and technology: a collection of reviews from nature journals*. 2010, World Scientific. p. 11-19.
427. Islam, S.E., et al., *Facile and Cost-Efficient Synthesis of Quasi-0D/2D ZnO/MoS₂ Nanocomposites for Highly Enhanced Visible-Light-Driven Photocatalytic Degradation of Organic Pollutants and Antibiotics*. *Chemistry*, 2018. **24**(37): p. 9305-9315.
428. Wang, T., et al., *MoS₂-Based Nanocomposites for Electrochemical Energy Storage*. *Adv Sci (Weinh)*, 2017. **4**(2): p. 1600289.
429. Stankovich, S., et al., *Graphene-based composite materials*. *Nature*, 2006. **442**(7100): p. 282-6.
430. Jayabalan, T., M. Manickam, and S.N. Mohamed, *NiCo₂O₄-graphene nanocomposites in sugar industry wastewater fed microbial electrolysis cell for enhanced biohydrogen production*. *Renewable Energy*, 2020. **154**: p. 1144-1152.
431. Kang, J., et al., *Fabrication of the SnO₂/α-Fe₂O₃ Hierarchical Heterostructure and Its Enhanced Photocatalytic Property*. *The Journal of Physical Chemistry C*, 2011. **115**(16): p. 7874-7879.
432. Li, Y., et al., *Hetero-structured MnO-Mn₃O₄@rGO composites: Synthesis and nonenzymatic detection of H₂O₂*. *Mater Sci Eng C Mater Biol Appl*, 2021. **118**: p. 111443.
433. Zeng, F.Y., et al., *Facile construction of Mn₃O₄-MnO₂ hetero-nanorods/graphene nanocomposite for highly sensitive electrochemical detection of hydrogen peroxide*. *Electrochimica Acta*, 2016. **196**: p. 587-596.
434. Bang, G.S., et al., *Effective liquid-phase exfoliation and sodium ion battery application of MoS₂ nanosheets*. *ACS Appl Mater Interfaces*, 2014. **6**(10): p. 7084-9.
435. Hu, Y., et al., *Synthesis of monodispersed single-crystal compass-shaped Mn₃O₄ via gamma-ray irradiation*. *Materials Letters*, 2006. **60**(3): p. 383-385.
436. Wu, X., et al., *Mn₃O₄ nanocube: an efficient electrocatalyst toward artificial N₂ fixation to NH₃*. *Small*, 2018. **14**(48): p. 1803111.

437. Narayani, L., et al., Mechanism of high temperature induced phase transformation and magnetic properties of Mn₃O₄ crystallites. *Journal of Magnetism and Magnetic Materials*, 2019. **476**: p. 268-273.
438. Luo, Y., et al., Probing the surface structure of α -Mn₂O₃ nanocrystals during CO oxidation by operando Raman spectroscopy. *The Journal of Physical Chemistry C*, 2012. **116**(39): p. 20975-20981.
439. Han, Y.F., et al., Controlled synthesis, characterization, and catalytic properties of Mn₂O₃ and Mn₃O₄ nanoparticles supported on mesoporous silica SBA-15. *Journal of Physical Chemistry B*, 2006. **110**(48): p. 24450-24456.
440. Bernard, M.C., et al., Electrochromic reactions in manganese oxides: I. Raman analysis. *Journal of the Electrochemical Society*, 1993. **140**(11): p. 3065.
441. Rani, B.J., et al., Synthesis and characterization of hausmannite (Mn₃O₄) nanostructures. *Surfaces and Interfaces*, 2018. **11**: p. 28-36.
442. McIntyre, N. and D. Zetaruk, X-ray photoelectron spectroscopic studies of iron oxides. *Analytical Chemistry*, 1977. **49**(11): p. 1521-1529.
443. Oku, M., K. Hirokawa, and S. Ikeda, X-ray photoelectron spectroscopy of manganese—oxygen systems. *Journal of Electron Spectroscopy and Related Phenomena*, 1975. **7**(5): p. 465-473.
444. Qiu, Y., et al., One-dimensional hierarchical MoO₂-MoS_x hybrids as highly active and durable catalysts in the hydrogen evolution reaction. *Dalton Transactions*, 2018. **47**(17): p. 6041-6048.
445. Wu, M., et al., Heterostructural composite of few-layered MoS₂/hexagonal MoO₂ particles/graphene as anode material for highly reversible lithium/sodium storage. *International Journal of Energy Research*, 2020. **44**(1): p. 518-527.
446. Wu, K.H., et al., Structural Origin of the Activity in Mn₃O₄-Graphene Oxide Hybrid Electrocatalysts for the Oxygen Reduction Reaction. *ChemSusChem*, 2015. **8**(19): p. 3331-9.
447. Aswathy, R., M. Ulaganathan, and P. Ragupathy, Mn₃O₄ nanoparticles grown on surface activated graphite paper for aqueous asymmetric supercapacitors. *Journal of Alloys and Compounds*, 2018. **767**: p. 141-150.
448. Brabers, V.A.M., F.M. Vansetten, and P.S.A. Knapen, X-Ray Photoelectron-Spectroscopy Study of the Cation Valencies in Nickel Manganite. *Journal of Solid State Chemistry*, 1983. **49**(1): p. 93-98.
449. Salavati-Niasari, M., F. Davar, and M. Mazaheri, Synthesis of Mn₃O₄ nanoparticles by thermal decomposition of a [bis(salicylidiminato)manganese(II)] complex. *Polyhedron*, 2008. **27**(17): p. 3467-3471.
450. Nesbitt, H.W. and D. Banerjee, Interpretation of XPS Mn(2p) spectra of Mn oxyhydroxides and constraints on the mechanism of MnO₂ precipitation. *American Mineralogist*, 1998. **83**(3-4): p. 305-315.
451. Tian, Z.Y., et al., Synthesis of the Catalytically Active Mn₃O₄ Spinel and Its Thermal Properties. *Journal of Physical Chemistry C*, 2013. **117**(12): p. 6218-6224.
452. Daripa, S., et al., Mn₃O₄ nanocluster-graphene hybrid for energy storage and electrochemical sensing application. *Ionics*, 2019: p. 1-9.
453. Kortidis, I., et al., Characteristics of point defects on the room temperature ferromagnetic and highly NO₂ selectivity gas sensing of p-type Mn₃O₄ nanorods. *Sensors and Actuators B-Chemical*, 2019. **285**: p. 92-107.

454. Li, Y.Y., et al., *Hetero-structured MnO-Mn₃O₄@rGO composites: Synthesis and nonenzymatic detection of H₂O₂*. *Materials Science & Engineering C-Materials for Biological Applications*, 2021. **118**: p. 111443.
455. Yang, S.L., et al., *Synthesis of Mn₃O₄ nanoparticles/nitrogen-doped graphene hybrid composite for nonenzymatic glucose sensor*. *Sensors and Actuators B-Chemical*, 2015. **221**: p. 172-178.
456. Yang, S.L., et al., *One-pot synthesis of Mn₃O₄ nanoparticles decorated with nitrogen-doped reduced graphene oxide for sensitive nonenzymatic glucose sensing*. *Journal of Electroanalytical Chemistry*, 2015. **755**: p. 15-21.
457. Si, P., et al., *A hierarchically structured composite of Mn₃O₄/3D graphene foam for flexible nonenzymatic biosensors*. *Journal of Materials Chemistry B*, 2013. **1**(1): p. 110-115.
458. Chang, X., et al., *Enhanced Surface Reaction Kinetics and Charge Separation of p-n Heterojunction Co₃O₄/BiVO₄ Photoanodes*. *J Am Chem Soc*, 2015. **137**(26): p. 8356-9.
459. Si, P., et al., *A hierarchically structured composite of Mn₃O₄/3D graphene foam for flexible nonenzymatic biosensors*. *Journal of Materials Chemistry B*, 2013. **1**(1): p. 110-115.